

AD-A216 754

NCEL

Technical Report

DTIC
ELECTE
JAN 10 1990
S B D

DTIC FILE COPY

R-927

September 1989

By G. Warren

Sponsored By Naval Facilities
Engineering Command

LATERALLY LOADED PARTIALLY PRESTRESSED CONCRETE PILES

ABSTRACT This report contains findings of an extensive test program on laterally loaded, partially prestressed concrete fender piles. The study included service load range as well as post-ultimate behavior and failure modes. Partial prestressing to 600 psi was sufficient to close flexural cracks caused by cyclic load in the service load range. The best performing configuration was an 18- by 18-inch section with 20 1/2-inch-diameter prestress strands in a rectangular configuration confined by No. 3 ties with 3-inch pitch. The configuration, in 65-foot lengths, can be expected to perform well under cyclic load, have an ultimate energy capacity greater than 30 ft-kips, and a post-ultimate energy capacity of more than 60 ft-kips. Anchorage, shear, and bond are more than adequate and the failure mode will be in flexure. ACI equations for flexural capacity and stiffness (Young's Modulus) do not adequately predict high strength. Field tests are required on the fendering systems to determine their load environment.



90 01 10 169

NAVAL CIVIL ENGINEERING LABORATORY PORT HUENEME CALIFORNIA 93043-5003

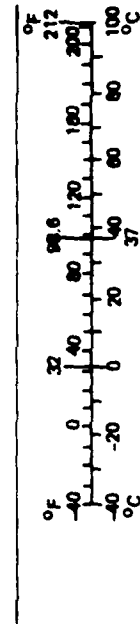
METRIC CONVERSION FACTORS

Approximate Conversions to Metric Measures

Symbol	When You Know	Multiply by	To Find	Symbol
LENGTH				
in	inches	*2.5	centimeters	cm
ft	feet	30	centimeters	cm
yd	yards	0.9	meters	m
mi	miles	1.6	kilometers	km
AREA				
in ²	square inches	6.5	square centimeters	cm ²
ft ²	square feet	0.09	square meters	m ²
yd ²	square yards	0.8	square meters	m ²
mi ²	square miles	2.6	square kilometers	km ²
	acres	0.4	hectares	ha
MASS (weight)				
oz	ounces	28	grams	g
lb	pounds	0.45	kilograms	kg
	short tons (2,000 lb)	0.9	tonnes	t
VOLUME				
tsp	teaspoons	5	milliliters	ml
Tbsp	tablespoons	15	milliliters	ml
fl oz	fluid ounces	30	milliliters	ml
c	cups	0.24	liters	l
pt	pints	0.47	liters	l
qt	quarts	0.95	liters	l
gal	gallons	3.8	liters	l
ft ³	cubic feet	0.03	cubic meters	m ³
yd ³	cubic yards	0.76	cubic meters	m ³
TEMPERATURE (exact)				
°F	Fahrenheit temperature	5/9 (after subtracting 32)	Celsius temperature	°C

Approximate Conversions from Metric Measures

When You Know	Multiply by	To Find	Symbol
LENGTH			
millimeters	0.04	inches	in
centimeters	0.4	inches	in
meters	3.3	feet	ft
meters	1.1	yards	yd
kilometers	0.6	miles	mi
AREA			
square centimeters	0.16	square inches	in ²
square meters	1.2	square yards	yd ²
square kilometers	0.4	square miles	mi ²
hectares (10,000 m ²)	2.5	acres	
MASS (weight)			
grams	0.035	ounces	oz
kilograms	2.2	pounds	lb
tonnes (1,000 kg)	1.1	short tons	
VOLUME			
milliliters	0.03	fluid ounces	fl oz
liters	2.1	pints	pt
liters	1.06	quarts	qt
liters	0.26	gallons	gal
cubic meters	35	cubic feet	ft ³
cubic meters	1.3	cubic yards	yd ³
TEMPERATURE (exact)			
Celsius temperature	9/5 (then add 32)	Fahrenheit temperature	°F



*1 in = 2.54 (exactly). For other exact conversions and more detailed tables, see NBS Misc. Publ. 286, Units of Weights and Measures, Price \$2.25, SO Catalog No. C13.10:286.

REPORT DOCUMENTATION PAGE			Form Approved OMB No. 0704-0188	
Public reporting burden for this collection of information is estimated to average 1 hour per response, including the time for reviewing instructions, searching existing data sources, gathering and maintaining the data needed, and completing and reviewing the collection of information. Send comments regarding this burden estimate or any other aspect of this collection of information, including suggestions for reducing this burden, to Washington Headquarters Services, Directorate for Information Operations and Reports, 1215 Jefferson Davis Highway, Suite 1204, Arlington, VA 22202-4302, and to the Office of Management and Budget, Paperwork Reduction Project (0704-0188), Washington, DC 20503.				
1. AGENCY USE ONLY (Leave blank)		2. REPORT DATE Sep 1989		3. REPORT TYPE AND DATES COVERED Not final - FY86 to FY88
4. TITLE AND SUBTITLE LATERALLY LOADED PARTIALLY PRESTRESSED CONCRETE PILES			5. FUNDING NUMBERS PE - Y1316-01-006-910 WU — DN665019	
6. AUTHOR(S) G. Warren				
7. PERFORMING ORGANIZATION NAME(S) AND ADDRESS(ES) Naval Civil Engineering Laboratory Port Hueneme, CA 93043-5003			8. PERFORMING ORGANIZATION REPORT NUMBER TR-927	
9. SPONSORING / MONITORING AGENCY NAME(S) AND ADDRESS(ES) Naval Facilities Engineering Command Alexandria, VA 22332			10. SPONSORING / MONITORING AGENCY REPORT NUMBER	
11. SUPPLEMENTARY NOTES				
12a. DISTRIBUTION / AVAILABILITY STATEMENT Approved for public release; distribution is unlimited.			12b. DISTRIBUTION CODE	
13. ABSTRACT (Maximum 200 words) This report contains findings of an extensive test program on laterally loaded, partially prestressed concrete fender piles. The study included service load range as well as post-ultimate behavior and failure modes. Partial prestressing to 600 psi was sufficient to close flexural cracks caused by cyclic load in the service load range. The best performing configuration was an 18- by 18-inch section with 20 1/2-inch-diameter prestress strands in a rectangular configuration confined by No. 3 ties with 3-inch pitch. The configuration, in 65-foot lengths, can be expected to perform well under cyclic load, have an ultimate energy capacity greater than 30 ft-kips, and a post-ultimate energy capacity of more than 60 ft-kips. Anchorage, shear, and bond are more than adequate and the failure mode will be in flexure. ACI equations for flexural capacity and stiffness (Young's Modulus) do not adequately predict high strength. Field tests are required on the fendering systems to determine their load environment.				
14. SUBJECT TERMS Partial prestress, fender piles, cyclic load, energy absorption, spalling, bond, flexure, shear, crack control, softening			15. NUMBER OF PAGES 266	
			16. PRICE CODE	
17. SECURITY CLASSIFICATION OF REPORT Unclassified	18. SECURITY CLASSIFICATION OF THIS PAGE Unclassified	19. SECURITY CLASSIFICATION OF ABSTRACT Unclassified	20. LIMITATION OF ABSTRACT UL	

CONTENTS

	Page
PURPOSE.	1
PROBLEM BACKGROUND	1
TEST OBJECTIVE	2
SCOPE	2
Configuration A	3
Configuration B	4
Configuration C	4
Configuration D	4
Configuration E	4
Configuration F	4
Configuration G	5
Response Measurements	5
Materials	5
TEST SETUP	5
Long Spans	6
Short Spans	6
INSTRUMENTATION AND DATA ACQUISITION	7
Long Spans	7
Short Spans	8
TEST PROCEDURES	9
Long Span Monotonic Loading	10
Long Span Cyclic Loading	10
Short Span Monotonic Test Procedures	10
Short Span Cyclic Loading	11
DATA REDUCTION	12
Curvature	12
Energy Absorption	13
Long Pile Tests	14
Short Pile Tests	14



For	
<input checked="" type="checkbox"/>	<input type="checkbox"/>
<input type="checkbox"/>	<input type="checkbox"/>
Distribution	
By	
Distribution/	
Availability Codes	
Dist	Avail and/or Special
A-1	

	Page
RESULTS	14
Concrete Mechanical Properties	14
Monotonic Response	15
Energy Absorption	16
Fiber-Reinforced Concrete	17
Increased Prestressing	17
Lightweight Concrete	18
Spiral Geometry	18
Cyclic Loading	18
ANALYSIS	20
Concrete Strength	20
Effect of Concrete Prestress	20
Spiral Spacing	21
Cyclic Response	22
Error Analysis	22
SUMMARY AND RECOMMENDATIONS	23
Effects of Prestress	24
Concrete	24
Confinement Reinforcement and Strand Arrangement	25
FUTURE RESEARCH	25
ACKNOWLEDGMENT	26
REFERENCES	26
APPENDIXES	
A - Test Pile Fabrication	A-1
B - Test Results	B-1

PURPOSE

This report presents the results of a test program on partially prestressed concrete fender pile concepts. The pile concepts and tests support a Test and Evaluation Master Plan (TEMP) of June 1984 entitled "Development of Prestressed Concrete Fender Piles" (Ref 1). This project is part of the Ports Systems Project of the Shore and Offshore Facilities Program. The tests not only governed the course of the fender pile program but uncovered essential findings in material and structural behavior for application to design, analysis, and life cycle of other waterfront facilities, partial and fallen prestressed concrete, and high strength concrete.

PROBLEM BACKGROUND

The Naval Facilities Engineering Command (NAVFAC), through the Naval Civil Engineering Laboratory (NCEL), has initiated a project to develop prestressed concrete fender piles for use at Navy port facilities. This project consisted of designing and detailing promising concepts, which was accompanied by analytical investigation of mechanical behavior and flexural energy absorbing characteristics. This was followed by three cycles of testing, evaluating, and redesigning the concepts.

This report covers the test and evaluation program and implications on design. The design of the complete pier fender system is shown schematically in Figure 1. The economic advantage of concrete fender piles over wood and steel, and the development of analytical models for flexural design are covered in References 2 through 4. The main emphasis of the analytical efforts was to maximize the flexural energy absorbing characteristics of the piling prior to spalling the concrete cover while controlling the reaction force to the pier.

A fender pile must be able to flexurally withstand service berthing impacts with little or no damage. However, it is realistic to expect an "extreme" berthing event that will occur at some rare interval during the lifetime of the fender pile. A fender pile must be capable of withstanding an extreme event while sustaining spall damage to the concrete cover to avoid exposing permanently deformed reinforcing steel. Although this damage is not defined as pile failure since a significant amount of energy can be absorbed after spalling and prior to collapse, spalling of the concrete with the resulting exposed steel and permanent deflection would require that the pile be replaced. Service berthing impacts have been defined as 70 ft-kips of energy or less while an extreme berthing event has been defined as 140 ft-kips of energy (Ref 3). A goal was set for individual, 65-foot fender piles (Figure 1) to be capable of sustaining an ultimate flexural energy capacity of at least 20 ft-kips prior to any permanent damage (such as concrete spalling).

TEST OBJECTIVE

The primary objective of laboratory testing was to demonstrate fender pile energy absorption characteristics and provide test results to verify the analysis techniques used to develop the more promising concepts. Behavior and performance were compared as functions of the various parameters among configurations.

The configurations evolved to control construction costs, retard crack growth, and reduce end reactions while maximizing energy capacitance at service loads and post-ultimate range. The tests further demonstrated the cyclic behavior of partially prestressed concrete in flexure. A major function of prestress was to control crack width and growth to preclude the use of coated strands for corrosion control. Through cyclic testing, the limits of pile response under repeated service loadings before unacceptable damage were determined. The objectives were met through mechanical testing and measuring the load-deformation response.

The goal of cyclic response was to sustain 80 percent of ultimate load energy (16 ft-kips for a 65-foot span) for 125 load cycles at a single load point without damage to the compression zone, and to control residual crack width to less than 0.012 inch. It is recognized that cycling load at a single point to a constant level in the laboratory is more severe than field service where load will vary in magnitude and location along the length of the pile. With the load point moving along the span and the possibility of autogenous crack healing, the residual crack widths in service will not be as severe. The residual crack width limit was set from American Concrete Institute (ACI) recommendations and previous work (Ref 3).

SCOPE

The testing was limited to lateral loading and simple supports on rollers. Although load repetition was included, loading was applied slowly without any dynamic effects.

Seven configurations were evaluated (Figure 2, A through G). Within each configuration the prestress strand arrangement was held constant while other parameters were varied. The following parameters were varied among the configurations and within each configuration:

1. Prestress force
2. Confinement steel (spiral) ratio and spacing
3. Confinement steel configuration
4. Concrete strength
5. Concrete type
6. Addition of conventional longitudinal reinforcing
7. Lateral ties (additional to spiral)
8. Length of shear span

A total of 31 pile specimens were fabricated and laboratory tested. Piles of all configurations except Configuration G were detailed by ABAM Engineers who prepared construction drawings and technical specifications for casting by J. H. Pomeroy, Inc., of Petaluma, California.

Piles fabricated by Pomeroy were numbered consecutively from MK1 through MK29 (MK15 was not fabricated). Three Configuration G piles were detailed by William L. Simon and Associates. Raymond International Builders prestress plant in Long Beach, California, fabricated Configuration G piles which were denoted as COL01, COL02, and COL03. Physical dimensions, constituents, and material properties for the configurations were drawn and tabulated on the construction drawings and documents in Appendix A. All concepts employed 1/2-inch-diameter, 7-wire, Grade 270 prestressing strands. Pile sections were detailed in a balanced flexural design; that is, the steel reached limiting steel stress (270 ksi) simultaneously as the concrete reached limiting strain (0.003) (Ref 5).

The specimens were tested in two-span lengths. The first series of specimens included MK1 through MK8. They were 60 feet 3 inches in length, and were tested in a span of 58 feet with concentrated loads at 15 feet from one support. Hereafter, these tests will be referred to as the long span tests. The 60-foot lengths presented unnecessary fabrication expenditures and handling problems. Test objectives could be met with shorter, more manageable lengths. Ultimate moment, ultimate strain, effect of confinement, and other parameters are independent of length. Further, within the elastic range, none of these parameters are dependent on the load location. Consequently, the remaining specimens were cast 33 feet in length and tested in 30-foot spans with a concentrated load at midspan (except two tests on MK13 and MK14, with loads applied 7 feet from a support to establish the effect of high shear on tendon anchorage). In addition to the cast 33-foot specimens, undamaged 35-foot sections from MK3, MK5, MK6, and MK8 were also tested in 30-foot spans. All 30-foot span tests will be herein referred to as the short span tests.

Details of all configurations are tabulated in Table 1. The spiral configurations, cross ties, lightweight (LW) concrete, and fiber reinforcement (FR) were attempts to improve post-ultimate behavior by confinement of concrete in the compression zone. Spiral shape tradeoff must weigh the larger confined cross-sectional area provided by a rectangle against the more efficient confinement shape provided by a circle. Since rectangular confinement shape may lead to premature spalling of the unconfined cover as the interior compressive forces tend to alter its shape, it was suspected that the rectangular spiral would be less efficient than the circular in post-ultimate response even though a larger area of the section is confined by a rectangular spiral.

Configuration A

Seven test piles were cast with 20 prestress tendons arranged in a circular pattern tied with W11 wire (ASTM A82 Grade 70) circular spiral with a 3-inch design pitch. (Measured pitch varied from 2 to 3.5 inches.) MK1 through MK3, MK7, MK8, and MK29 used normal weight concrete (8,000-psi design strength) while MK4 used lightweight concrete (7,000-psi design strength). Lightweight concrete with a lower modulus was expected to be more energy absorbant under service load. The design prestress was 60 ksi per strand in MK1 through MK4 for an effective

concrete prestress of 567 psi. MK29 had a slight increase in effective concrete prestress to 600 psi. The effective prestress force was increased to a design value of 150 ksi per strand to produce an effective concrete prestress of 1,417 psi in MK7 and MK8.

Configuration B

Two test piles were cast as MK5 and MK6 using normal weight concrete. Prestressing tendons were arranged in a rectangular pattern confined by no. 3-bar (ASTM A615 Grade 60), square spiral and cross ties. The spiral pitch was 3 inches and the cross tie spacing was 6 inches. The design effective prestress was 60 ksi per strand to produce an effective concrete prestress of 567 psi. No. 6 longitudinal bars were placed at midheight of the cross section.

Configuration C

Thirteen piles were cast in Configuration C with 16 prestress strands with an effective prestress of 48 ksi per strand for an effective concrete prestress of 450 psi. The strands were arranged in a symmetric, rectangular configuration with W5 wire square spiral. MK9 through MK14 and MK20 and 21 had 3-inch pitch single wire spiral. MK16 and MK17 had 4-1/2-inch pitch single spiral, while MK18 and MK19 had 6-inch pitch single spiral. MK23 had 3-inch pitch, doubled wire spiral. All piles of Configuration C were cast with normal weight concrete but MK20 and MK21 were fiber reinforced (see Appendix A).

Configuration D

Two piles were cast in Configuration D with the same strand configuration and prestress force as Configuration C. However, No. 6 longitudinal bars were added to the cross section at midheight and No. 3 cross ties were added at 6-inch spacing. MK22 had double W5 wire spiral with 3-inch pitch, while MK24 had single W5 spiral at 3-inch pitch.

Configuration E

Three test piles, MK25 through MK27, were cast in Configuration E using normal weight concrete with 20 strands in a different pattern than Configuration B (strand centroid nearer to the extreme compression and tension faces) and prestressed to an effective level of 600 psi. Double wrapped W5 wire square spiral with 3-inch pitch was used in MK25 and MK26, while a single wrap, 3-inch pitch W5 spiral was used in MK27. No cross ties or conventional reinforcing was employed.

Configuration F

MK28 was cast with normal weight concrete in Configuration F with the same prestress level and configuration as Configuration E but using No. 3 stirrups at 3-inch spacing as confinement reinforcing.

Configuration G

This concept differs from all the others by employing the least number of prestress strands and smallest cross-sectional area while using higher strength concrete (12,000-psi design strength). Configuration G utilized 14 prestress strands in an unsymmetric pattern. To provide a uniform concrete prestress of 540 psi, each strand layer was pretensioned in proportion to the product of number of strands per layer and distance from the section centroid. Initial strand tension varied from 30.4 kips in each of the two top strands to 8.7 kips in each of the six bottom strands. W6.5 wire rectangular spiral was employed. COLO1 had 4-inch spiral pitch while COLO2 and COLO3 had a 6-inch spiral pitch.

Response Measurements

Load-displacement and the following load-strain characteristics were determined by the tests: cracking limit, elastic limit, ultimate strength, cover spalling, and the extent of the plastic zone. Collapse characterization, maximum displacement, ruptured prestressing tendons, and spalled concrete zones were also documented when encountered prior to reaching maximum displacement constraints. A constraint displacement was set at 36 inches for the load point (an operational constraint based on pier geometry).

Measured strains in the pile section were used to locate the neutral axis in bending and to estimate the stress/force in the prestressing steel. Material strain correlated to loading is very important in validation of behavioral analytical models for prestressed piles.

Materials

Normal weight concrete for the specimens designated MK was designed for a 28-day strength of 8,000 psi and a prestress release strength of 4,500 psi. Two-inch fibers were added to the mix of MK20 and MK21 in accordance with ACI 544.1R-82. Normal weight concrete for the COLO designated specimens was designed for a 28-day cylinder strength of 12,000 psi. Silica fume, fly ash, and super plasticizers were used to obtain the high strengths. Silica fume with limits on tricalcium aluminate (6 to 10 percent) also adds to the concrete durability and should help in corrosion control. Lightweight concrete for MK4 was designed for a 28-day strength of 7,000 psi. Prestressing strains were ASTM A416 Grade 270 stress relieved, low relaxation. Wire spirals were ASTM A82 cold drawn Grade 70. All conventional reinforcement was ASTM A615 Grade 60.

TEST SETUP

The load tests were conducted on the rail test system embedded in the concrete floor of Building 570 at NCEL. The piles were laterally loaded to produce maximum moment at the load point. Figure 3 is a photograph of the test frame during a load test. The test frame and fixtures were fabricated from standard AISC sections. Machined rollers were employed at each reaction point and the load point was pinned

(laterally restrained). The compressor-driven hydraulic load system consisted of four, 6-inch-diameter rams with 4-foot strokes. Maximum hydraulic pressure was 1,800 psi. The rams, which were laying horizontally, applied lateral loading to the pile in a plane parallel to the floor, bending the pile about its major (strongest) axis. The compression face of the pile (hydraulic ram load side) was the "top" of the pile at casting. The entire test assembly was anchored to the rail system embedded in the floor. Load and reactions were applied through 8- by 14-inch bearing pads consisting of a 1-inch steel plate with 1/2-inch plywood for bearing distribution. The pile weight was supported at 15-foot intervals on greased teflon strips. The piles rested on their "sides" on two teflon strips with a grease layer between them and were easily positioned by hand after the piles were placed on the supports with forklifts. The piles were fabricated with a 3/8-inch side draft for easy form removal. This implies that the compression face (top) was 3/4 inch wider than the tension face.

Long Spans

A schematic of the long span loading arrangement is shown in Figure 4. The pile lengths were 60 feet 3 inches and the test length was 58 feet with shear spans of 15 feet and 43 feet on either side of the load point. The end of the test pile of the short shear span was marked "SA" while the end of the long span was marked "EA" during fabrication. The reactions were:

$$R_{EA} = 0.26P \text{ kips}$$

and

$$R_{SA} = 0.74P \text{ kips}$$

The maximum moment was (at the point of load):

$$M_p = 11.13P \text{ kip-ft}$$

where P is the applied concentrated load in kips.

Short Spans

The shorter piles were single point loaded at midspan except MK13A and MK14A (MK13 and MK14 were retested after cycling the load at midspan), which were loaded 7 feet from the SA end support as shown in the schematic of Figure 5. The spans were 30 feet. In addition to the 33-foot cast specimens, undamaged 35-foot lengths of previously tested 60-foot specimens MK2, MK5, MK6, and MK8 were also tested in 30-foot spans (MK2A, MK5A, MK6A, and MK8A). End reactions for midspan loading were:

$$R_{EA} = R_{SA} = 0.5P \text{ kips}$$

and maximum moment at the point of load was:

$$M_p = 7.5P \text{ kip-ft}$$

Since the prestress strands were subject to much larger service stress ranges than encountered by conventional prestressed members, the Poisson effect on the strands required a longer anchorage to fully develop the strand tensile strength. MK13A and MK14A were tested to verify that the full sectional moment capacity could be developed prior to an anchorage failure in a 7-foot shear span. End reactions for MK13A and MK14A were:

$$R_{EA} = 0.203P \text{ kips}$$

$$R_{SA} = 0.797P \text{ kips}$$

and maximum moment for MK13A and MK14A was:

$$M_p = 5.58P \text{ kip-ft}$$

INSTRUMENTATION AND DATA ACQUISITION

Sensors were selected for obtaining a direct analog of load, strain, and deflection. Houston Scientific gages (Figure 6) with a linear range of 5 feet were used for large displacements near the load point. Bourne's linear potentiometers (Figure 7) with a 1-foot gage length were used at the other locations. Six-inch length, paper back, wire SR-4 strain gages were attached to the exterior surface of the piles (sides, top, and bottom). Internal strain gages were embedded in the compression zone of selected piles.

A 100-kip capacity Baldwin SR-4 load cell was used to measure the applied jacking load, P . The load cell had a spherical head that simulated a pinned (laterally restrained) load point. It was calibrated in NCEL's 400,000-pound test machine prior to the pile tests.

To measure crack widths during selected tests (including all cyclic tests), crack gages were placed across cracks in the vicinity of the load point. Avongard gages (Figure 8) used in the long pile tests had a range of 10 mm and estimated resolution of 0.05 mm. Electronic gages (clip gages shown in Figure 9) employed in the shorter length tests had a range of 13 mm and a resolution of 0.003 mm or better. Calibration curves were derived for the crack gages by comparison with known lengths.

Long Spans

A total of 20 channels of data were taken during each long span test. A schematic of strain and deflection gage locations with identifying notations is given in Figure 4. Deflection was measured at nine locations along the pile span using linear potentiometers. The locations were: the load point, five points on the 43-foot shear span, and three points on the 15-foot shear span.

SR-4 strain gages in sets of three were mounted on the upper side of the specimens at three locations: at the load point, and at the middle of each shear span (Figure 4). A set of three included gages mounted near extreme tension fiber, neutral axis, and extreme compression fiber. A photograph of a set of three gages mounted to the side of the test pile is shown in Figure 10. All SR-4 electrical resistance strain gages were calibrated by shunting known resistances across one arm of the Wheatstone bridge circuit.

Concrete strain was also measured in the interior of MK1, MK2, MK4, MK5, and MK7 (in both tension and compression zones) at the point of load application using Reinforced Concrete Strain Meters manufactured by Carlson Electronics of Campbell, California (Ref 6). The strain meters were 3-foot-long rods hollowed to contain strain sensing devices (Figure 11). The rods were threaded to bond to the concrete. The strain sensing device contained two electrical resistance strain sensing elements. One wire increased in length and resistance with strain while the other decreased. The ratio of electrical resistance was directly proportional to length change and the total resistance was directly related to temperature. The strain sensing elements were wired into a Wheatstone bridge. The strain meters were used with a Carlson MA-4 Test Set which provided a readout of resistance and ratio values. Calibration constants were supplied by the manufacturer. Figure 12 is a photograph of a concrete strain meter with the MA-4 Test Set.

The pretensioning in the elastic wire elements was adjusted to provide full linear range in either compression or tension. The meters placed in the compression zone were preset by the manufacturer for full range in compression while those placed in the tension zone were preset for full tension. The meters were tied in place to the spiral cage adjacent to a top and bottom prestress tendon (Figure 13). Lead wires were run out through the compression face about 3 feet from the meters.

The long span test data chain for transferring electronic signals from all the sensors, except the Carlson meters, is shown by schematic in Figure 14. Signals carrying the effects of the various mechanical actions (strain, deflection, etc.) were transmitted by cable to amplifiers with carrier signal generators onto a data logger for analog-to-digital conversion and printout. Validyne SG71 signal conditioners/amplifiers were employed for all data channels. The data logger, a programmable Digistrip III by Kaye Instruments, Inc., provided an LED readout and an integral printer for permanent record. The Digistrip III included two microprocessors (one for data acquisition and one for output operations), which controlled data scan and acquisition, scaling to engineering units, and output readout and printing. Sensor inputs were sequentially scanned (manual mode of operation) as outlined in the TEST PROCEDURES section of this report, and the analog signals were converted to digital form and printed out with appropriate conversion factors to the correct engineering units (inch, in/in, etc.). Time of incremental recording was included and the engineering terms and units were preprogrammed for printout also.

Short Spans

Fifteen or more parameters were continuously recorded during the tests of the shorter piles. These included: load, six strains

(external and internal gages), six displacements, and two or three crack widths. Deflection and strain transducer locations are shown in Figure 5.

Six SR-4 electrical resistance strain gages were epoxied along the pile depth at the point of load application. Two were located on the compression face (extreme compression fiber) near the corners of the two sides, one on the tension face, and three on the side at 2, 3.5, and 5 inches from the compression face. Figure 15 is a photograph showing external strain gage installation. An Eaton internal strain gage (6 inch, CG129) was embedded inside the spiral of the compression zone. Crack widths were measured with clip gages fabricated similar to the ones described in ASTM E399. The clip gages were typically employed in pairs as shown in Figure 9. Upon failure, the crack widths at the crack gage locations were checked with a caliber.

All 16 sensor outputs were processed through a Validyne Model MC1 signal conditioner/amplifier, then recorded on a Honeywell 101 magnetic tape recorder. Six channels (deflection and internal strain) were branched to a backup recording on a TEAC R-71 cassette recorder. Loadpoint displacement, load, and maximum compression strain was monitored in real time for continuous test control using a Honeywell 1858 strip chart recorder. Further process control was provided by real time plots of load versus loadpoint deflection on a Houston Instrument 100 Recorder X-Y pen plotter. Figure 16 is a data chain chart of the short pile tests.

TEST PROCEDURES

Using forklifts, the test piles were placed in the load frame onto silicon greased teflon pads supporting the pile's weight. Final positioning was done by hand. All instrumentation was attached after positioning the pile in the test frame. All SR-4 electrical resistance strain gages and deflection gage fixtures were epoxied to the test piles 24 hours in advance of the load tests. The instrumentation was checked, calibrated, and zeroed 30 minutes before starting the loading. Concrete cylinder tests were made to determine the concrete strength and stress-strain properties. Concrete stress-strain curves were derived for only the first eight specimens, MK1 through MK8, to be used in the development of the analytical model for the piles. These concrete stress-strain curves are given in Appendix B while concrete strengths are tabulated in Table 1.

Pretest readings of the Carlson meters embedded in the long piles provided average concrete strain for estimating prestress loss and current prestress. These values are tabulated in Table A-1 of Appendix A.

Two types of quasi-static tests, monotonic and cyclic, were conducted at deflection rates of 1 in/sec. The loading in monotonic tests was increased until the pile failed in flexure or the deflection limit was reached. In cyclic tests the loading was applied and removed repeatedly in an attempt to simulate pile service conditions. Both monotonic and cyclic tests were conducted on all configurations. After completion of cyclic loadings in the "service load range," piles were loaded to failure.

Long Span Monotonic Loading

The long span tests were load controlled prior to ultimate load when the pile behavior was somewhat linear, and were deflection controlled after ultimate load while the pile was deforming more plastically. After an initial preload of approximately 3,000 pounds, the load increments were maintained at 1,000 pounds. Loading was controlled by the hydraulic loading ram operator, who monitored the output from the load cell with a digital voltmeter. After ultimate loading, displacement increments of 1/2 inch were applied to the test pile. At each increment, all electronic gages were scanned, recorded, and printed with the data logger. Ratio and resistance readings from the internal gages (when present) were made with the MA-4 Test Set. The test proceeded until the prestress strands on the tension face failed or when the deflection limit was reached. Deflection limits on the long span tests were set at 36 inches. Post-test conditions were documented by photographs and spall zone characteristics were noted.

Long Span Cyclic Loading

Cyclic tests proceeded as in the monotonic tests except that the piles were unloaded and reloaded in the working range prior to their ultimate load for up to 37 cycles. A preload was applied prior to the first cycle, wherein the concrete tensile strength was slightly exceeded producing at least 3 cracks on the tension face near the load point. Three cracks were marked for application of Avondgard crack gages. After releasing the load, the crack gages were applied across the completely closed cracks with quick setting epoxy and allowed to set securely before starting the first complete load cycle. Avongard crack gages were examined for crack width changes to determine if the prestress forces were sufficient to close the concrete tensile cracks after the load was removed. MK1 was cycled to 15 kips, 18 kips, 20 kips, and 35 kips while MK2 was cycled to 25 kips and 35 kips. Test increments were similar to the monotonic tests and crack progress was marked on the pile surfaces. After the load cycling was completed, the piles were loaded to failure as in the monotonic tests.

Short Span Monotonic Test Procedures

Monotonic tests proceeded at a continuous and constant deflection rate of 1 in/sec until all the tension strands failed or the deflection limit was reached; whereupon, the load was removed. The deflection limits on the short spans were set at 30 inches so the monotonic tests were completed in 30 seconds or less.

MK3A, MK6A, MK8A, MK9, MK10, MK23, and MK24 were loaded monotonically to failure. MK16, MK17, MK18, MK20, MK22, COLO1, and COLO2 were first precracked then monotonically loaded to failure. MK13A and MK14A were monotonically loaded to failure 7 feet from the support after being subjected to midspan cyclic loading (MK13 and MK14, respectively).

Short Span Cyclic Loading

A service load level of 80 percent of the ultimate energy corresponds to a maximum moment of 326 kip-ft and a load of 43.4 kips in the short piles loaded at midspan. Cyclic loading of the short piles was set at levels below the maximum service level. Cyclic loading was continuously applied at the rate of 1 in/sec, from zero to a constant load level of 40 to 80 percent of the ultimate load energy. Depending on the survivability of the compression zone and the residual crack width, load levels were step increased and the cyclic process continued. If the specimens could not attain or maintain the previous cyclic load level due to deterioration of the compression zone, then deformation was continued until failure or deflection limits were reached.

Short piles and cycled load levels were as follows:

MK5A	250 cycles to 43.4 kips
then	100 cycles to 50.0 kips
then	100 cycles to 55.0 kips
MK11	259 cycles to 43.4 kips (could not maintain 43.4 kips on cycle 260)
MK12	300 cycles to 33 kips
then	200 cycles to 38.5 kips
MK13	100 cycles to 43.4 kips (no cyclic failure)
MK14	100 cycles to 43.4 kips (no cyclic failure)
MK19	100 cycles to 41.2 kips (no cyclic failure)
MK21	10 cycles to 43.4 kips (no failure during cyclic loading)
MK25	200 cycles to 43.4 kips
MK26	50 cycles to 38 kips
then	50 cycles to 40 kips
then	50 cycles to 42 kips
then	50 cycles to 44 kips
then	11 cycles to 46 kips
MK27	150 cycles to 40 kips
then	50 cycles to 42 kips
then	117 cycles to 44 kips
MK28	150 cycles to 39 kips
then	100 cycles to 42 kips

	then	100 cycles to 44 kips
	then	148 cycles to 46 kips
MK29		150 cycles to 38 kips
	then	100 cycles to 40 kips
	then	52 cycles to 42 kips
COL03.		250 cycles to 43.4 kips

Successive cyclic load levels were selected considering concrete cumulative compression fatigue from proceeding cycles and residual crack width (crack closure) on the tension face. Concrete fatigues rapidly when stressed in excess of 75 percent of the ultimate compressive strength and deteriorates the compression zone which reduces flexural capacity. Residual tension crack widths of 0.012 inch or more were considered unsatisfactory in preventing strand corrosion while in service. During cyclic load tests, the compression zone was closely monitored visually and by strain gages for evidence of deterioration while crack gages continuously sensed crack opening. Thus, the load level and number of cycles were determined at which compression zone deteriorated and/or crack closure exceeded 0.012 inch. Whenever a pile satisfactorily resisted a series of cycles at a given load level, the load level was increased and the pile was subjected to another series. The final load cycle was extended to failure except for MK13 and MK14, which was monotonically loaded to failure at 7 feet from the support after being subject to 100 load cycles at midspan.

DATA REDUCTION

Deflection and strain were plotted as a function of applied load and moment. Moment-curvature relationships were obtained from loading, cross-section strain, and post-ultimate deflection. Energy absorption was also calculated as a function of load and deflection.

Curvature

Curvature for moment-curvature relationships was determined from strain readings (assuming linear distribution of strain across the section) prior to ultimate load and from deflection gages during post-ultimate loading. Prior to ultimate load, cross-section strain values at the load point (including internal gage readings) were fitted to a linear relationship and curvature was determined from:

$$\phi = \epsilon_c / C \quad (\mu \text{ strain/in})$$

where ϵ_c is the concrete strain at the outermost compression fiber and C is the depth from the outermost compression fiber to the neutral axis.

After ultimate load, deflection values from the load point deflection gage and the two adjacent gages (one on either side) were used in a curvature relationship derived from the equation of a circle in Cartesian coordinates where the point of origin is the lowest point on the circle:

$$x^2 + y^2 + Dx + Ey = 0$$

and the radius of curvature, R, is determined from:

$$R = \frac{1}{2} \sqrt{D^2 + E^2}$$

For the deflected pile, choosing the load point as the origin and displacement differentials as Y values on either side of the load point (at X = +24 and -24 inch), the radius of curvature can be determined by solving 2 equations with 2 unknowns:

$$R = \frac{3}{(Y_l + Y_r)} \sqrt{4(Y_l^2 + Y_r^2 + 8)^2 + (Y_l - Y_r)^2 (Y_l Y_r - 4)^2}$$

from which the curvature is obtained:

$$\phi = 1/R$$

where Y_l and Y_r are the differences between the load point deflection and the deflections measured at points 24 inches on either side of the load point. Curvature was obtained only for those test piles with internal gages and those piles with three or more strain gages across the compression zone.

Energy Absorption

The energy (external work), E, absorbed by the test piles, was obtained from the area of the load-deflection response at the point of load:

$$E = \int P D_p$$

where P is the applied load increment and D_p is the deflection at the applied load.

Energy increments were calculated from products of load and deflection increments:

$$\Delta E_n = ((P_n + P_{n-1})/2)(D_n - D_{n-1})$$

where the subscripts n and n-1 designate consecutive data points. Running values of total energy were calculated and tabulated for each data point:

$$E_n = E_{n-1} + \Delta E_n$$

The total absorbed energy at the end of the test was:

$$E = (1/2) \sum_{n=1}^N (P_n + P_{n-1})(D_n - D_{n-1})$$

where N is the total number of data points.

Long Pile Tests

Data from the data logger printout were loaded into the data base program, SYMPHONY, on an IBM PC. After statistical analysis, deflected shapes were also derived as a function of loading. The calculated parameters were also plotted using SYMPHONY. In addition to the computerized data base, other observed parameters during cyclic loading such as crack width and growth, change in stiffness, shifting of the neutral axis, and general deterioration were incorporated with strain and deflection for a qualitative assessment of prestress loss.

Short Pile Tests

Similar parameters were analyzed for the short piles. Data from the FM analog tapes were digitized using an analog-to-digital conversion board in the PC, or with a Norland NI 2000A Waveform and Data Analysis System. Deflection, strain, curvature, and energy were plotted directly from the Norland to an X-Y plotter while the digitized data on the PC were statistically smoothed and plotted with SYMPHONY.

RESULTS

Data plots of the load response are presented in sets for each specimen in Appendix B. The data sets also include stress-strain plots from concrete cylinders as well as photographs of the test piles showing crack patterns and spalling. Summaries of the load responses are tabulated in Table 2 including ultimate deflection, energy absorption, and other observed data. "Ultimate" data values are defined as those values related to maximum loading (or moment) where concrete spalled in the compression zone. Cyclic test results are tabulated in Table 3 and include residual strain and residual crack widths.

Configurations B and E with normal weight concrete (MK5, MK6, and MK28) demonstrated the best overall structural results by absorbing the most energy and loading as well as exhibiting more strain softening and plasticity while sustaining the least damage at ultimate loading. Plastic behavior is characterized by a constant load as deformation increases; whereas, strain softening shows a distinct load decrease with increased deformation.

Concrete Mechanical Properties

In addition to the cylinder tests made at prestress transfer, tests were conducted on representative cylinders of each pile for strength, f'_c and stress-strain curves. Strengths are tabulated in Tables 1 through 3 while stress-strain plots with Young's Modulus are provided with the long pile data sets in Appendix B. Two types of tests were conducted: (1) a test in accordance with ASTM C469, and (2) a test with SR-4 electrical strain gages applied to the cylinders. Both gave similar results; however, the ASTM C469 measurements were terminated prior to failure to protect the test frame and gages from the energy release of the failure process. The stiffness of the test machine caused a rapid,

explosive failure so it was not possible to define the descending portion of the stress-strain curve after ultimate strength.

The ACI equation relating Young's modulus of concrete, E_c , to its unit weight, w , and compressive strength, f'_c :

$$E_c = 33w^{1/3} \sqrt{f'_c}$$

tends to overestimate the stiffness derived from the measured stress-strain behavior. The ACI equation was not intended for use with high strength concrete. A relationship for high strength concrete developed by Morales (Ref 7) better fits the test results:

$$E_c = (4,0000 \sqrt{f'_c} + 1.0 \times 10^6)(w/145)^{1.5}$$

The normal weight concrete averaged 145 lb/ft³, while the lightweight concrete was 121 lb/ft³.

Monotonic Response

Appendix B contains photographs and data plots of load-deflection, moment-curvature, deflection distribution, energy deflection, moment-energy, residual crack width, and load-strain for all piles. A summary of ultimate responses is given in Table 2. Deformation (deflection and curvature) response of the piles to lateral load was linear up to ultimate load and could be characterized by a bilinear relationship with a transition region. The initial elastic response occurred prior to cracking on the tension face of the cross section. The response then transitioned to another linear curve with about 1/5 as much stiffness (depending on prestress and concrete strength) up to ultimate loading where the concrete cover in the compression zone spalled due to lack of confinement. The ultimate compressive strain was 0.003 or larger. In the short span tests, bilinear response was observed up to an ultimate load of about 55 kips with a transition at cracking near 17 kips. Example preultimate load-deflection plots for 30-foot span tests are given in Figure 17.

Spalling the concrete cover at ultimate loading resulted in a sudden loss in load carrying capacity directly related to the loss of concrete area. The compression concrete fractured longitudinally and along the spiral layer from the edge of the load bearing plate for a distance into the short shear span ("AE" end) of the test piles (see photographs in Appendix B). Concrete spalling severely damaged the piles. A pile in service would be permanently deformed and would require replacement after ultimate loading. Since the concrete spalled along the spiral, reducing the area of the compression zone, depth of concrete clear cover, and spiral geometry are major factors in determining the moment carrying capacity after ultimate loading. Thus, the loss after spalling was greater for Configuration A with circular spirals than for all configurations with the rectangular spirals or ties.

After concrete spalling and the subsequent loss in load carrying capacity, there was strain softening and/or plastic deformation response until the prestress tendons on the tension side of the cross section

started to rupture (or in the cases of MK18, MK19, and MK25 through MK28 the strands did not all rupture but continued to carry a high load as the strands slipped through the concrete after bond breakdown). Example load-deflection plots showing post-ultimate response are given in Figure 18. The prestressing tendons of the circular pattern (Configuration A) broke in sequence while those of the rectangular patterns all failed at once or slipped through the concrete as the bond broke down and limiting deformation was attained. Failure was designated at the point of tensile strand rupture or when deflection limits were exceeded even though the test piles continued to carry load.

Spalling of the cover at ultimate load in the short span tests was accompanied by a load loss of about 10 percent and was followed by a plastic and strain softening response. Behavior was consistent for all Configuration C piles except that strain softening was nonexistent in MK20, MK21, and MK23. Strain softening was so prevalent in MK9, MK10, MK18, and MK19 that it increased the energy dissipation by over 300 percent beyond ultimate energy levels.

Slippage of the tension strands was noted in the piles with lower lateral confinement. Slippage and bond failure was characterized by spalling of the tension face cover and longitudinal cracks along the pile side at the tension strand level. The slippage was greatest for the largest spiral pitch (6 inches). Spalling and cracking on the tension face reached several feet on either side of the load point in MK18 and MK19. Little distress in spiral reinforcement was observed, but rupture occurred in one wrap of COL03 and yielding was observed in one wrap of MK7.

After cover spalling, the highest energy release was observed when the core concrete would gradually crush in the case of wider spiral pitch (as in COL01). This increased the distance between the centroid of the compression zone and the neutral axis from the top surface, and shortened the internal moment arm with all or most of the tension strands unbroken. The cause to this behavior seems to be lack of confinement. Further, wider spiral pitch allowed unbonding of the strands over several feet from the point of maximum moment (MK18 and MK19). In the presence of more confinement reinforcement, all strands broke soon after compression concrete spalling (COL02, MK22, and MK23). Lower concrete strength may have been a secondary factor when combined with less confinement.

Curvature, ϕ , was derived from cross-sectional strain data. The neutral axis moved from the uncracked section centroid (prior to tensile cracking) steadily toward the compression face as ultimate load was approached. The neutral axis probably dropped just prior to ultimate loading (cracks ceased to progress into the compression zone), but this could not be verified due to limitations of the strain gages. Moment-curvature plots are included in Appendix B.

Energy Absorption

Energy was plotted versus deflection and moment for each test and presented in the data sets of the Appendix B. The energy-deflection curves were characteristically "S" shaped. There was little energy in the initial elastic response. Similarly, the energy leveled off after

strand rupture or bond failure and the load capacity began to fall toward zero. Energy values at ultimate load and at failure (total energy) are tabulated in Table 2. Configurations A and B (long piles) reached energy levels well over 30 ft-kips prior to ultimate load. MK5 reached 63 ft-kips at failure. Average ultimate energy for the short piles was about 23 ft-kips with failure energy 2 to 5 times greater. Examples of moment-energy plots are given in Figure 19.

Initial stiffness of Configuration G piles was greater than other configurations except those of highest prestress (MK7 and MK8) (Figure 17). Higher stiffness resulted in less energy absorption prior to ultimate load. Spalling of the concrete cover at ultimate load resulted in a greater percentage loss of compression concrete and a significant resistance loss. Post-ultimate response included softening and finally rupturing of tensile strands. The tests were terminated after exceeding a midspan displacement limit. Not all tension strands ruptured at test termination. The maximum energy absorption was comparable to other configurations. Configuration G failure zones extended over larger areas than observed in the other configurations. The extent of the failure zone in itself presents no problem, but it is indicative of ability to absorb energy - a result of bond breakdown which also causes excessive crack width at service loading. Bond failure was caused by lower prestress in the tension strands coupled with lack of confinement. The spiral cage of COLO1 remained intact while several wraps ruptured in COLO2 and COLO3. The 6-inch spiral pitch of the latter two resulted in lower energy levels than COLO1, which had a 4-inch pitch. The opposite was found in other configurations.

Fiber-Reinforced Concrete

The steel fibers of MK20 and MK21 provided better concrete confinement after ultimate strength. Fiber-reinforced concrete produced higher ultimate load (15 percent higher). There was less compression zone loss and smaller decrease in internal moment arm which resulted in a premature and sudden failure of the tension strands before the fiber confinement could fully benefit the post-ultimate ductile behavior. This design oversight could have been corrected with lower strength concrete or more prestressing strands. Due to the early rupture of the strands, these two piles demonstrated the lowest overall energy dissipation.

Increased Prestressing

Within Configuration A, the two specimens (MK7 and MK8) that were prestressed 2-1/2 times more than all other configurations sustained no ultimate loading enhancement. However, the stiffness of MK7 and MK8 was almost twice that of the others which resulted in half the energy absorption at ultimate loading (20 to 22 ft-kip). Energy absorption at failure was also substantially less for higher prestress force. Higher prestressing force may have caused greater distress to the confinement reinforcement. There was spiral yielding in MK7.

Small prestress force changes did not cause noticeable stiffness differences (Figure 17). However, the lowest prestress used in Configuration C resulted in the highest post-ultimate energy capacity. For

example, MK9, MK10, MK18, and MK19 sustained from 4 to 5 times the ultimate energy through the post-ultimate range (Table 2). This energy capacity was developed at a sacrifice of strand slippage (bond break-down) and large crack openings having undesirable consequences in the cyclic behavior.

Lightweight Concrete

Without confinement, the release of energy through spalling at ultimate load was much more dramatic with lightweight concrete test pile MK4. The post-ultimate load loss was almost half the ultimate load and was the worst of the piles tested. The relative strength of bond between paste and aggregate is greater in the lightweight matrix than the comparable normal weight concrete. Without a relatively weak transition zone between paste and aggregate for crack arresting, the concrete fracture process at spalling progressed unchecked through the aggregate as easily as the paste. Thus, the spall zone was larger for MK4 than was generally found with the other test piles. The prestress strands of MK4 ruptured at failure prior to full development of the confined strength of the concrete. The 3-3/4-inch spiral spacing in the spall zone had little effect on the plastic behavior of MK4.

Spiral Geometry

Spiral reinforcing for concrete confinement benefits post-ultimate load carrying capacity and the extent of the plastic behavior. Square ties confined more of the compression zone and resulted in the smallest compression spall zone for the smallest post-ultimate load carrying loss. Spiral spacing (2 to 3.5 inches) had little effect on the plastic behavior, but the rectangular configuration was superior due to the prestress strand configuration. After concrete spalling, square ties bend (curved) outward between bends (see photos in Appendix B), as expected, with no sign of yielding. The spiral of MK7 yielded and necked down at one point. The isolated spiral yielding of MK7 or the failure in the COLO3 spiral may have been anomalies or side effects of the higher prestress force since none of the other spirals showed any indication of yielding.

Cyclic Loading

Table 3 summarizes the cyclic test results including residual crack width, maximum concrete compressive strain, absorbed energy, and visual inspection of the compression zone for each cyclic load level. The distinct bilinear response observed in the single load cycle to failure was less apparent in subsequent load cycling. Crack lengths grew slowly with each cycle but abruptly increased with load step increases. Cyclic load-deflection, residual crack width measurements, and load-to-failure plots are given in Figures 20 through 22 for MK25 (Configuration E). Similar plots are provided for circular spiral Configuration A (MK29) in Figures 23 through 25. Measured tensile strain at peak load increased slightly with each cycle as did the curvature and the deflection. The neutral axis at ultimate load had shifted to within 5 inches of the compression face.

During the cycling process, displacement and curvature increased at a given loading and residual deformation remained after load removal. No doubt there was some loss in prestress but not enough to keep tensile cracks from partially closing when load was removed. There was slippage over the crack surfaces as evidenced by powdered concrete falling from open cracks. Residual crack opening (load removal) remained less than 0.012 inch after 100 cycles at 80 percent of ultimate energy for Configurations B and E. Continued cycling produced more prestress loss, which kept cracks from closing completely and caused residual crack width to increase (Figures 21 and 24).

If damage was not incurred in the compression concrete, then flexural strength was not reduced from straight, monotonic loading. On long span piles with the load cycled 35 times, the cracking closed to less than 0.05 mm. There was no compression concrete damage, so ultimate capacity and energy levels were not impaired by the cycling process. On the other hand, MK25 through MK29 did not attain full capacity because of sustained damage to the compression concrete. Only cyclic loads were applied to MK25 through MK29, which were cycled until the compression zone spalled rendering them incapable of sustaining the cycling load level. MK25 through MK29 were subsequently loaded to failure.

Cyclic loading also induced compression zone deterioration in piles MK5A, MK11, MK13, and MK19. MK11 showed compression zone deterioration (cracking) after 40 cycles at a load level equivalent to 80 percent of ultimate energy. MK13 was damaged after 50 cycles at 80 percent of ultimate energy, while MK19 was damaged after 80 cycles at 70 percent of ultimate energy. MK13 and MK19 were able to maintain their respective load levels after 100 cycles, while MK11 could not sustain cycling to 80 percent of ultimate energy after spalling occurred at 259 cycles and it was subsequently loaded to failure on cycle 260. MK5A (Configuration B) was capable of sustaining the greatest amount of load cycling. Compression zone deterioration was observed after 480 cycles. It was apparent that deterioration of the compression zone occurred within 100 cycles if the concrete strain exceeded 0.0022/in/in.

Configuration C exhibited the worst residual crack widths with cyclic loading. It was difficult to sustain cyclic loading without residual crack widths exceeding 0.012 inch. Large residual cracks and deflection are results of compression zone deterioration which was triggered by excessive concrete compression strain. MK12, loaded at the equivalent of 40 percent of the ultimate energy level, exhibited crack widths of 0.011 inch or less after 100 cycles. The other specimens of Configuration C sustained residual crack widths of at least 0.05 inch after 100 cycles at 80 percent energy level. In contrast, MK5A (Configuration B) exhibited 0.011 inch maximum residual crack width after a total of 450 cycles.

Cyclic tests of the fiber-reinforced concrete resulted in the fibers being pulled loose along crack surfaces and preventing crack closure. At the end of ten cycles the residual crack opening was 0.017 inch, compared to half of that or less for other tests at the same load level.

Cycling load from 0 to 43 kips (80 percent ultimate energy) produced a concrete compression strain differential of about 0.00225 in/in in COL03 (Configuration G). After 250 load cycles, the residual crack opening was 0.038 inch and residual midspan deflection was 1.4 inch.

ANALYSIS

The test results in the preultimate (services load) range agree well with the analysis methodology and computer program developed by ABAM Engineers (Ref 3) and the use of the Morales Equation to determine concrete stiffness. ACI equations for Young's Modulus predicted overly stiff piles resulting in a more conservative analysis with less energy and smaller displacement predictions. The most accurate refinement to the analytical approach would be to use measured concrete stress-strain curves and experimental values of concrete spall strain, but this is not recommended due to the complexity. A complete explanation of the analytical approach appears in References 3 and 4.

Configuration C was the most energy absorbent. However, due to the low prestress, this configuration was poor in cyclic behavior (crack control and compression concrete deterioration). To correct these shortcomings, Configuration E and F were derived with four additional prestress strands and increased prestress force. This enhanced the service load range without sacrificing energy capacity.

Concrete Strength

Except for the 12,000-psi concrete of Configuration G, concrete strength had little effect on the monotonic energy capacity up to ultimate load. The high strength concrete was stiffer resulting in smaller deflections offsetting any increase in ultimate load. In contrast, lower concrete strength enhanced the post-ultimate energy absorption capacity.

Effect of Concrete Prestress

Fender piles as flexural members were most effective when prestressed to about 1/3 that which a normal, axial load bearing pile would be prestressed. Prestressing had a major impact on the flexural stiffness, energy capacity, crack width opening, and to a lesser degree, bonding and compression zone deterioration under cyclic loading. The lowest effective prestress (450 psi) exhibited the highest energy absorption, but crack width opening and compression zone deterioration was unsatisfactory at the desired service load limits. The highest effective prestress (1,417 psi) resulted in a very stiff pile with low energy capacity. The other two levels of prestress (568 and 600 psi) yielded a more satisfactory response.

Prestressing at levels comparable to axial load-bearing members (1,417 psi in Configuration A) resulted in unnecessary stiffness and higher reaction forces for a given energy level (or a lower energy level for a given reaction). On the other hand, partial prestressing increases from 450 psi to 600 psi resulted in better crack control,

without sacrificing stiffness and energy absorption. Based on the cyclic response of MK25 through MK29, 600-psi effective prestress provides the best tradeoff of energy capacity with crack width and compression zone deterioration.

Spiral Spacing

The majority of monotonic tests were conducted with W5 wire spirals and a 3-inch pitch, which was equivalent to spiral percentage, p_s , of 0.43 percent. There was no apparent effect of confinement reinforcement on ultimate load or stiffness. There was considerable range of energy absorption results due to variation of other parameters, particularly concrete strength. However, the average value of failure energy absorption of specimens with a 3-inch spiral pitch was less than those with 4.5-inch pitch ($p_s = 0.32$ percent), which was less than those with 6-inch pitch ($p_s = 0.21$ percent). Likewise, doubling the spiral (MK22, MK23) lowered the energy capacity from a single wrap. The greater post-ultimate energy absorption was attributed to bond breakdown on the tension face. This caused longitudinal cracks (accompanied by wider transverse cracking) along the prestress strands allowing the strands to slip through the concrete accompanied by larger rotations and displacements with slower load decrement.

On the compression face, little can be gained by increasing the post-ultimate confinement strength of the concrete within the configurations since the strands ruptured on the tension face. There is little doubt that the full, confined concrete strength was not reached. Fully developing the confined strength would allow for larger rotations and the increased concrete strain would lower the neutral axis. Lowering the neutral axis increases the compression zone and increases the compression force of the bending couple which would have to be balanced by an increase in tension force. Since an increase in the tension forces would be achieved by some combination of increasing the number, size, or strength of the prestressing strands and increasing the bond capacity of steel, increasing the plastic deformation region of the test configurations does not seem realistic. Enclosing a larger area of the compression zone by spiral would also increase the load carrying and energy absorbing characteristics. However, this takes away from the 2 inches of minimum cover for spiral and strand corrosion protection.

It cannot be shown that the cross ties and added conventional steel at midheight in Configurations B and D enhanced the flexural performance of the piles. The enhanced performance of these configurations can be attributed to rectangular strand configuration and lower prestress.

Pile Configurations B, E, and F (normal weight concrete), in 65-foot lengths, can sustain a design working energy absorption of 15 ft-kips and a "rare event" energy level of 30 ft-kips (ultimate strength). Placing the test pile designs in perspective for other lengths: the deflection at the load point, D_p , is proportional to the pile length, L , and the longer shear span, B ; while the load carrying capacity, P_u , is proportional to L/B . For pile lengths of 65 feet, it is expected^u that the deflection at ultimate moment will increase by 16 percent over the 58-foot length test values while the load will decrease by 4 percent. This results in a less stiff pile with a higher energy

absorption capacity. The failure displacement will be less than 36 inches. Shortening the pile will increase stiffness and result in less deflection at higher loads for a given ultimate moment. For a length of 45 ft, P_u will be 11 percent greater than the 58-foot test values while the ultimate deflection will be about 30 percent less than the tests. Similar values can also be derived from the short pile test results.

Cyclic Response

Unfortunately, the characteristics that enhance energy absorption under monotonic loading are detrimental to cyclic load response. That is, low concrete strength and wide spiral spacing (low percentage of confinement reinforcement) results in bond release and high concrete strain enhancing energy capacity, but presents poor crack control (increased residual crack widths) and rapid compression concrete deterioration.

The concrete strengths of MK25 through MK29 did not attain design strengths of 8,000 psi (test strengths range from 7,070 psi to 7,420 psi). However, the performance of these piles and the configurations represented were superior to most of the other piles under cyclic loading. This can be attributed to the increase in effective concrete prestress to 600 psi, the increased number of prestress strands (20), and more efficient strand configuration (in Configurations E and F). Configuration F (MK28) was the best performer of this group and was only equalled by MK5A. This configuration is better than Configuration E because of deformations on the confinement steel employed in MK28 (also employed in MK5). After 150 cycles at a load of 39 kips maximum residual crack width 0.009 inch, and 50 more cycles at 42 kips, the crack width was only 0.011 inch with no damage to the compression concrete. This compares with a residual crack width of 0.015 inch after 150 cycles of 38 kips on circular spiral configuration in MK29. It is also noted that when strand stress did not exceed 200 ksi (model prediction) and concrete compression strain did not exceed 0.002 in/in (model prediction and measured), then no damage was sustained in the compression zone and crack width was controlled within desirable limits.

Error Analysis

Errors of the results taken directly from instrument readings (deflection, strain, load) are a function of the instrumentation reliability but are estimated to be no more than 5 percent. Errors in the energy results which are products of two instrument values could be somewhat higher. The values of curvature are the least reliable; although the strain readings are reliable within 5 percent, the internal gages could not be accurately located during specimen fabrication because of reinforcing cage flexibility. Curvature values have errors from 5 to 20 percent (higher errors associated with location of the Carlson meters). The curvature derivation from deflections also contributed to the higher errors.

The Carlson strain meters and other internal strain gages are no doubt superior to the SR-4 electrical resistance strain gages. Embedded in the concrete adjacent to the steel stands, the strain meter provided

change in length in the steel also. The meter measured average strain regardless of cracking because the rod was bonded to the concrete by its threaded ends. The possible reliability errors associated with curvature results are mainly due to the lack of confidence in locating the strain meter position rather than the strain record.

Load cycling presented two more problems regarding internal strain meters. There is no doubt that the elastic limit was exceeded in the steel rod encasing the strain sensor ($F_y = 72$ ksi). However, due to its 240-ksi strength, the elastic steel wire sensor continued to exhibit a linear resistant-strain response until there was a load reversal (cycling or post-ultimate load loss). The load cycling to higher load may have also broken down the bond between the strain meter rod and concrete while the concrete near its ultimate strain (0.003) also exhibited permanent set and nonlinearity. Therefore, response from the strain meters was suspect at the highest load cycles. Further, the meters ceased to reflect a realistic average tension strain for post-ultimate response because of wide cracks concentrated near meter midlength.

The Eaton internal strain gages used on the short piles performed better than the strain meters under cyclic load. However, the gage lost capacity after spalling of the compression concrete cover. Internal strain gages could not be used on the tension side because they are only 6 inches in length (which was the average crack spacing).

SUMMARY AND RECOMMENDATIONS

Several objectives were accomplished with the extensive pile test program. Comparisons were made for seven prestressing schemes and configurations. Evaluations were made of the effects of the following parameters and variables on monotonic and cyclic load response:

1. Prestress force
2. Prestress strand arrangement
3. Confinement steel
4. Concrete strength
5. Concrete type
6. Addition of conventional reinforcing
7. Lateral ties (additional to spiral)
8. Length of shear span

Energy absorbing relationships for load ranges of zero up to pile failure based on lateral load-deflection are provided. Moment-curvature relationships, deflected shapes, and limiting concrete and steel strains were also determined. All of these will verify and support analytical modeling and were necessary to establish design criteria and limitations. The results are applicable to design and analysis of other concrete structures in marine/industrial environments, to full and partially prestressed concrete, and to high strength concrete elements.

Effects of Prestress

It has been demonstrated that partial prestressing (600 psi) is sufficient to control crack widths to less than 0.012 inch precluding the use of coated prestressing strands or cathodic protection for corrosion prevention. However, if the pile's ultimate capacity is exceeded and the cover concrete is spalled, the exposed confinement steel and the strands will corrode more rapidly than conventional concrete steel due to the prestress.

Although a circular spiral would appear to be more efficient than a rectangular shape for confining the concrete at high loads, the greater confinement area offered by the rectangular shape more than offsets this effect. Balanced flexural designs with partial prestress, normal weight concrete, rectangular strand patterns with square spiral ties were definitely superior in load carrying capacity, energy absorption, and post-ultimate behavior. Other pile configurations that included higher prestress, higher strength concrete, and circular spirals and strand patterns absorbed less energy. The highest prestress almost doubled the preultimate stiffness with half the total energy absorbing capacity. Likewise, lightweight concrete did not show any significant structural benefits because of the need for extra confinement.

A major advantage of partial prestressing is the control of cracking and crack widths at service loads. It is reasonable, for repetitive loading, that the upper limit of usable elastic energy for service conditions (i.e., frequent impacts and load cycles) be set at 16 ft-kips per pile (for a 65-foot length pile). This should keep cracks closing to within 0.012 inch of being completely closed. Configurations B, F, and E in 65-foot spans can be designed for at least 30 ft-kips ultimate energy absorption and still provide more than 100 percent energy reserve to failure of the prestressed tendons. Ultimate energy capacity of the circular reinforcement pattern is about 35 ft-kips and about 40 ft-kips for the rectangular pattern. Failure energy of 50 ft-kips can be obtained for the circular configuration compared to over 70 ft-kips for the rectangular configuration.

Prestress level in the strands should be 60 ksi. Lower prestress may result in bond failure and higher prestress significantly increases the flexural stiffness and reduces the energy capacity. A minimum effective concrete prestress of 600 psi should be provided to offset tensile stresses during pile handling and driving and for crack control while in service.

Concrete

It is reasonable to use a balanced design and limit the concrete spall strain to 0.003 (including prestress). The Morales equation (Ref 7) or another relationship accounting for high strength concrete should be used for Young's Modulus of concrete, rather than the ACI equation.

Concrete strength should be 8,000 psi. Although the piles always exhibit a compression failure mode at ultimate strength, tight control of 28-day cylinder strength to 8,000 psi insures a better combination of

higher post-ultimate energy dissipation and design service load level. A lower strength degrades crack control and a higher strength increases stiffness unnecessarily.

Details obtained from the fiber-reinforced concrete were limited, but the addition of fibers did not seem to bring any substantial advantage beyond an ultimate strength that was 15 percent above average. Crack closure was impaired and overall energy dissipation was lowest. Since the cost per pile is doubled by the addition of fibers, fiber-reinforced concrete piles are not recommended.

Confinement Reinforcement and Strand Arrangement

Confinement requirements for flexural fender piles are different from fully prestressed, axial load bearing piles. Bond is not as serious with axially compressed members and the confinement is used to insure full compression strength development. On the other hand, for a laterally loaded fender pile, lateral reinforcement confines the compression concrete on one face while resisting tensile splitting around the tension strands (bond failure) on the opposite face. Confinement tradeoffs were made to allow some deformation and rotation through strand slippage to insure energy absorption while controlling crack widths and providing proper compression confinement.

Rectangular confinement reinforcement equivalent of No. 3 ties with a 3-inch pitch and a yield strength of 60 ksi should be used because it performed the best of all confinement arrangements. Deformed reinforcement is superior to smooth wire in a rectangular shape because of the enhancement to bond strength during cyclic load. Cross ties do not enhance confinement at service loads and do not substantially benefit post-ultimate behavior. Smooth circular spiral can be employed but is less efficient in load resistance and the design capacity must be adjusted downward for reduced section efficiency. There will be at least a 30 percent decrease in total energy capacity for the same number of prestress strands. On the other hand, there are two advantages to circular spiral: (1) the ease and availability of spiral fabrication and, (2) the average clear cover provides more corrosion protection than rectangular patterns (wider residual crack widths accompany greater clear cover).

Strand Configurations B, E, and F with 600-psi concrete prestress and 8,000-psi concrete strength will maintain a cyclic service load limit equal to 80 percent of ultimate energy capacity while keeping residual crack width less than 0.012 inch and maximum compression concrete strain less than 0.0021 in/in (no compression zone damage).

FUTURE RESEARCH

The reaction forces expected from the concrete piles may be harsher on ships than wood for a given energy input from the ship. Camels or rub strips may be required for concrete fender pile applications. This will require further investigation after trial field installations to determine if it is a problem. Field tests should be conducted over 5 or more years with internal strain gaged pile, which will provide not only

a measure of pile performance but will serve as transducers for measurement of loads and impacts during berthings. Observations should continue over the installation lifetime.

The multiaxial state of stress in high strength concrete (confinement plus prestress) results in a higher compression capacity than currently allowed by conventional analysis (ACI). The ultimate strength, rectangular stress block coefficients currently being employed by ACI need reevaluation for high strength concrete applications.

The ultimate capacity of high strength concrete was limited by spalling of the concrete away from the compression face while failure was triggered by splitting of the concrete away from the tensile strands. These graphically demonstrated the impact of the fracture process and a limitation of structural concrete design. A complete understanding of fracture methodology and the variables affecting it must be acquired to develop techniques to mitigate spalling on the compression face and longitudinal splitting on the tensile side of high strength concrete structural elements. Ultimately, concrete fracture mechanics methodology must be developed for successful crack control in reinforced concrete.

ACKNOWLEDGMENT

Mr. Robert Julian, General Engineer, was the principal investigator of the program to develop a prestressed concrete fendering system. Dr. Javier Malvar, Associate Research Engineer, University of California, Los Angeles, directed the task of testing the short span piles. The author and Dr. Malvar were assisted by Mr. David Corrente, Engineering Technician, who prepared all test layouts and Mr. Michael Hanks, Electronics Technician, who prepared sensors and performed the instrumentation setups. All participants made equal contributions to the successful completion of the test program.

REFERENCES

1. Naval Facilities Engineering Command. NAVFAC TEMP: Development of prestressed concrete fender piles. Washington, DC, Jun 1984.
2. _____. Contract Report TM53-84-04: Concrete fender pile study. San Bruno, CA, T.Y. Lin International, Mar 1984.
3. Naval Civil Engineering Laboratory. Contract Report CR 86.009: Prestressed concrete fender piles - Analysis and final pile detailing. Washington, DC, ABAM Consulting Engineers, 4 Feb 1986.
4. _____. Contract Report CR 88.003: Development, analysis, design, and fabrication of prestressed concrete fender piles - Analyze test results. Washington, DC, ABAM Consulting Engineers and Ben C. Gerwick, Inc., Nov 1987.

5. W. L. Simon. Personal communication, William L. Simon & Associates, Denver, CO, Dec 1986.
6. R. W. Carlson. "Manual for the use of strain meters and other instrumentation for embedment in concrete structures," Fourth Edition, Berkley, CA, 1975.
7. Salvador Martinez Morales. Short-term mechanical properties of high strength lightweight concrete, Ph D Thesis, Department of Structural Engineering, Cornell University, Ithaca, NY, Aug 1982.

Table 1. Specimen Geometry

Pile Number	Configuration	Concrete Strength (psi)	Number of Strands	Effective Strand Prestress (ksi)	Effective Concrete Prestress (psi)	Spiral Size	Measured Spiral Pitch
MK1	A	9310	20	60	565	W11	2-
MK2	A	9410	20	60	565	W11	2-1/2
MK3	A	8980	20	60	565	W11	2-1/2
MK4	A	6300 (LW)	20	60	565	W11	3-3/4
MK5	B	9870	20	60	565	No. 3	3
MK6	B	8430	20	60	565	No. 3	3
MK7	A	9360	20	150	1417	W11	3
MK8	A	8600	20	150	1417	W11	3-3/4
MK9	C	8200	16	60	450	W5	3
MK10	C	7600	16	60	450	W5	3
MK11	C	8030	16	60	450	W5	3
MK12	C	8790	16	60	450	W5	3
MK13	C	8700	16	60	450	W5	3
MK14	C	8600	16	60	450	W5	3
MK16	C	8520	16	60	450	W5	4-1/2
MK17	C	8660	16	60	450	W5	4-1/2
MK18	C	8660	16	60	450	W5	4-1/2
MK19	C	8650	16	60	450	W5	4-1/2
MK20	C	9020 (FR)	16	60	450	W5	6
MK21	C	9020 (FR)	16	60	450	W5	6
MK22	D	8670	16	60	450	2-W5	3
MK23	C	8360	16	60	450	2-W5	3
MK24	D	8950	16	60	450	W5	3
MK25	E	7360	16	63.7	600	2-W5	3
MK26	E	7300	20	63.7	600	2-W5	3
MK27	E	7190	20	63.7	600	W5	3
MK28	F	7070	20	63.7	600	No. 3	3
MK29	A	7420	20	63.7	600	W11	3
COLO1	G	11500	14	VARIED	540	W6.5	4
COLO2	G	11500	14	VARIED	540	W6.5	6
COLO3	G	12500	14	VARIED	540	W6.5	6

NOTE: LW = Lightweight concrete.

FR = Steel fiber-reinforced concrete.

Table 2. Load-to-Failure Test Results

Pile	Concrete Strength (psi)	Span	Loading (monotonic or cyclic)	Cracking Moment (kip/ft)	Ultimate Moment (kip/ft)	Ultimate Deflection (in.)	Ultimate Energy (ft/kip)	Total Energy (ft/kip)	Ultimate Strain (10^{-6})*
MK3	898C	58	M	110	409	18.7	38	50	3300
MK3A	900C	30	M	-	433	7.9	34	48	3320
MK4	630C	58	M	90	369	17	26	39	3280
MK5	987C	58	M	90	455	18.3	42	63	3210
MK6	8430	58	M	110	455	17.7	40	67	3310
MK6A	850C	30	M	-	420	7.4	25	50	3290
MK7	9360	58	M	180	425	10	22	37	2950
MK8	8600	58	M	200	421	9.1	20	38	3050
MK8A	8600	30	M	-	408	5	22	34	3280
MK9	8200	30	M	131	439	8.2	26	98	3600
MK10	7600	30	M	148	417	7.5	22	78	3200
MK13	8700	30	M at 7ft	141	435	5.7	25	74	3300
MK14	8660	30	M at 7ft	141	437	5.9	26	46	3600
MK16	8520	30	M	150	430	8.1	25	59	3400
MK17	8660	30	M	149	417	7.9	23	60	3600
MK18	8650	30	M	145	434	7.9	24	84	3600
MK20	9020	30	M	152	461	8	28	42	3800
MK22	8670	30	M	120	405	7.8	22	76	3900
MK23	8360	30	M	130	398	8.2	25	48	3600
MK24	8950	30	M	128	414	7.9	25	77	3900
COL01	11500	30	M	122	477	8	27	97	
COL02	11500	30	M	123	443	7.4	24	49	
MK1	9310	58	C/M**	120	445	19.8	38	46	(200)* 2600
MK5A	9900	30	C/M**	90	455	18.3	14	54	(600)* 3200
MK11	8030	30	C/M**	142	325	10.8	17	56	(1000)* 4100
MK12	8790	30	C/M**	142	421	7.6	20	60	(1100)* 2300
MK19	8840	30	C/M**	136	393	8	18	94	
MK21	9080	30	C/M**	157	453	8.2	26	50	(300)* 3800

Table 2. Continued

File	Concrete Strength (psi)	Span	Loading (monotonic or cyclic)	Cracking Moment (kip/ft)	Ultimate Moment (kip/ft)	Ultimate Deflection (in.)	Ultimate Energy (ft/kip)	Total Energy (ft/kip)	Ultimate Strain (10 ⁶)*
MK2	9140	58	C**	110	422	16.8	32	43	3000
MK25	7360	30	C**	124	386	5.8	12	88	-
MK26	7300	30	C**	127	345	5.4	11	82	-
MK27	7190	30	C**	115	330	4.8	9	72	-
MK28	7070	30	C**	105	345	5.5	11	72	-
MK29	7420	30	C**	116	315	5.3	10	57	-
COL03	12500	30	C**	126	429	7.2	15	64	-

*Number in parenthesis indicate residual strain at the end of the cyclic loading

**Final cycle response after various service load cycles.

Table 3. Cyclic Load Test Results

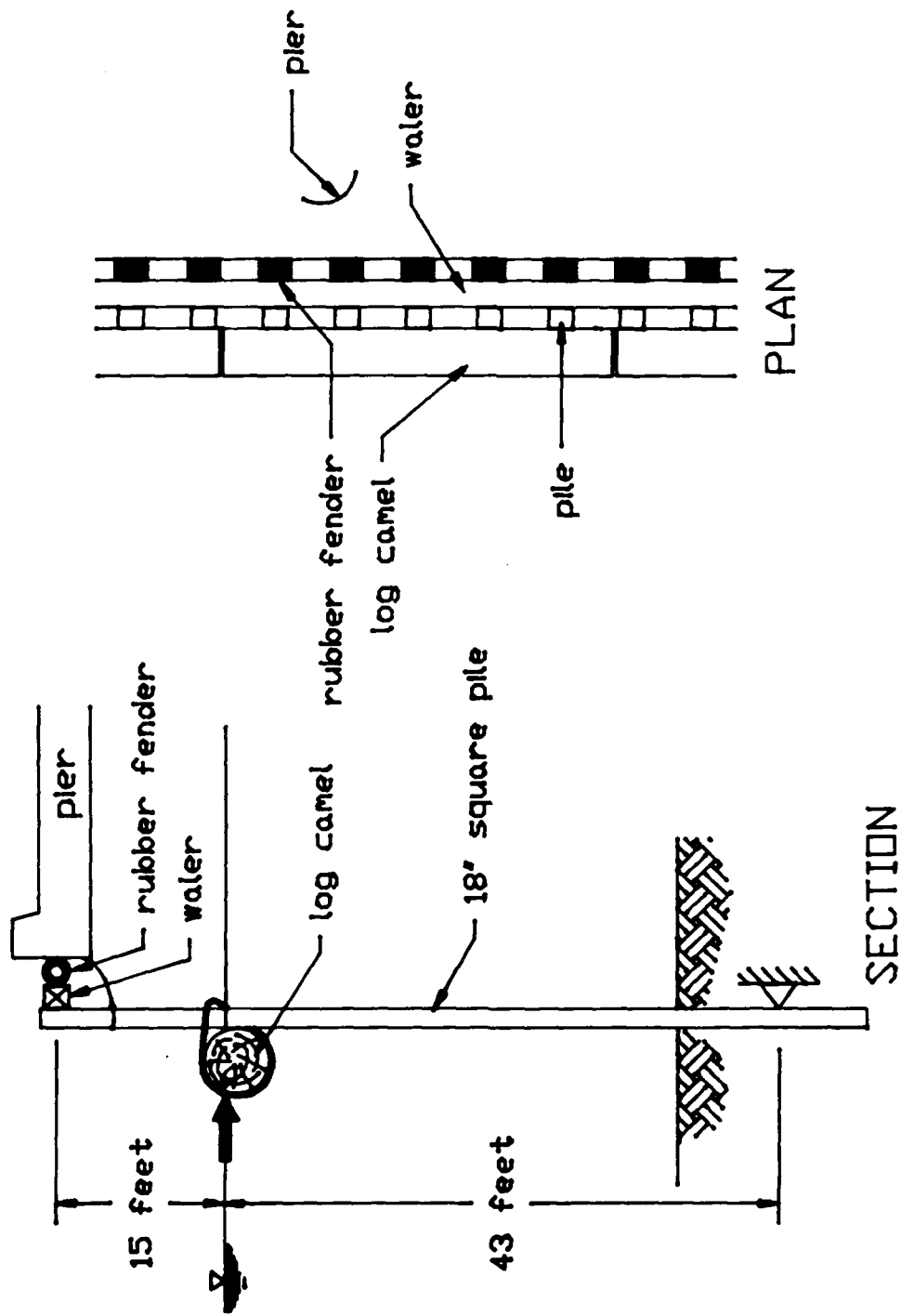
Pile	Concrete Prestress (psi)	Concrete Strength (psi)	Number of Cycles	Load (kips)	Closed Crack Width (in.)	Measured Concrete Strain (uE)*	Model Concrete Strain (uE)	Measured Energy Per Cycle (ft/kips)**	Model Energy Per Cycle (ft/kips)**	Model Steel Stress (ksi)	Compression Zone Damage
MK11	450	8000	209	43.4	.190	2610	2500	12	12	237	Yes
MK12	450	8800	300	33	.020	1620	1550	6	6	180	No
			200	38.5	.035	2190	1850	7.6	8.5	210	No
MK13	450	8700	100	43.4	.058	2370	2300	12.1	12	235	Yes
MK14	450	8700	100	43.4	.051	2250	2300	11.9	12	235	No
MK19	450	8800	100	41.2	.054	2220	2100	11	10.5	226	Yes
MK21	450	9000	10	43.4	.017	2130	2300	10.8	12	235	No
MK5A	568	9900	250	43.4	.004	1560	1850	8	8.6	187	No
				50	.007	1900	2250	9.5	12.2	219	No
MK25		7360	1	55	.009	2260	2700	12.5	15.6	238	Yes
			50	43.4	.004	1832 (0)	2200	10.5	8.9	202	No
			50		.014	2130 (186)		9.4			
			100		.020	2292 (260)					
			150		.023	2367 (335)					
			200		.029	2404 (372)					
MK26		7300	Last	51.5	-	-	-	87.8	-	-	No
			1	38	.008	1593 (0)	1786	6.5	6.2	174	
			50		.009	2016 (126)		6.1			
			50	40	.012	2452 (322)	1933	6.7	7.1	184	No
			50	42	.021	2827 (536)	2100	7.8	8.1	195	No
			50	44	.027	3207 (431)	2282	8.8	9.3	206	No
			11	46	-	-	2471	9.6	10.5	217	Yes
			Last		-	-		81.5	-	-	-
MK27		7190	1	40	.006	1711 (66)	1958	7.8	7.1	185	No
			50		.011	2160 (261)		7.1			
			100		.015	2393 (374)					
			150		.020	2505 (457)					
			50	42	.026	2766 (616)	2127	8.4	8.2	196	No
			50	44	.031	2994 (682)	2290	9.1	9.1	206	Yes
			100		.036	-					
			117		-	-					
			Last		-	-		72	-	-	

Table 3. Continued

Pile	Concrete Prestress (psi)	Concrete Strength (psi)	Number of Cycles	Load (kips)	Closed Crack Width (in.)	Measured Concrete Strain (μE)*	Model Concrete Strain (μE)	Measured Energy Per Cycle (ft/kips)**	Model Energy Per Cycle (ft/kips)**	Model Steel Stress (ksi)	Compression Zone Damage
MK28	7070		1	39	.002	1578 (10)	1893	6.8	6.7	180	No
			50		.004	1747 (64)		6.3			
			100		.007	1950 (68)					
			150		.009	2044 (150)					
			50	42	.011	2307 (188)	2155	8.2	8.2	196	No
			100		.013	2382 (188)					
			50	44	.017	-	2340	9.1	9.4	207	Yes**
			100		.018	-					
			50	46	.024	-	2550	10.3	10.7	218	
			100		.034	-					
MK29	7420		148		-	-					
			Last		-	-					
			1	38	.004	1644 (37)	2081	72.2	-	195	No
			50		.008	1938 (98)		8.1	7.2		
			100		.010	2049 (112)					
			150		.015	2124 (167)					
			50	40	.023	2165 (130)	2300	8.8	8.4	209	Yes**
			100		.027	-					
			50	42	.033	-	2543	9.4	9.7	221	
			52		-	-					
COLO3			Last		-	-	-	56.8	-		
			250	43.4	.038	2250 (150)	2100	10.0	10.3	185	Yes

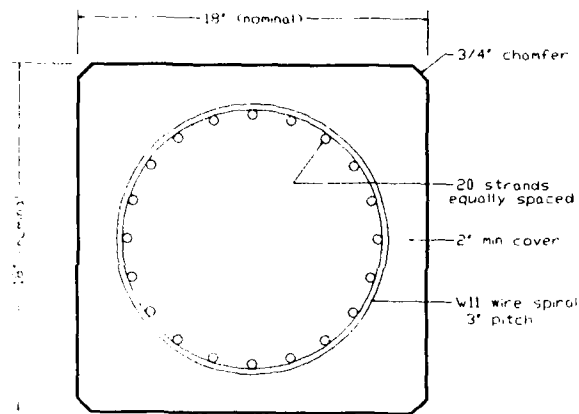
*Number in parenthesis are residual strains after load removed.

**The indicated energy corresponds to the first cycle. It is about 10 percent higher than for successive cycles at the same load level

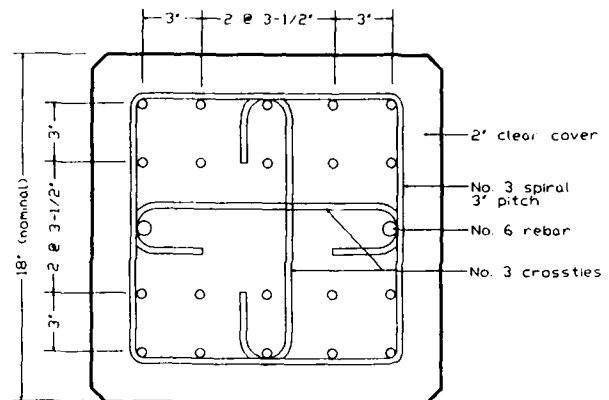


FENDER SYSTEM LAYOUT

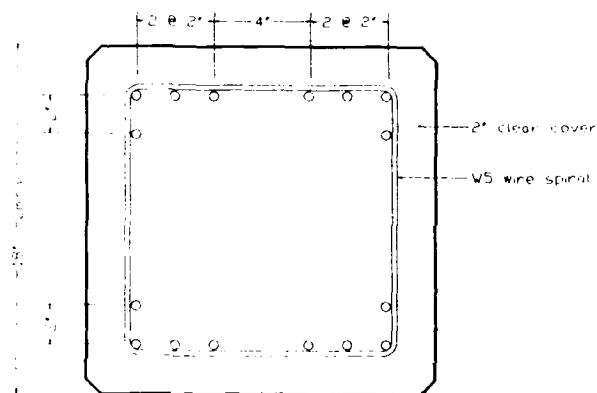
Figure 1. Schematic of prestress concrete fender system concept.



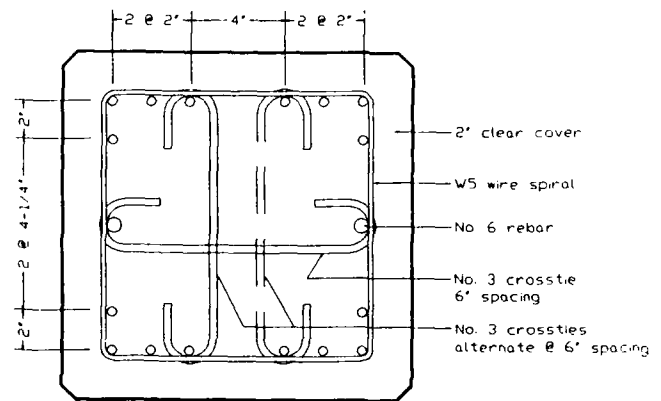
CONFIG (A)



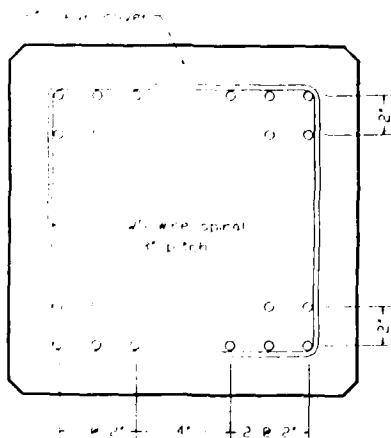
CONFIG (B)



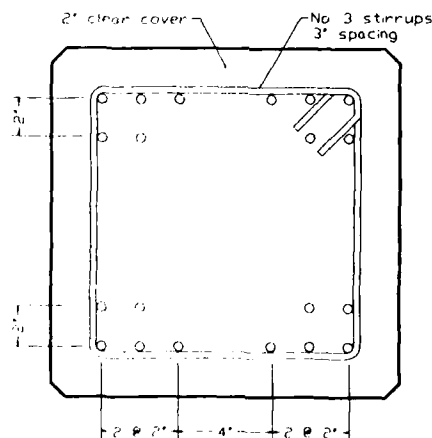
CONFIG (C)



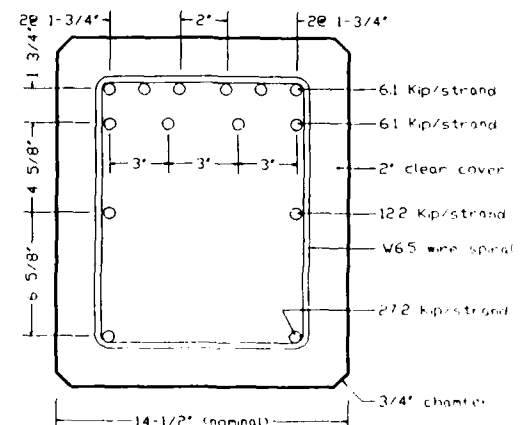
CONFIG (D)



CONFIG (E)



CONFIG (F)



CONFIG (G)

Figure 2. Prestress concrete fender pile cross-section configuration concepts.

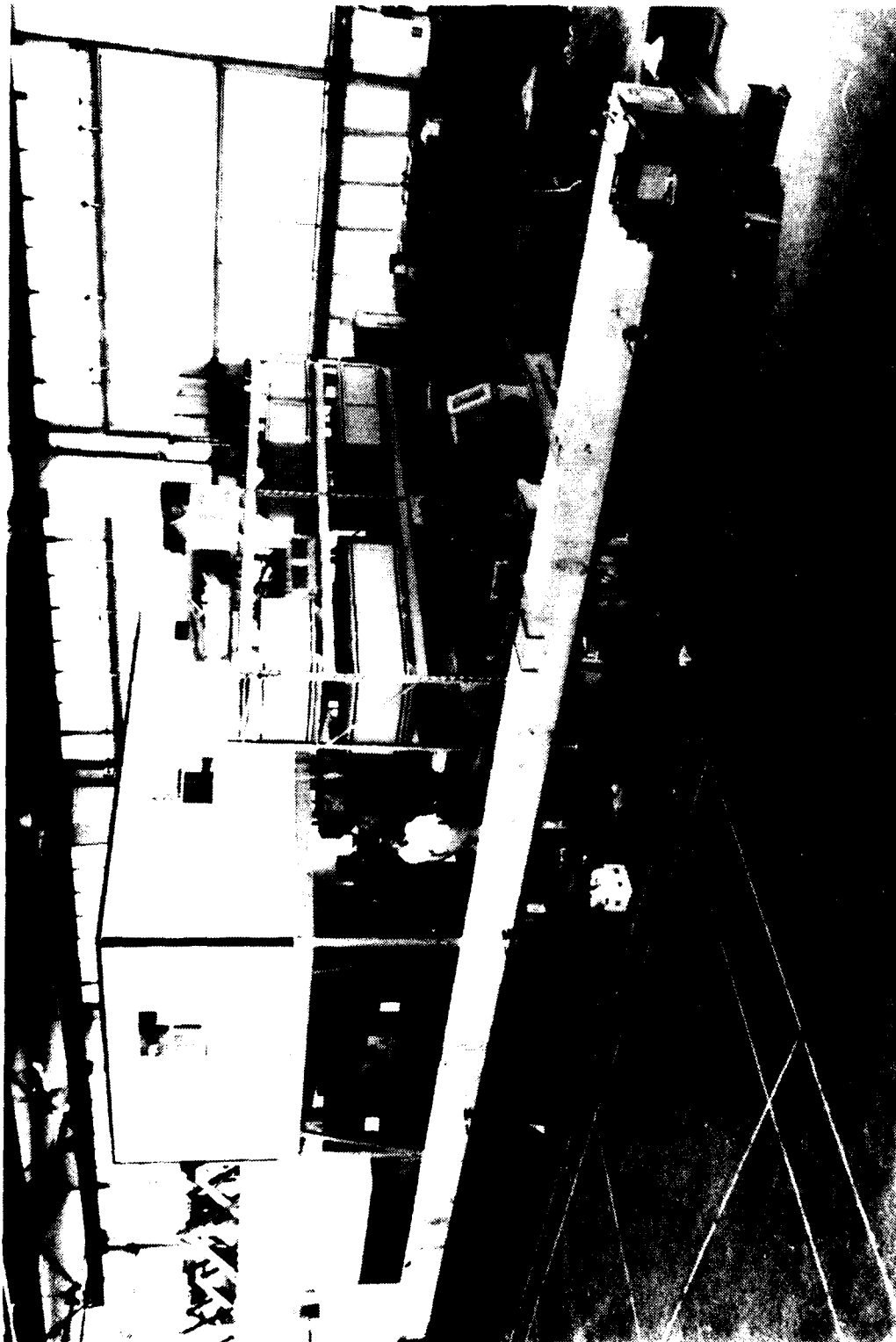


Figure 3. Photograph of laterally loaded test setup.

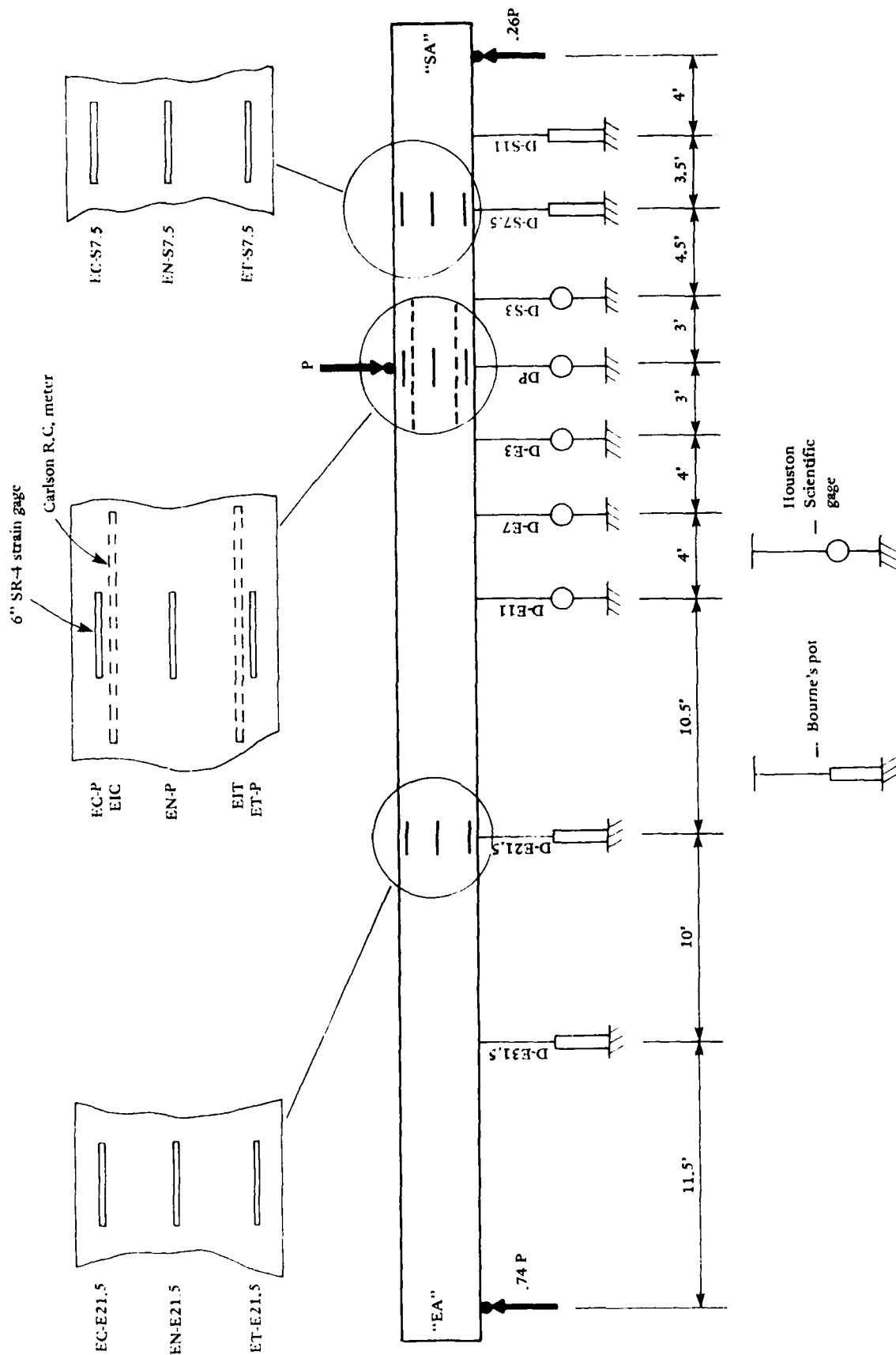


Figure 4. Deflection and strain gage layout for long span tests.

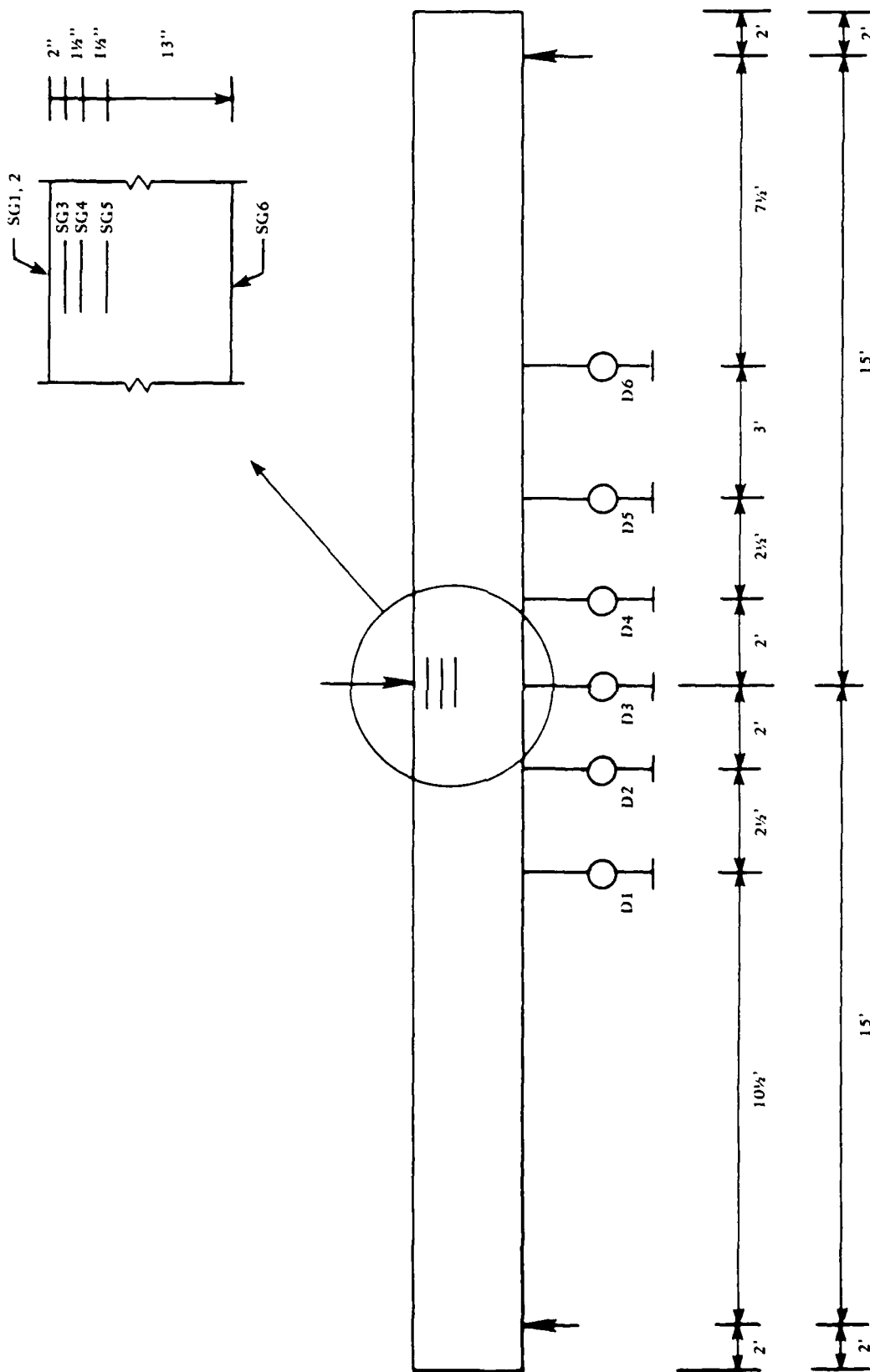


Figure 5. Loading schematic and gage layout for short span tests.

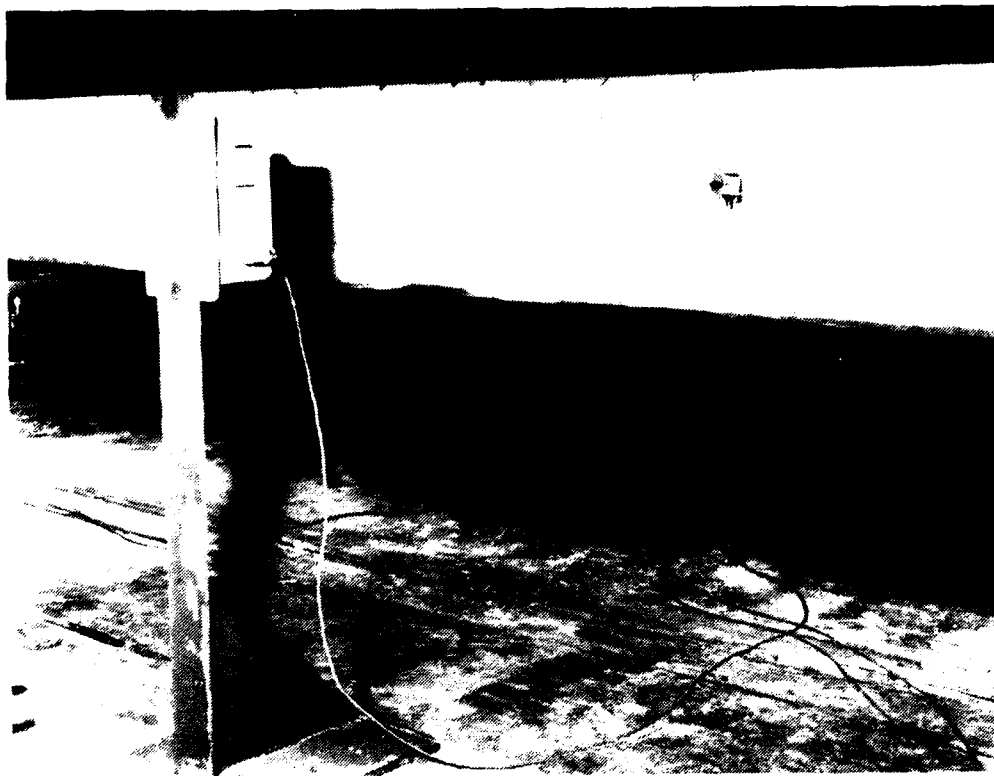


Figure 6. Houston Scientific linear potentiometer with 5-foot range.

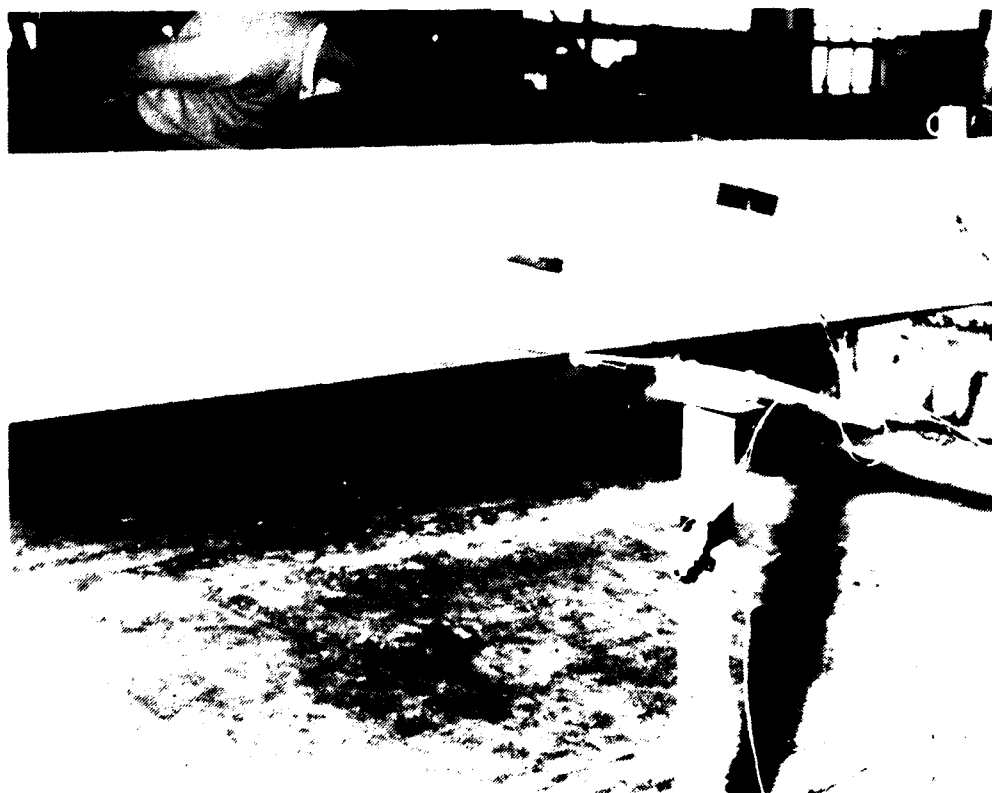


Figure 7. Bourne's linear potentiometer with 12-inch range.



Figure 8. Avongard crack gage.



Figure 9. Clip gages for crack width measurements.



Figure 10. SR-4 strain gages with bridges mounted to the side of test pile.

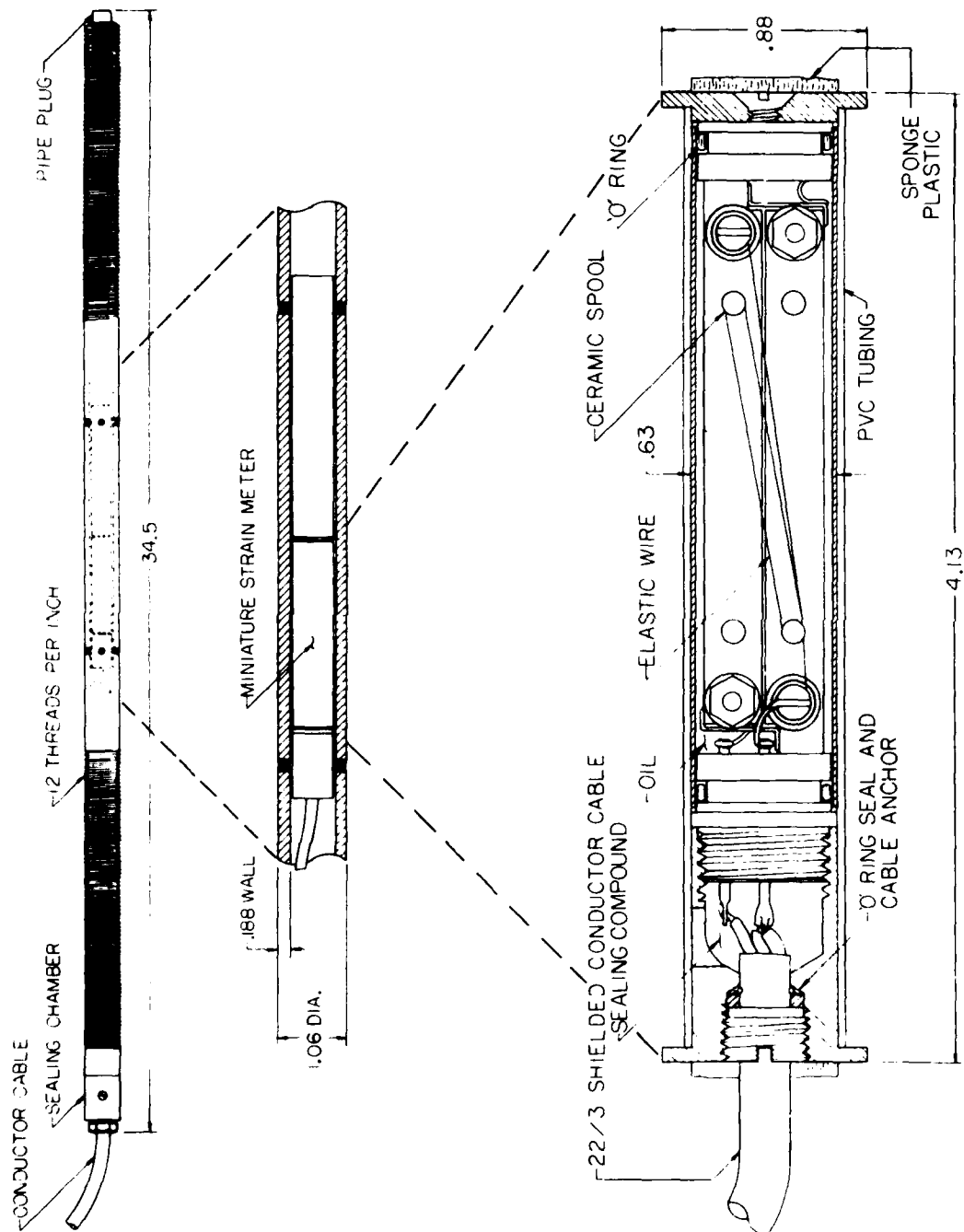


Figure 11. Carlson Reinforced Concrete (RC) strain meter.

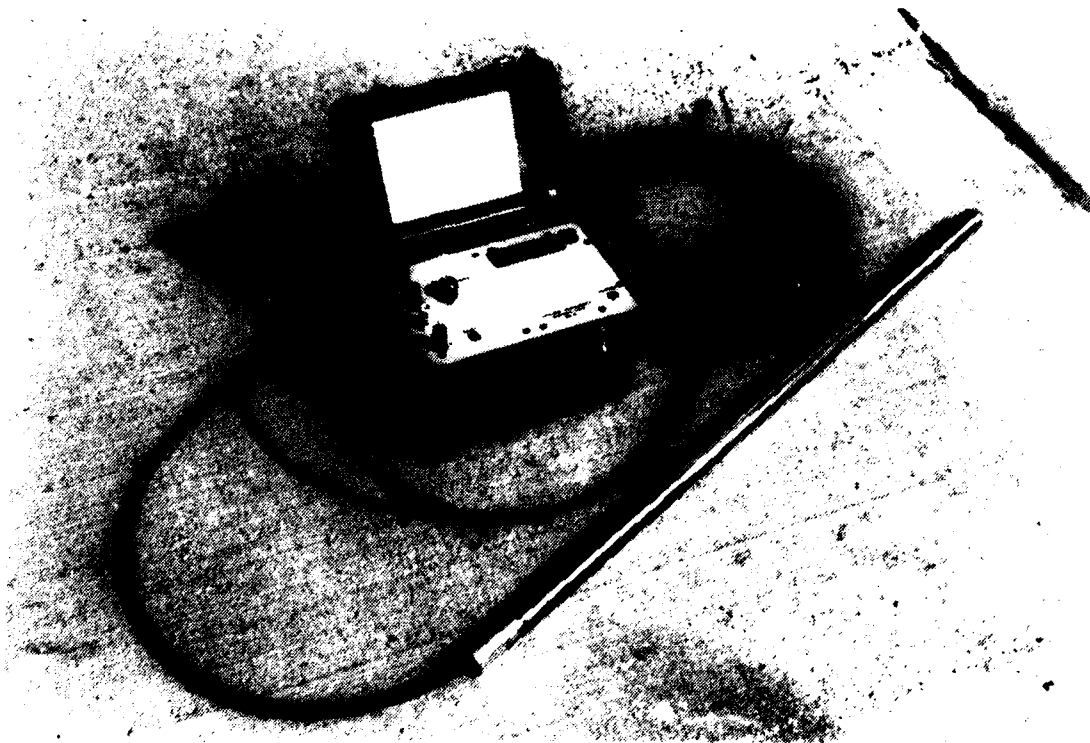


Figure 12. Carlson RC meter and MA-4 test set.

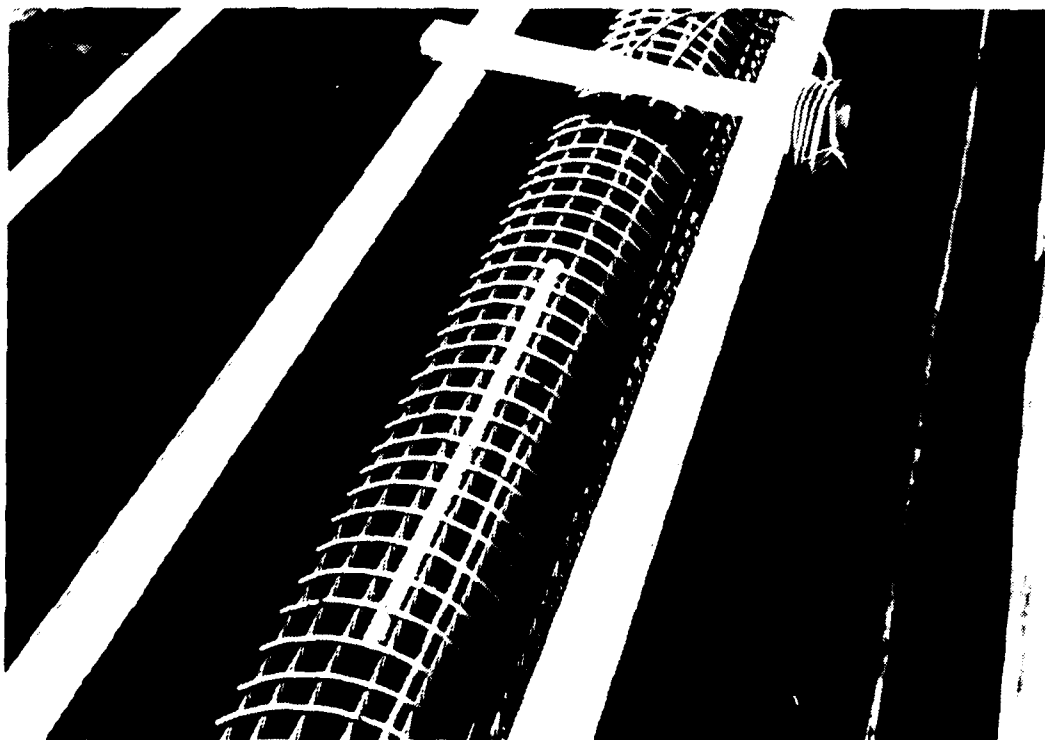


Figure 13. Carlson RC meter tied inside reinforcing cage at load point.

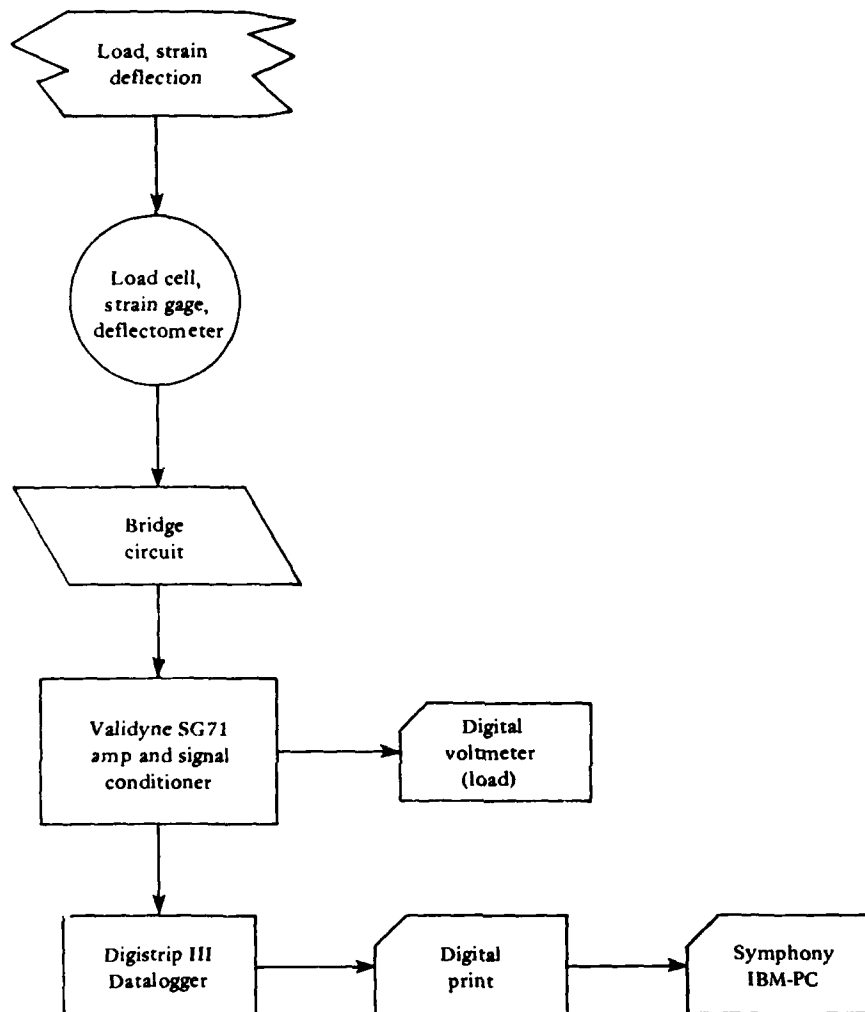


Figure 14. Data chain diagram for long span tests.



Figure 15. SR-4 strain gages location at point of load application.

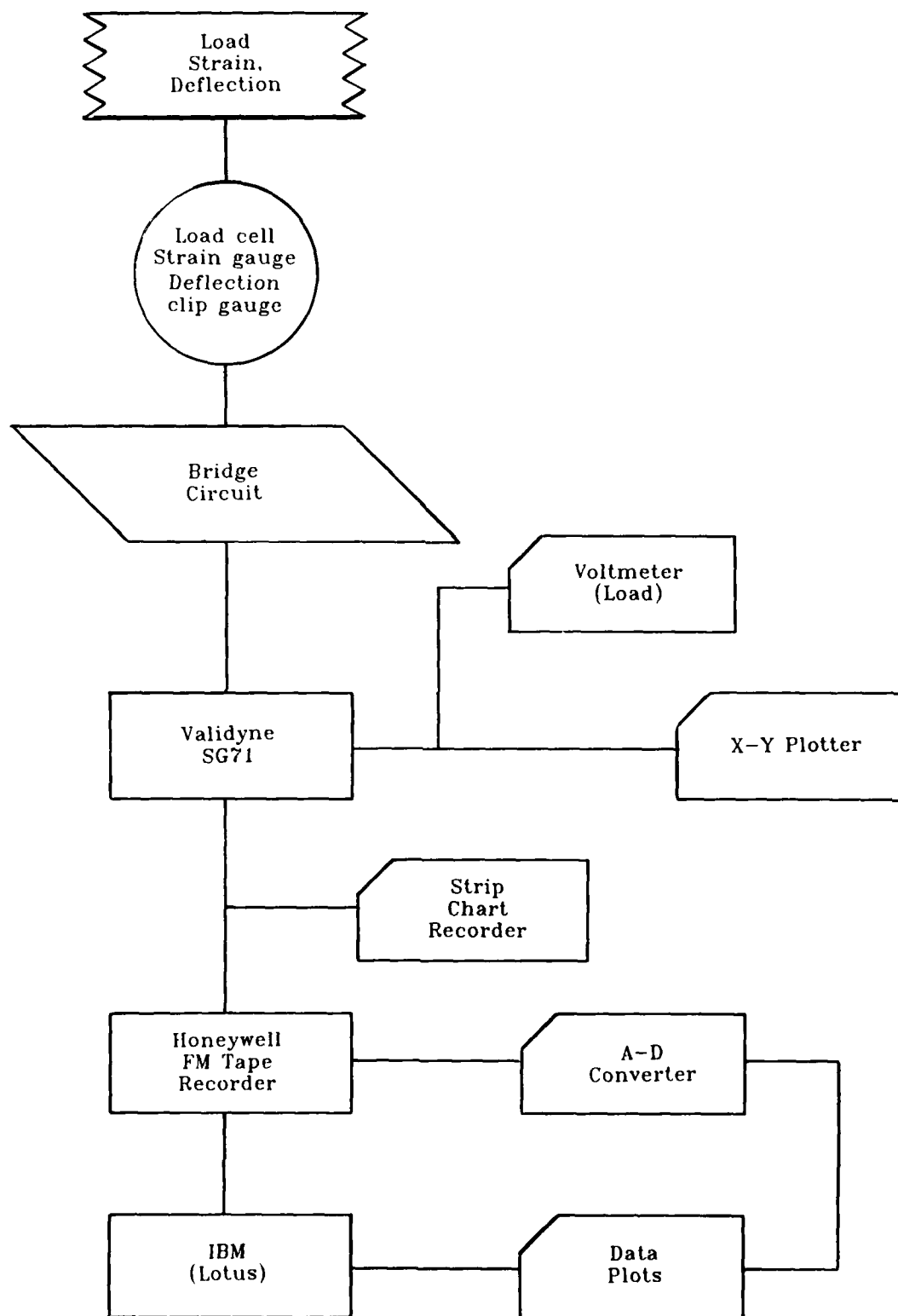


Figure 16. Data chain for short span tests.

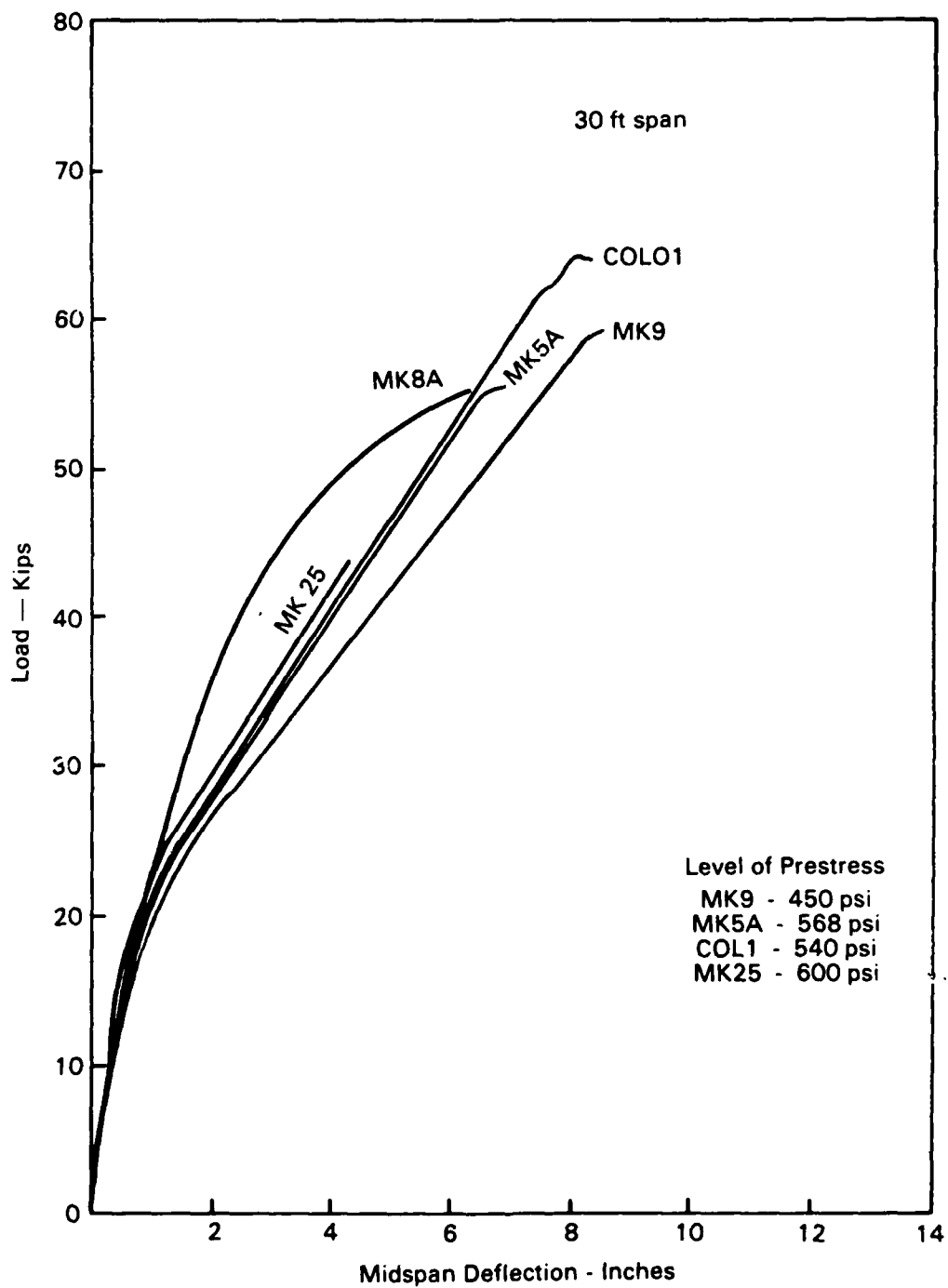


Figure 17. Preultimate load-deflection plots.

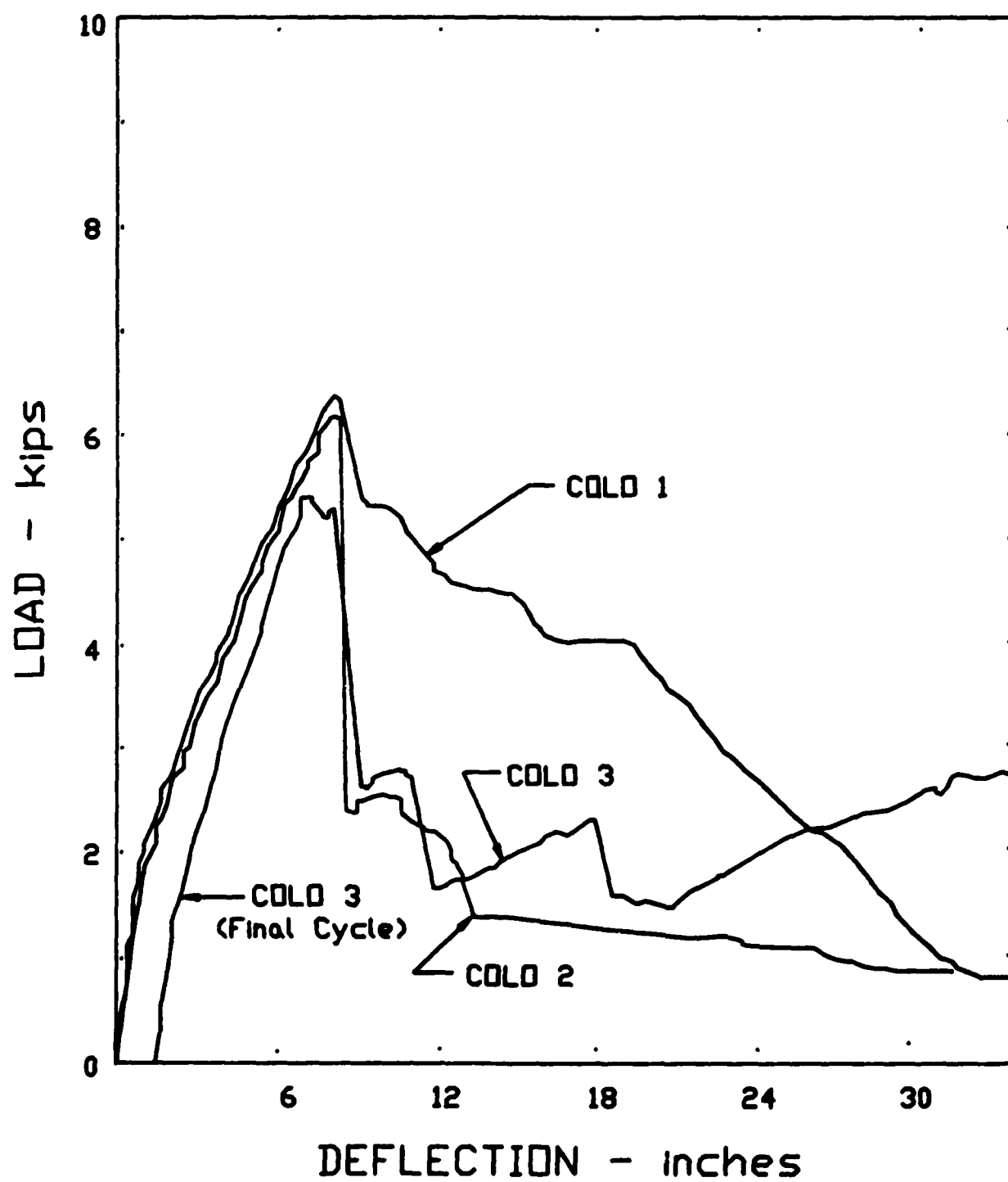


Figure 18. Load-deflection plots for COLO piles.

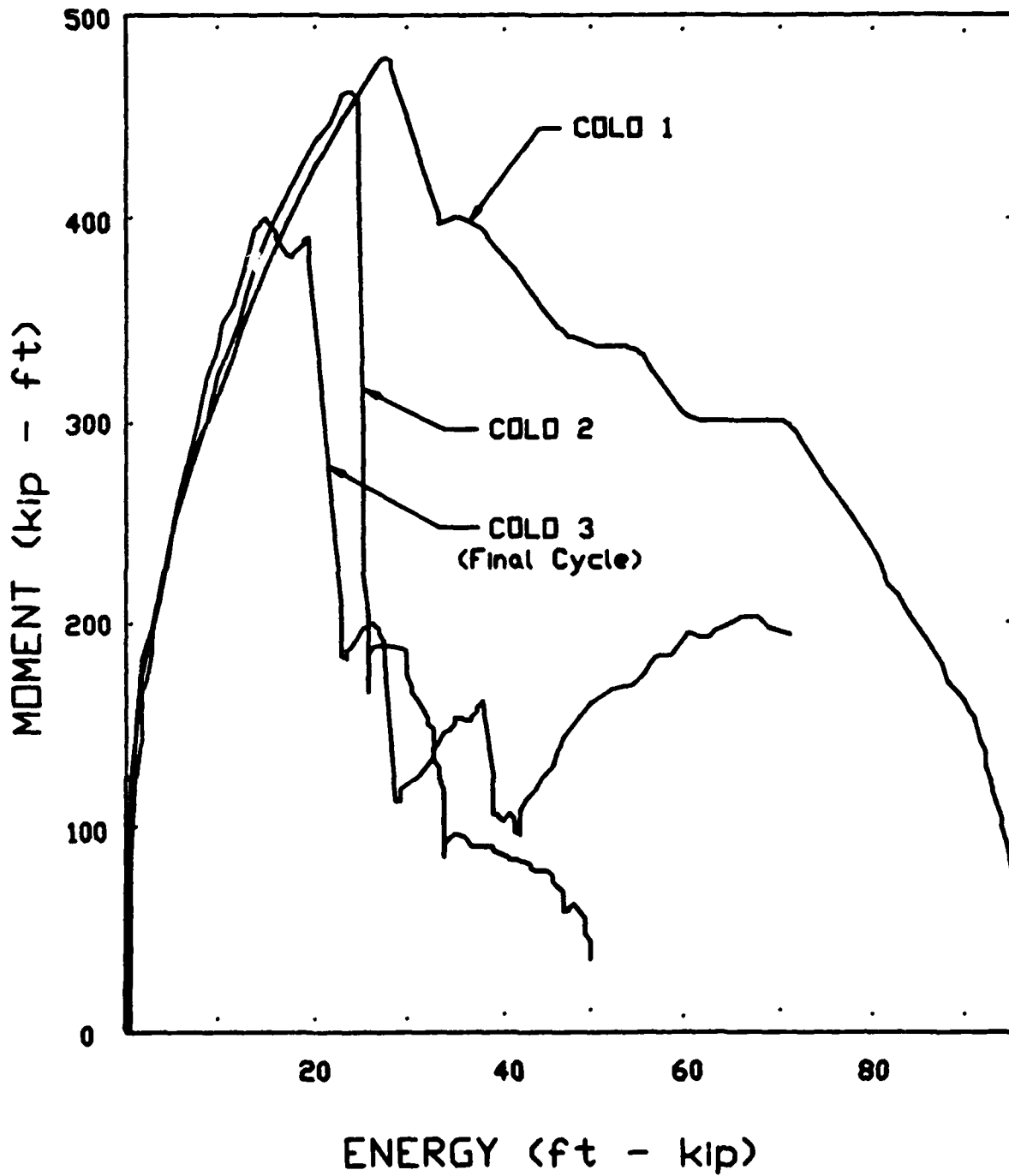


Figure 19. Moment-energy plots of COLO piles.

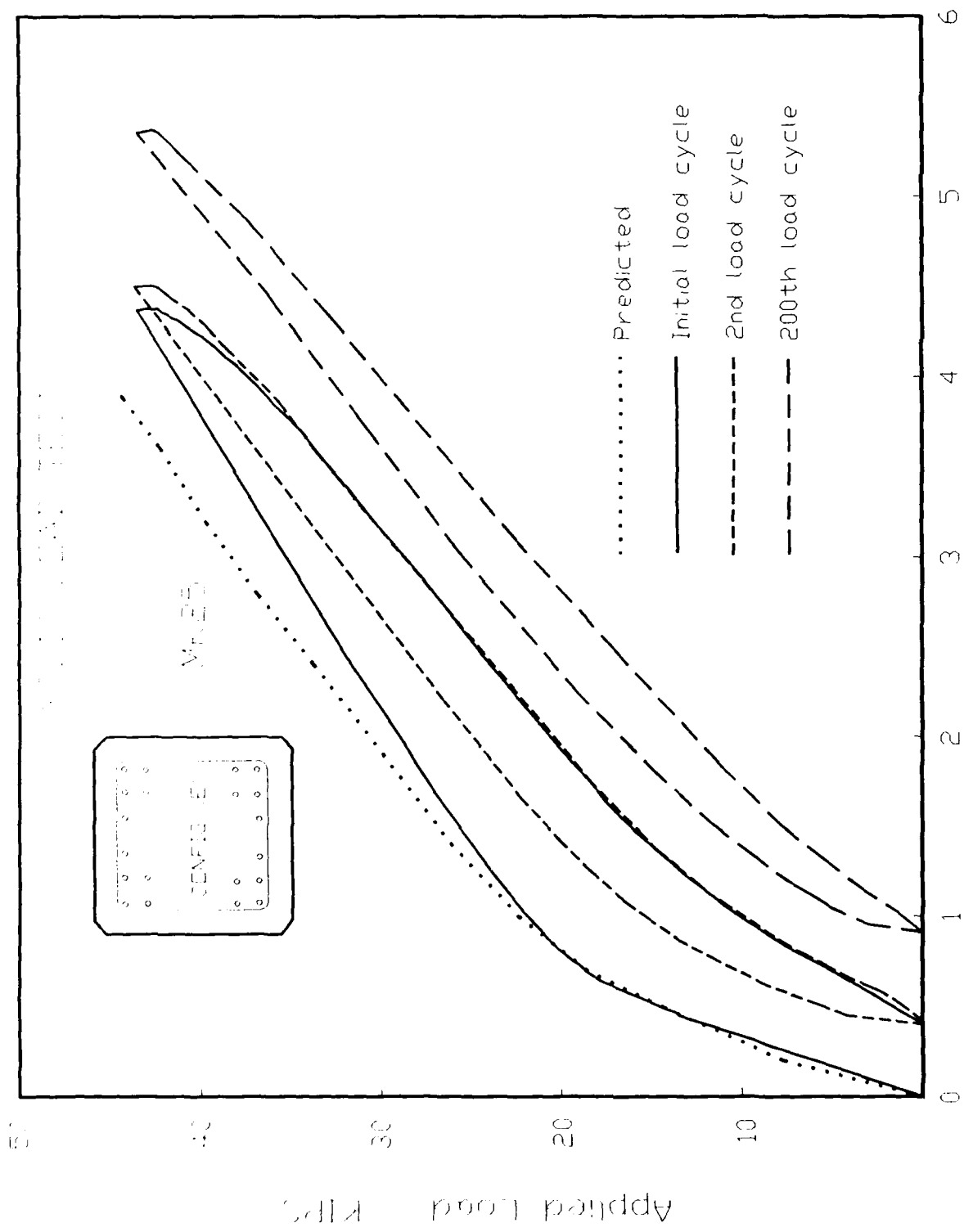


Figure 20. Cyclic load-deflection plots for MK25.

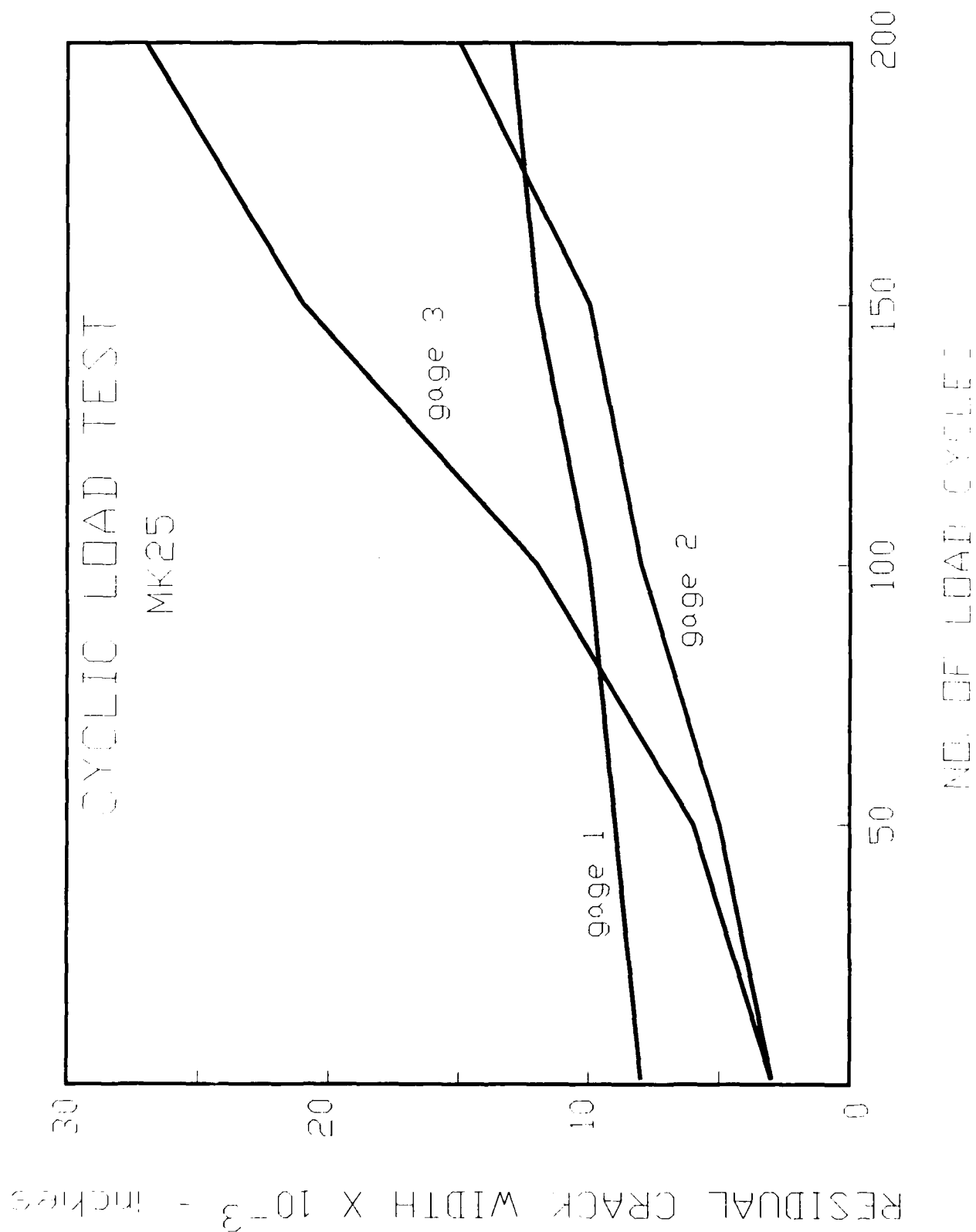


Figure 21. Residual crack width for MK25 during cyclic loading.

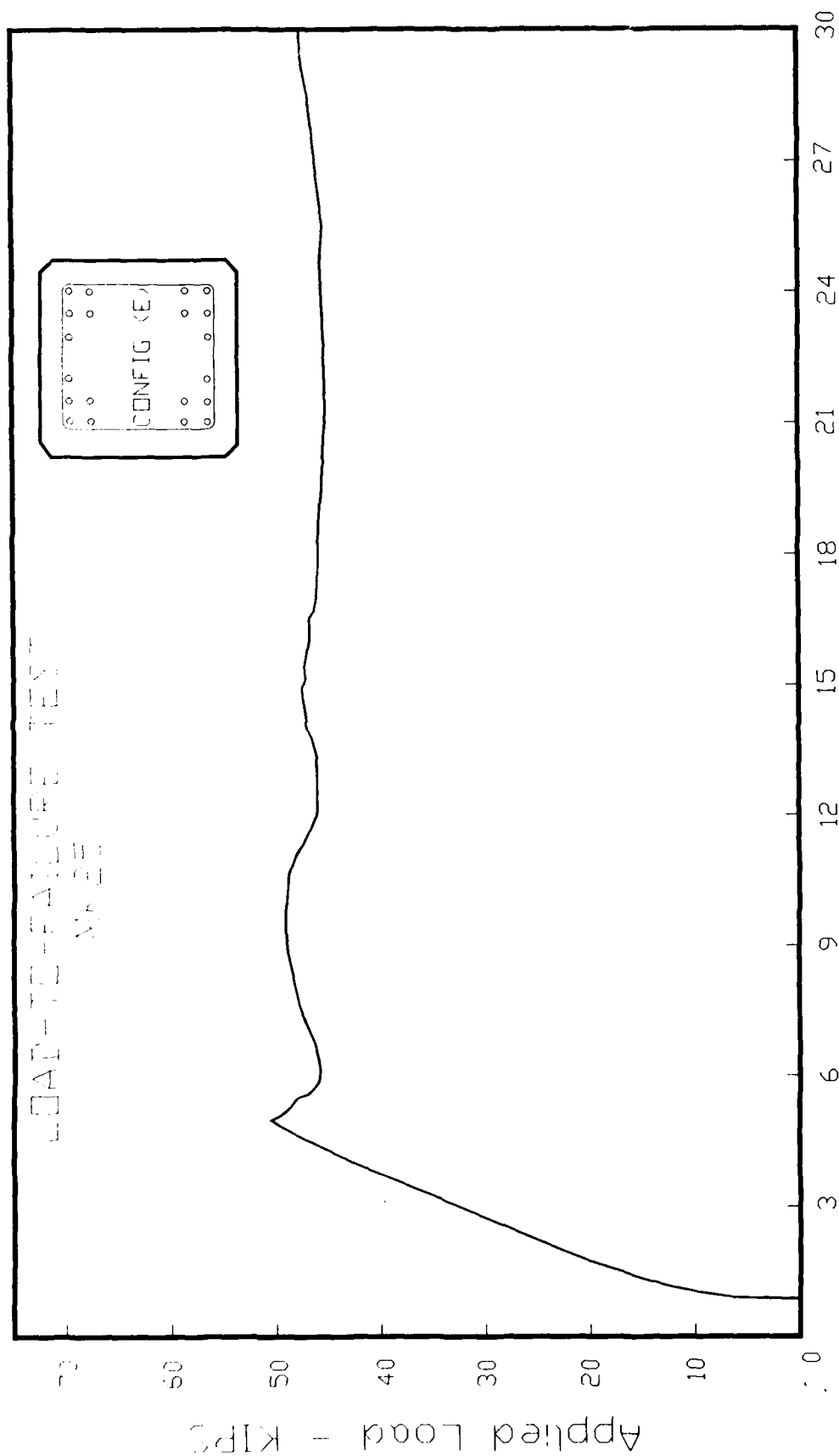


Figure 22. Final load-to-failure deflection plot for MK25 featuring extended plastic zone.

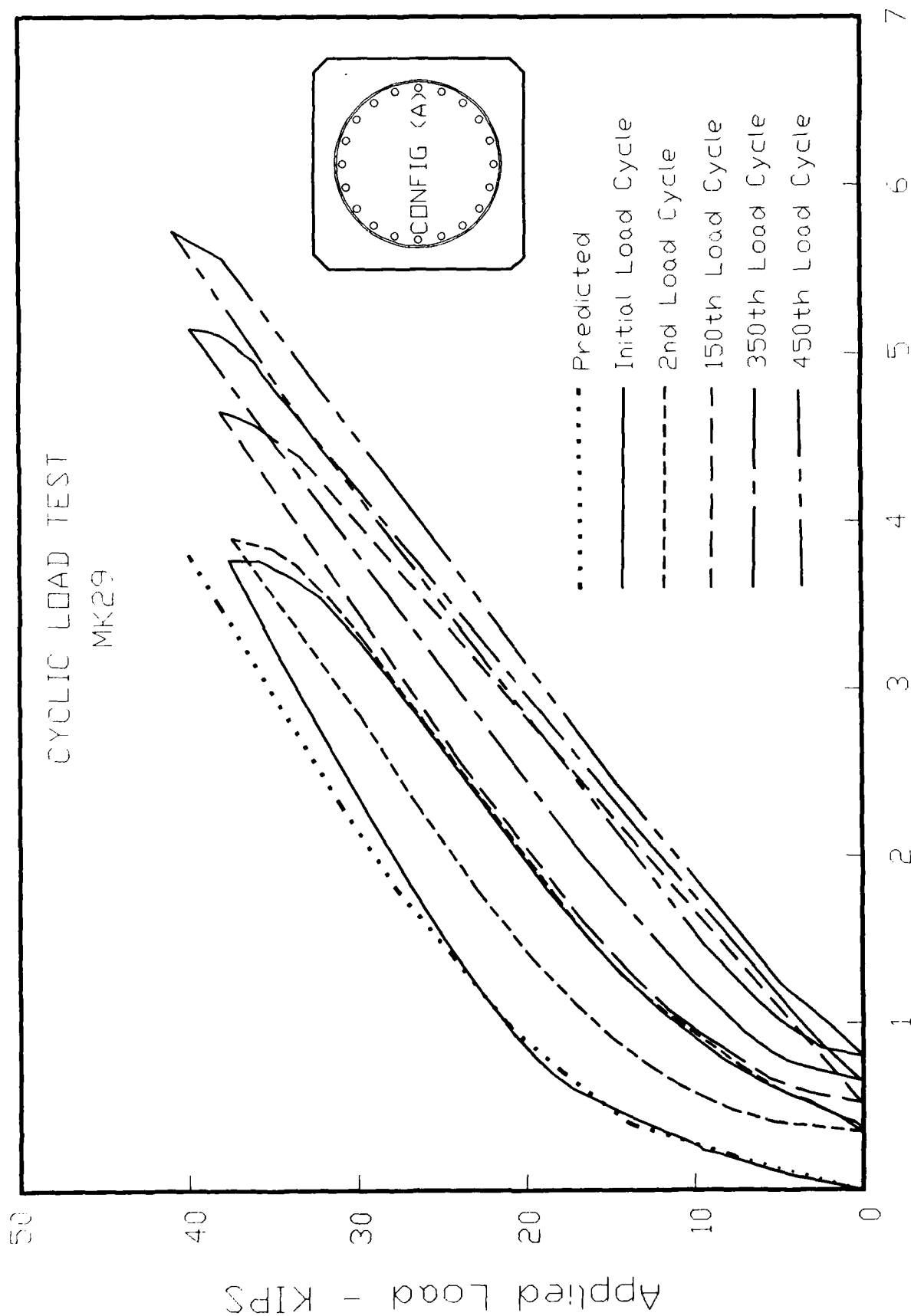


Figure 23. Cyclic load-deflection response of MK29.

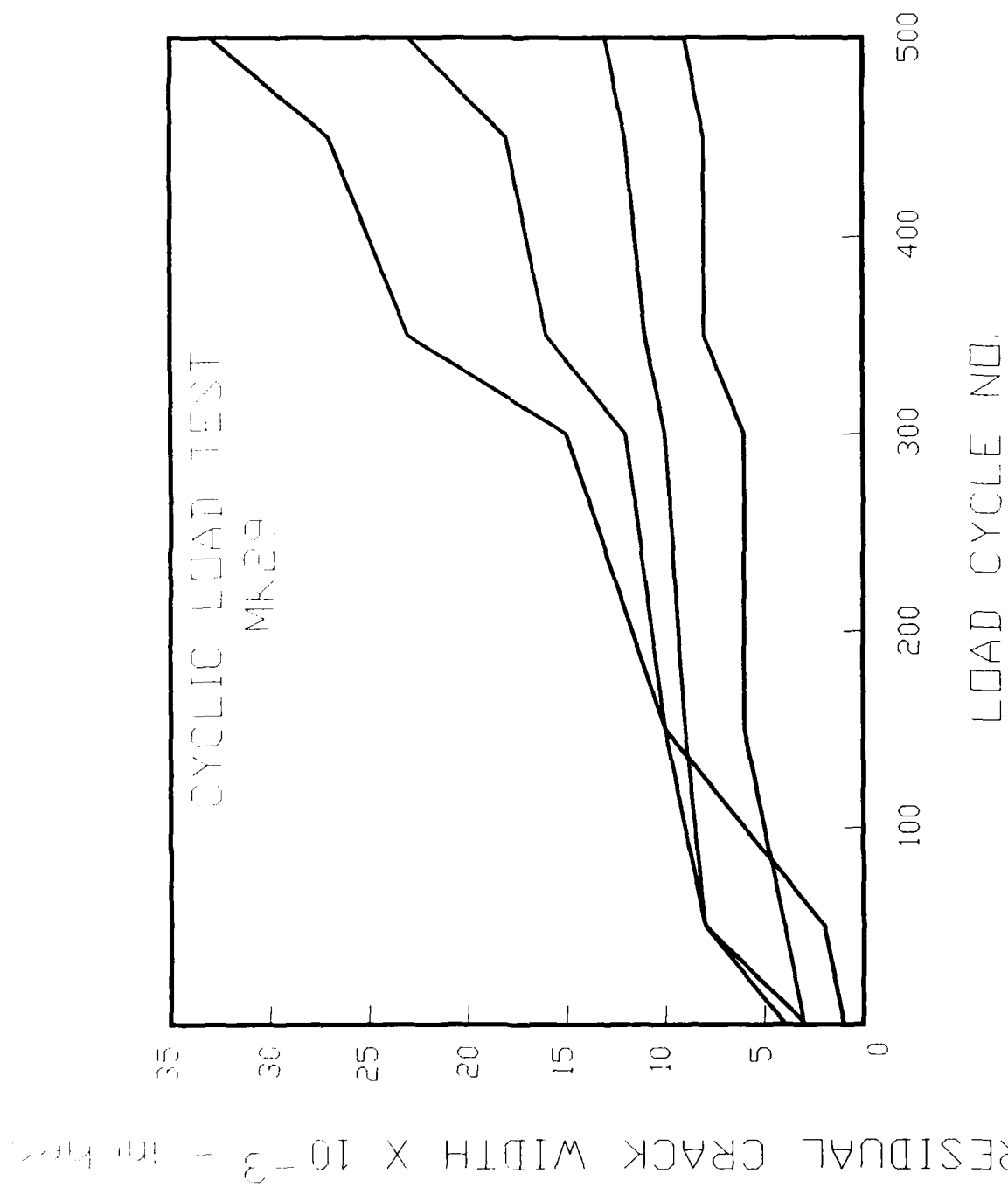


Figure 24. Residual crack width during load cycling of MK29.

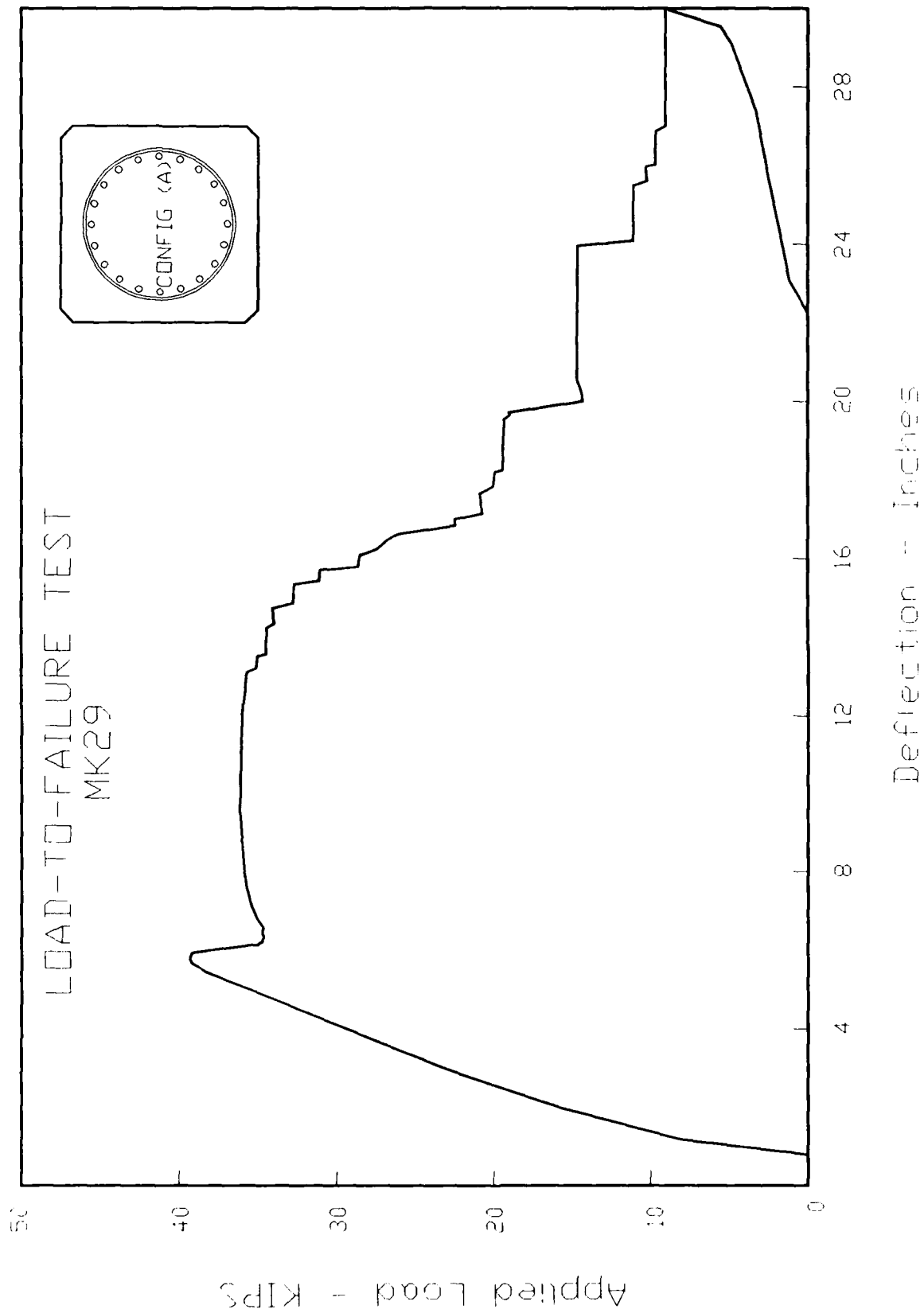


Figure 25. Final load-to-failure deflection plot for MK29 featuring short plastic zone and systematic tensile strand rupture.

Appendix A

TEST PILE FABRICATION

The test piles were fabricated in accordance with the construction drawings in Figures A-1 through A-12 by J. H. Pomeroy, Incorporated of Petaluma, California, and William L. Simons and Associates of Denver, Colorado. Figure A-13 shows the prestress tendon/spiral cage from the anchored end of MK1, MK2, and MK3. Figure A-14 shows the pouring of the second batch of concrete used to cast the first three piles.

The piles were cast in the morning and the prestress release was made the following morning. During the time period between casting and release, piles and test cylinders were steam cured. A cylinder break was made for each of the concrete batches just prior the the prestress release. Release strengths as well as prestressing are tabulated in Table A-1. After prestress release, the tendons were torched at the ends and the piles were removed from the forms by crane using lifting hooks and placed on blocks for air curing until shipment. Test piles were delivered by truck with a flatbed trailer where they were placed on timber supports outside the test lab or placed from the truck trailer directly onto the test frame using two forklifts lifting at the cast-in lifting hooks.

A-1/A-2

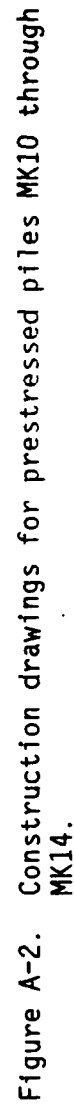
Table A-1. Test Pile Prestress

Test Pile	Prestress Transfer Strain ^a (μ in./in.)	Pretest Strain (μ in./in.)	Initial Prestress ^b (kips)	Prestress Loss ^c (kips)	Effective Prestress (kips)
MK1	50	190	207	17	190
MK2	46	192	207	17	190
MK4	82	293	214	26	188
MK5	212	306	207	27	180
MK7	646	770	515	68	447

^a Carlson RC meter readings.

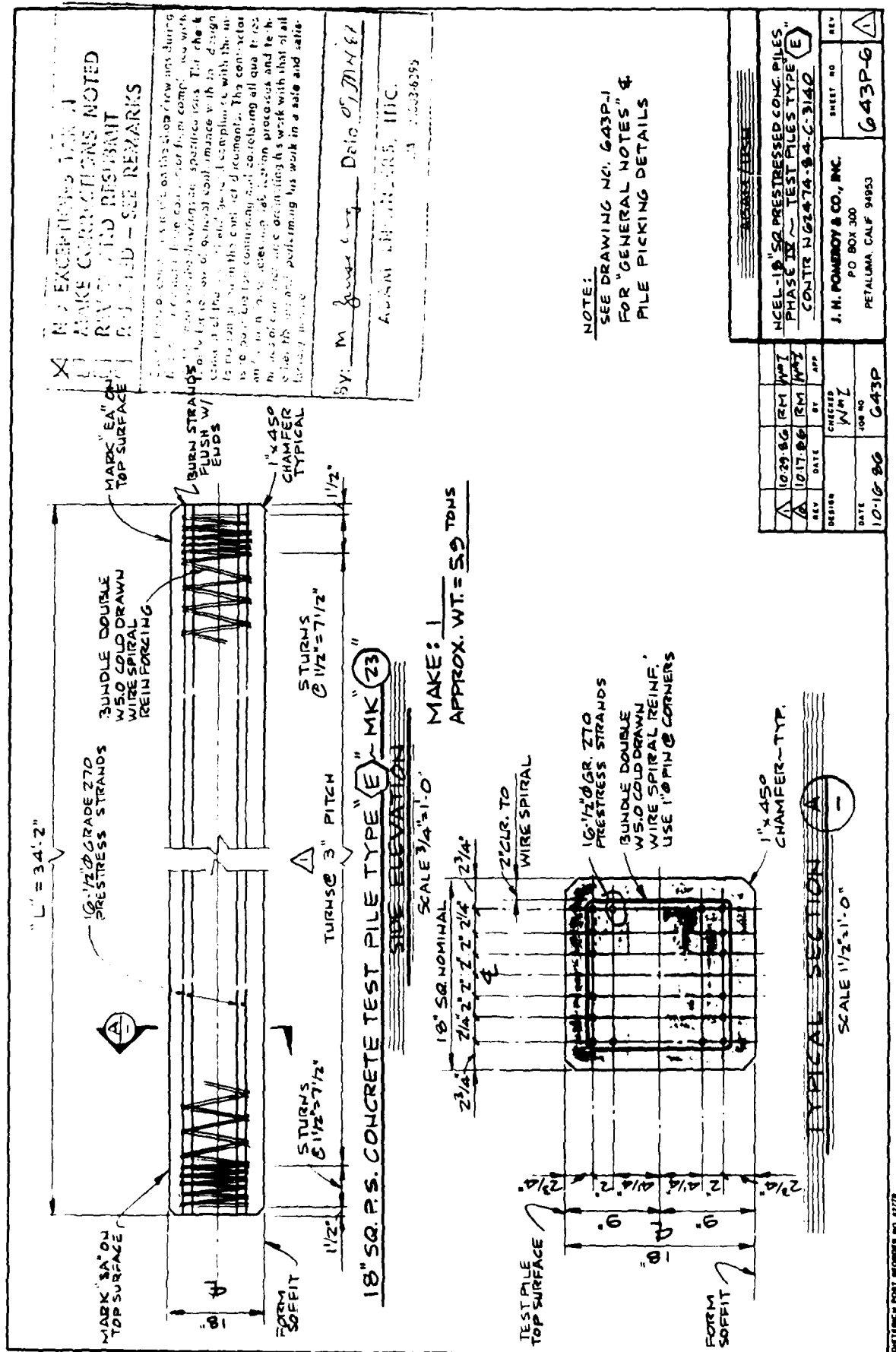
^b Design values.

^c $E_s = 29 \times 10^6$ psi and strand area = 0.153 in².



CONFIDENTIAL - ONLY MEMBERS NO 12218

A-6



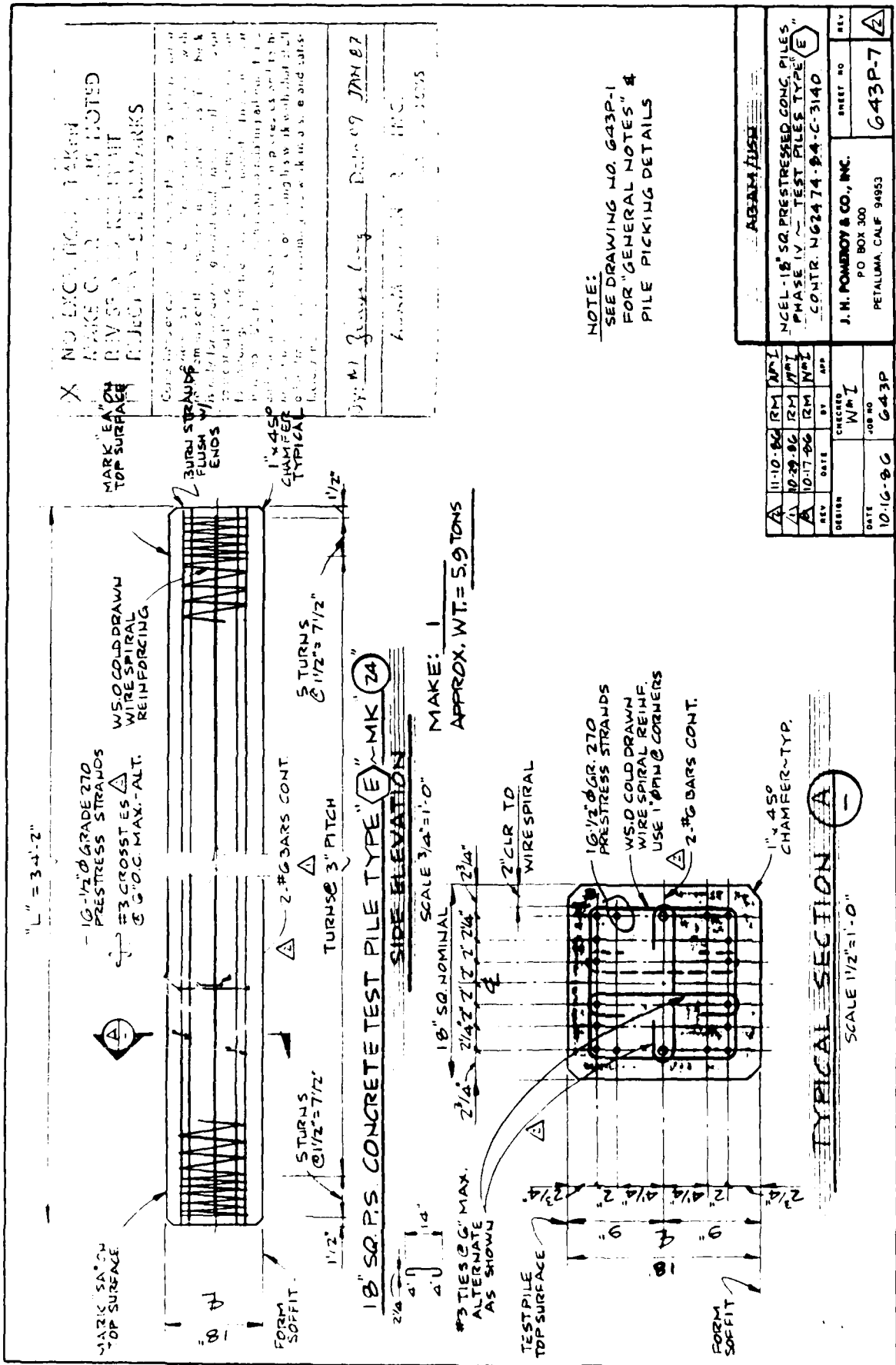


Figure A-7. Construction drawings of prestressed pile, MK24.

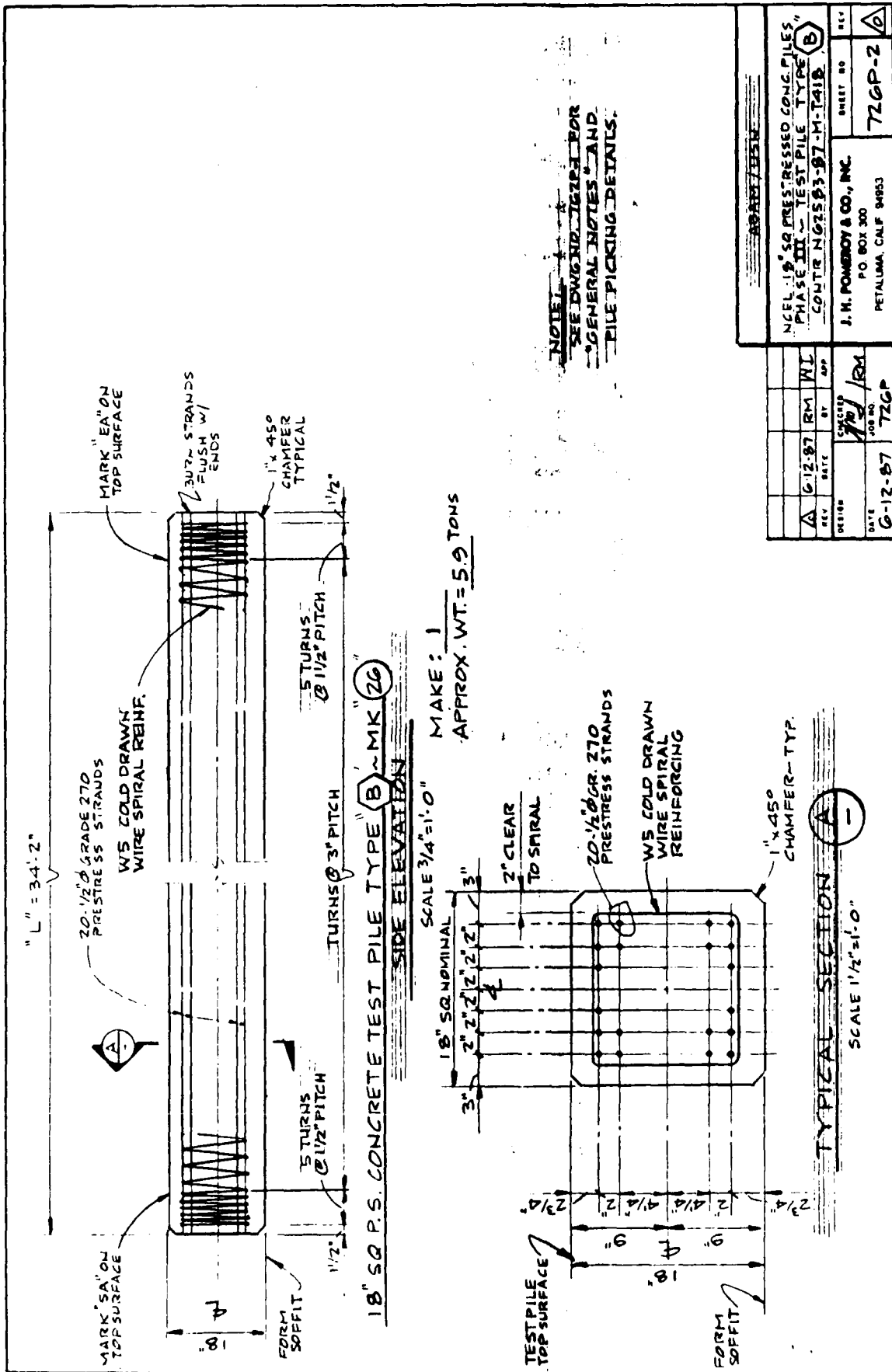
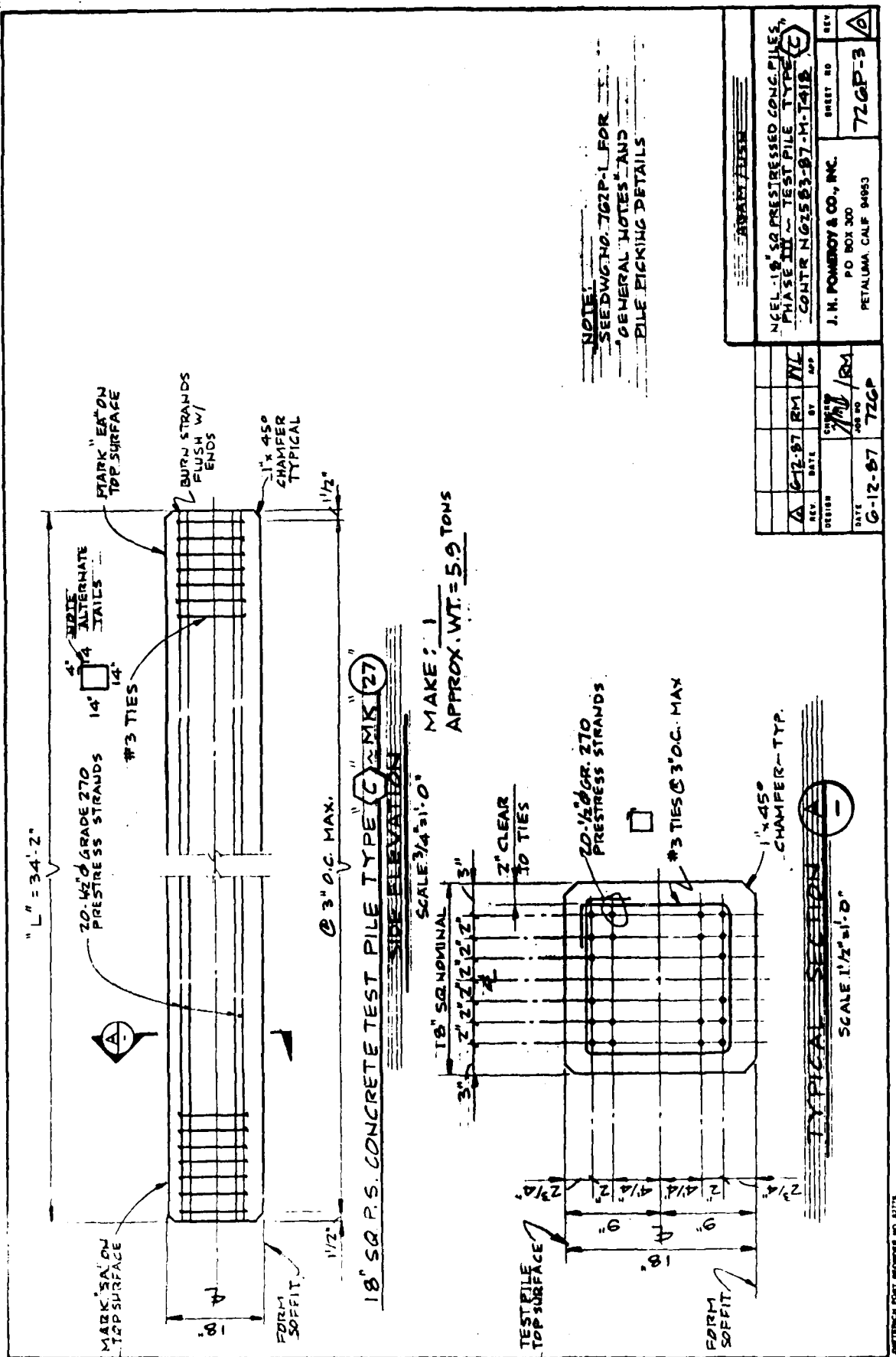


Figure A-9. Construction drawings for MK27.



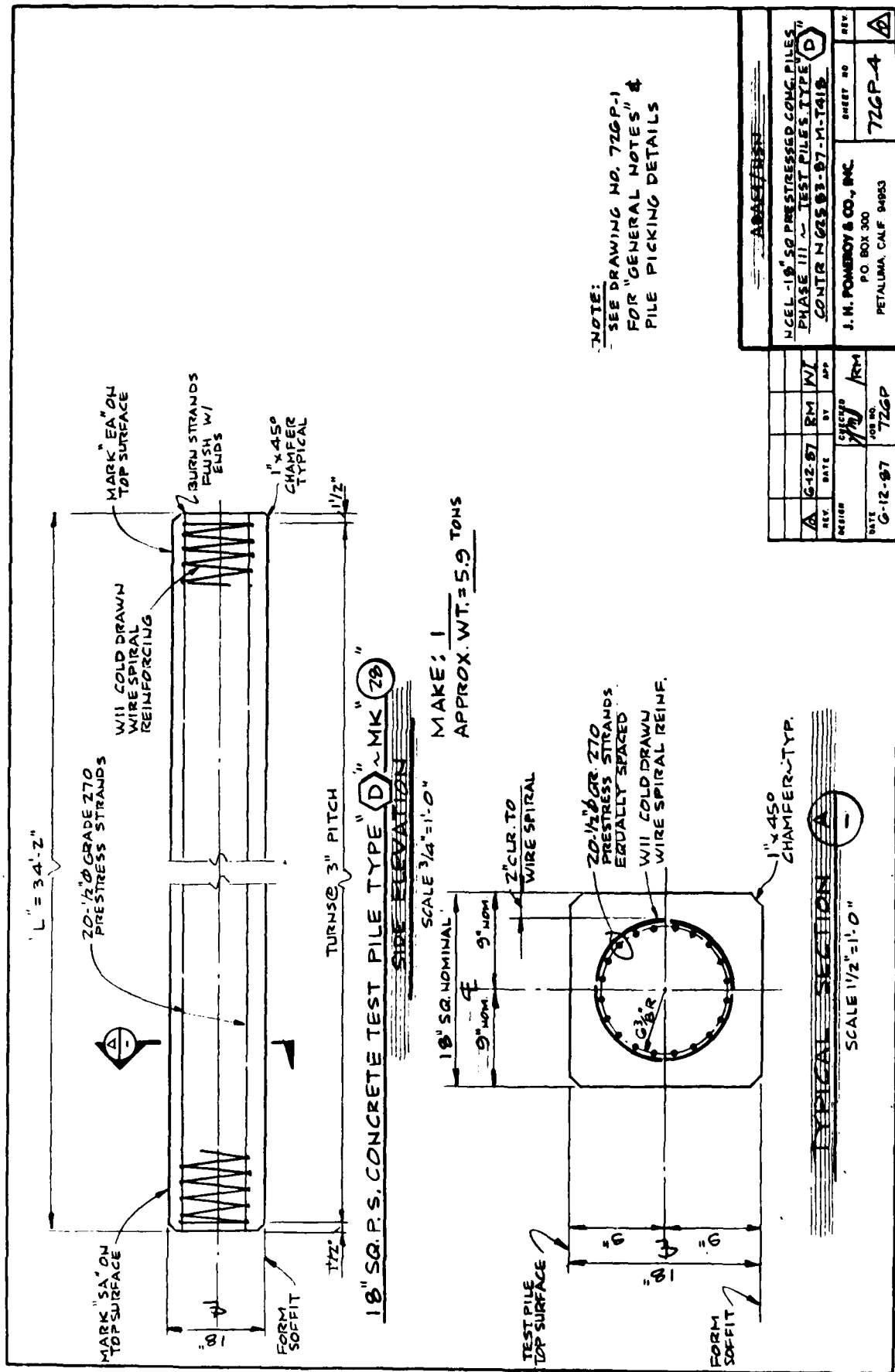
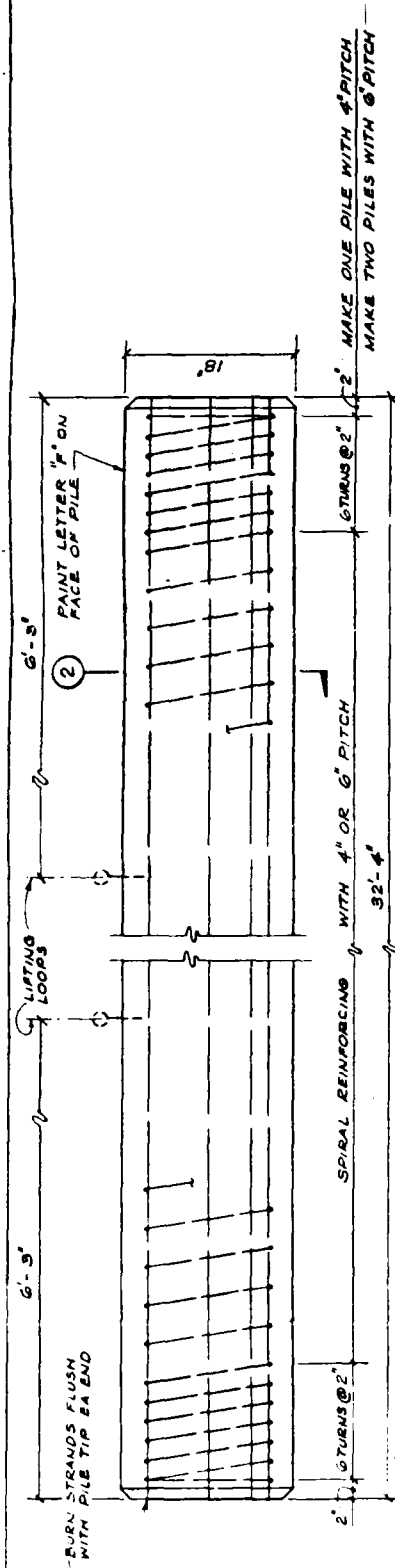
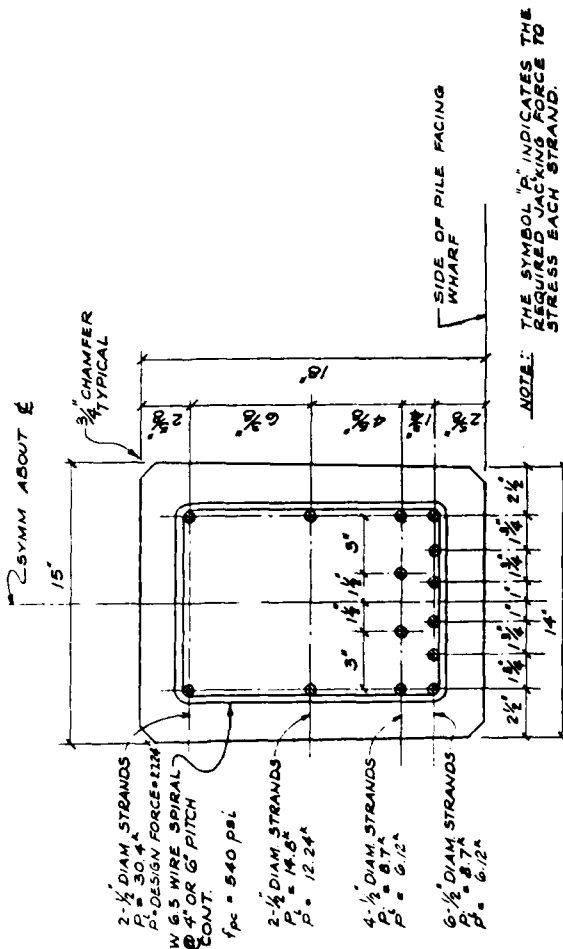


Figure A-11. Construction drawings for MK29.



14' x 18' PRESTRESSED CONCRETE PILE ①

SCALE: 1/8" = 1'-0"



PILE CROSS-SECTION ②

SCALE: 3" = 1'-0"

FABRICATION DETAILS - TEST UNITS			
NCEL - PRESTRESSED CONCRETE FENDER PILE			
SCALE: AS NOTED	REVISIONS:	DRAWN BY: NLS	APPROVED: NLS
DATE: DEC. '86			
WILLIAM L. SIMONS & ASSOCIATES CONSULTING STRUCTURAL ENGINEERS DENVER, (303) 439-2406			
S-1			



Figure A-12. Construction drawings for COL01 through COL03.

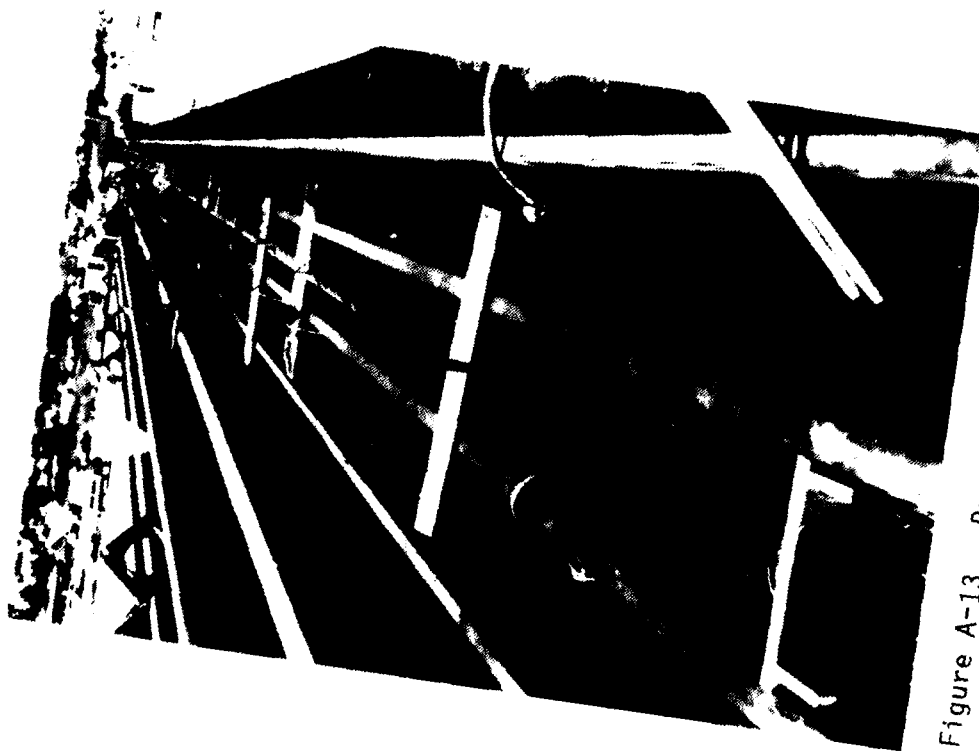


Figure A-13. Prestressed reinforcing cage for MK1 through MK3.



Figure A-14. Casting MK1 through MK3.

Appendix B
TEST RESULTS

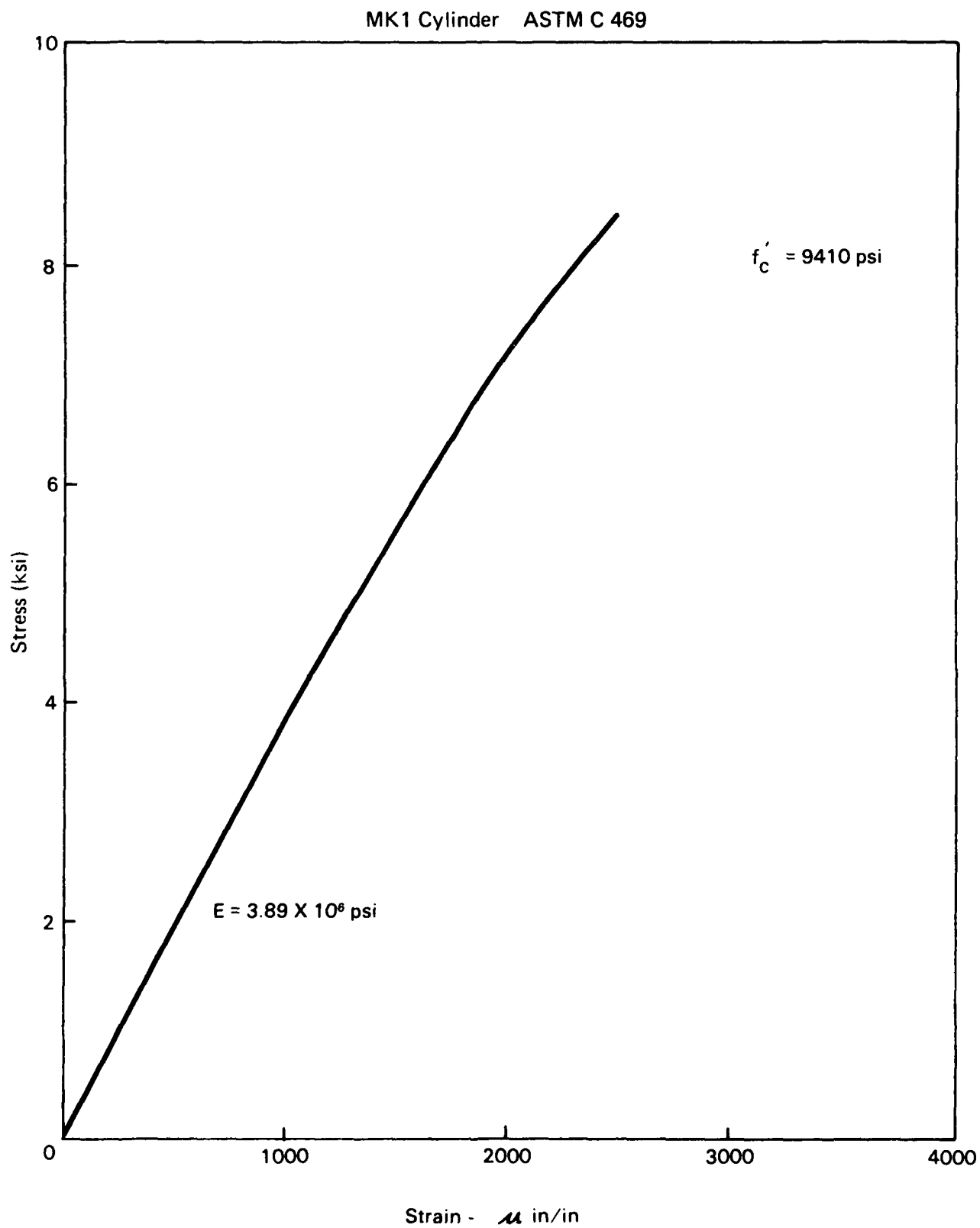


Figure B-1. Concrete stress-strain curve for MK1.

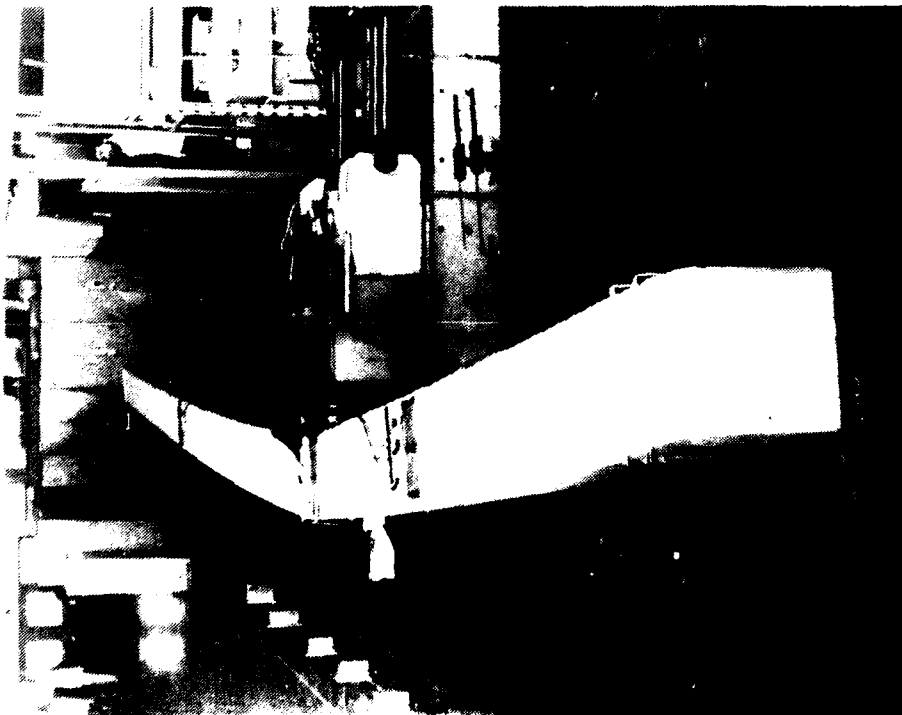


Figure B-2. MK1 post-ultimate displacement.



Figure B-3. MK1 compression spall zone after failure.



Figure B-4. MK1 post-failure tensile cracking at the load point.

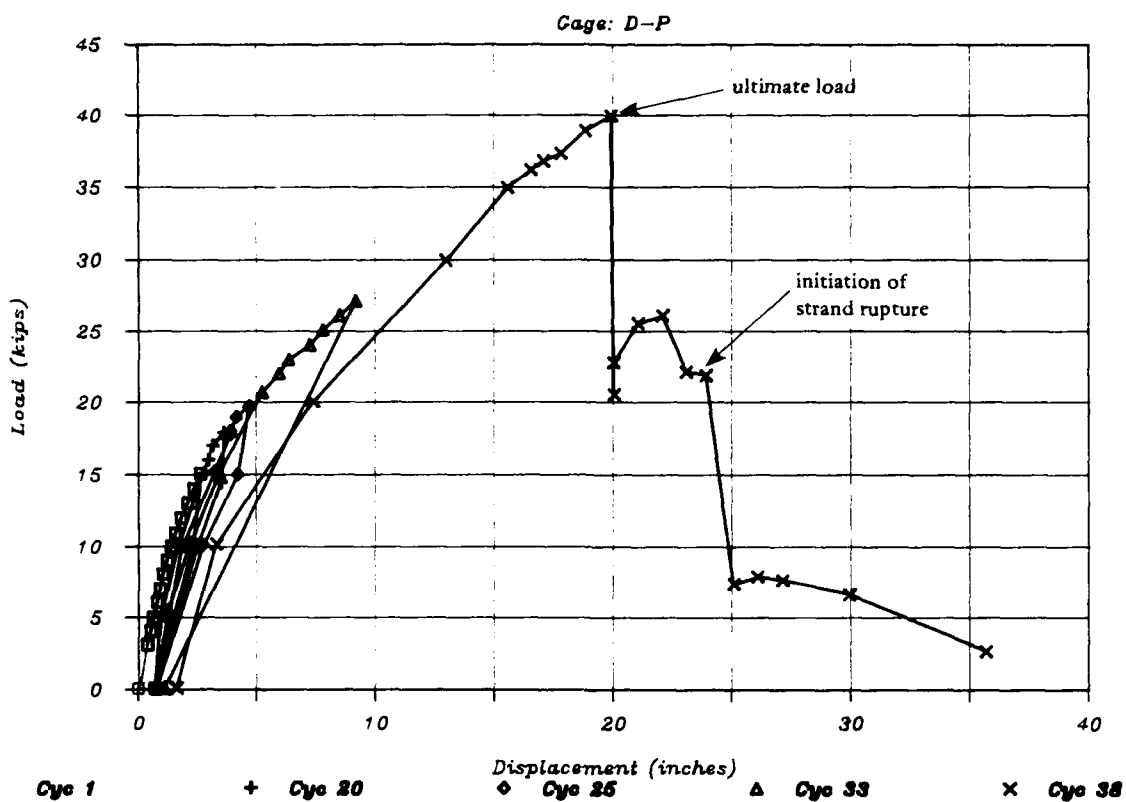


Figure B-5. MK1 load-displacement plot for cycles 20, 25, 33, and 38.

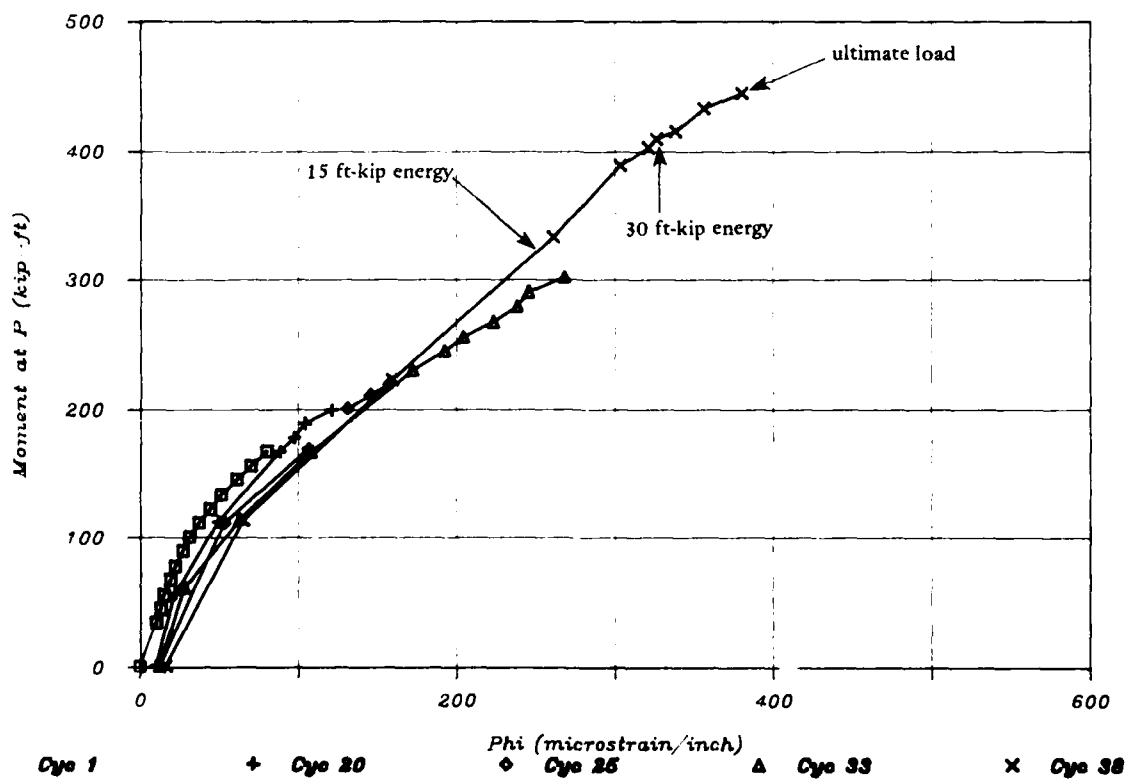


Figure B-6. MK1 moment-curvature plot for cycles 20, 25, 33, and 38.

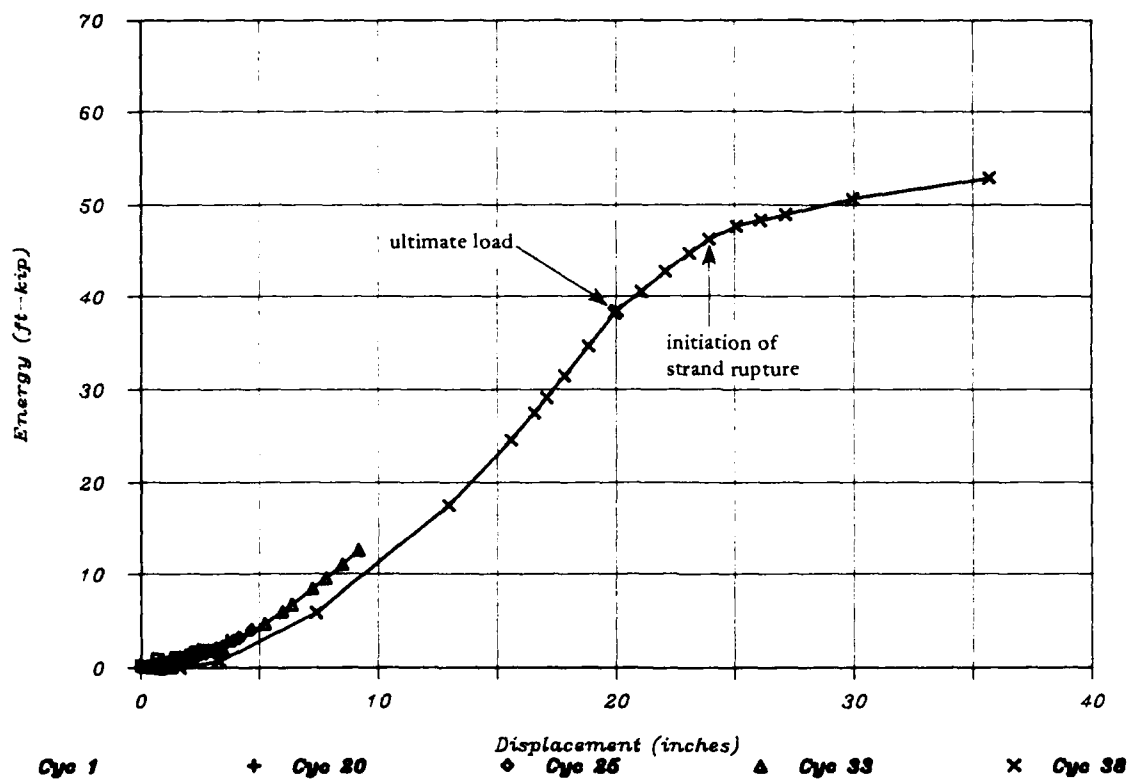


Figure B-7. MK1 energy-displacement plot for cycles 20, 25, 33, and 38.

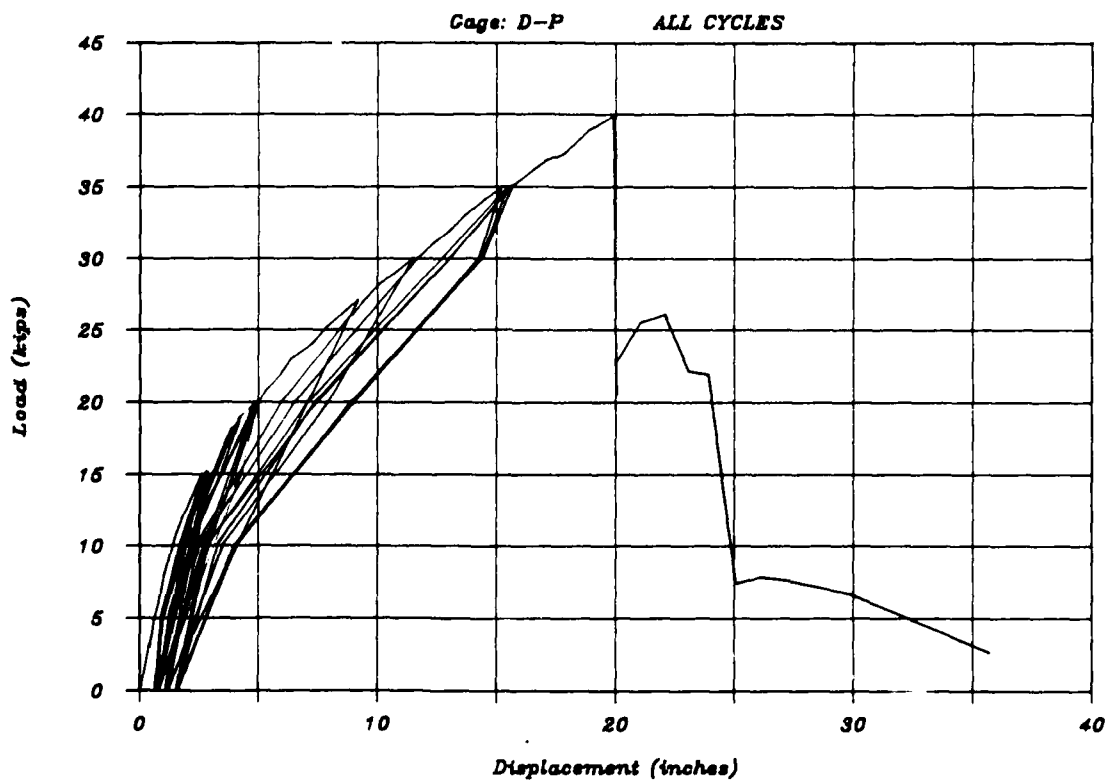


Figure B-8. MK1 load-displacement plot for all cycles.

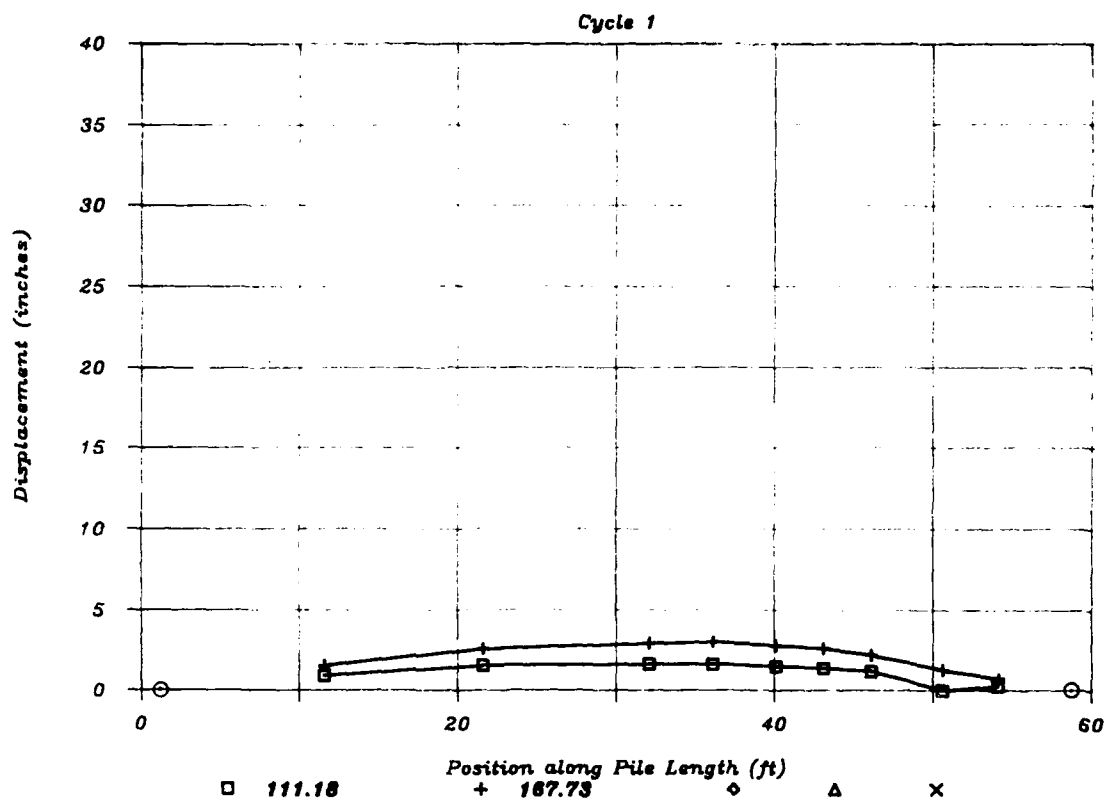


Figure B-9. MK1 first cycle deformed shape for $M = 111$ and 168 kip-ft.

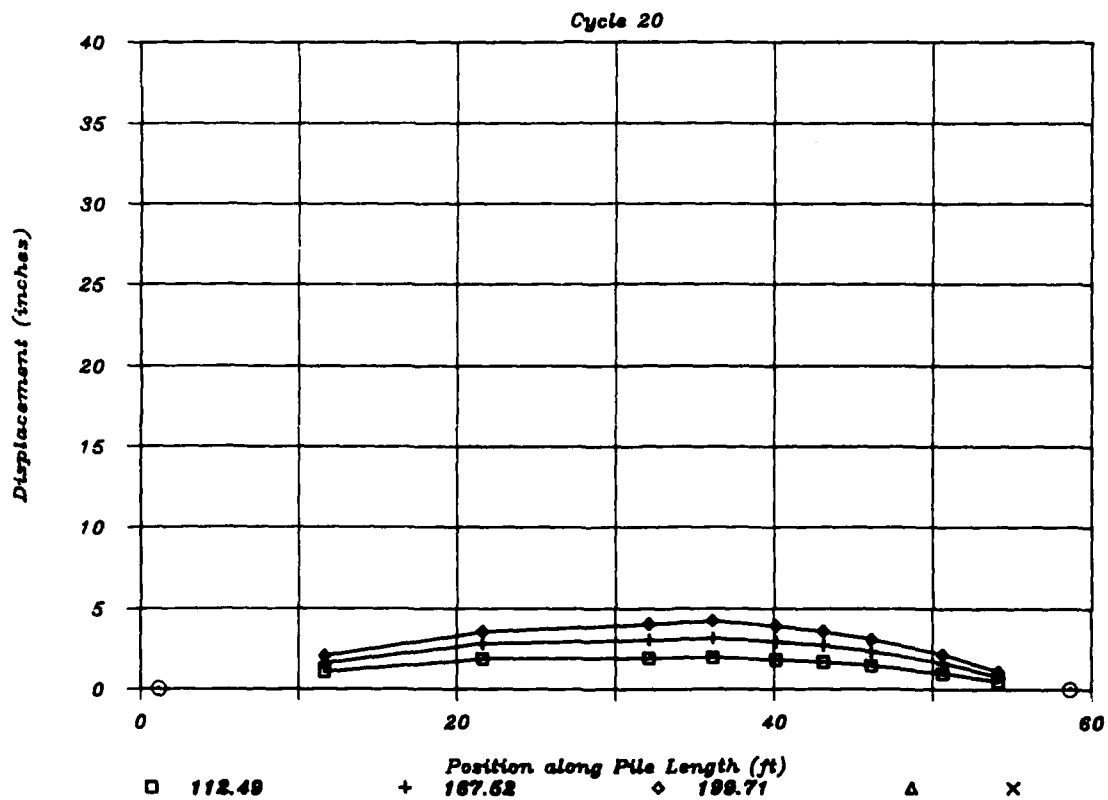


Figure B-10. MK1 cycle 20 deformed shape for $M = 112$, 168 , and 200 kip-ft.

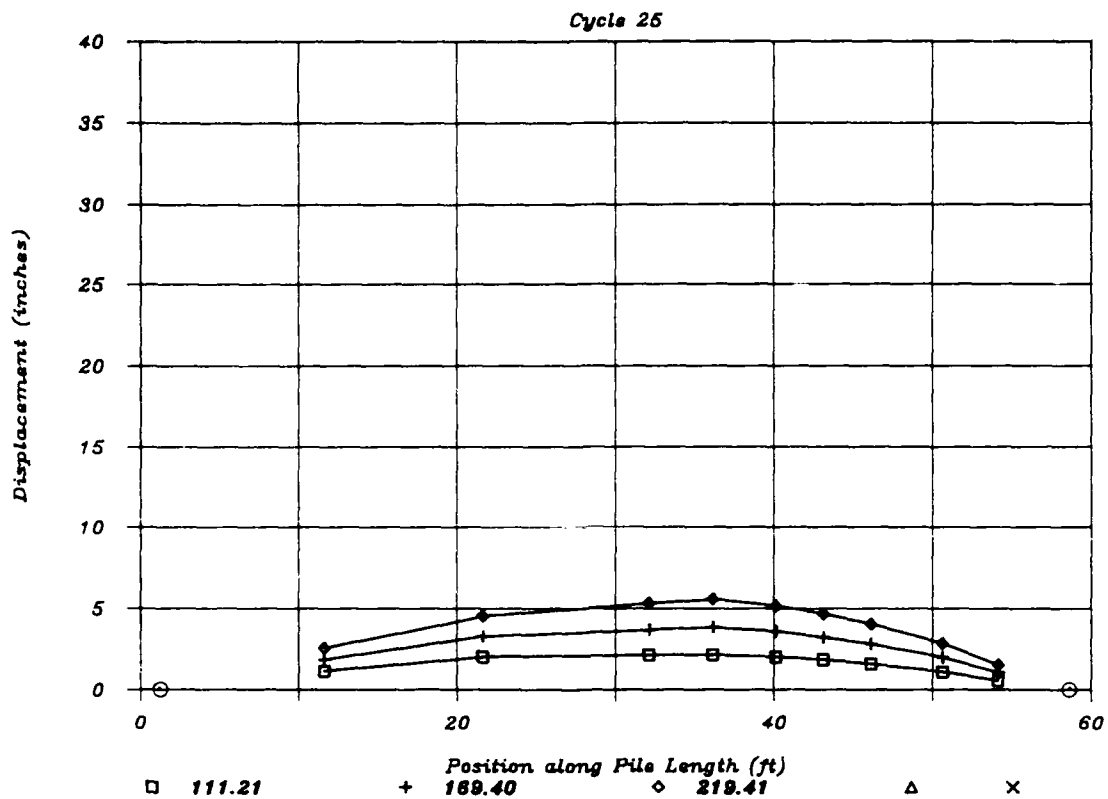


Figure B-11. MK1 cycle 25 deformed shape for $M = 111$, 169, and 219 kip-ft.

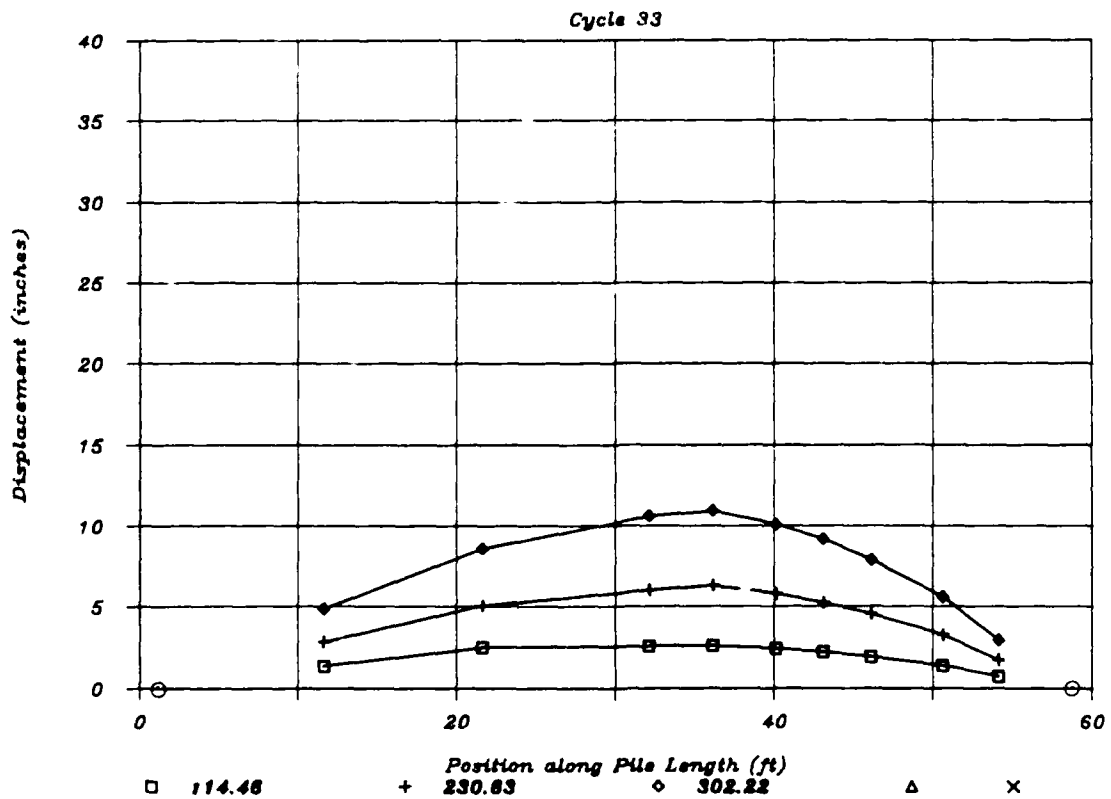


Figure B-12. MK1 cycle 33 deformed shape for $M = 114$, 231, and 302 kip-ft.

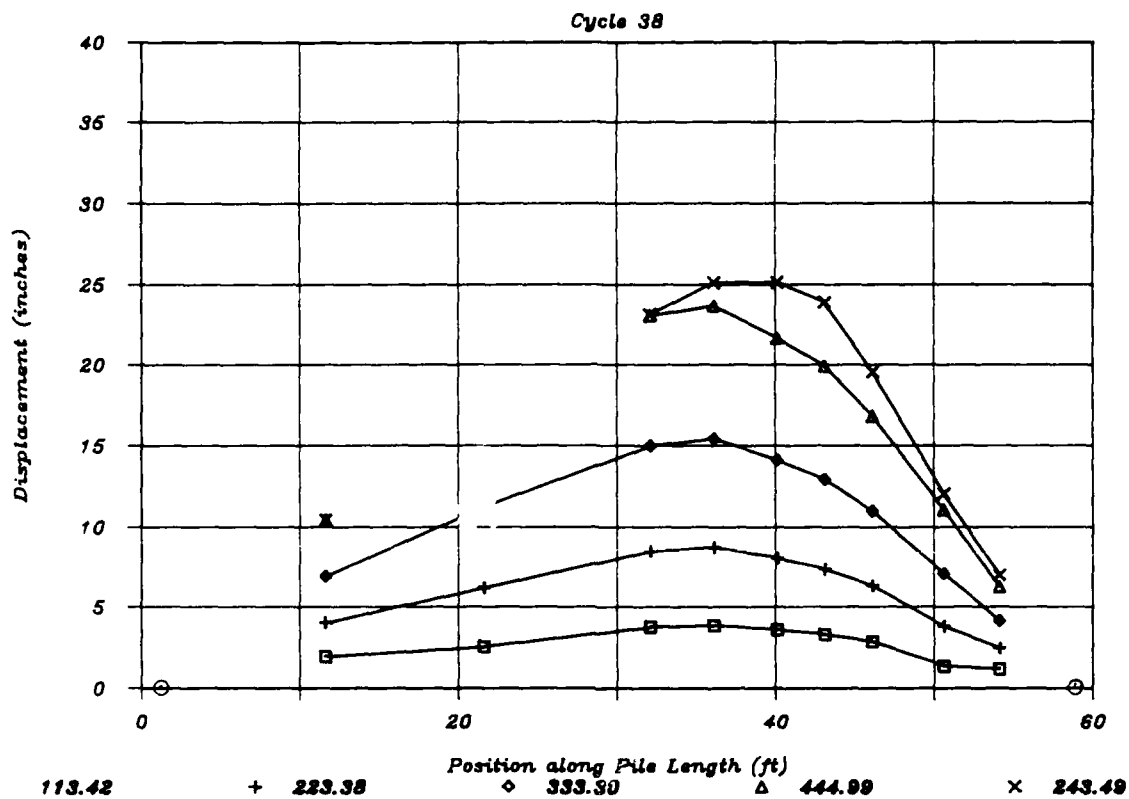


Figure B-13. MK1 final cycle deformed shape for $M = 113, 223, 333, 445,$ and 243 kip-ft.

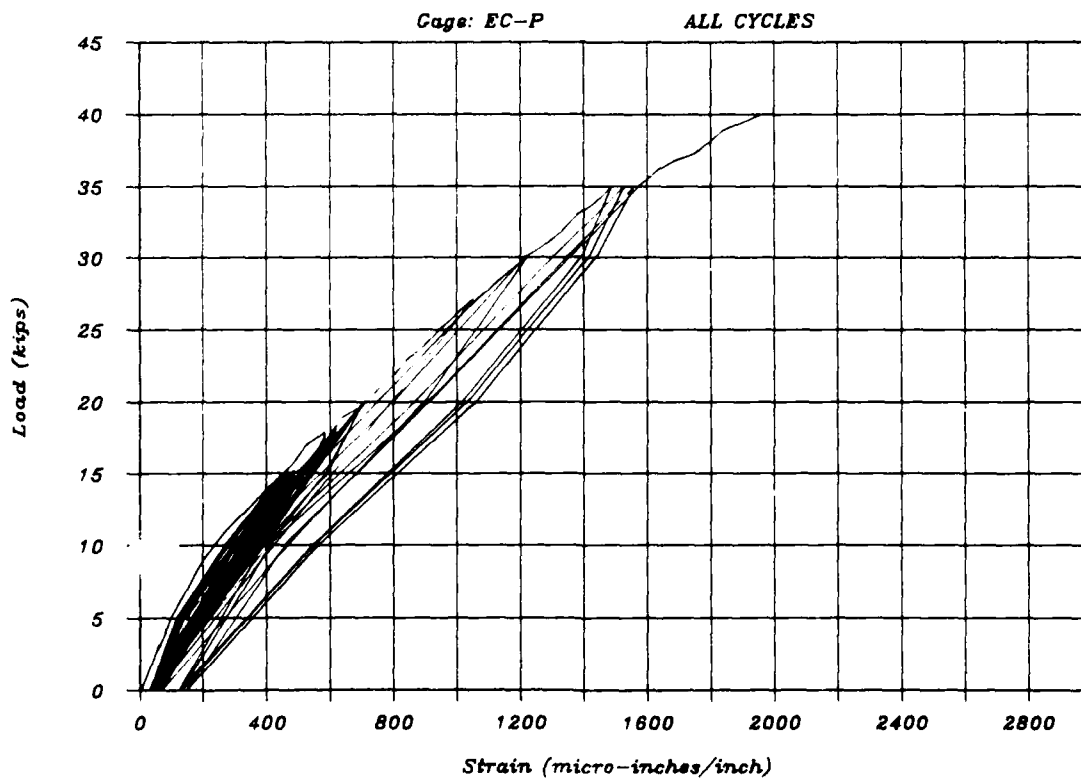


Figure B-14. MK1 load-compression strain for all cycles.

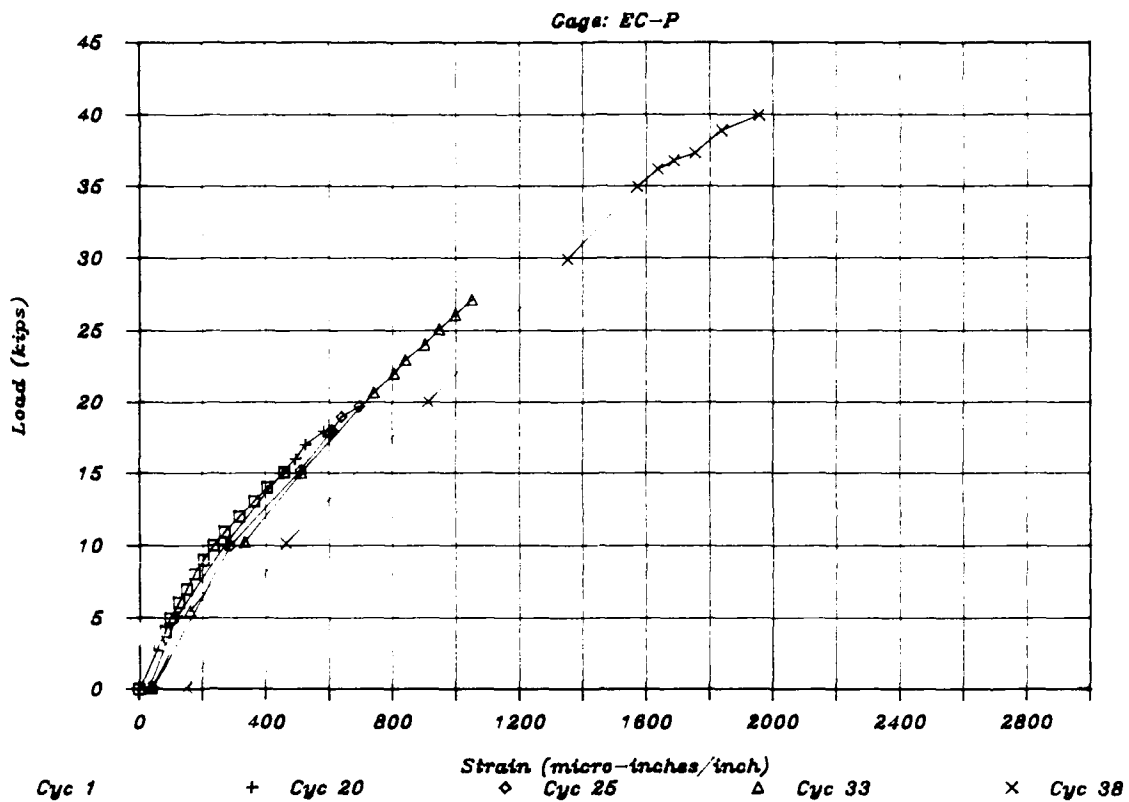


Figure B-15. MK1 load-compression strain for cycles 1, 20, 25, 33, and 38.

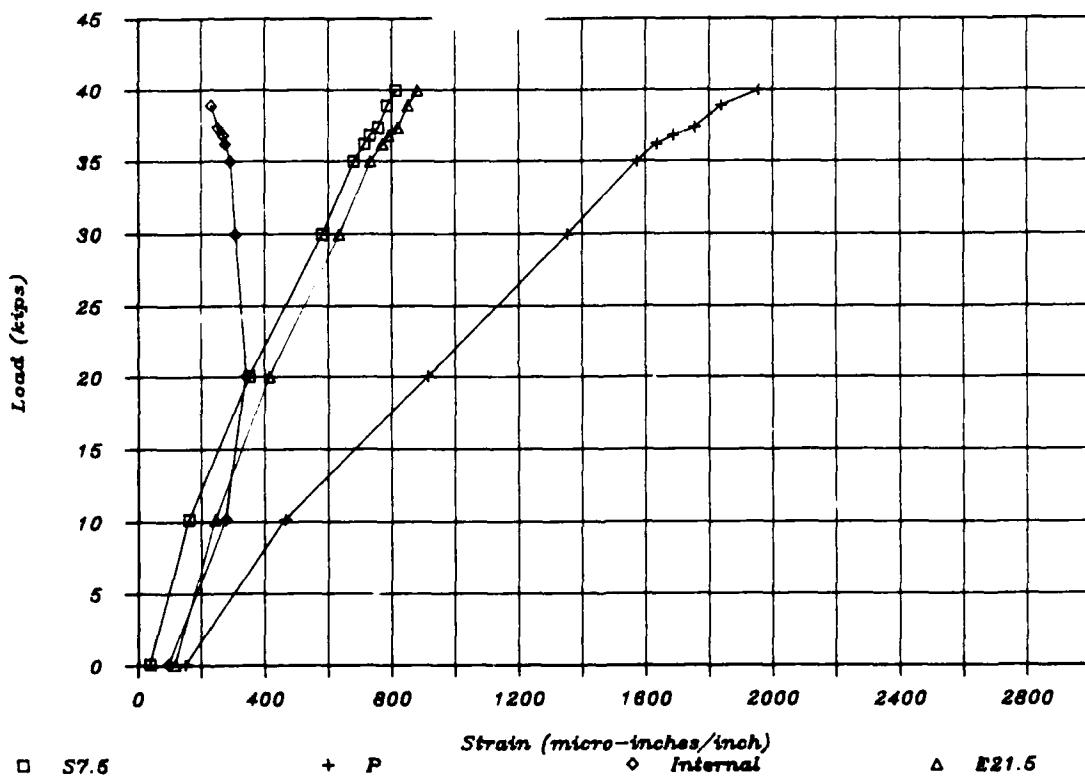


Figure B-16. MK1 final cycle compression strain - all gages.

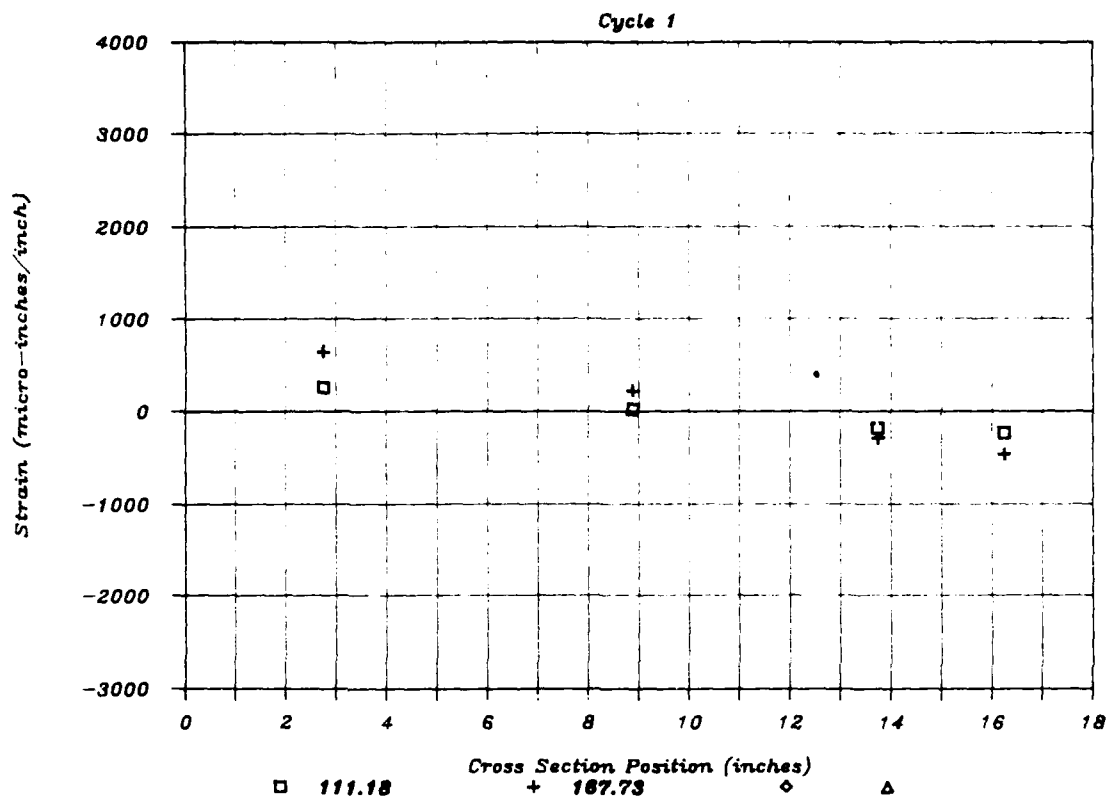


Figure B-17. MK1 load point cross-section strain - cycle 1.

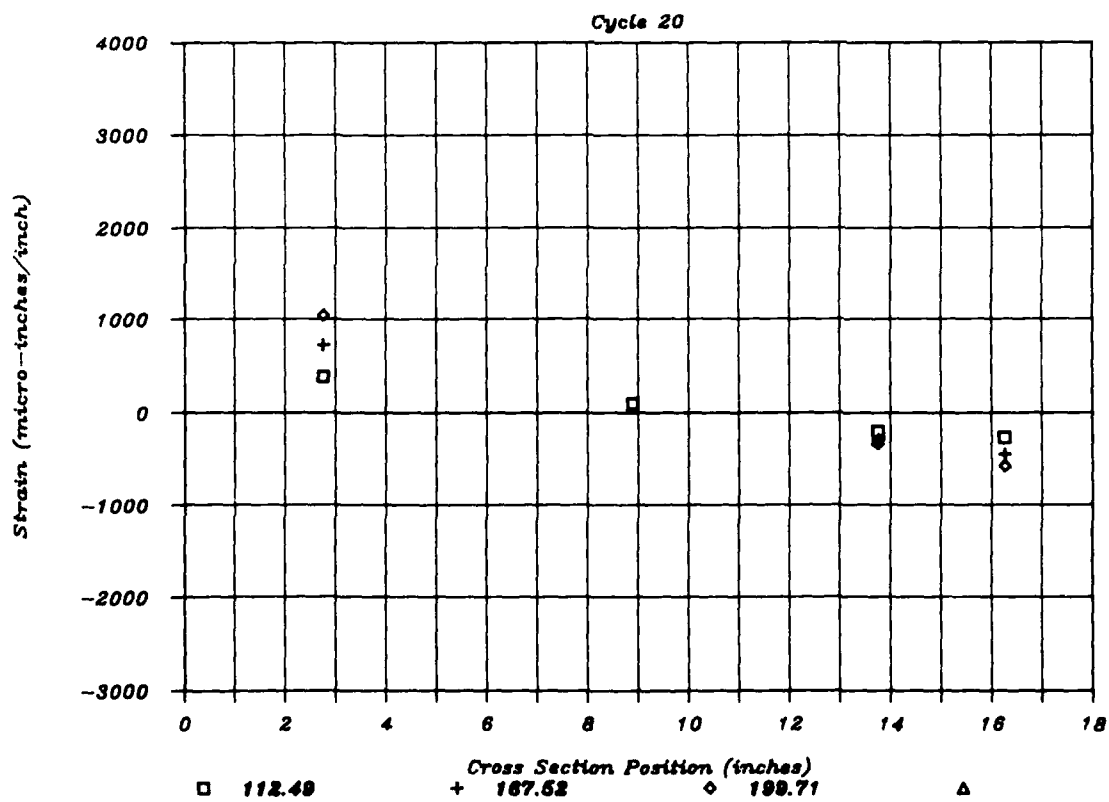


Figure B-18. MK1 load point cross-section strain - cycle 20.

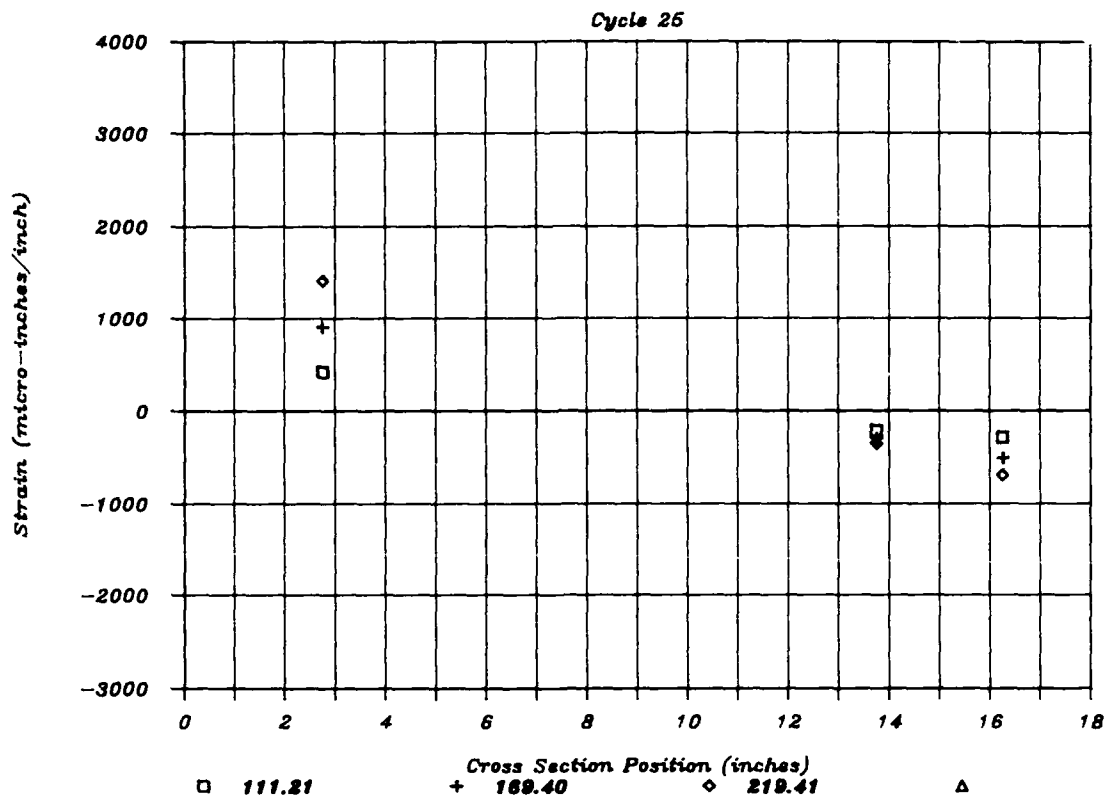


Figure B-19. MK1 load point cross-section strain - cycle 25.

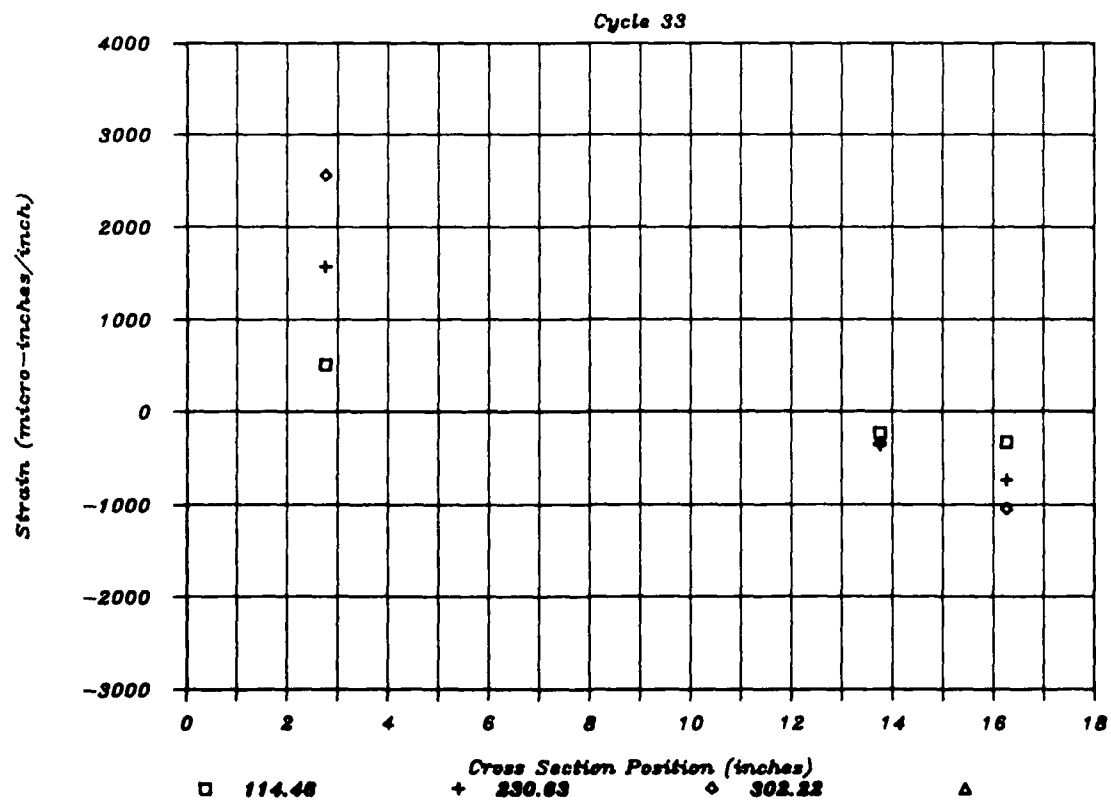


Figure B-20. MK1 load point cross-section strain - cycle 33.

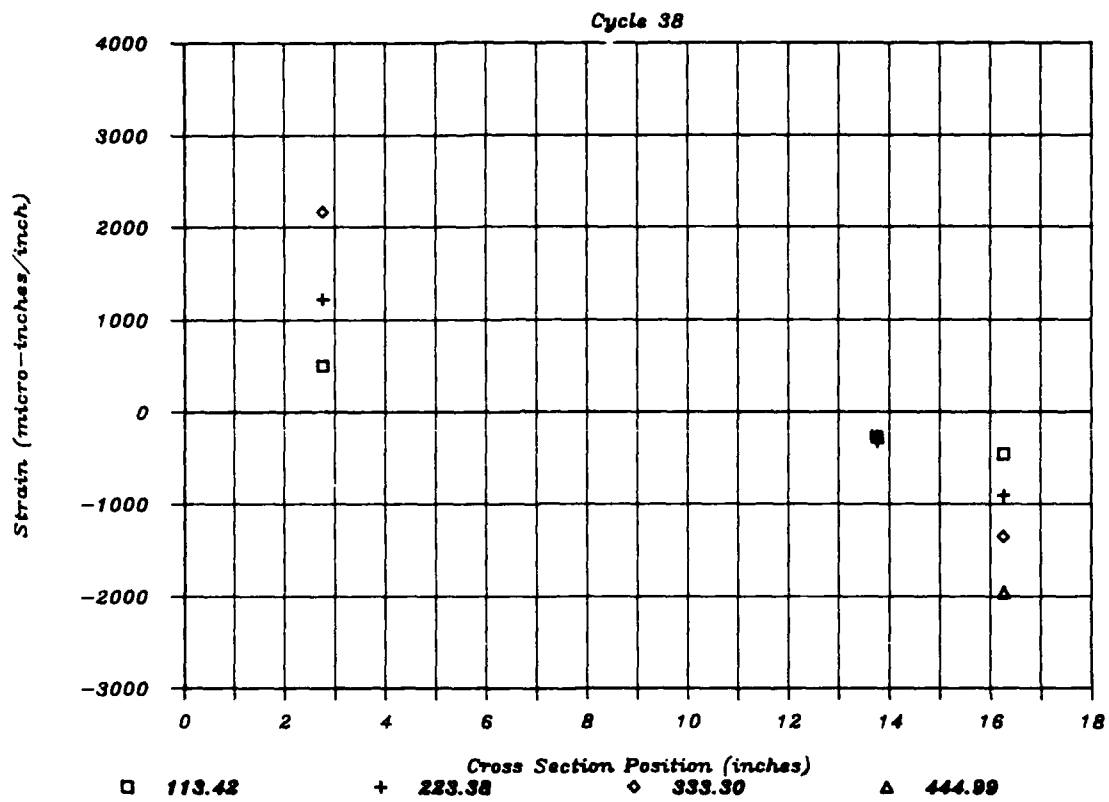


Figure B-1. MK1 load point cross-section strain - final cycle.

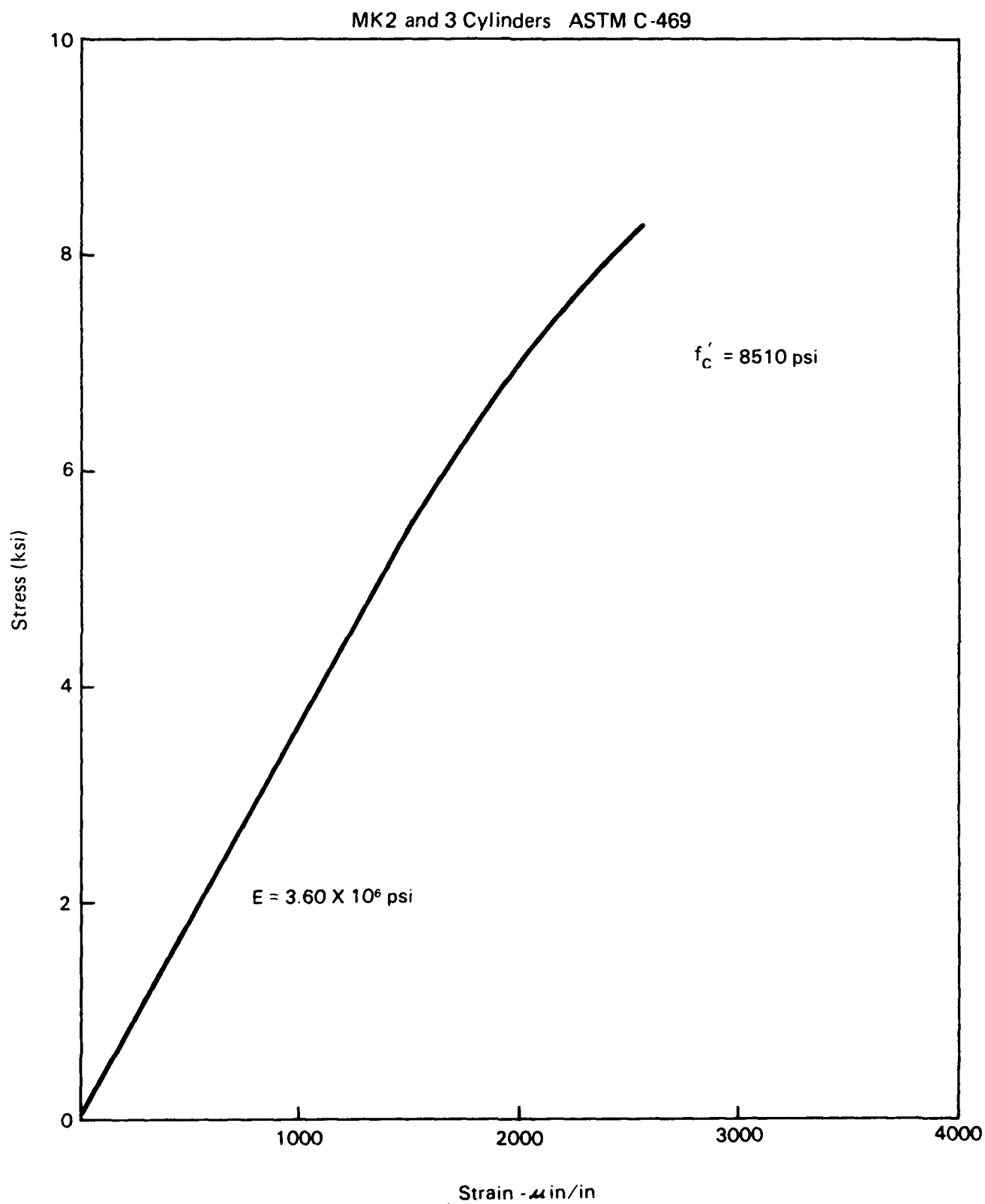


Figure B-22. Concrete stress-strain curve for MK2 and MK3.

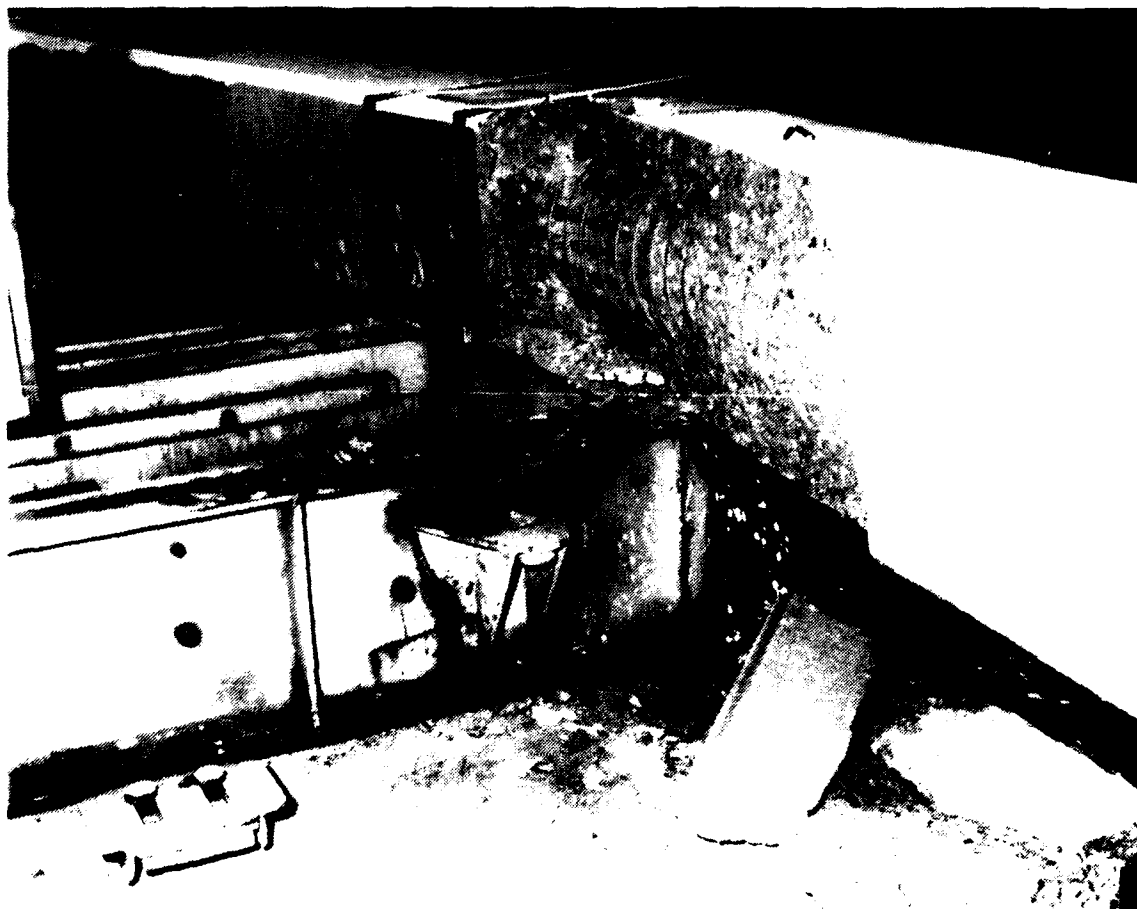


Figure B-23. MK2 spall zone after failure.

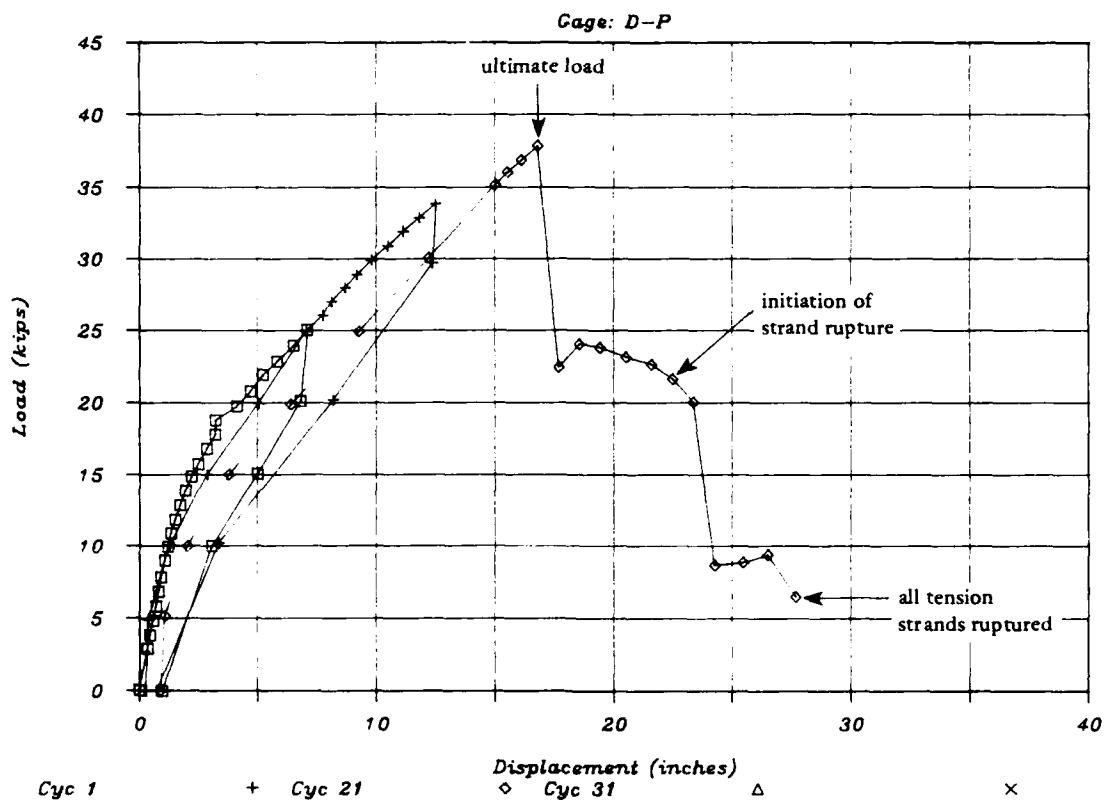


Figure B-24. MK2 load-displacement plot for cycles 1, 21, and 31.

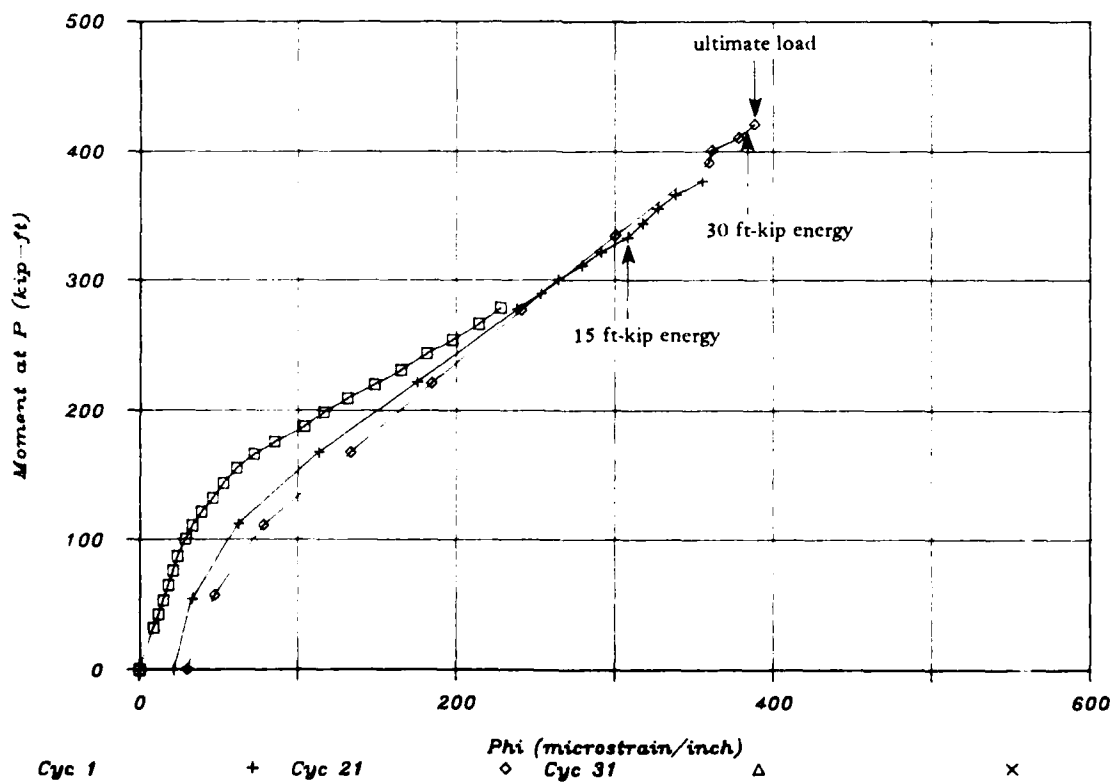


Figure B-25. MK2 moment-curvature plot for cycles 1, 21, and 31.

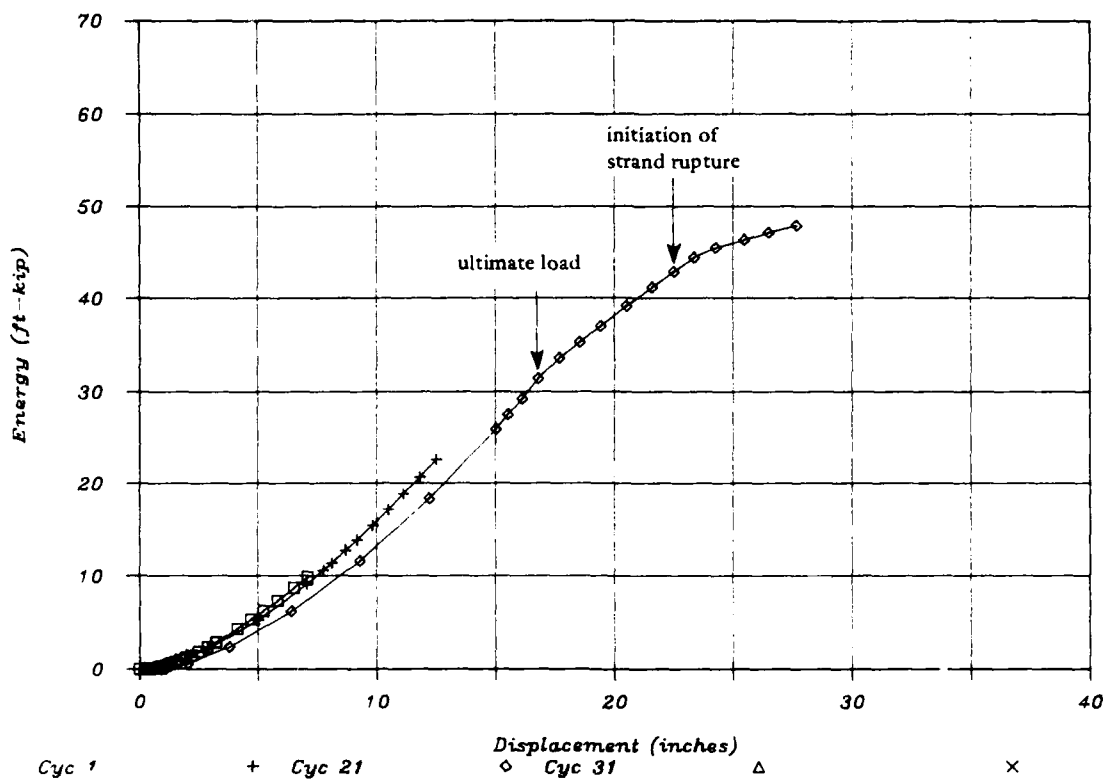


Figure B-26. MK2 energy-displacement plot for cycles 1, 21, and 31.

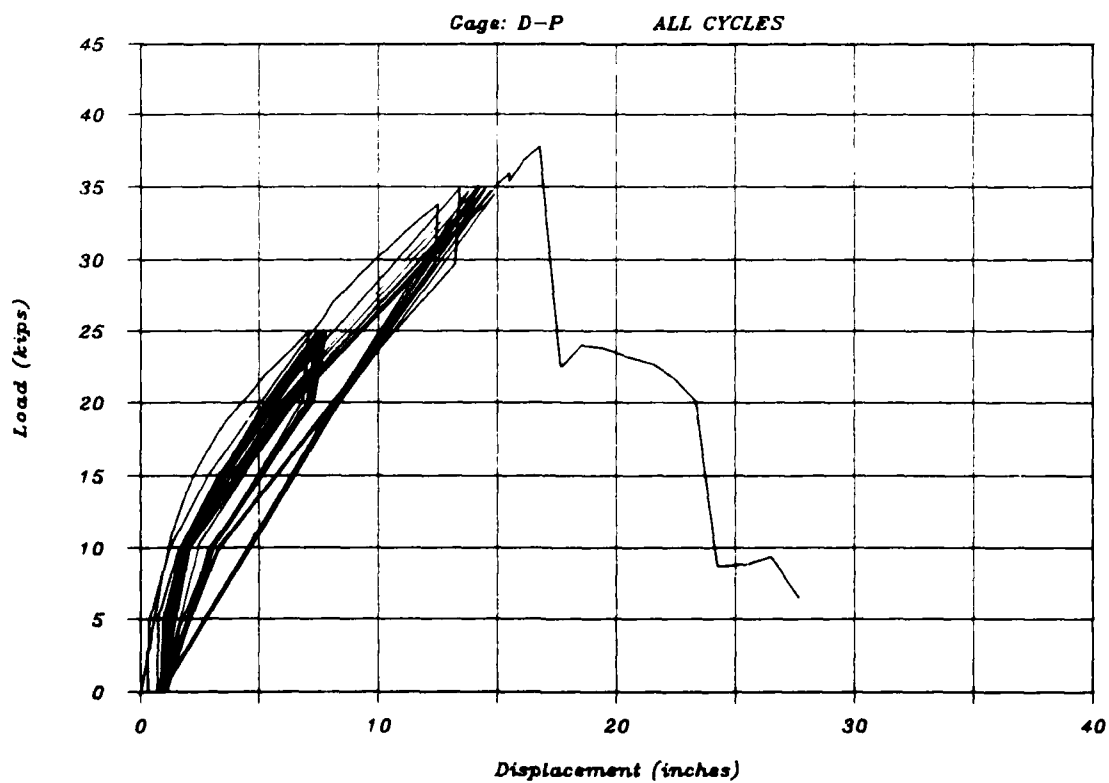


Figure B-27. MK2 load-displacement plot for all cycles.

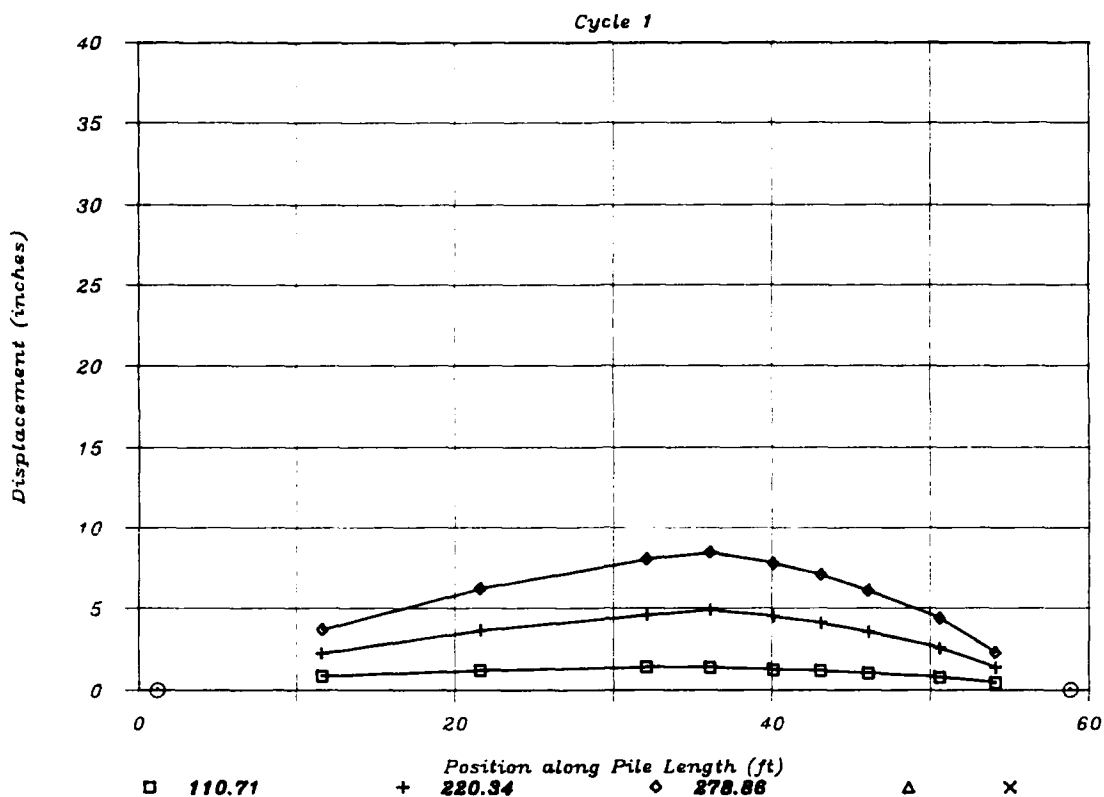


Figure B-28. MK2 first cycle deformed shape for $M = 111, 220,$ and 279 kip-ft.

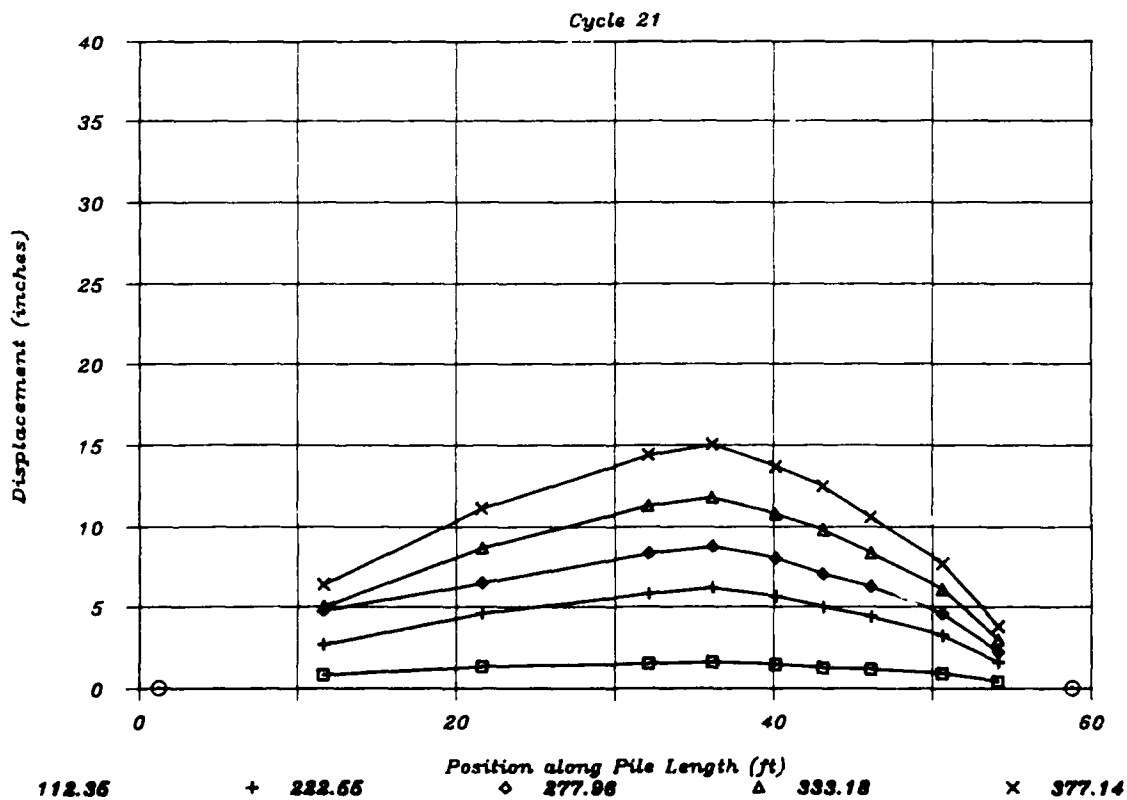


Figure B-29. MK2 cycle 21 deformed shape for $M = 112, 223, 278, 333,$ and 377 kip-ft.

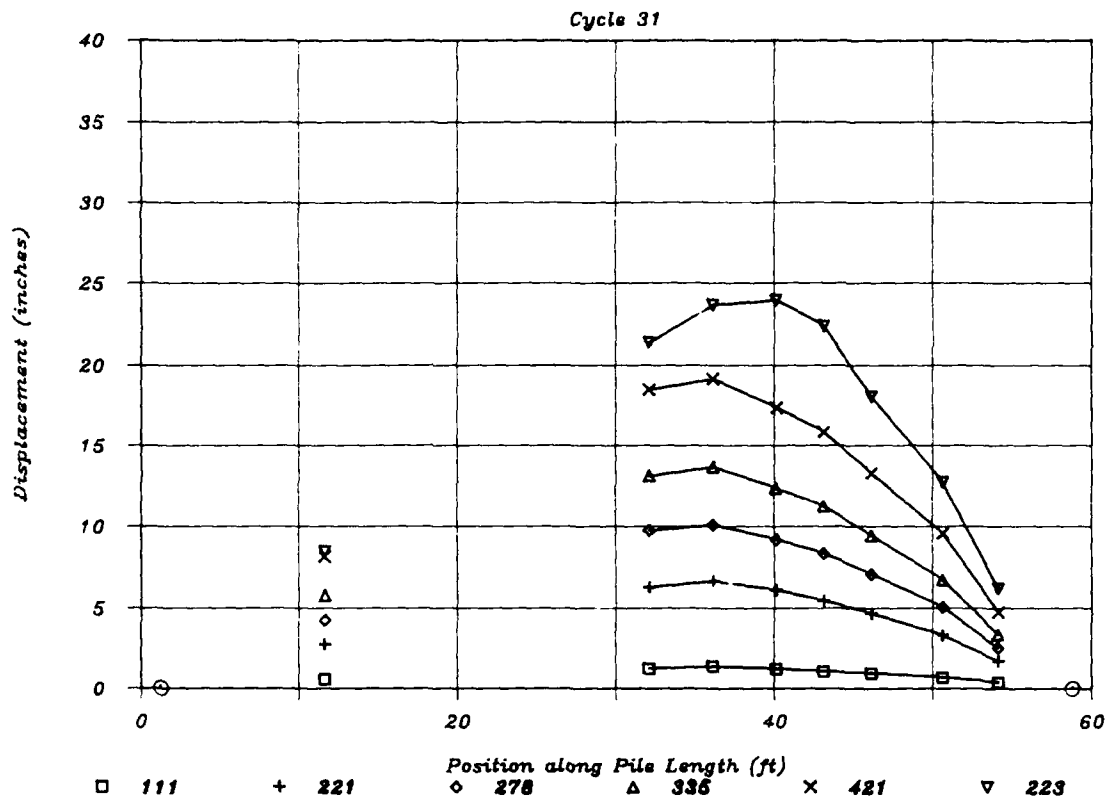


Figure B-30. MK2 final cycle deformed shape for $M = 111, 221, 278, 336, 421,$ and 223 kip-ft.

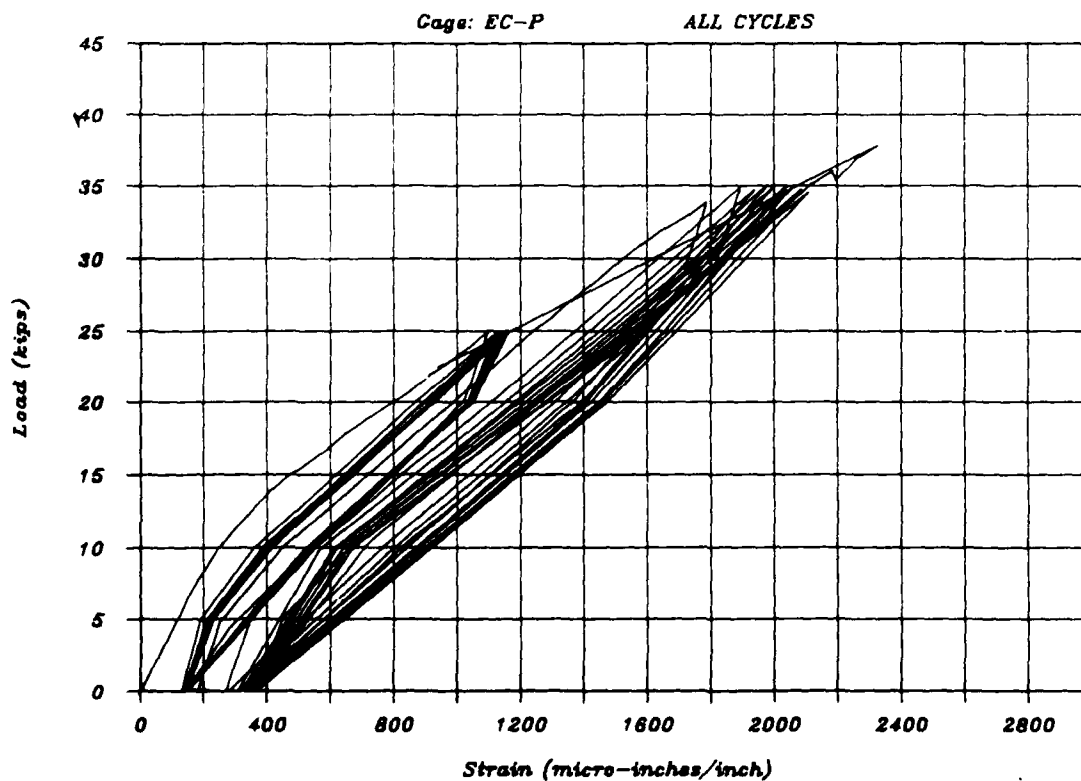


Figure B-31. MK2 load-compression strain for all cycles.

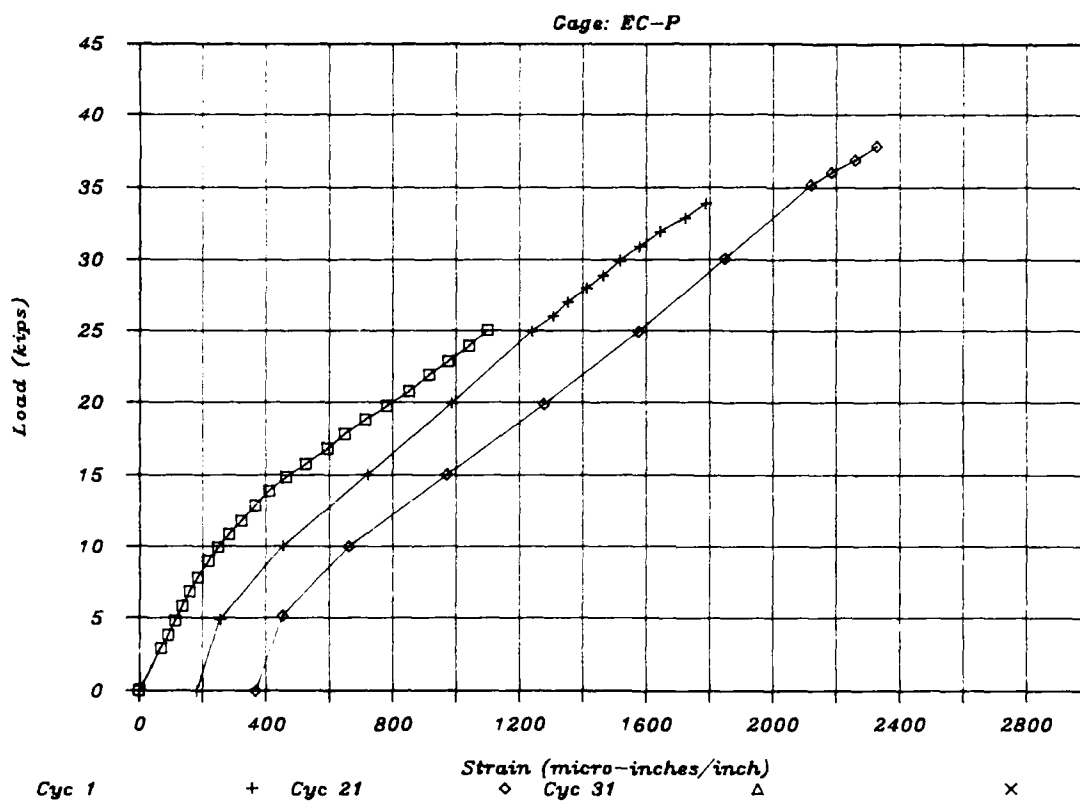


Figure B-32. MK2 load-compression strain for cycles 1, 21, and 31.

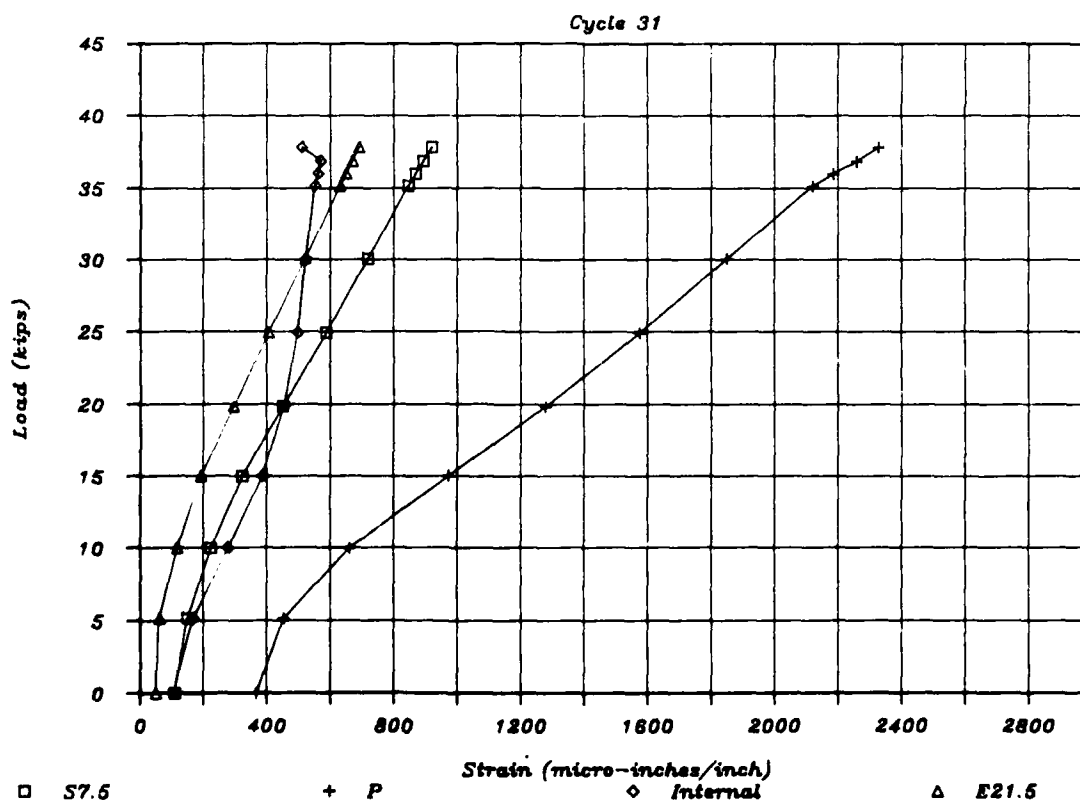


Figure B-33. MK2 final cycle load-compression strain - all gages.

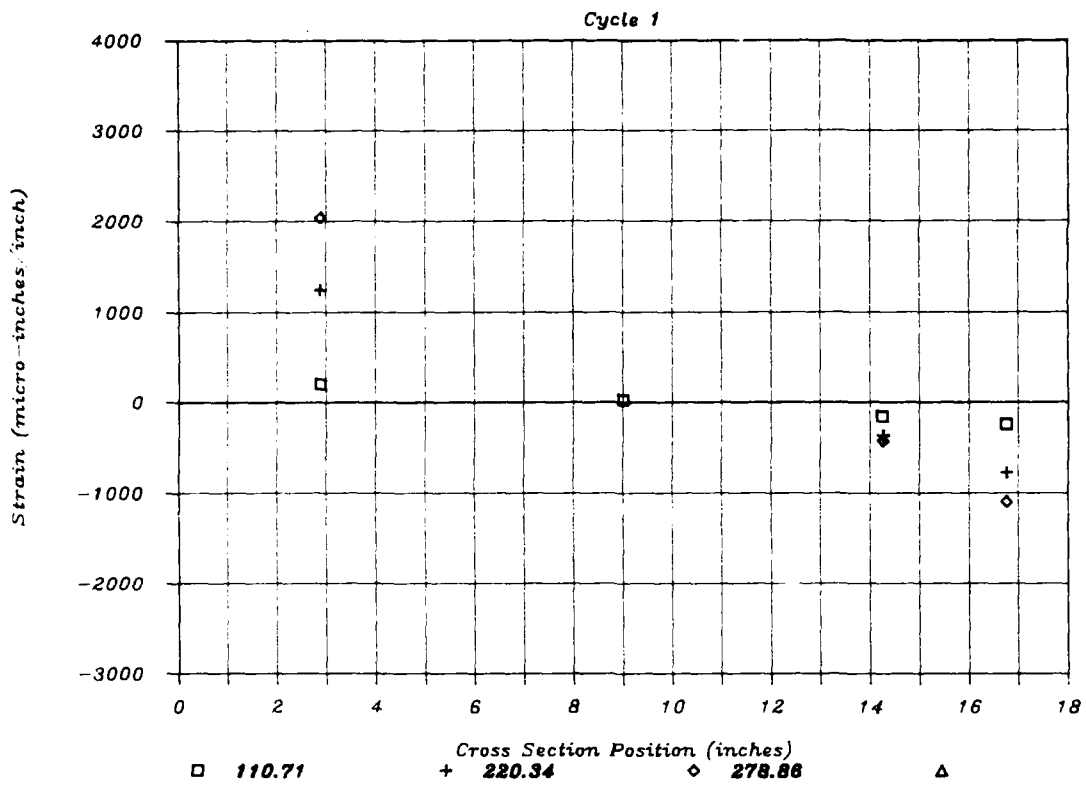


Figure B-34. MK2 load point cross-section strain - first cycle.

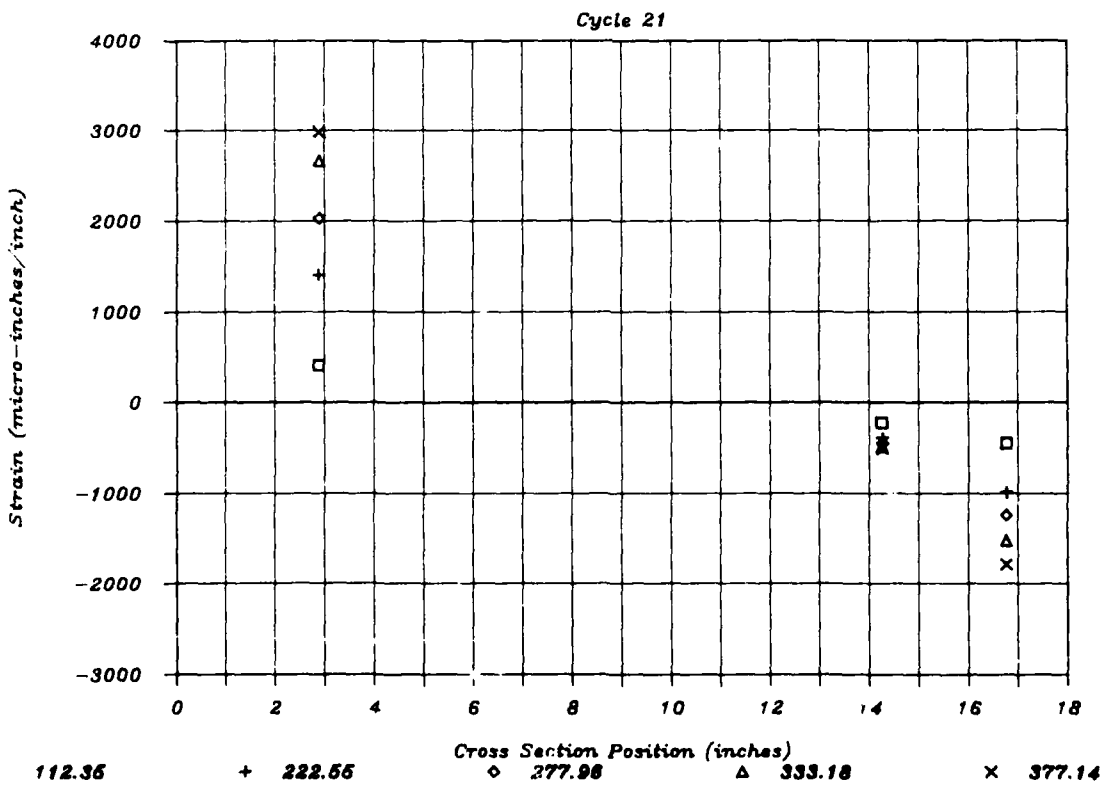


Figure B-35. MK2 load point cross-section strain - cycle 21.

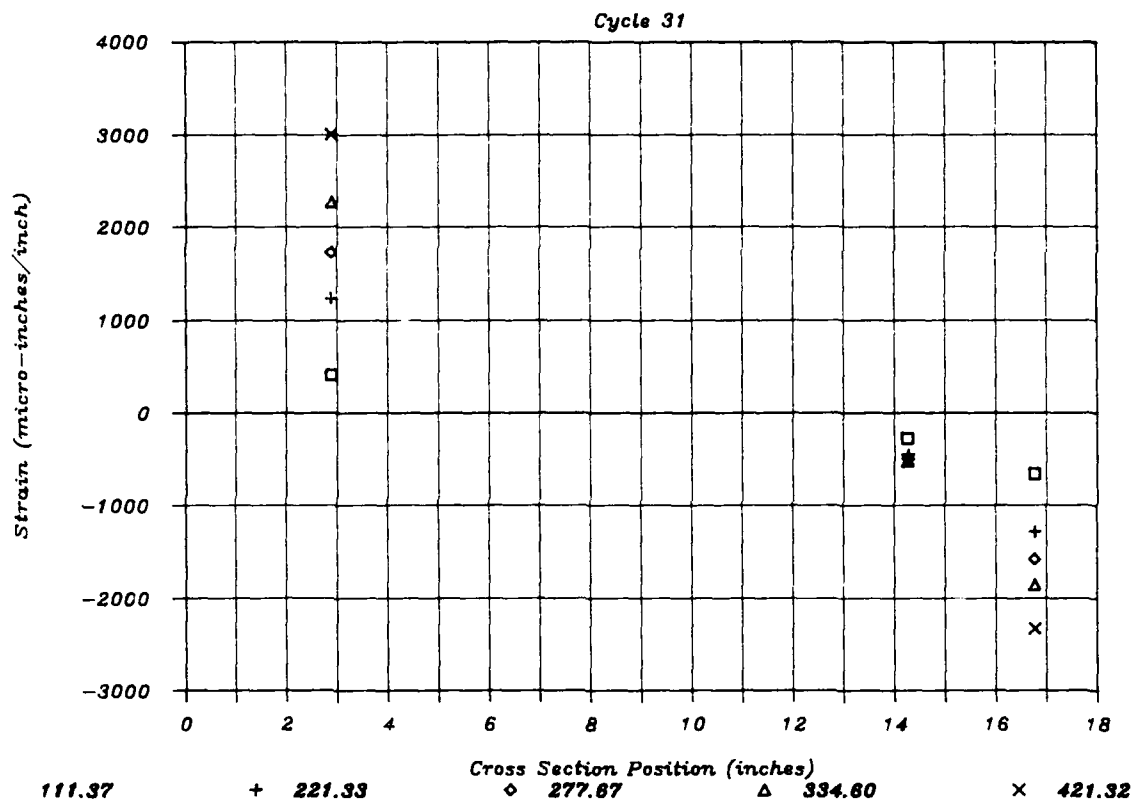


Figure B-36. MK2 load point cross-section strain - final cycle.



Figure B-37. MK3 post-ultimate displacement.



Figure B-38. MK3 failure displacement.



Figure B-39. MK3 spall zone after failure.

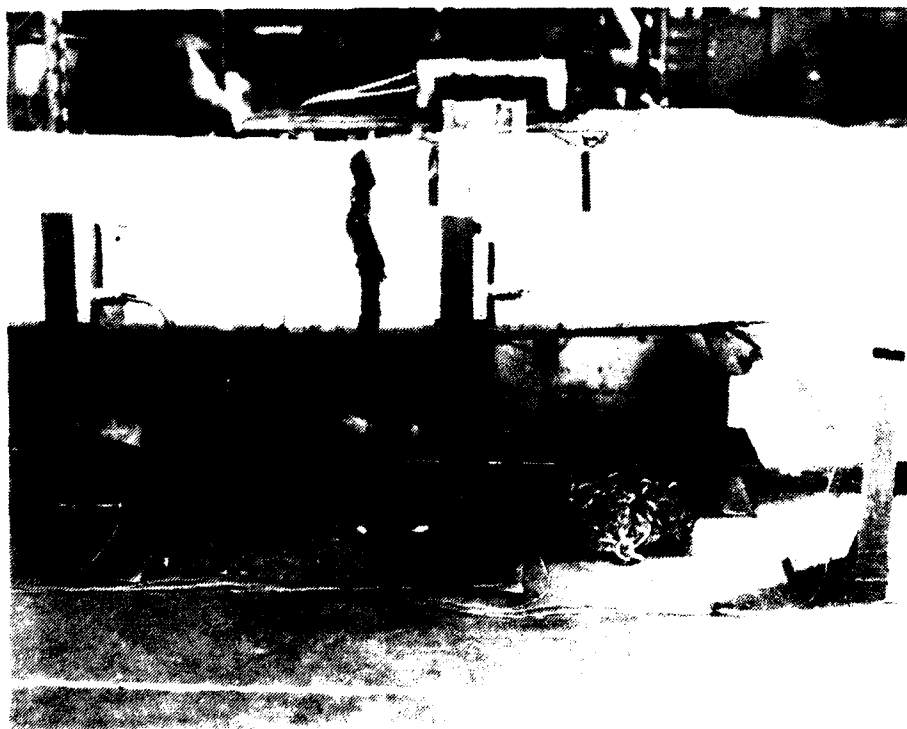


Figure B-40. MK3 tension face cracking at failure.

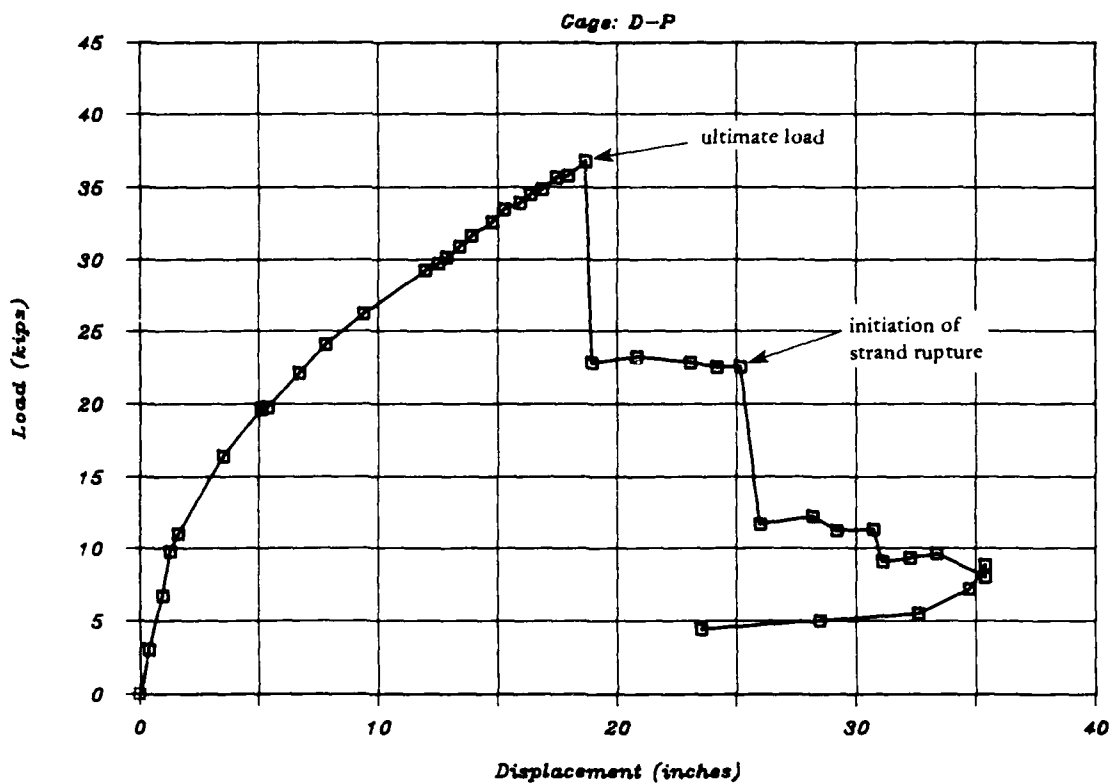


Figure B-41. MK3 load-displacement plot.

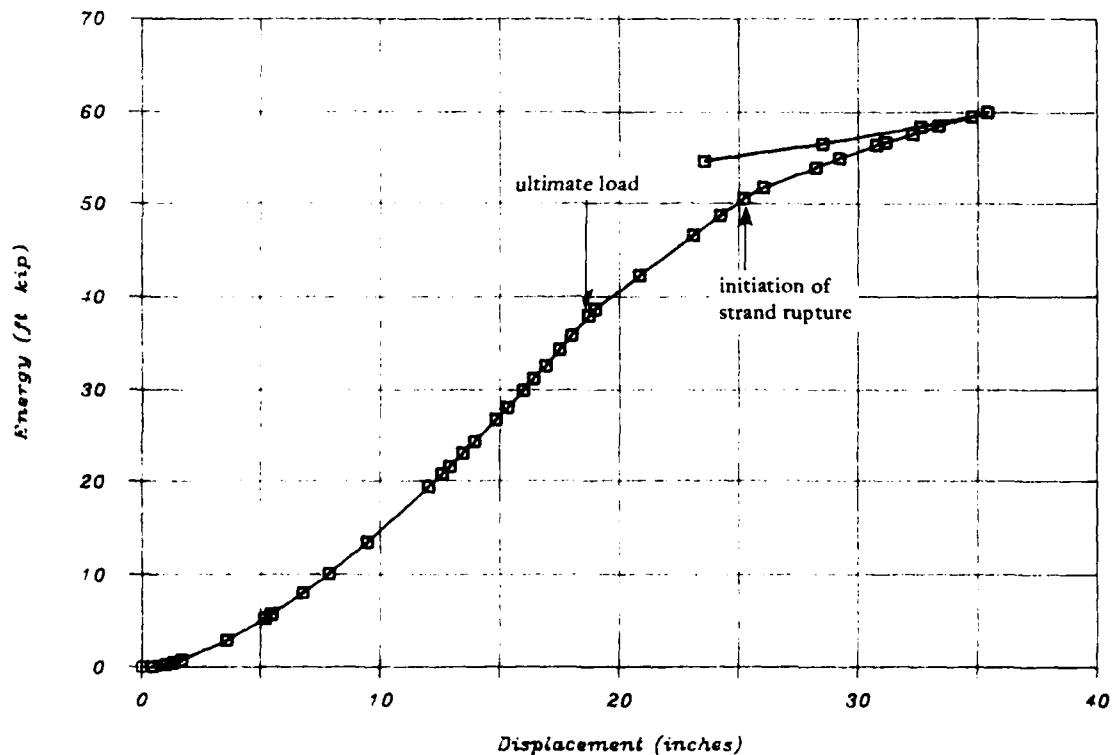


Figure B-42. MK3 energy-displacement plot.

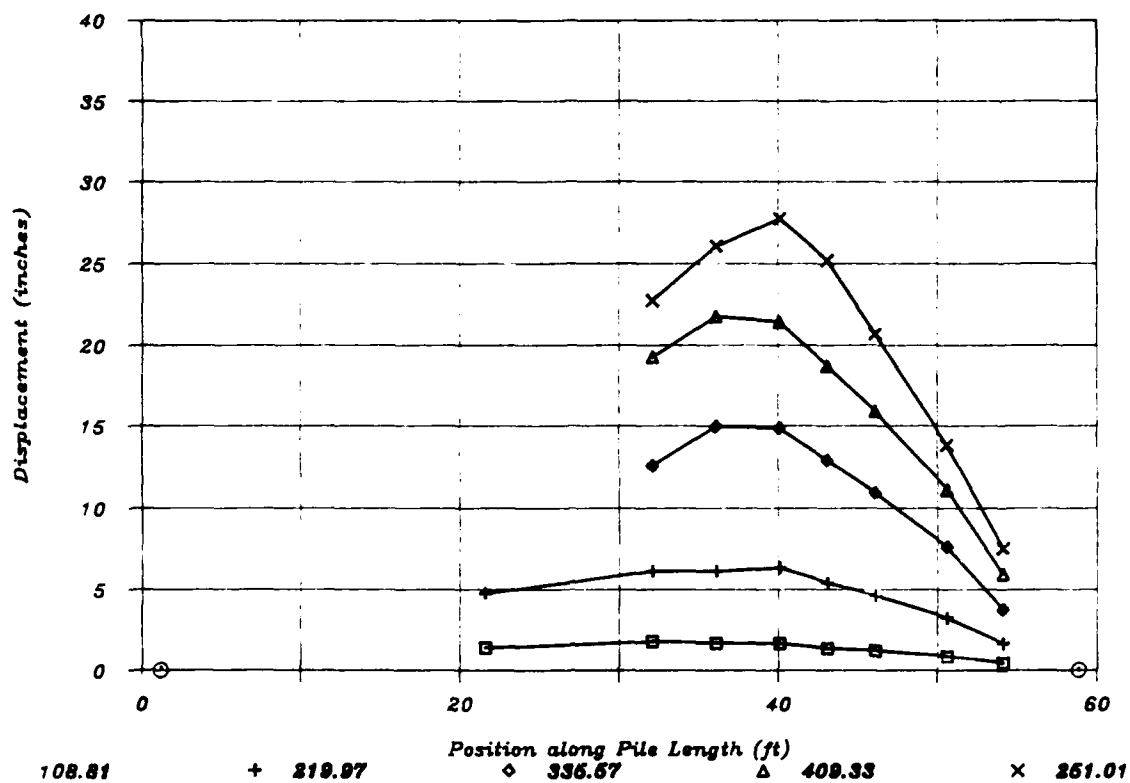


Figure B-43. MK3 deformed shape for M = 109, 220, 336, 409, and 251 kip-ft.

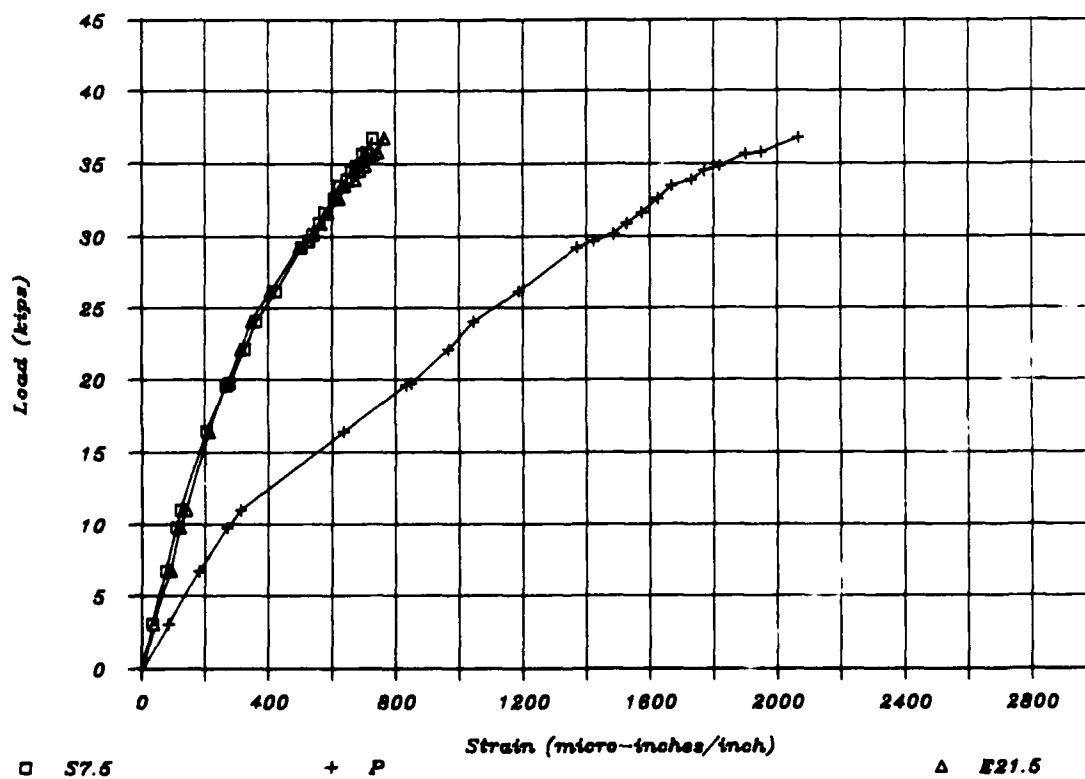


Figure B-44. MK3 load-compression strain - all gages.

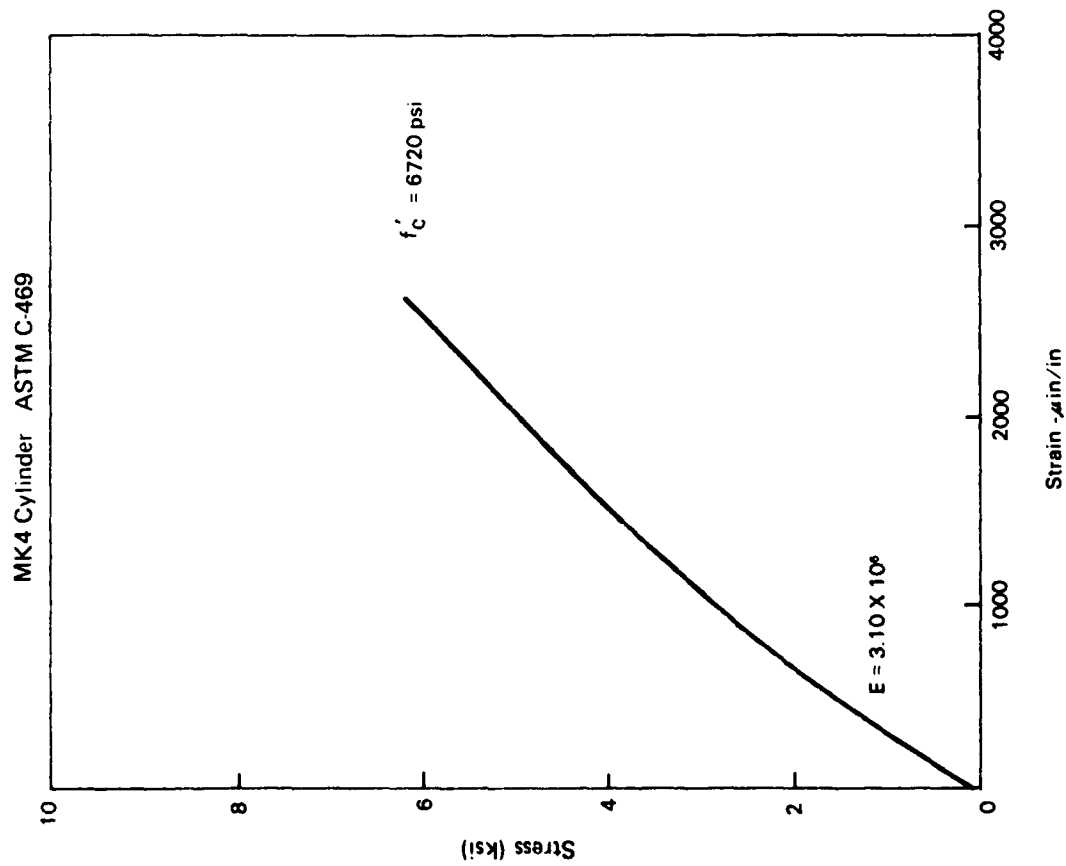


Figure B-45. Concrete stress-strain curve for MK4 (ASTM C-469).

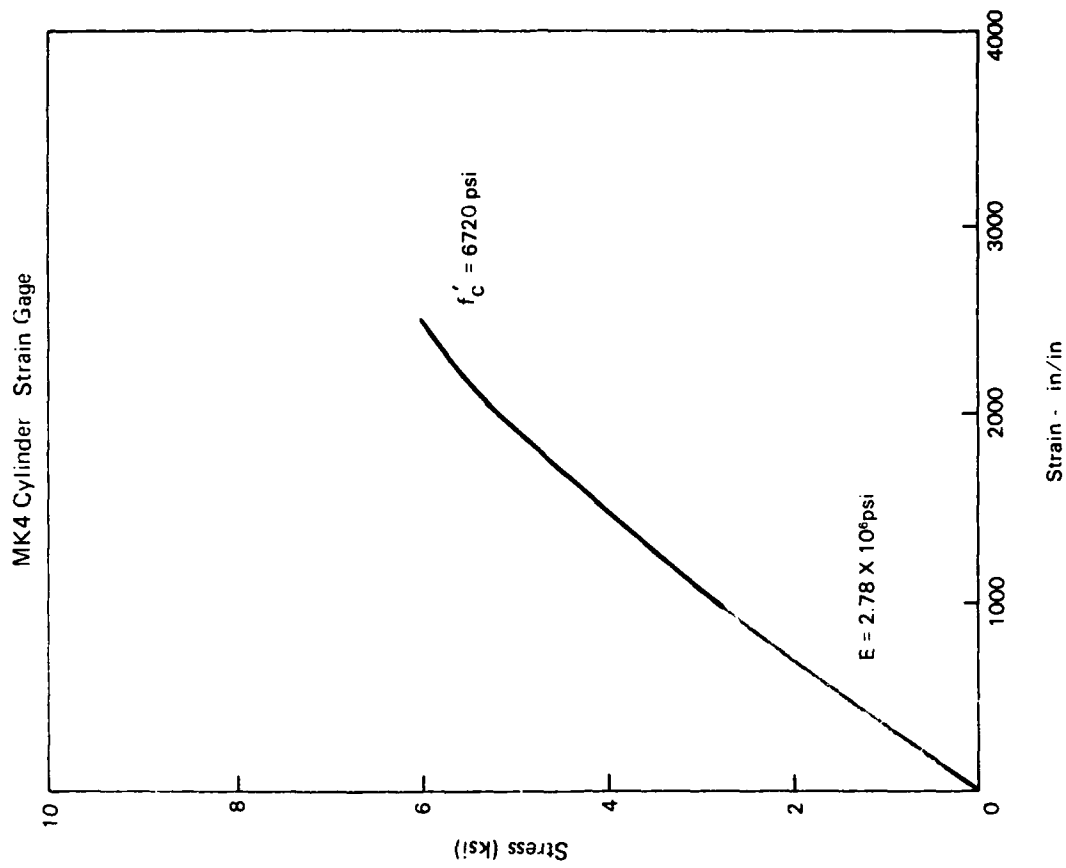


Figure B-46. Concrete stress-strain curve for MK4 (strain gage).

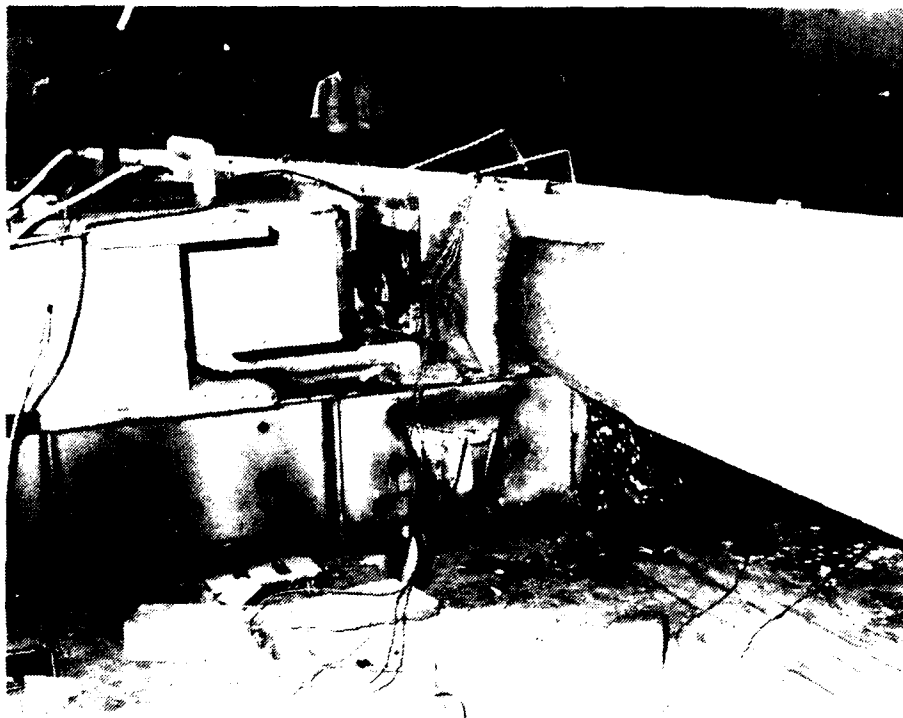


Figure B-47. MK4 compression spalling at ultimate load.

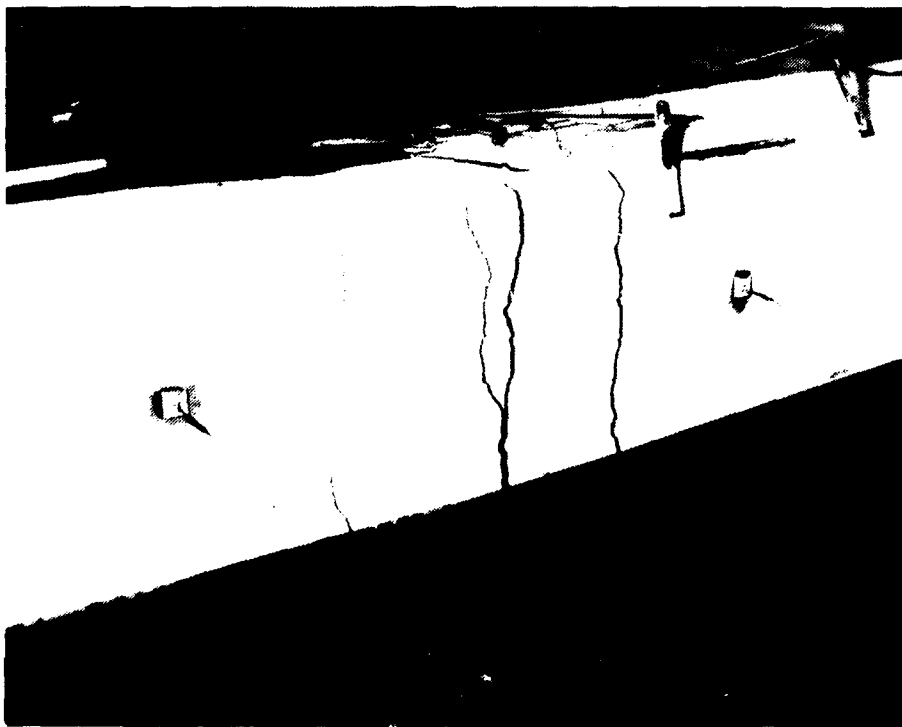


Figure B-48. MK4 load point tension face cracks at ultimate load.



Figure B-49. MK4 spall zone after failure load.



Figure B-50. MK4 failure near load point.

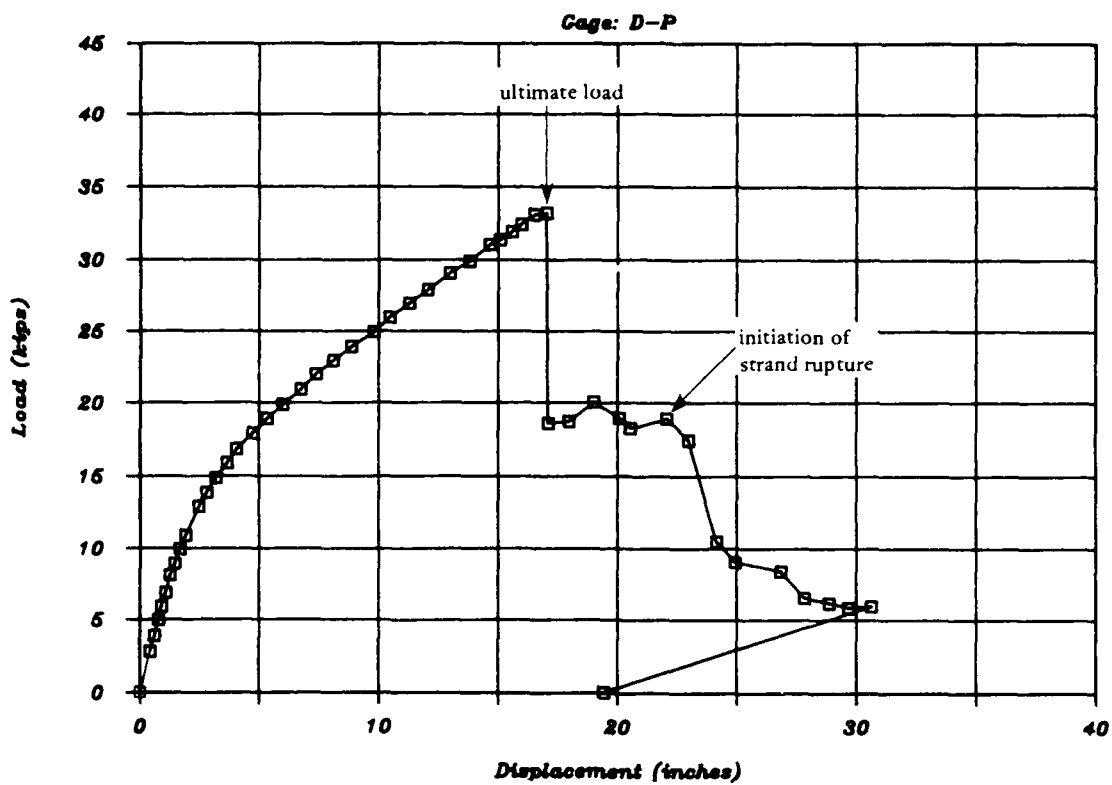


Figure B-51. MK4 load-displacement plot.

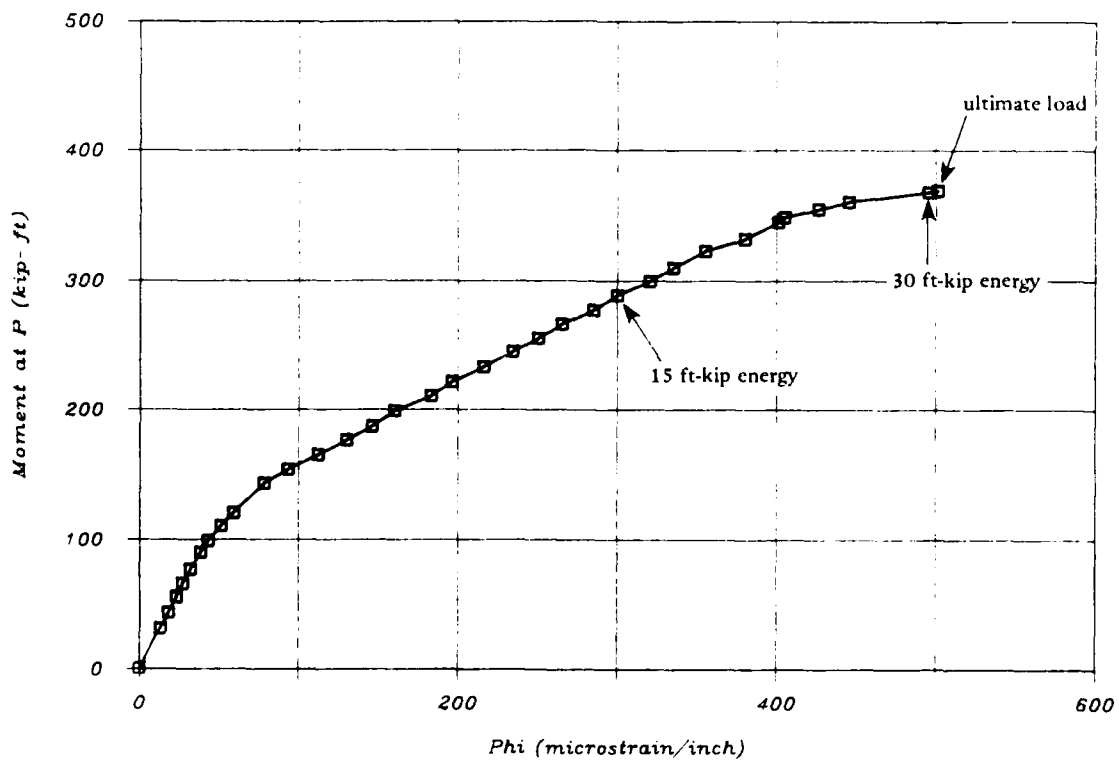


Figure B-52. MK4 moment-curvature plot.

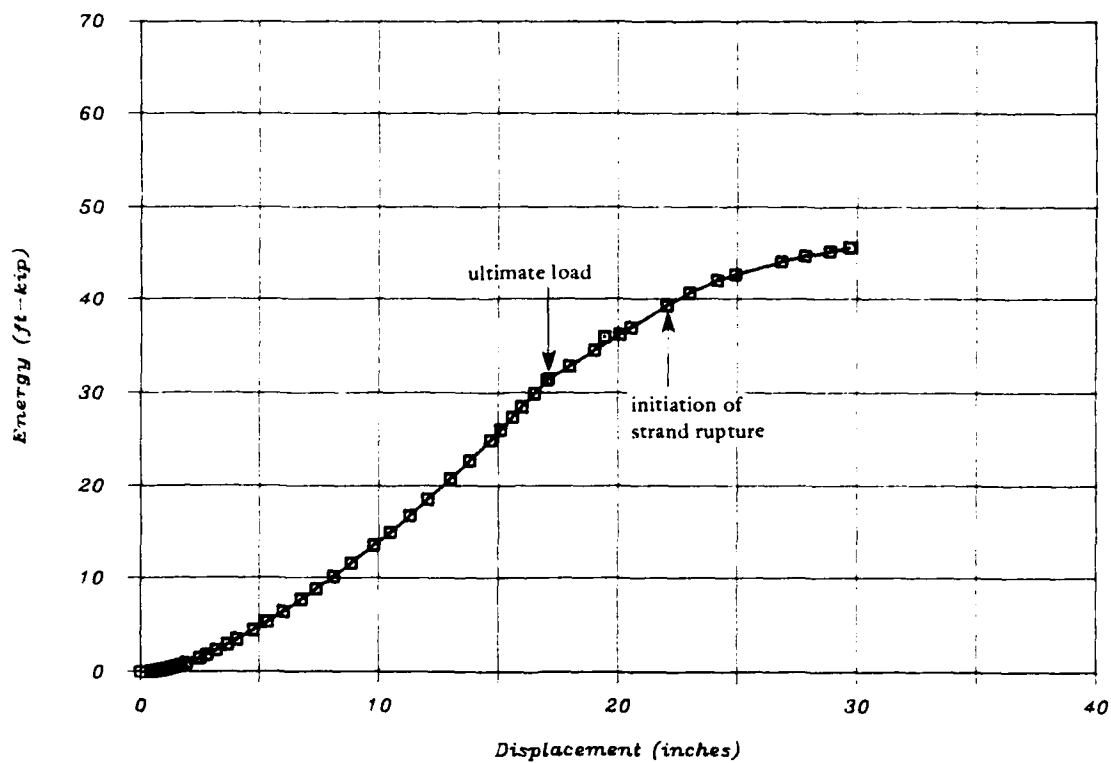


Figure B-53. MK4 energy-displacement plot.

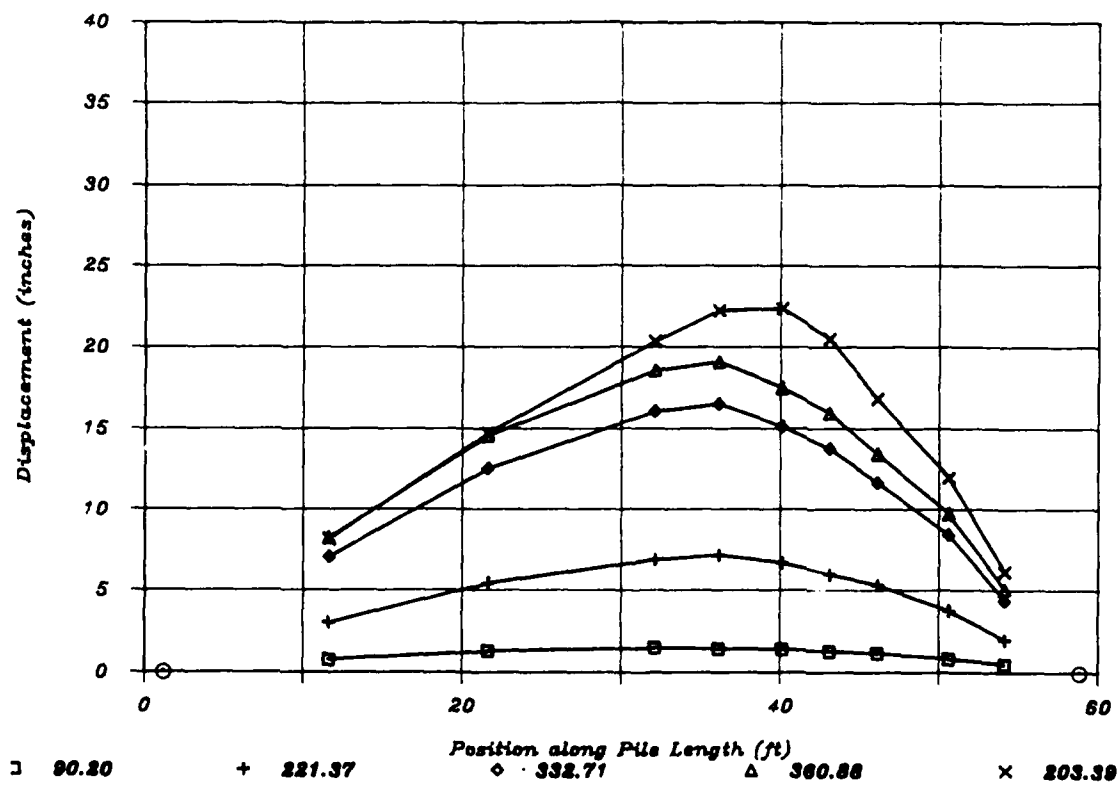


Figure B-54. MK4 deformed shape at $M = 90, 221, 333, 361,$ and 203 kip-ft.

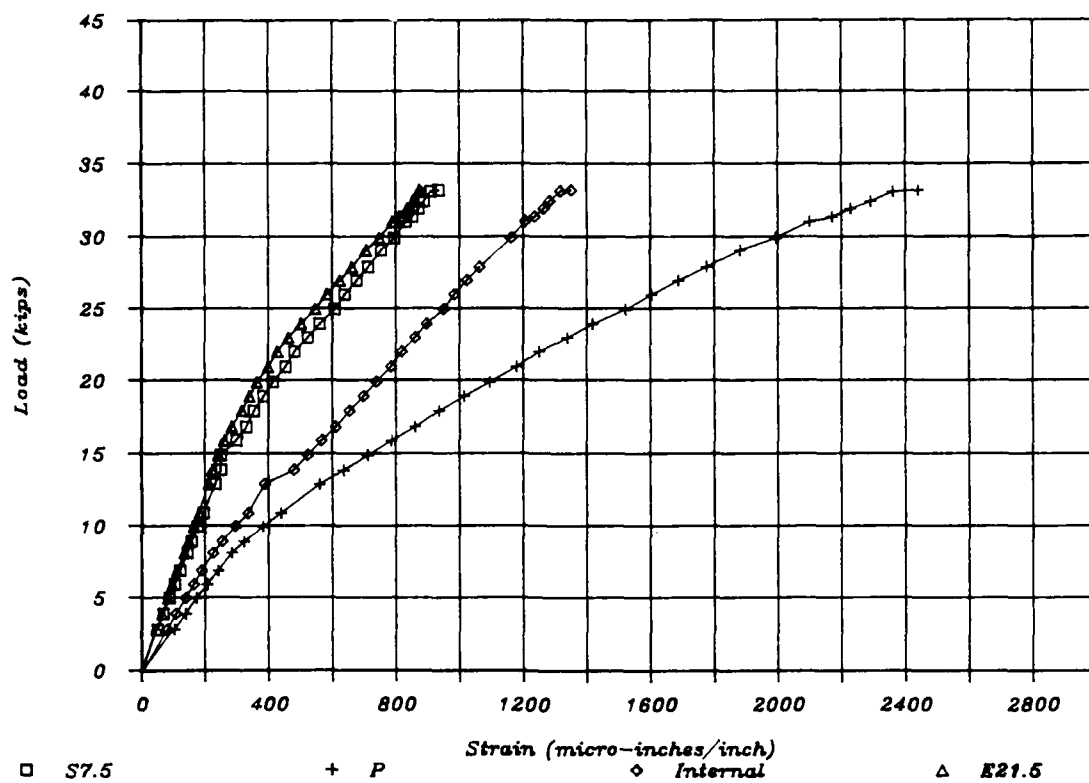


Figure B-55. MK4 load-compression strain - all gages.

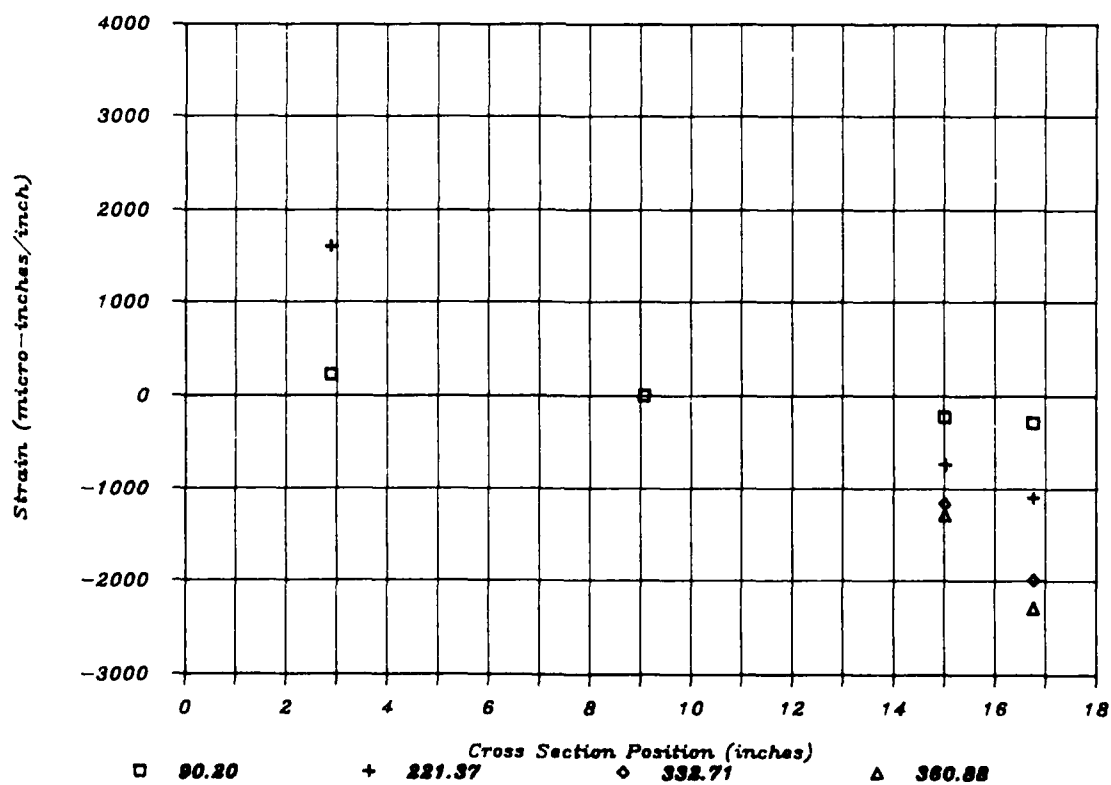


Figure B-56. MK4 load point cross-section strain at M = 90, 221, 333, and 361 kip-ft.

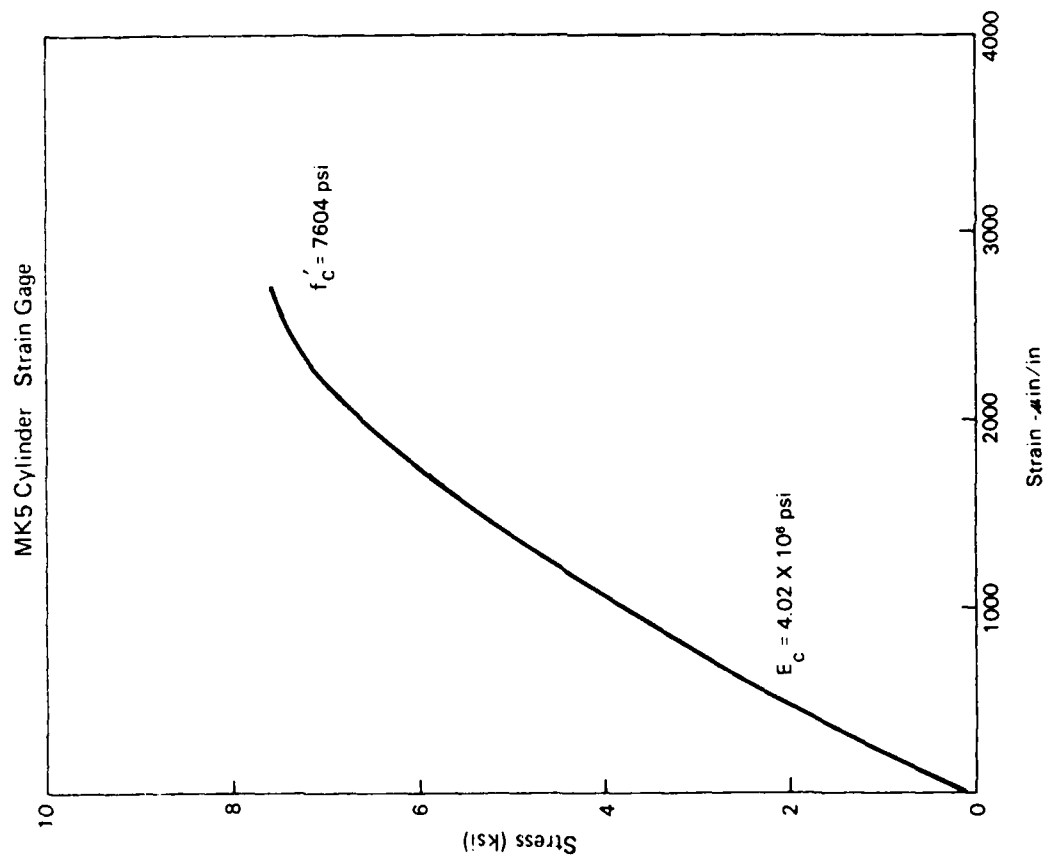


Figure B-57. Concrete stress-strain curve for MK5 (ASTM C-469).

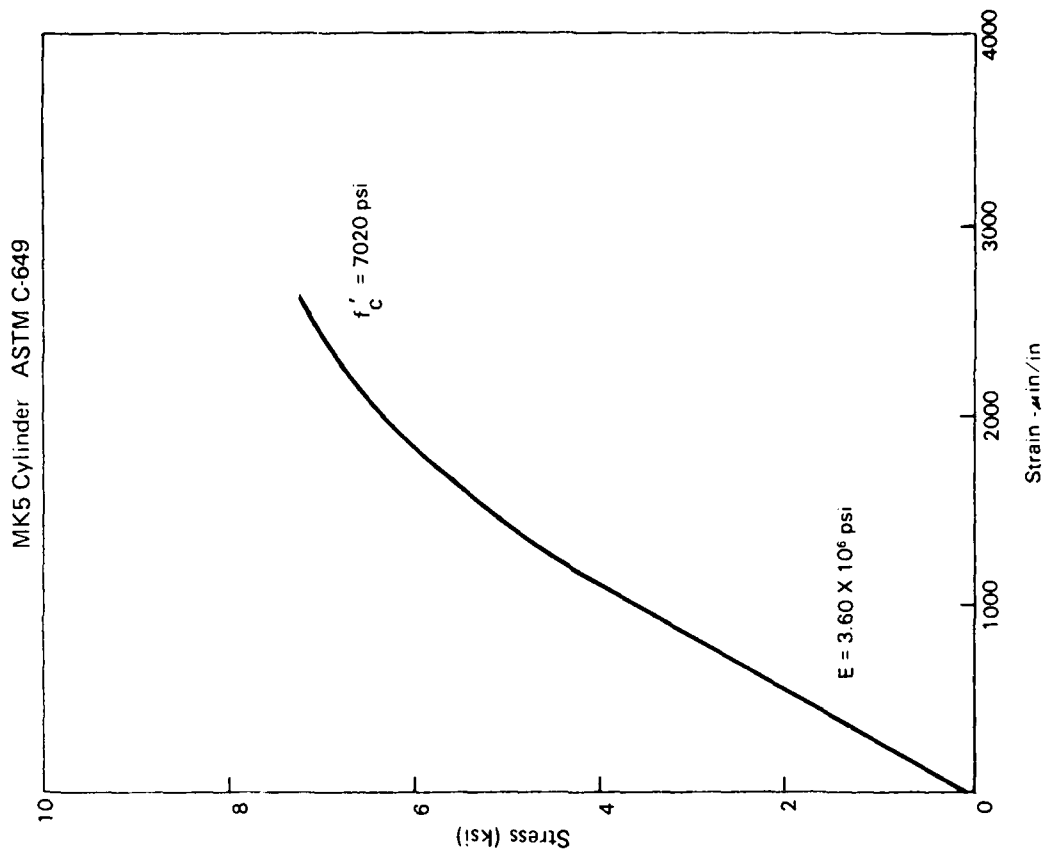


Figure B-58. Concrete stress-strain curve for MK5 (strain gage).

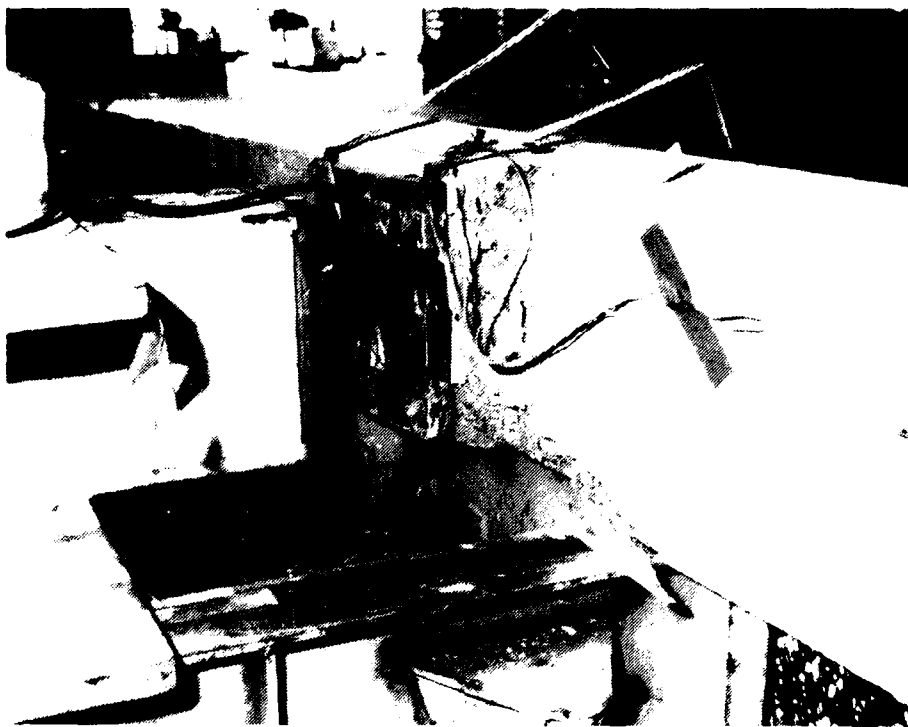


Figure B-59. MK5 concrete spall zone after ultimate load.



Figure B-60. MK5 spall zone after failure.

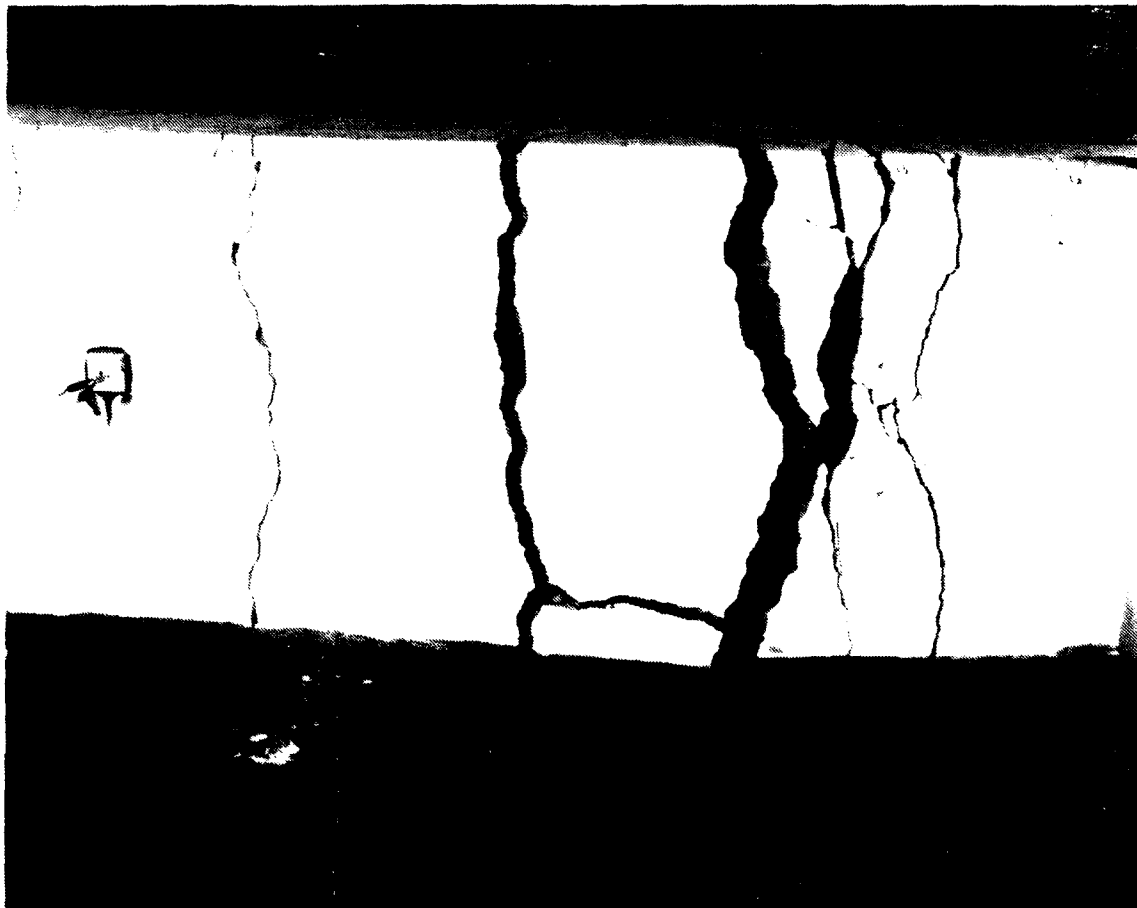


Figure B-61. MK5 tension face at load point after failure.

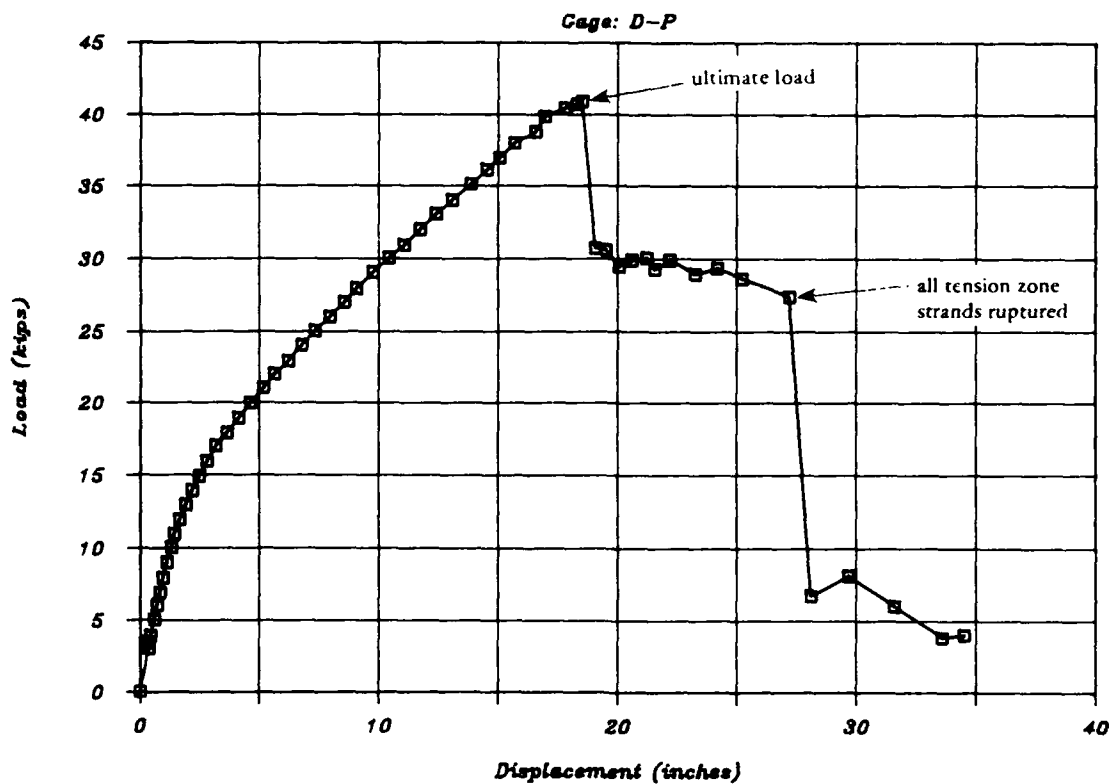


Figure B-62. MK5 load-displacement plot.

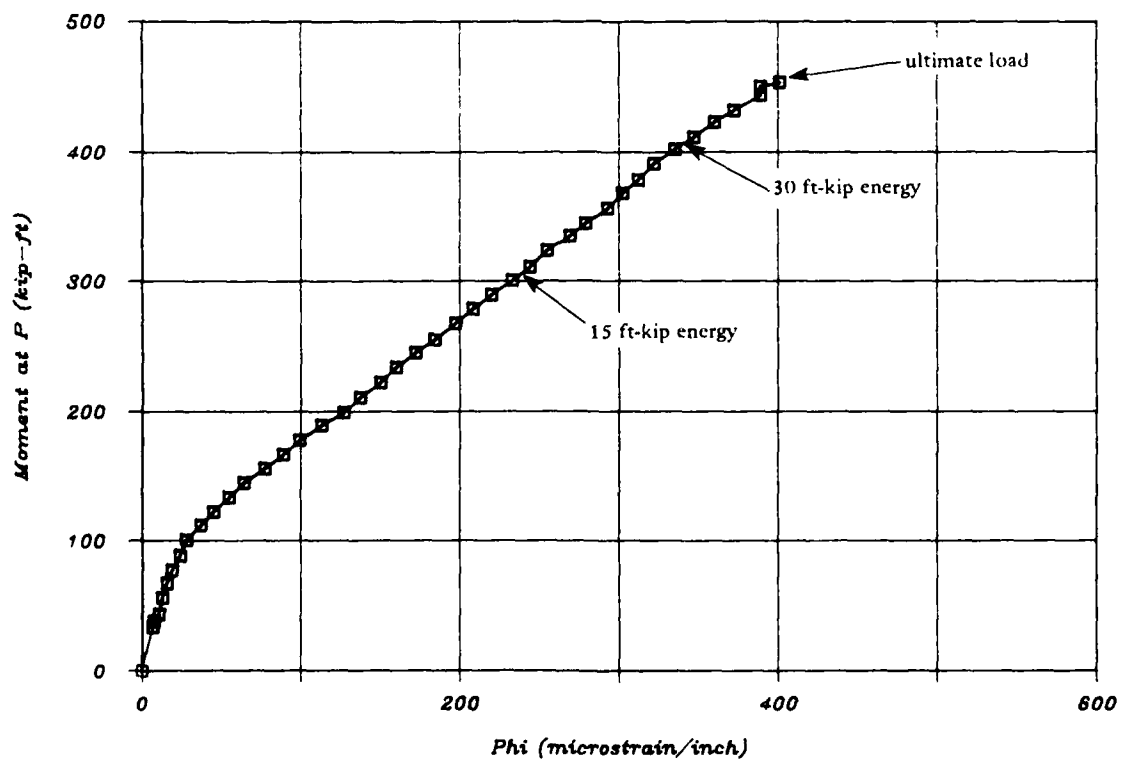


Figure B-63. MK5 moment-curvature plot.

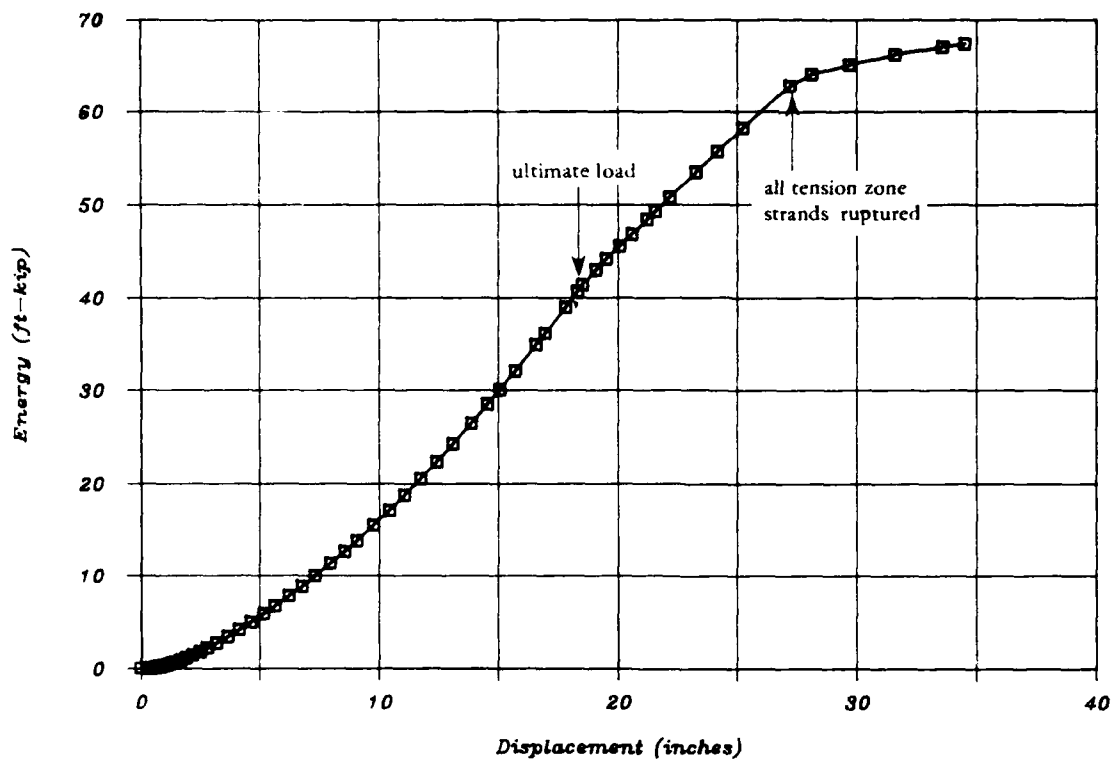


Figure B-64. MK5 energy-displacement plot.

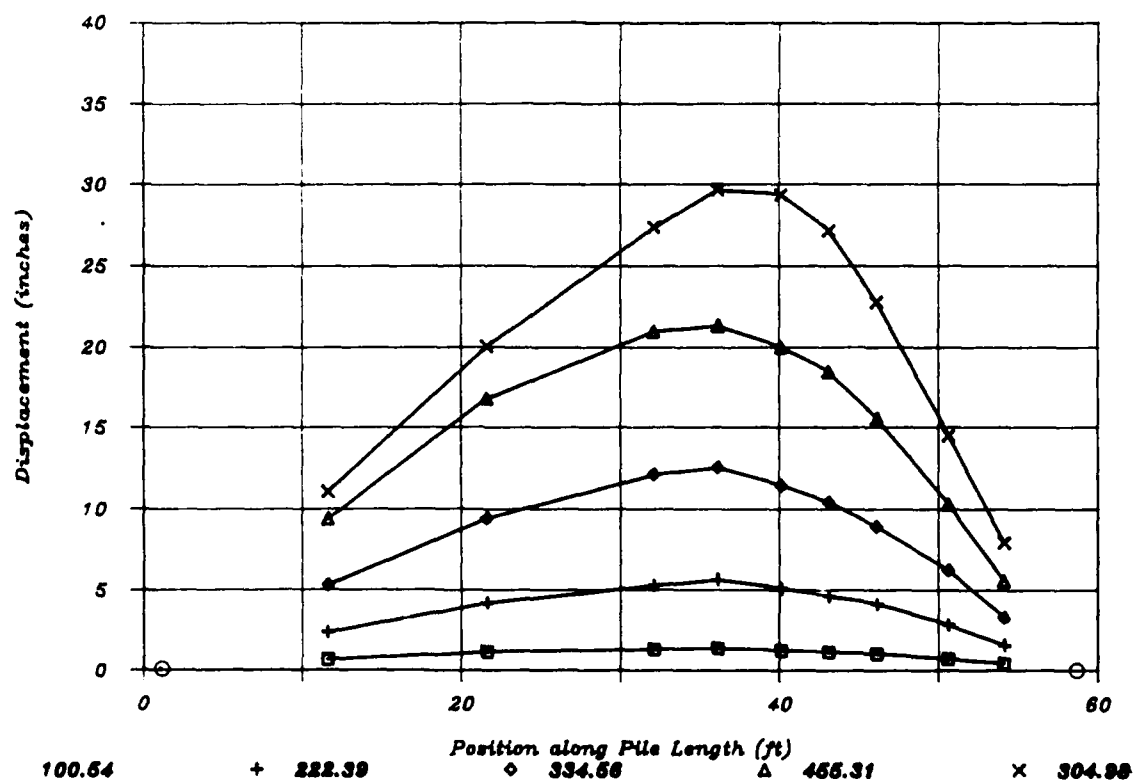


Figure B-65. MK5 deformed shape at $M = 101, 222, 335, 455,$ and 305 kip-ft.

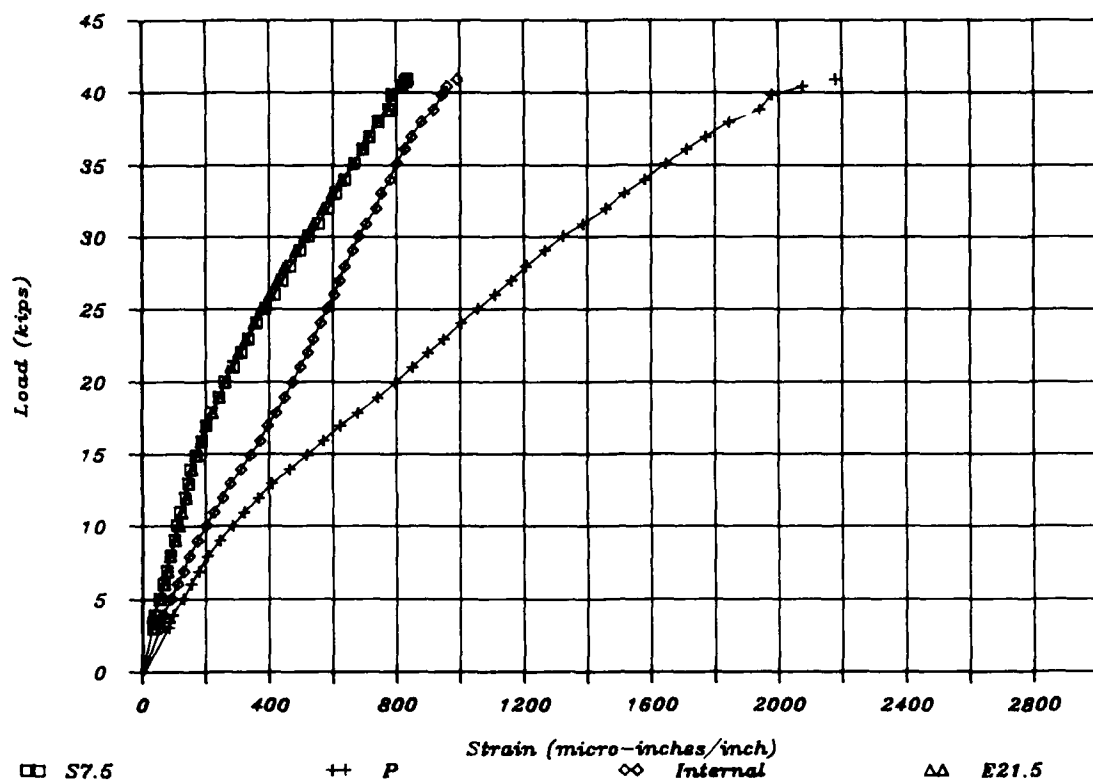


Figure B-66. MK5 load-compression strain - all gages.

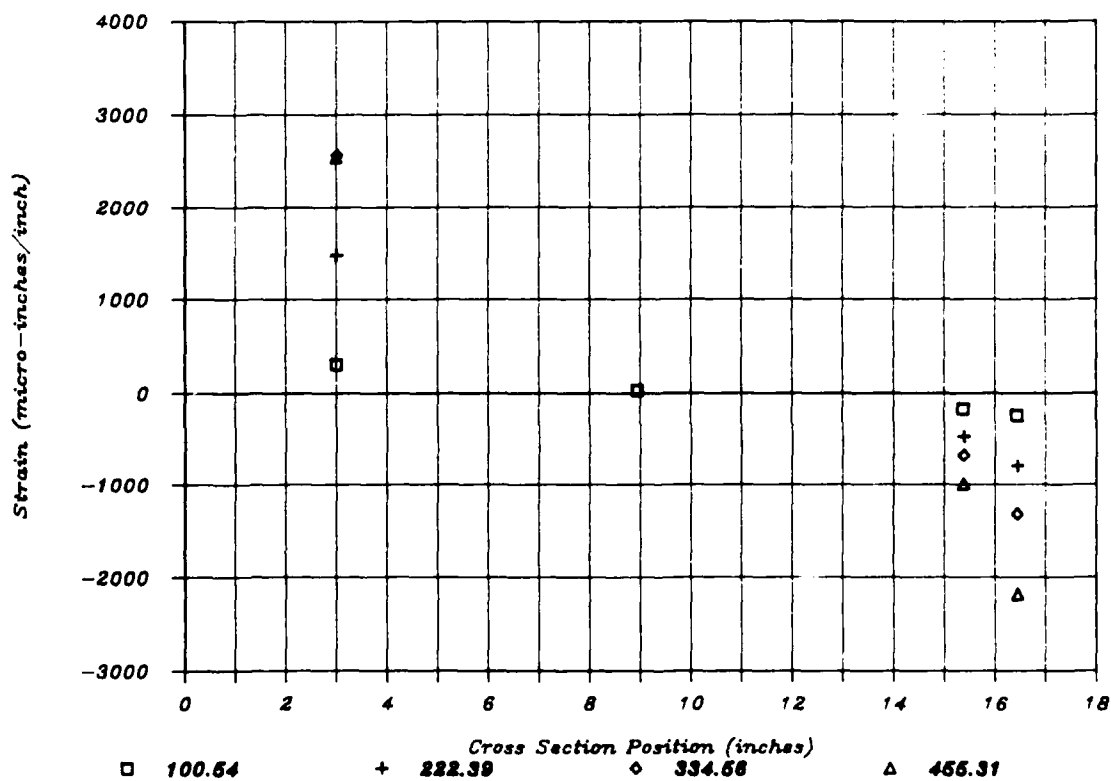


Figure B-67. MK5 load point cross-section strain at M = 101, 222, 335, 455, and 305 kip-ft.

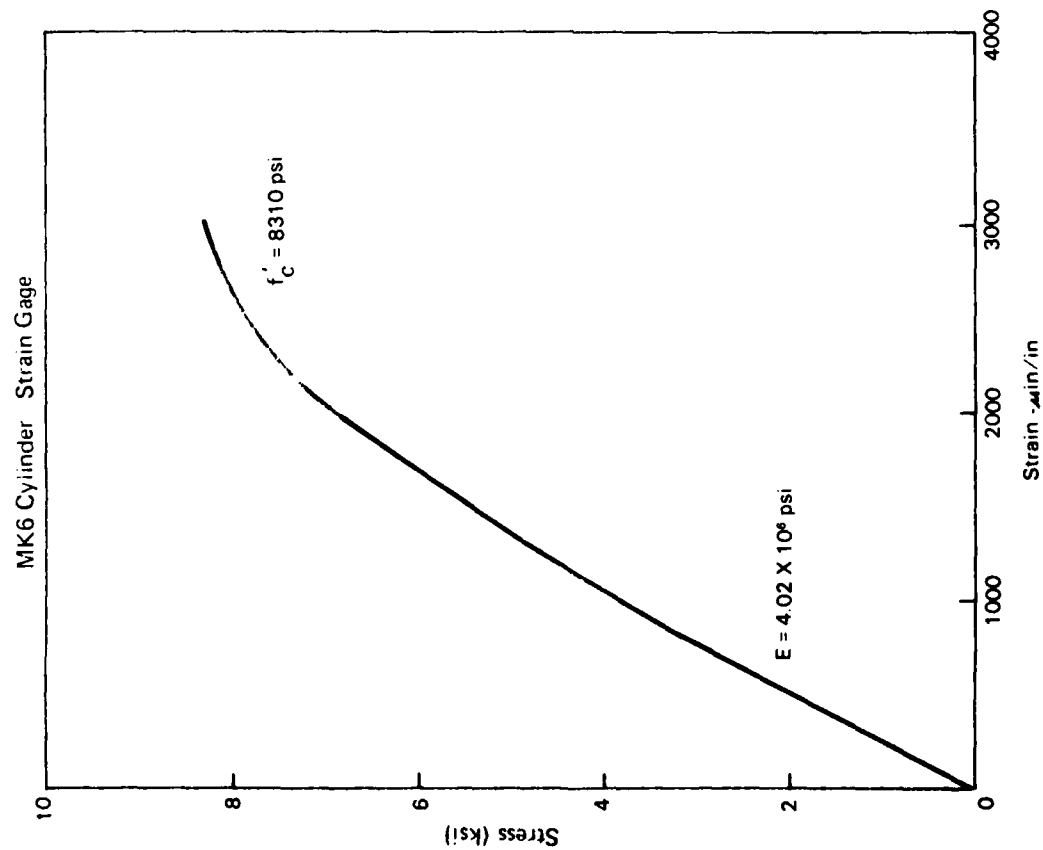


Figure B-68. Concrete stress-strain curve for MK6 (ASTM C-469).

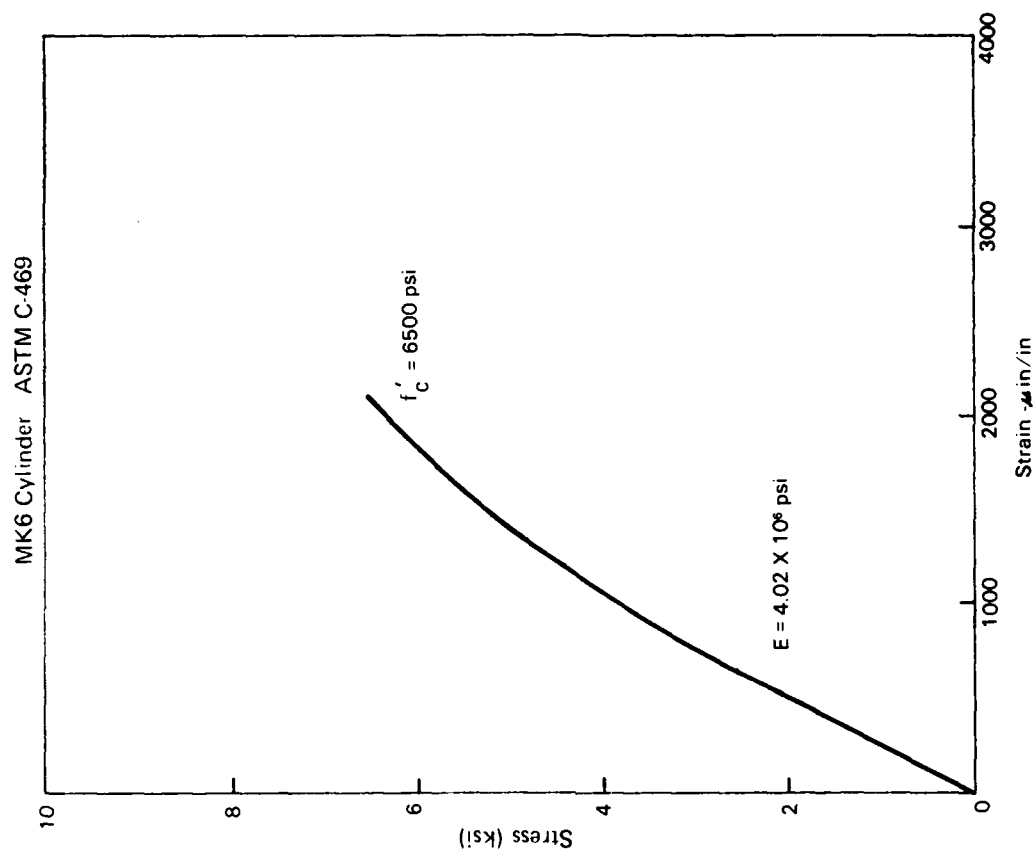


Figure B-69. Concrete stress-strain curve for MK6 (strain gage).

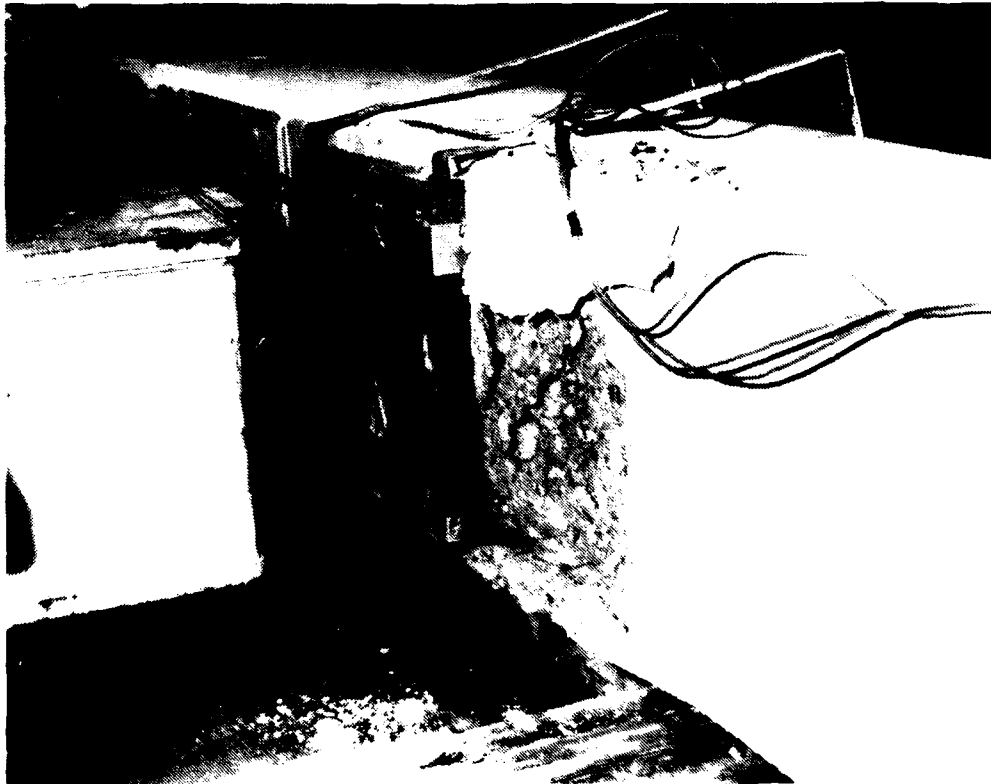


Figure B-70. MK6 concrete spalling at ultimate load.



Figure B-71. MK6 displacement at failure.



Figure B-72. MK6 spall zone after failure.

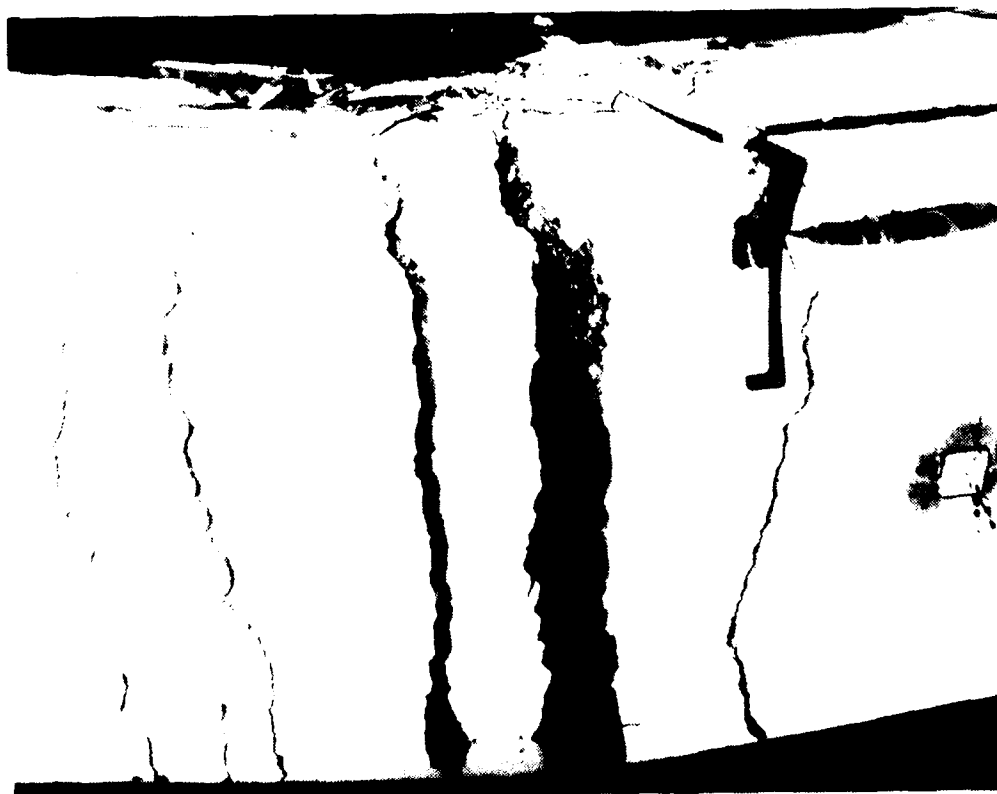


Figure B-73. MK6 post-failure tension face at load point.

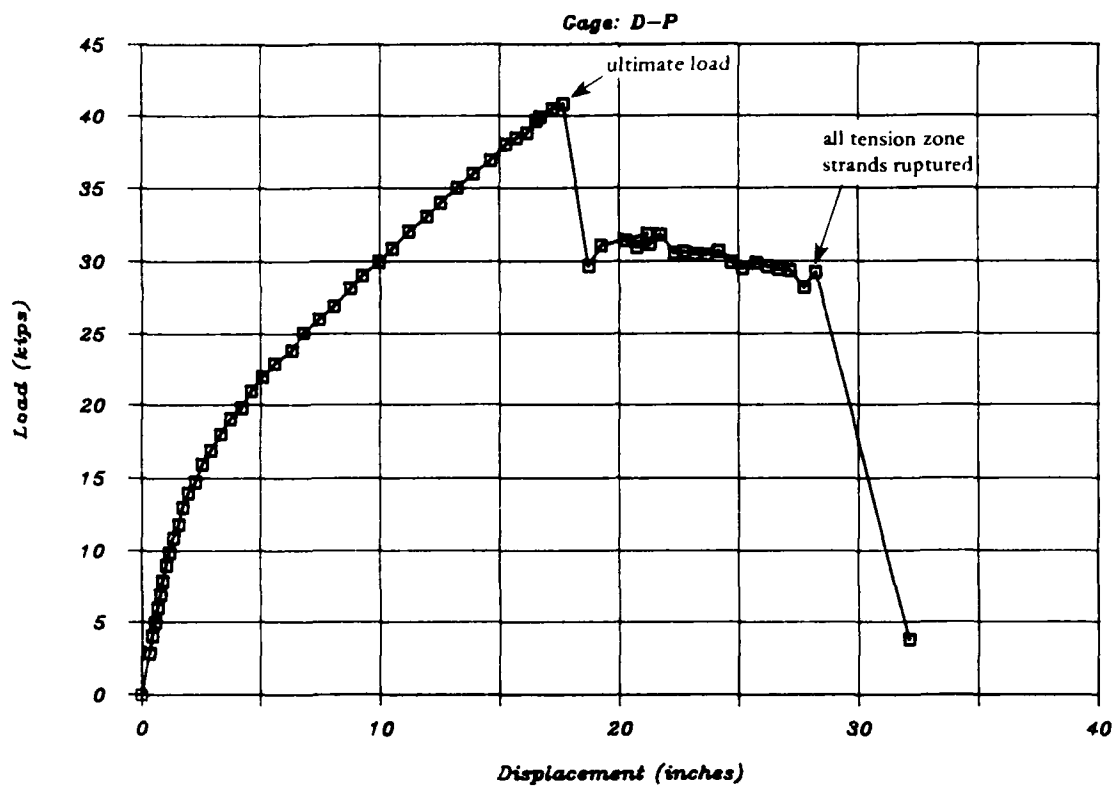


Figure B-74. MK6 load-displacement plot.

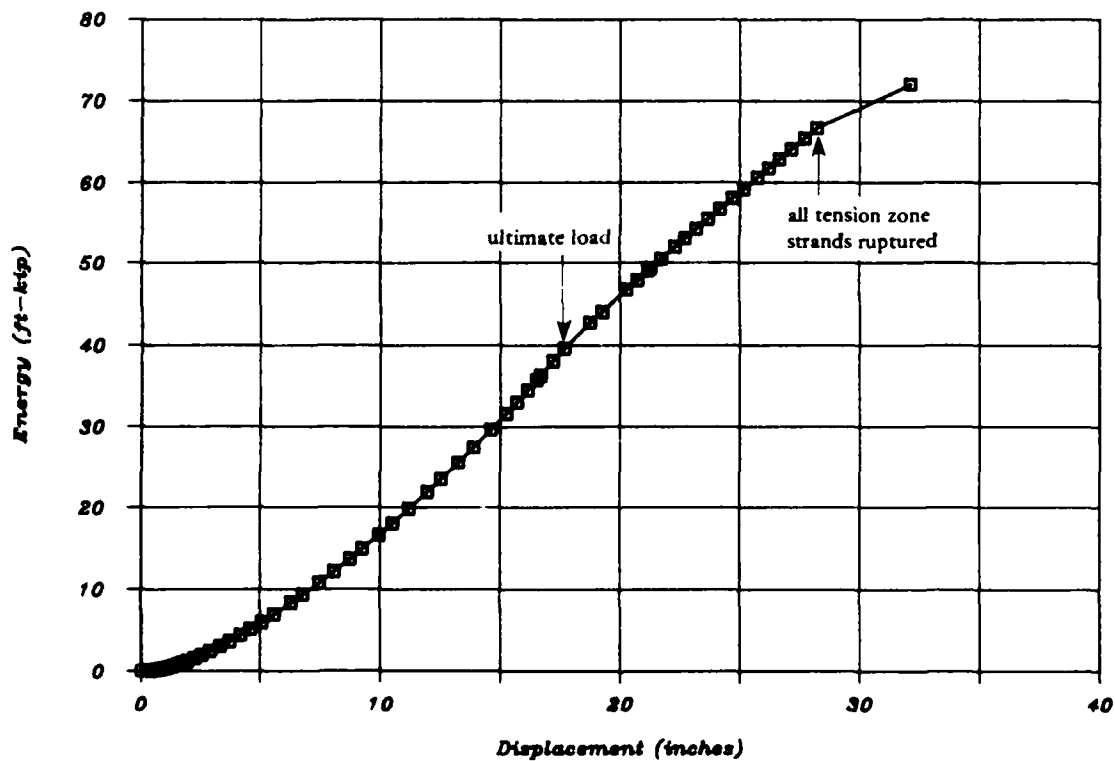


Figure B-75. MK6 energy-displacement plot.

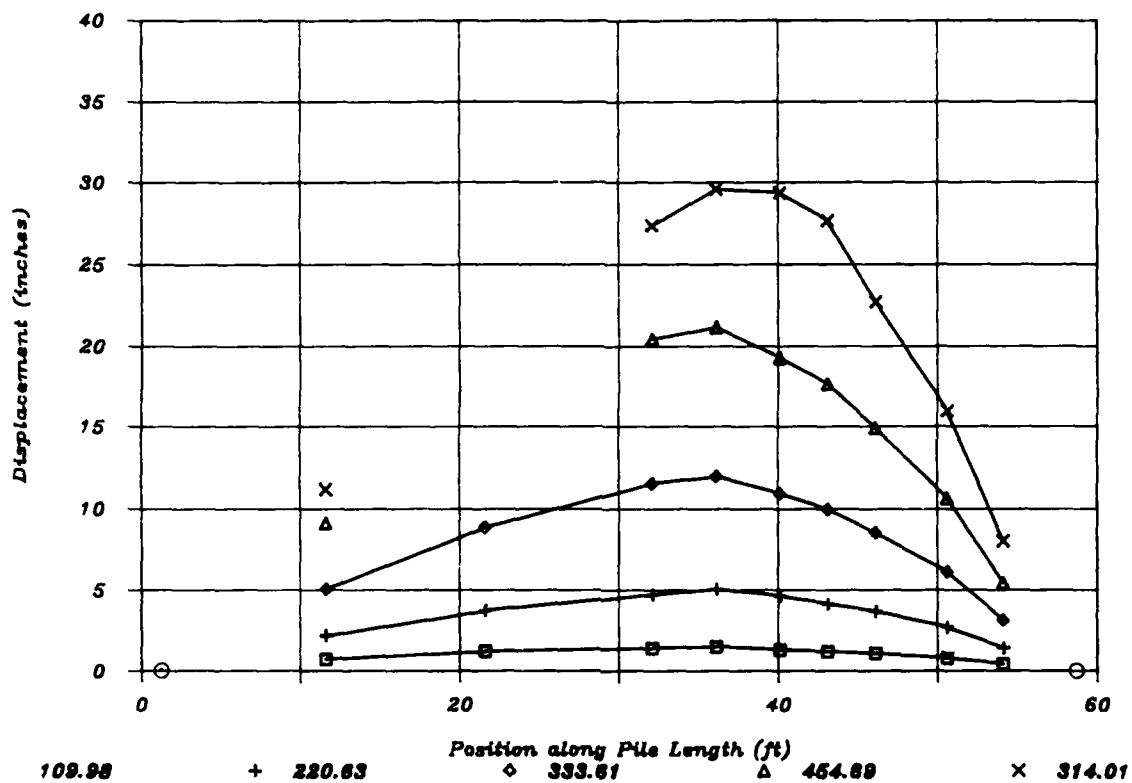


Figure B-76. MK6 deformed shape at $M = 110, 221, 334, 455,$ and 314 kip-ft.

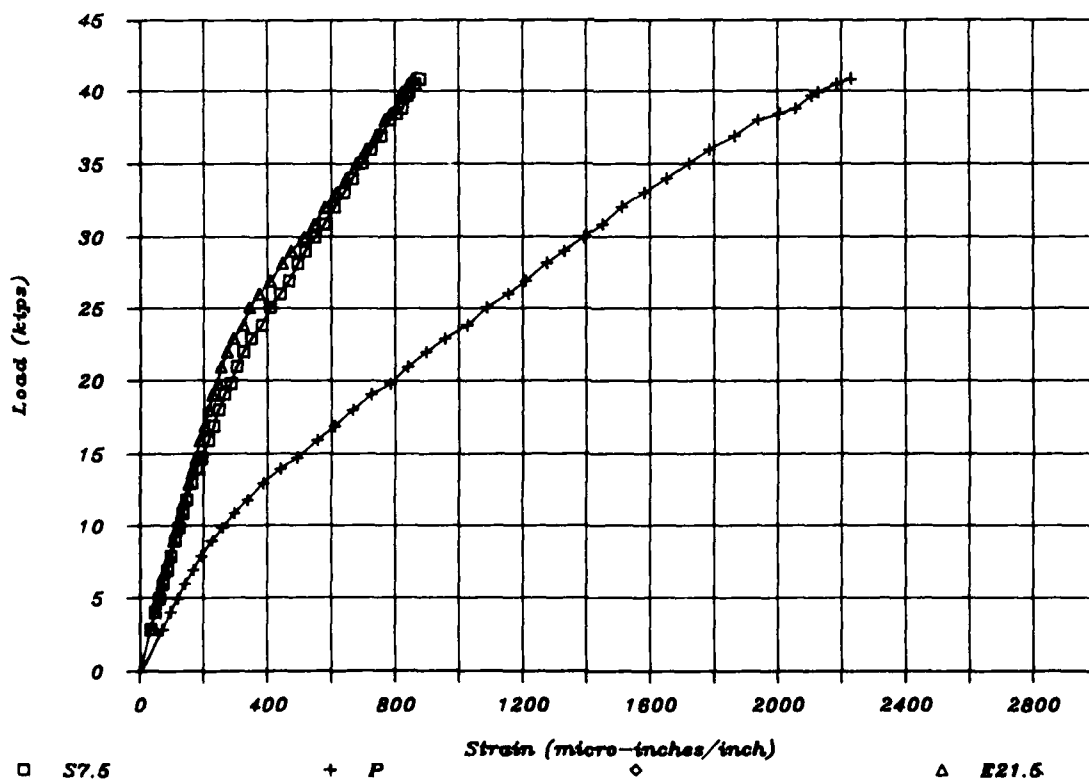


Figure B-77. MK6 load-compression strain - all gages.

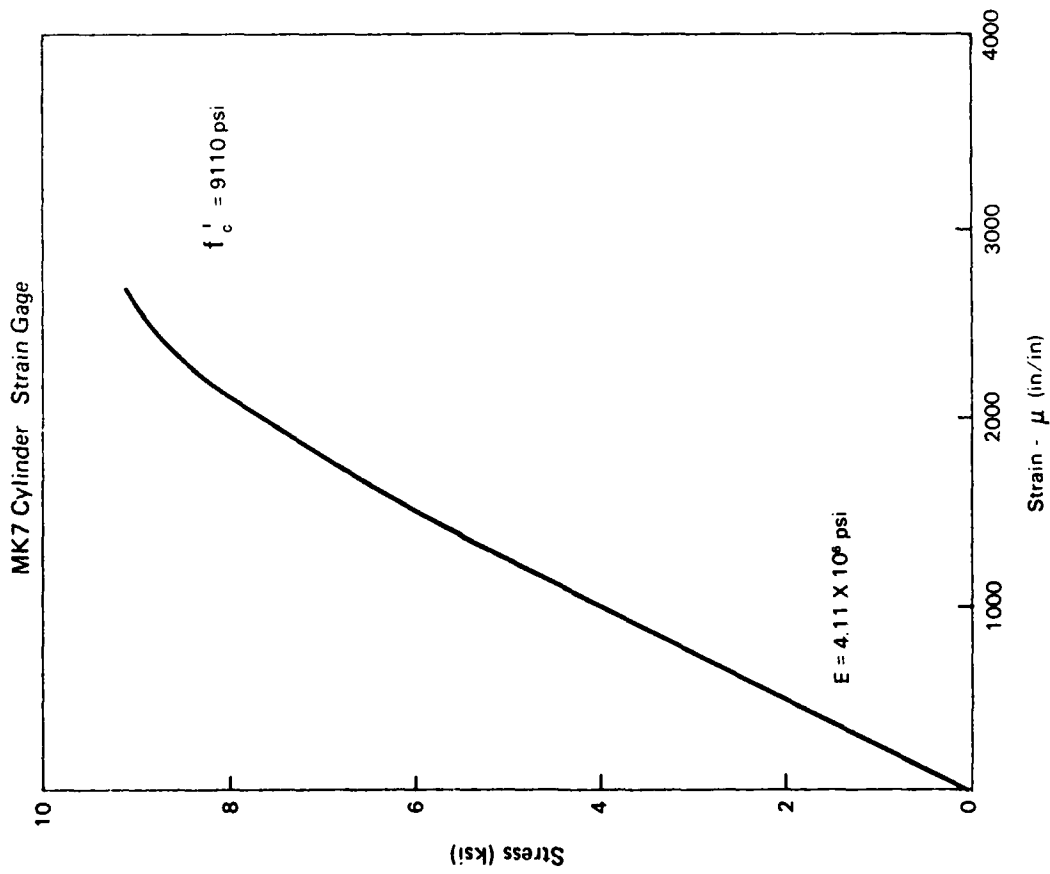


Figure B-78. Concrete stress-strain curve for MK7 (ASTM C-469).

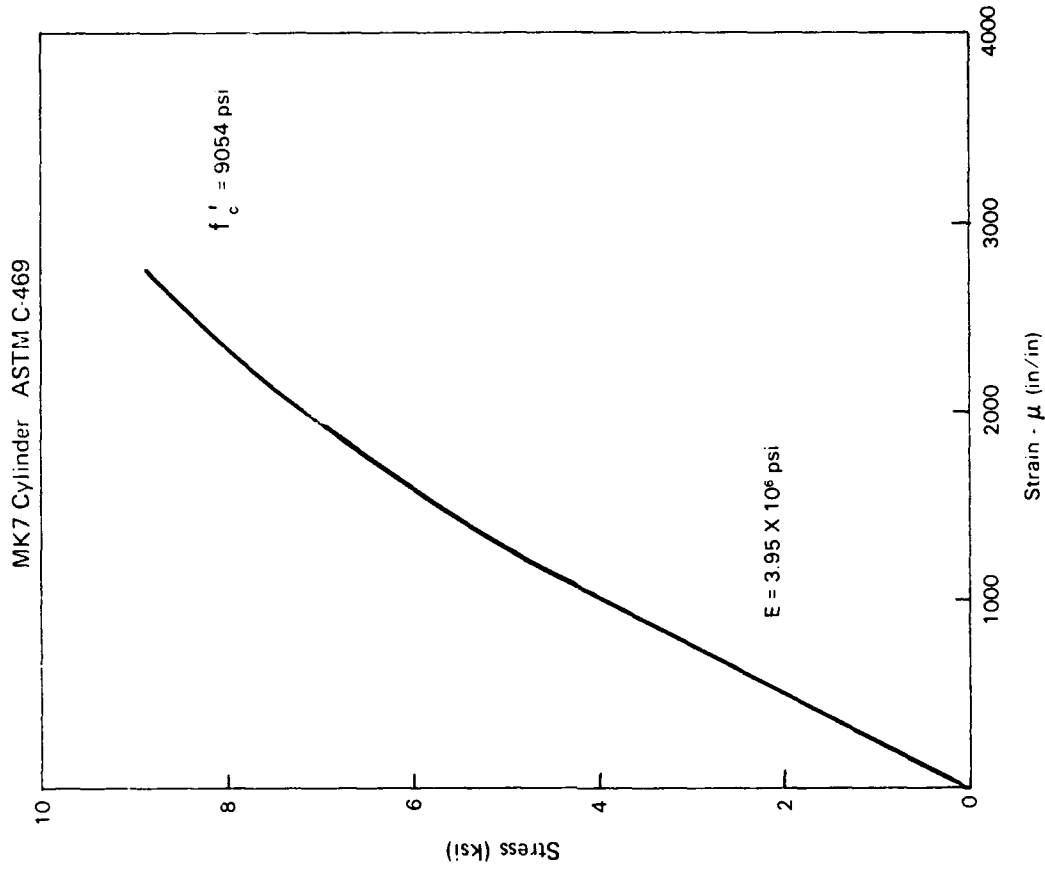


Figure B-79. Concrete stress-strain curve for MK7 (strain gage).



Figure B-80. MK7 post-failure spall zone.



Figure B-81. MK7 spiral yield and necking in the spall zone.

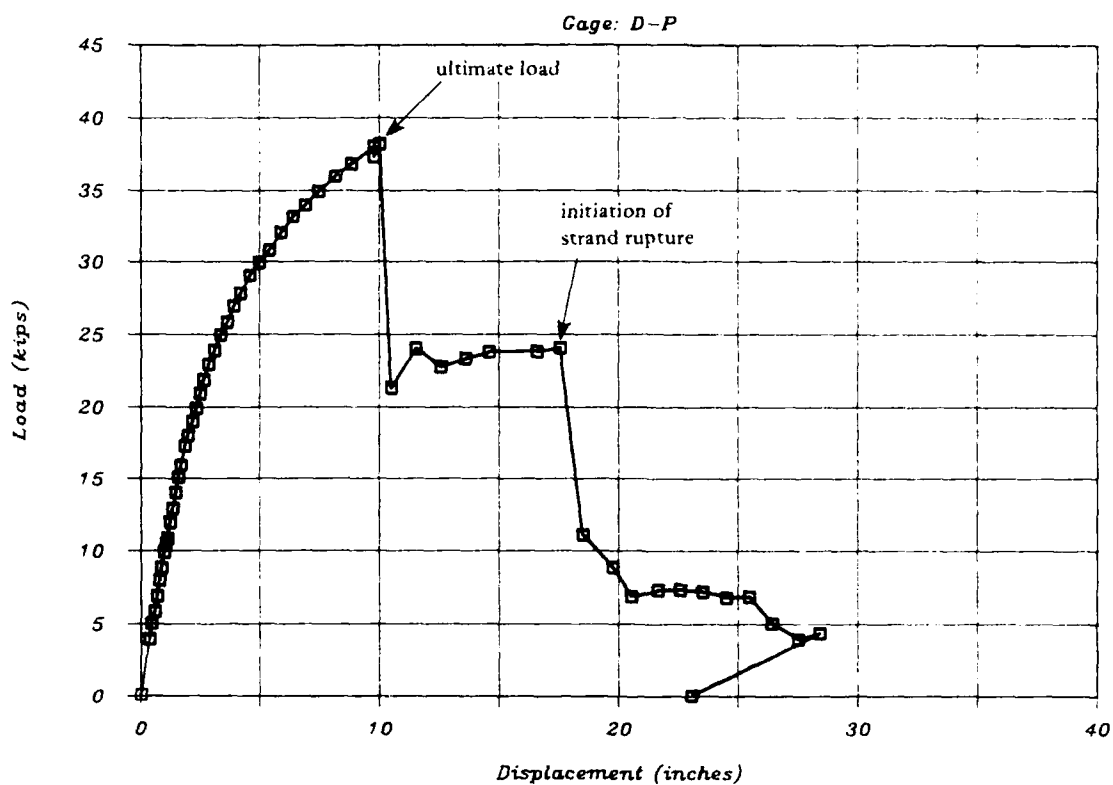


Figure B-82. MK7 load-displacement plot.

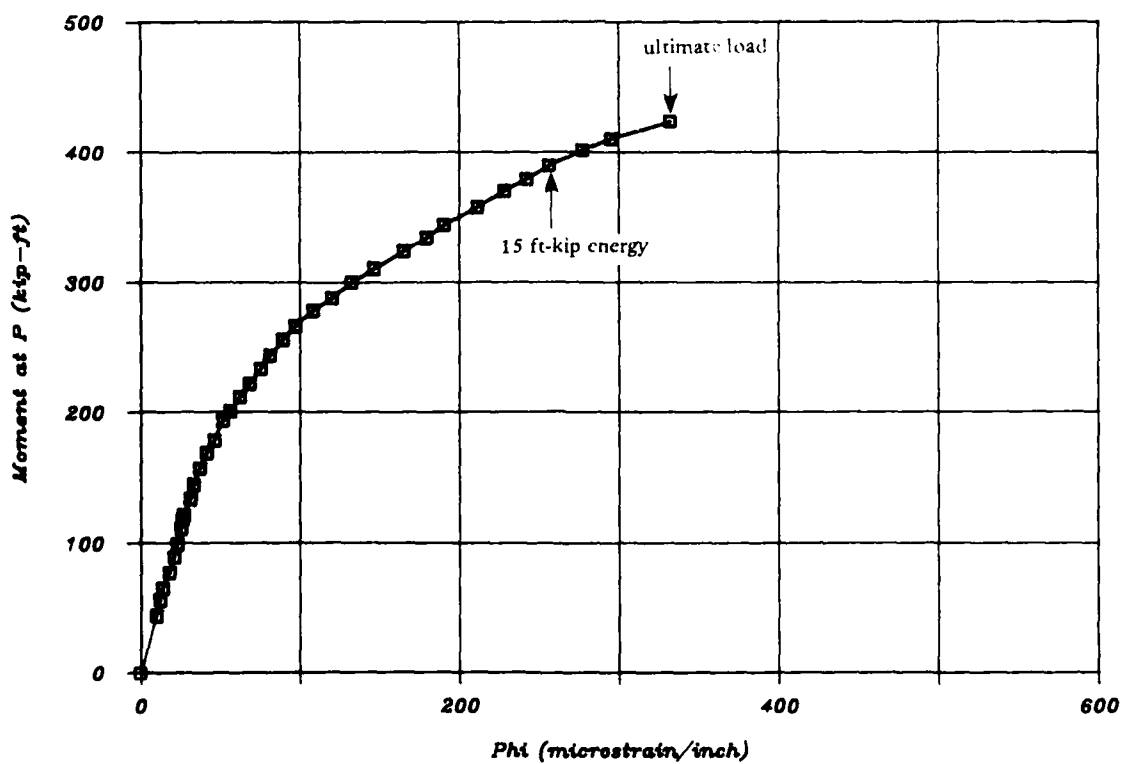


Figure B-83. MK7 moment-curvature plot.

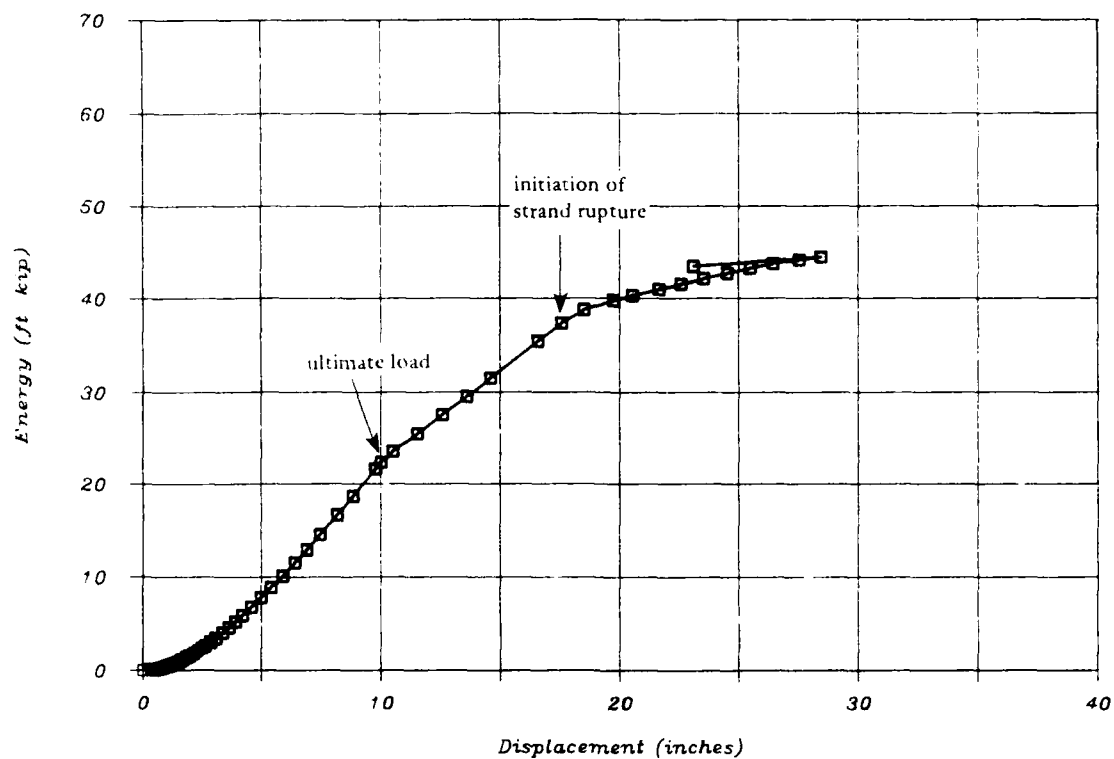


Figure B-84. MK7 energy-displacement plot.

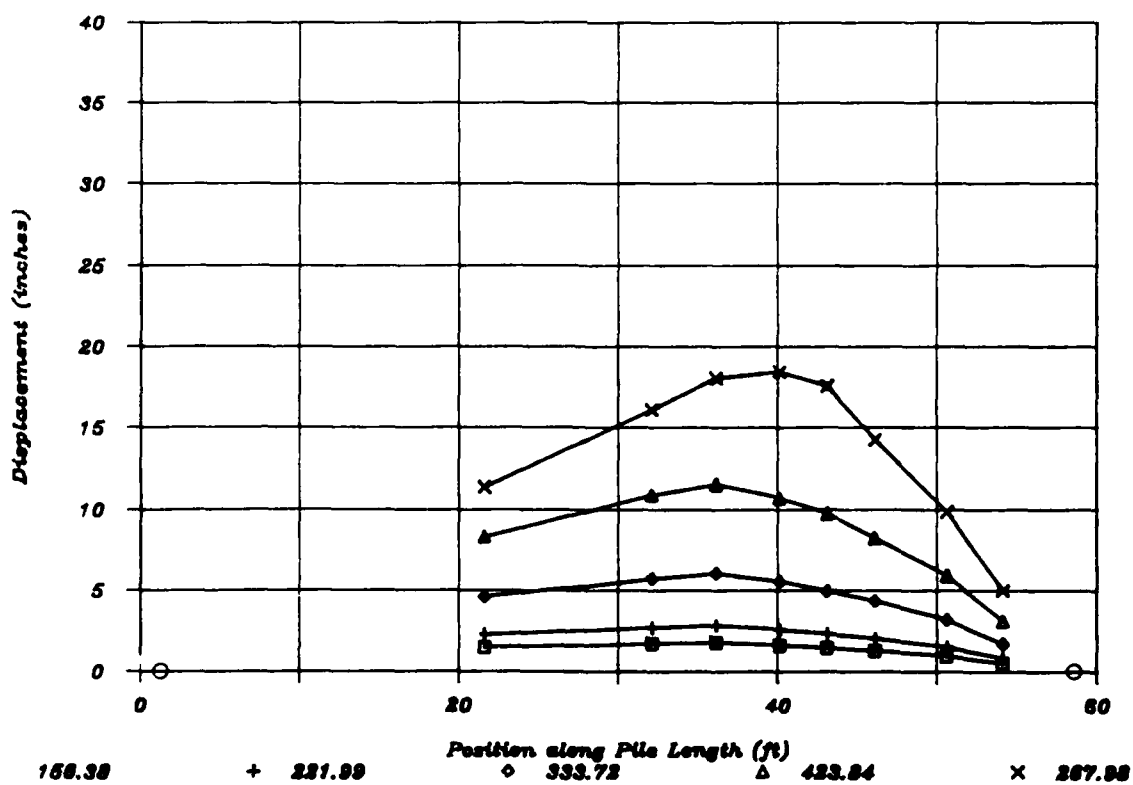


Figure B-85. MK7 deformed shape for M = 156, 222, 334, 424, and 268 kip-ft.

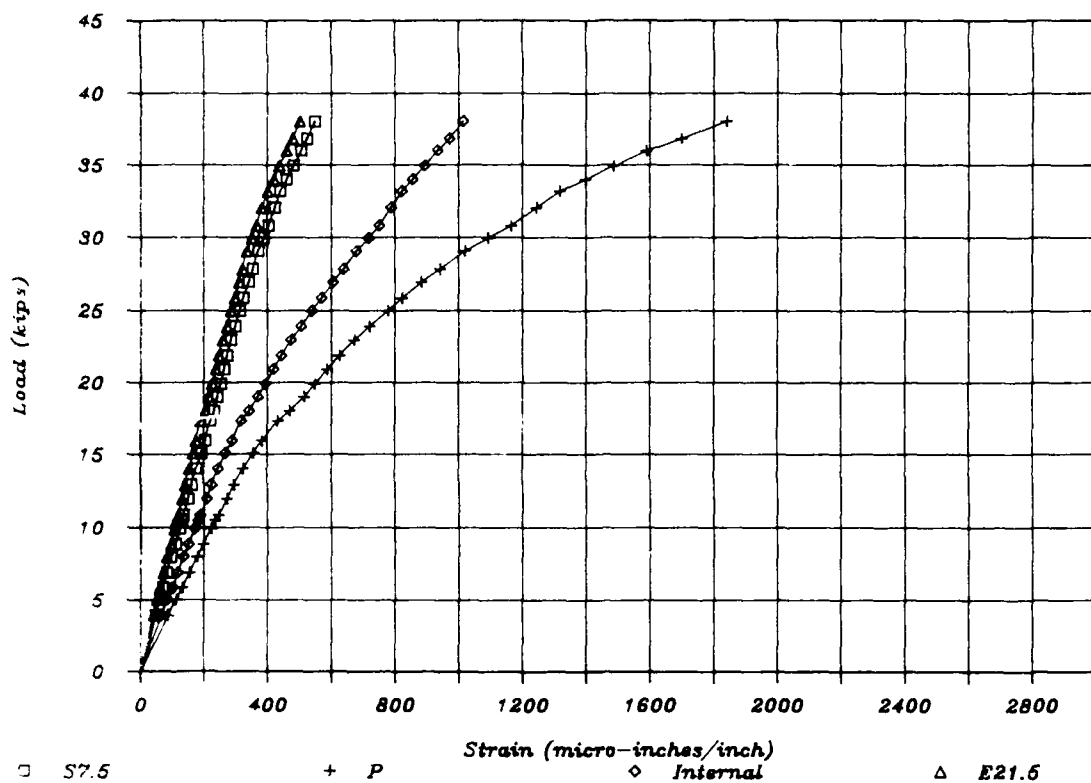


Figure B-86. MK7 load-compression strain - all gages.

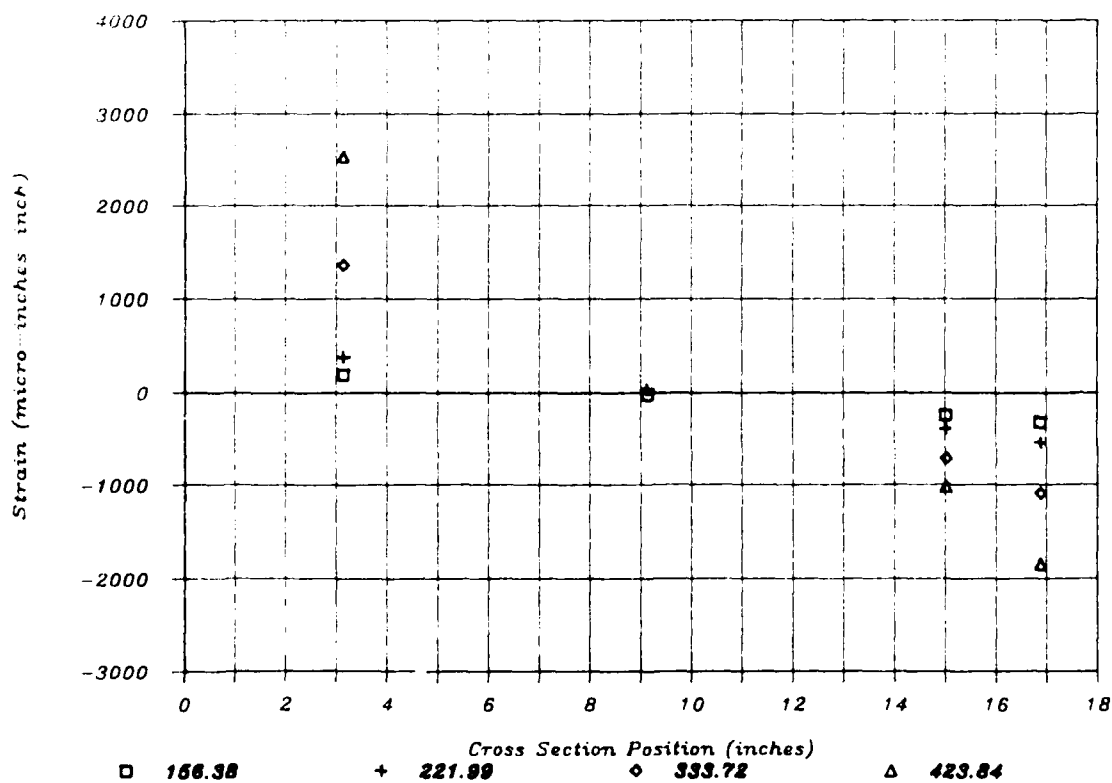


Figure B-87. MK7 load point cross-section strain for M = 156, 222, 334, and 424 kip-ft.

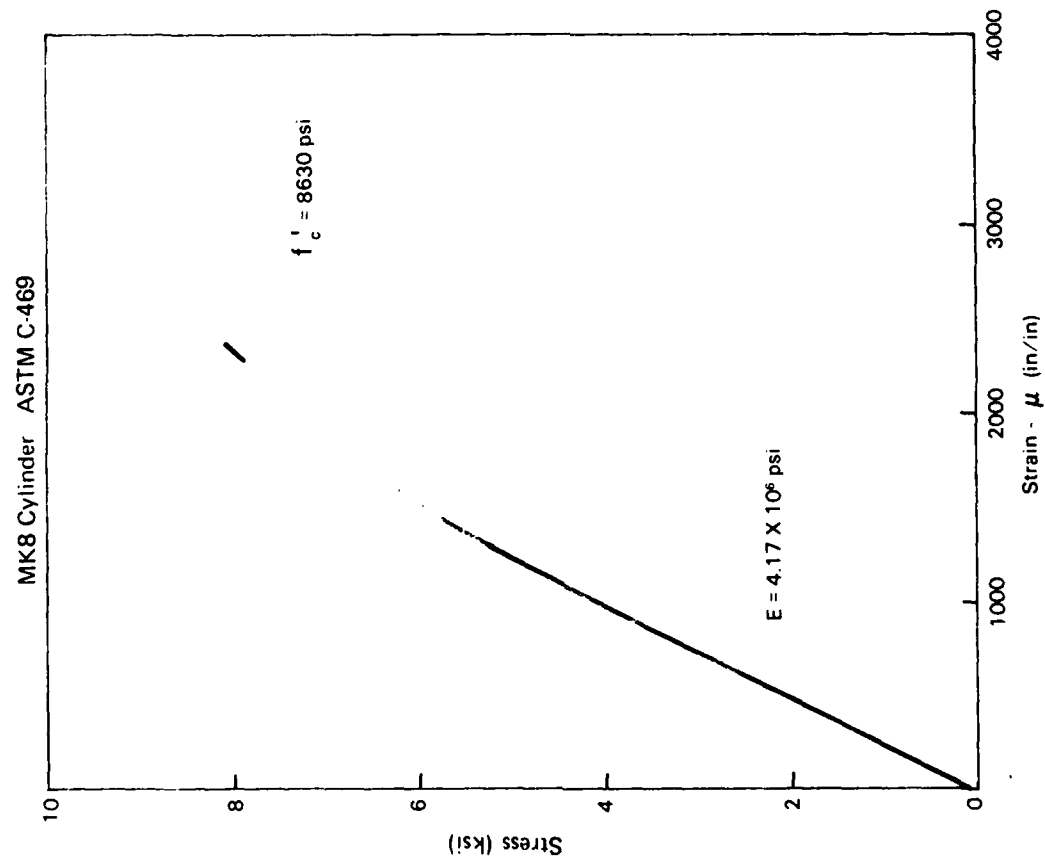


Figure B-88. Concrete stress-strain curve for MK8 (ASTM C-469).

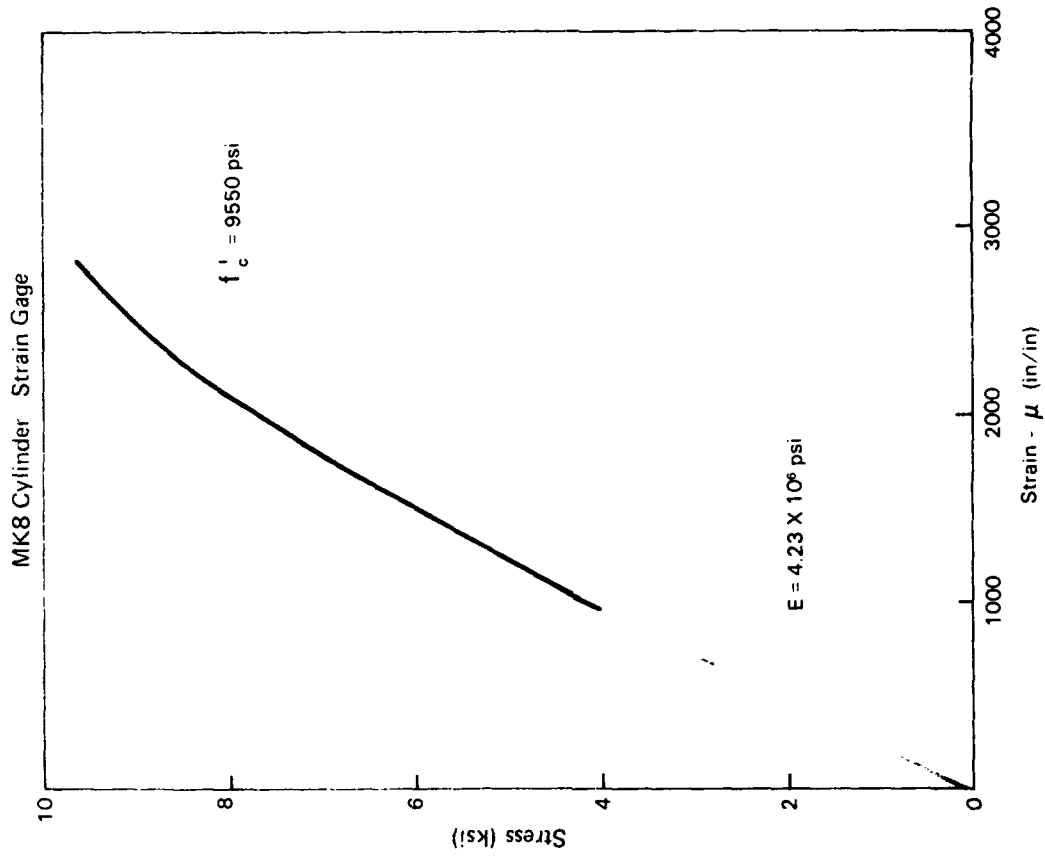


Figure B-89. Concrete stress-strain curve for MK8 (strain gage).

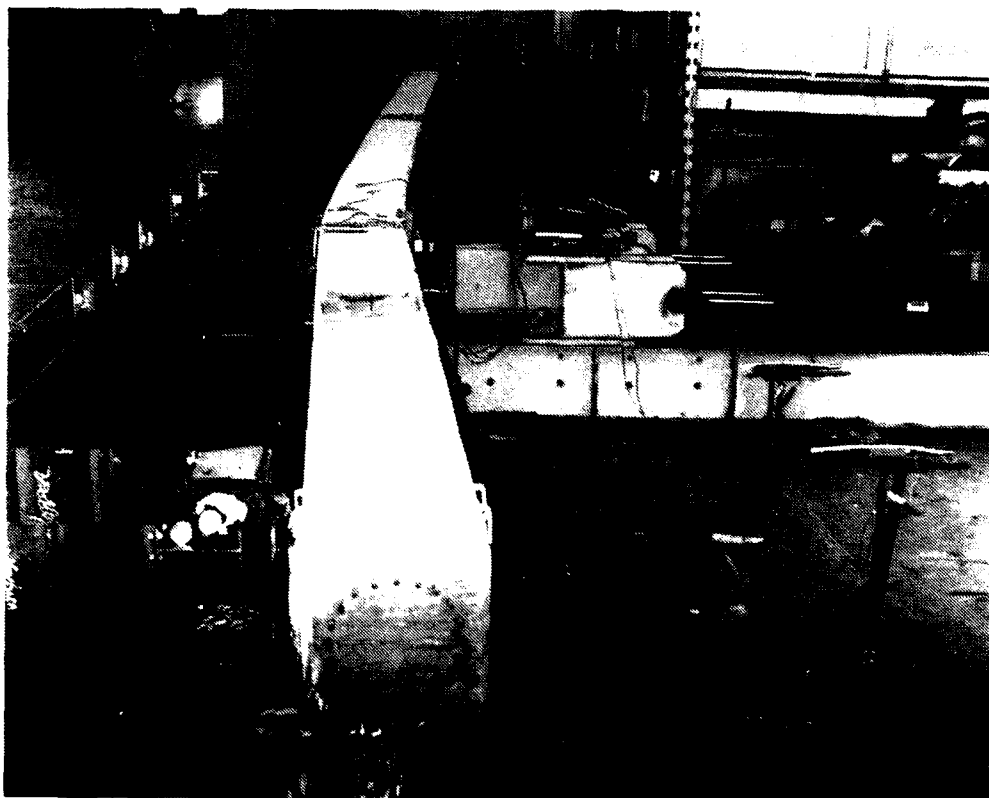


Figure B-90. MK8 ultimate load displacement.



Figure B-91. MK8 ultimate load spalling.

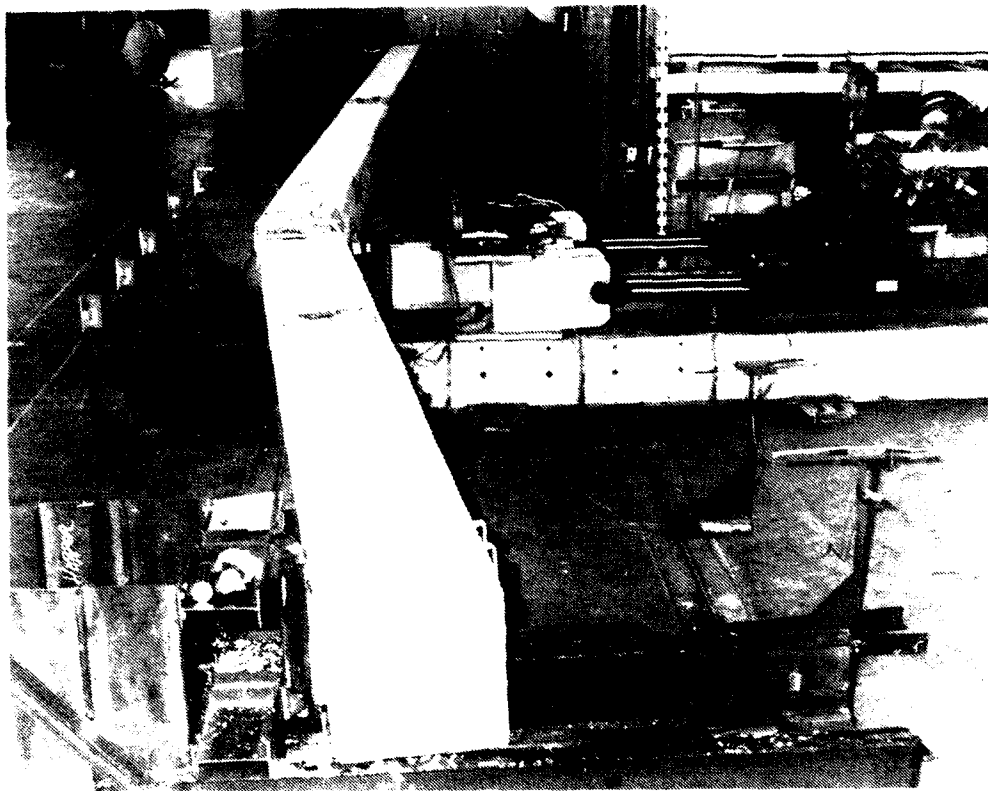


Figure B-92. MK8 failure displacement.

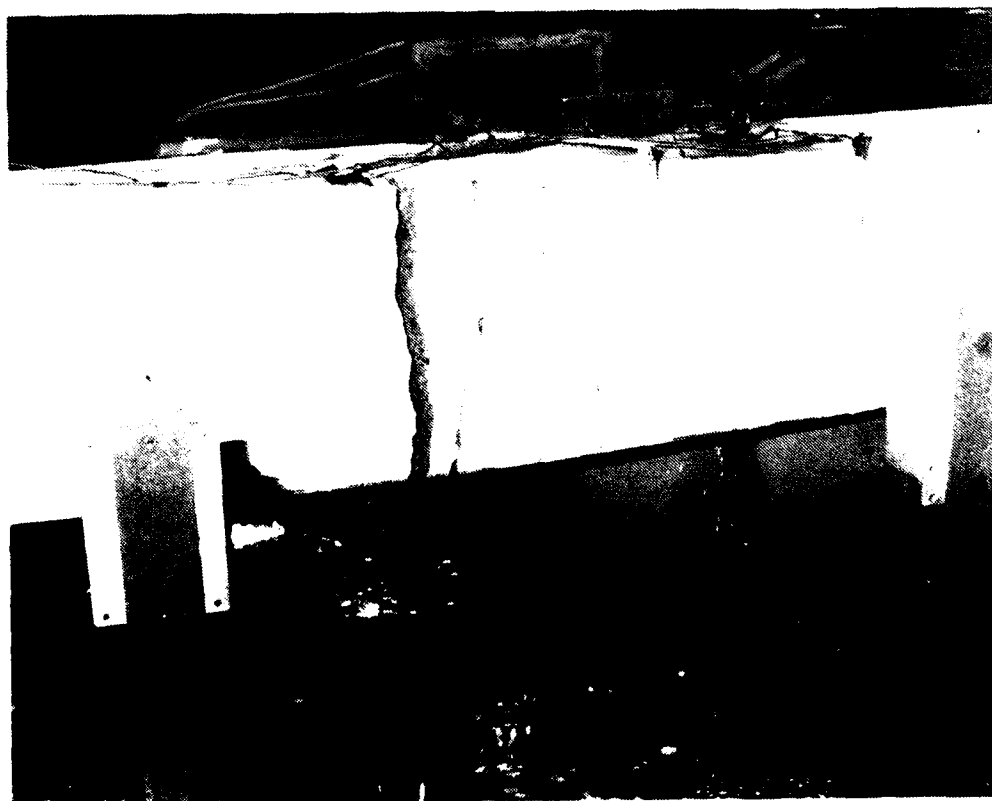


Figure B-93. MK8 load point tension face at failure.

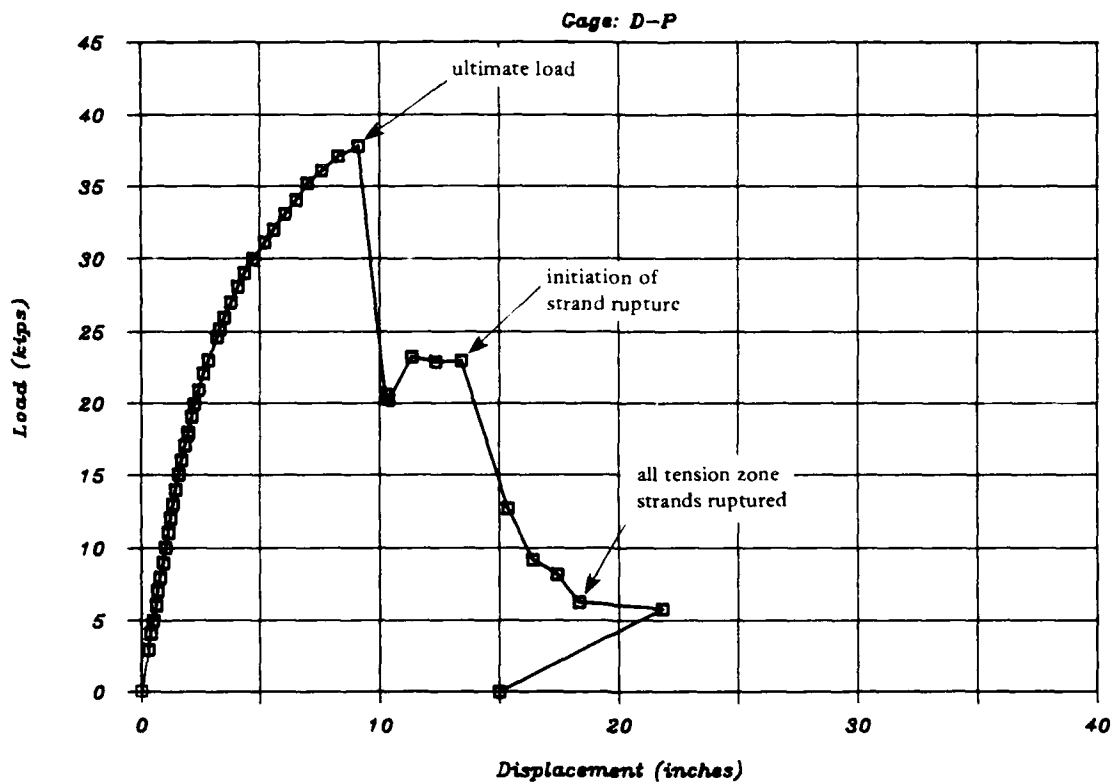


Figure B-94. MK8 load-displacement plot.

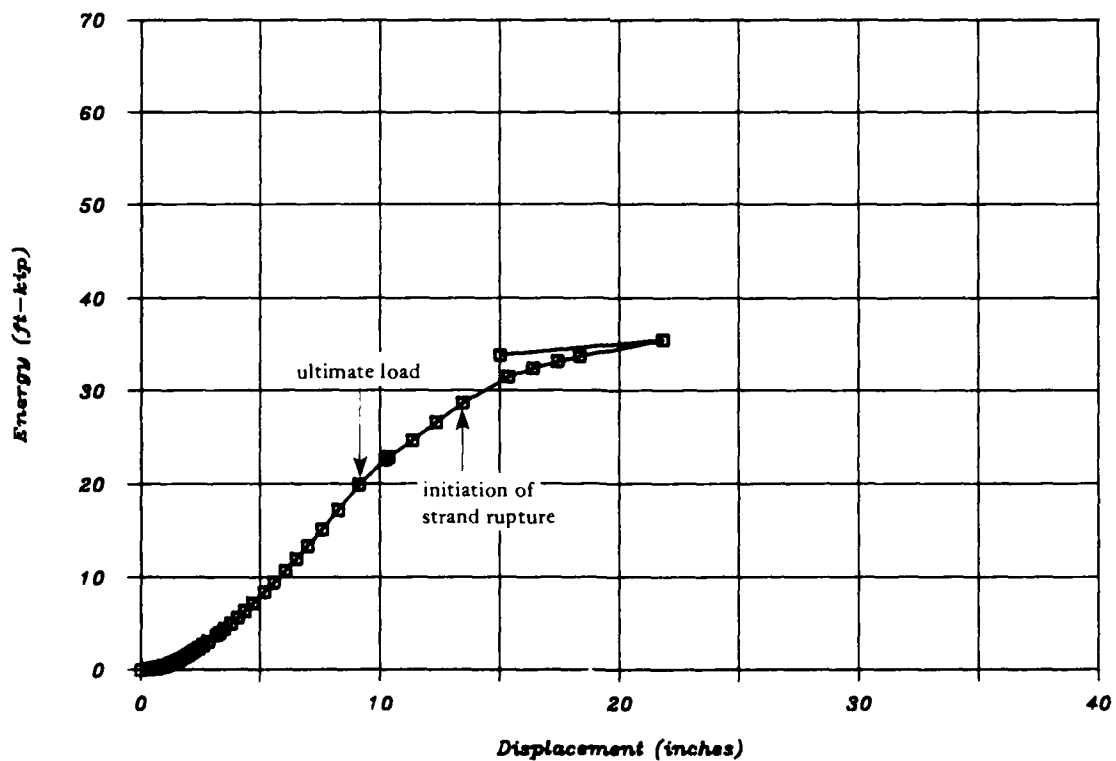


Figure B-95. MK8 energy-displacement plot.

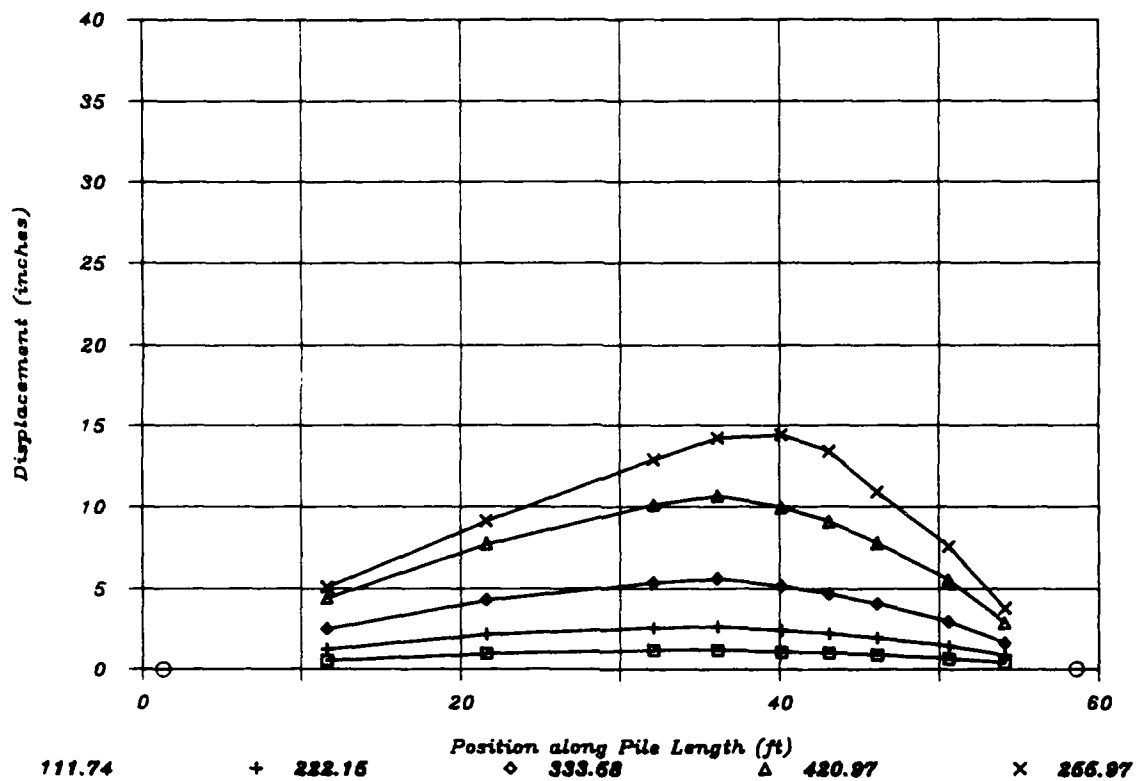


Figure B-96. MK8 deformed shape at $M = 112, 222, 334, 421,$ and 256 kip-ft.

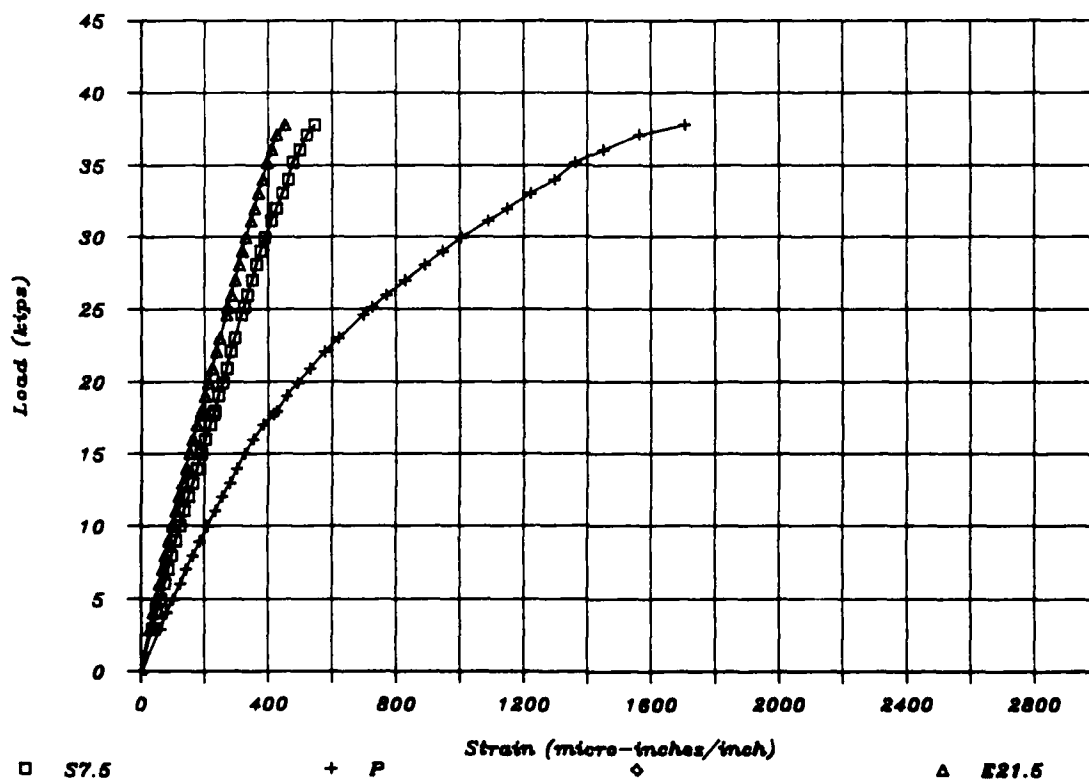


Figure B-97. MK8 load-compression strain - all gages.



Figure B-98. Compression spall zone of MK3A.

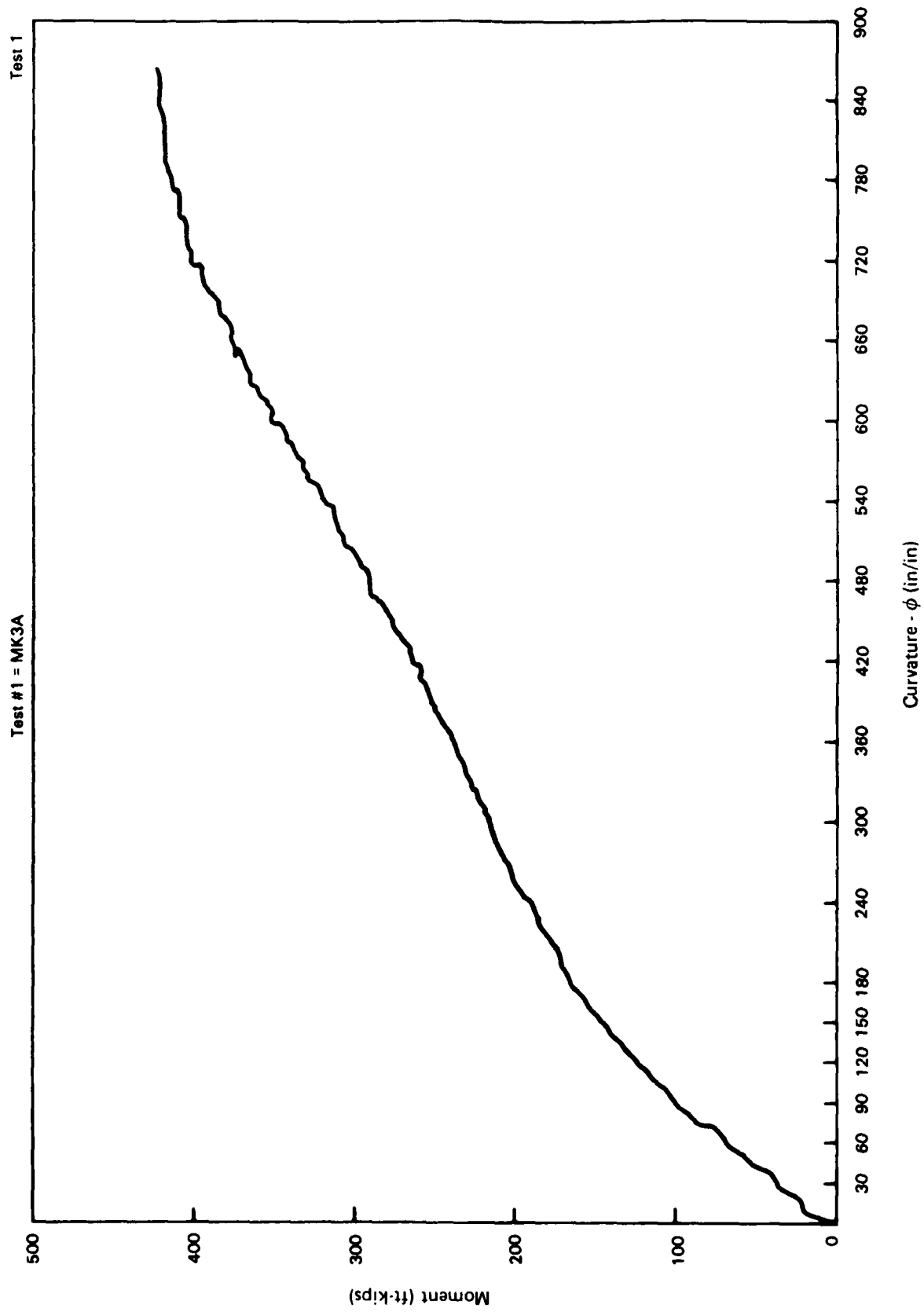


Figure B-99. Moment-curvature plot for MK3A.

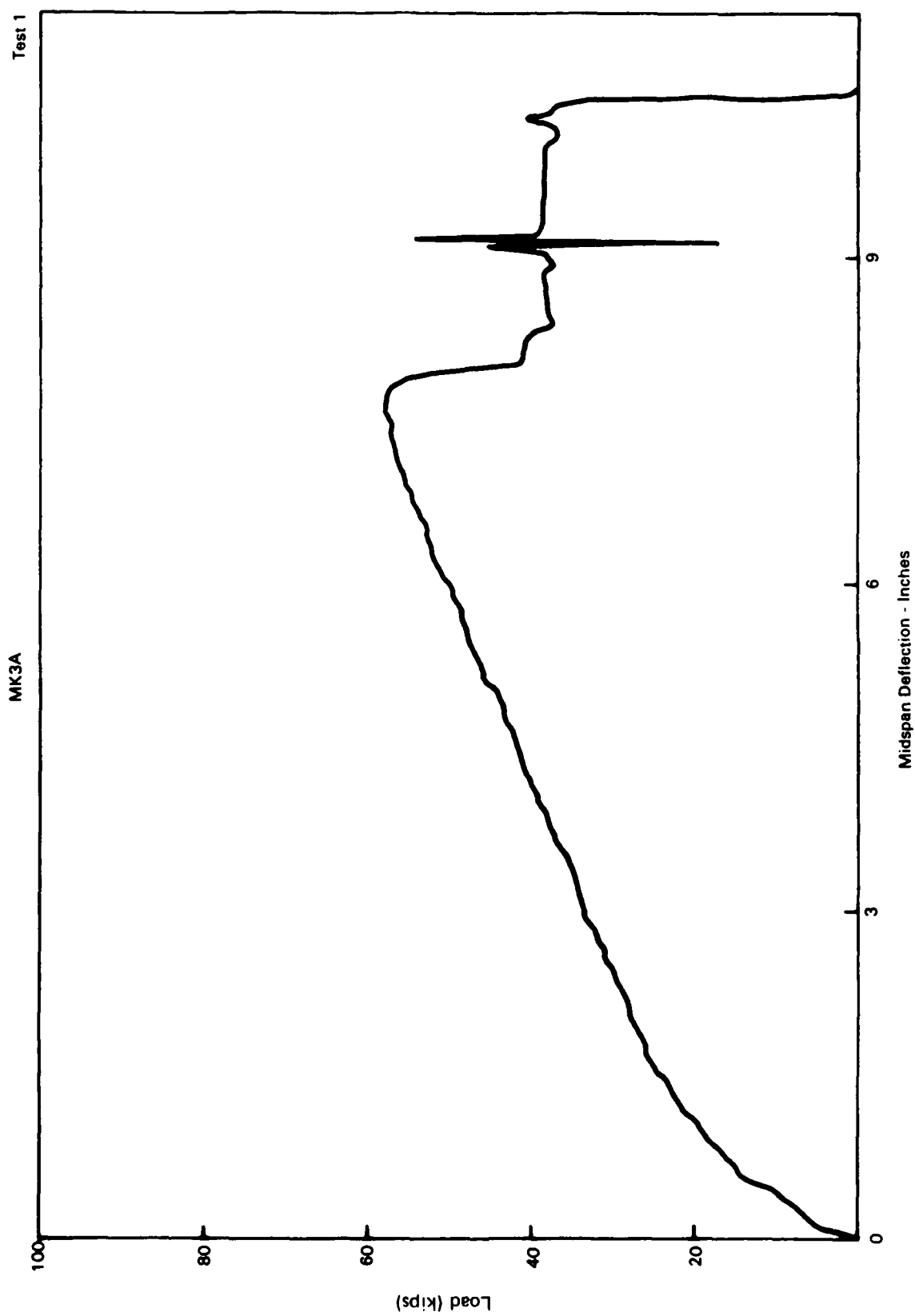


Figure B-100. Load-deflection plot for MK3A.

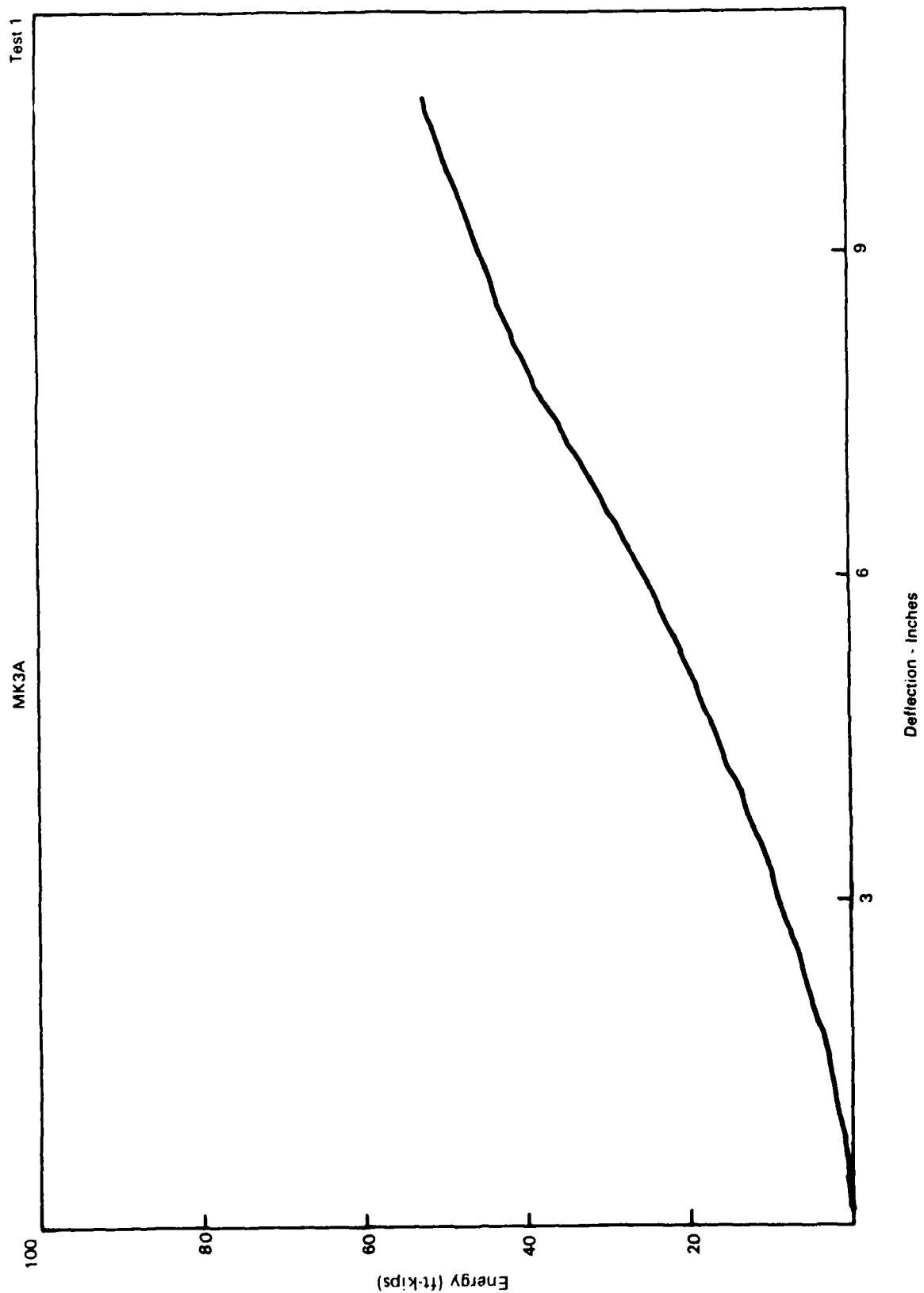


Figure B-101. Energy-deflection plot for MK3A.

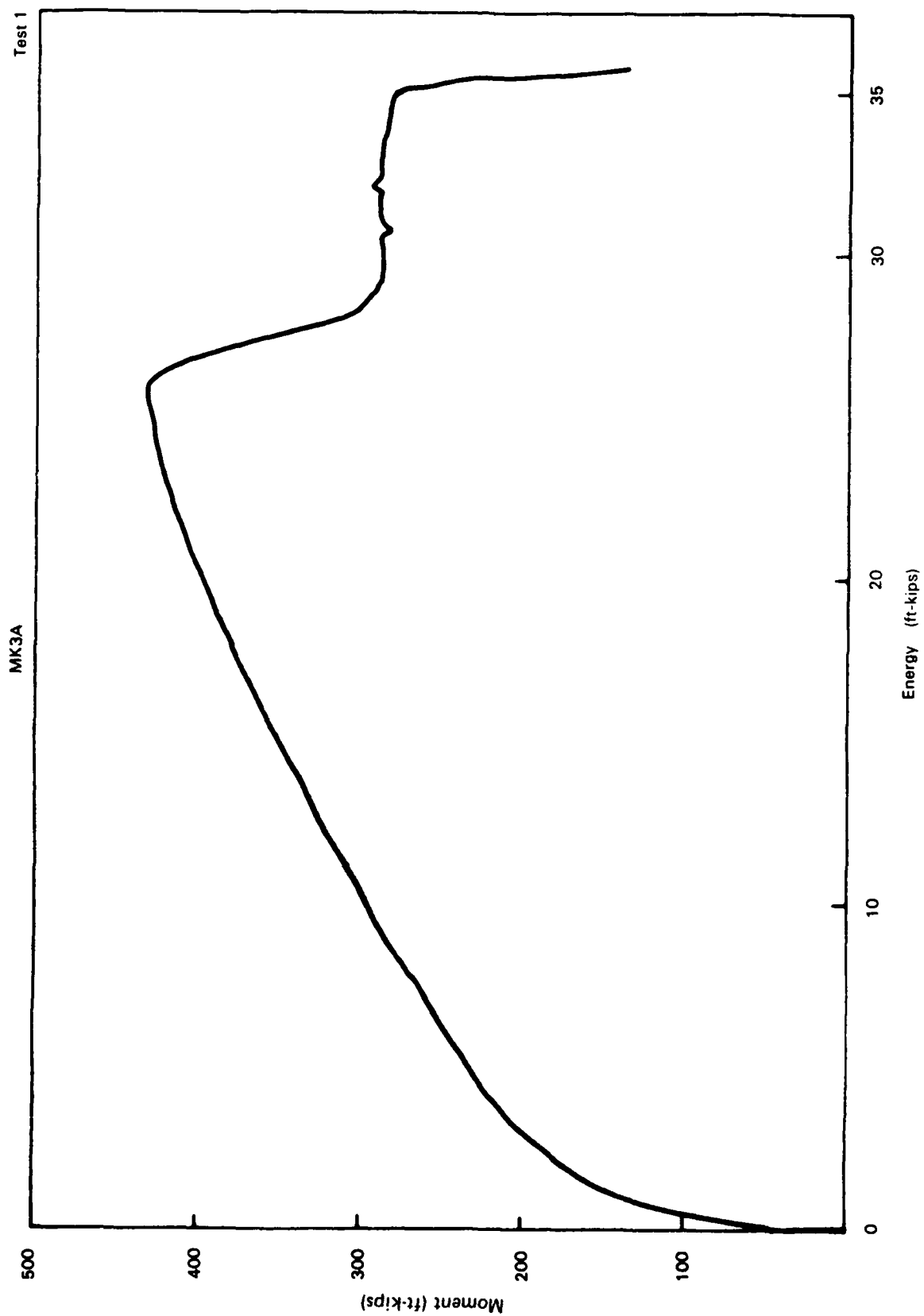


Figure B-102. Moment-energy plot for MK3A.

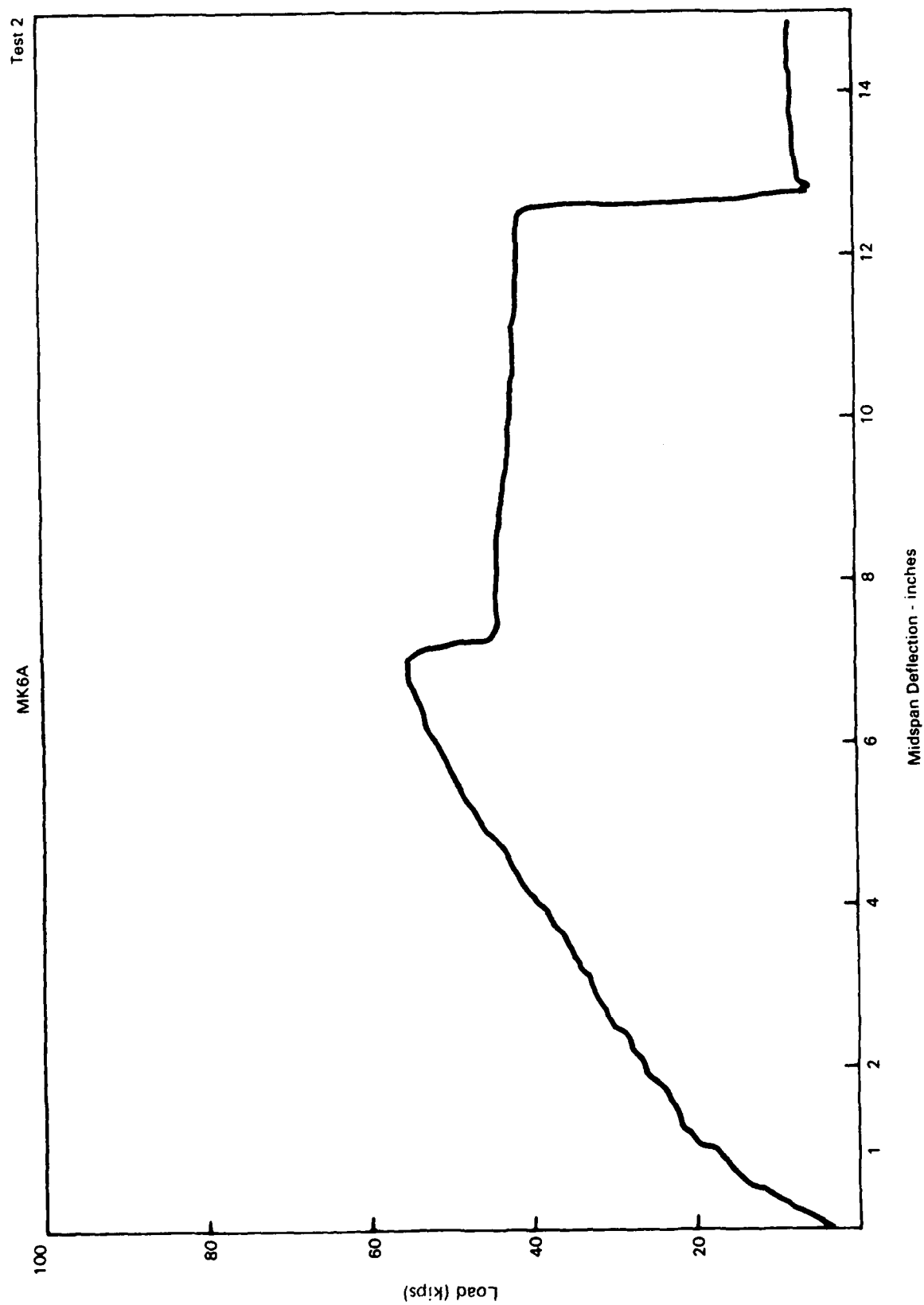


Figure B-103. Load-deflection plot for MK6A.

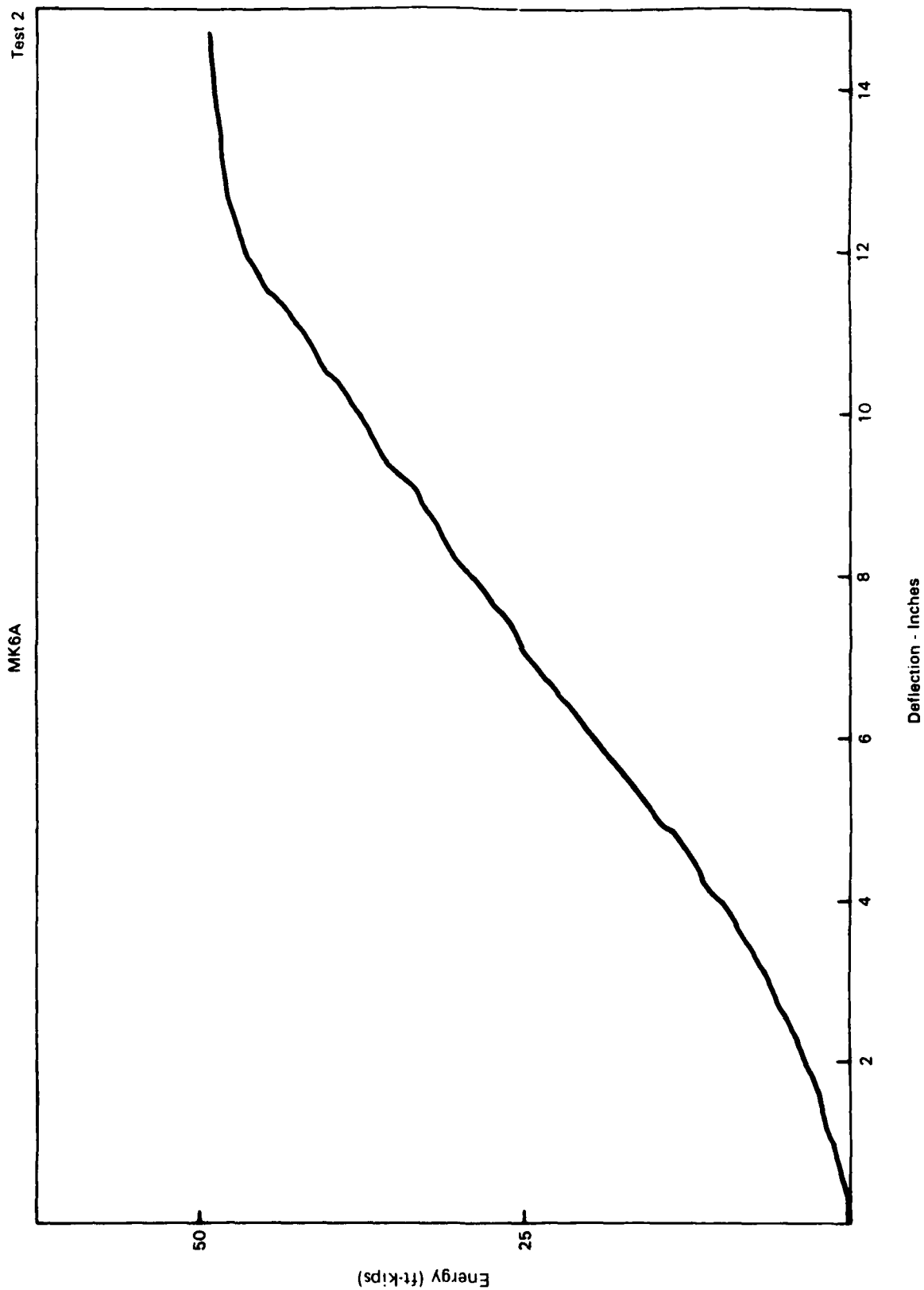


Figure B-104. Energy-deflection plot for MK6A.

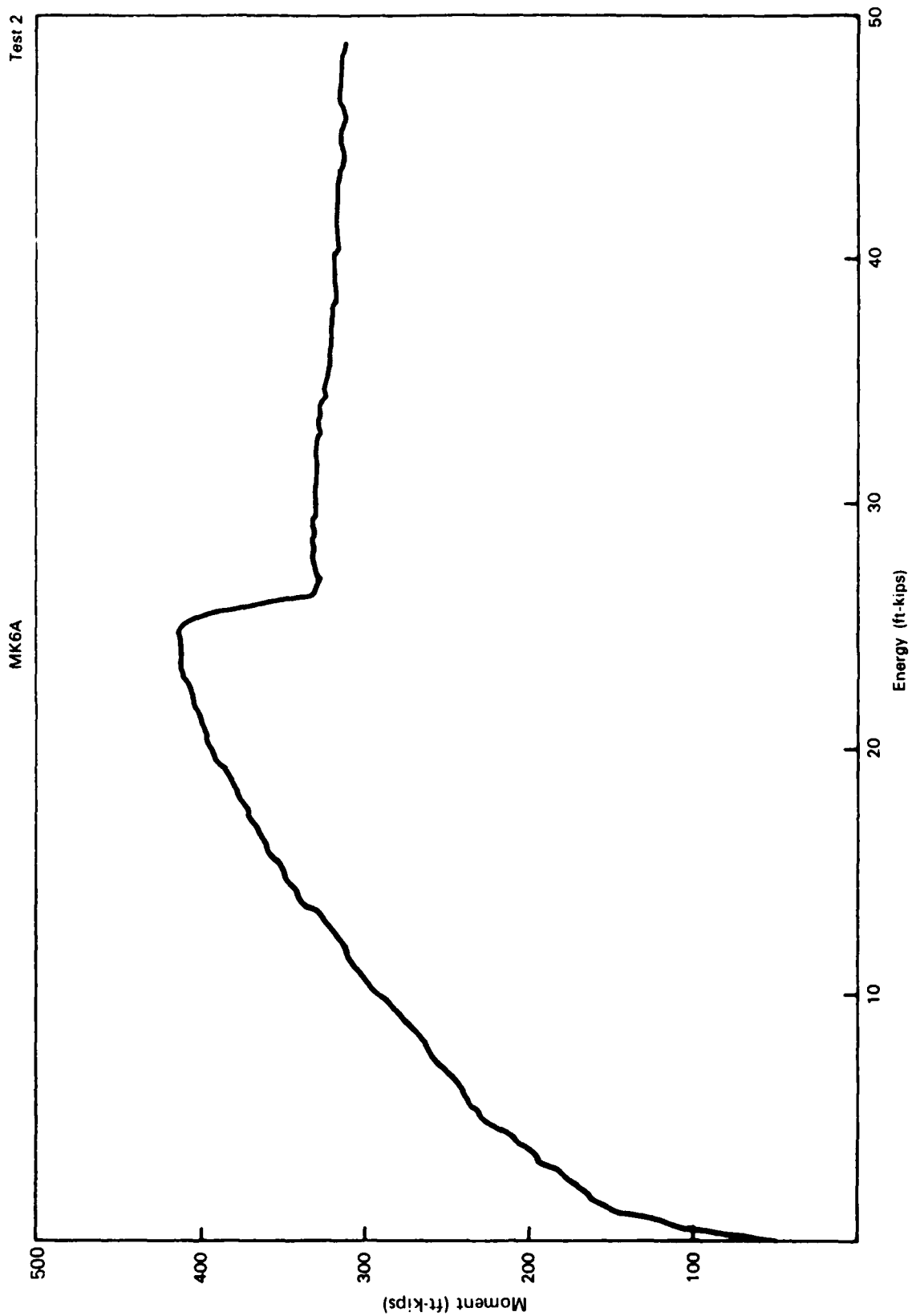


Figure B-105. Moment-energy plot for MK6A.

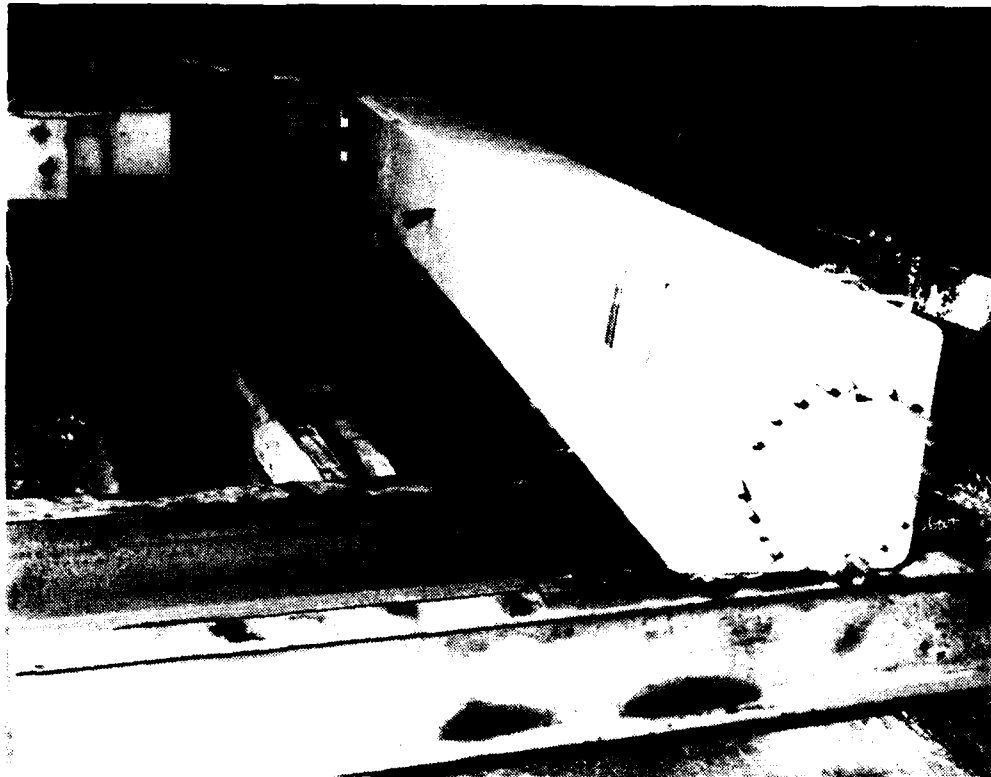


Figure B-106. Post-ultimate compression face of MK8A.



Figure B-107. Compression spall zone of MK8A.

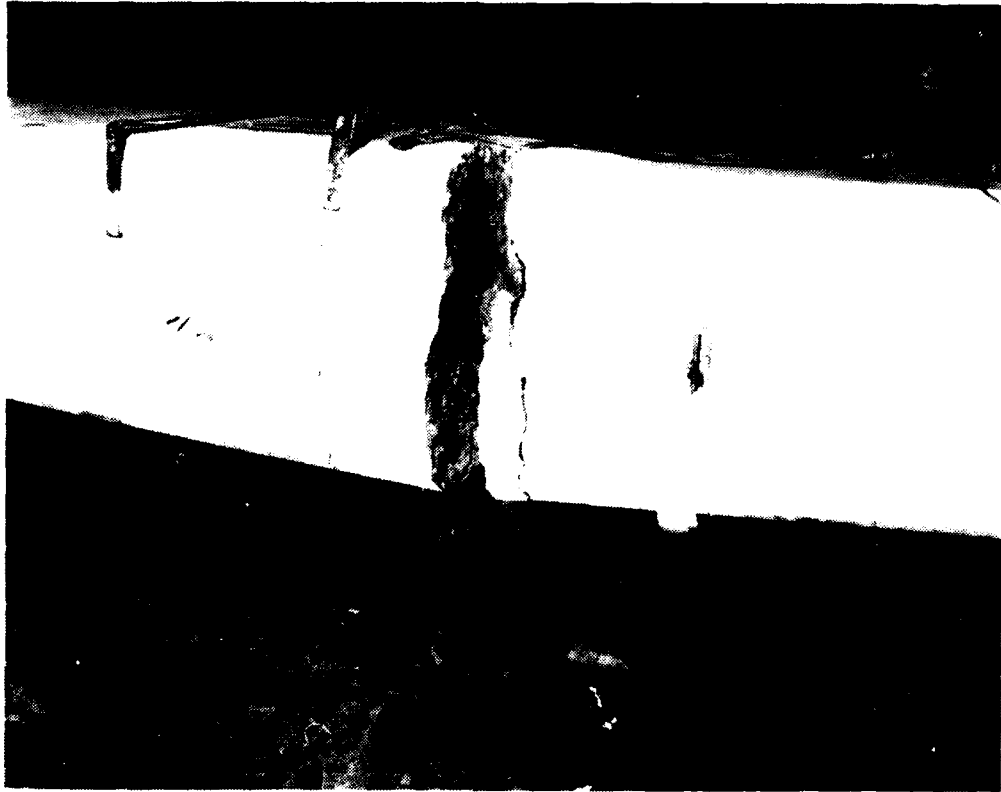


Figure B-108. Post-ultimate tension face of MK8A.

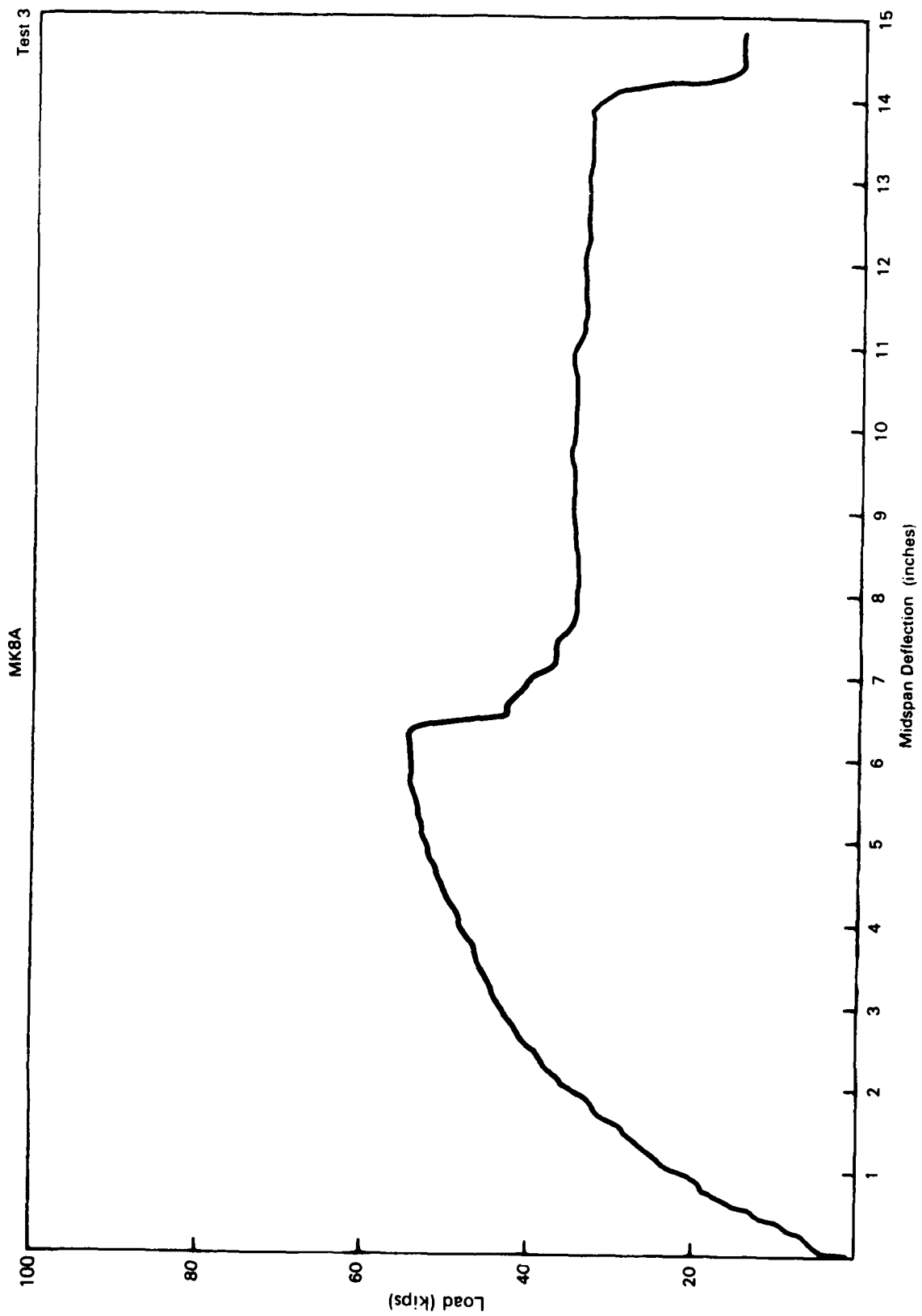


Figure B-109. Load-deflection plot for MK8A.

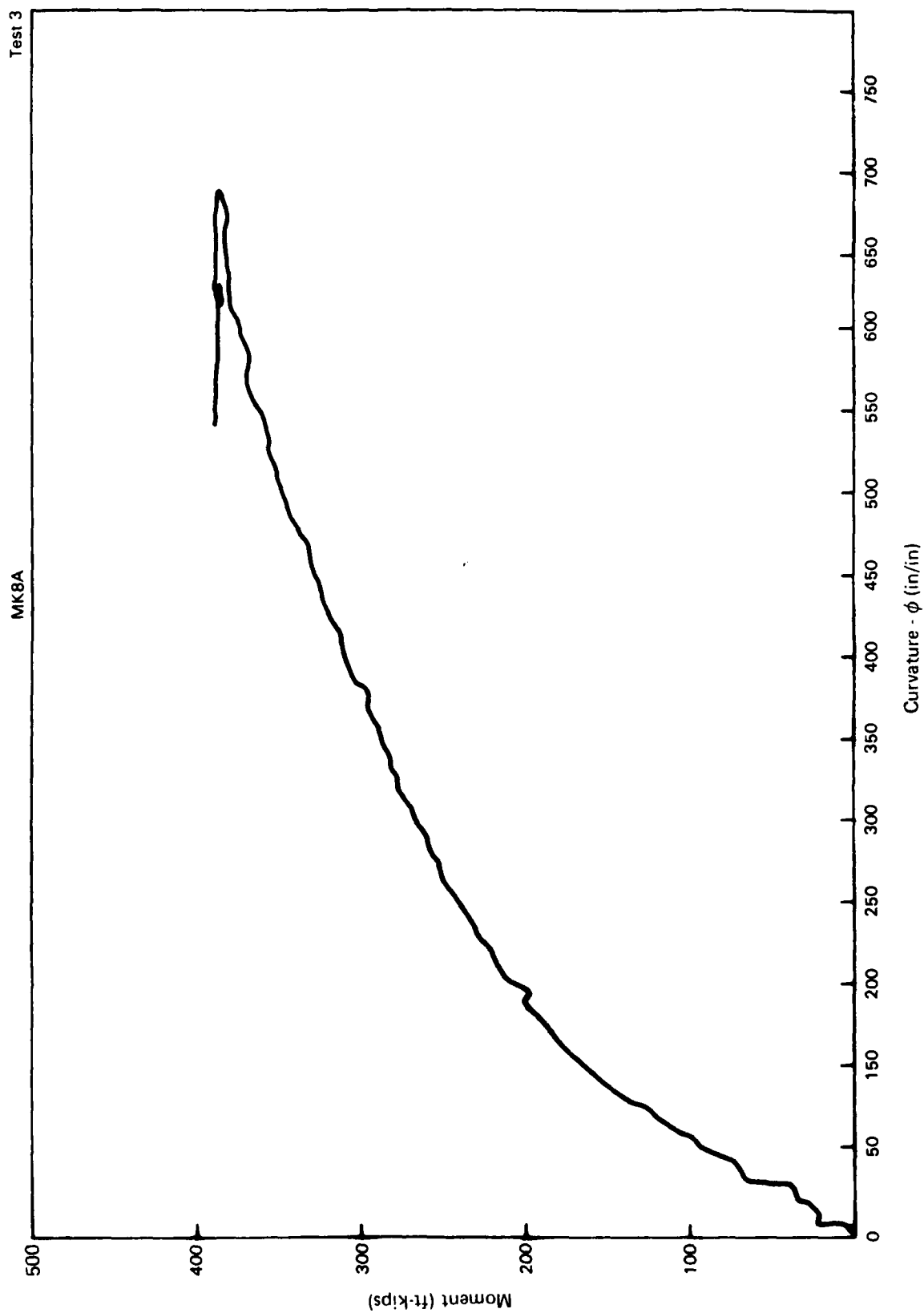


Figure B-110. Moment-curvature plots for MK8A.

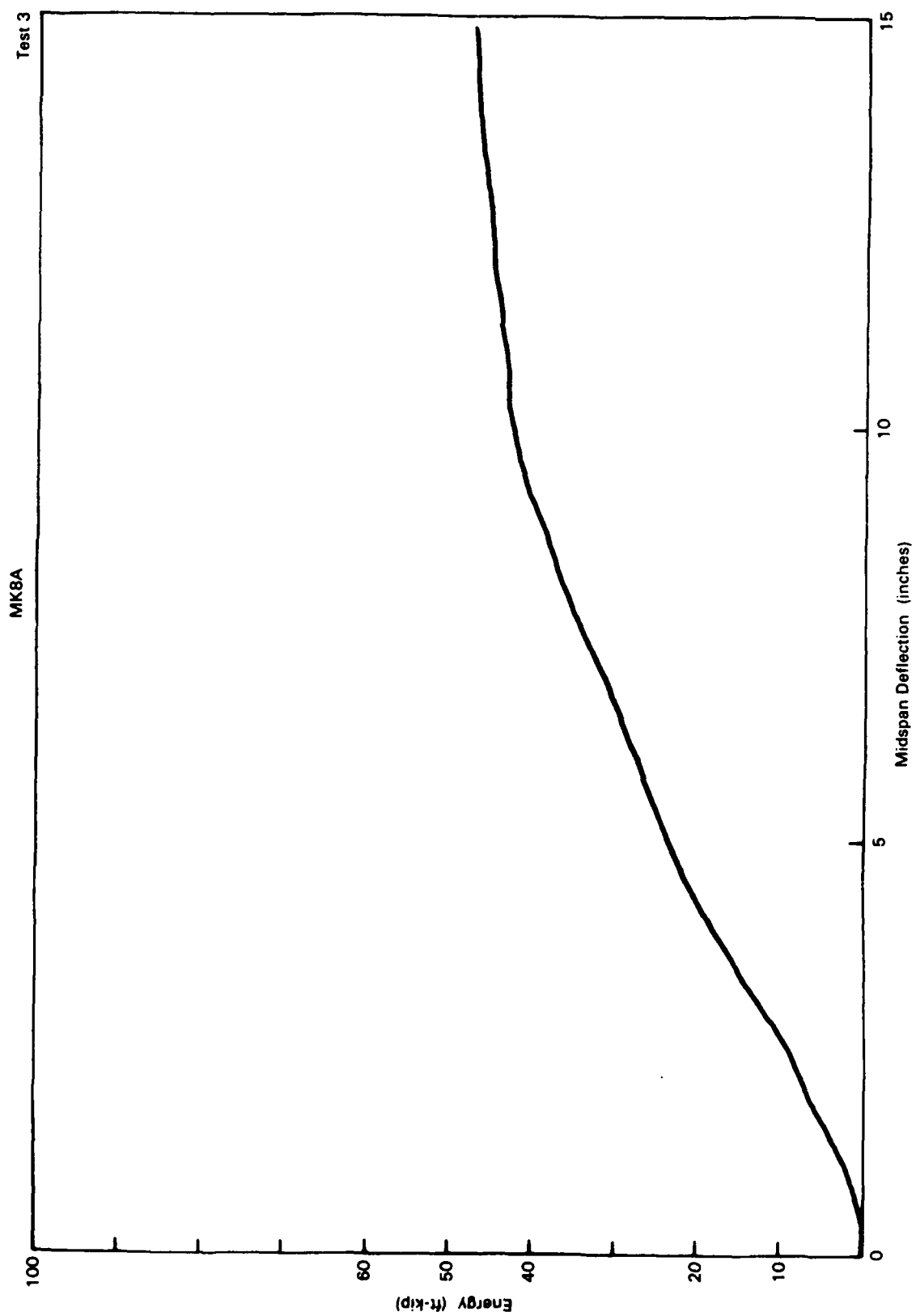


Figure B-111. Energy-deflection plot for MK8A.

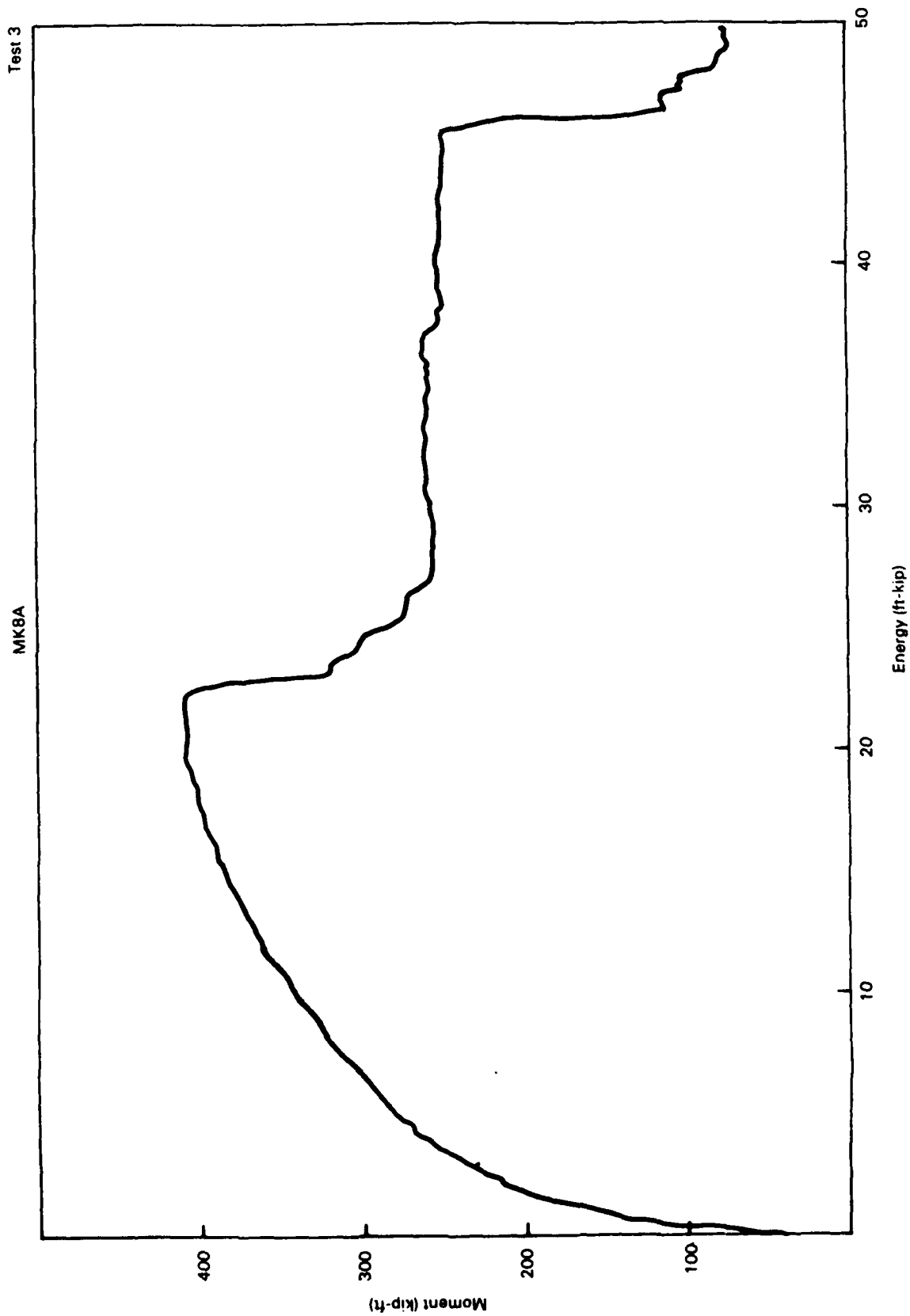


Figure B-112. Moment-energy plots for MK8A.

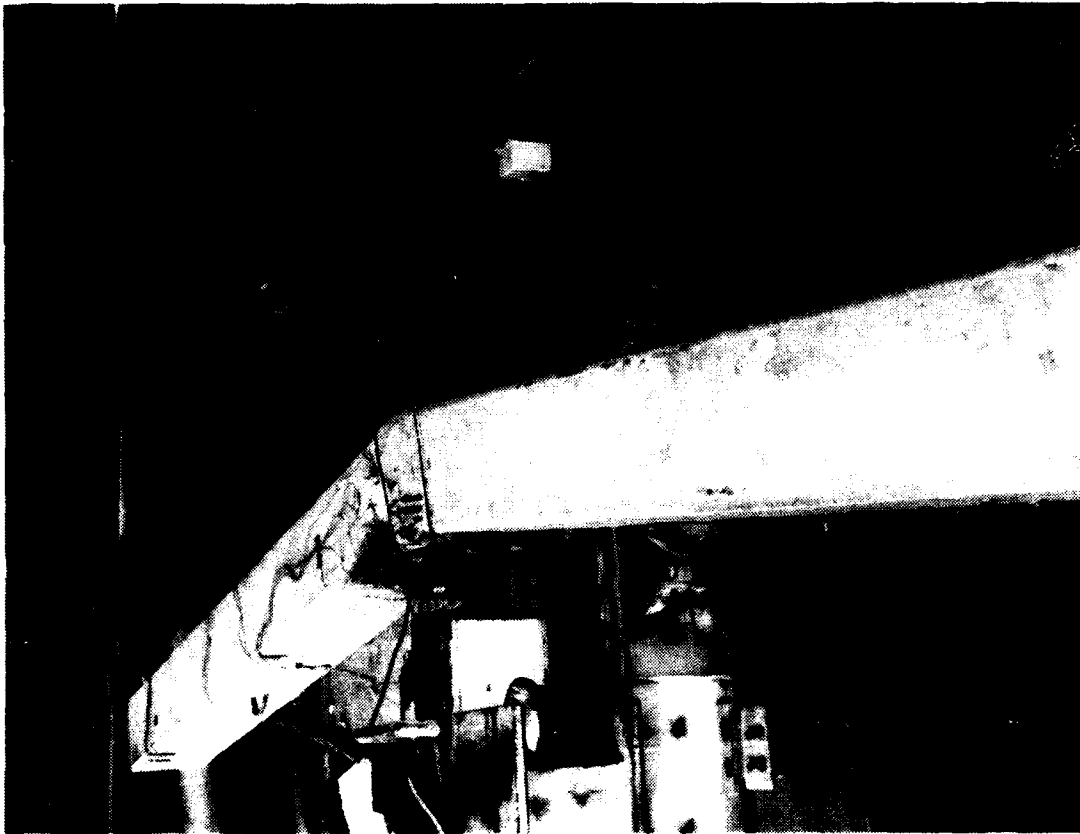


Figure B-113. MK9 deformed shape before and after spalling at ultimate load.

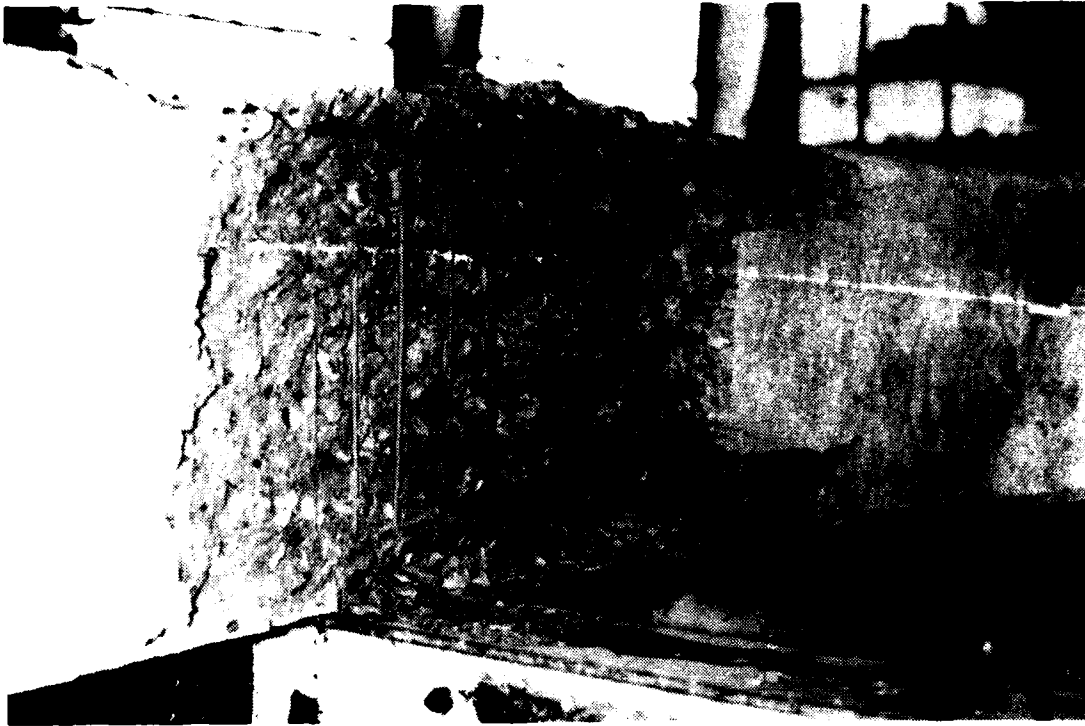


Figure B-114. MK9 compression spalling at failure.



Figure B-115. MK9 tension side at failure.

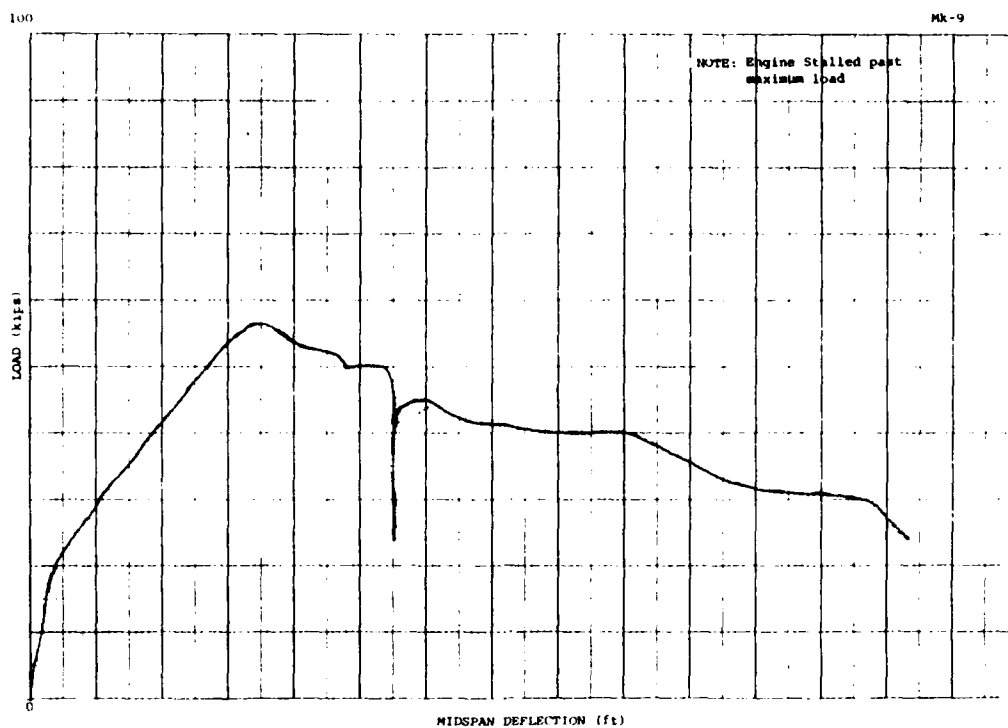


Figure B-116. MK9 load-deflection plot.

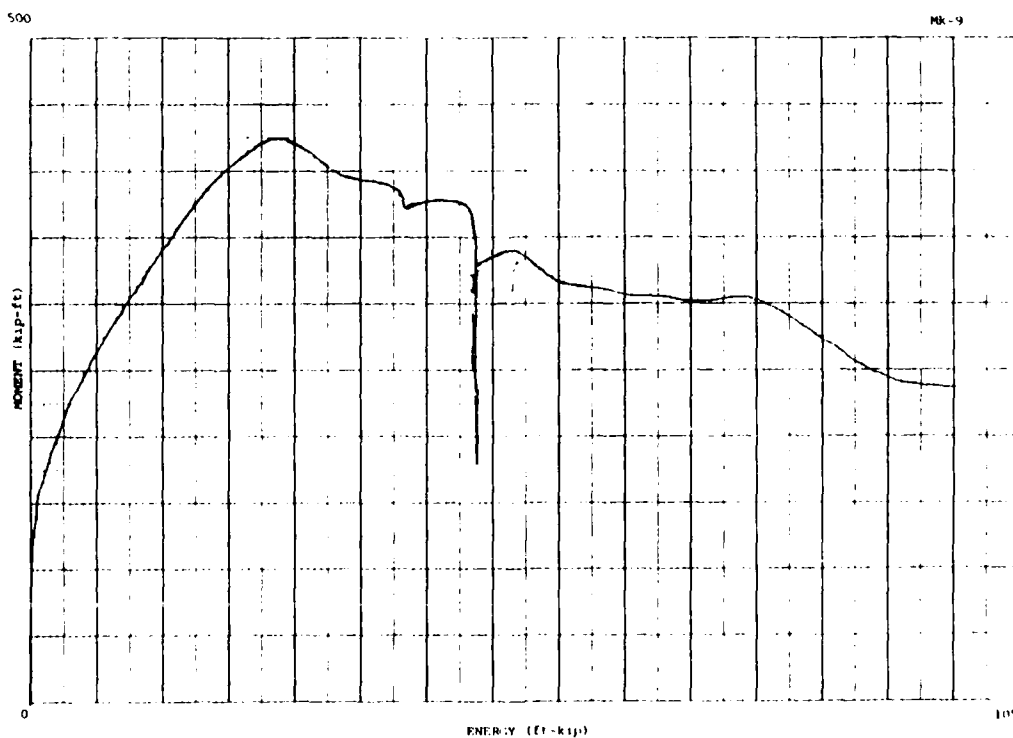


Figure B-117. MK9 moment-energy plot.

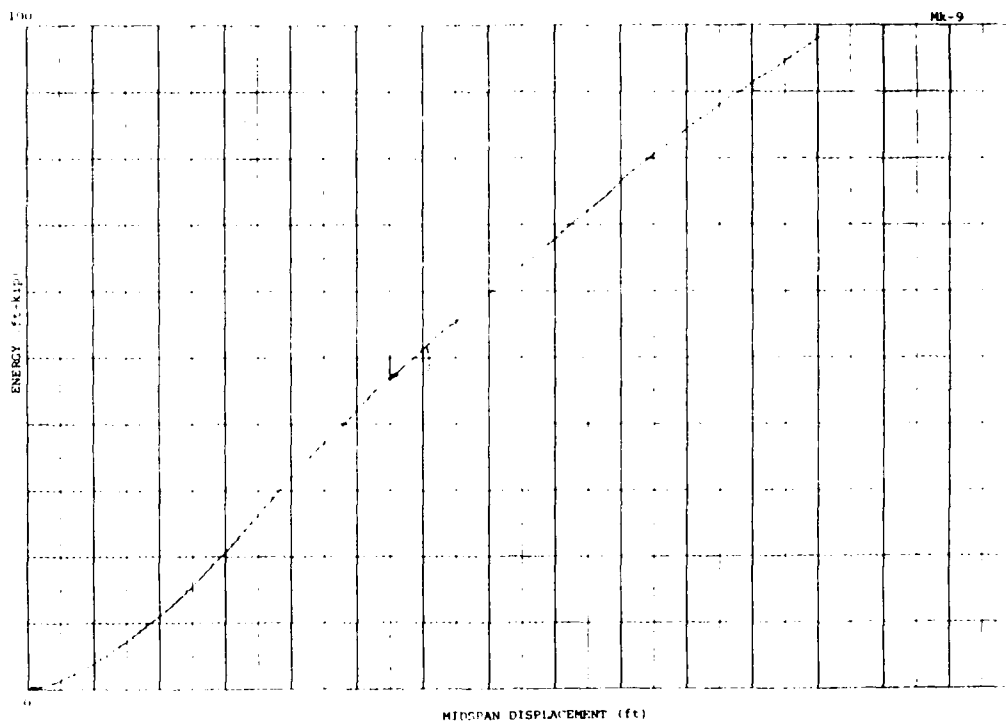


Figure B-118. MK9 energy-displacement plot.

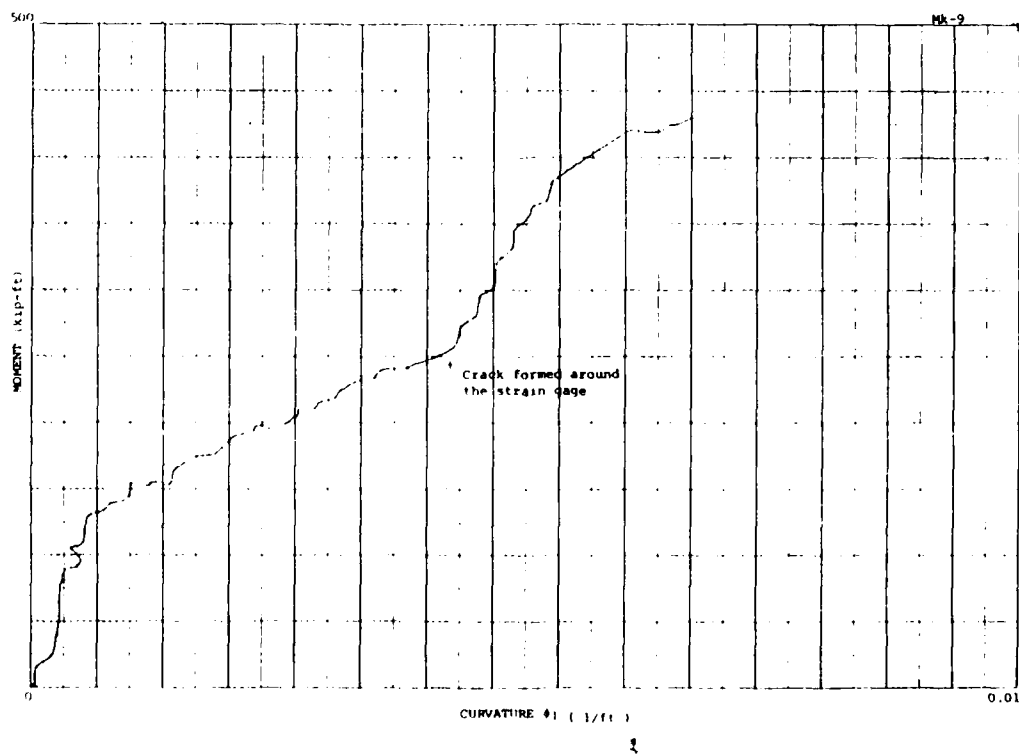


Figure B-119. MK9 moment-curvature plot.

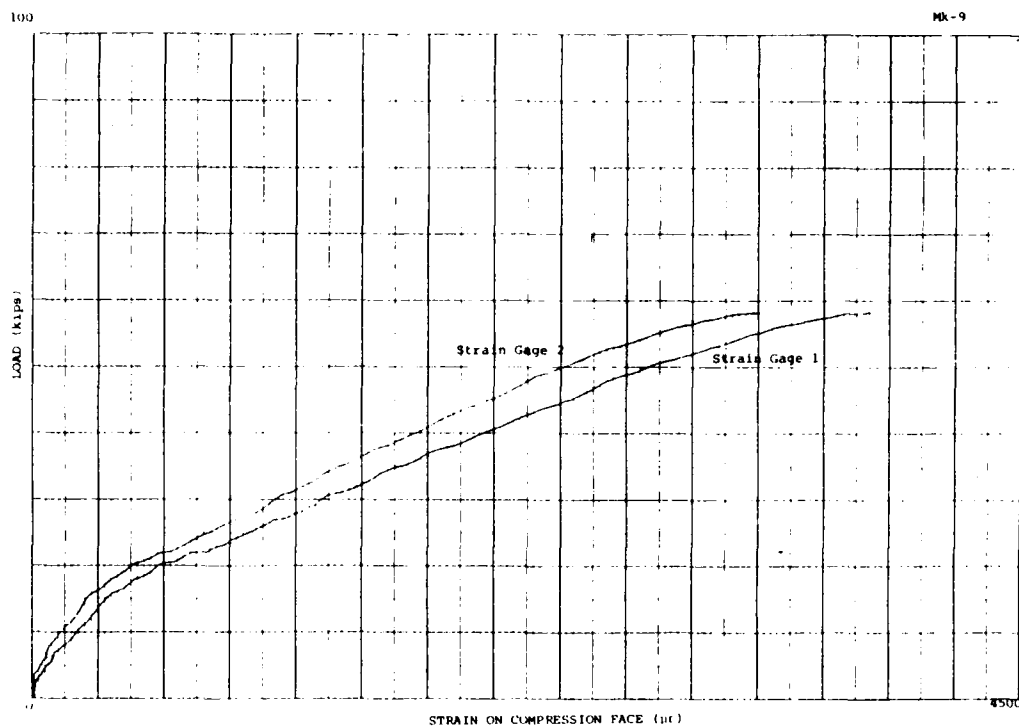


Figure B-120. Load-compression strain for MK9.

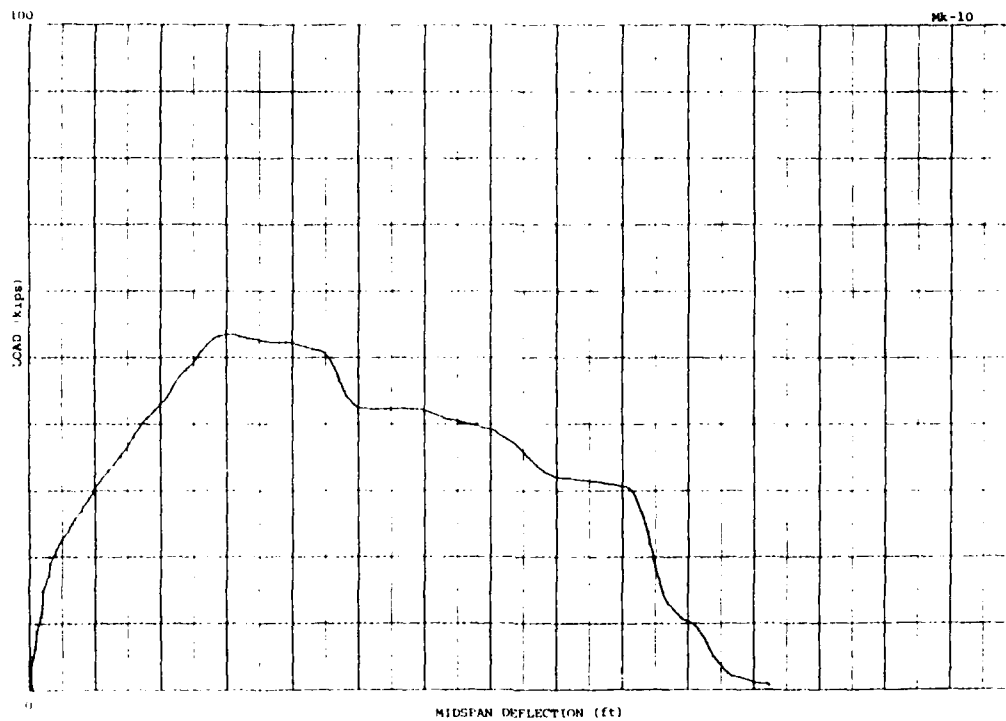


Figure B-121. MK10 load-deflection plot.

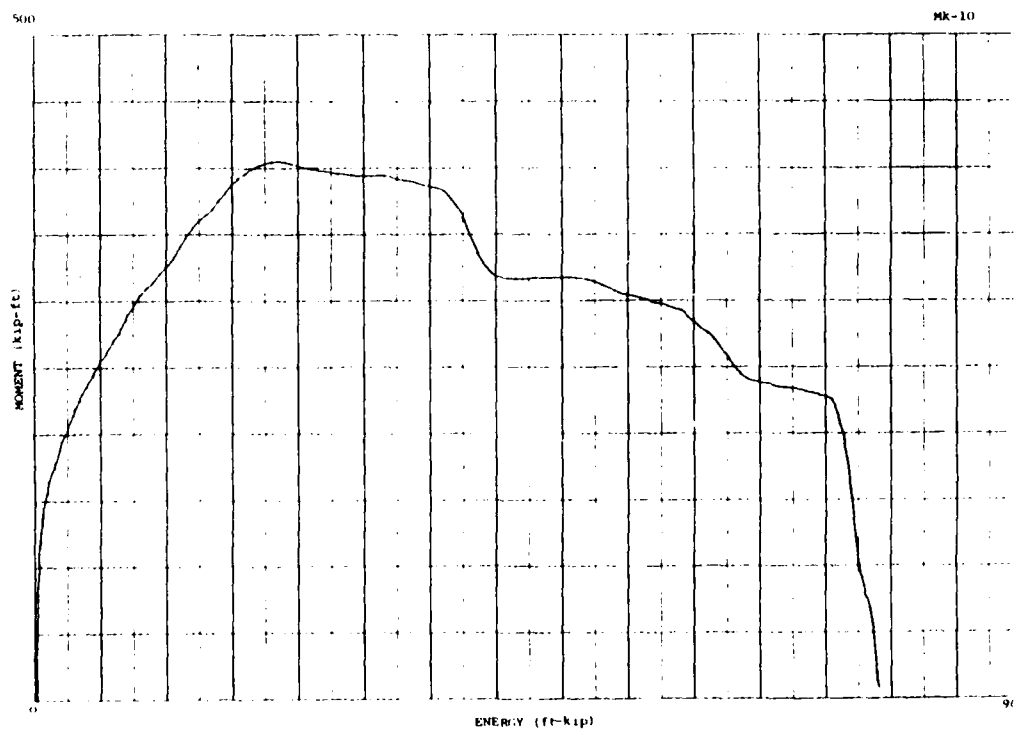


Figure B-122. MK10 moment-energy plot.

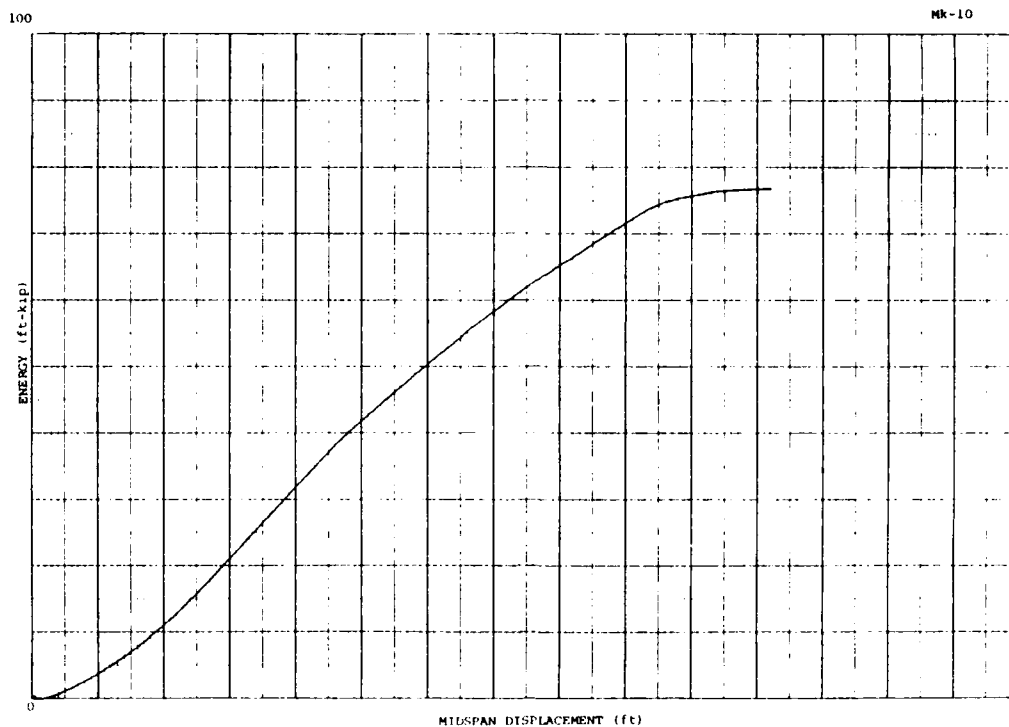


Figure B-123. MK10 energy-displacement plot.

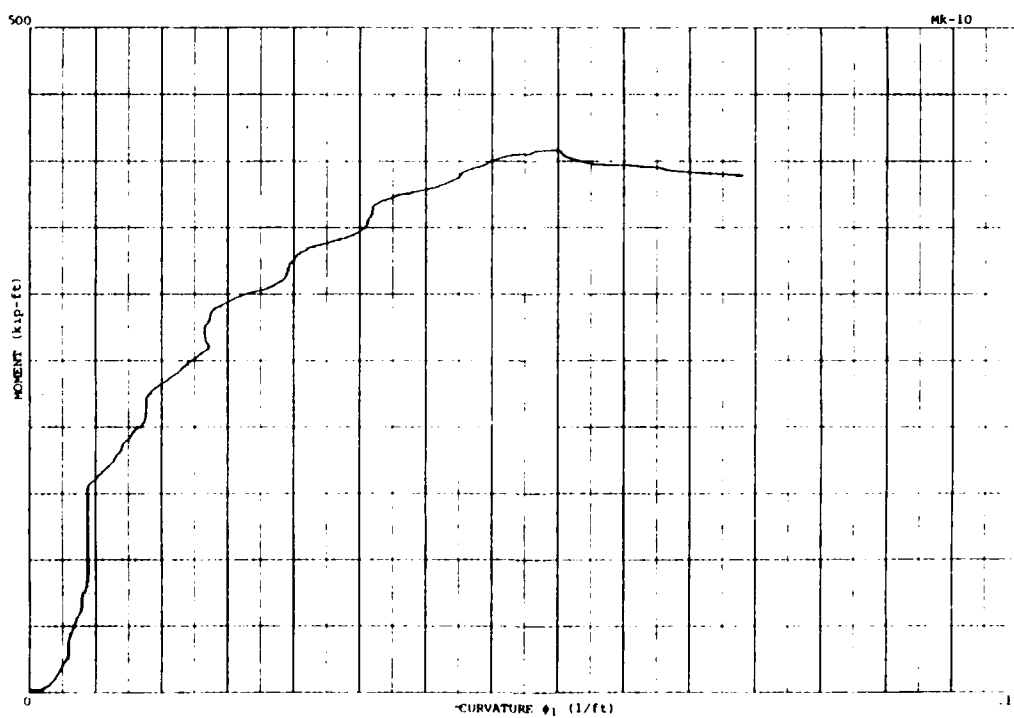


Figure B-124. MK10 moment-curvature plot.

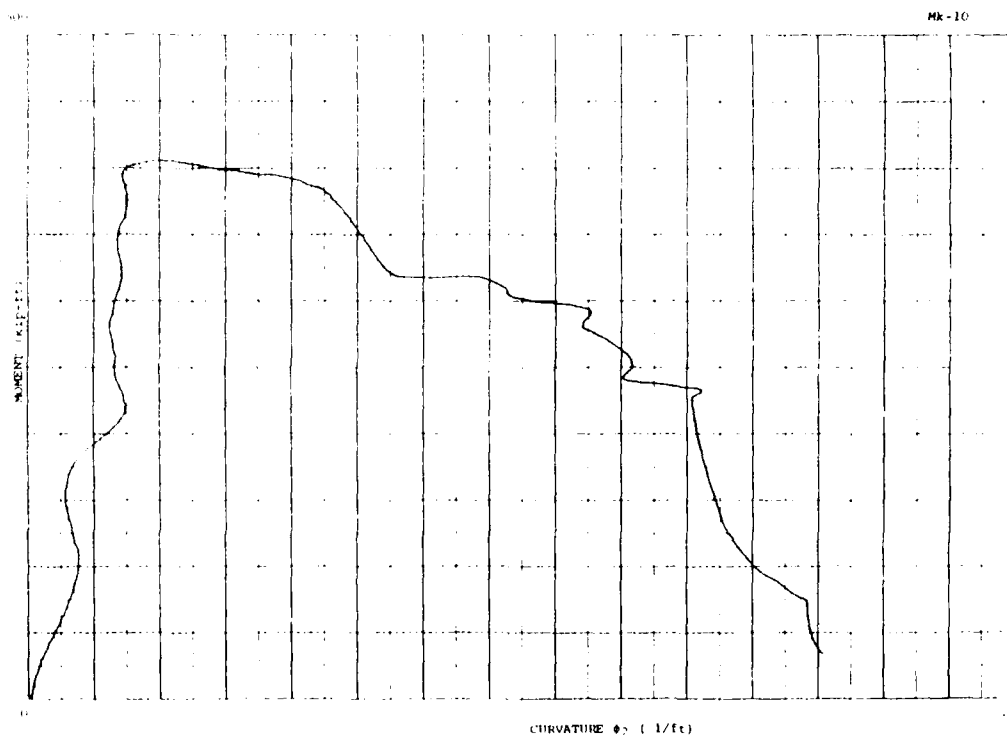


Figure B-125. MK10 moment-curvature plot.

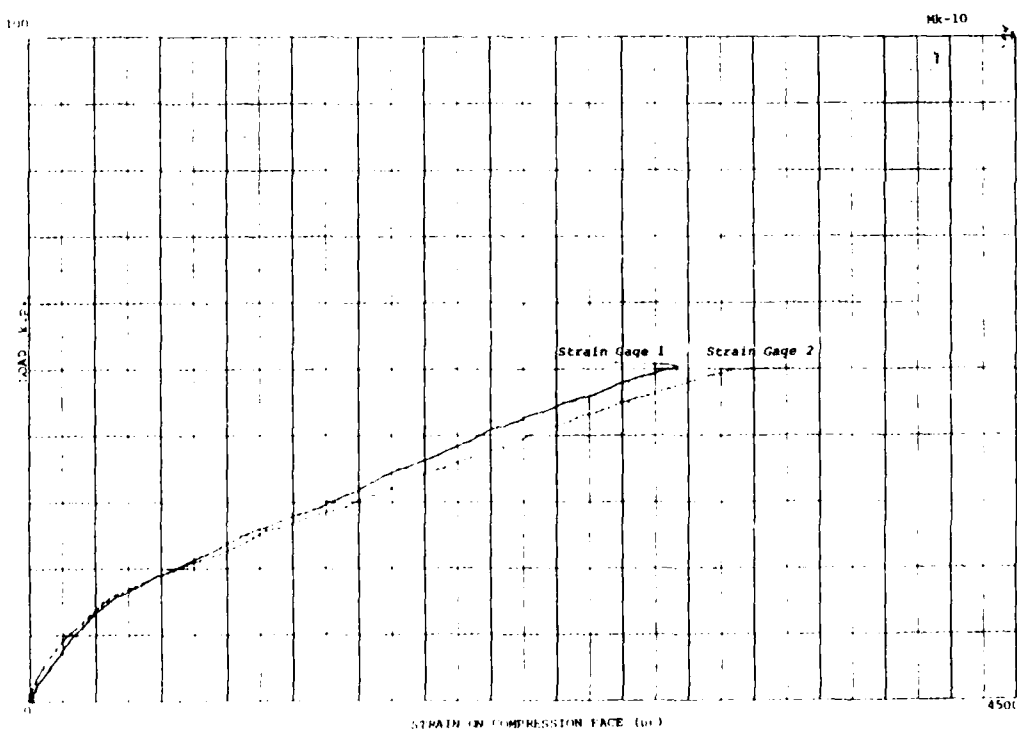


Figure B-126. MK10 compression strain.

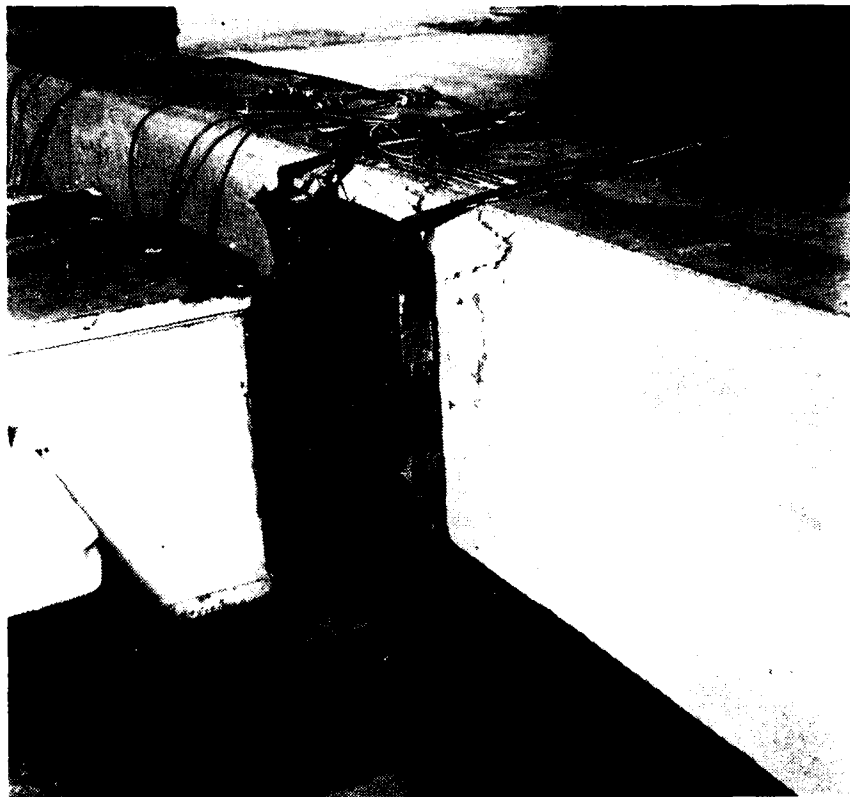


Figure B-127. MK11 compression zone deterioration after 120 and 209 cycles.

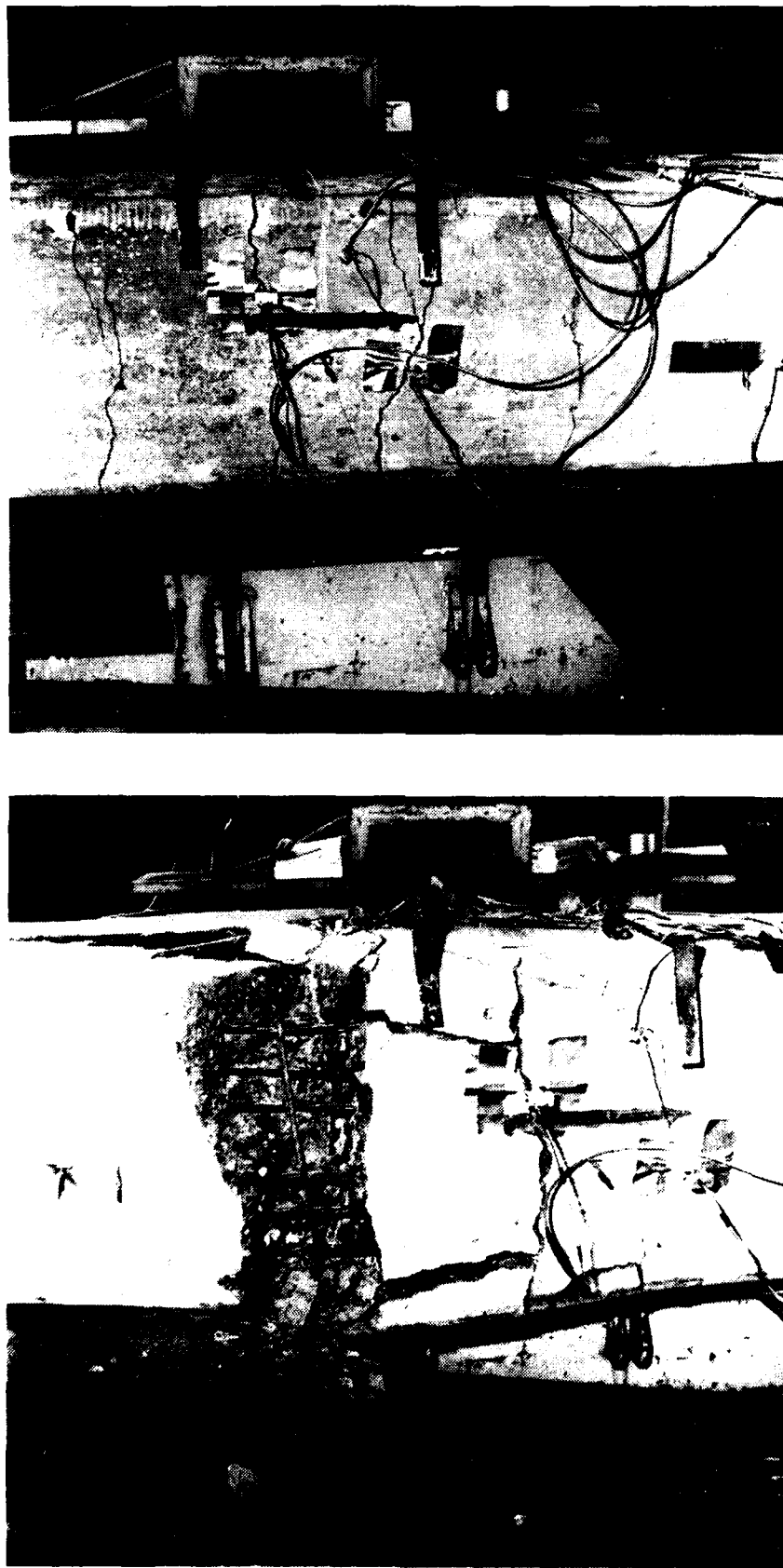


Figure B-128. MK11 tension face cracking after 120 and 209 cycles.

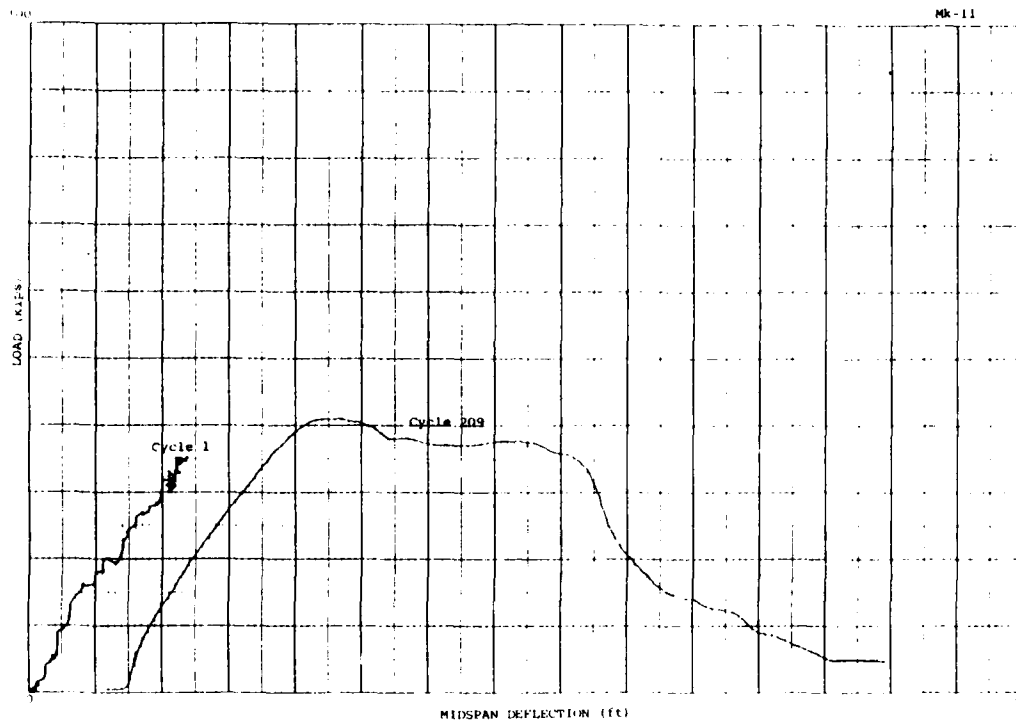


Figure B-129. MK11 load-deflection plot.

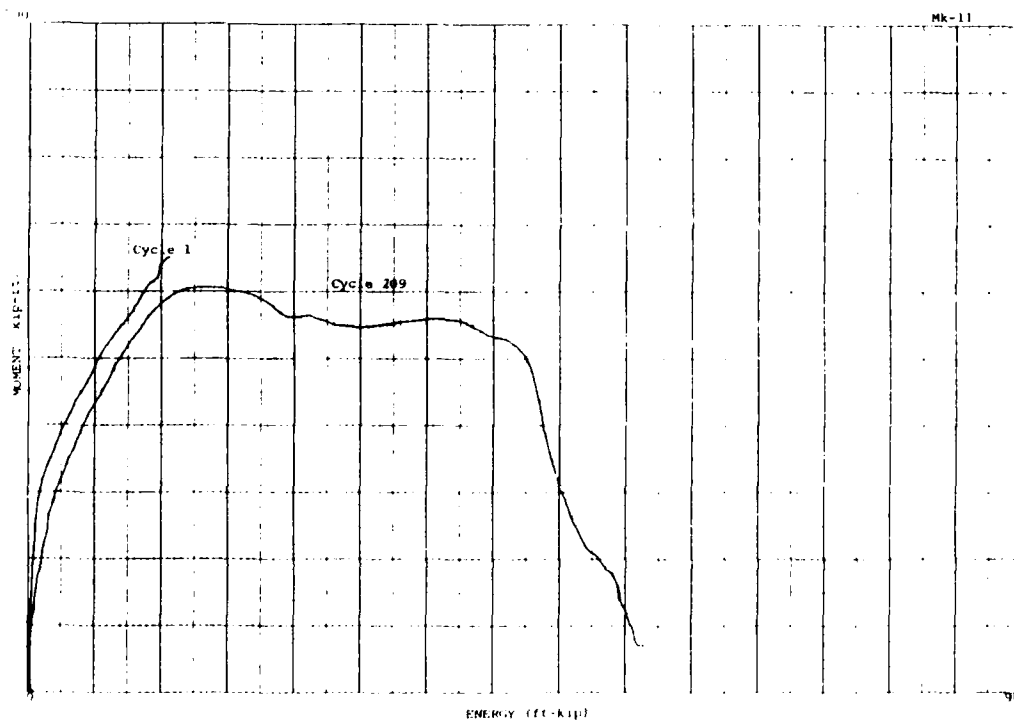


Figure B-130. MK11 moment-energy plot.

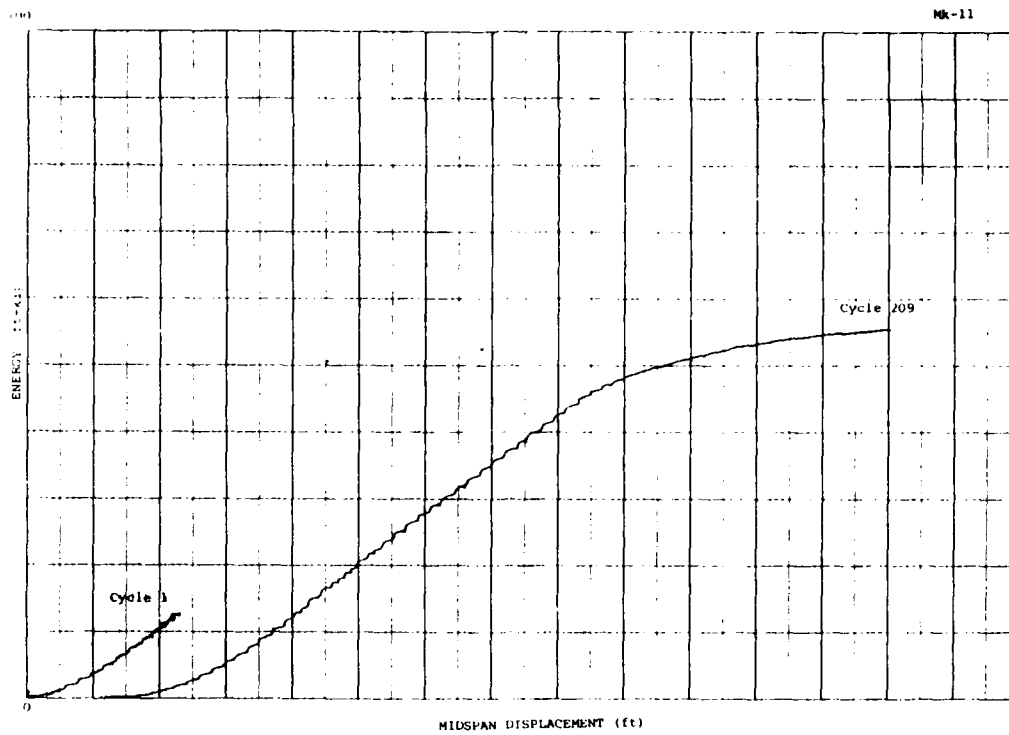


Figure B-131. MK11 energy-displacement plot.

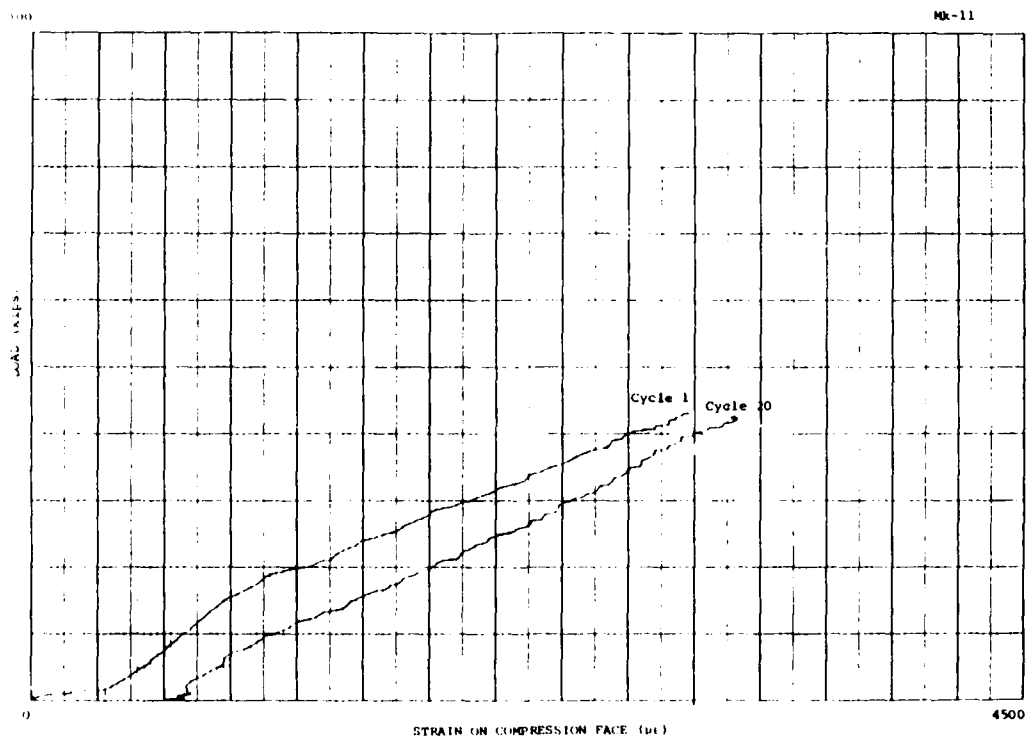


Figure B-132. MK11 compression strain.

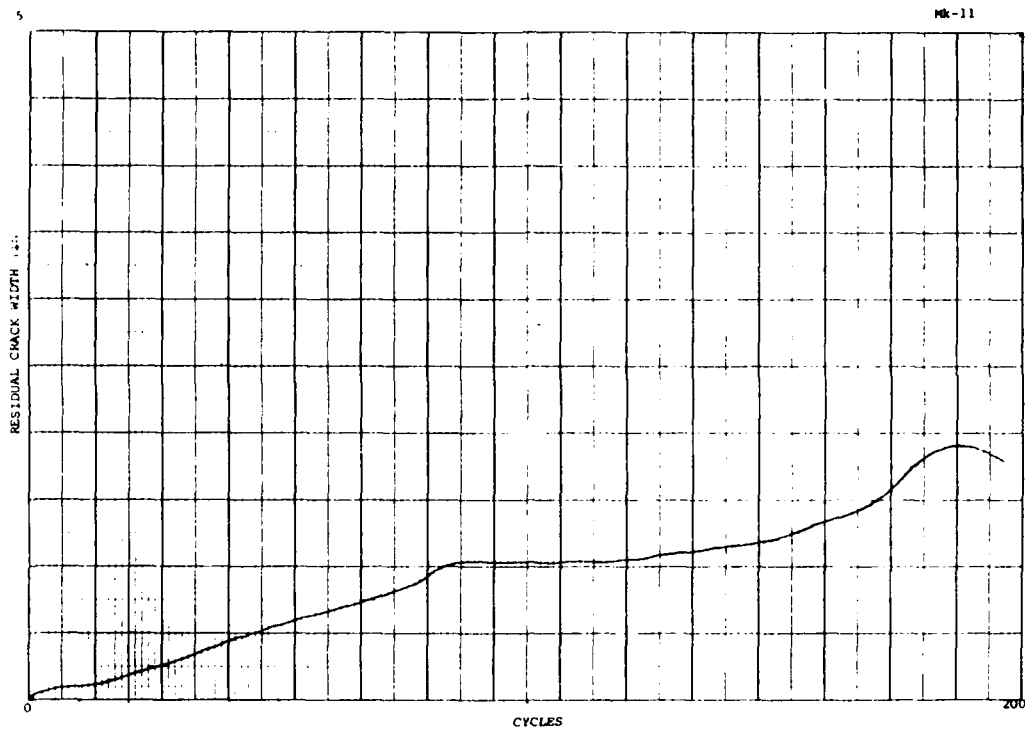


Figure B-133. MK11 crack width after load removal (at point of load).

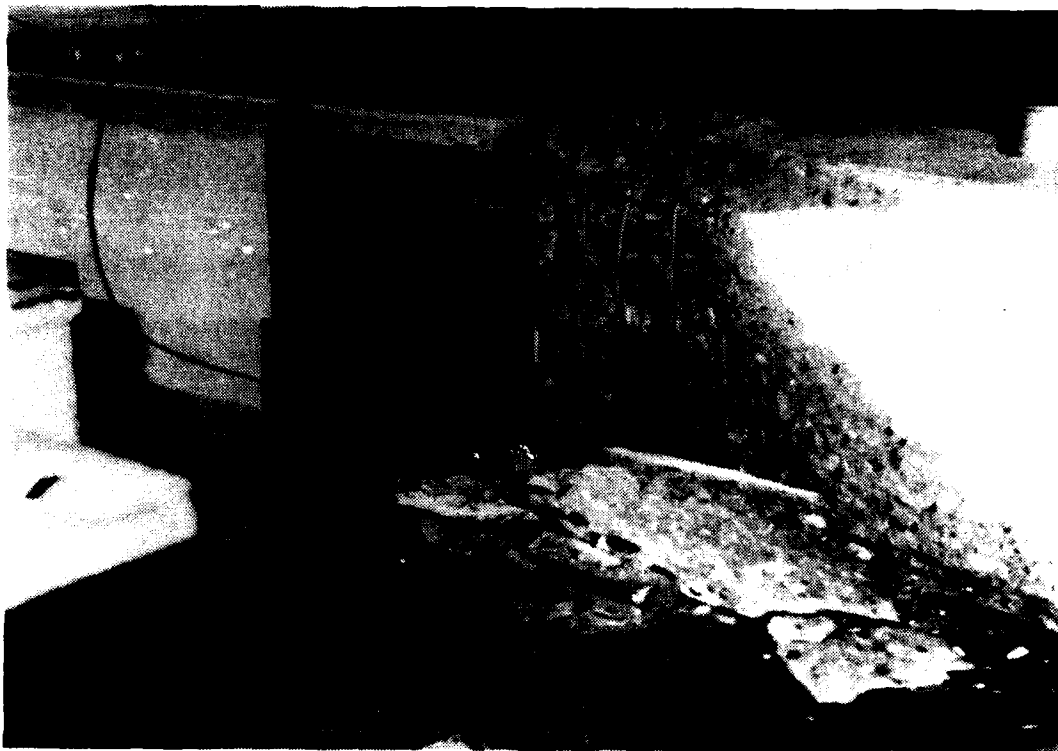


Figure B-134. MK12 compression spalling at failure.

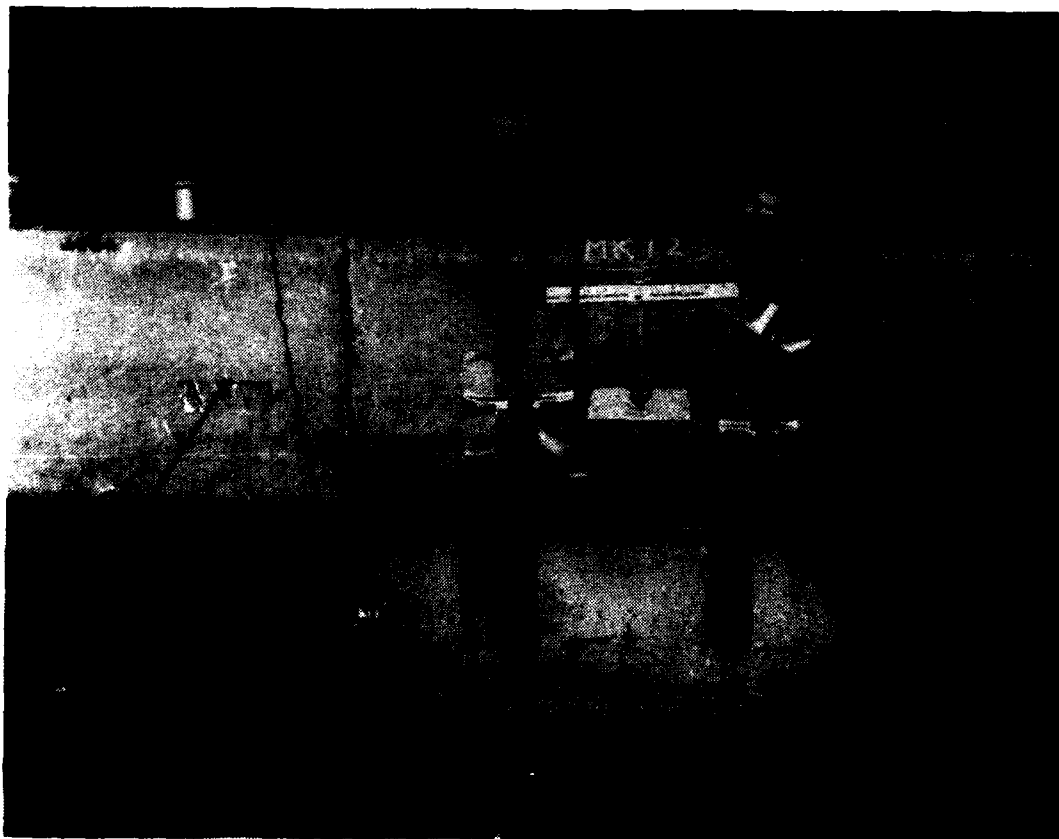


Figure B-135. MK12 tension cracking at failure.

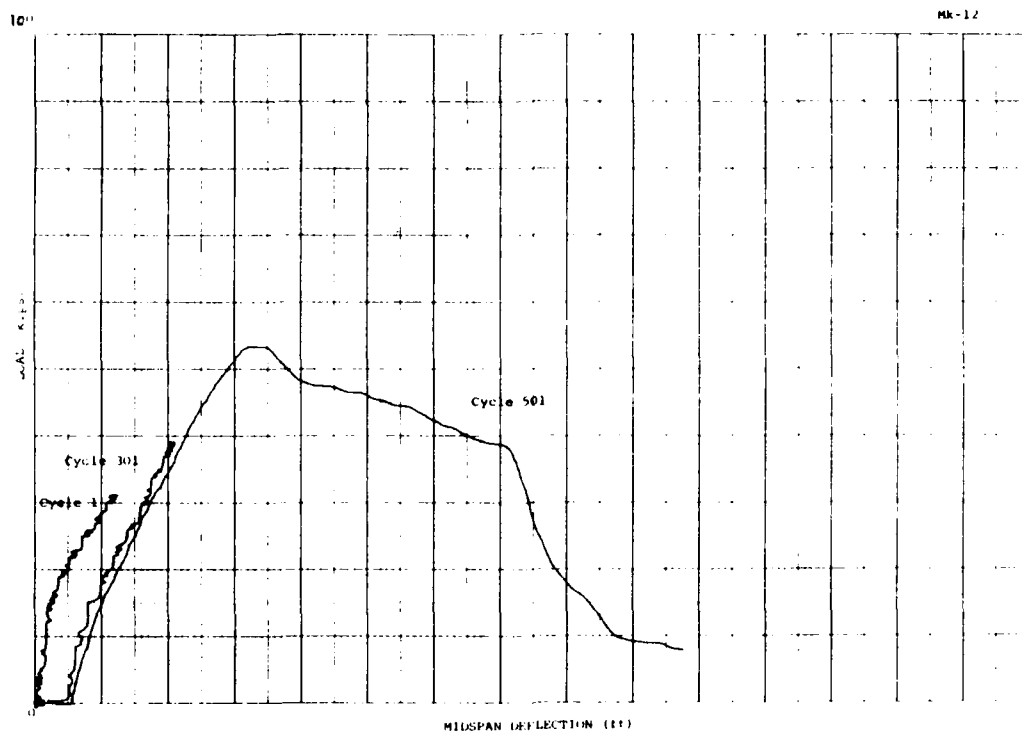


Figure B-136. MK12 load-deflection plot.

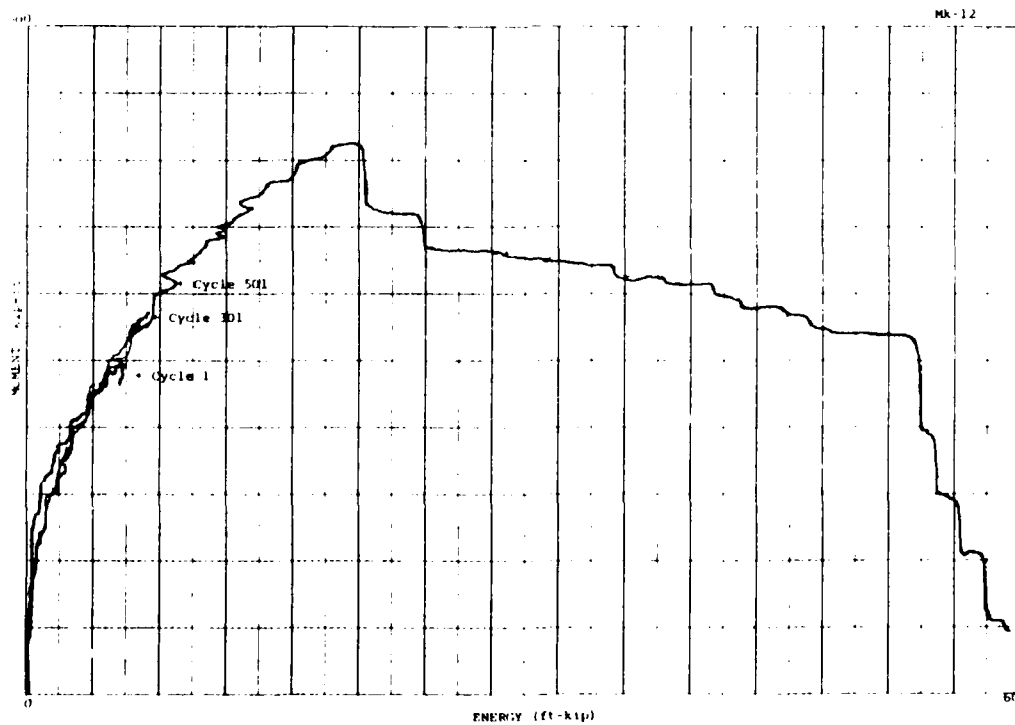


Figure B-137. MK12 moment-energy plot.

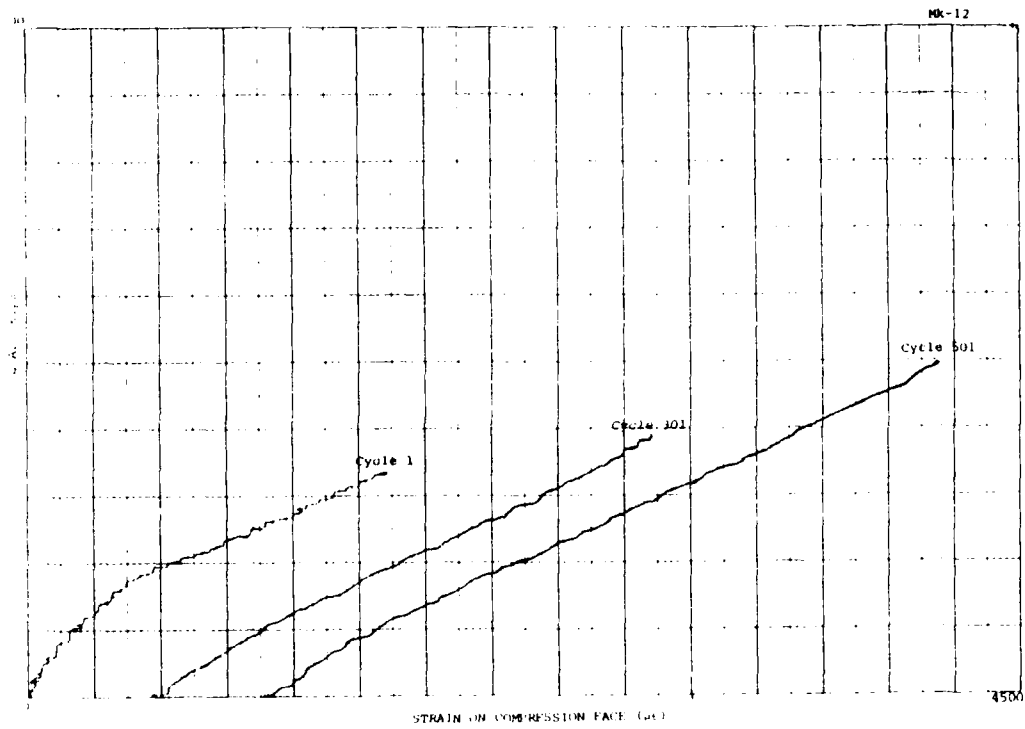


Figure B-138. MK12 compression strain at point of load.

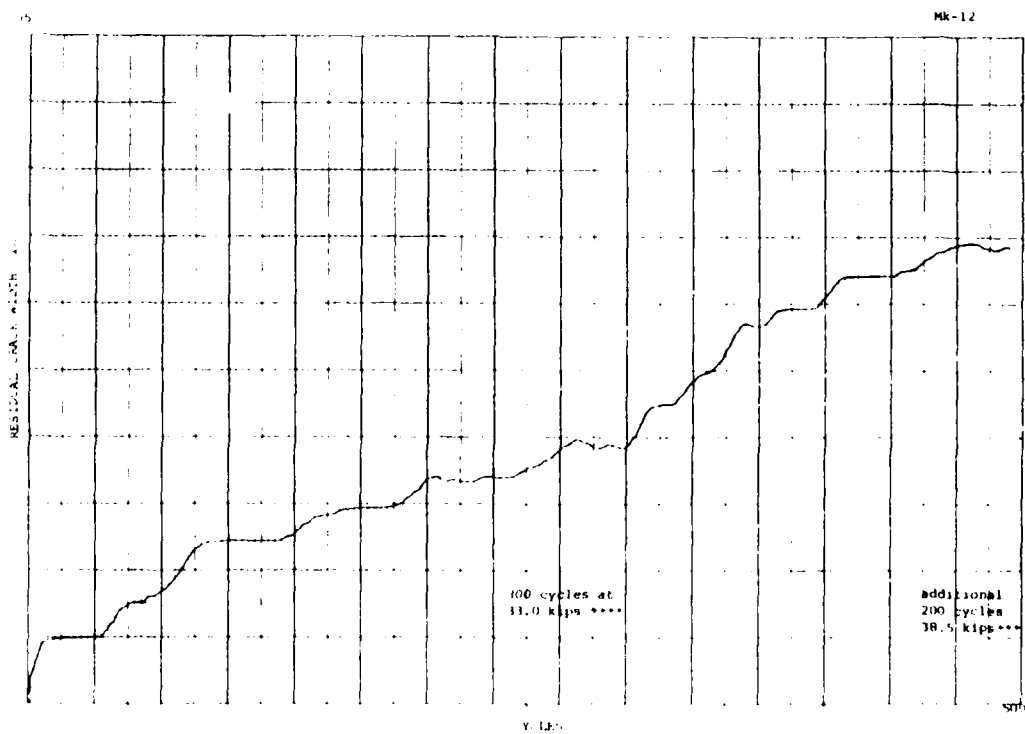


Figure B-139. MK12 crack width after load removal at point of load.

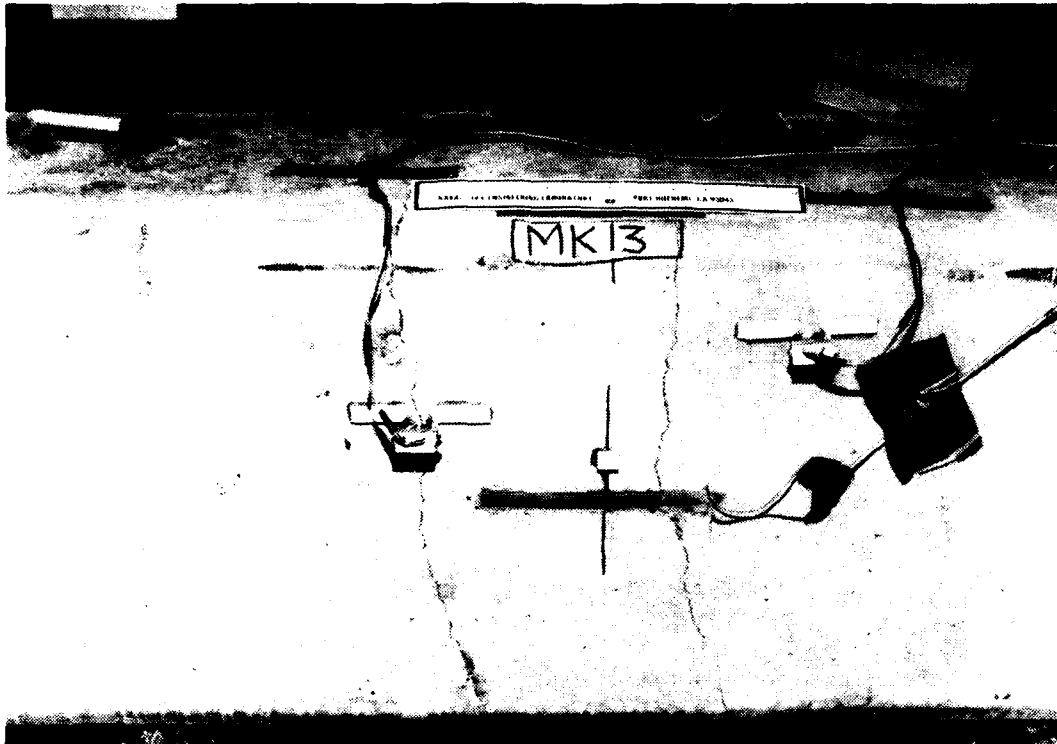


Figure B-140. MK13 tension crack after 100 cycles loaded at midspan.



Figure B-141. MK13 compression zone deterioration after 100 cycles.

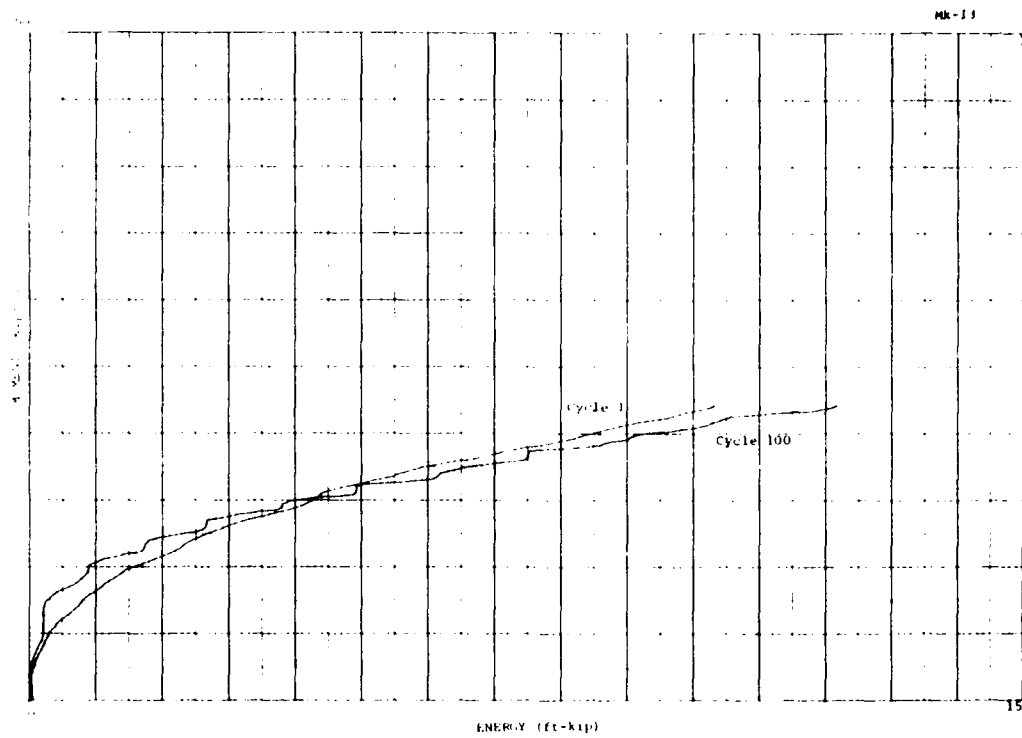


Figure B-142. MK13 moment-energy plot.

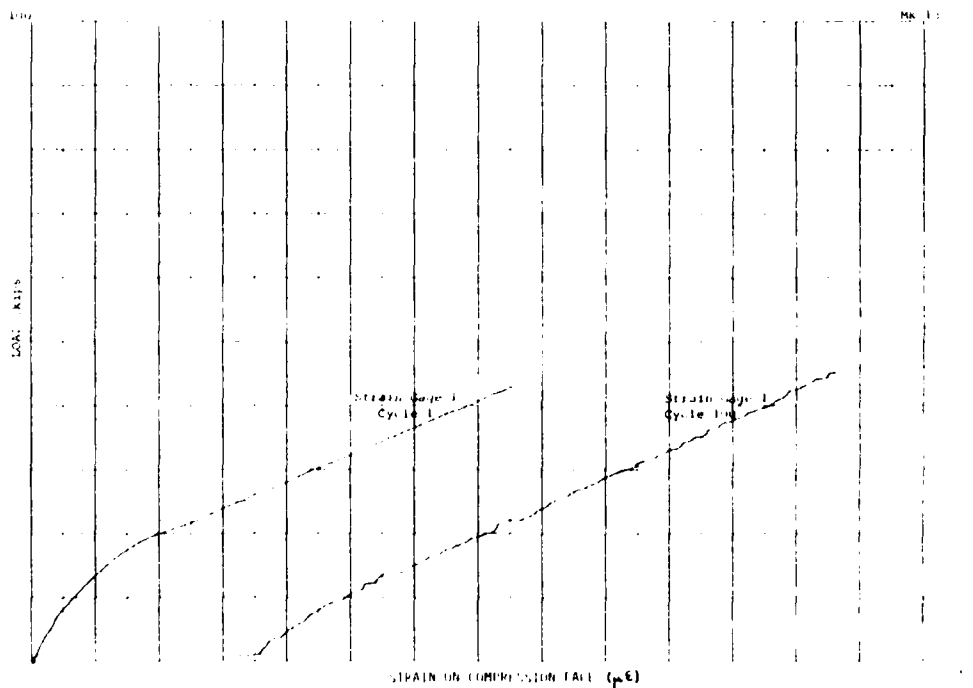


Figure B-143. MK13 compression strain at point of load.

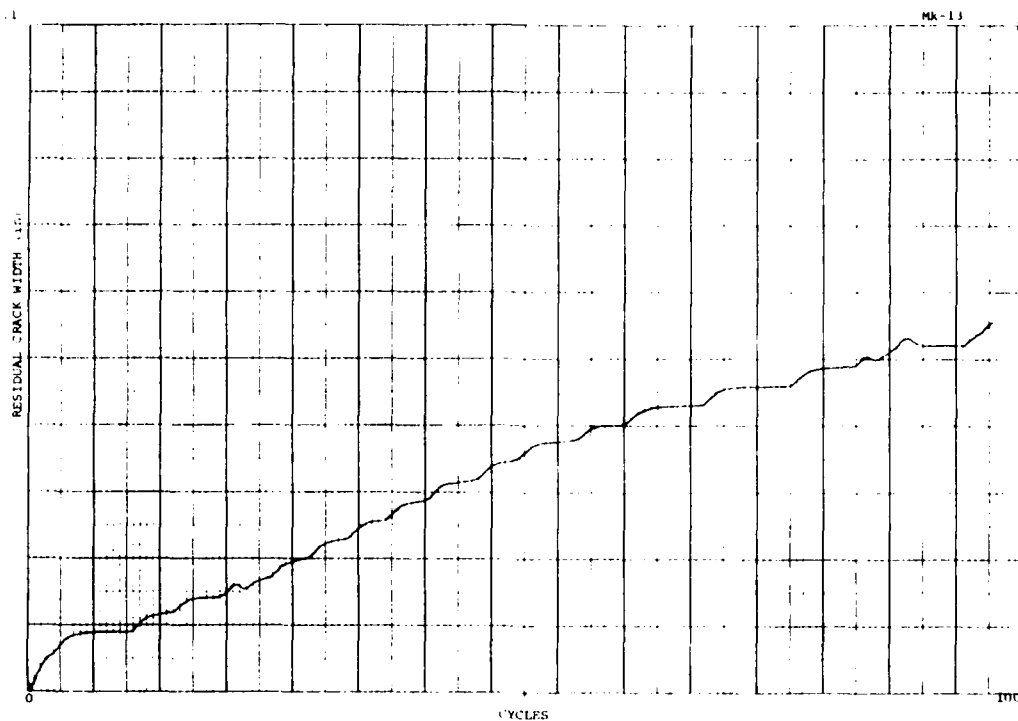


Figure B-144. MK13 crack width after load removal.

Note: MK13 was first subjected to 100 cycles with the load applied at midspan, then monotonically loaded to failure with the load applied at 7 feet from one support.

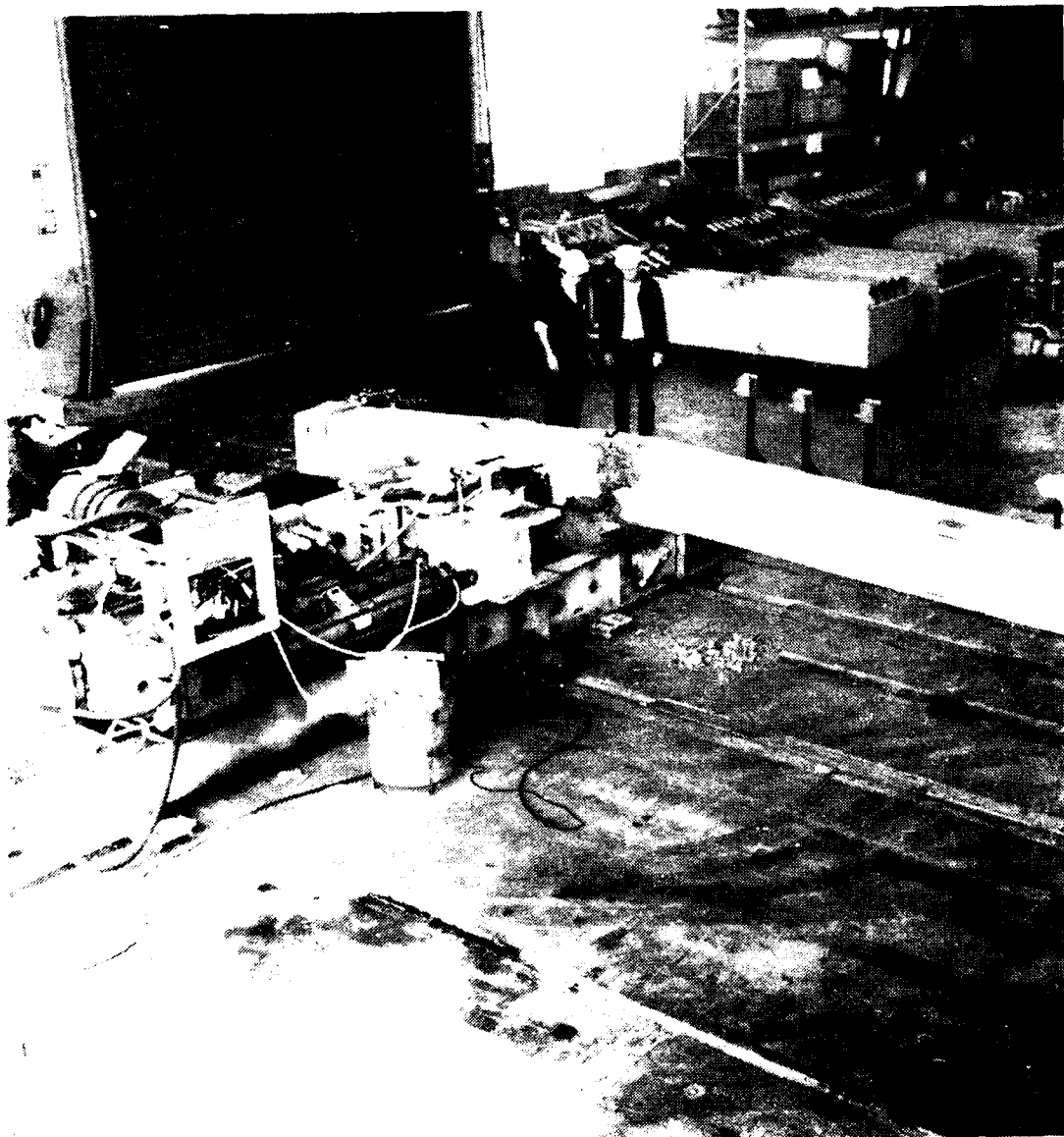


Figure B-145. MK13A monotonic loaded at 7 feet from one support.



Figure B-146. MK13A compression spalling at failure after monotonic loading.

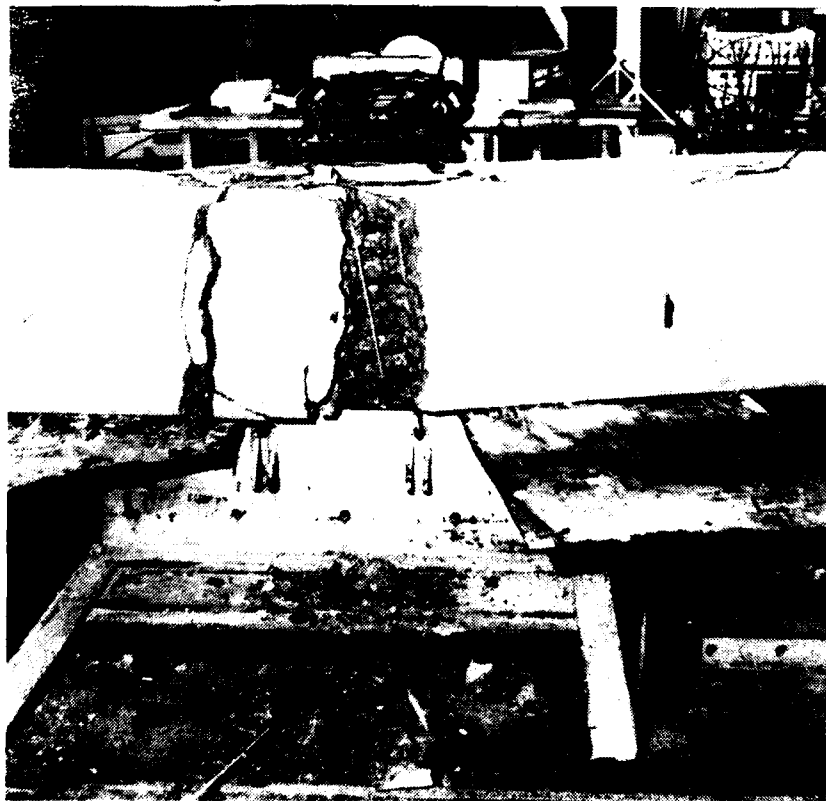


Figure B-147. MK13A tension cracking at failure.

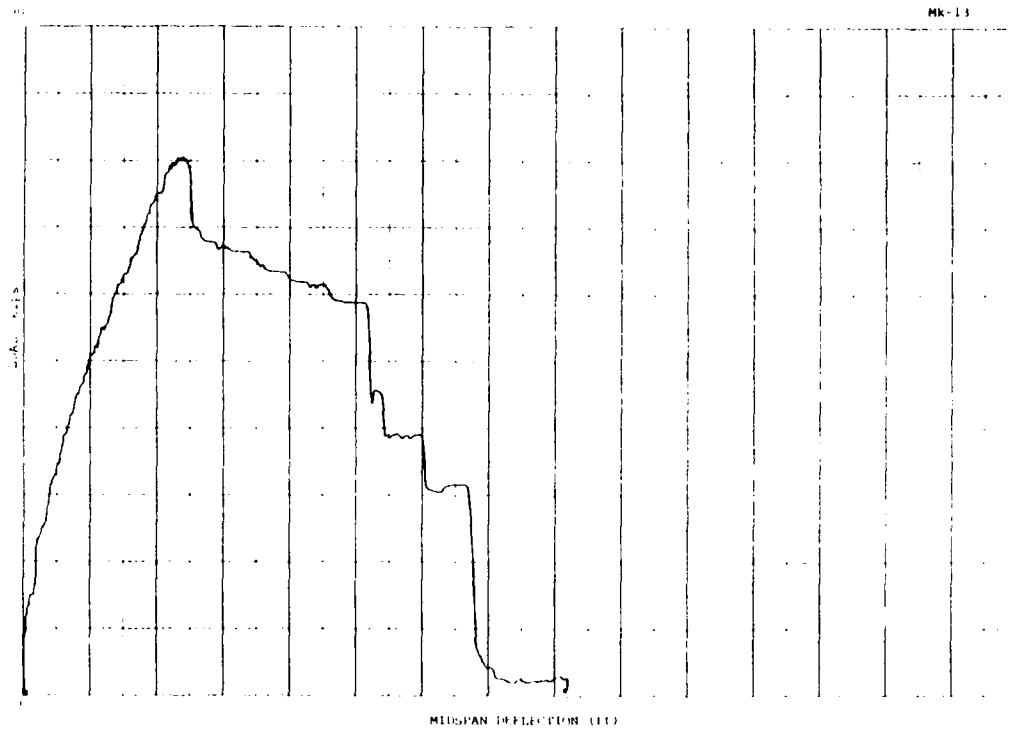


Figure B-148. MK13A load-deflection plot at point of load.

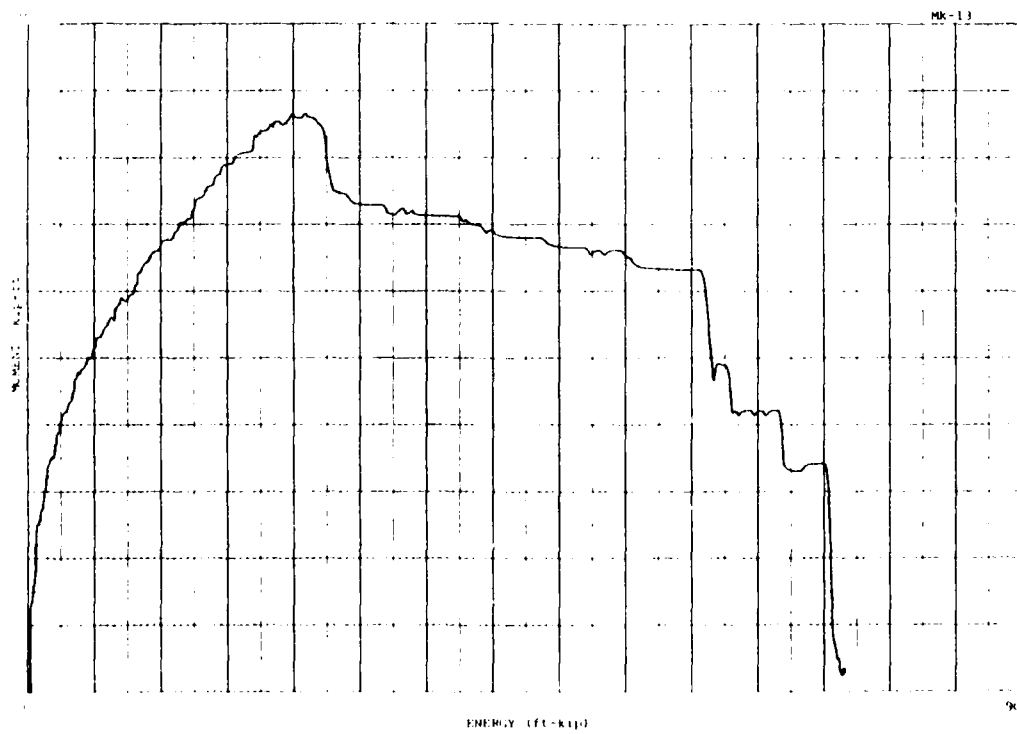


Figure B-149. MK13A moment-energy plot.

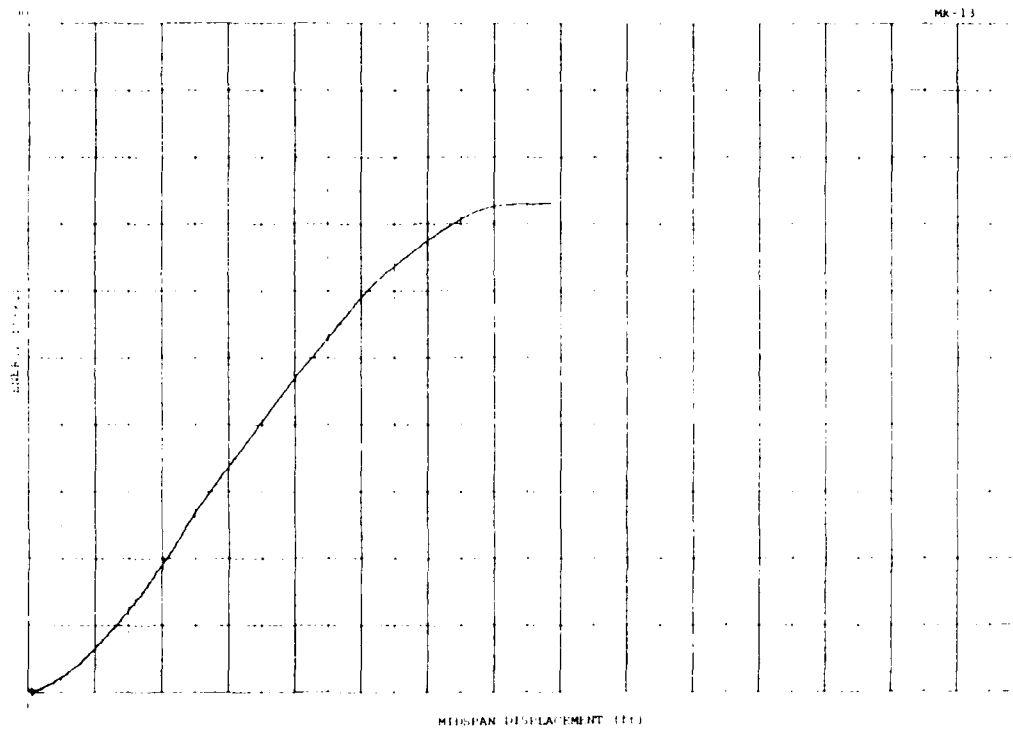


Figure B-150. MK13A energy-displacement plot.

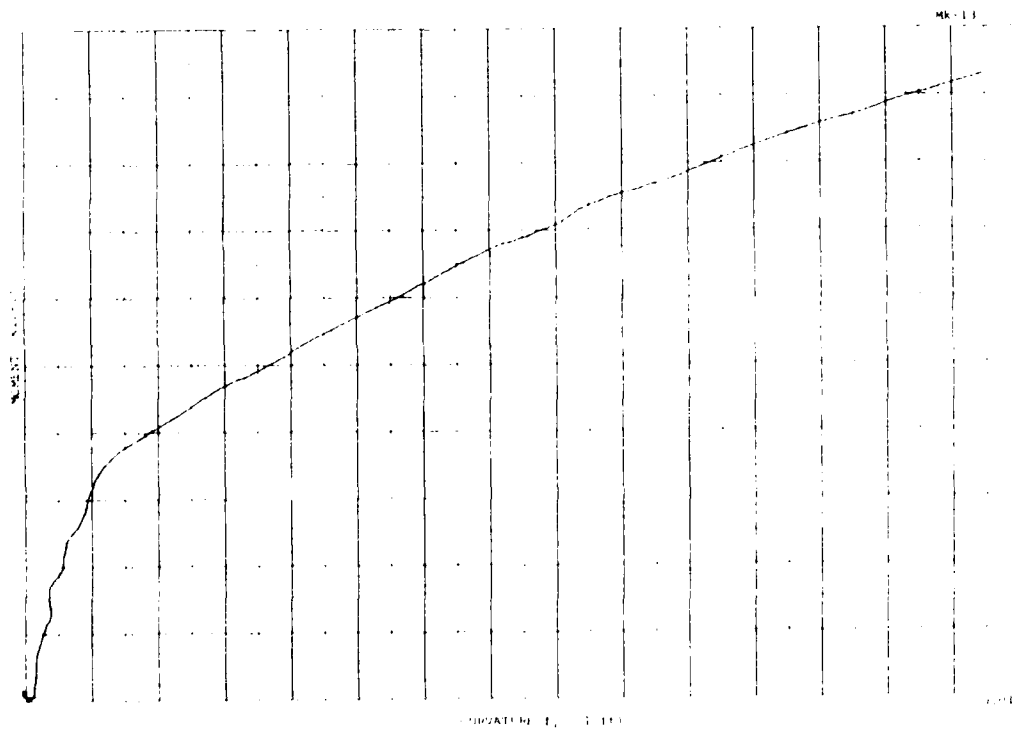


Figure B-151. MK13A moment-curvature plot prior to ultimate load.

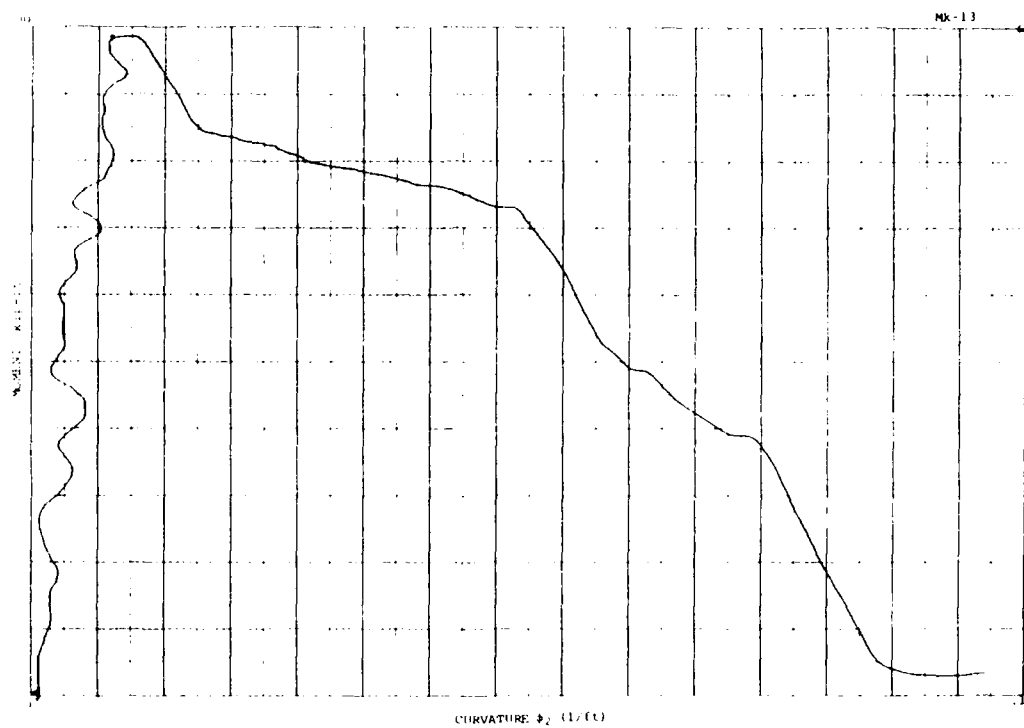


Figure B-152. MK13A moment-curvature plot to failure.

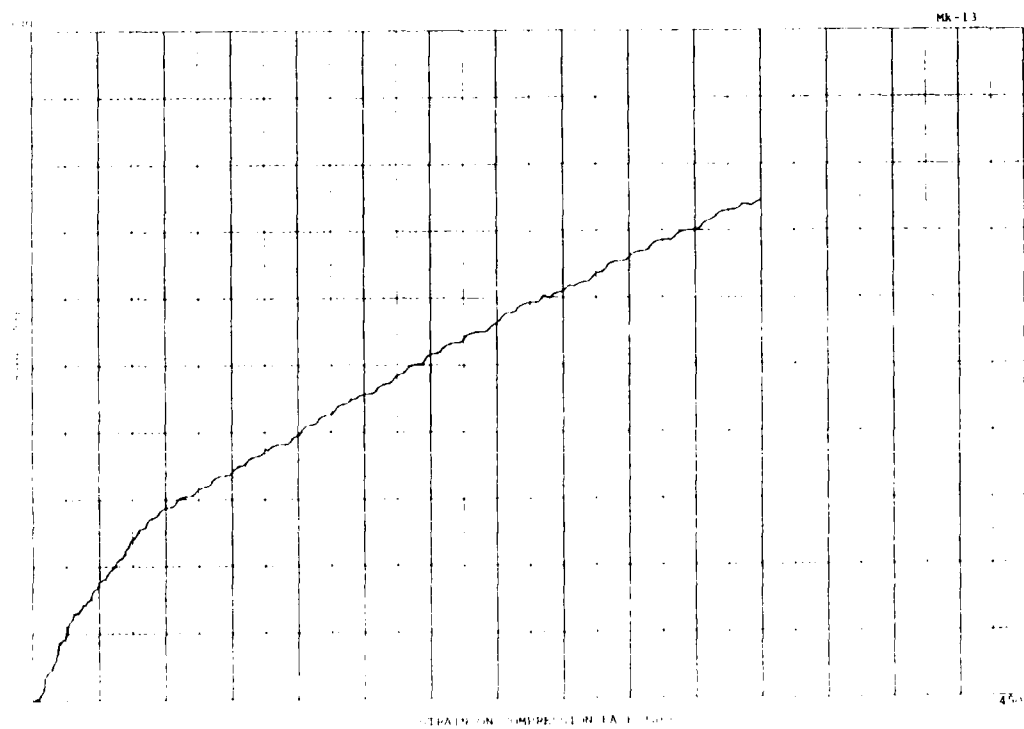


Figure B-153. MK13A compression strain.

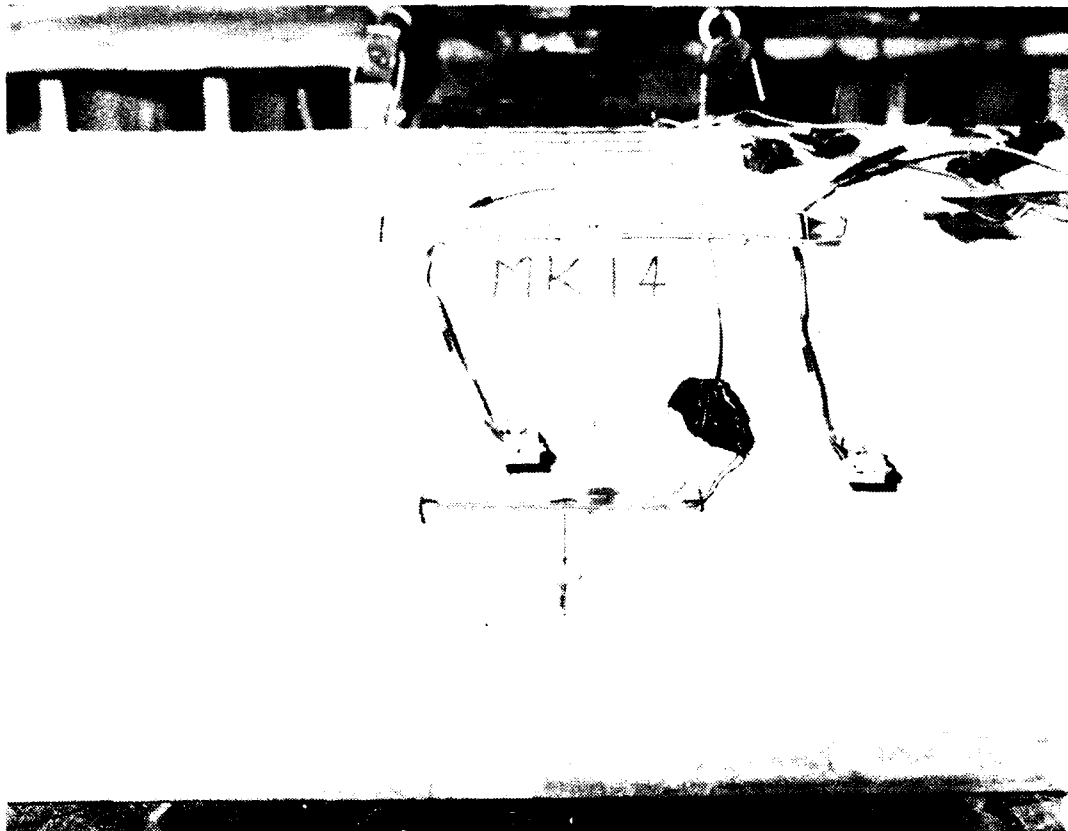


Figure B-154. MK14 tension crack after 100 cycles loaded at midspan.

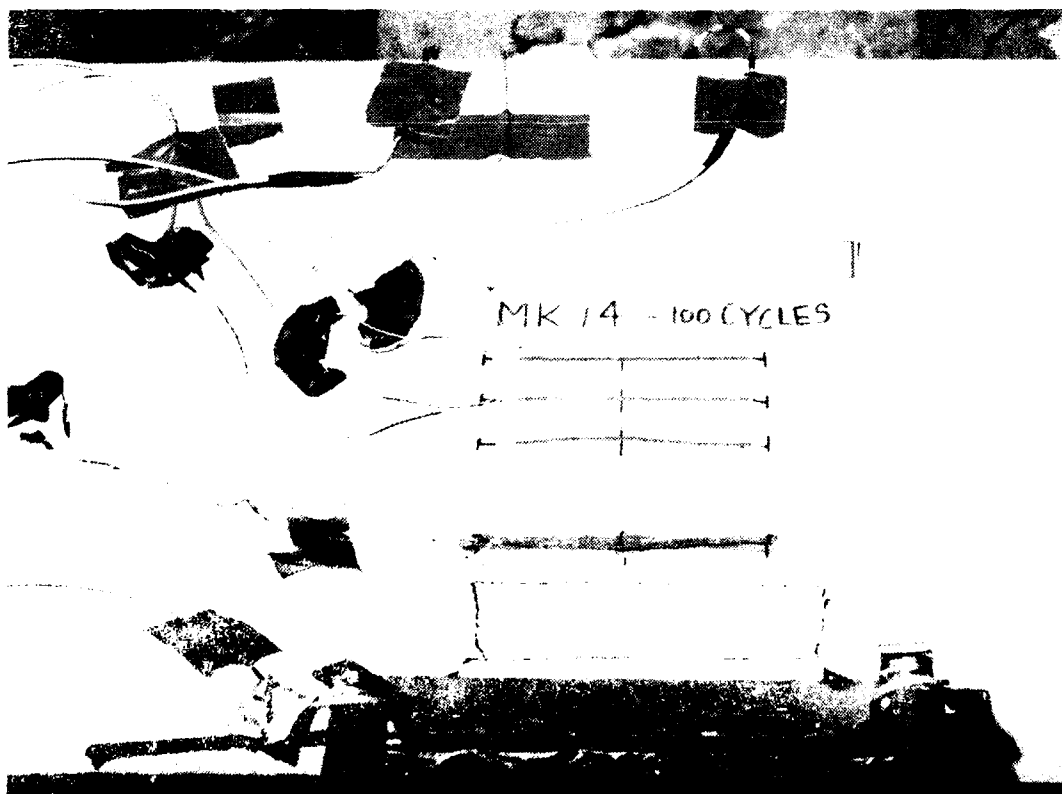


Figure B-155. MK14 compression face after 100 cycles.

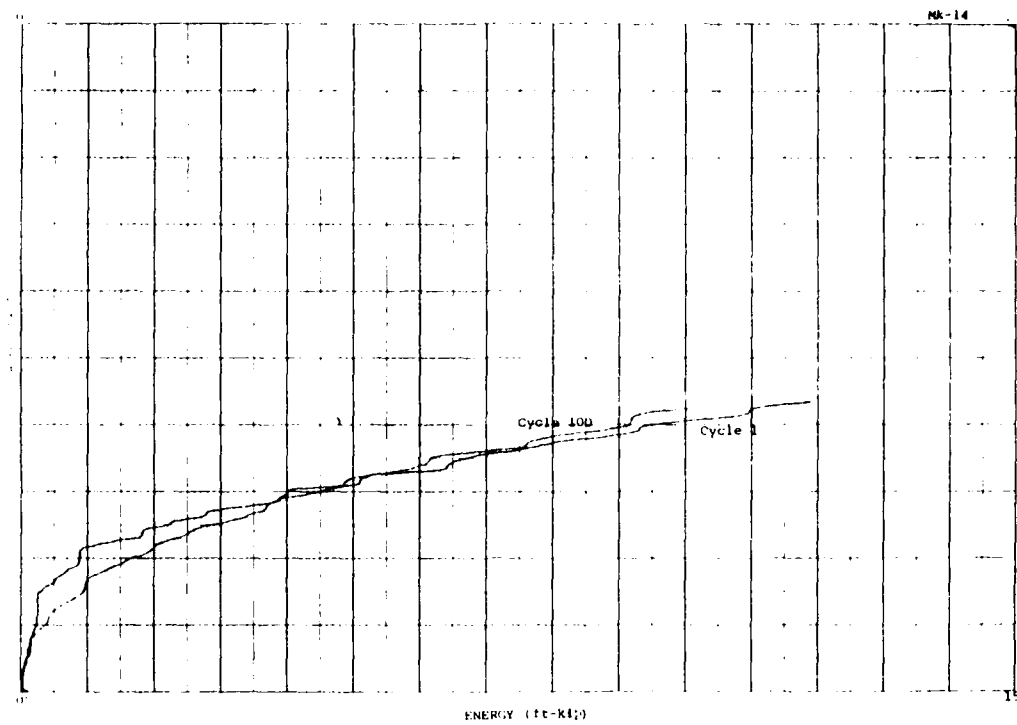


Figure B-156. MK14 moment-energy plot.

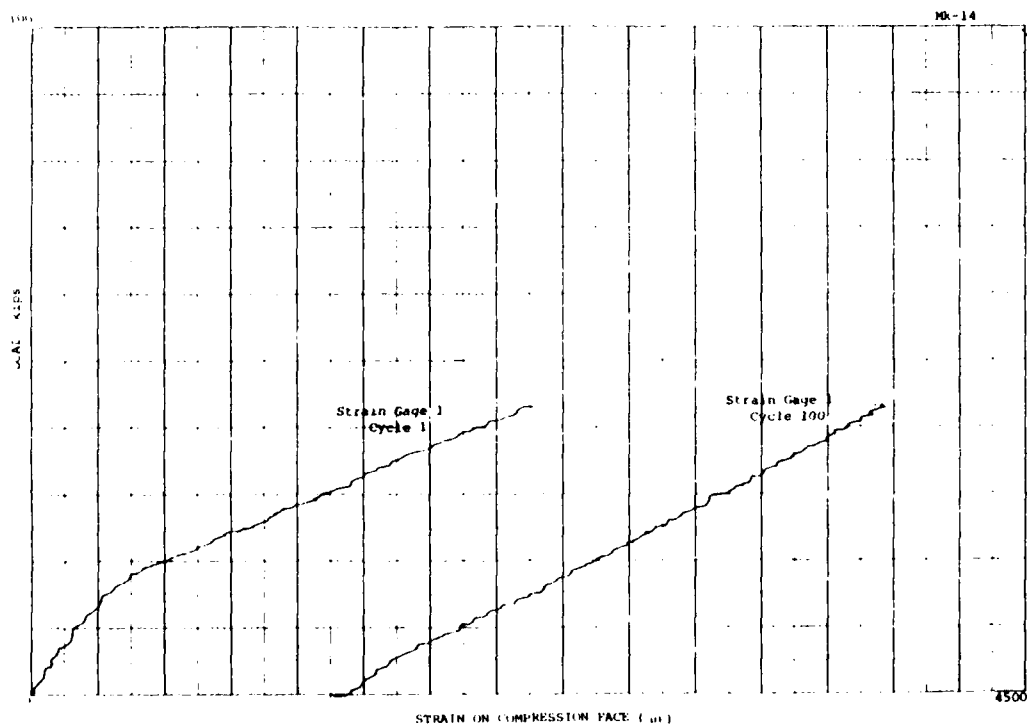


Figure B-157. MK14 compression strain.

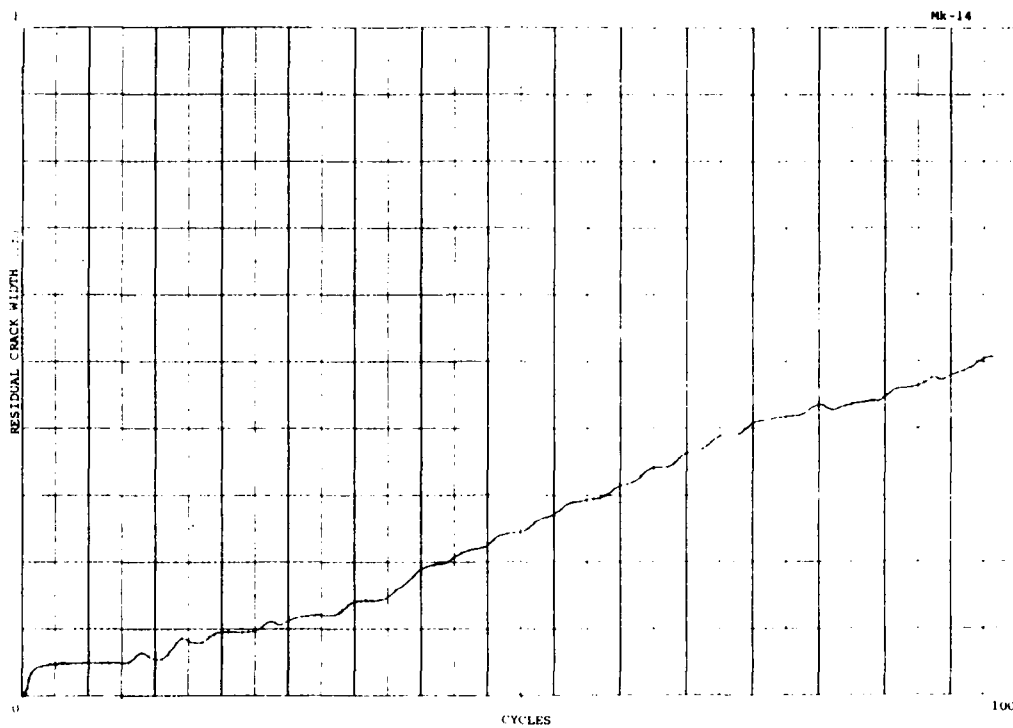


Figure B-158. MK14 crack width after load removal.

Note: MK14 was first subjected to 100 cycles with the load applied at midspan, then monotonically loaded to failure with the load applied at 7 feet from one support. Results of monotonic test follow on MK14A.

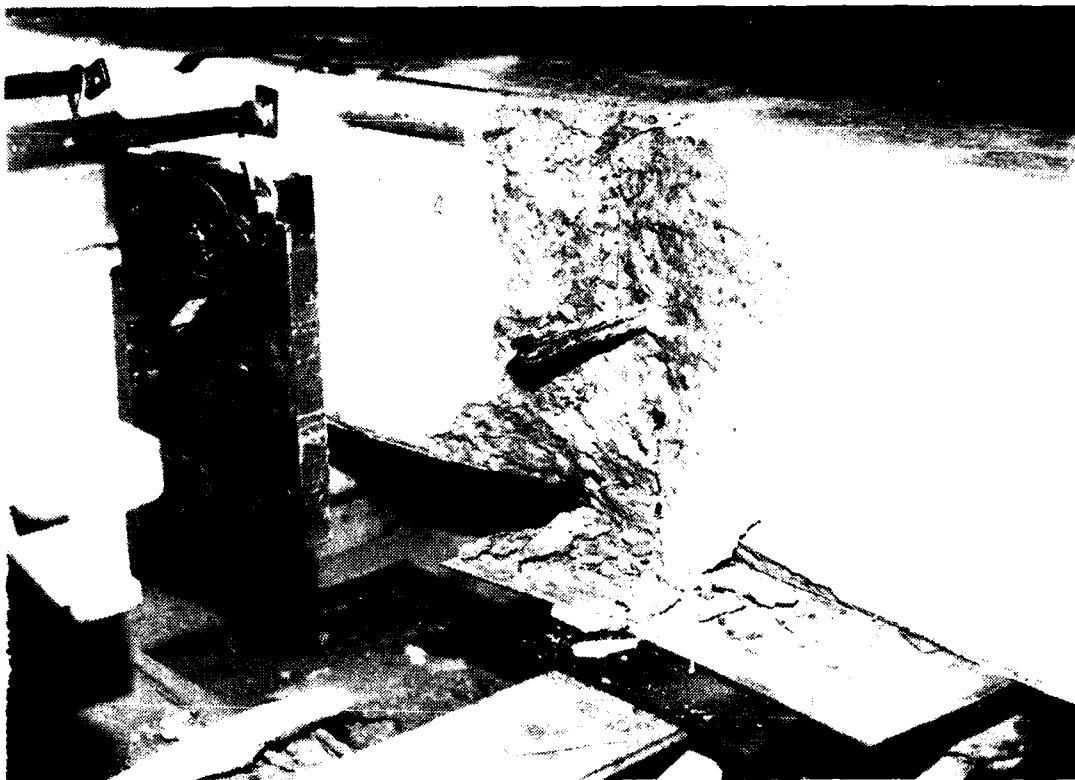


Figure B-159. MK14A compression spalling at failure monotonic load at 7 feet from support.

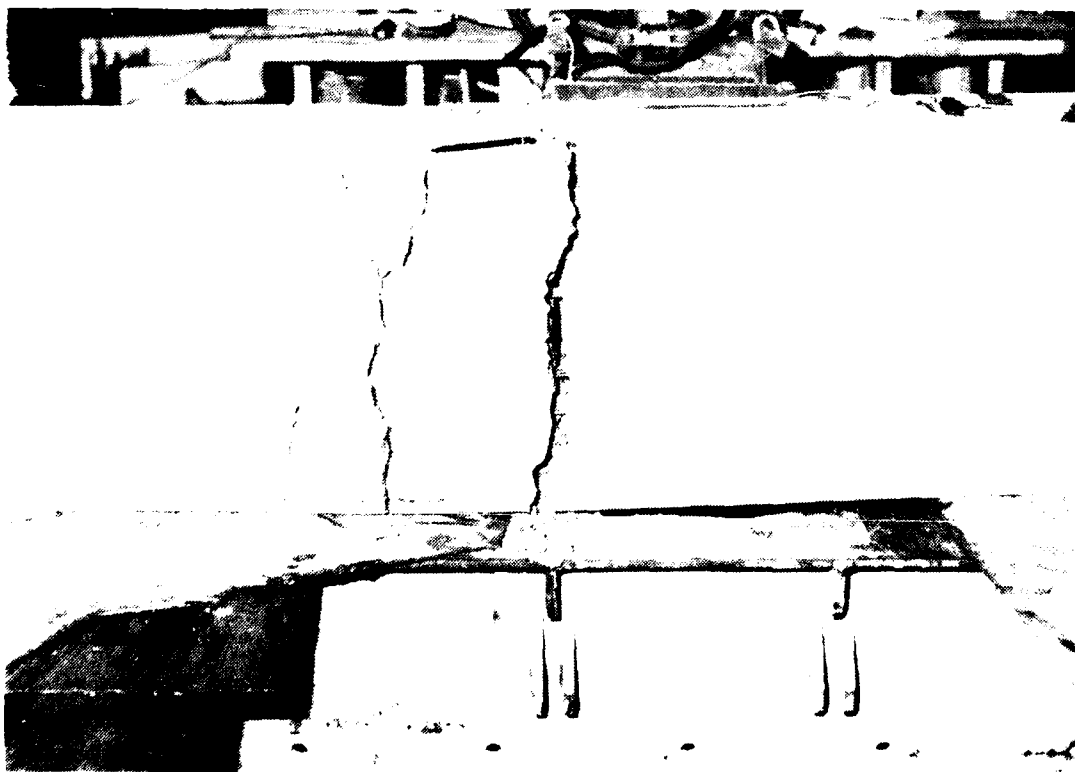


Figure B-160. MK14A tension cracks at failure.

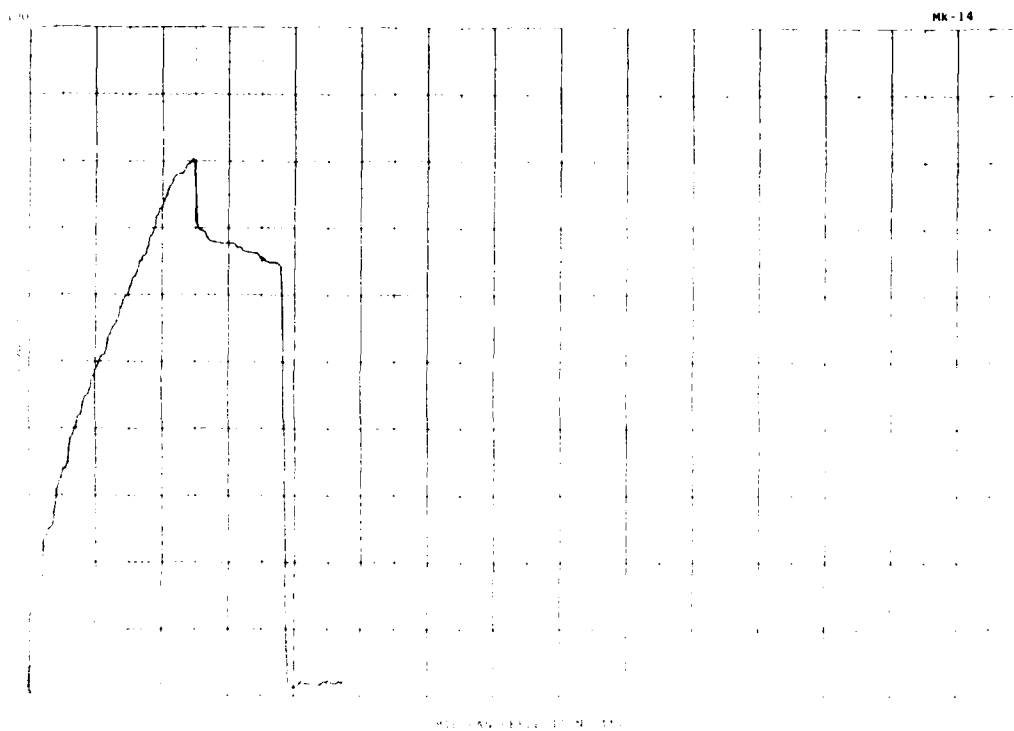


Figure B-161. MK14A load-deflection plot.

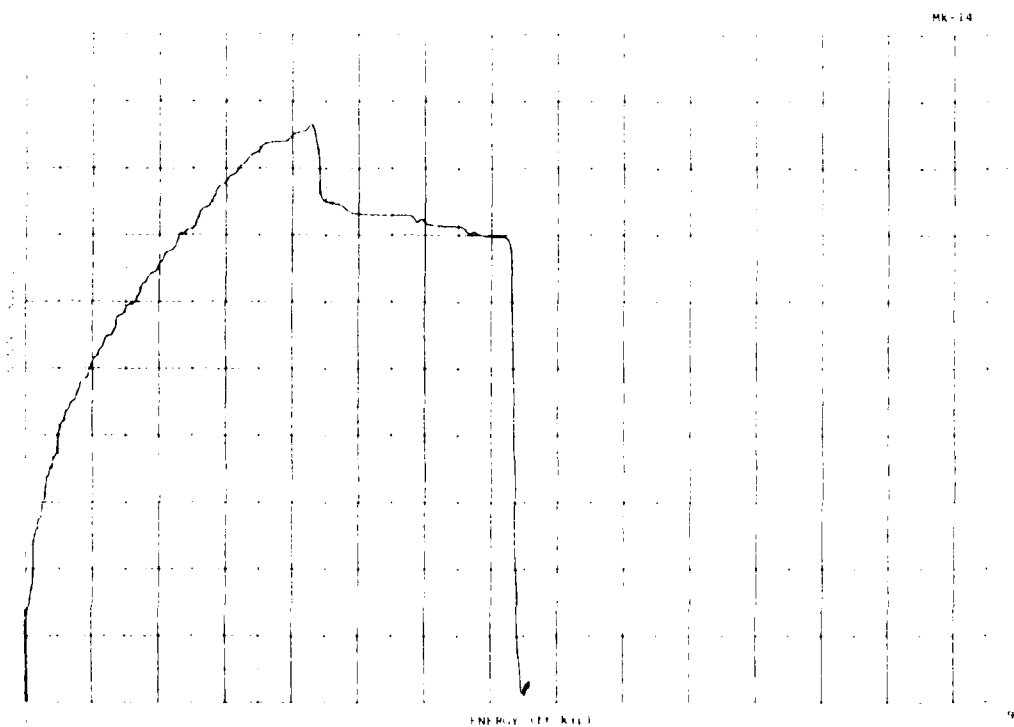


Figure B-162. MK14A moment-energy plot.

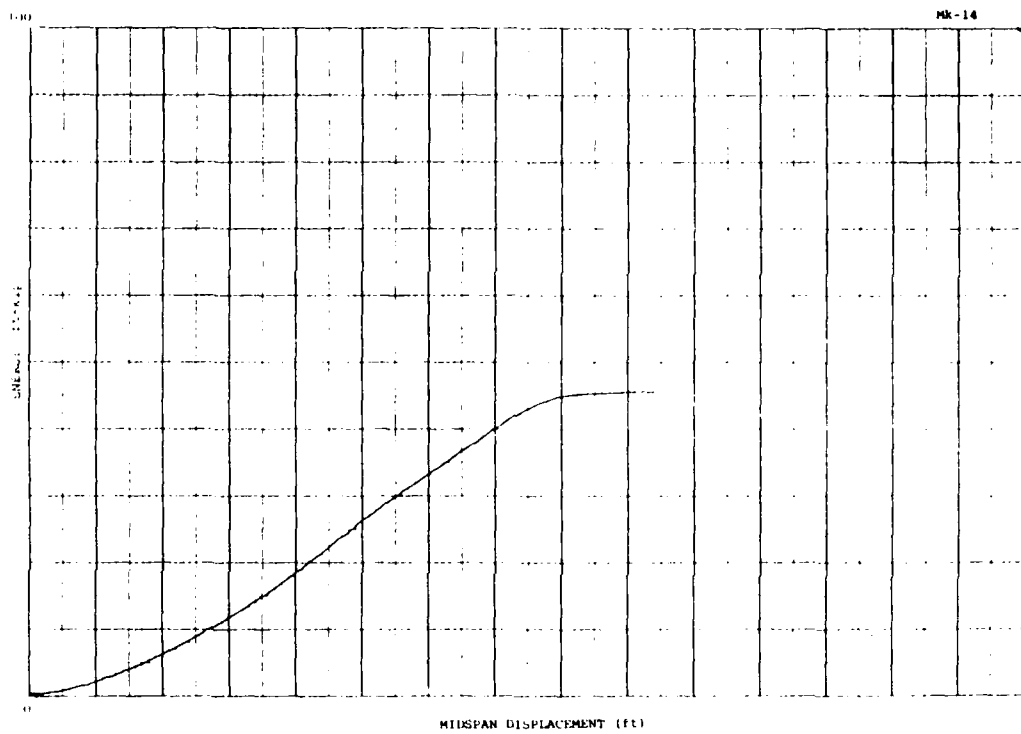


Figure B-163. MK14A energy-displacement plot (at point of load).

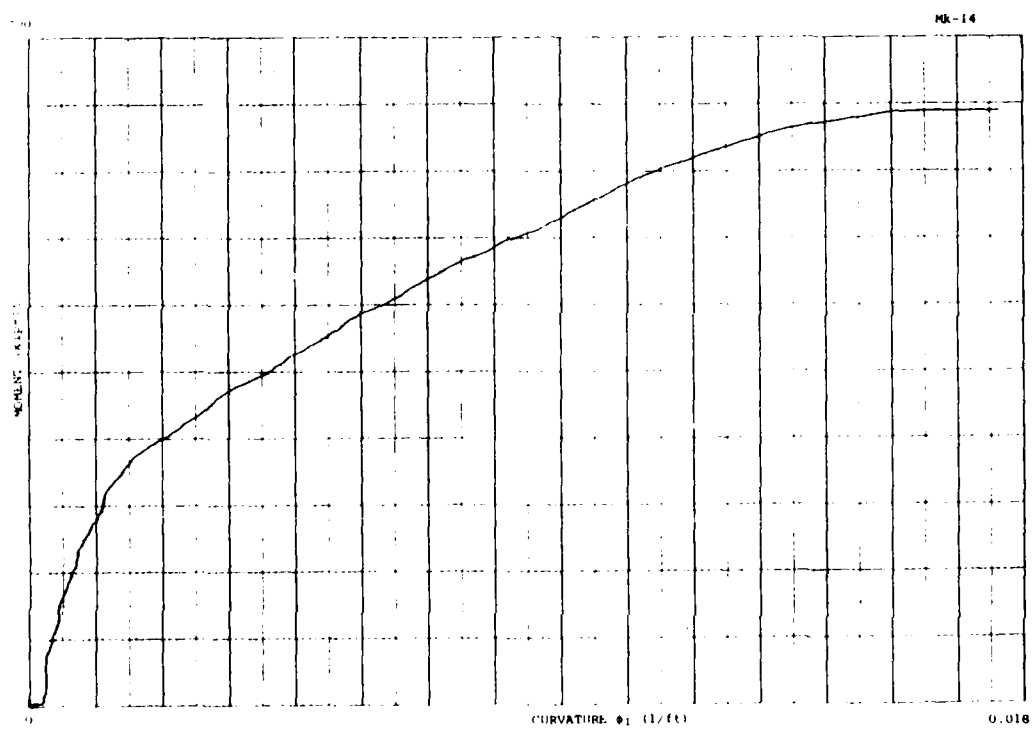


Figure B-164. MK14A moment-curvature plot before ultimate load.

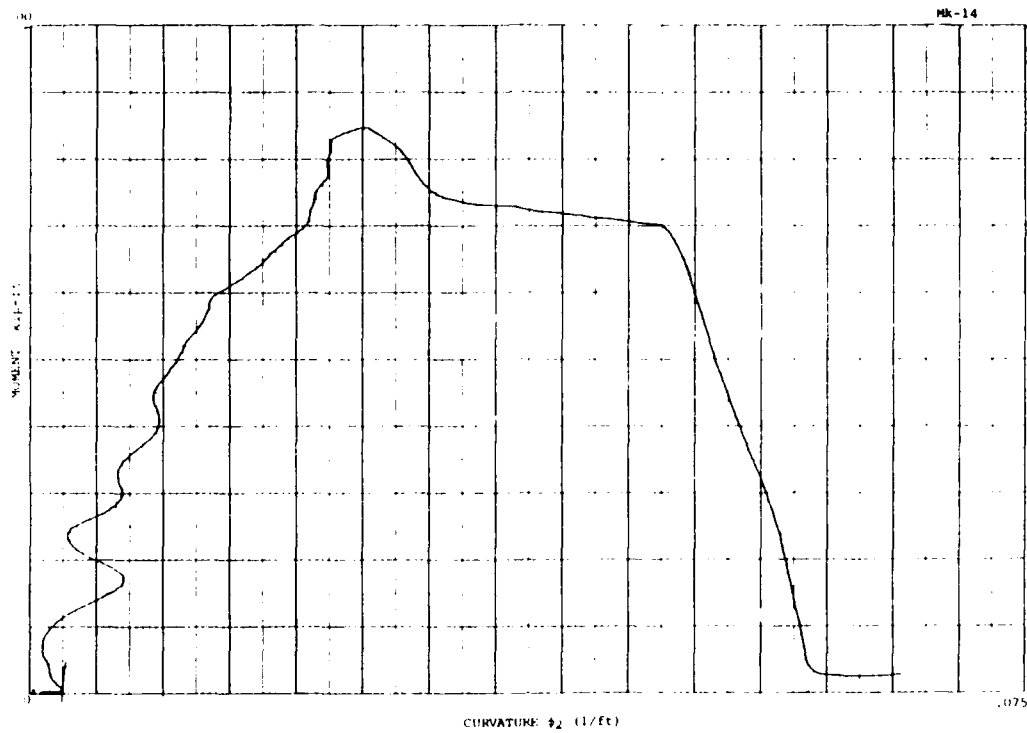


Figure B-165. MK14A moment-curvature plot to failure load.

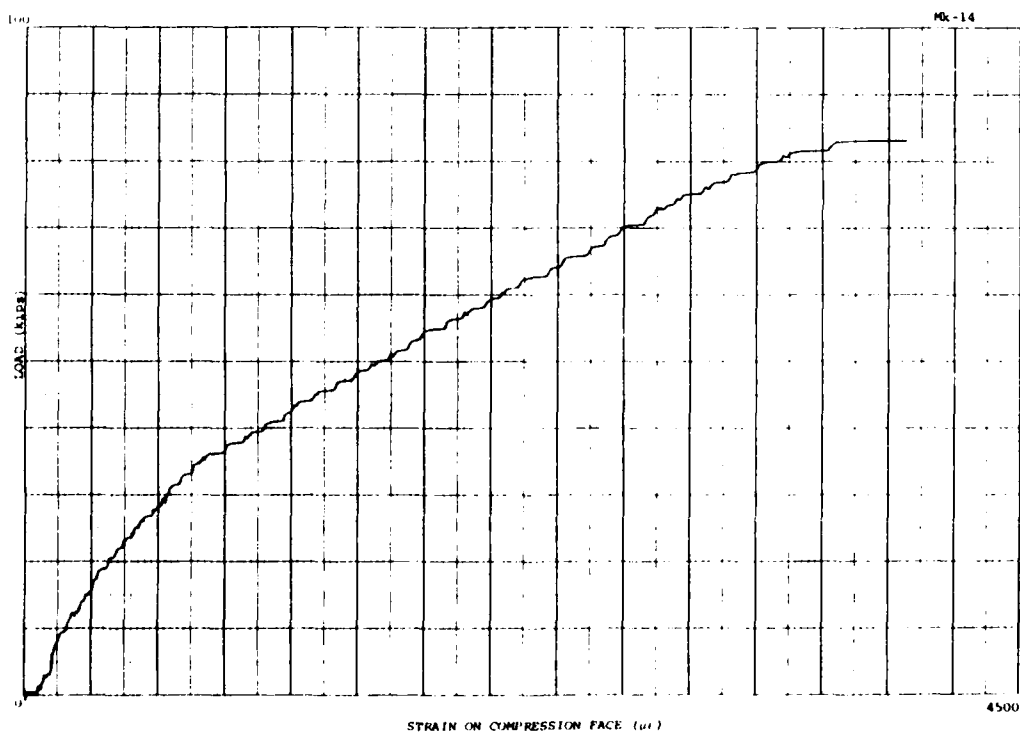


Figure B-166. MK14A compression strain.



Figure B-167. MK16 compression spalling at failure.



Figure B-168. MK16 tension cracking at failure.

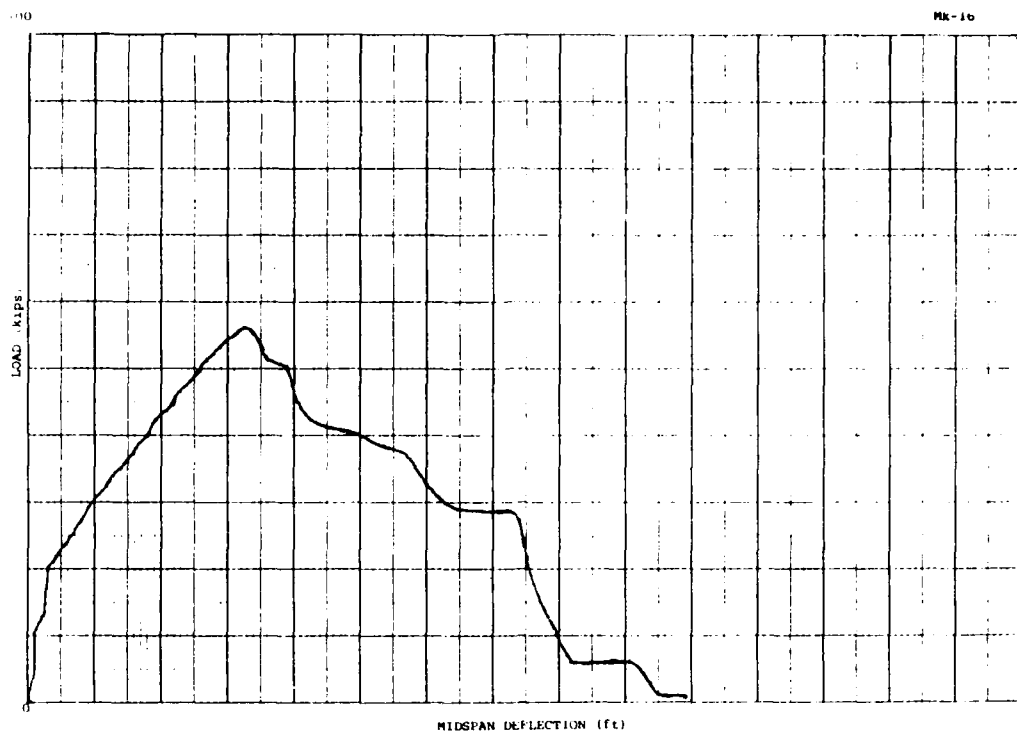


Figure B-169. MK16 load-deflection plot.

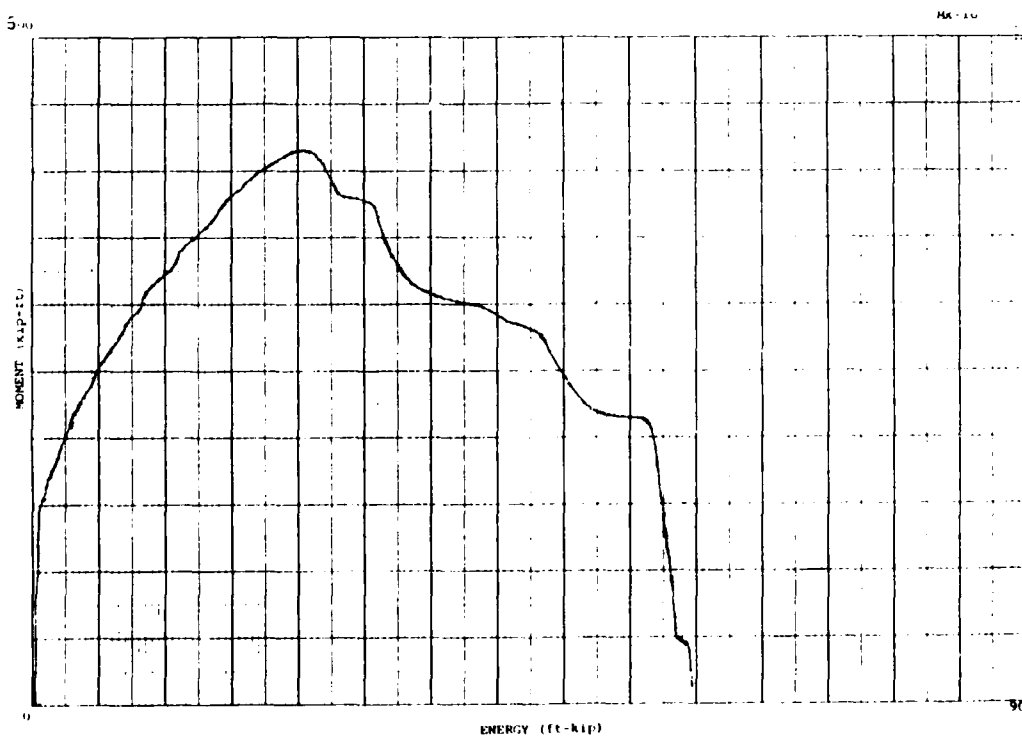


Figure B-170. MK16 moment-energy plot.

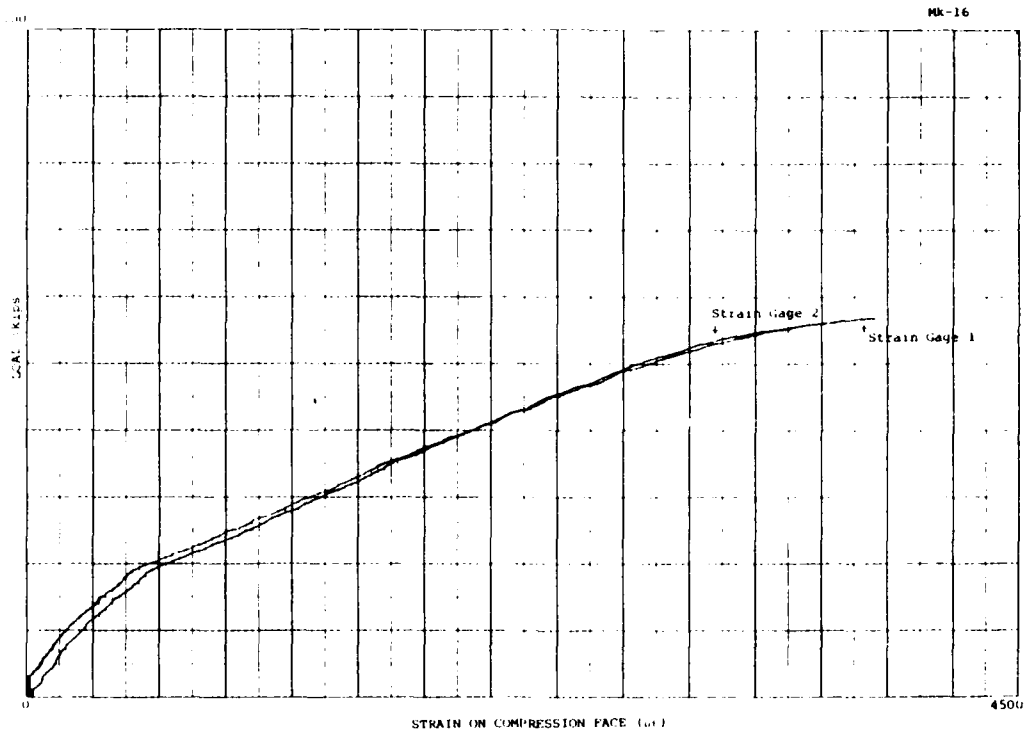


Figure B-171. MK16 compression strain.



Figure B-172. MK17 compression spalling at failure.

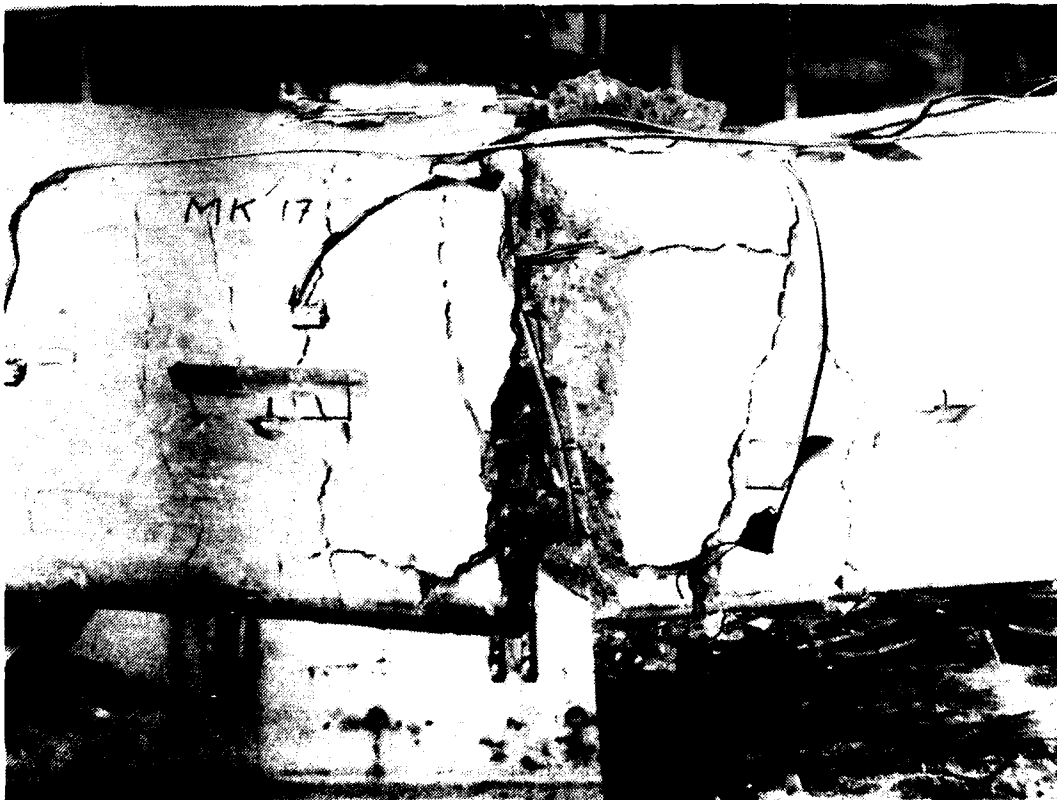


Figure B-173. MK17 tension cracking at failure.

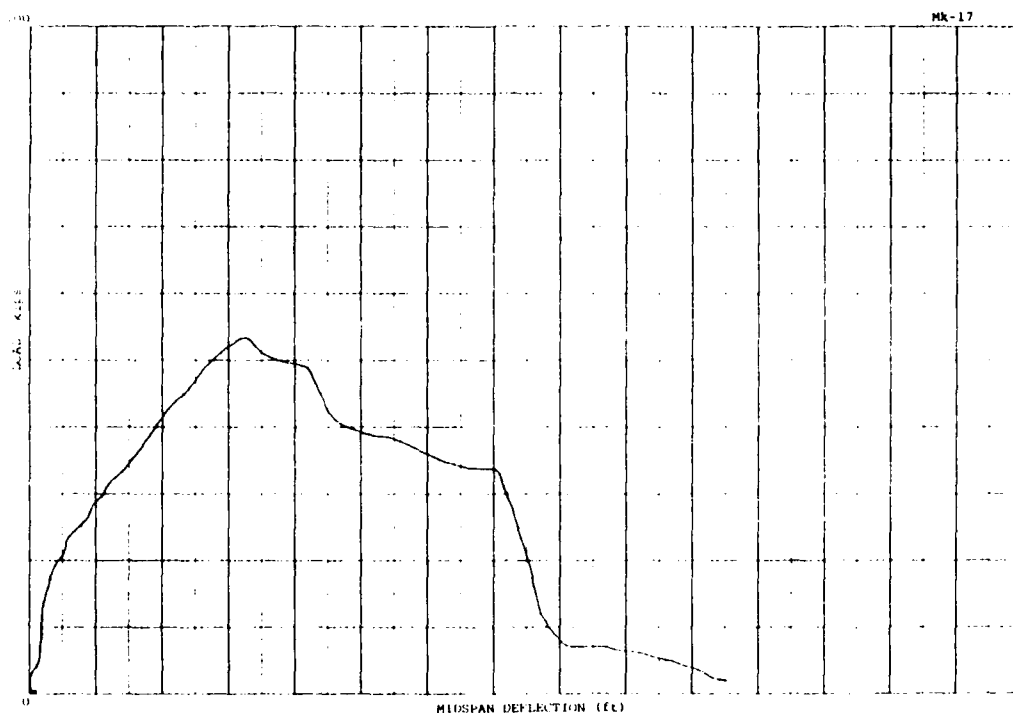


Figure B-174. MK17 load-deflection plot.

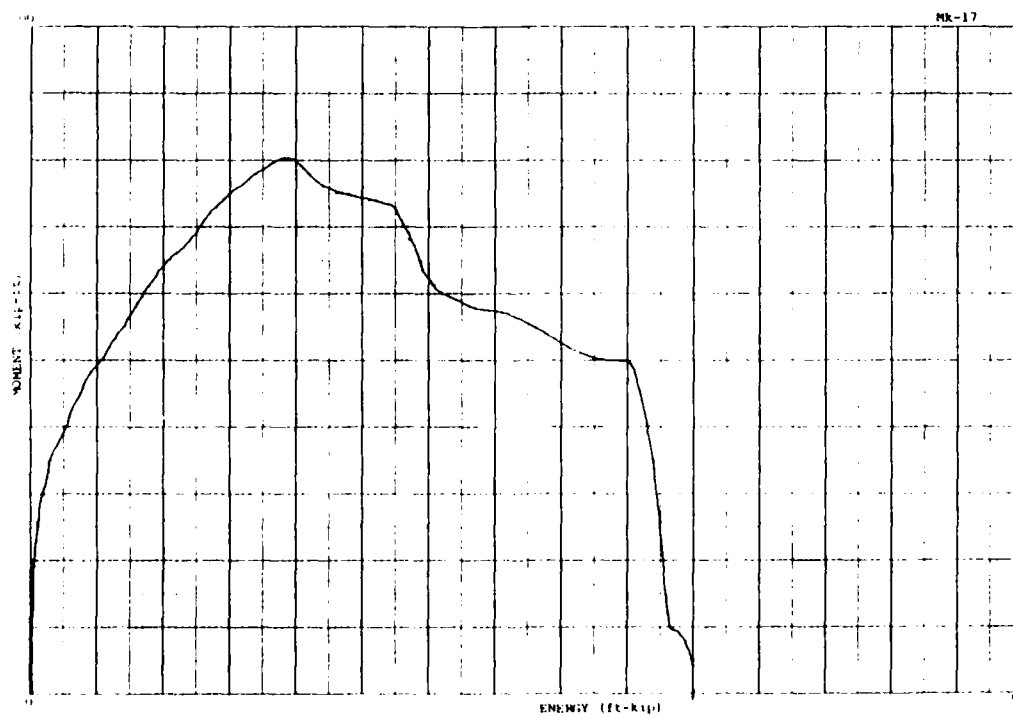


Figure B-175. MK17 moment-energy plot.

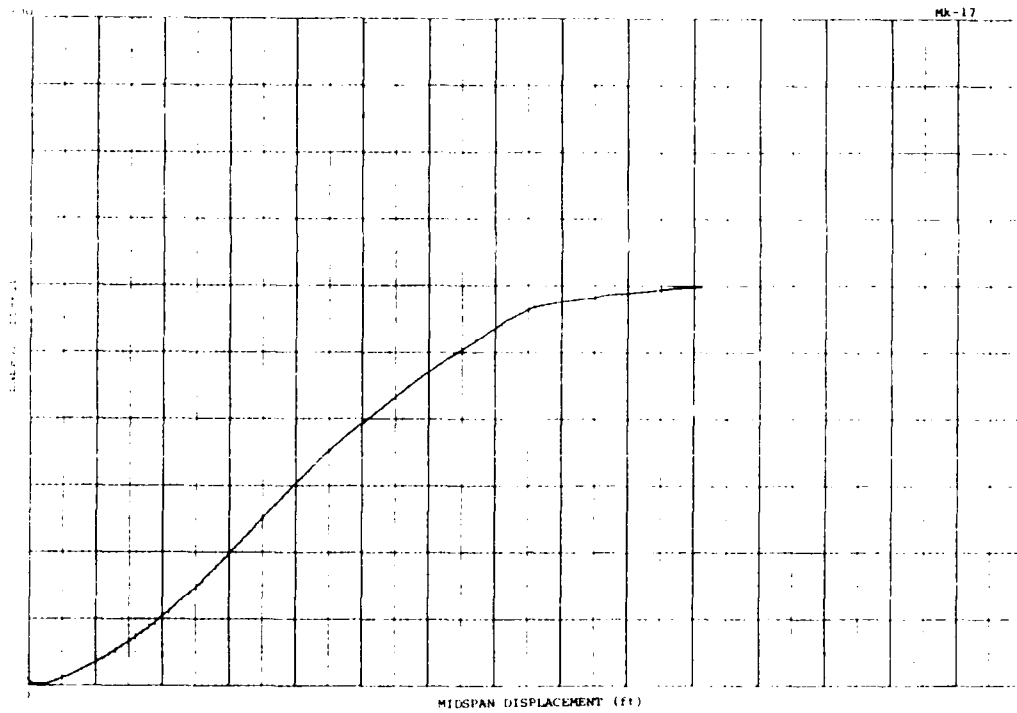


Figure B-176. MK17 energy-displacement plot.

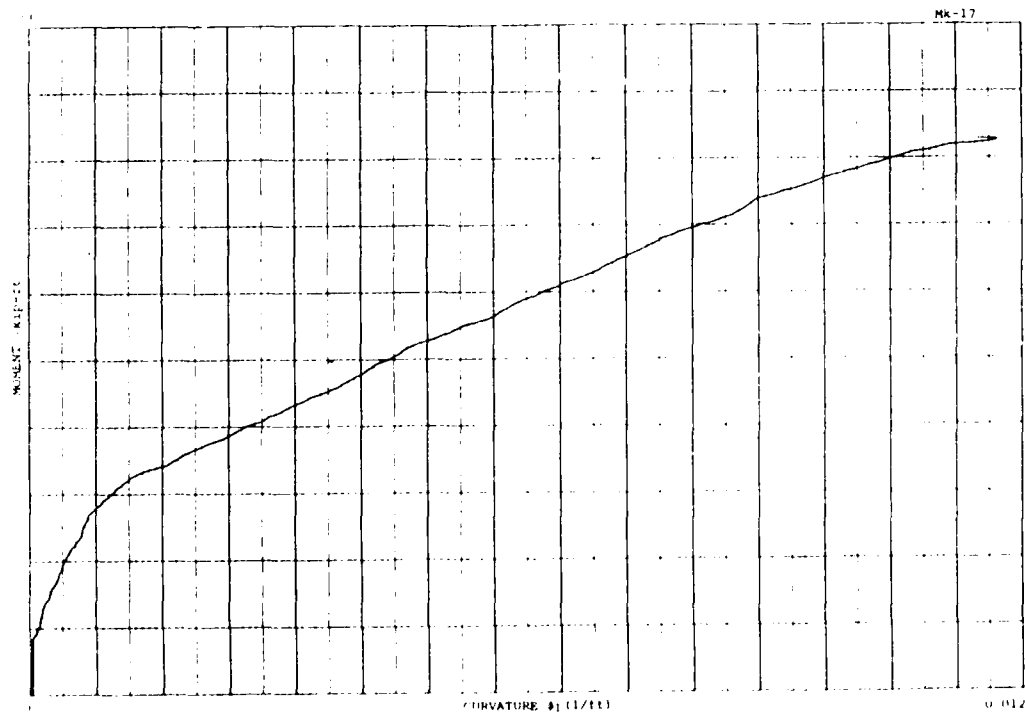


Figure B-177. MK17 moment-curvature plot.

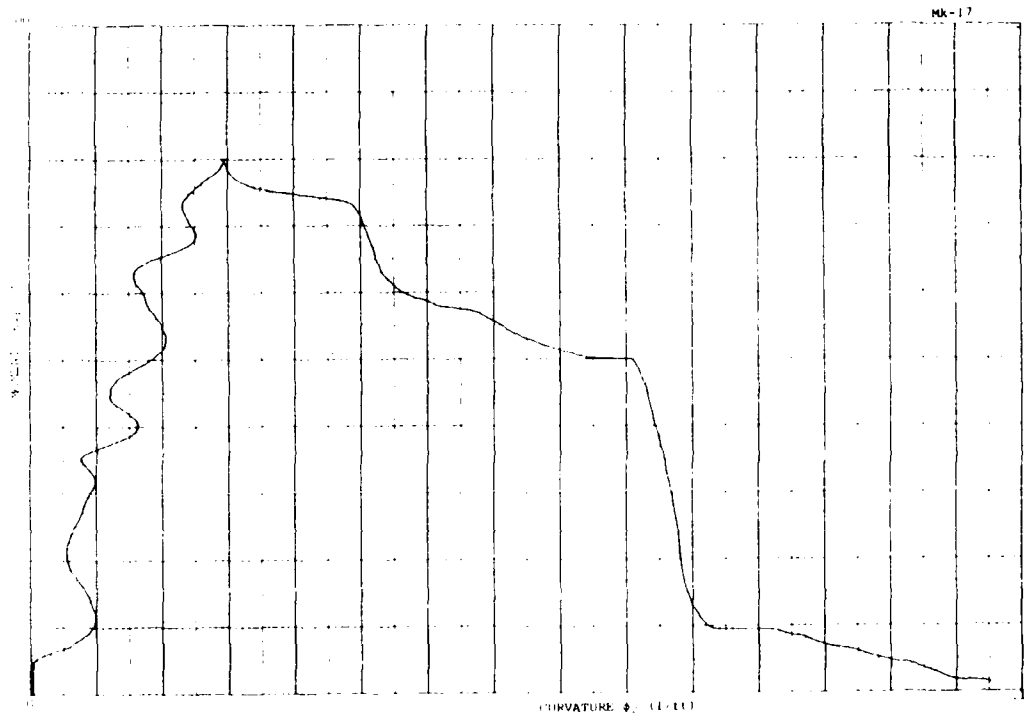


Figure B-178. MK17 moment-curvature plot.

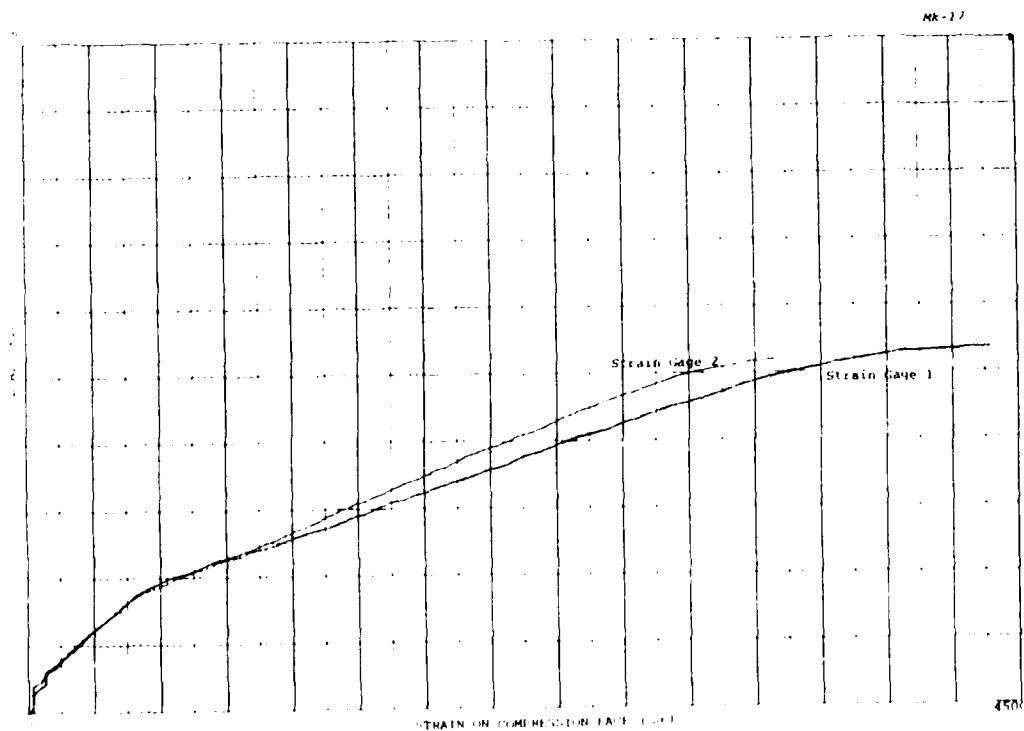


Figure B-179. MK17 compression strain.



Figure B-180. MK18 compression spalling at failure.

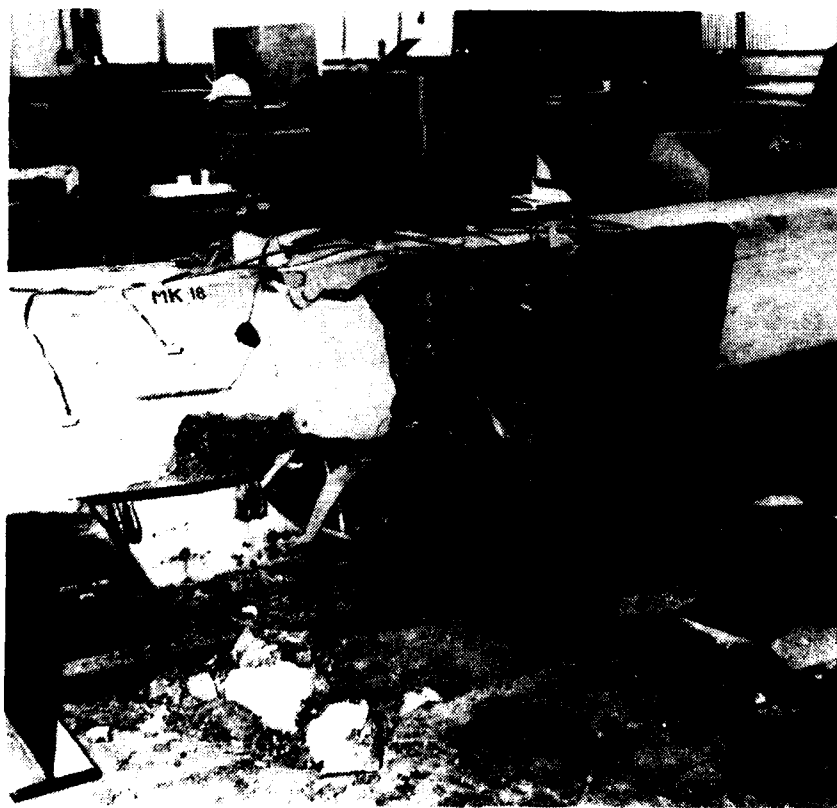


Figure B-181. MK18 tension spalling at failure.

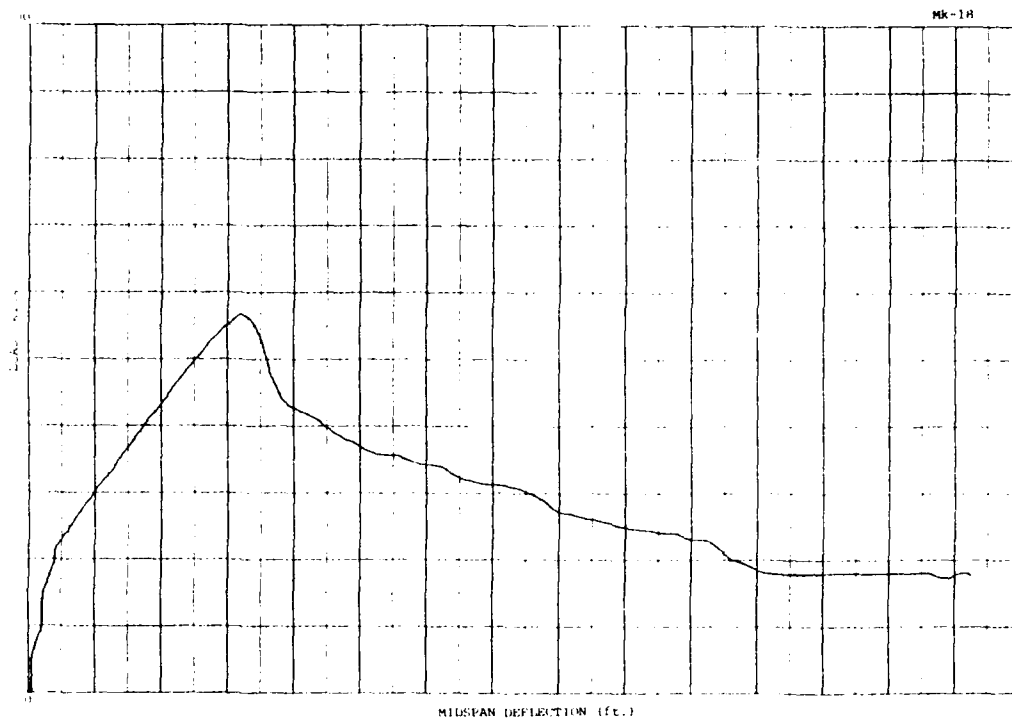


Figure B-182. MK18 load-deflection plot.

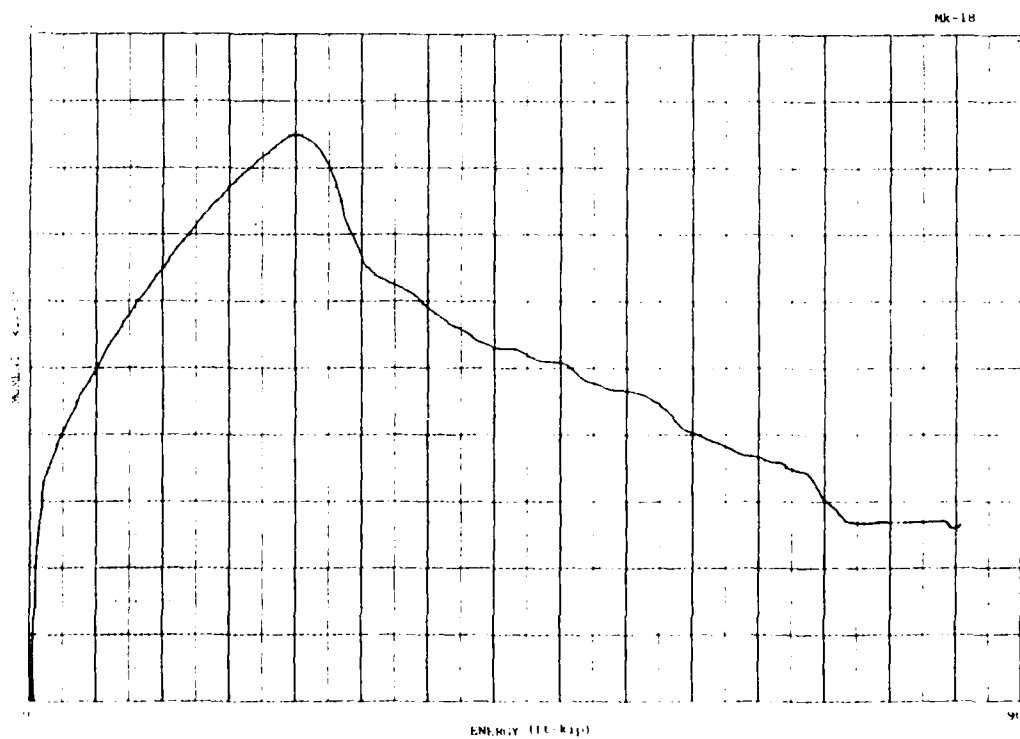


Figure B-183. MK18 moment-energy plot.

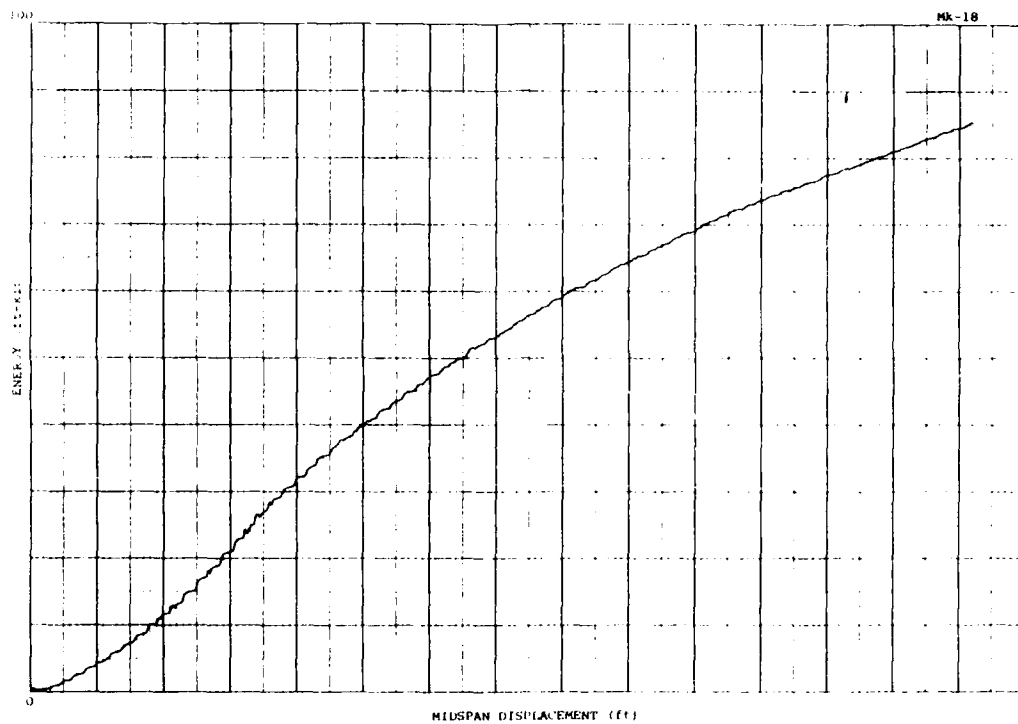


Figure B-184. MK18 energy-displacement plot.

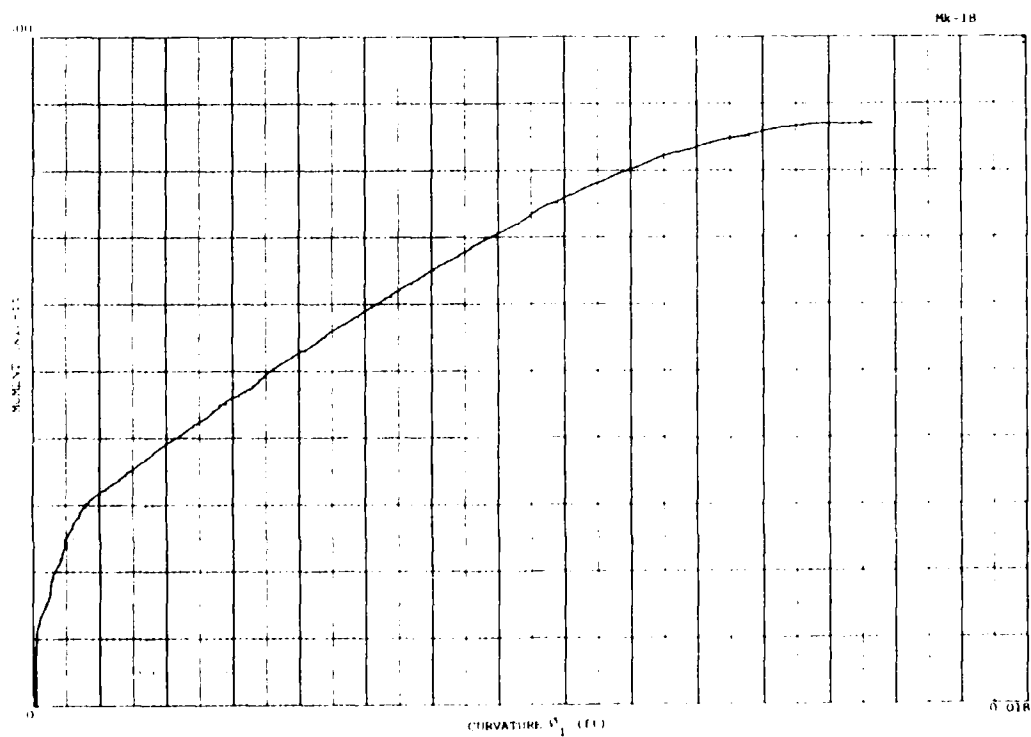


Figure B-185. MK18 moment-curvature plot.

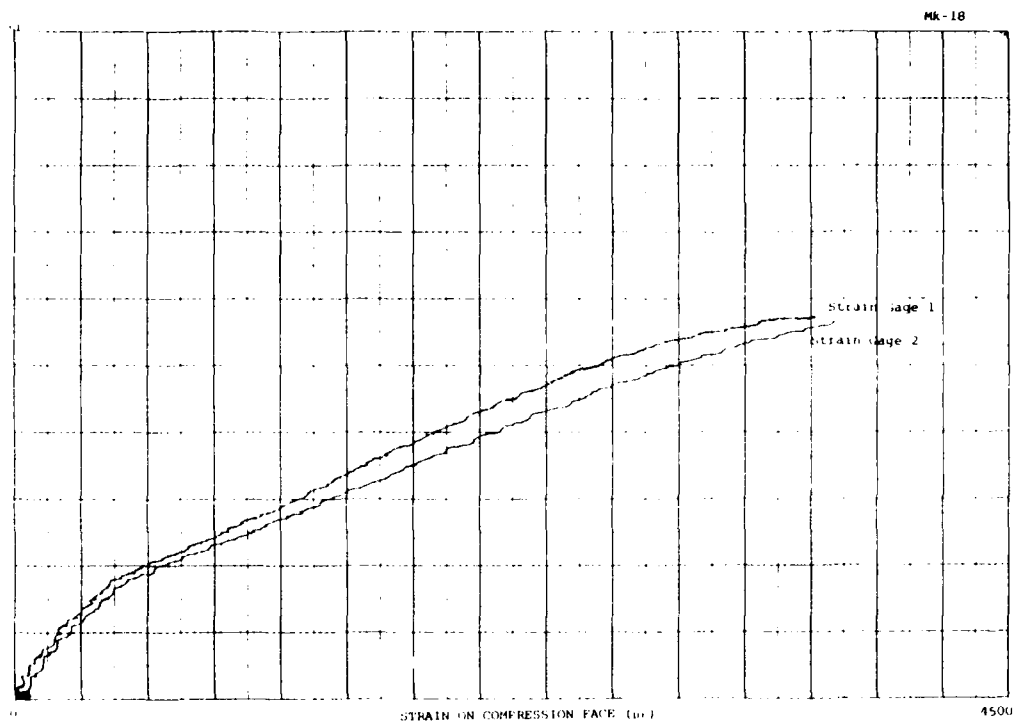


Figure B-186. MK18 compression strain.



Figure B-187. MK19 compression spalling at failure.

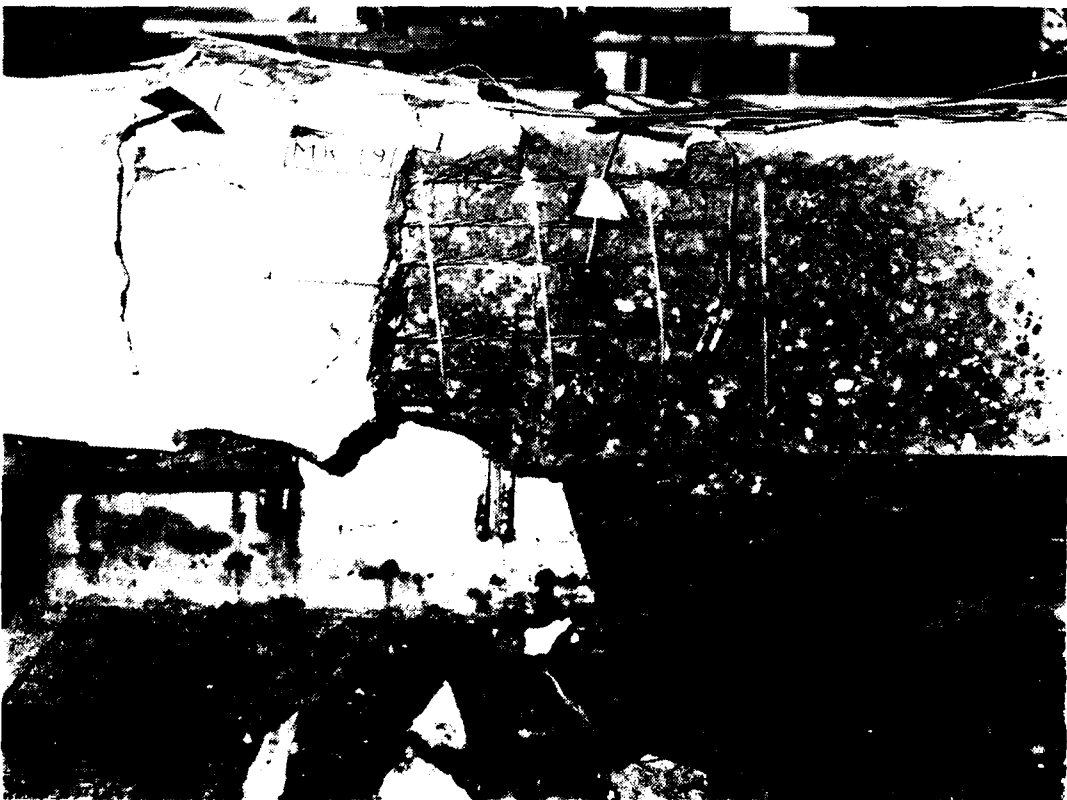


Figure B-188. MK19 tension spalling at failure.

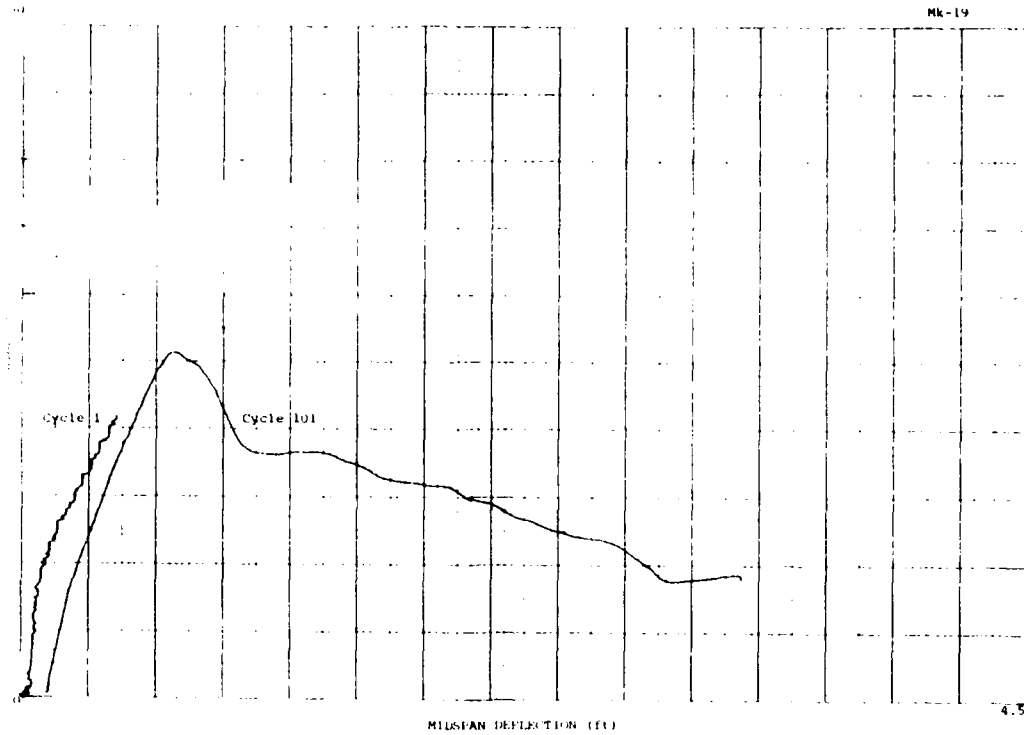


Figure B-189. MK19 load-deflection plot.

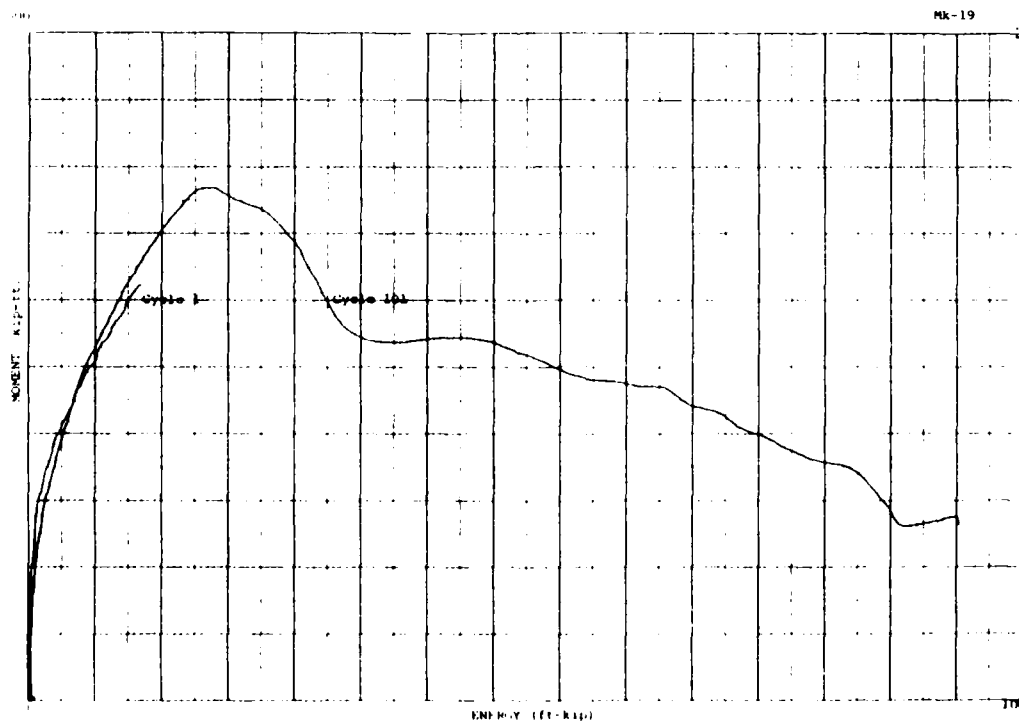


Figure B-190. MK19 moment-energy plot.

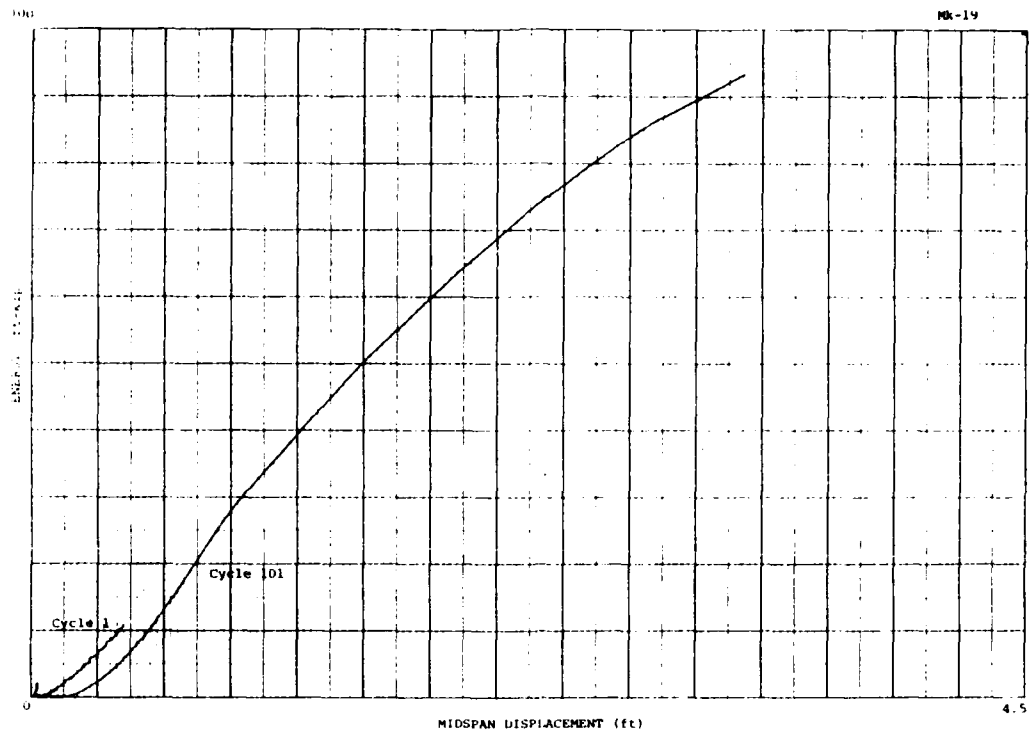


Figure B-191. MK19 energy-displacement plot.

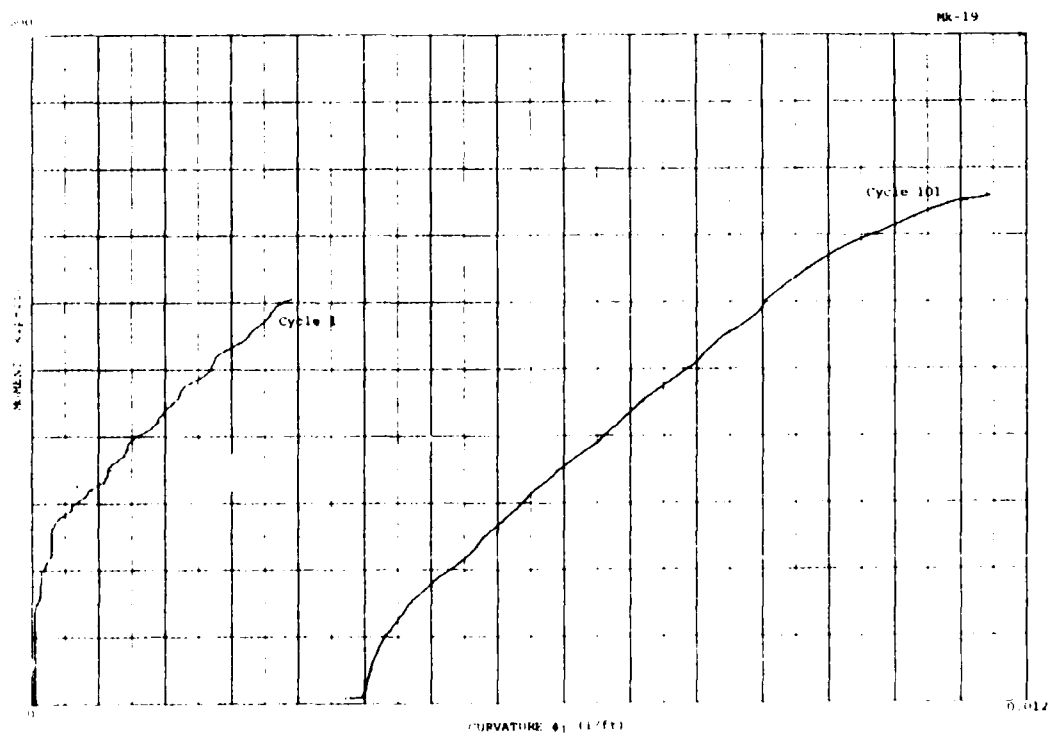


Figure B-192. MK19 moment-curvature plot.

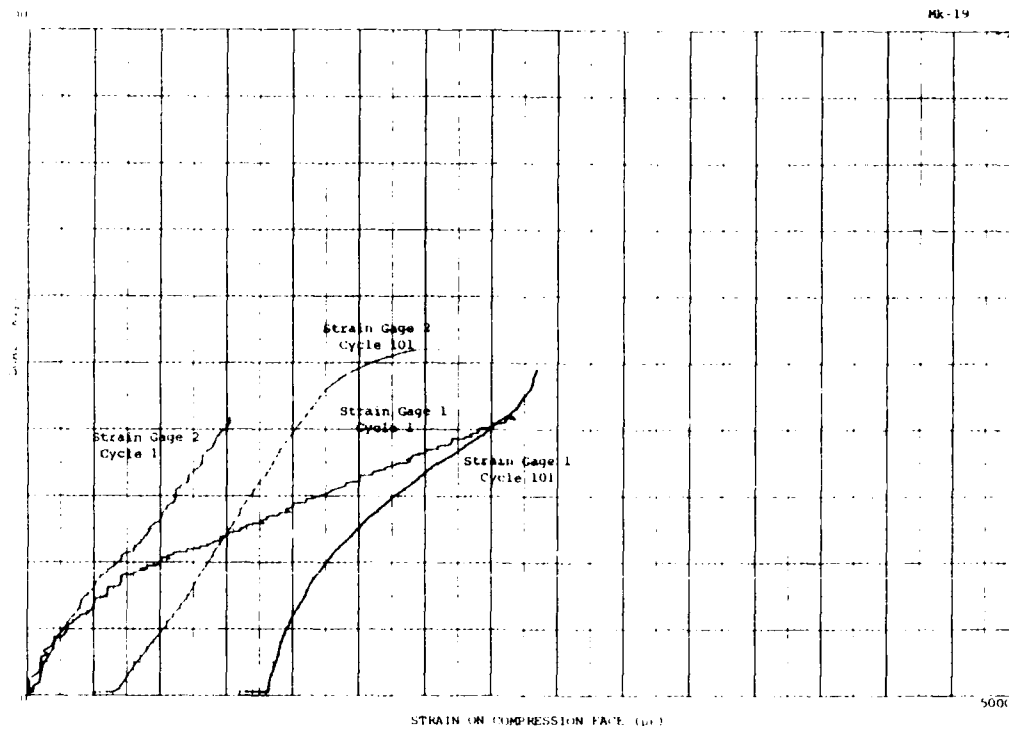


Figure B-193. MK19 compression strain.

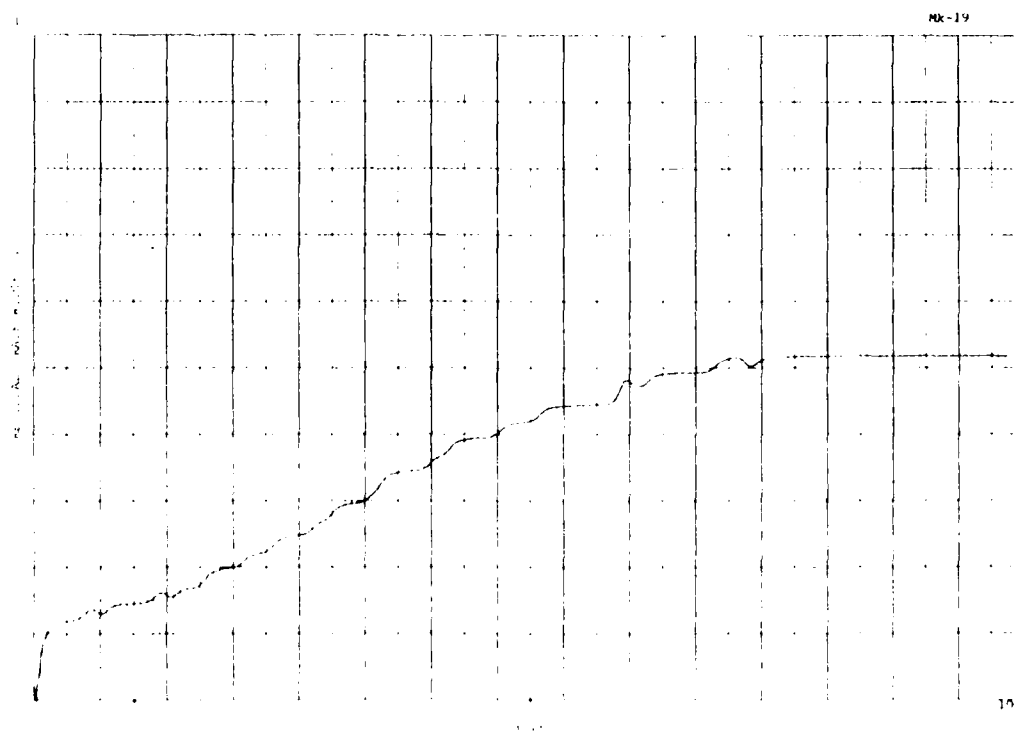


Figure B-194. MK19 crack width after load removal.

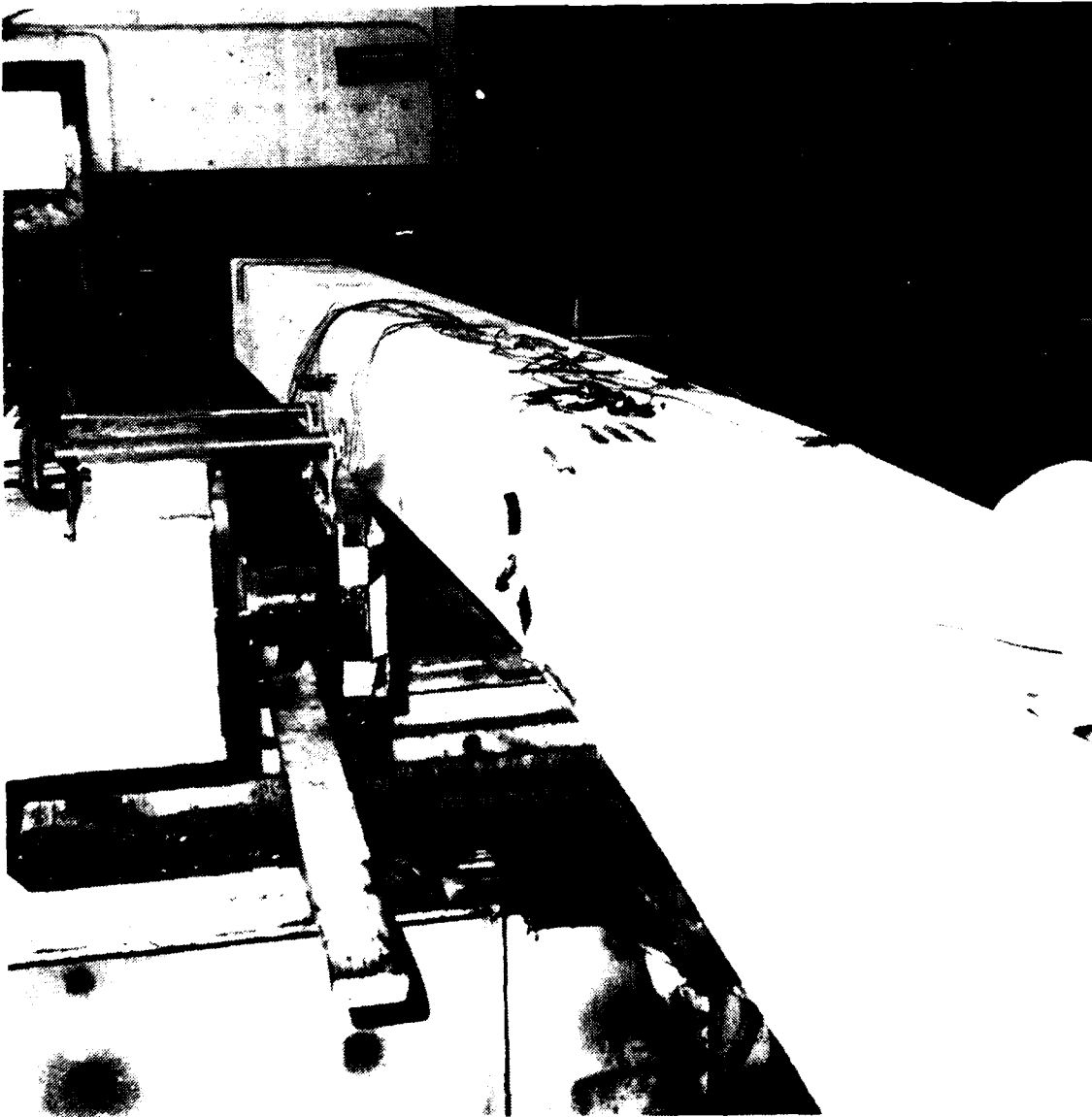


Figure B-195. MK20 at failure.

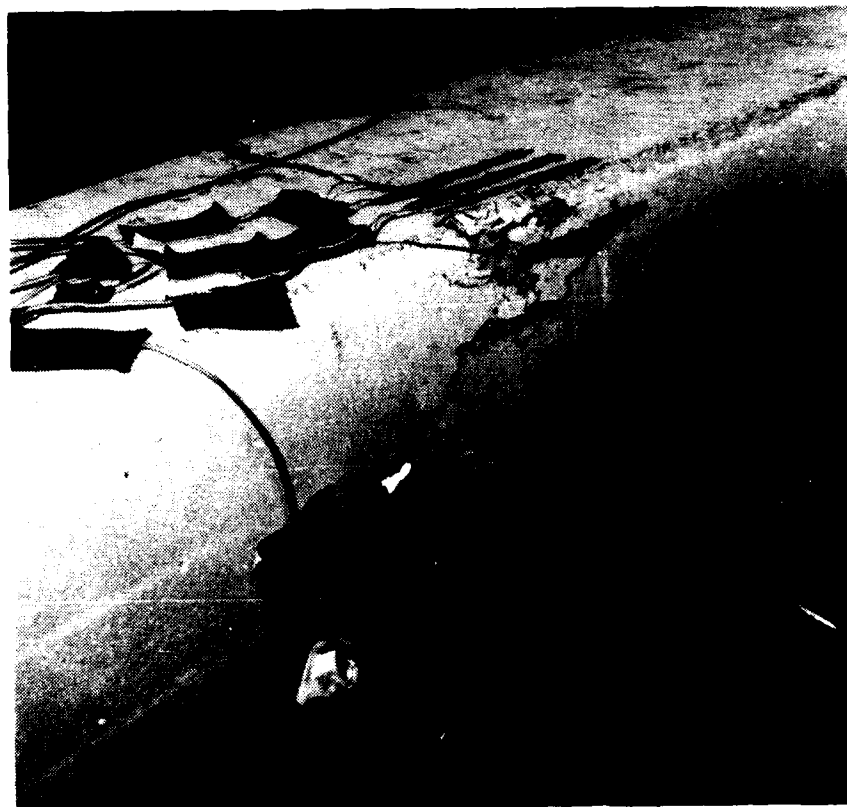


Figure B-196. MK20 compression face at failure.

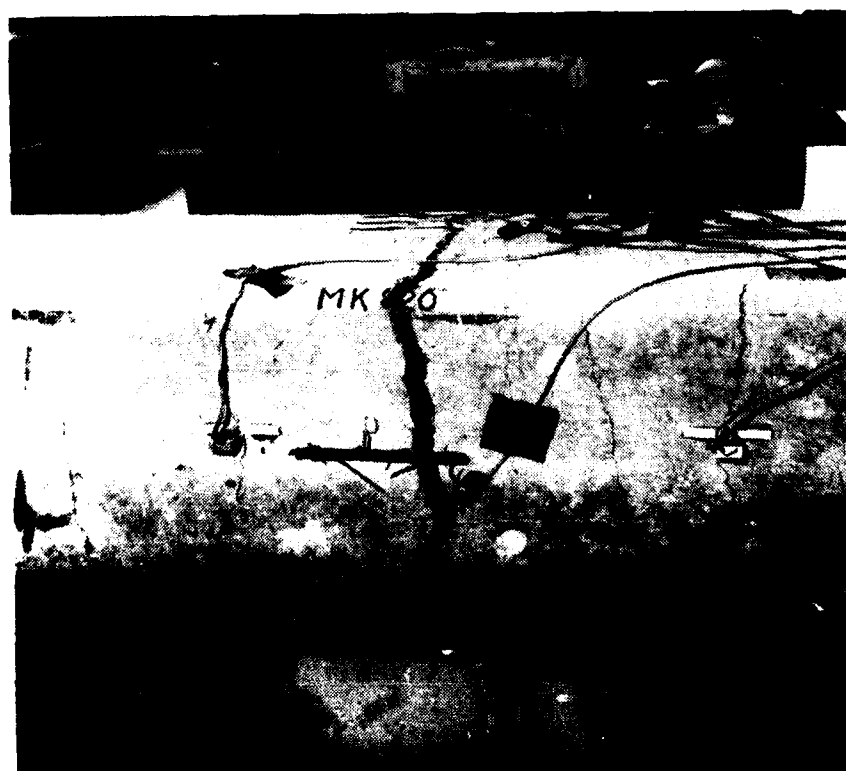


Figure B-197. MK20 localized cracking at failure.

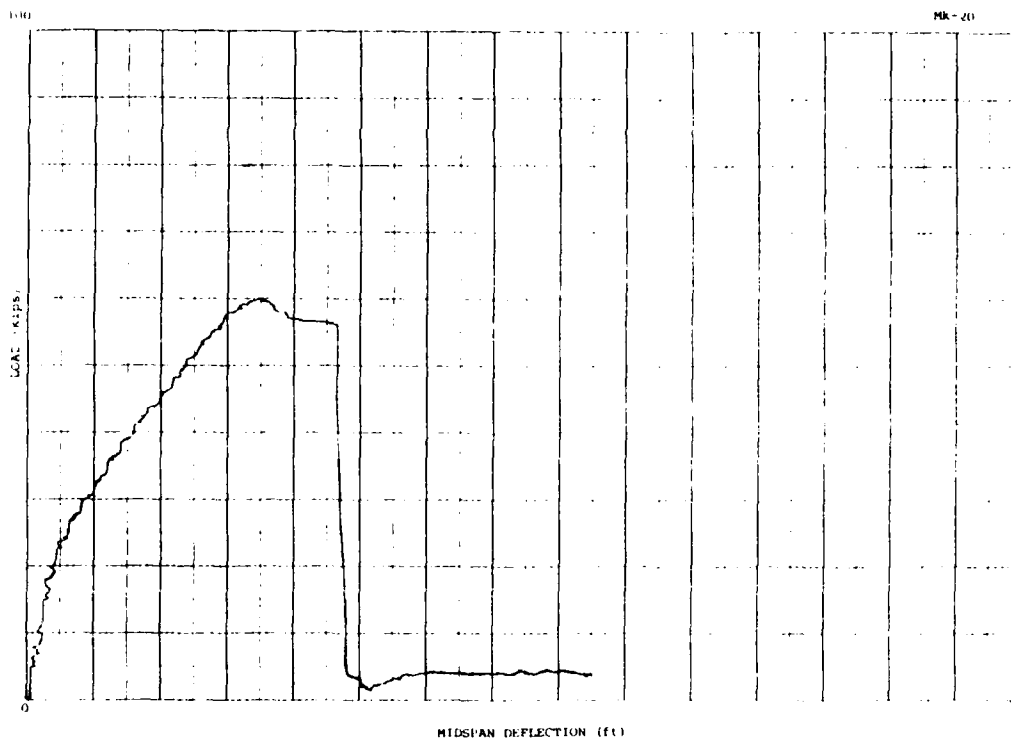


Figure B-198. MK20 load-deflection plot.

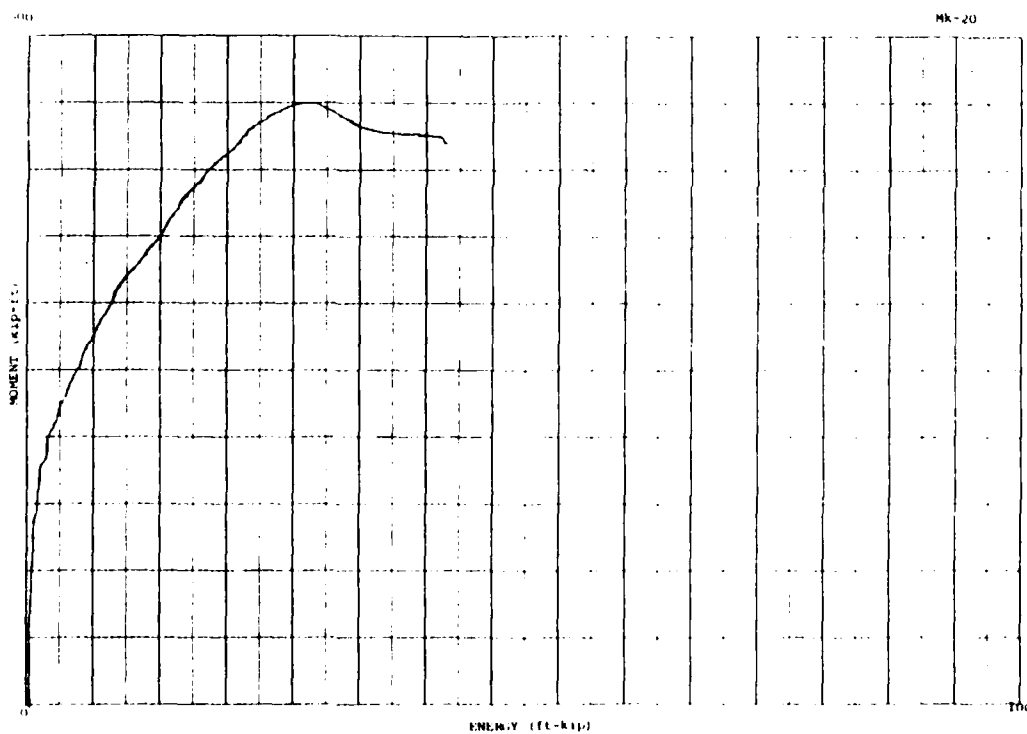


Figure B-199. MK20 moment-energy plot.

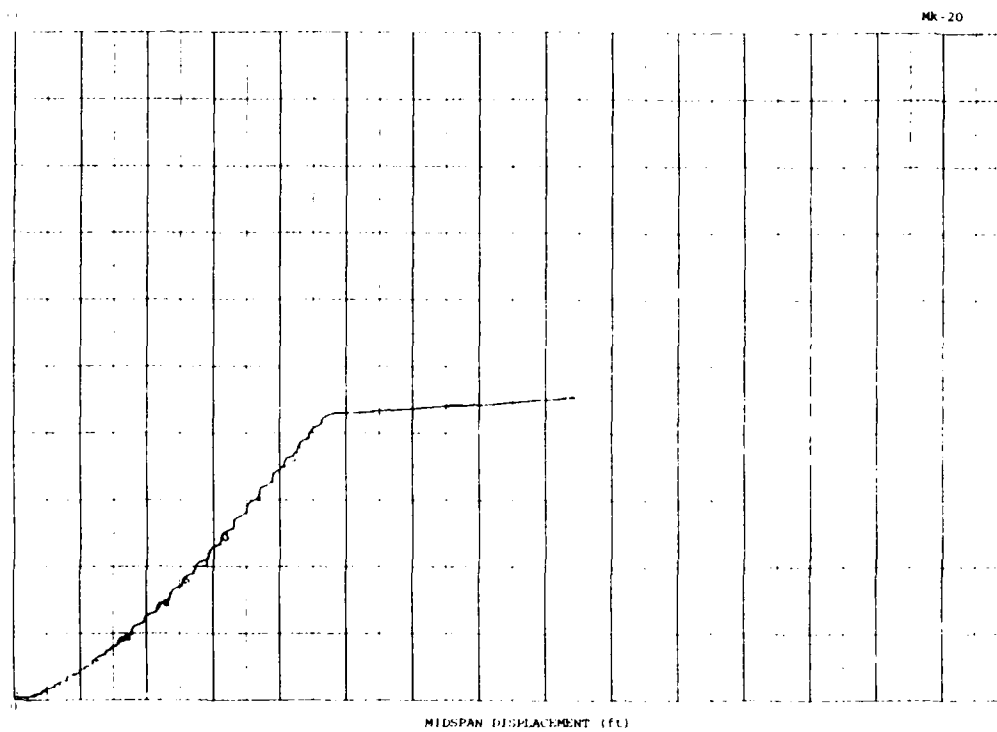


Figure B-200. MK20 energy-displacement plot.

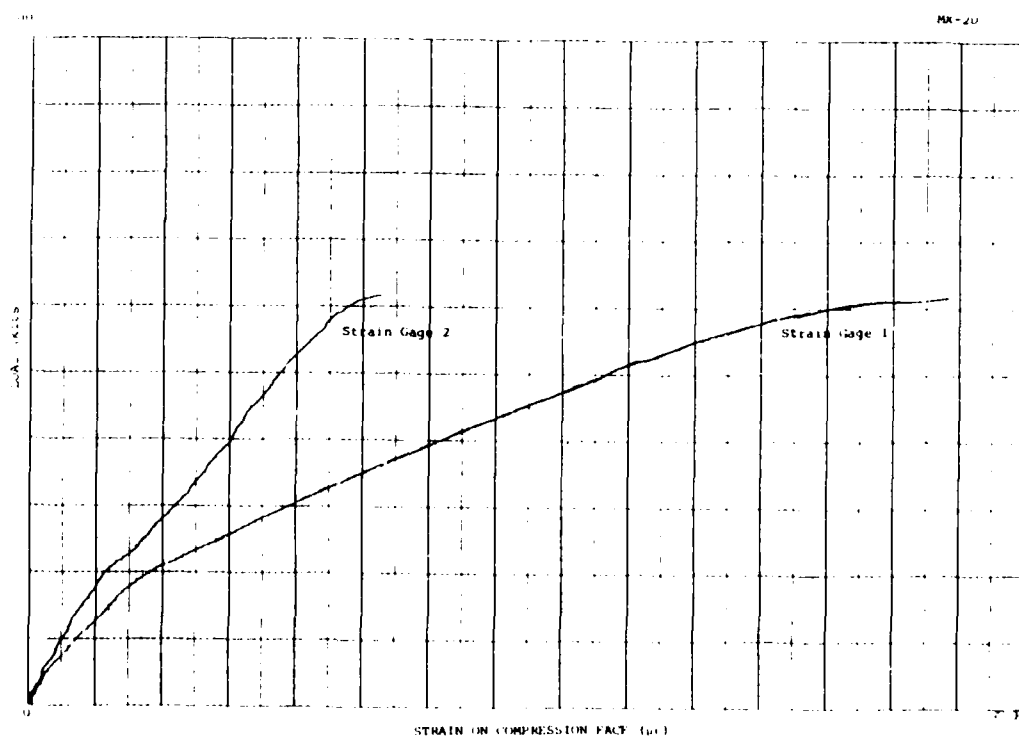


Figure B-201. MK20 compression strain.

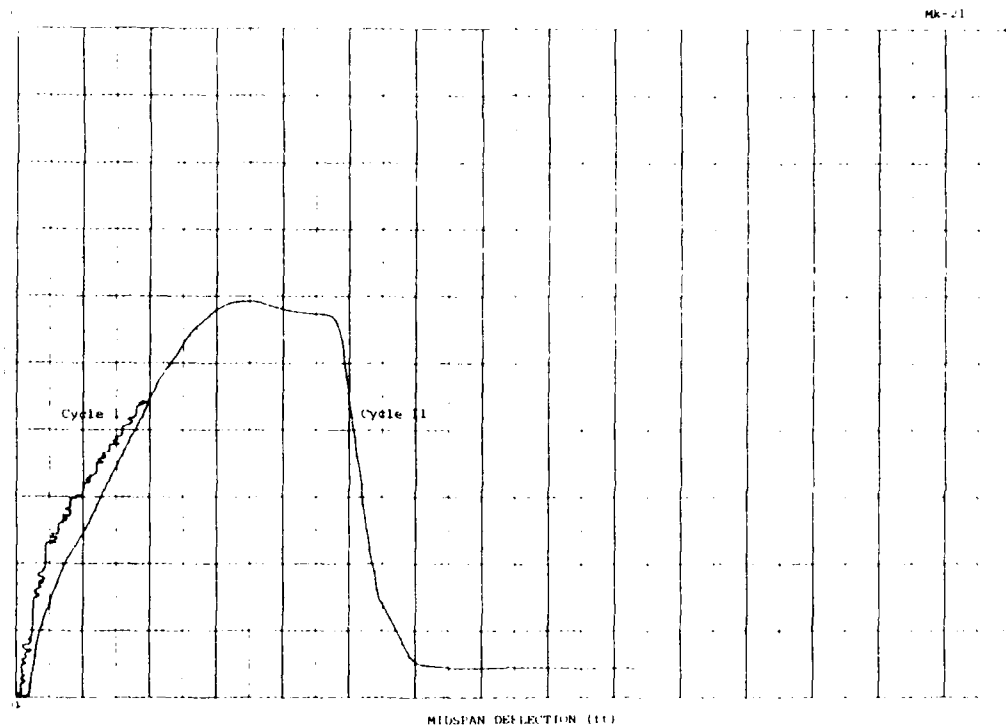


Figure B-202. MK21 load-deflection plot.

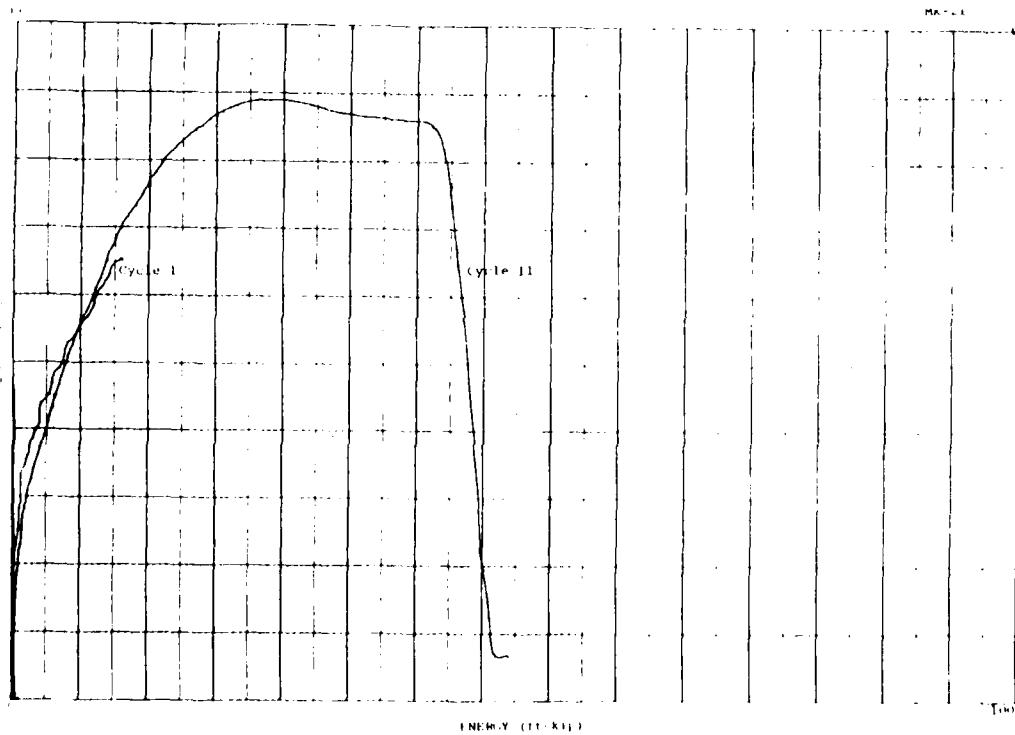


Figure B-203. MK21 moment-energy plot.

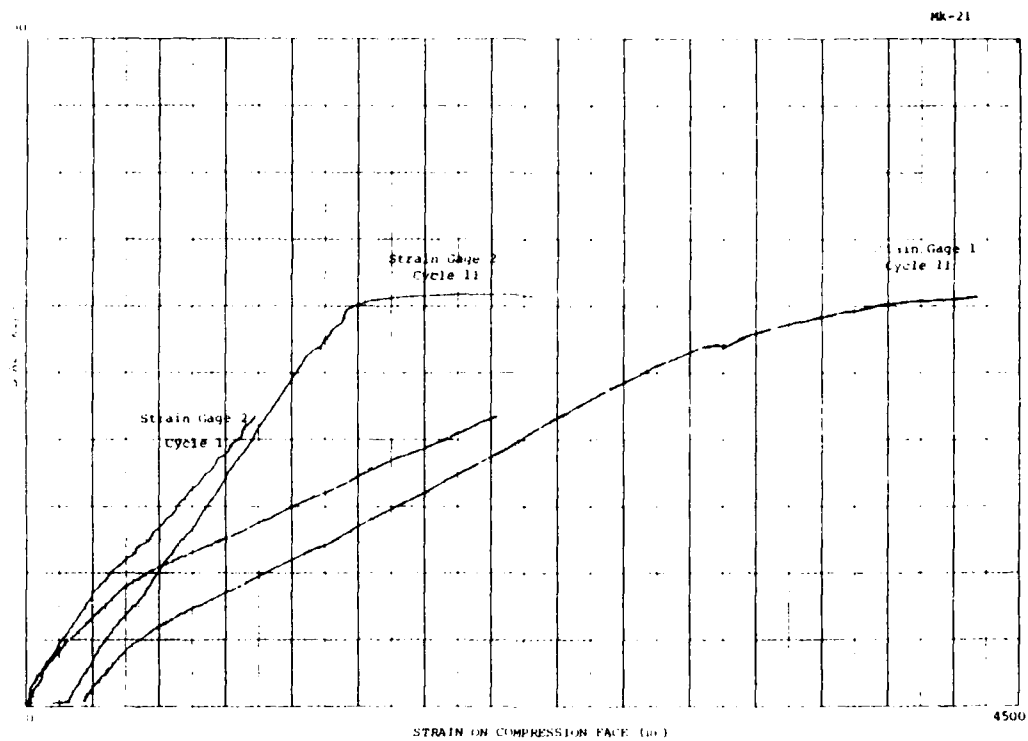


Figure B-204. MK21 compression strain.

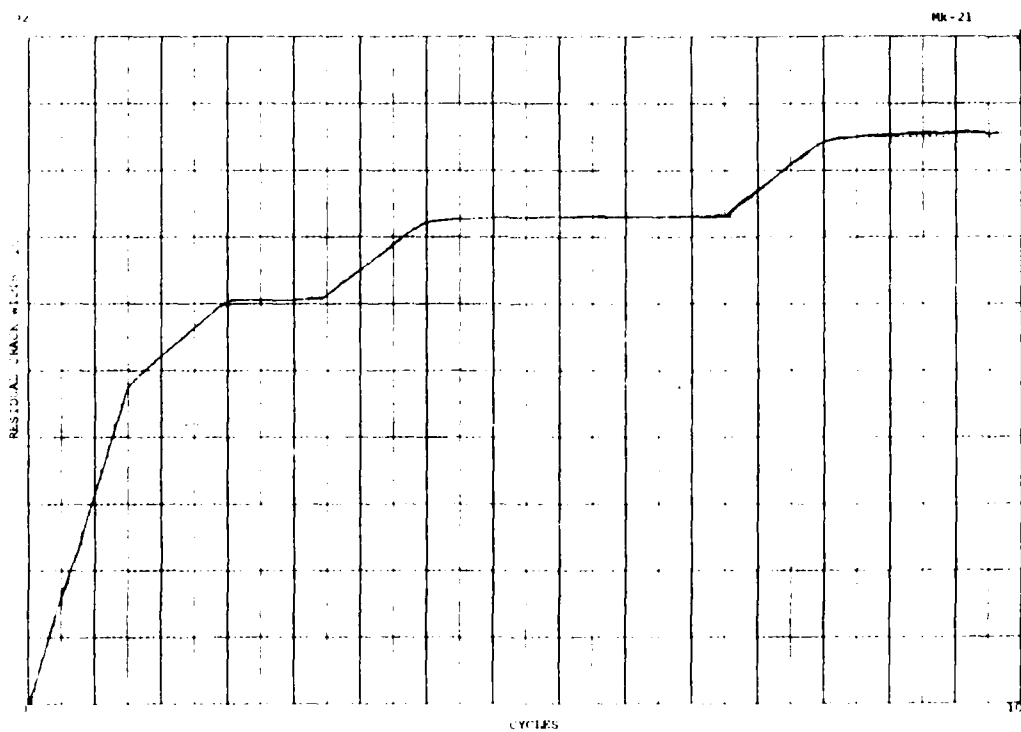


Figure B-205. MK21 crack width after load removal.

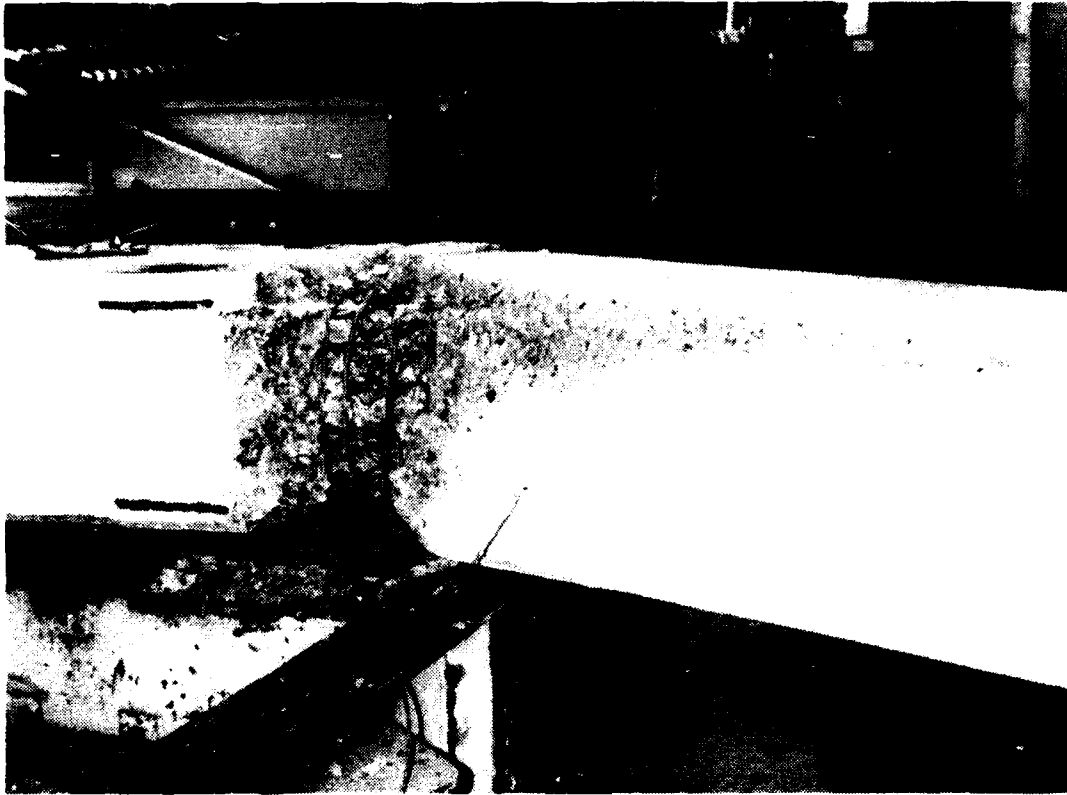


Figure B-206. MK22 compression spalling at failure.



Figure B-207. MK22 tension cracking at failure.

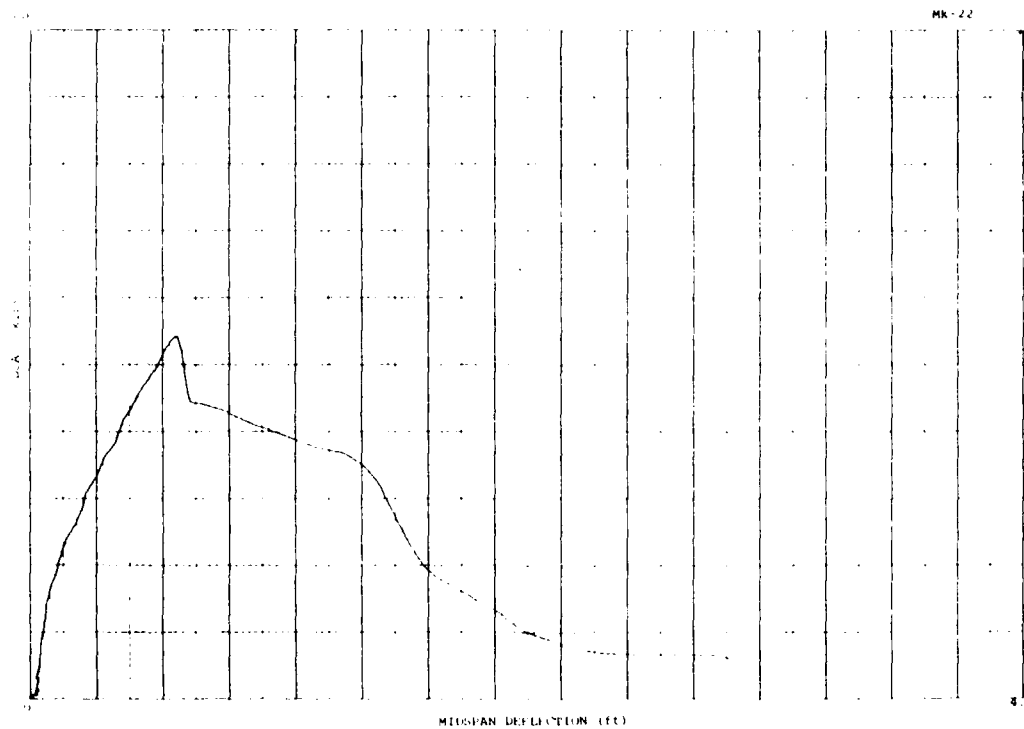


Figure B-208. MK22 load-deflection plot.

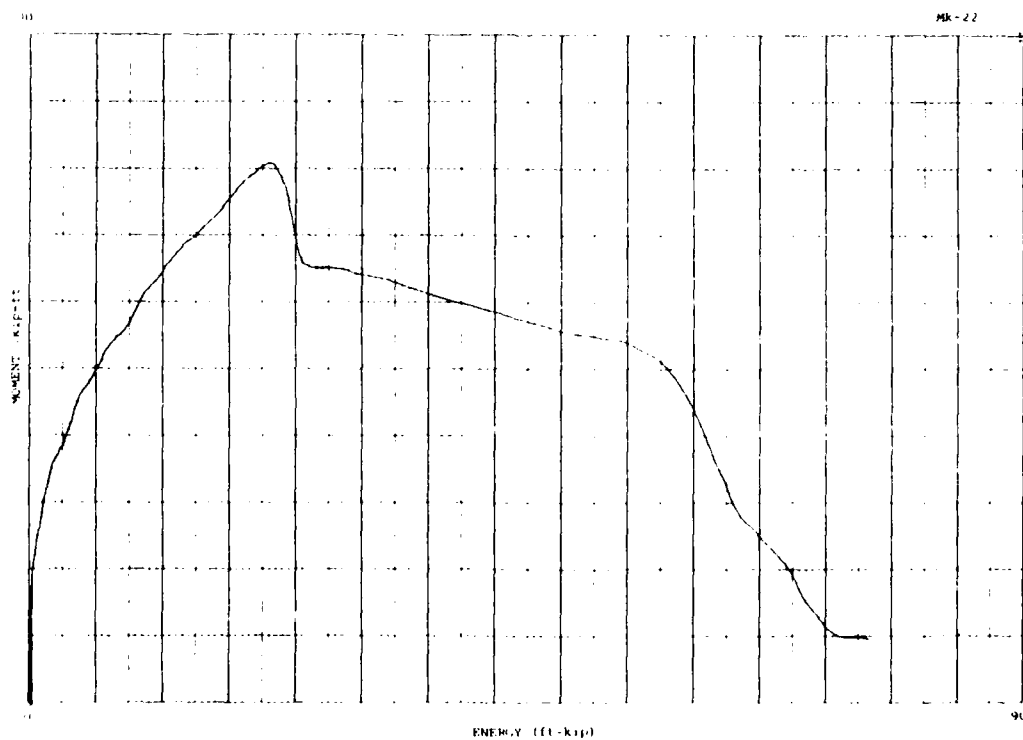


Figure B-209. MK22 moment-energy plot.

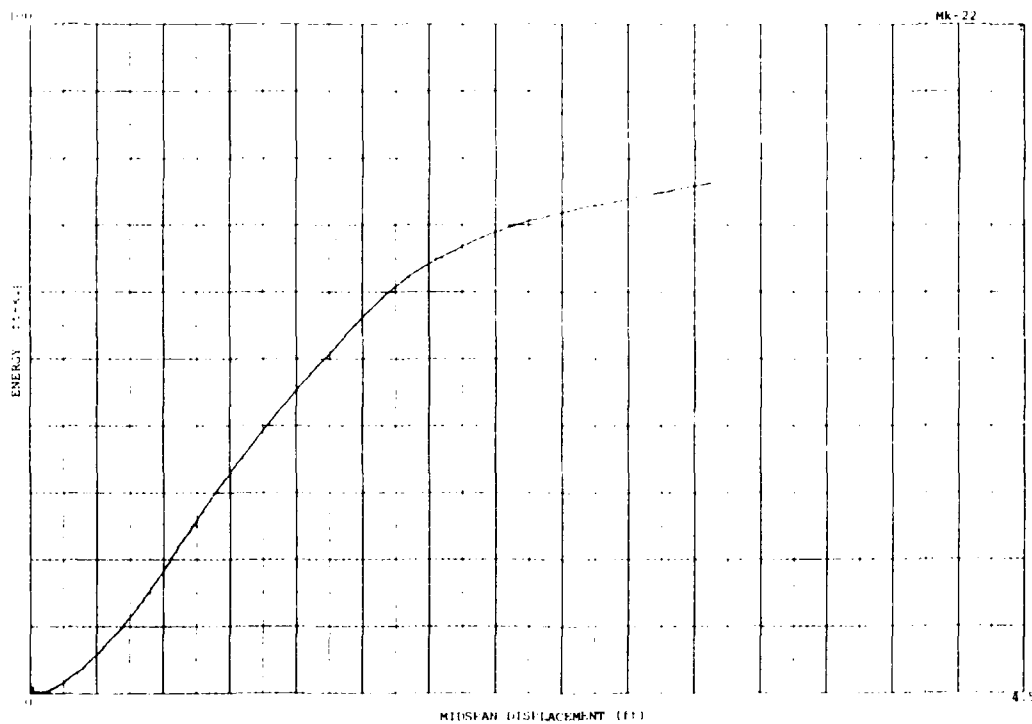


Figure B-210. MK22 energy-displacement plot.

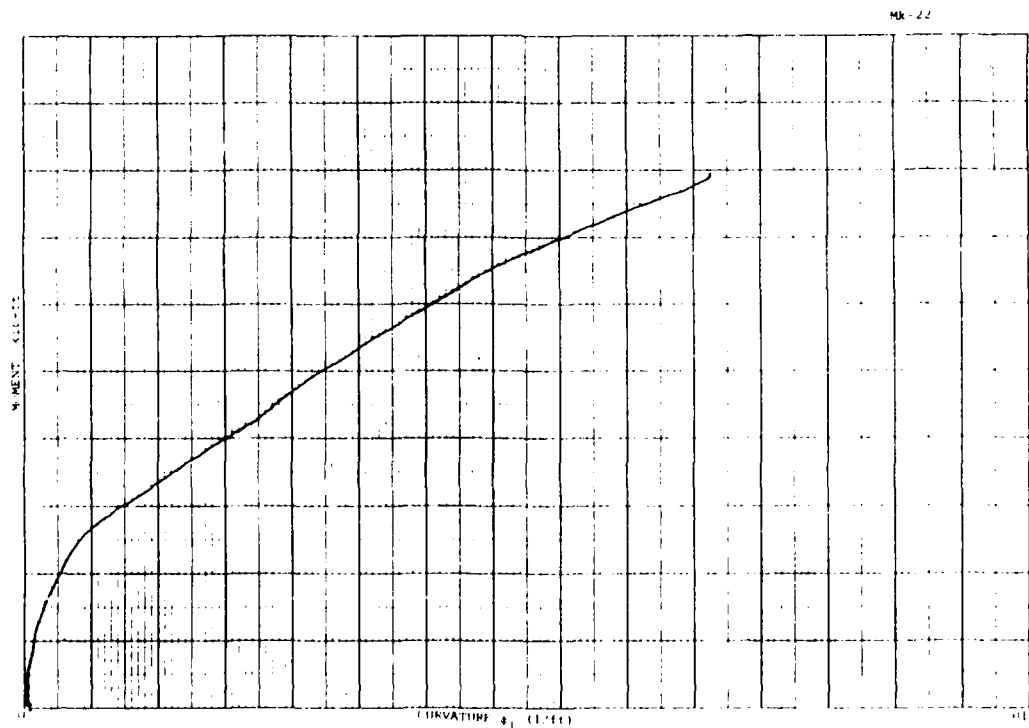


Figure B-211. MK22 moment-curvature plot.

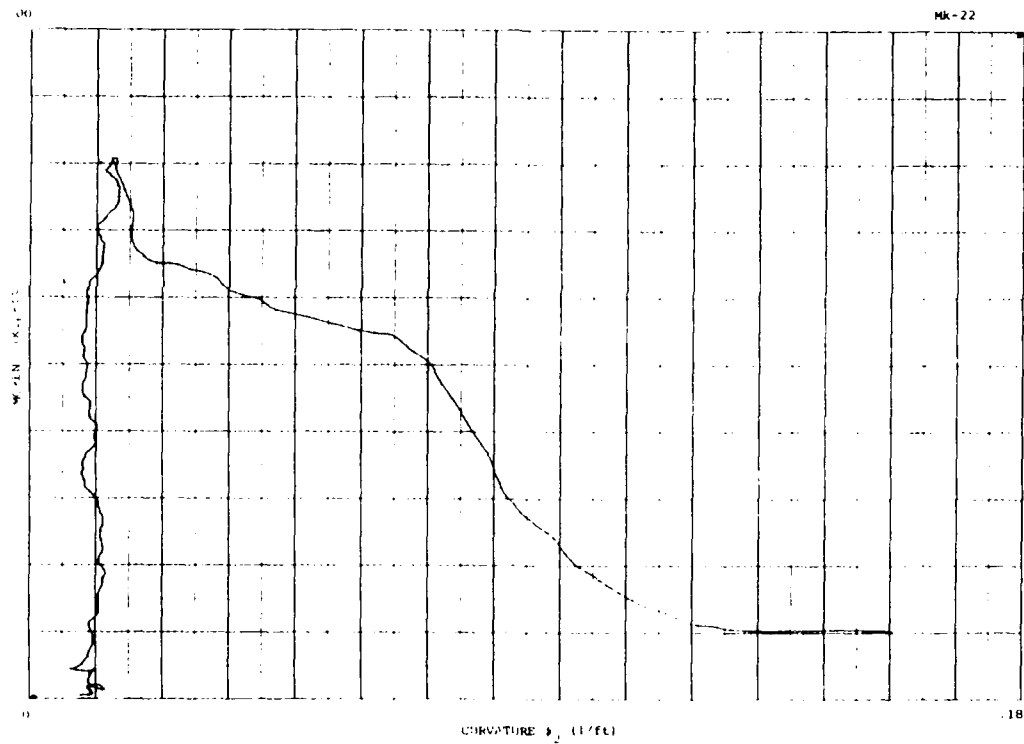


Figure B-212. MK22 moment-curvature plot.

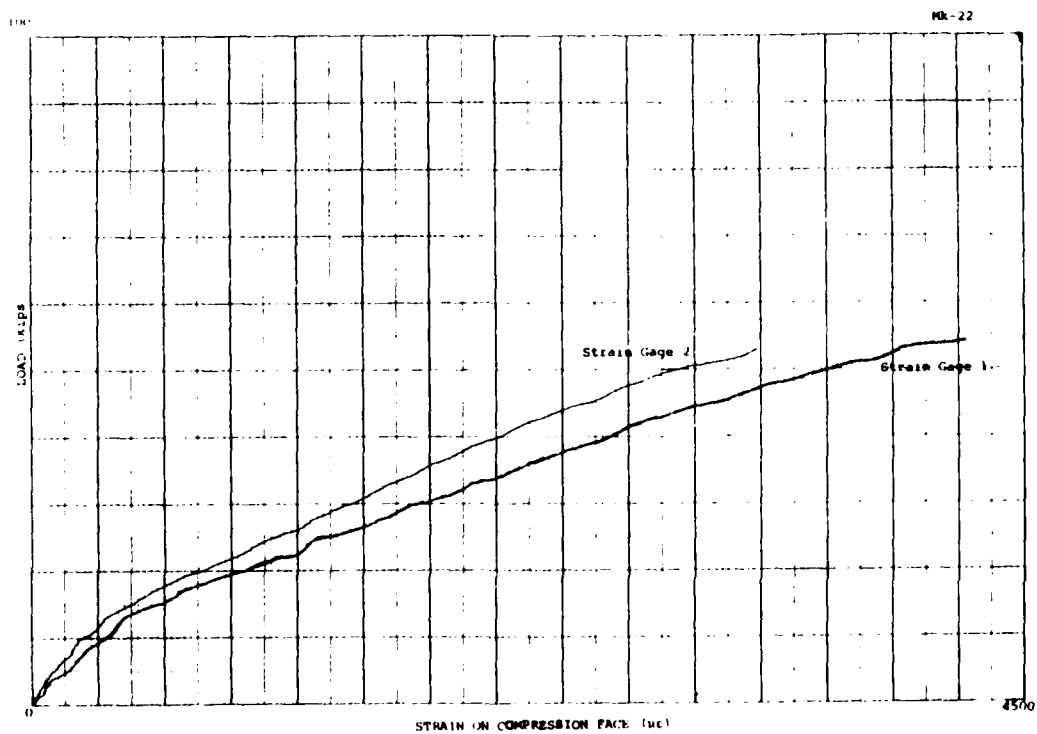


Figure B-213. MK22 compression strain.



Figure B-214. MK23 at failure.

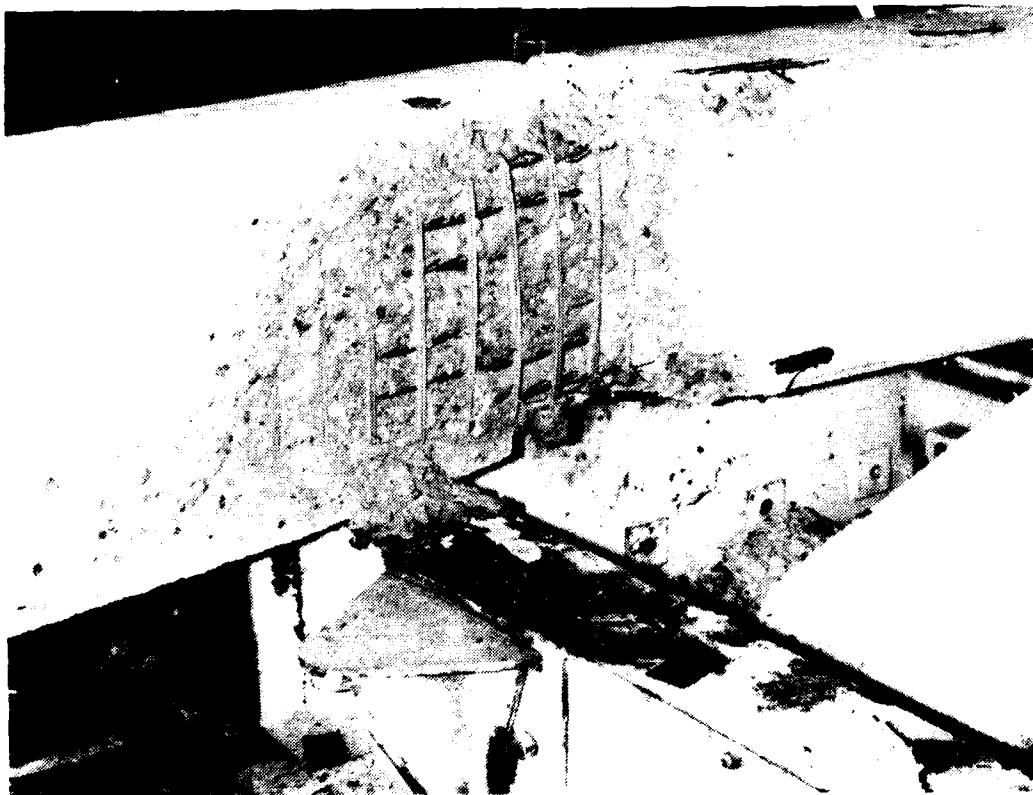


Figure B-215. MK23 compression spalling at failure.



Figure B-216. MK23 tension cracking at failure.

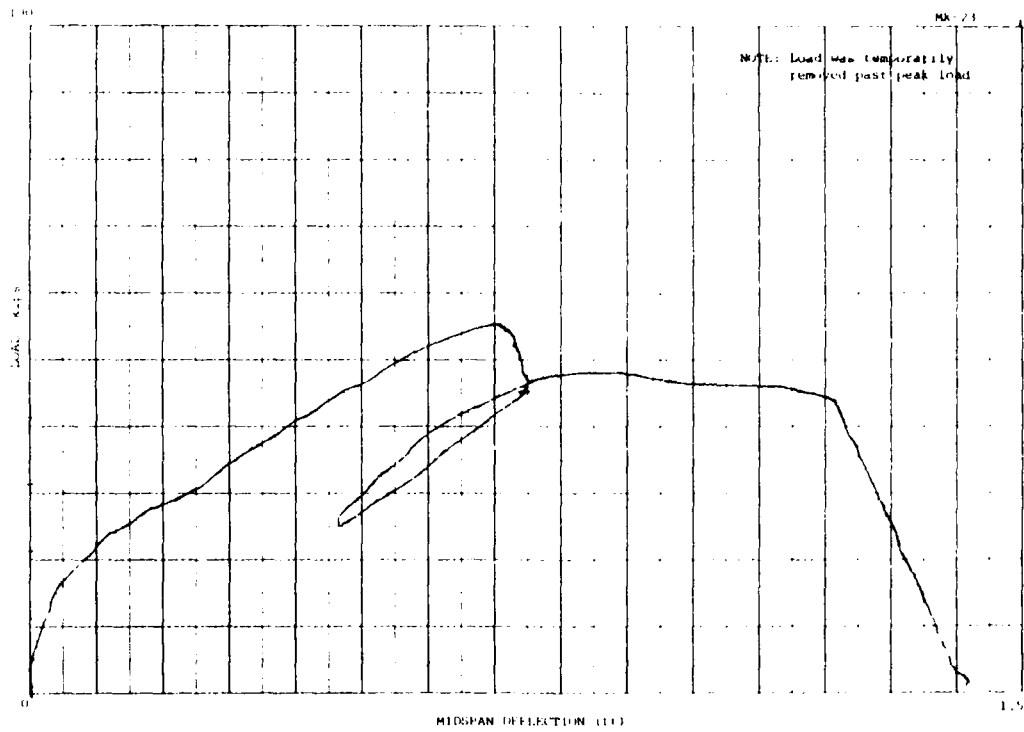


Figure B-217. MK23 load-deflection plot.

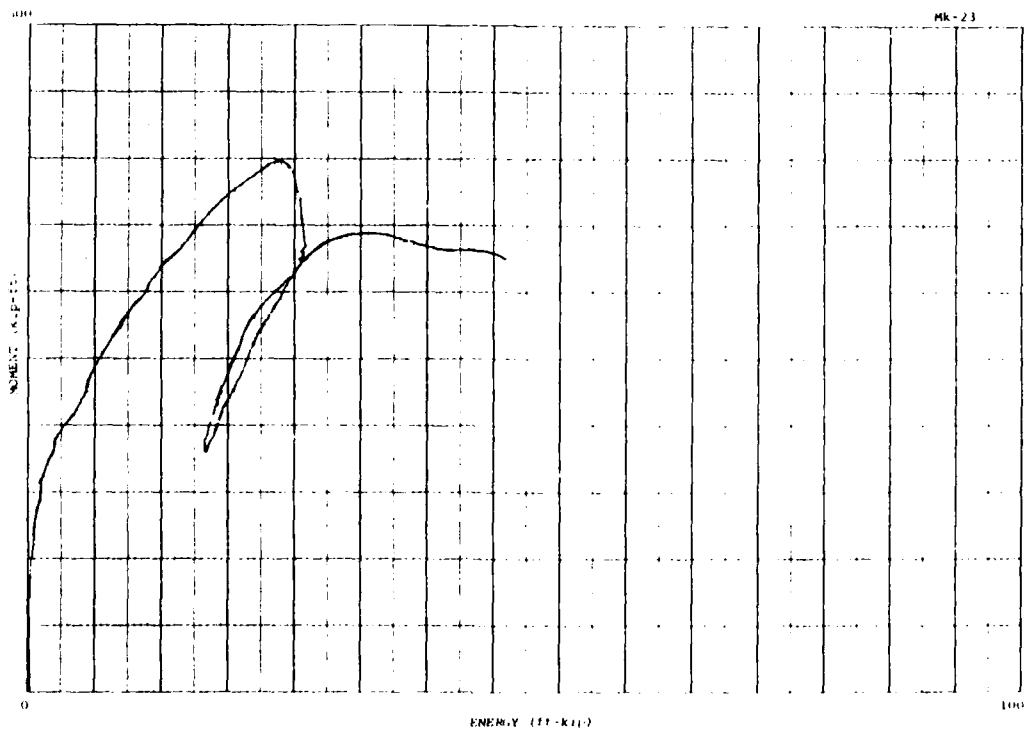


Figure B-218. MK23 moment-energy plot.

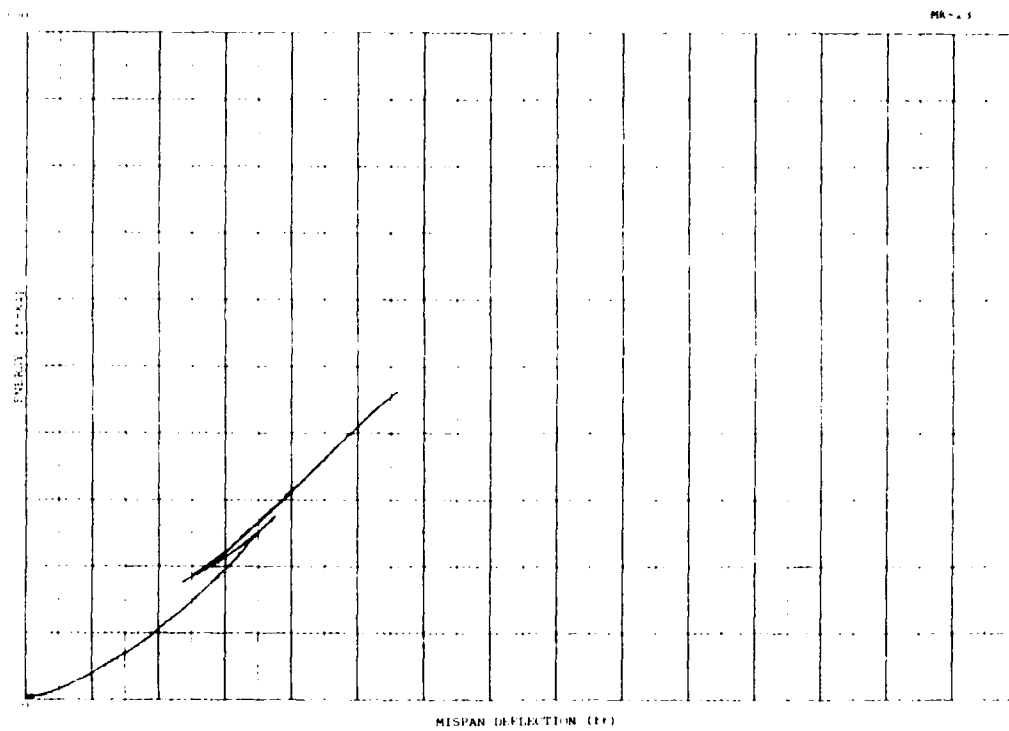


Figure B-219. MK23 energy-displacement plot.

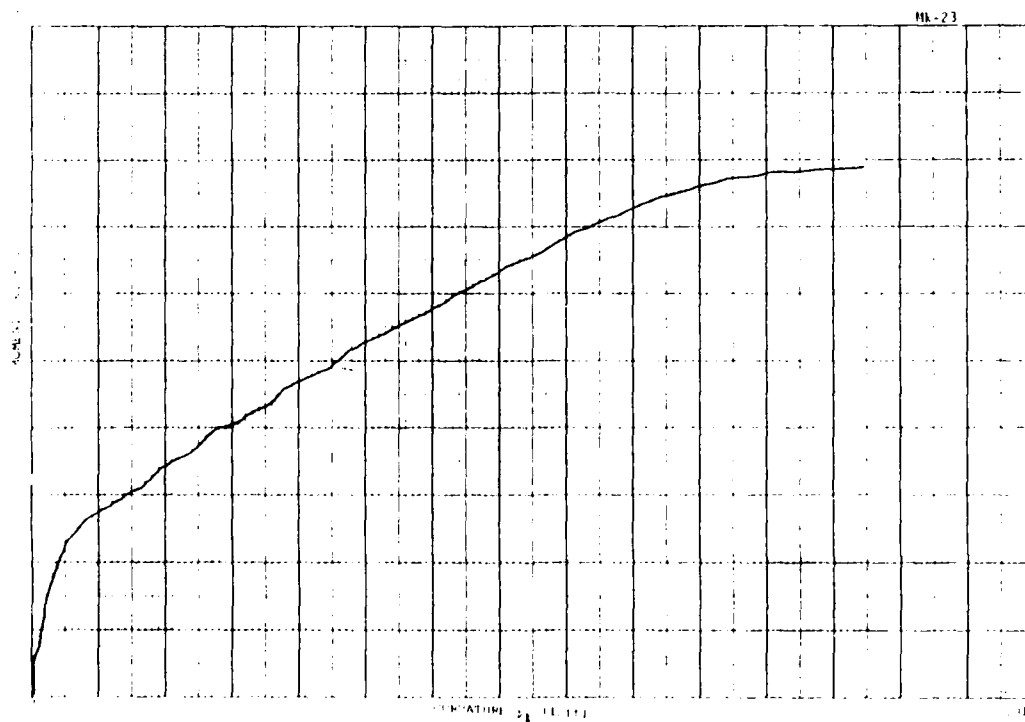


Figure B-220. MK23 moment-curvature plot.

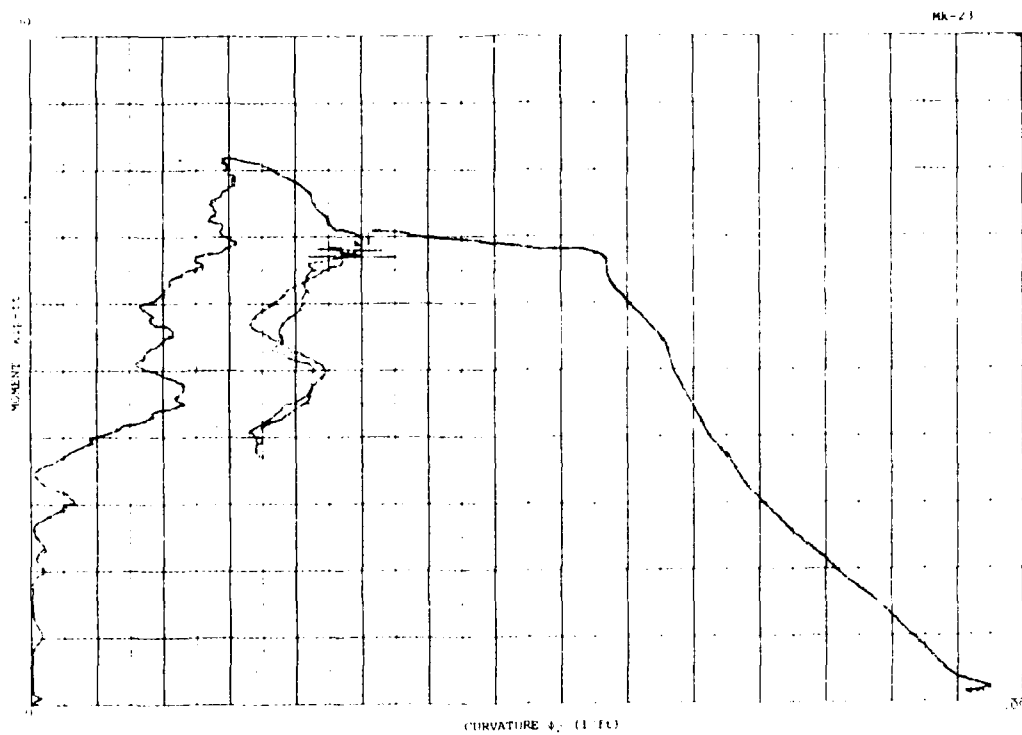


Figure B-221. MK23 moment-curvature.

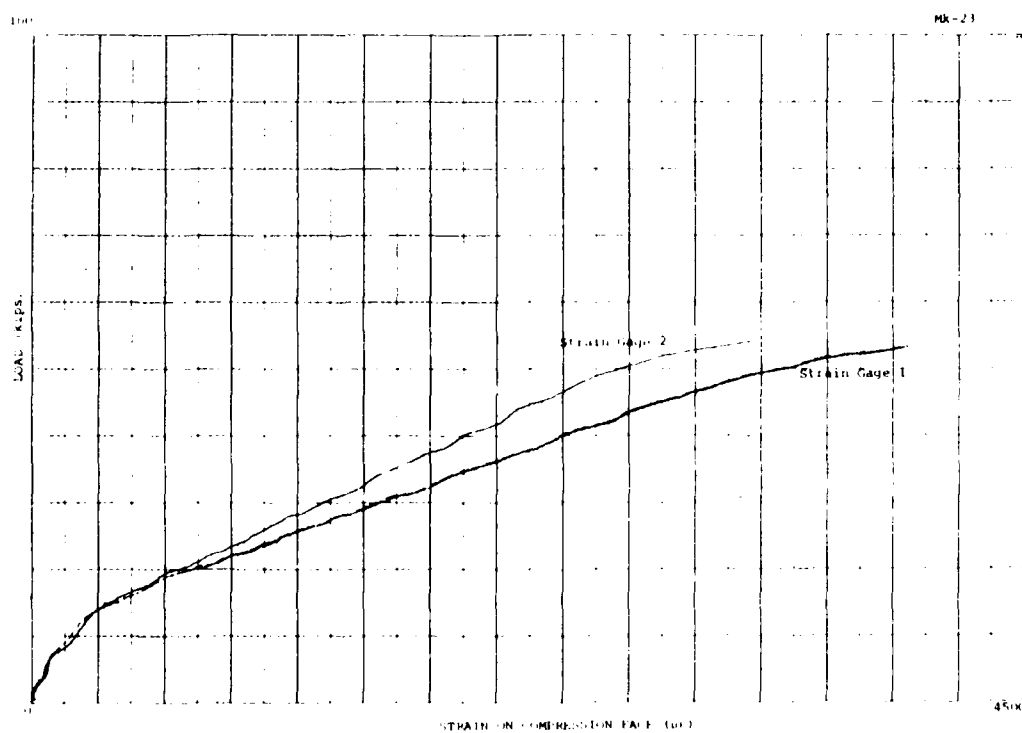


Figure B-222. MK23 compression strain.

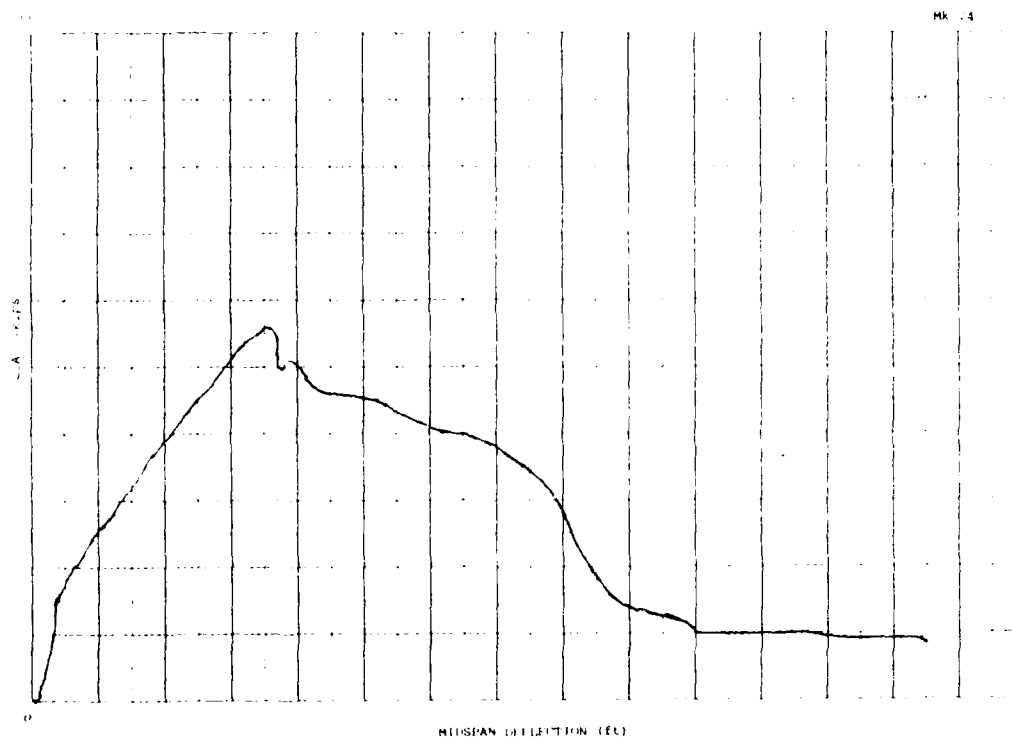


Figure B-223. MK24 load-deflection plot.

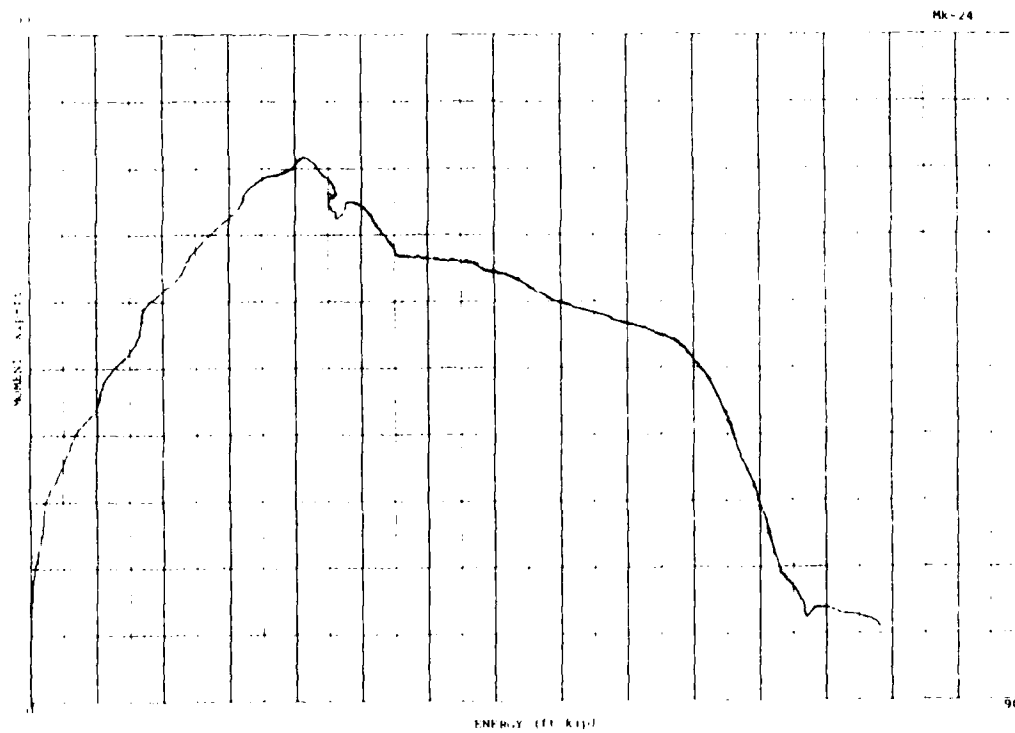


Figure B-224. MK24 moment-energy plot.

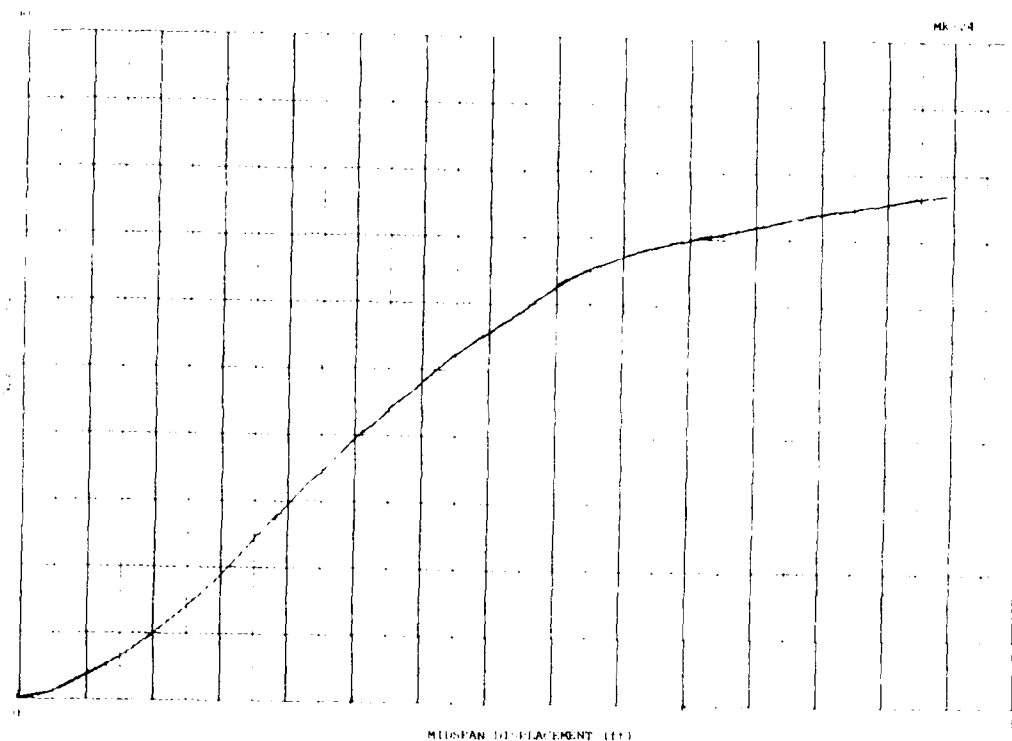


Figure B-225. MK24 energy-displacement plot.

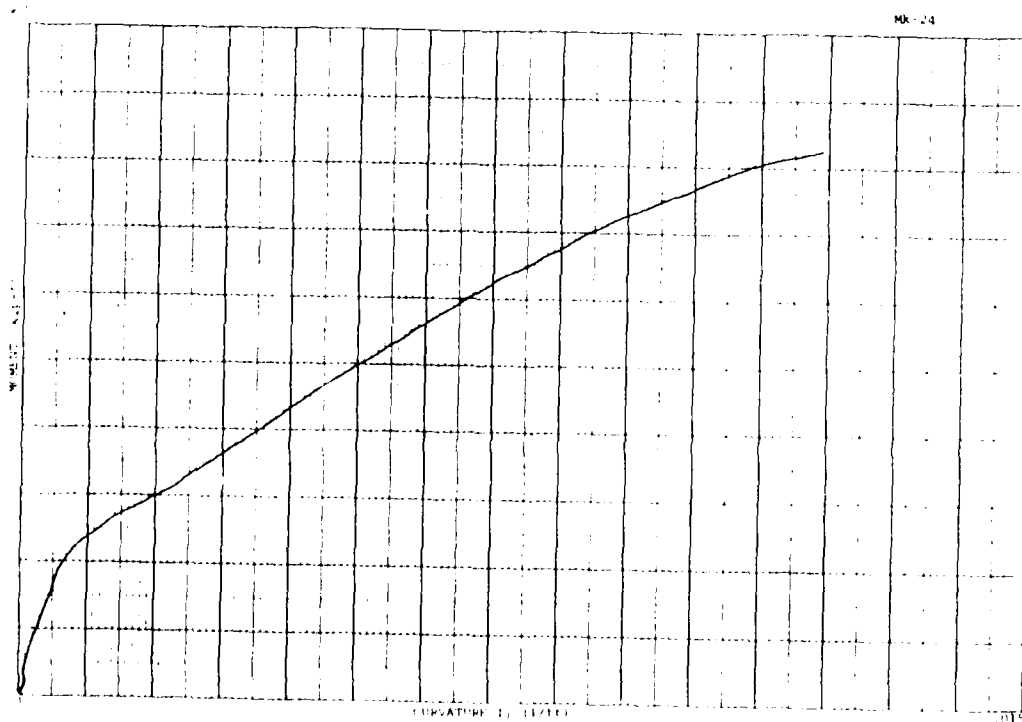


Figure B-226. MK24 moment-curvature plot.

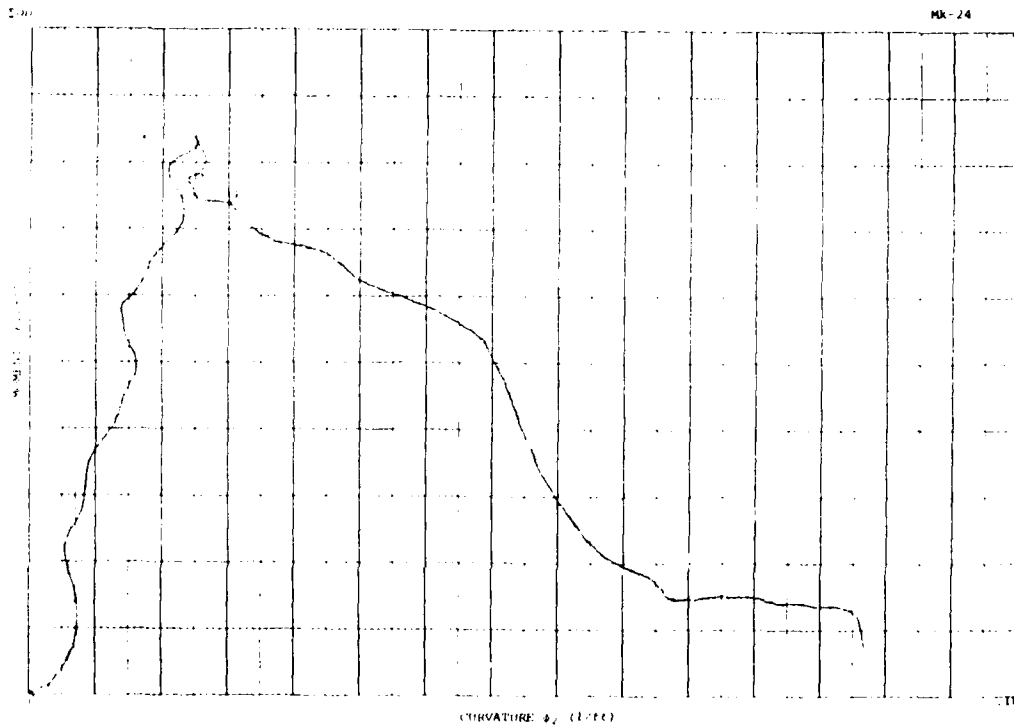


Figure B-227. MK24 moment-curvature plot.

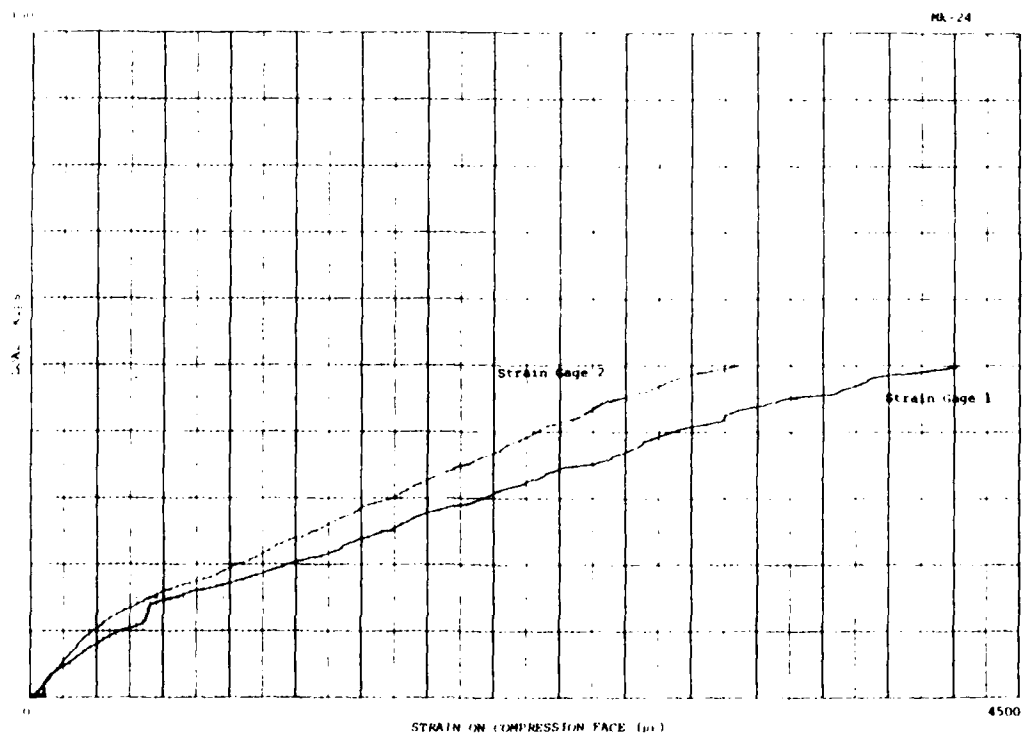


Figure B-228. MK24 compression strain.

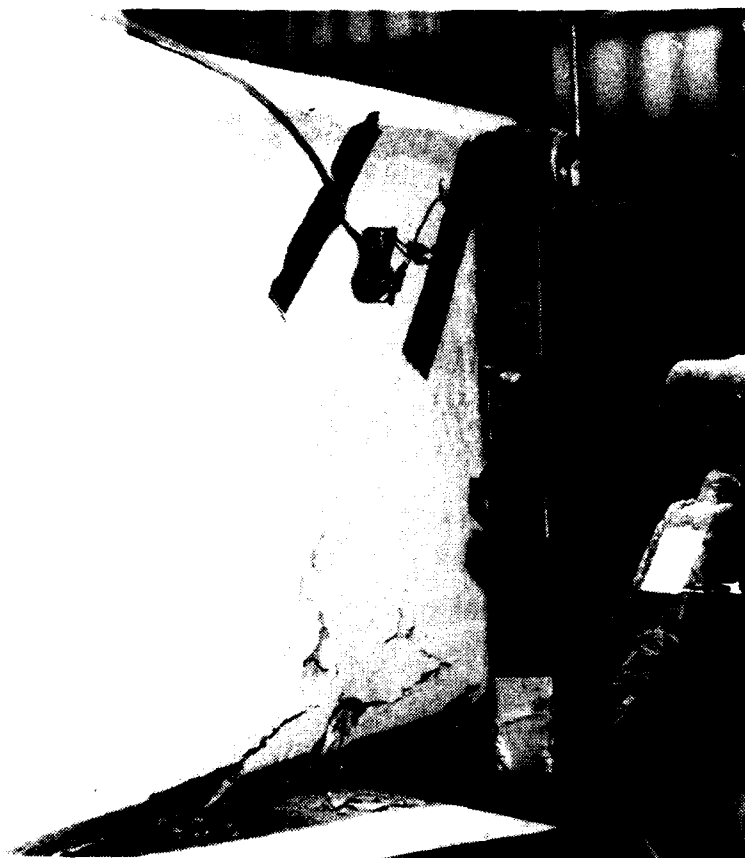


Figure B-229. MK5A compression zone deterioration after 450 cycles.



Figure B-230. MK5A tension face cracks after 450 cycles.



Figure B-231. MK5A compression spalling at failure.



Figure B-232. MK5A tension cracks at failure.

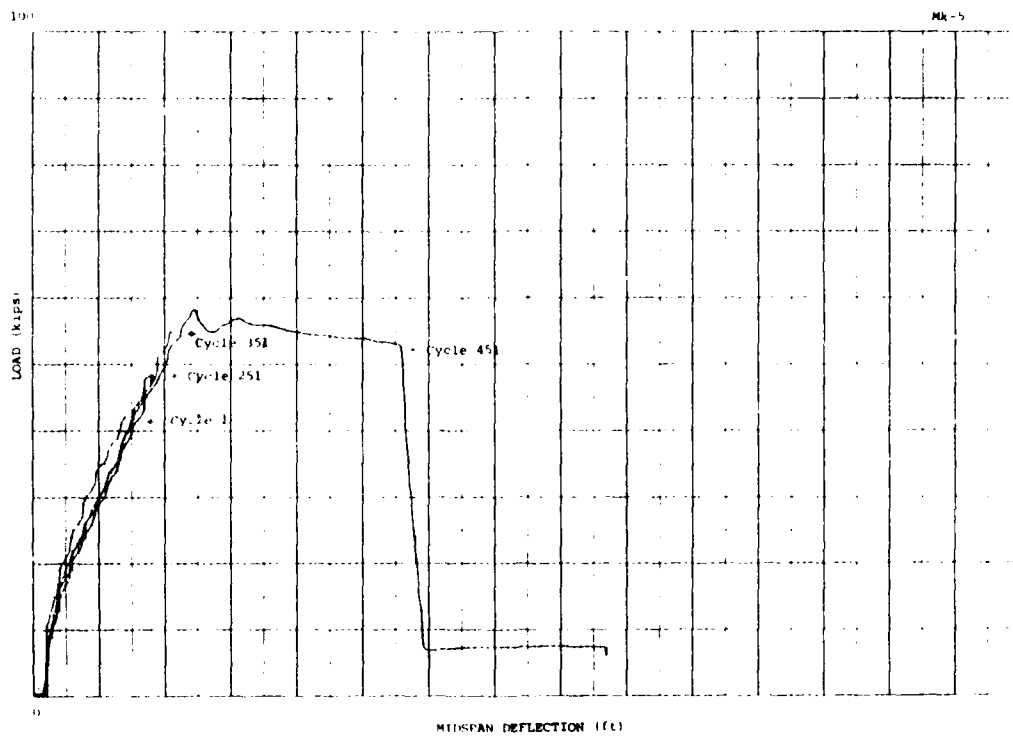


Figure B-233. MK5A load-deflection plot.

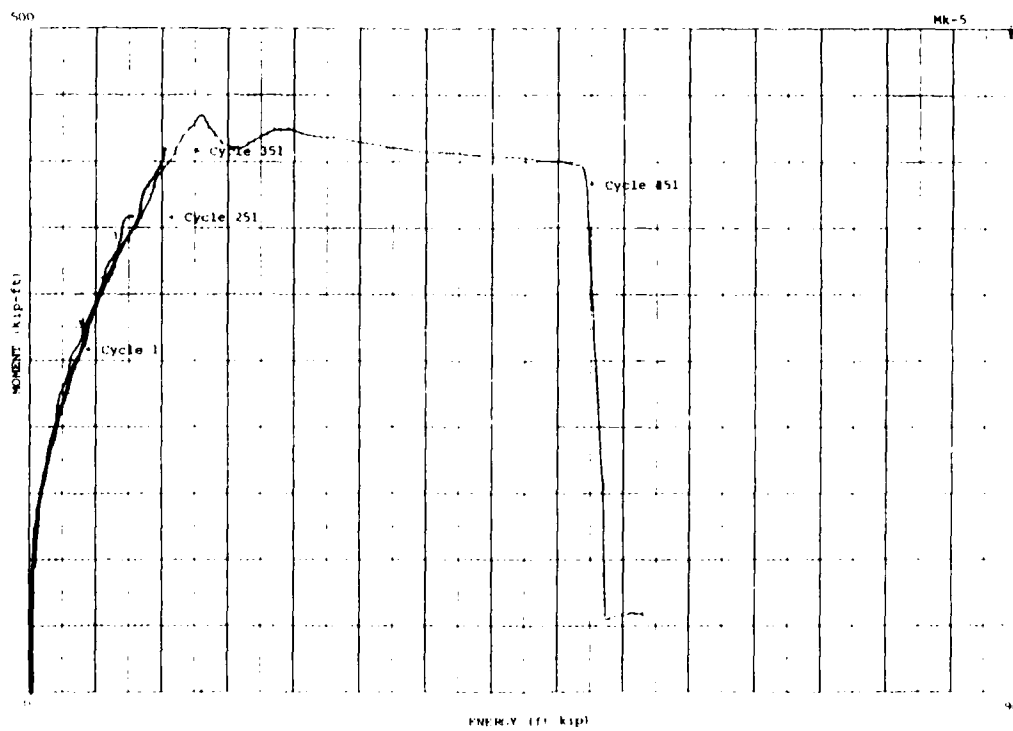


Figure B-234. MK5A moment-energy plot.

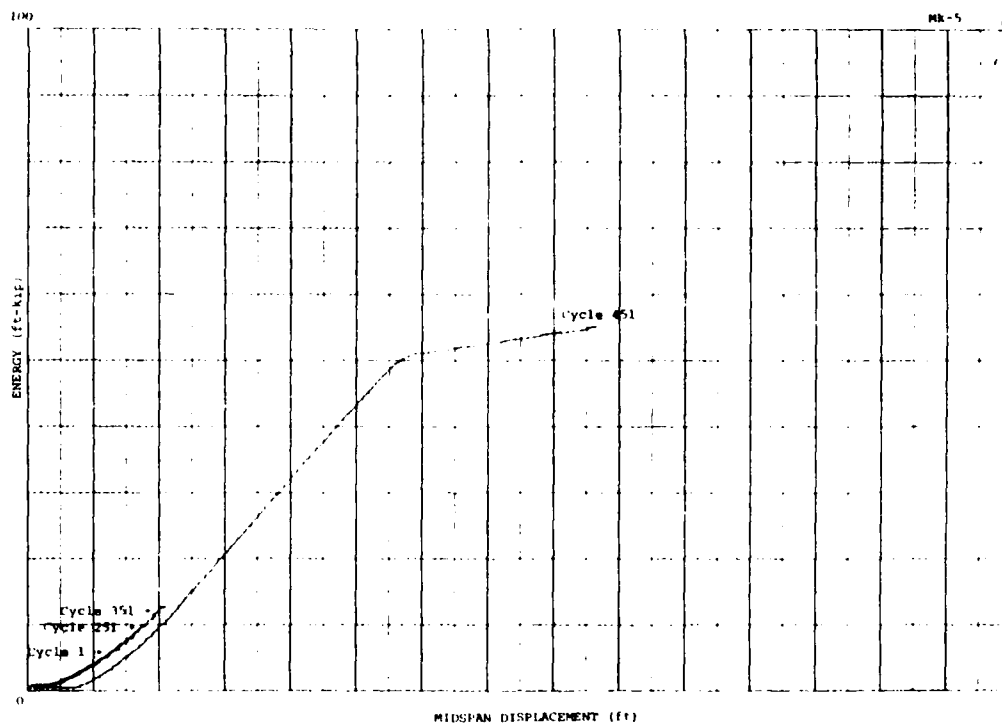


Figure B-235. MK5A energy-displacement plot.

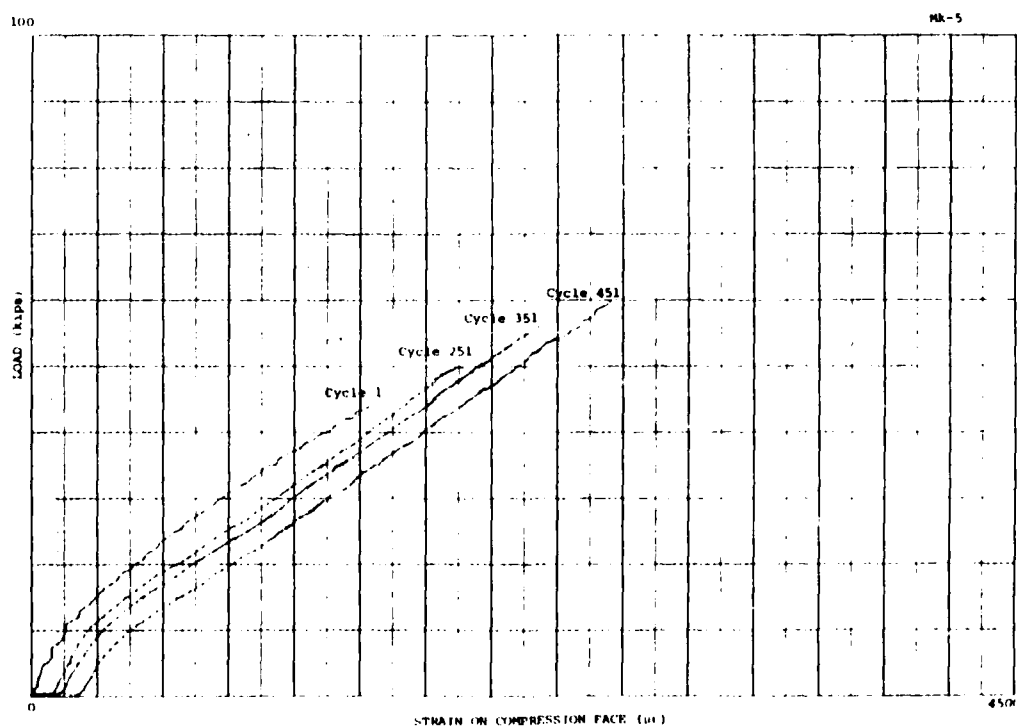


Figure B-236. MK5A compression strain.

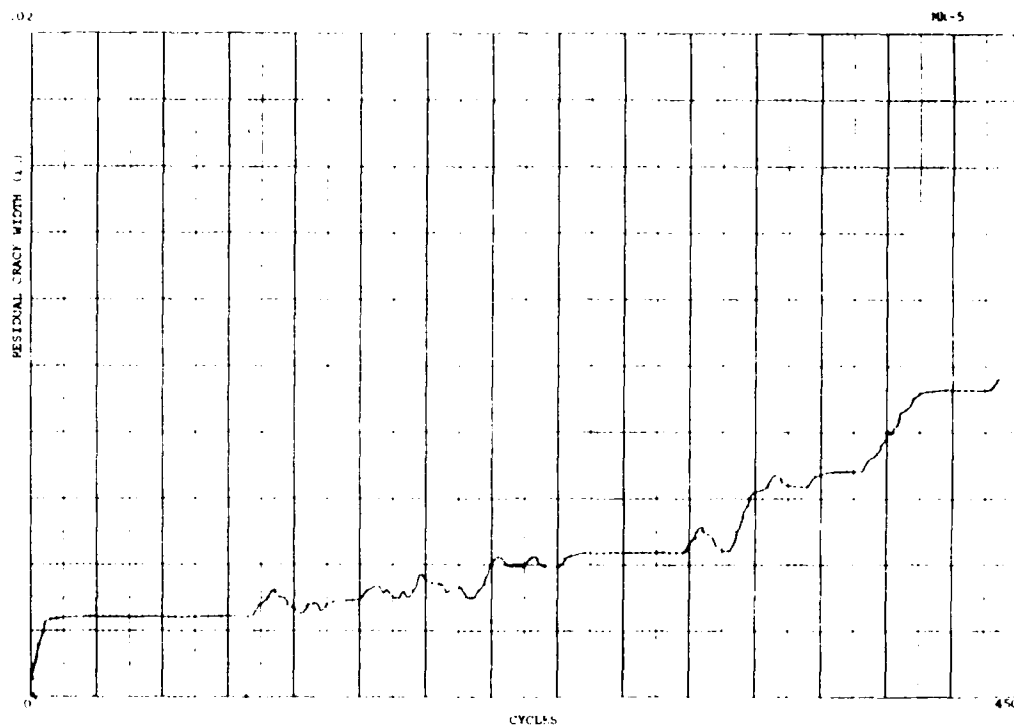


Figure B-237. MK5A crack width after load removal.

cycle 1 - E = 22.9 = 10.5
 cycle 2 - E = 20.4 = 9.4
 cycle 200 - E = 20.4

100 inkip = 18.2
 120 inkip = 21.8 = 10 ft.kip

MK 25 7/17/87 200 cycles

50

43.4

40

37.75

30

Load (Kips)
 B-138

20

17

10

0

1

2

4

5

6

Deflection - inches

Figure B-238. Continuous deflection response of MK25 to cyclic load.

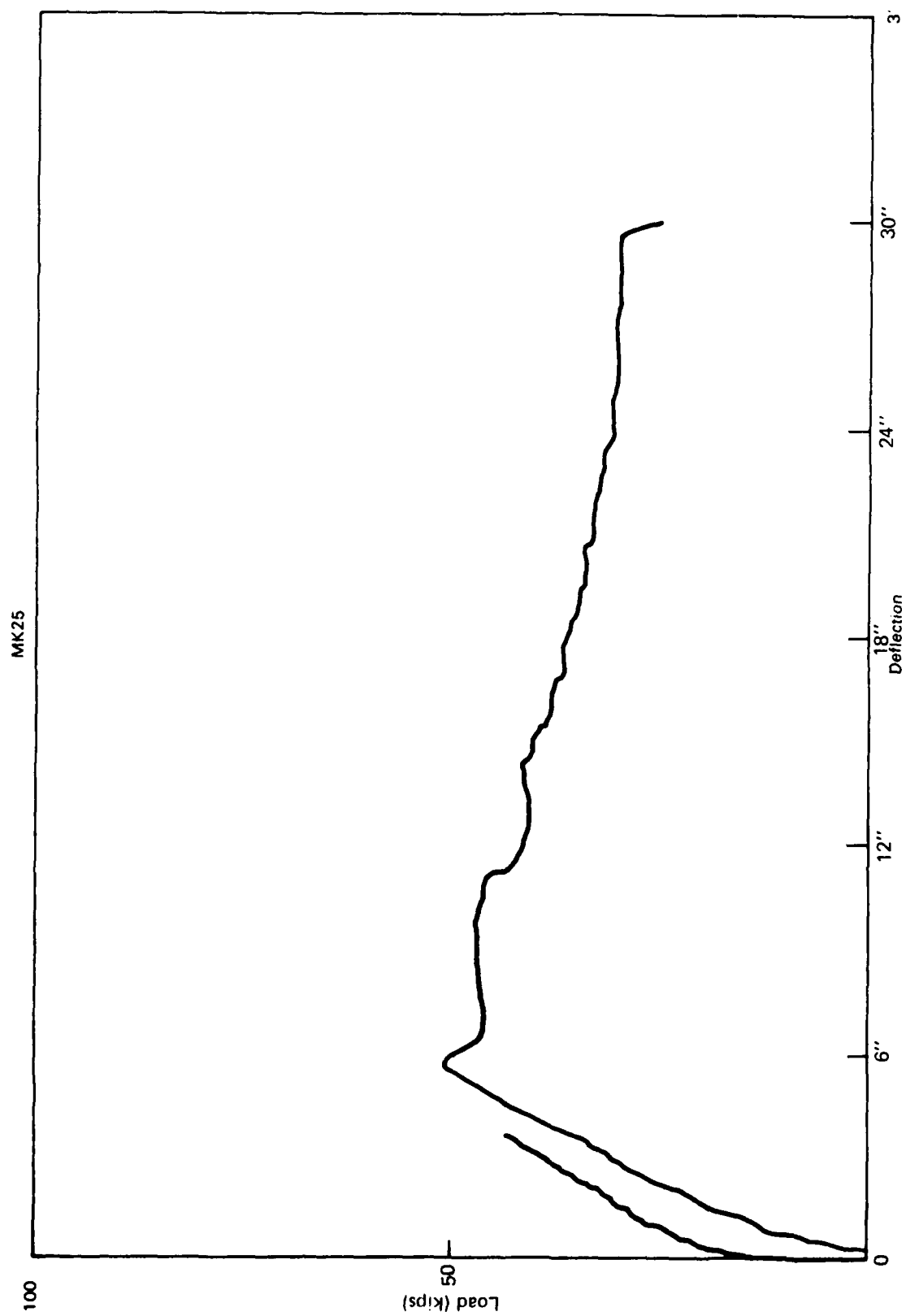


Figure B-239. First and final load-deflection plot of MK25.

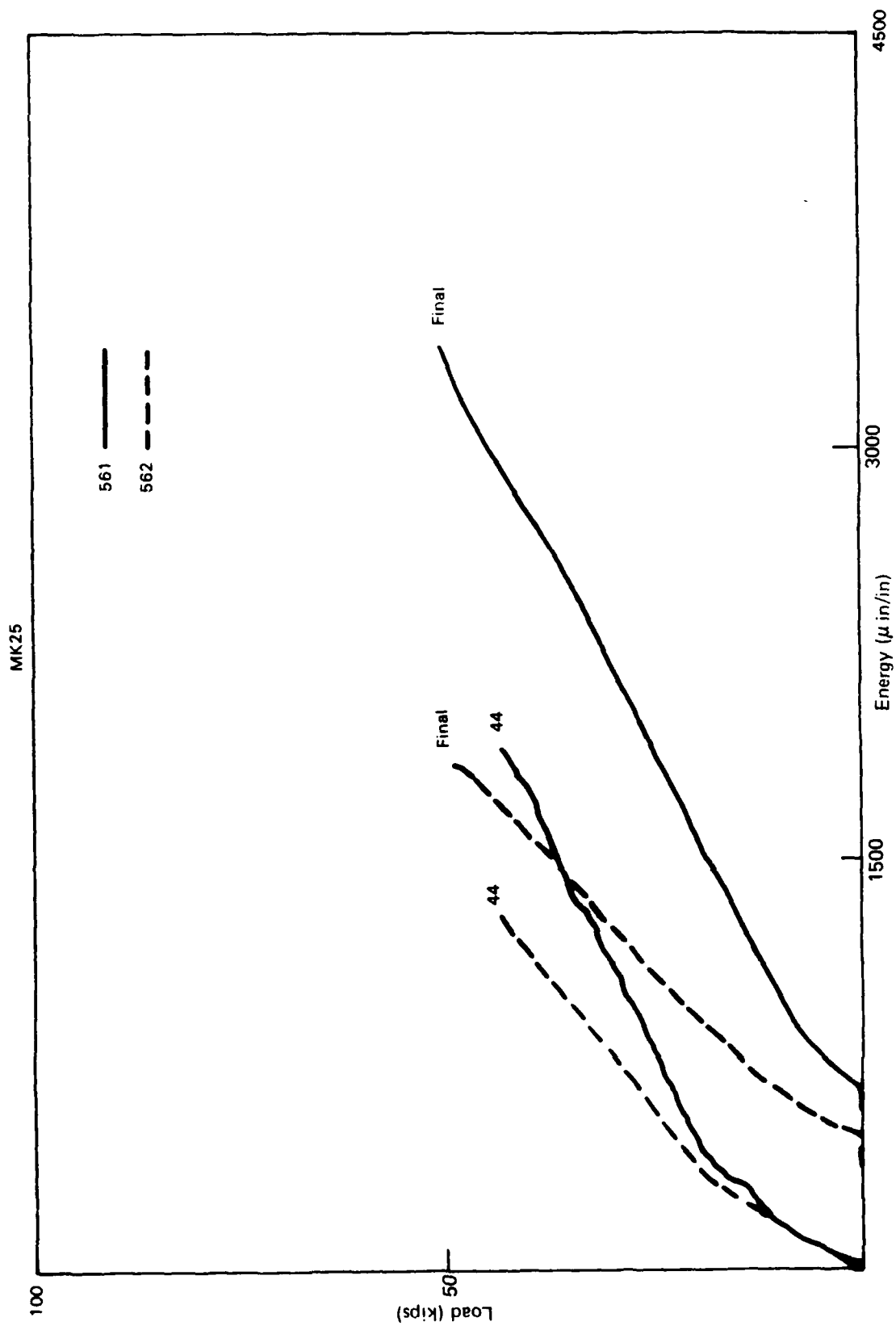


Figure B-240. Compression strain gage plots of MK25.

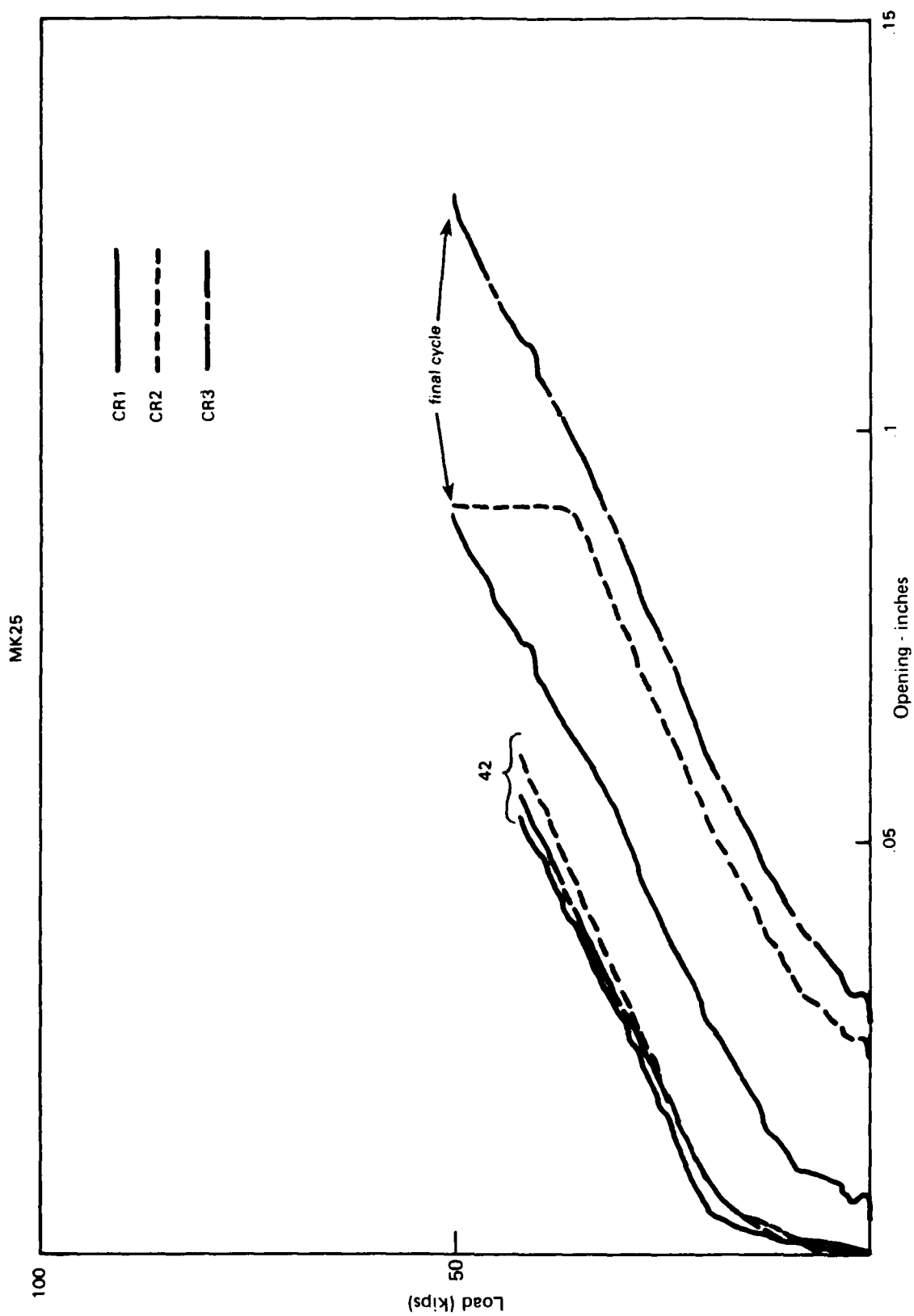


Figure B-241. Crack gage plots of MK25.

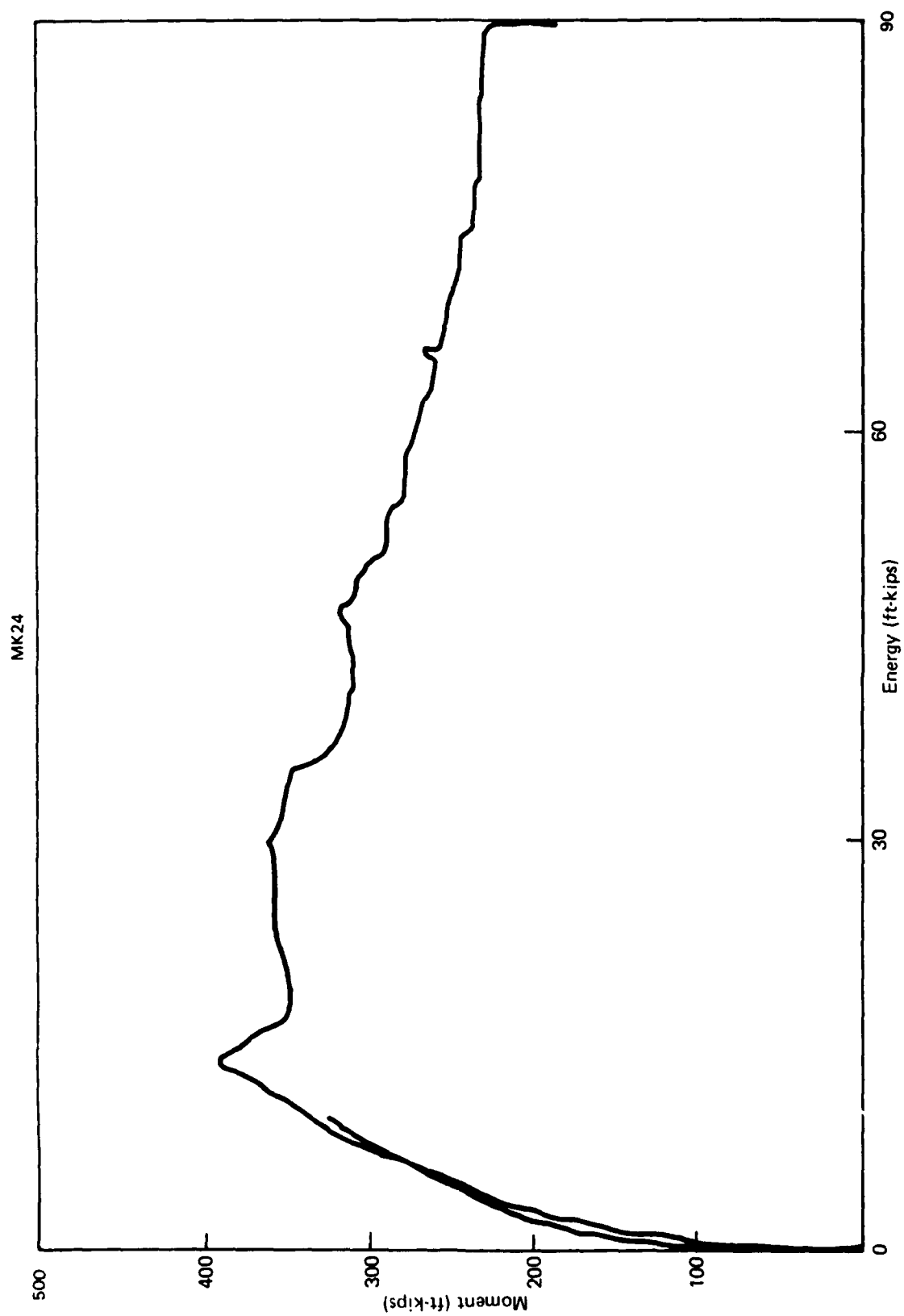
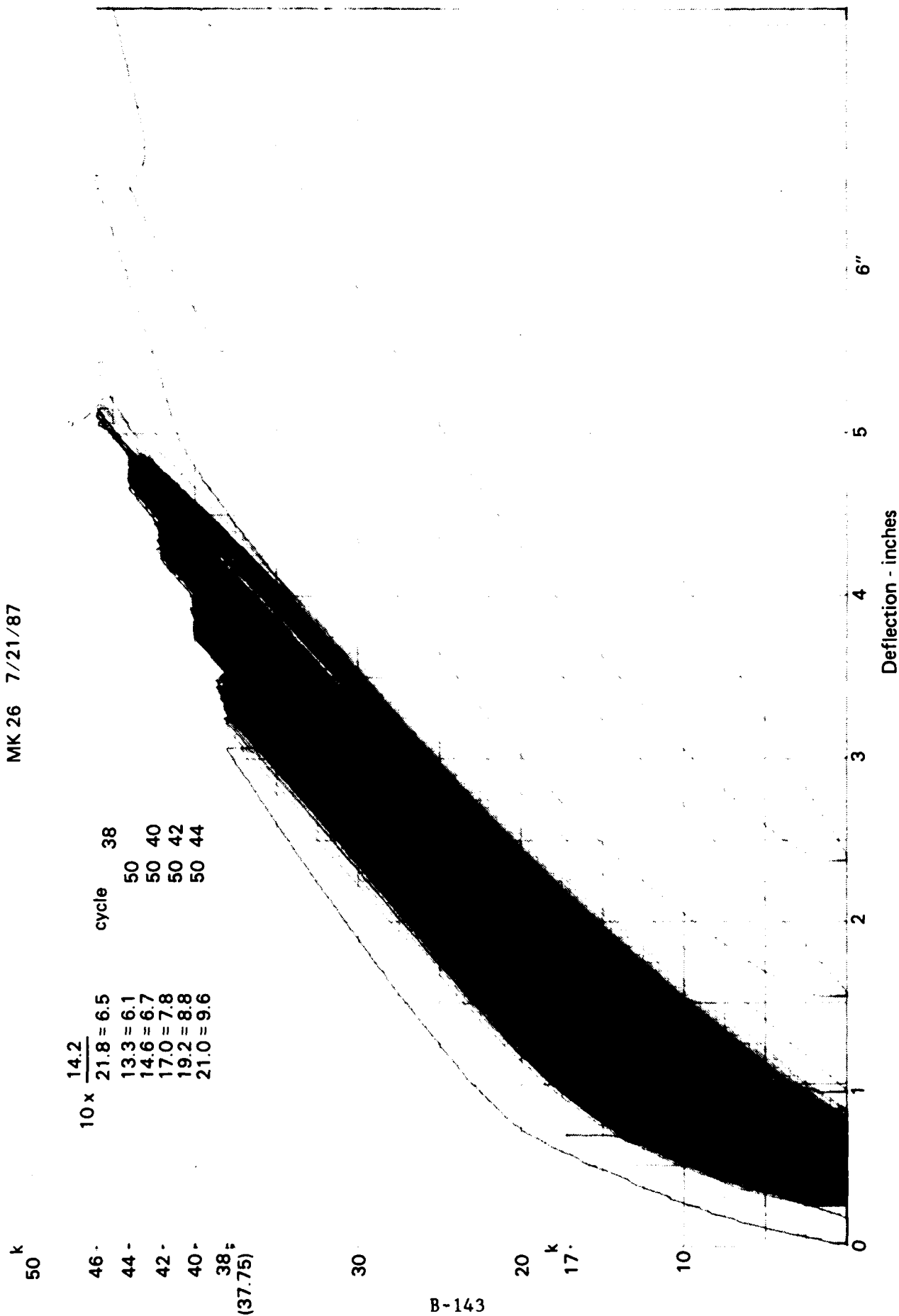


Figure B-242. Moment-energy plot first and final load on MK25.

MK 26 7/21/87



B-143

Figure B-243. Continuous deflection response of MK26 to cyclic load.

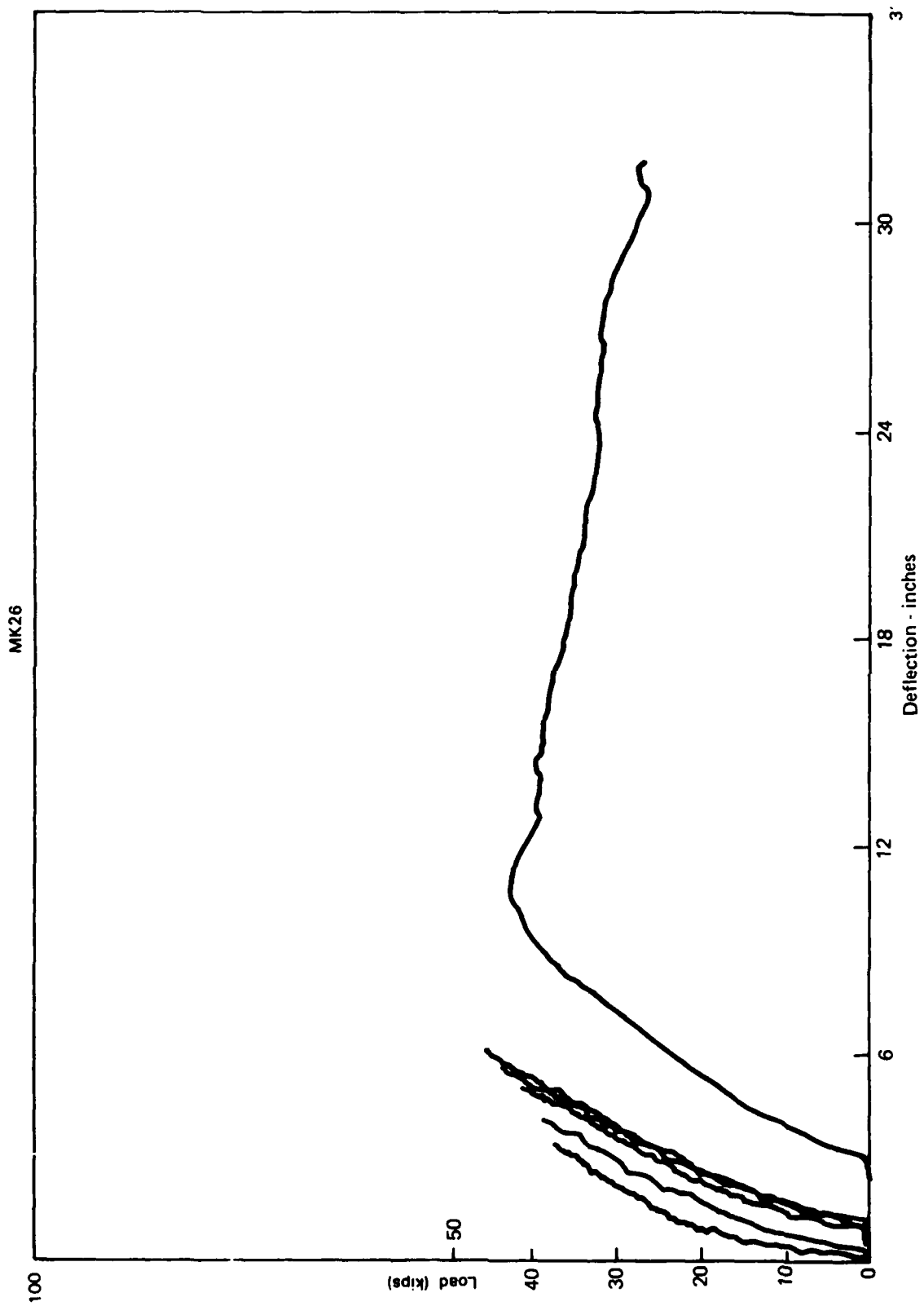


Figure B-244. Load-deflection plots of MK25.

MK26

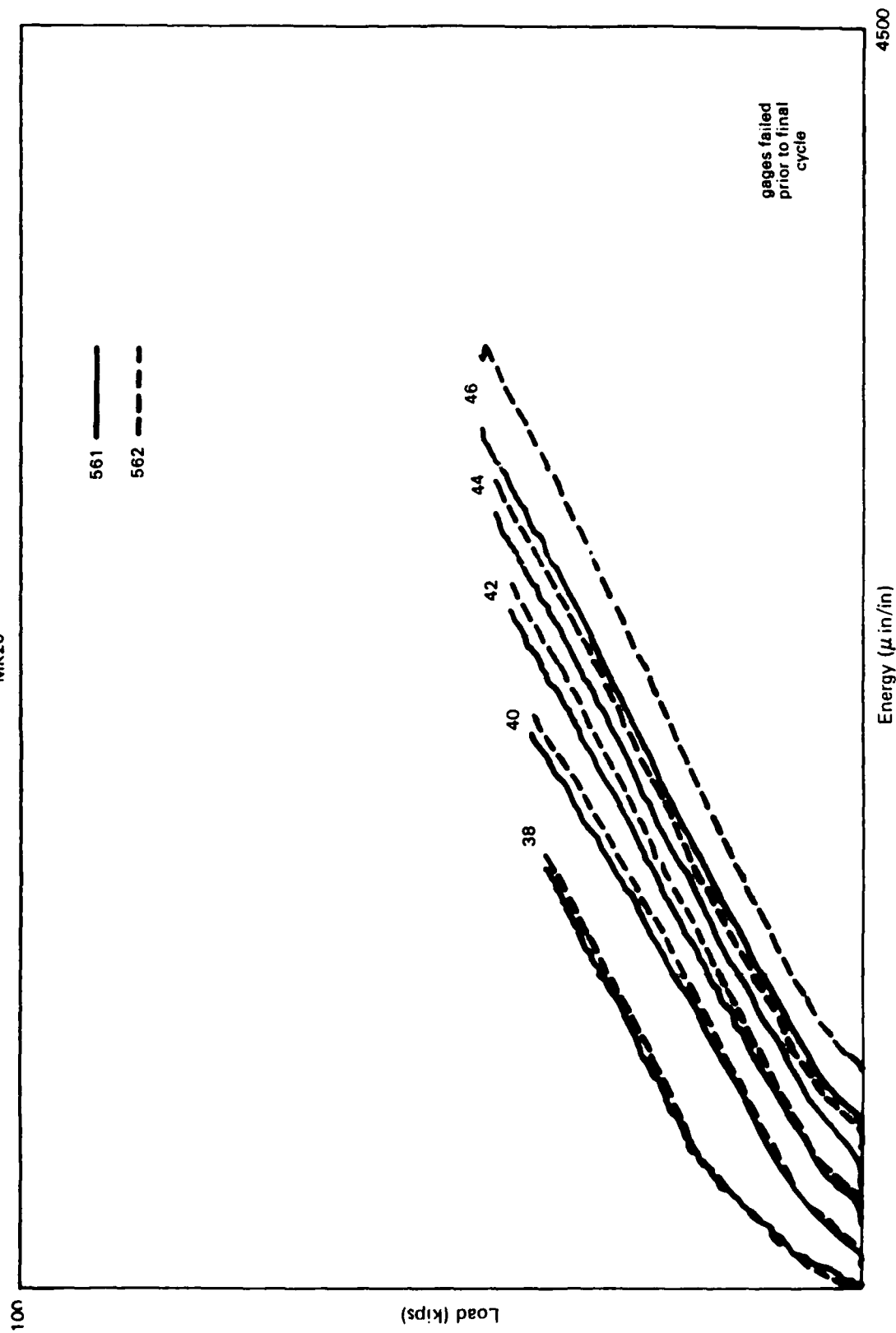


Figure B-245. Load-strain response of MK26.

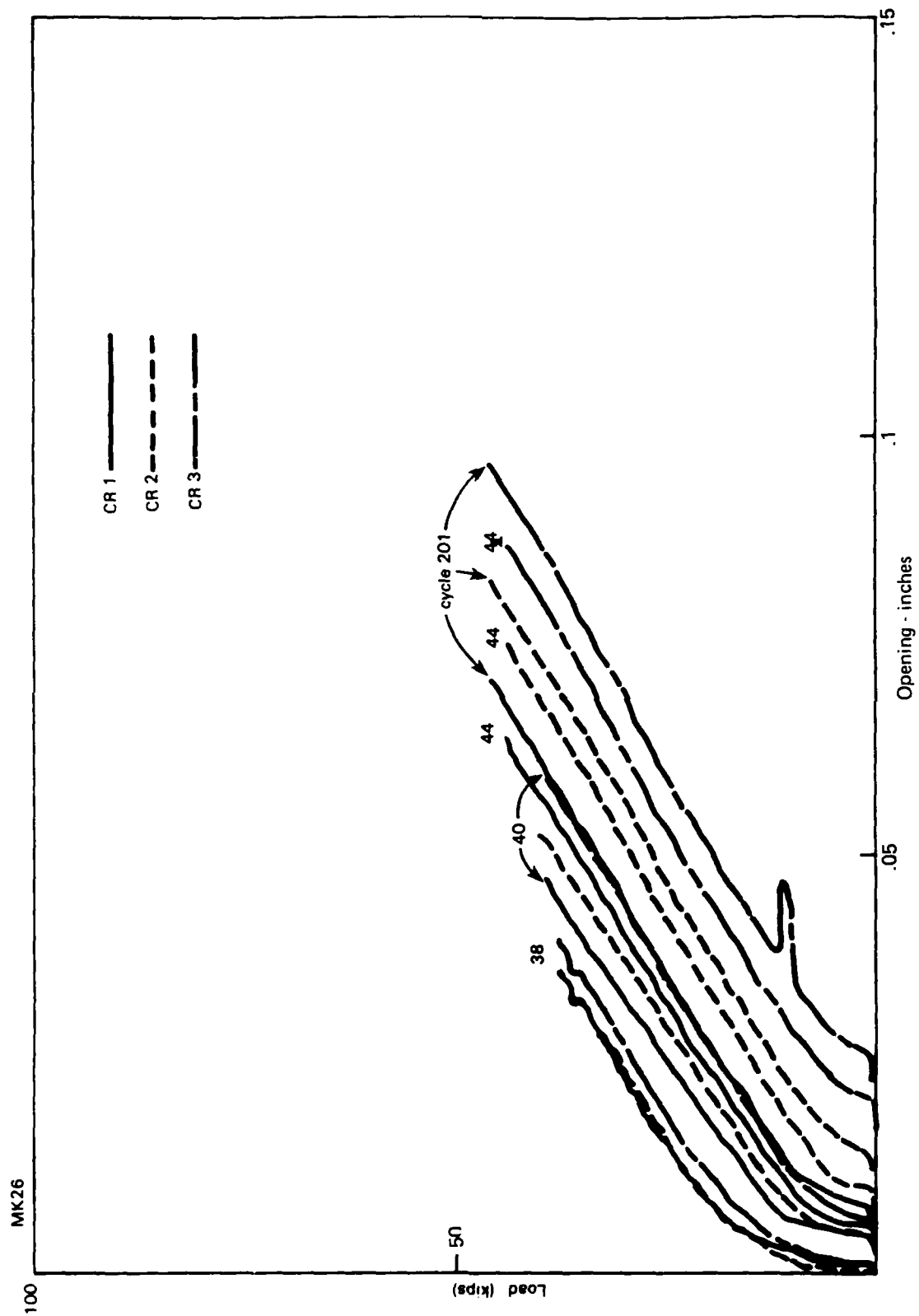


Figure B-246. Crack opening response of MK26.

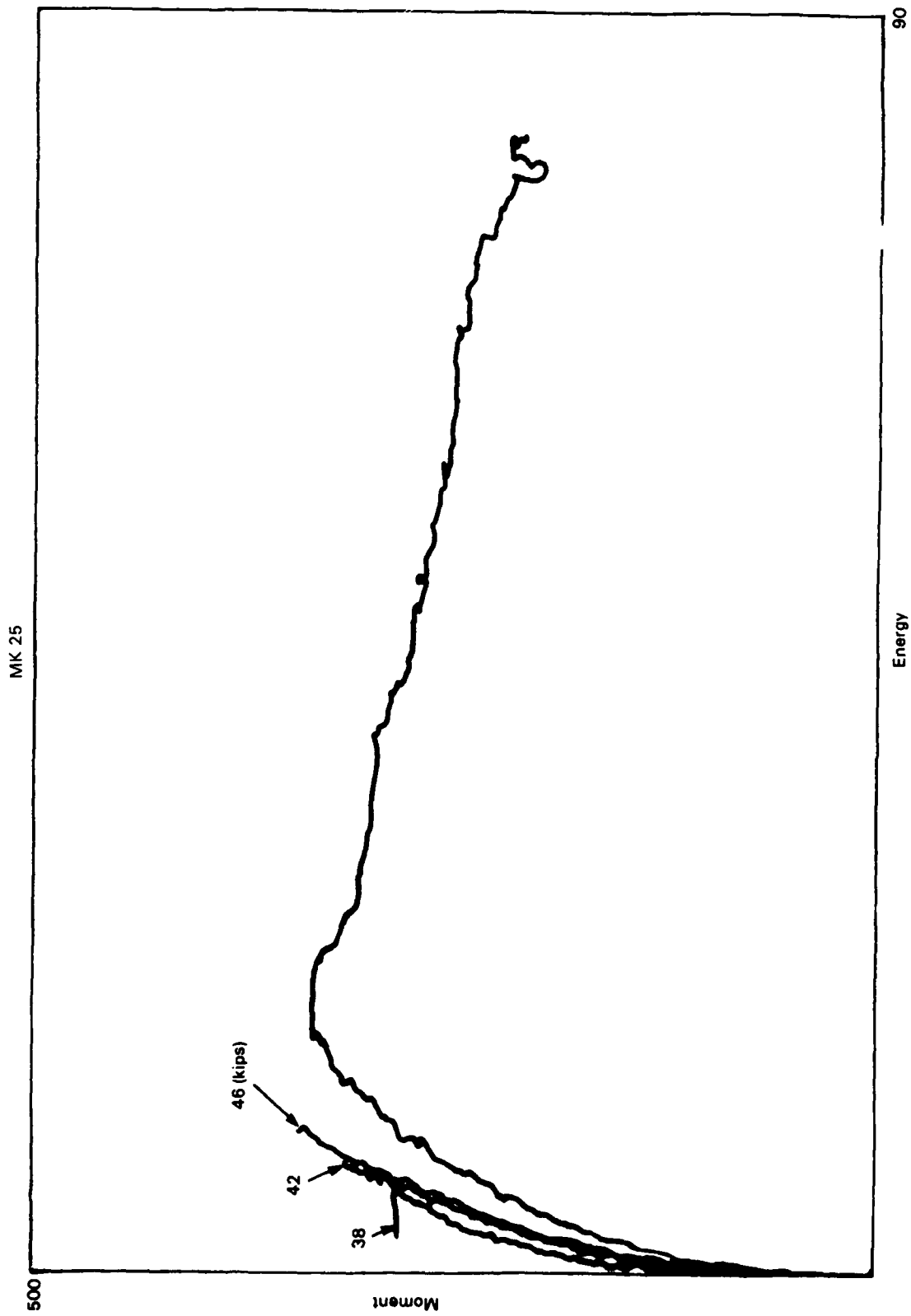


Figure B-247. Moment-energy plots for MK26.

MK 27 7/22/87

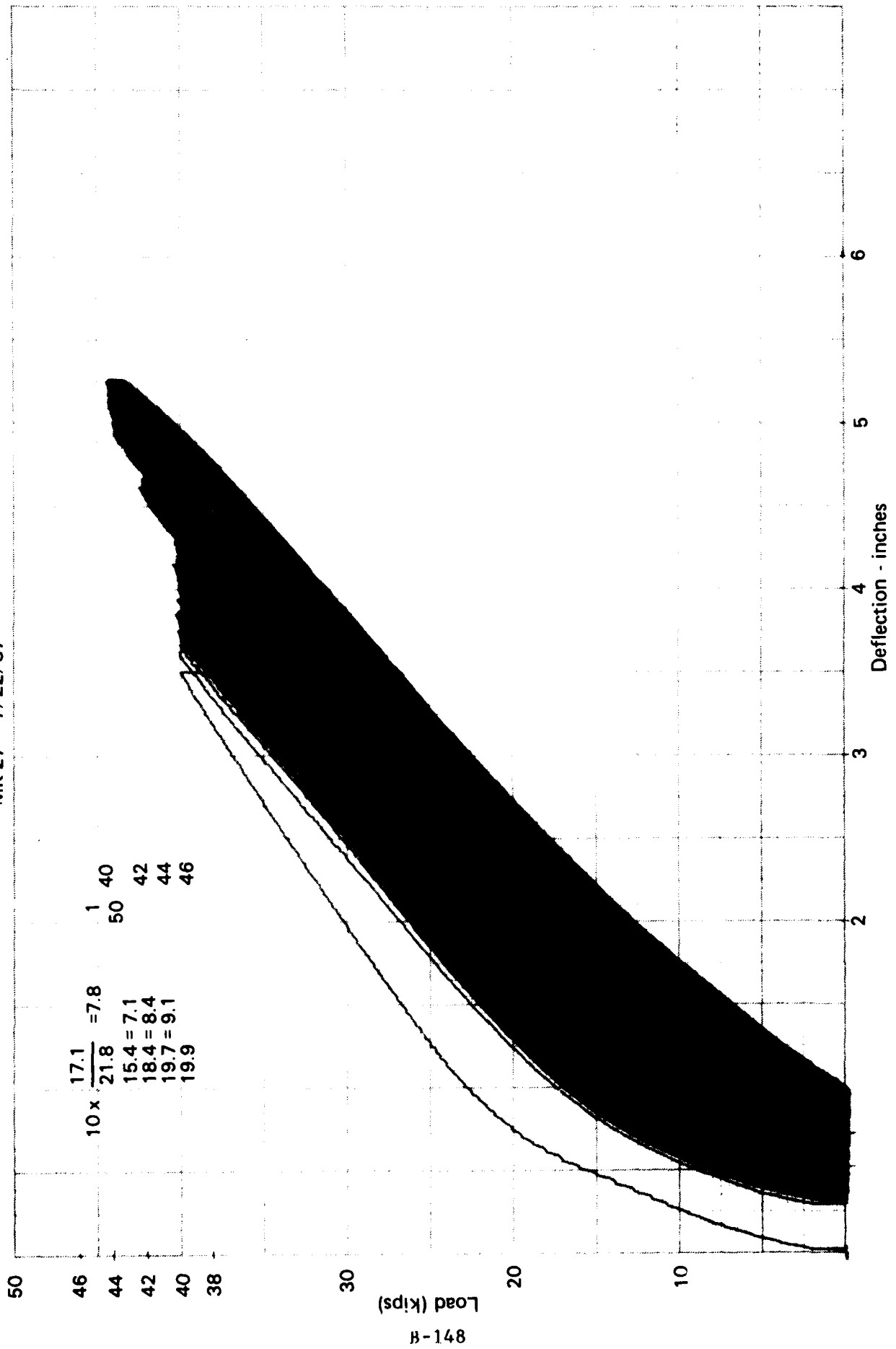


Figure B-248. Continuous load-deflection response of MK27.

MK 27 7/22/87

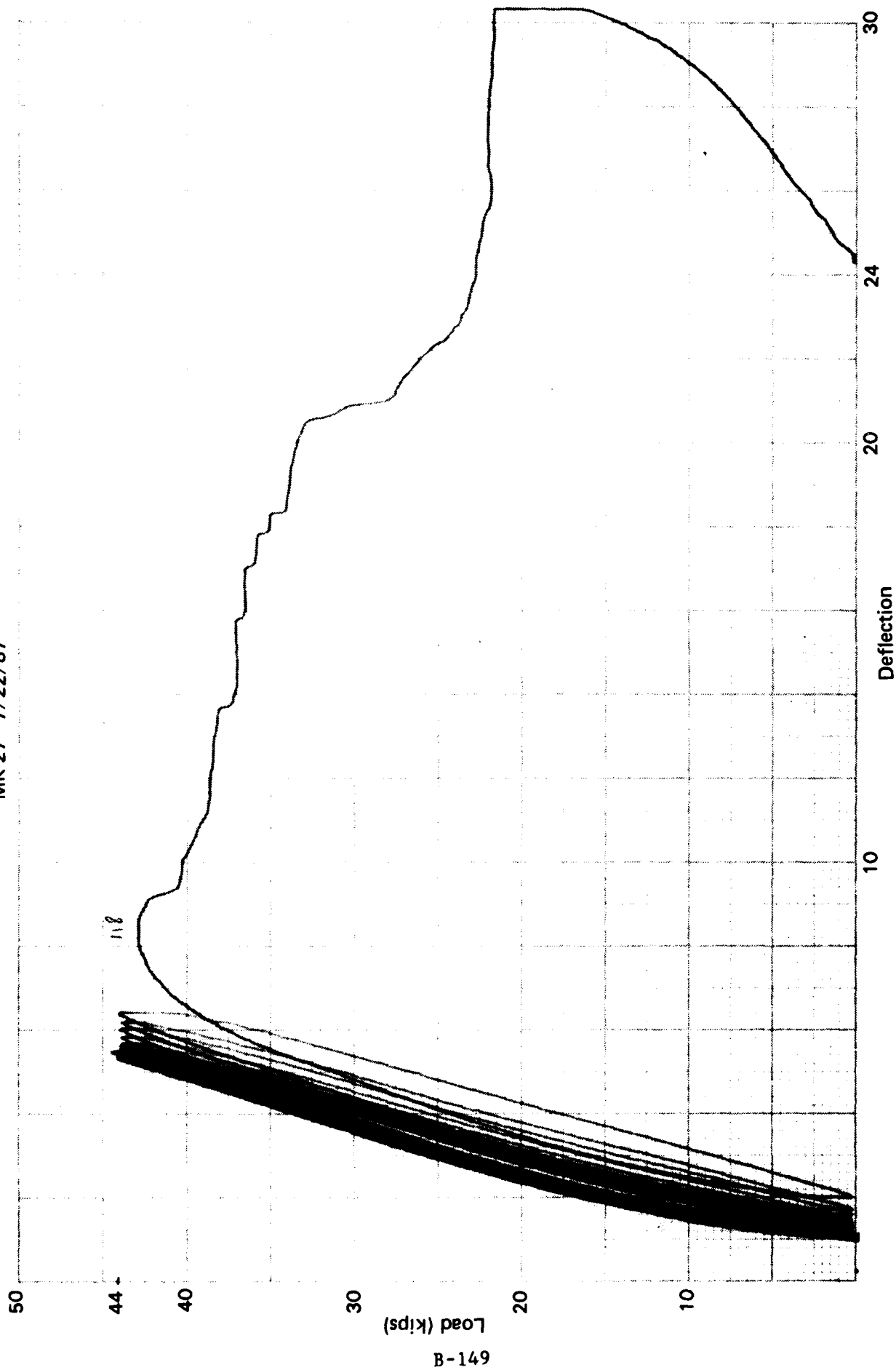


Figure B-249. Final load-deflection cycles of MK27.

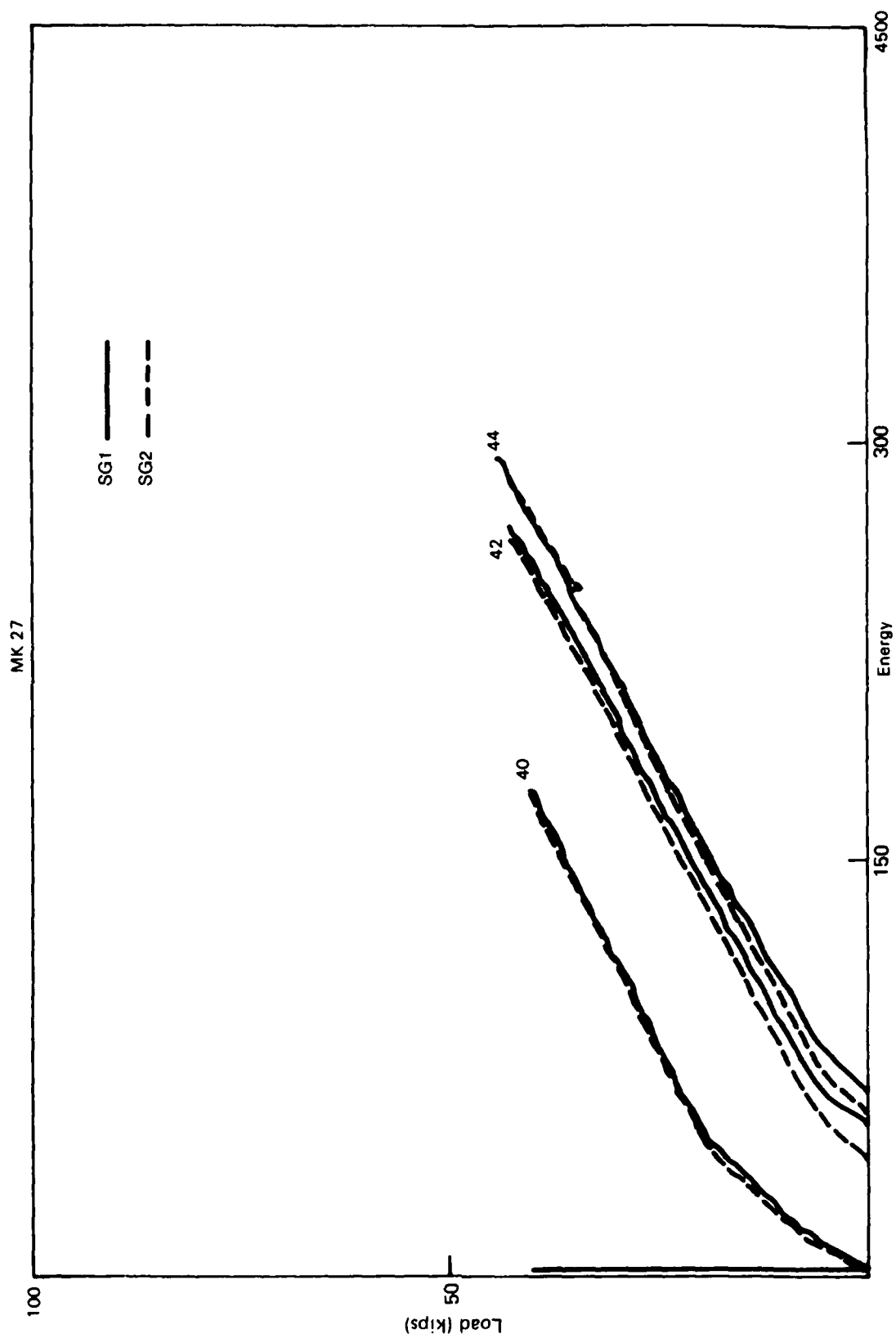


Figure B-250. Load-strain plots of MK27.

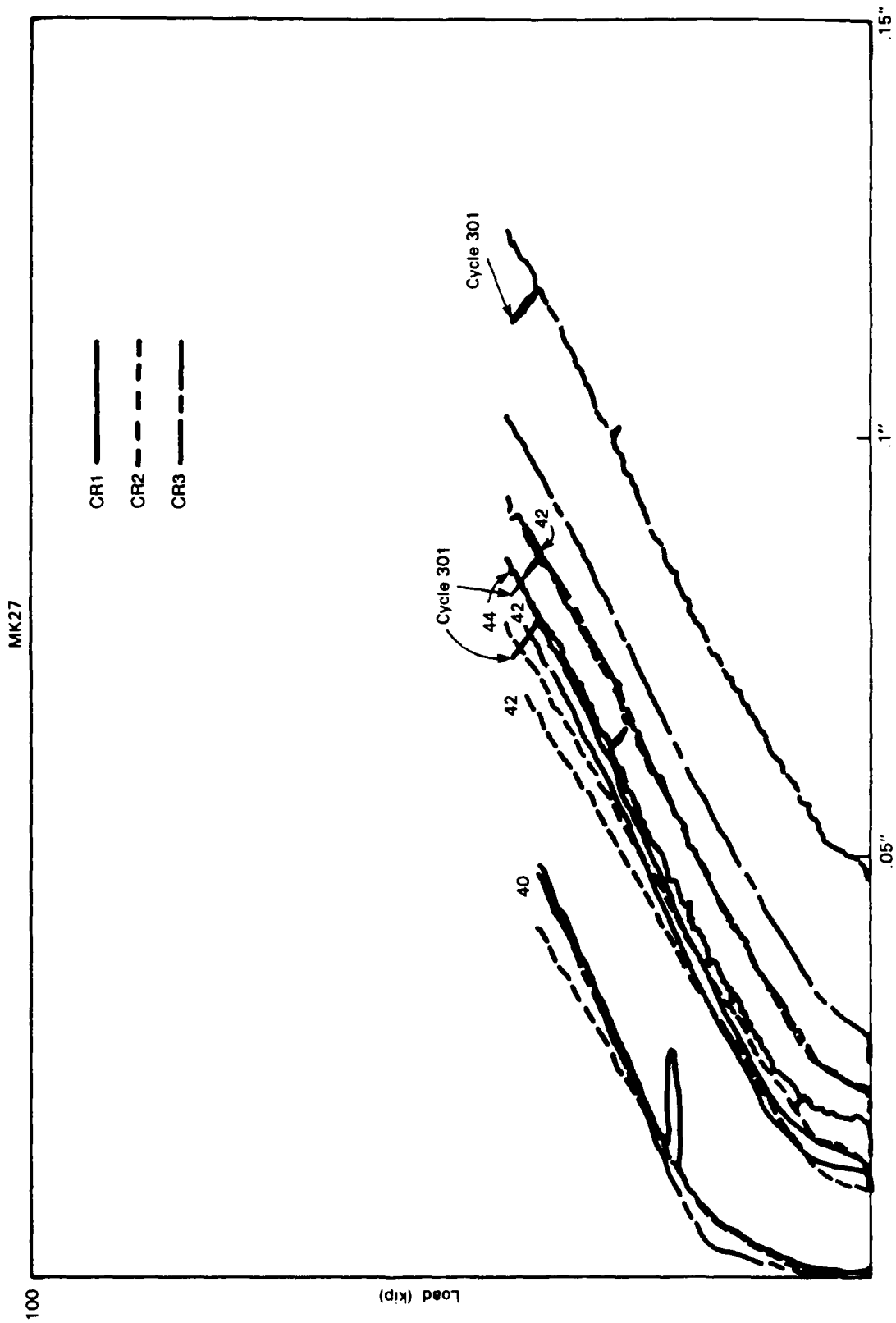


Figure B-251. Crack opening during cyclic load of MK27.

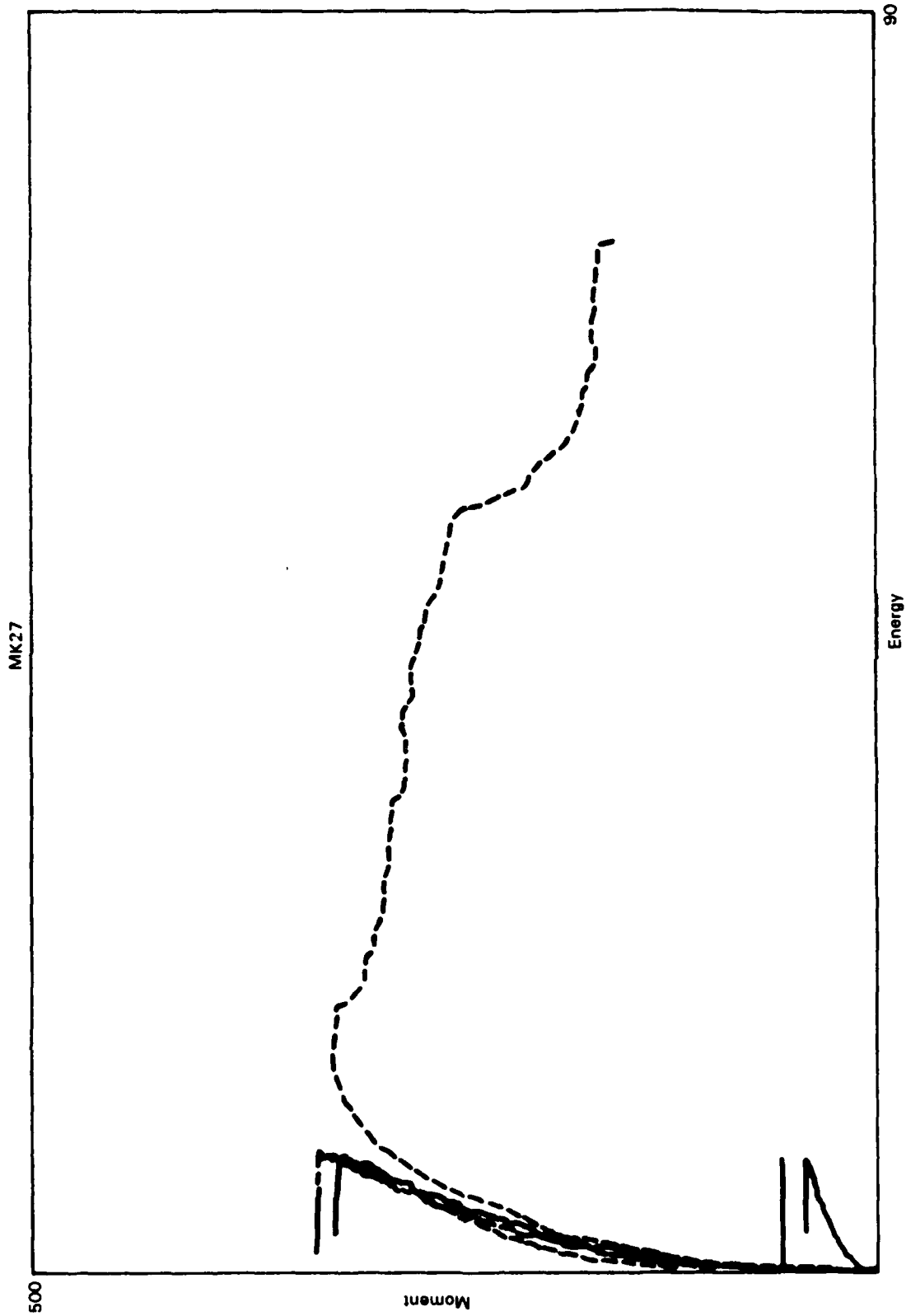
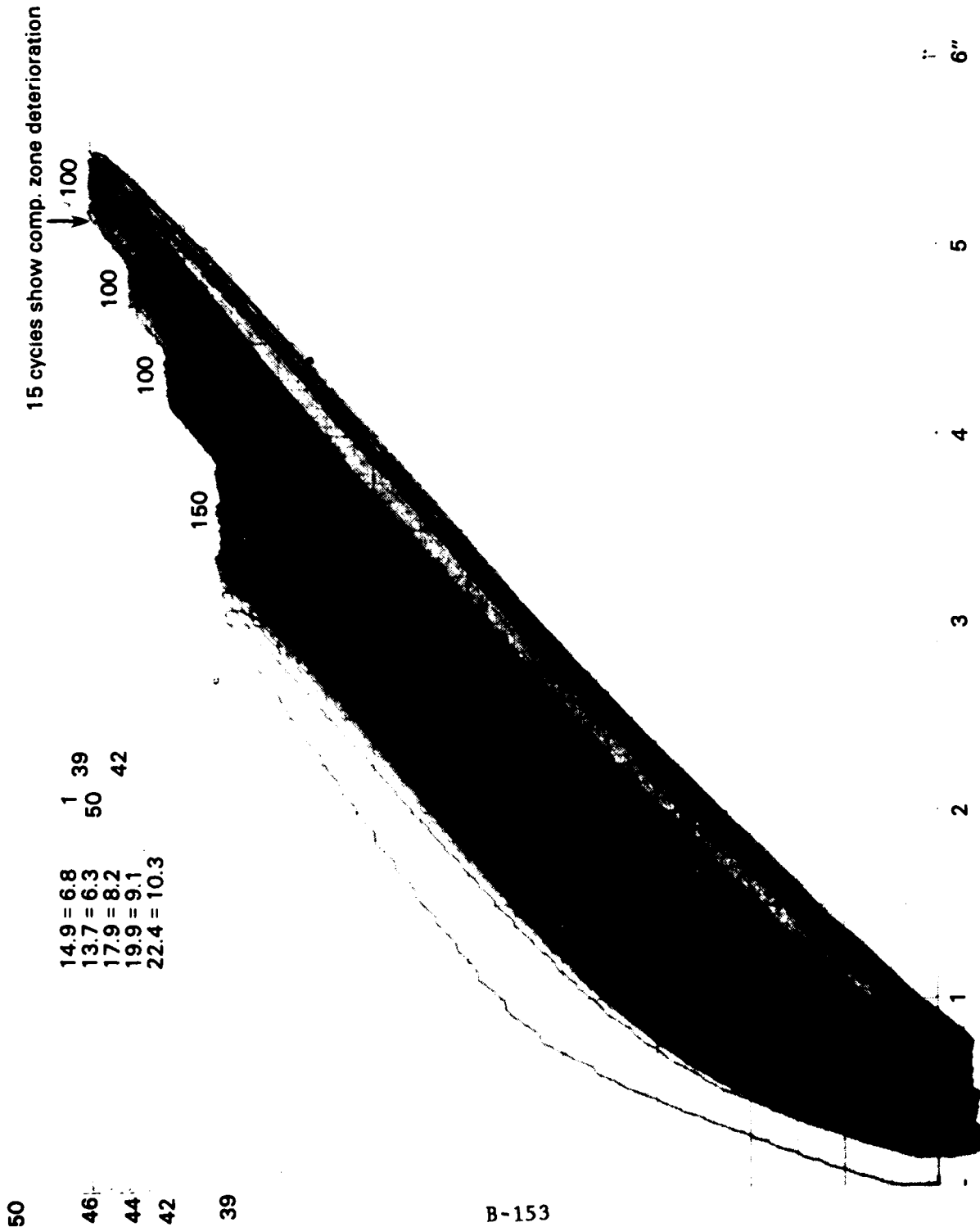


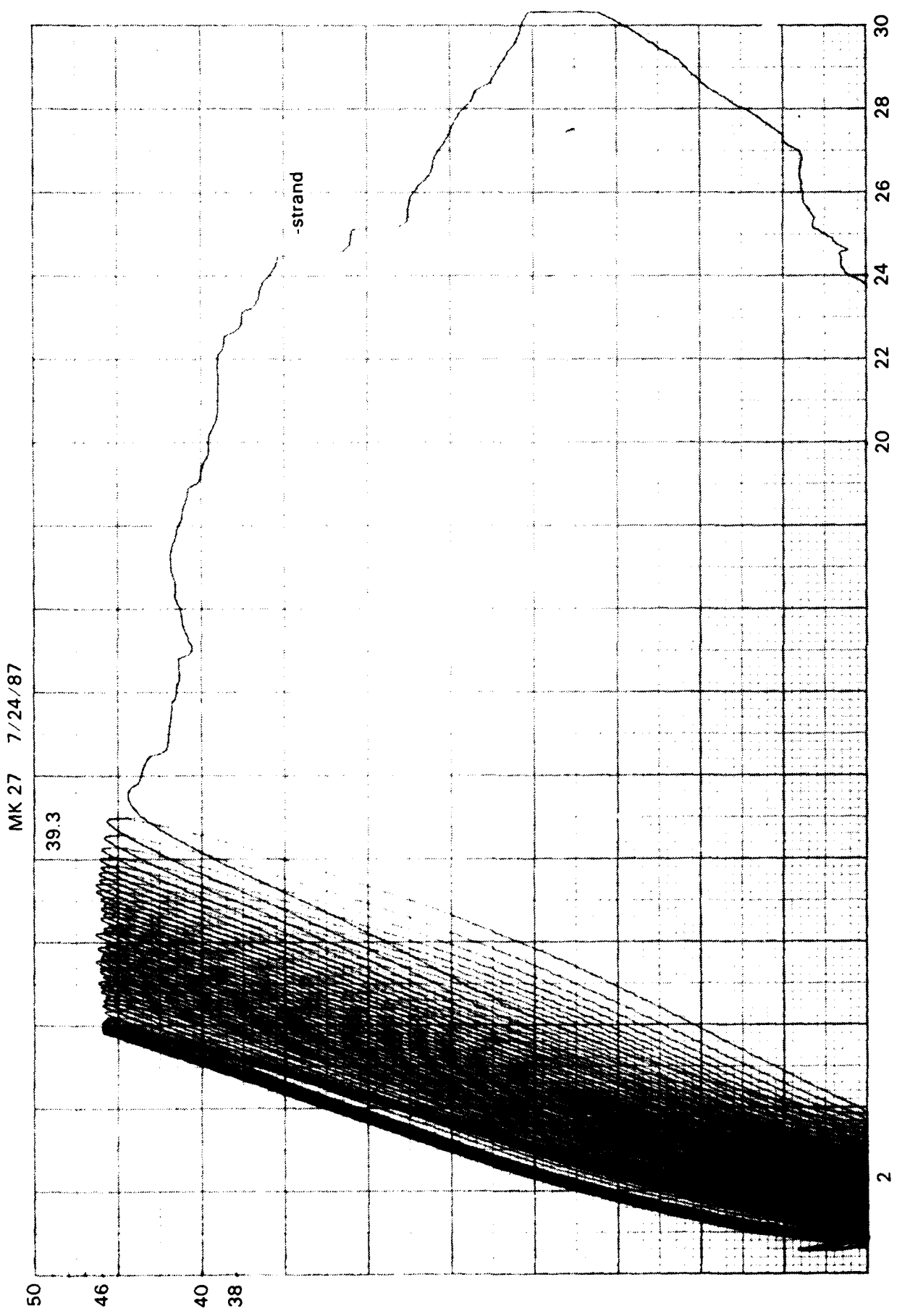
Figure B-252. Moment-energy plots for MK27.

MK 27 7/24/87



B-153

Figure B-253. Continuous service load cycling on MK28.



B-154

Figure B-254. Final load cycle on MK28.

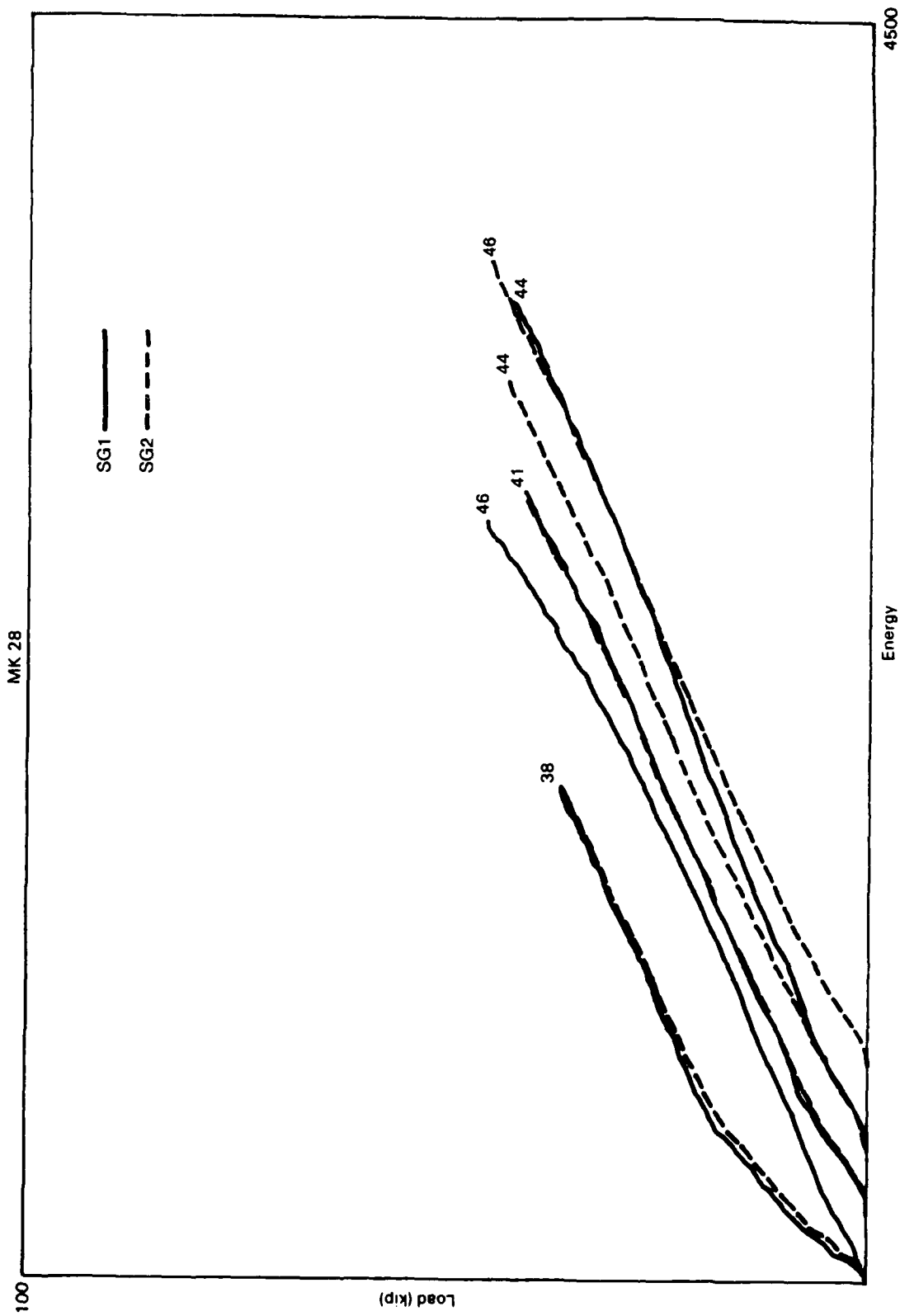


Figure B-255. Strain gage plots for MK28.

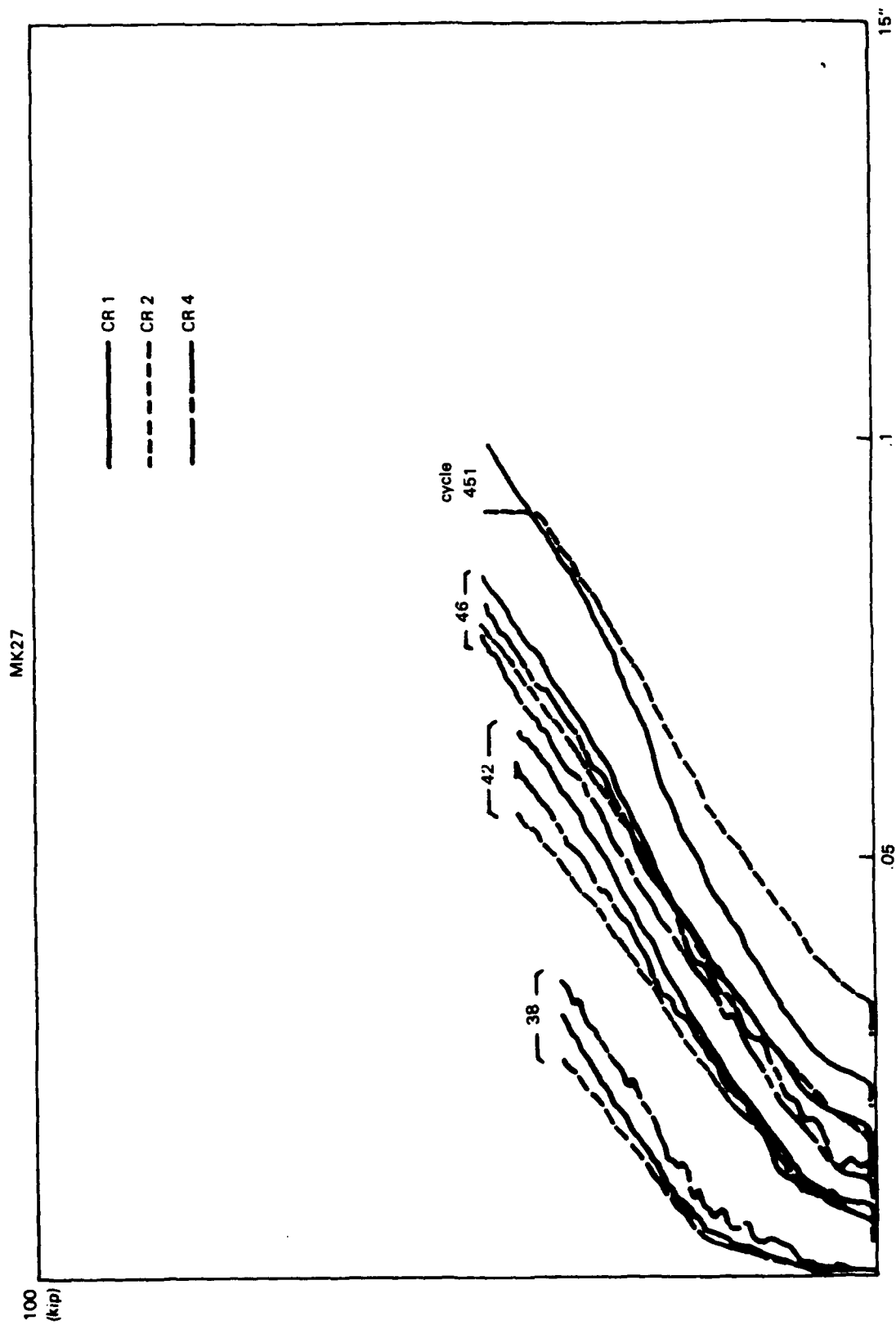


Figure B-256. Crack opening plots of MK28.

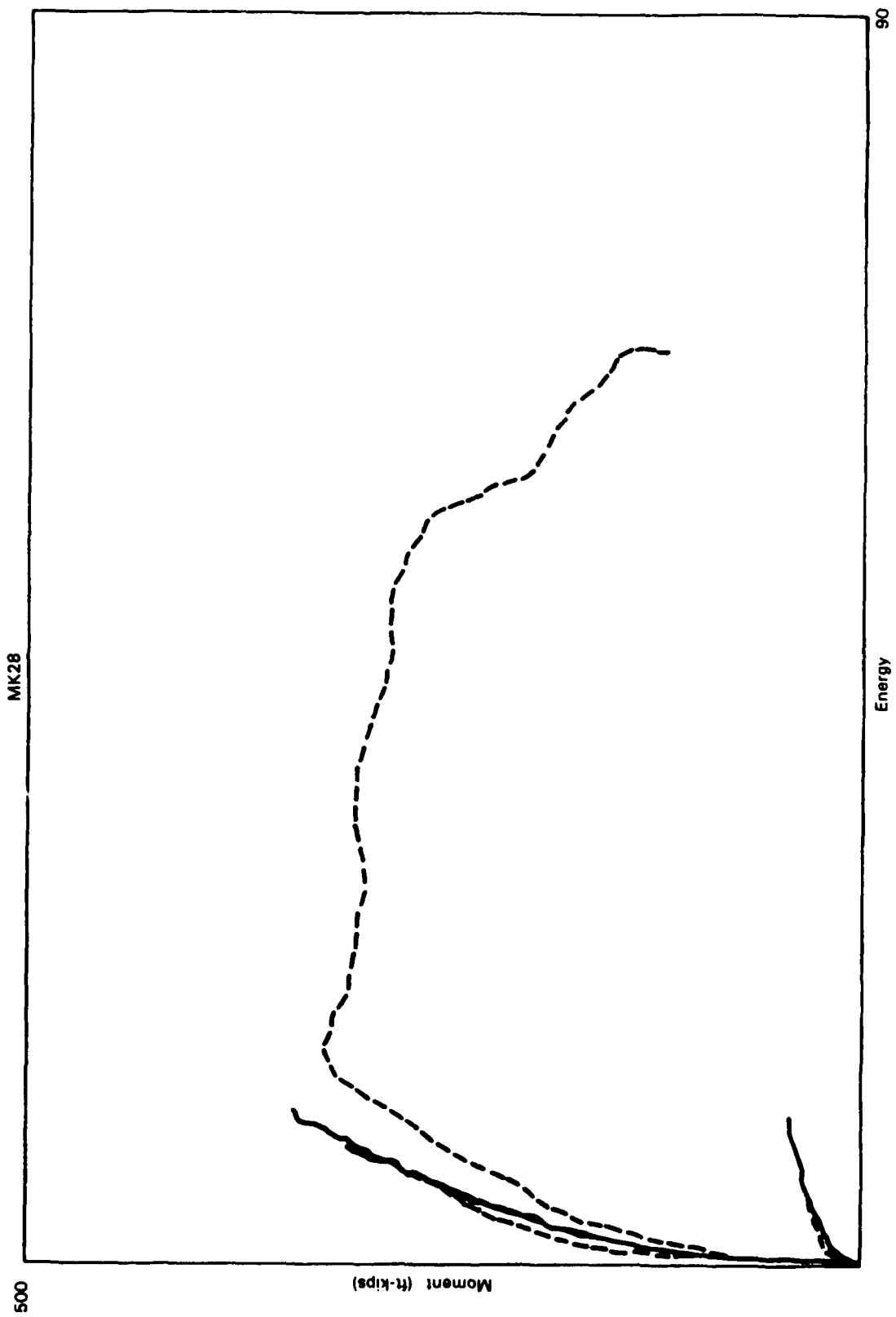


Figure B-257. Moment-energy plots for MK28.

MK 29 7/29/87

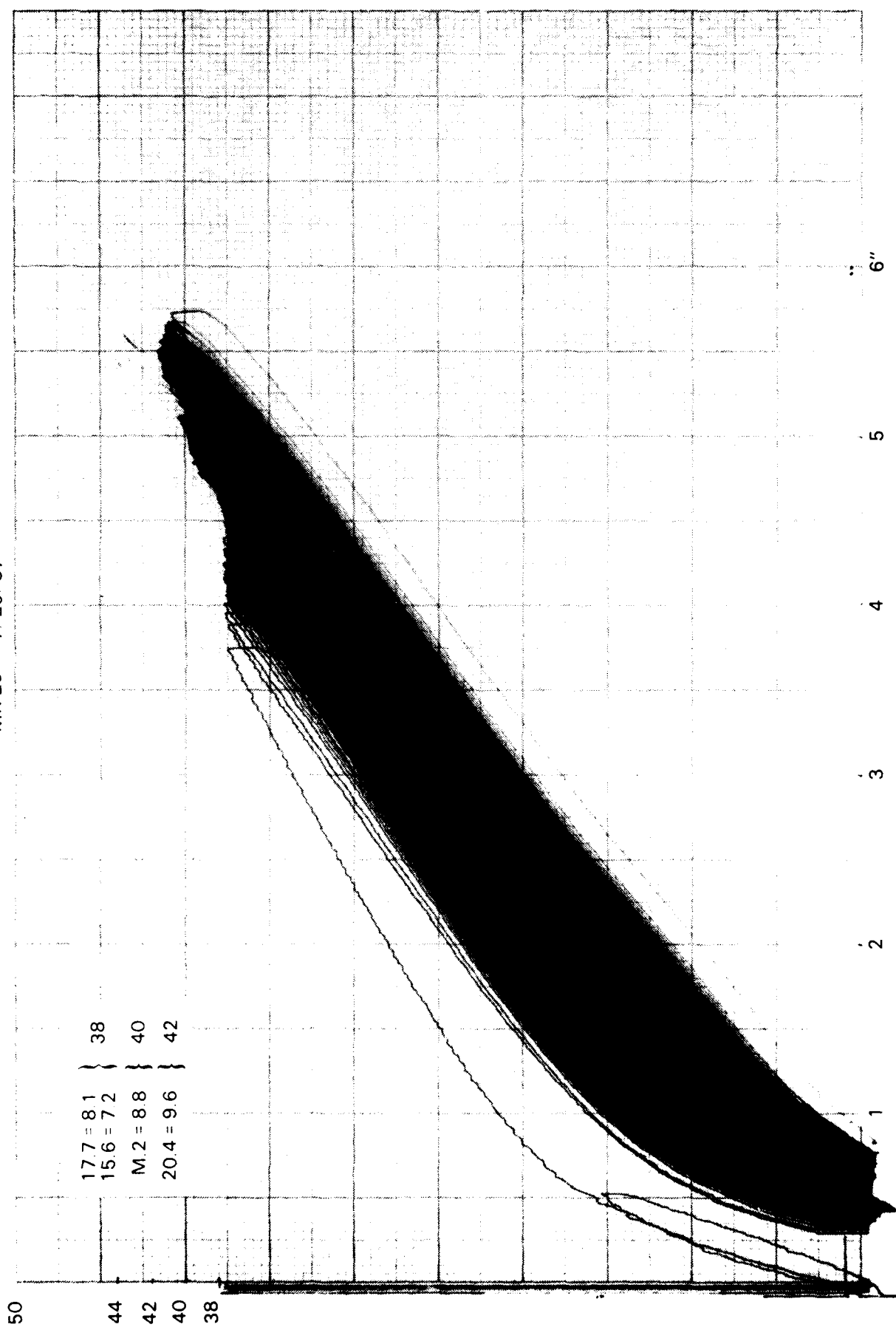


Figure B-258. Continuous deflection response to cyclic load on MK29.

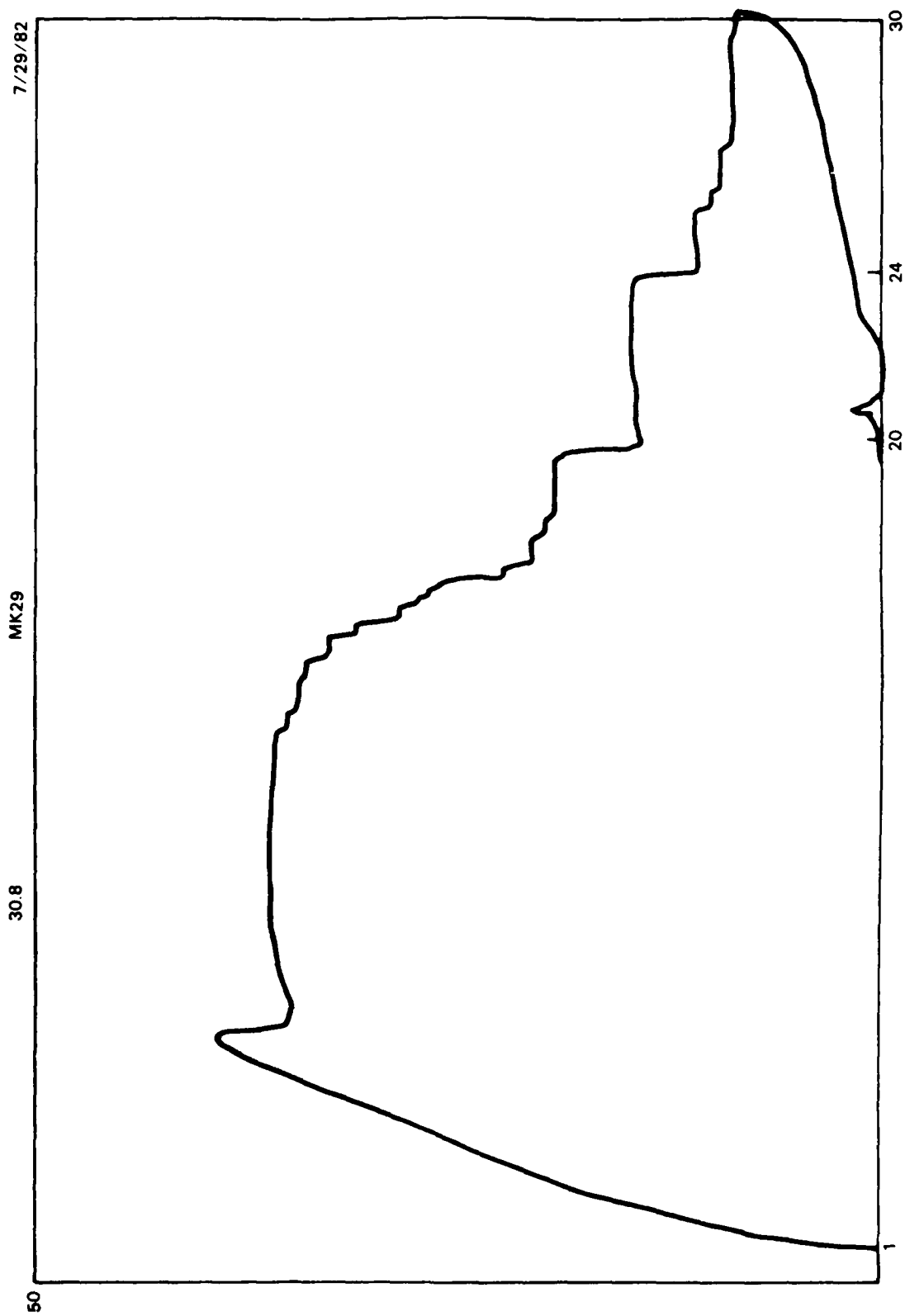


Figure B-259. Final cycling deflection on MK29.

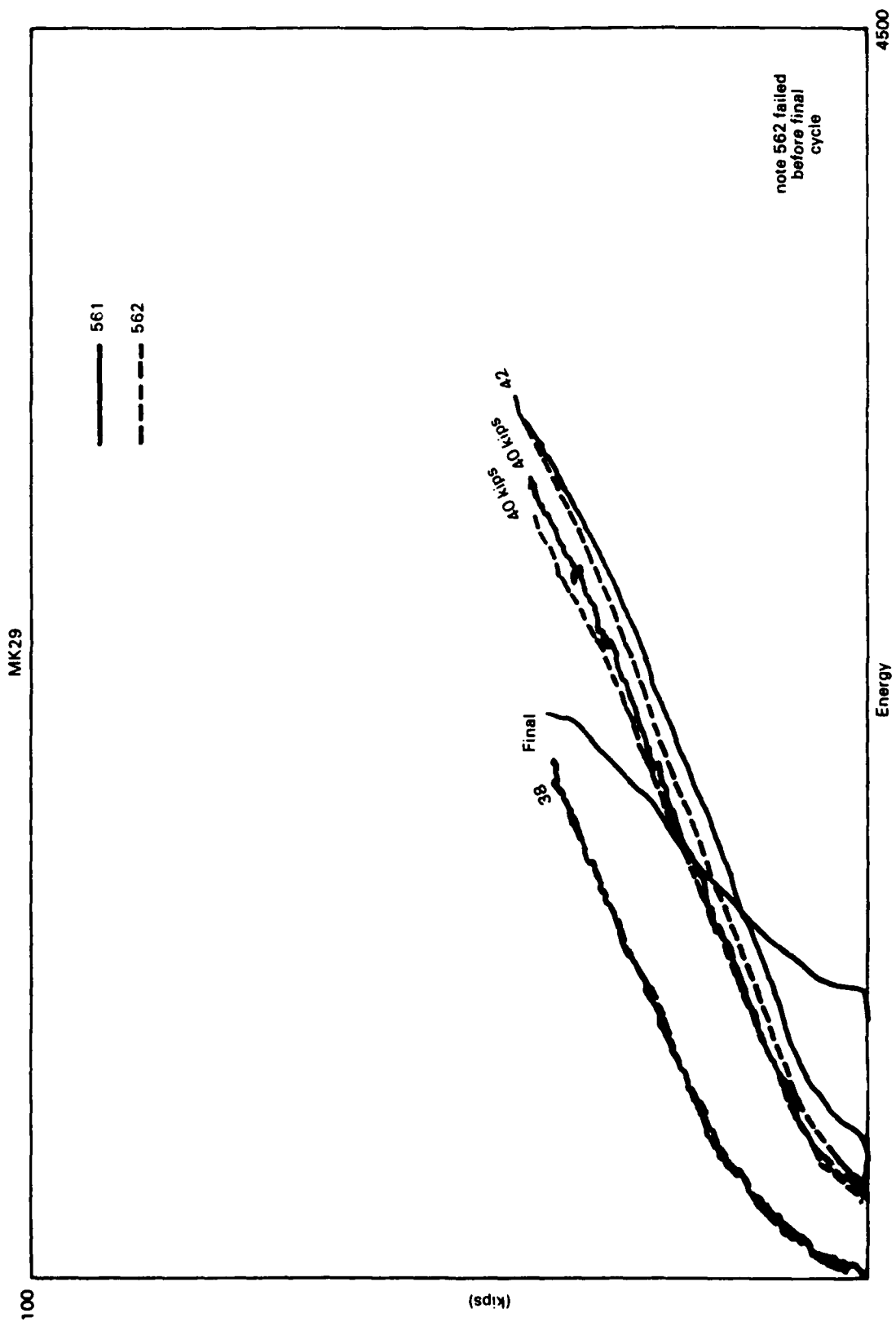


Figure B-260. Strain gage plot of MK29.

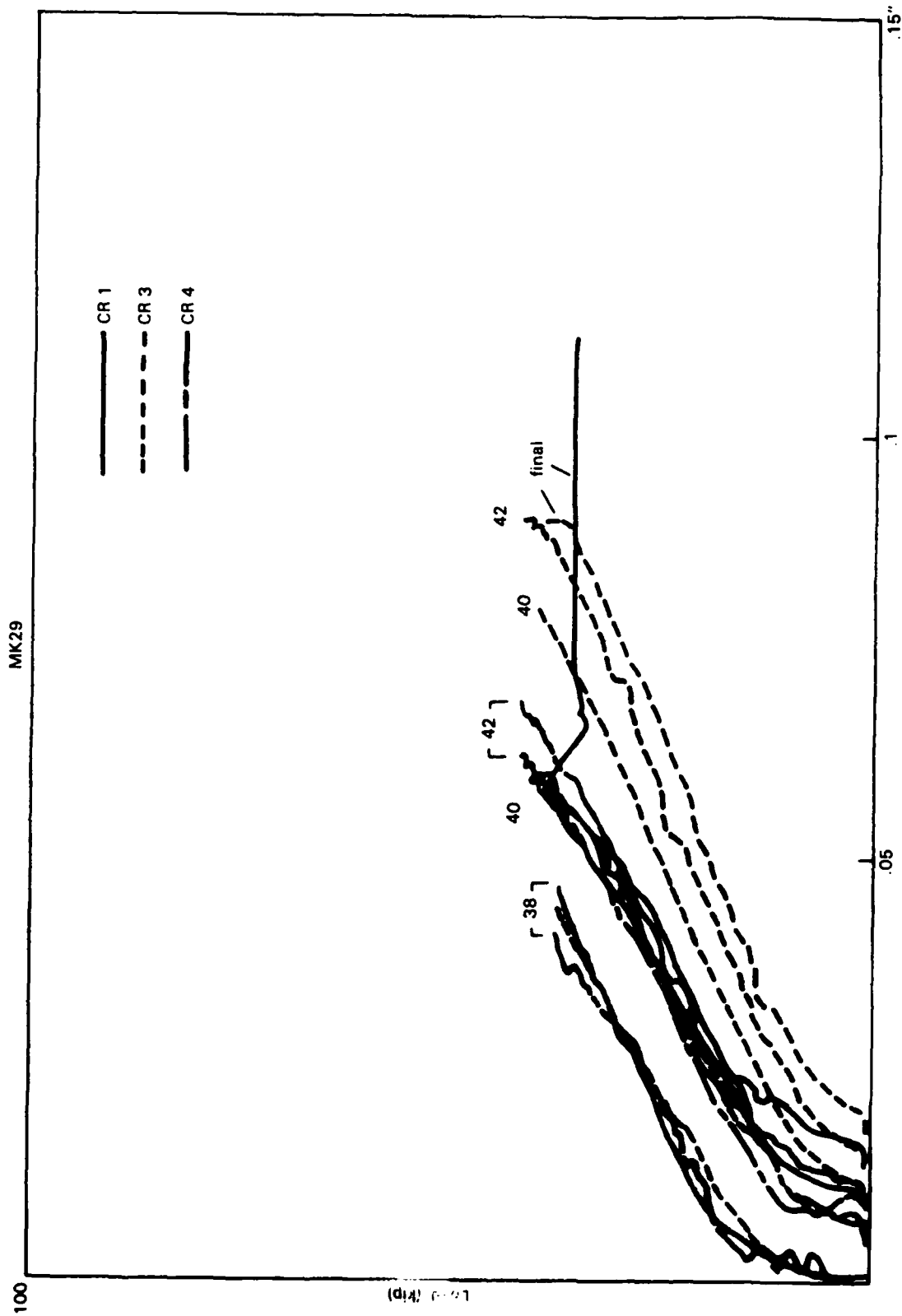


Figure B-261. Crack opening on MK29.

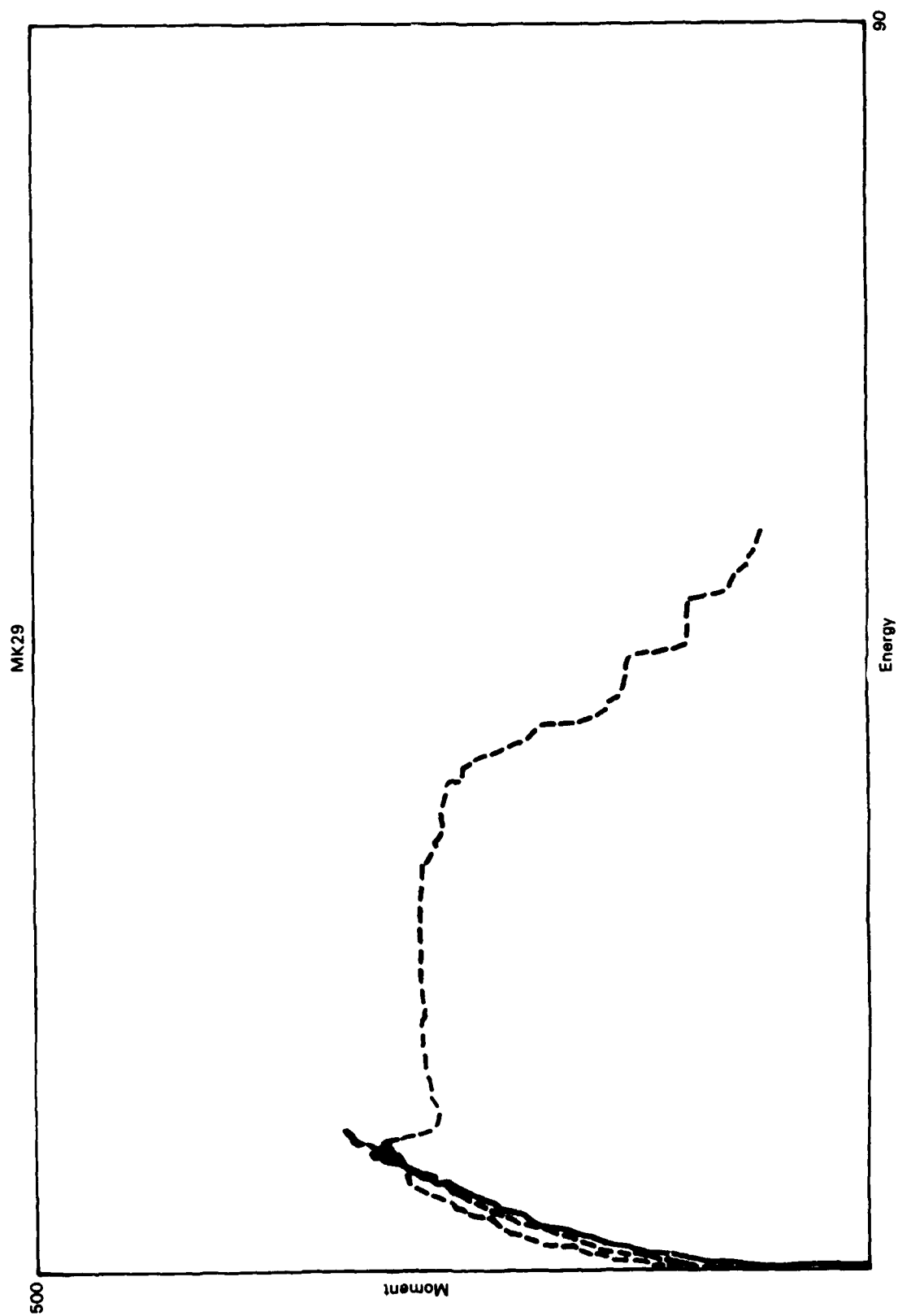


Figure B-262. Moment-energy plot for MK29.

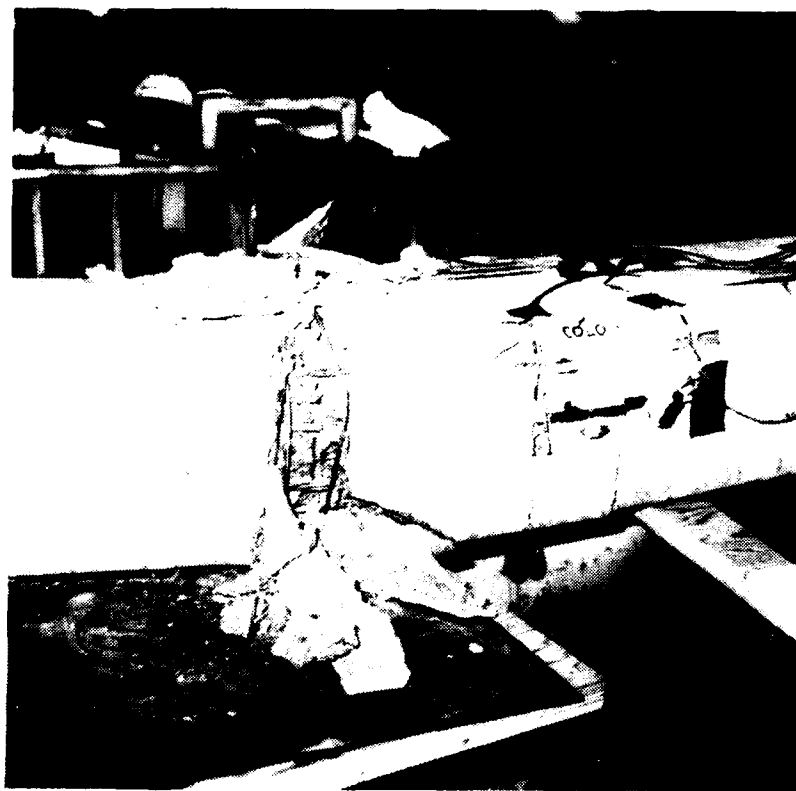


Figure B-263. Tension face after failure.

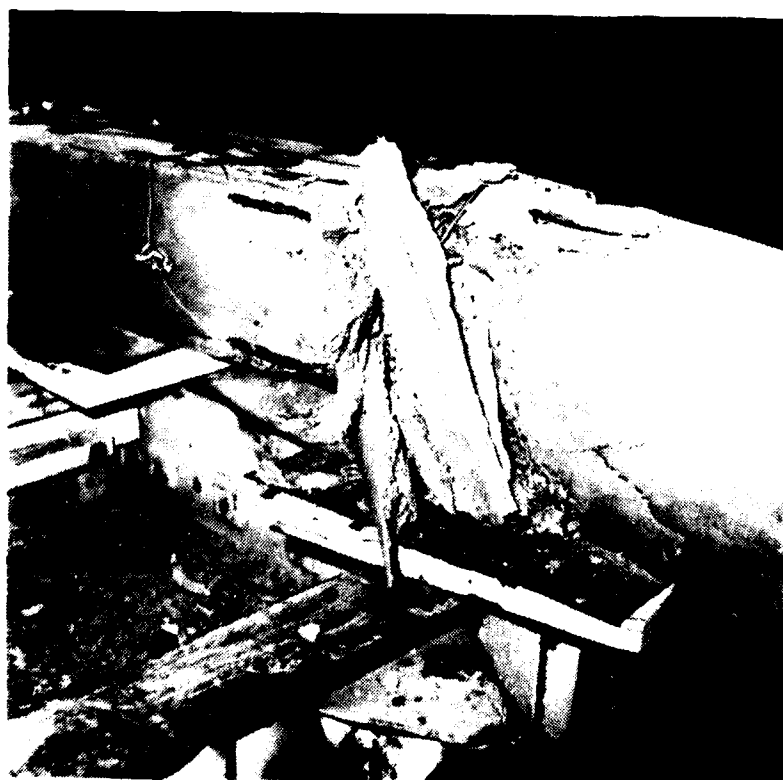


Figure B-264. Compression face after failure of COL01.

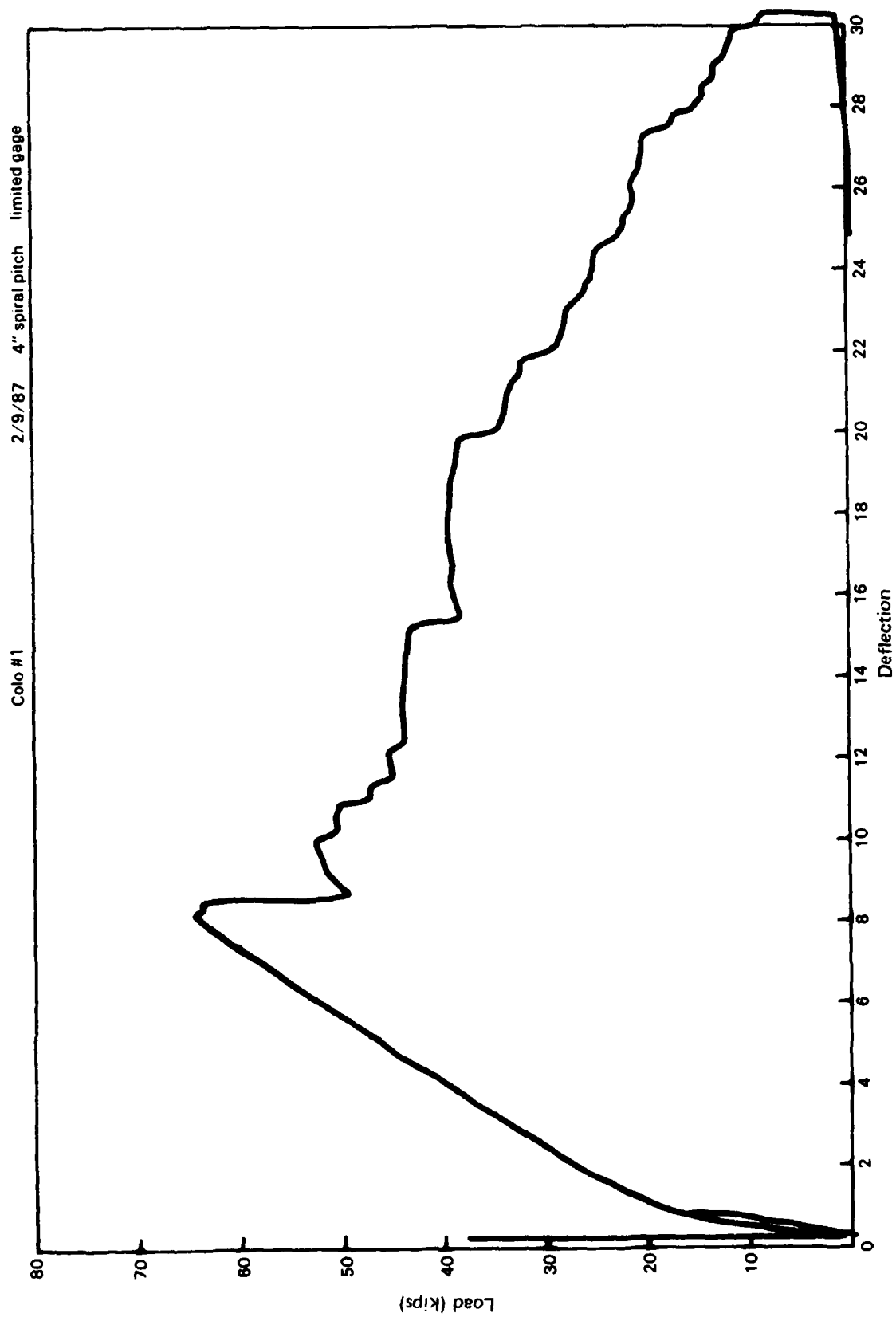


Figure B-265. Load-deflection response of COL01.

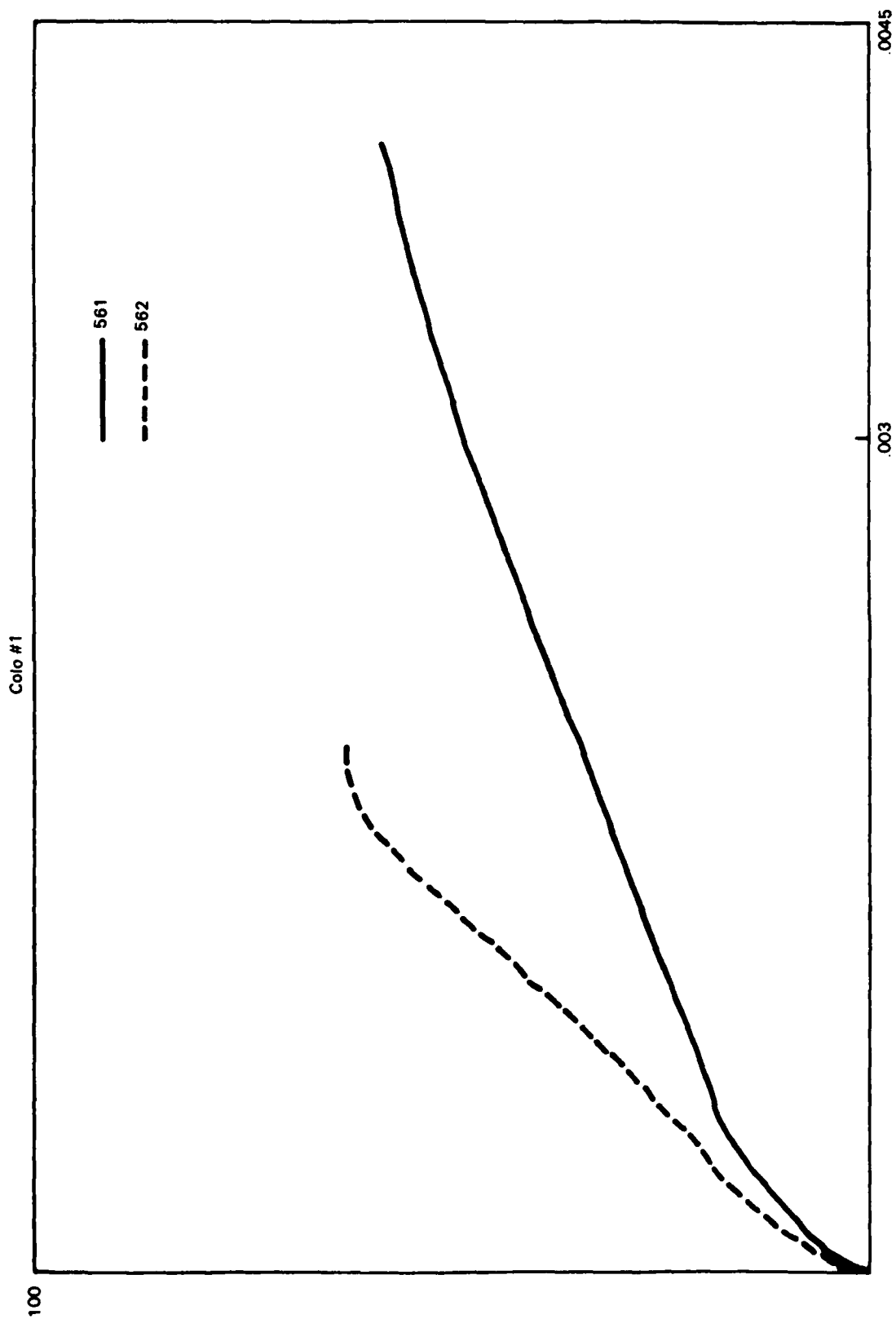


Figure B-266. Strain gage plots of COL01.

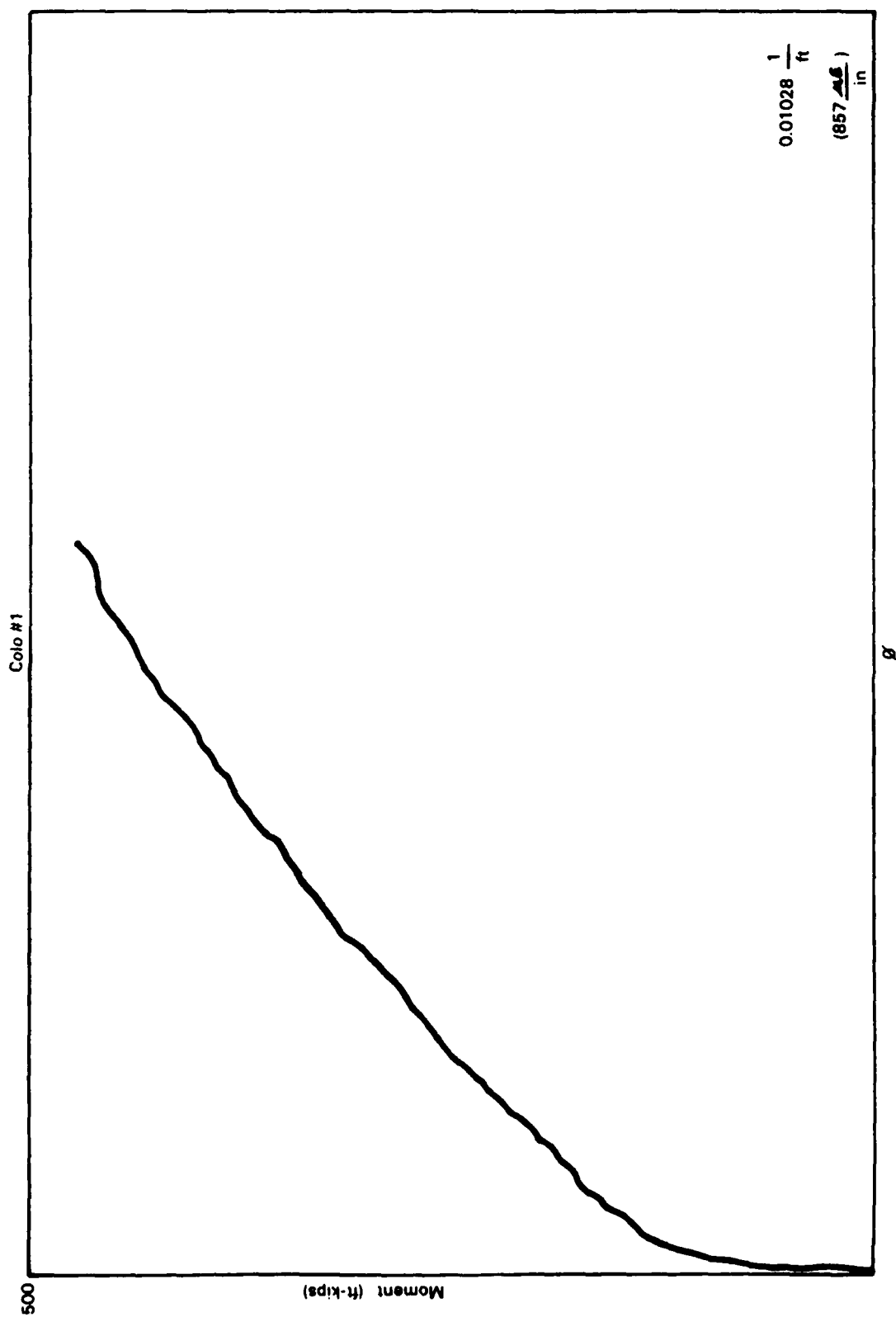


Figure B-267. Moment-curvature plot of COL01.

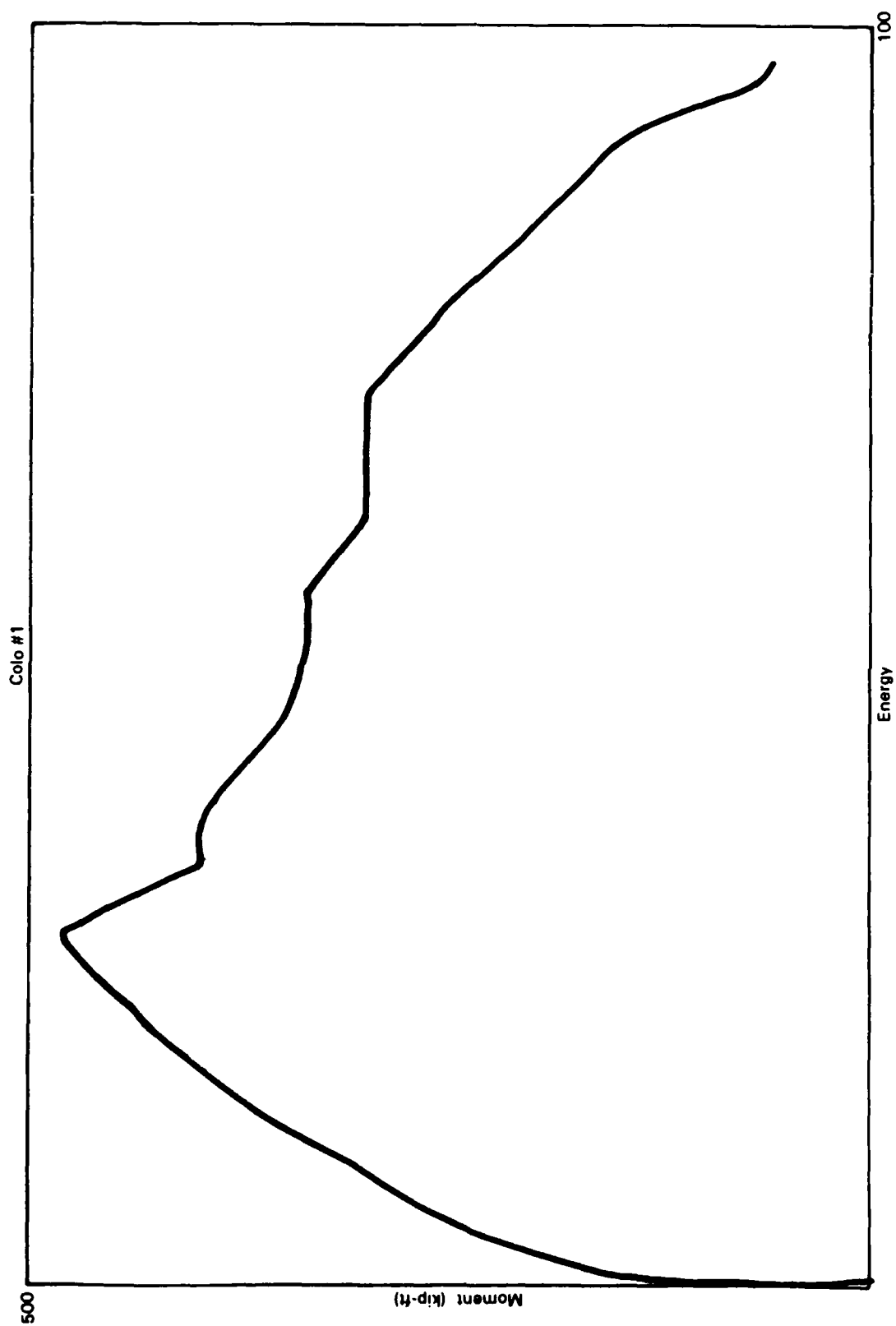


Figure B-268. Moment-energy plot for COL01.

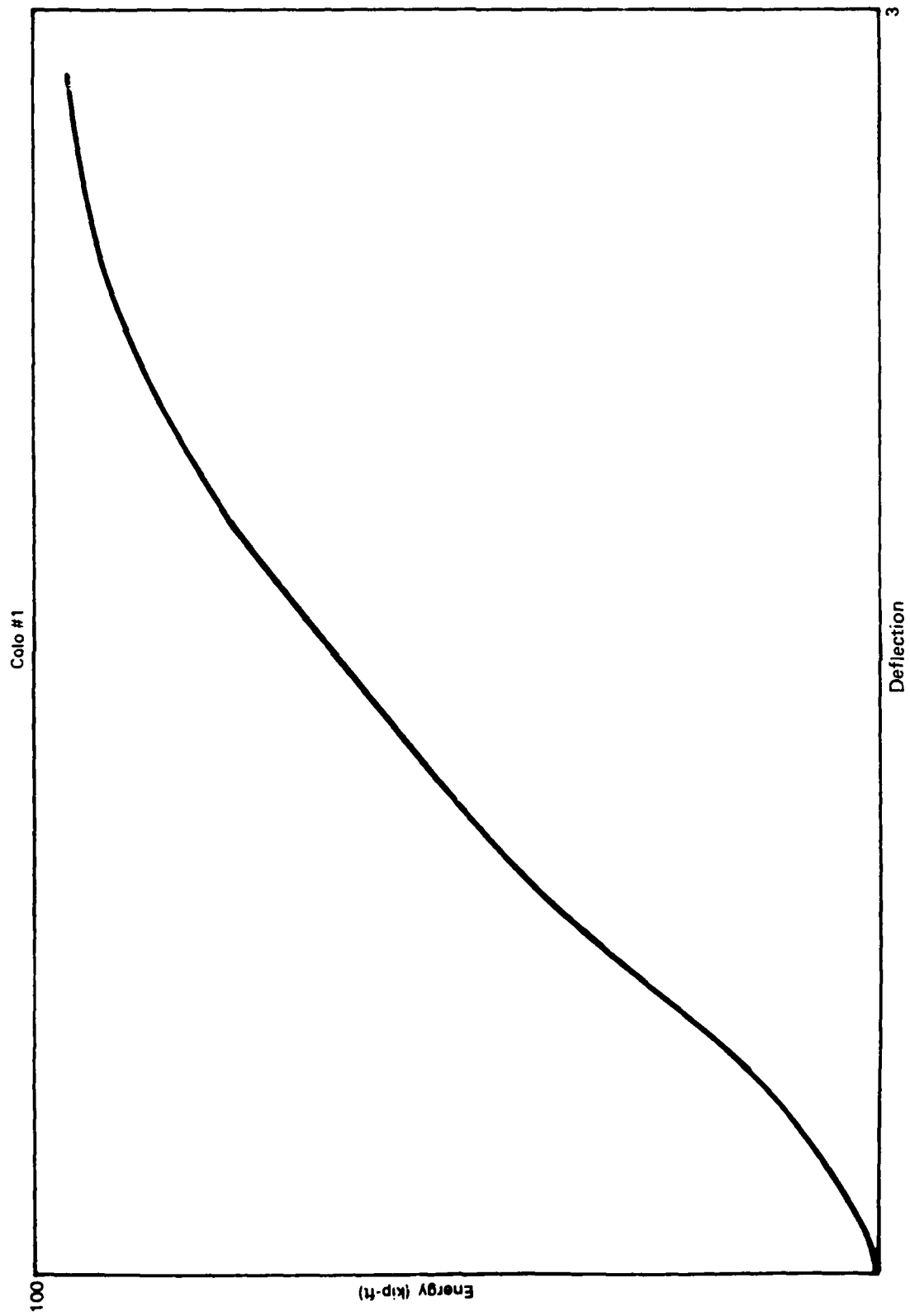


Figure B-269. Energy-deflection plot of COL01.



Figure B-270. Spalling zone on compression face of COL02.



Figure B-271. Tension face of COL02 at failure.

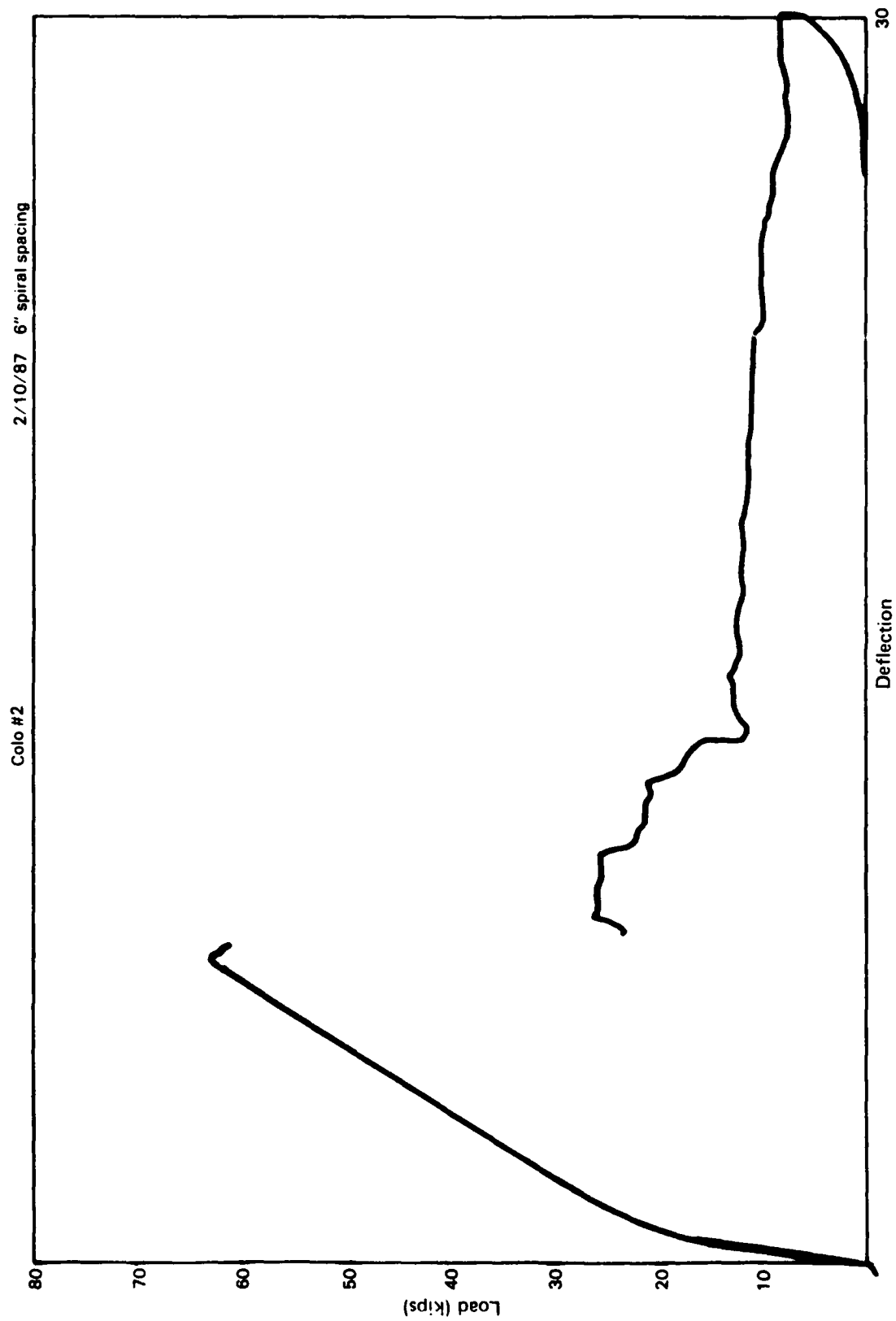


Figure B-272. Load-deflection plot for COL02.

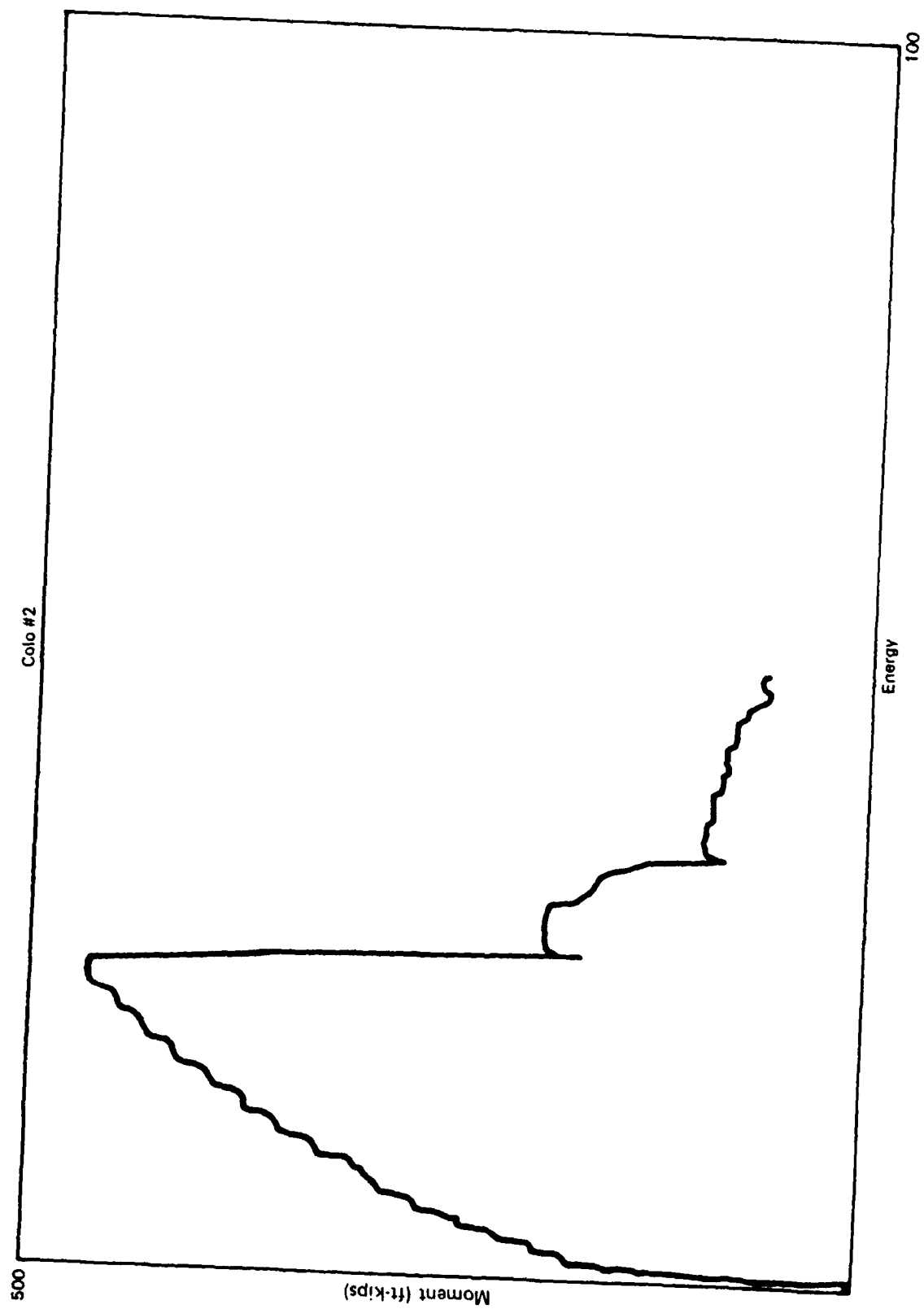


Figure B-273. Moment-energy plot for COL02.

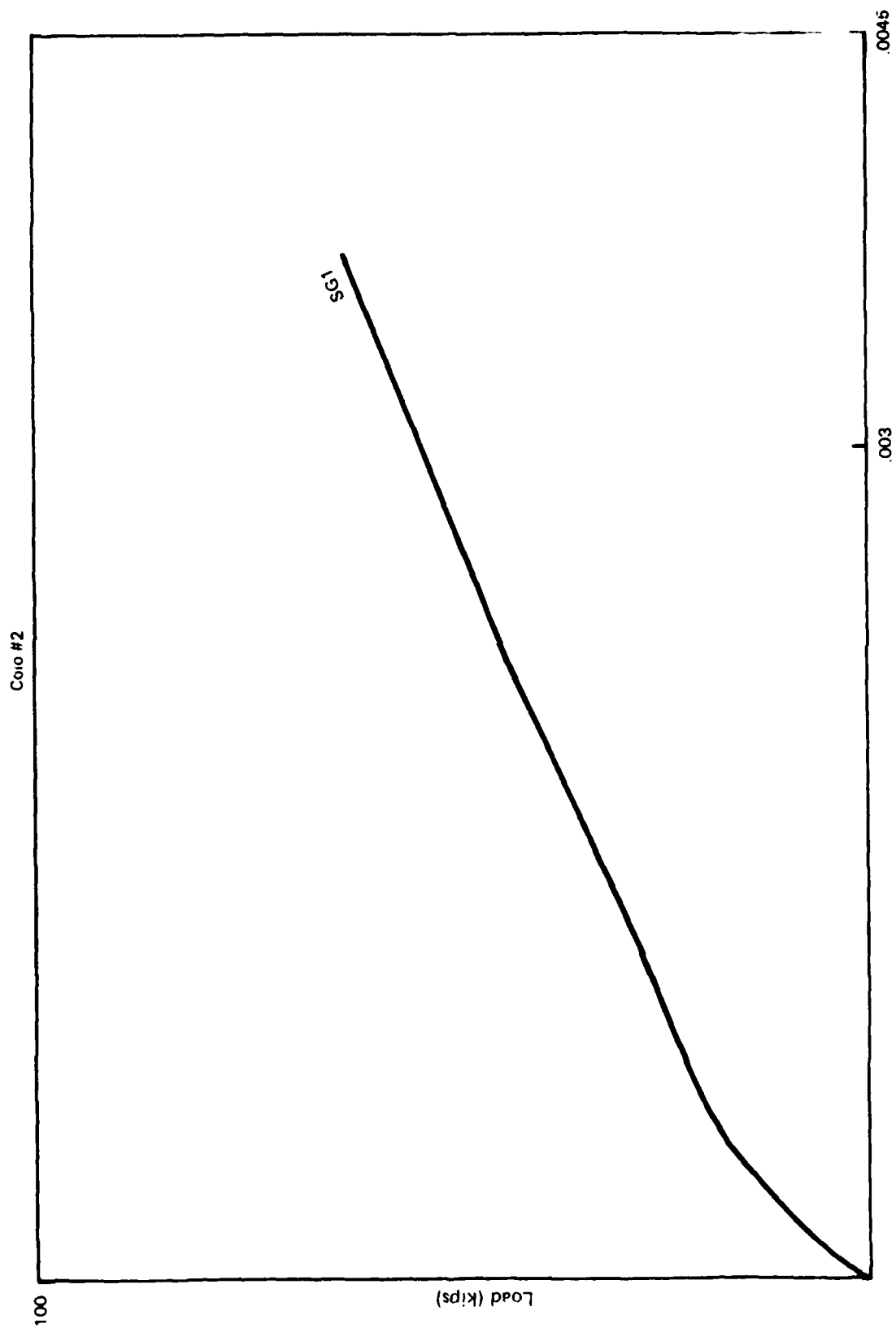


Figure B-274. Strain response of COL02.

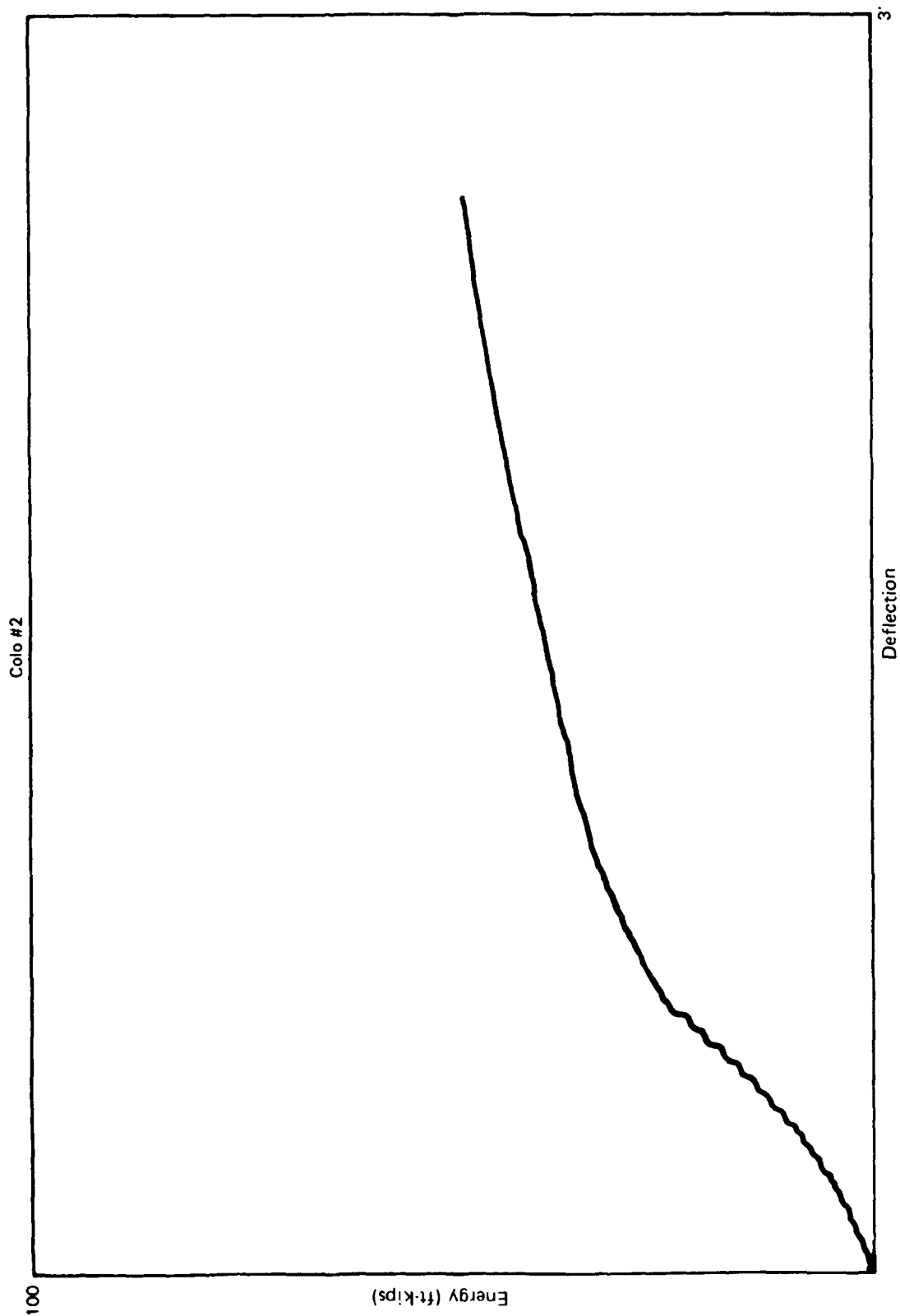


Figure B-275. Energy-deflection plot of COL02.

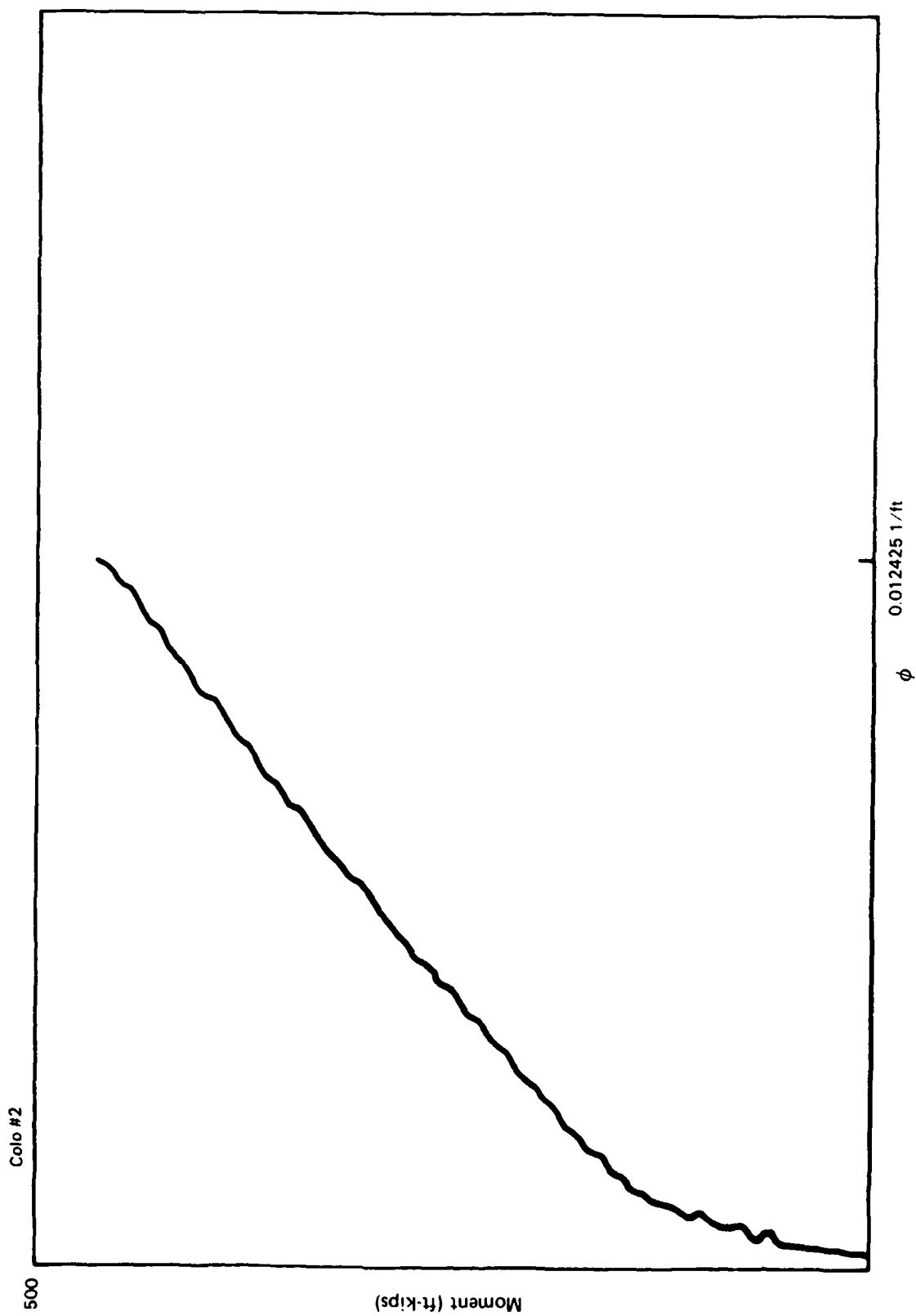


Figure B-276. Moment-curvature plot for COL02.



Figure B-277. Compression zone spall of COL03.



Figure B-278. Tension face of COL03 after failure.

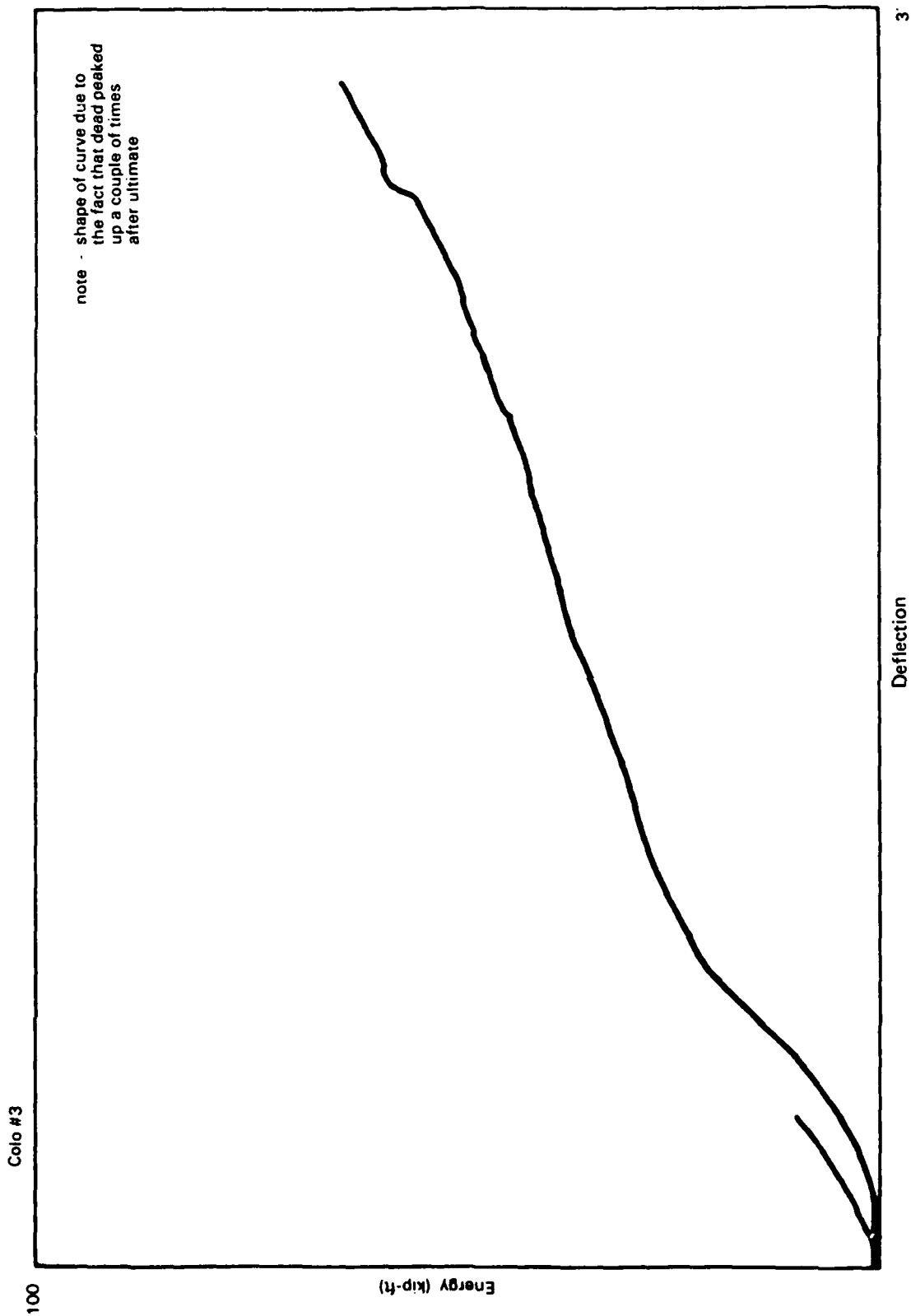


Figure B-279. Energy-deflection plot of COL03.

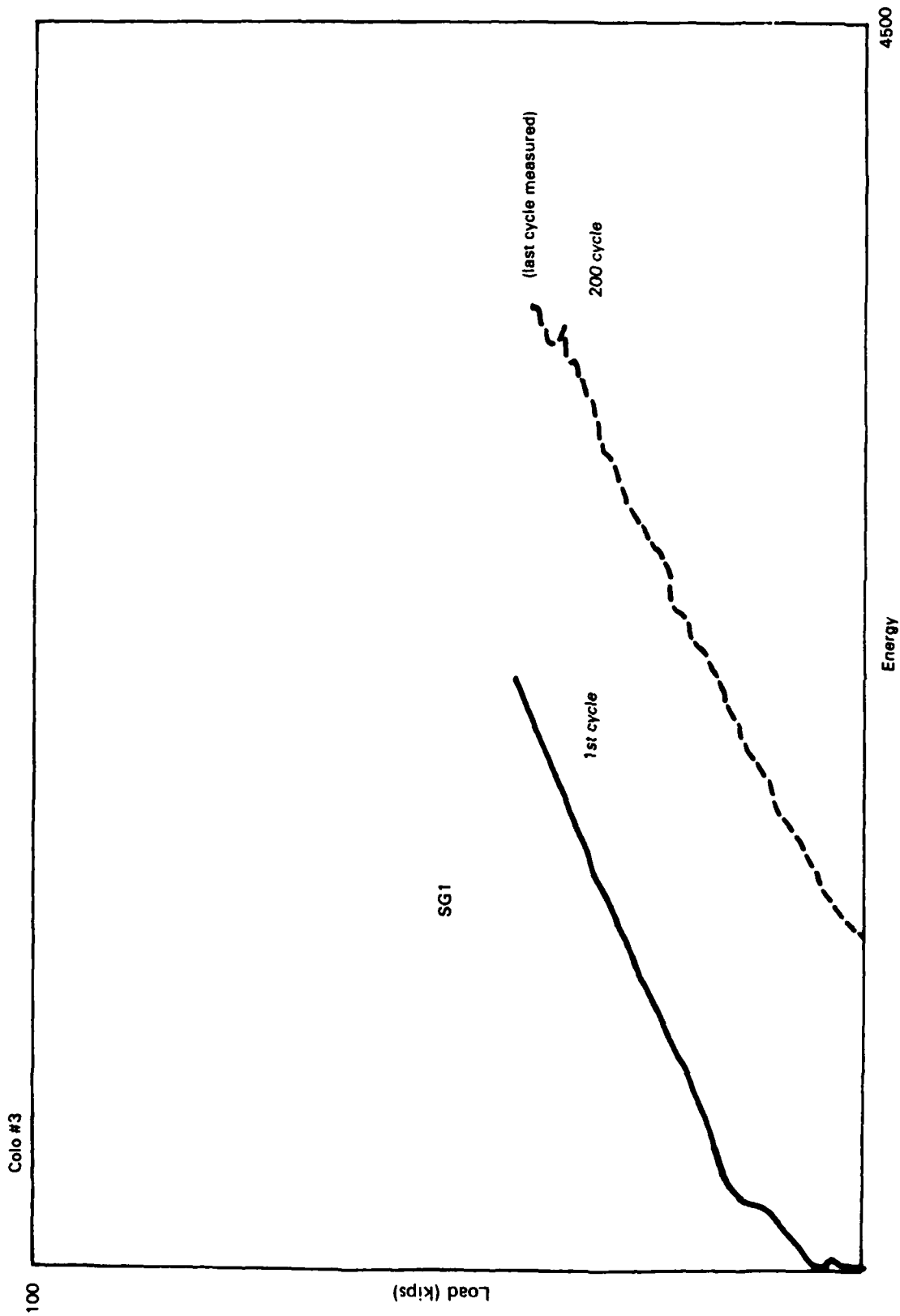


Figure B-280. Strain gage results from COL03.

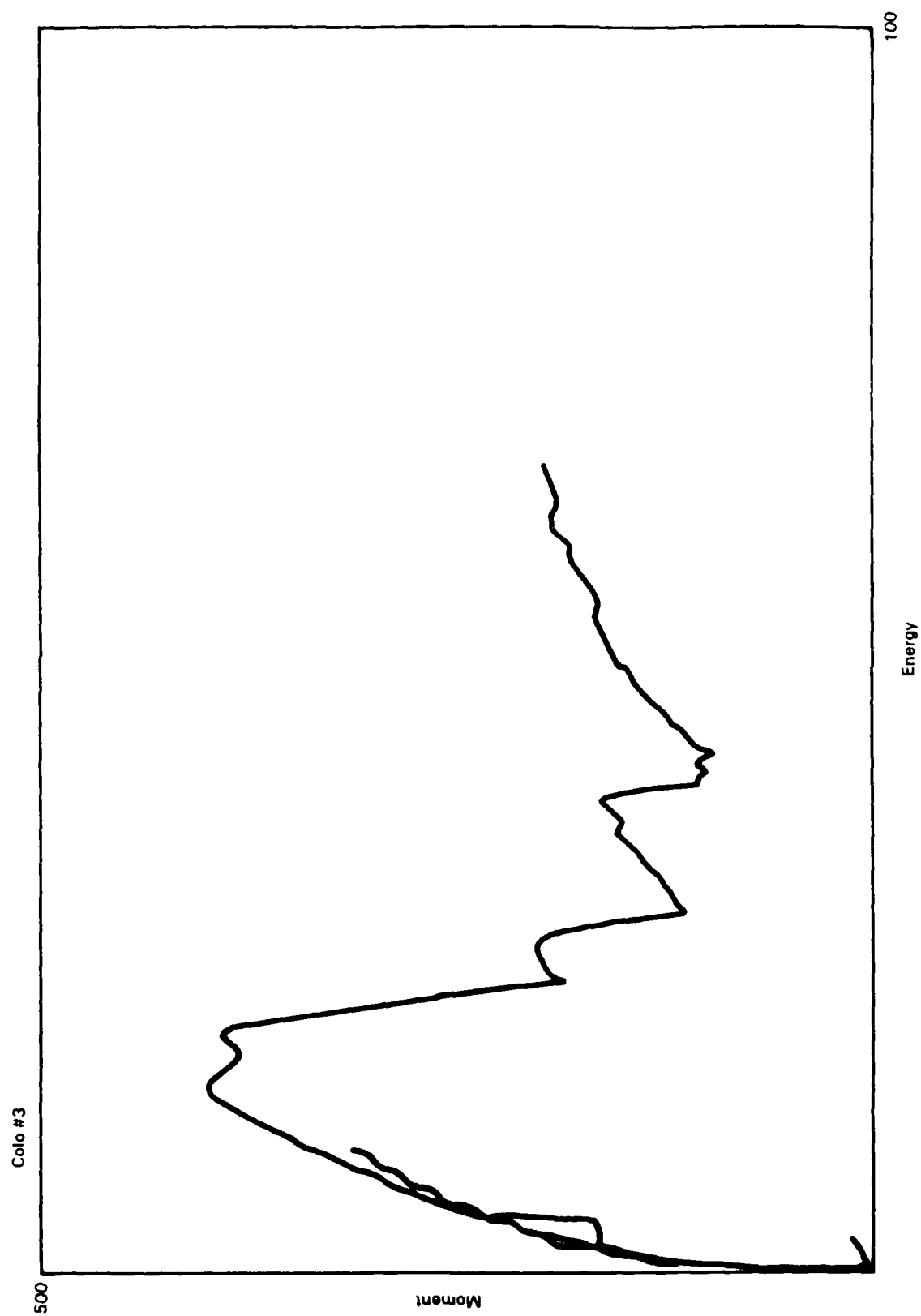


Figure B-281. Moment-energy curvature of COL03.

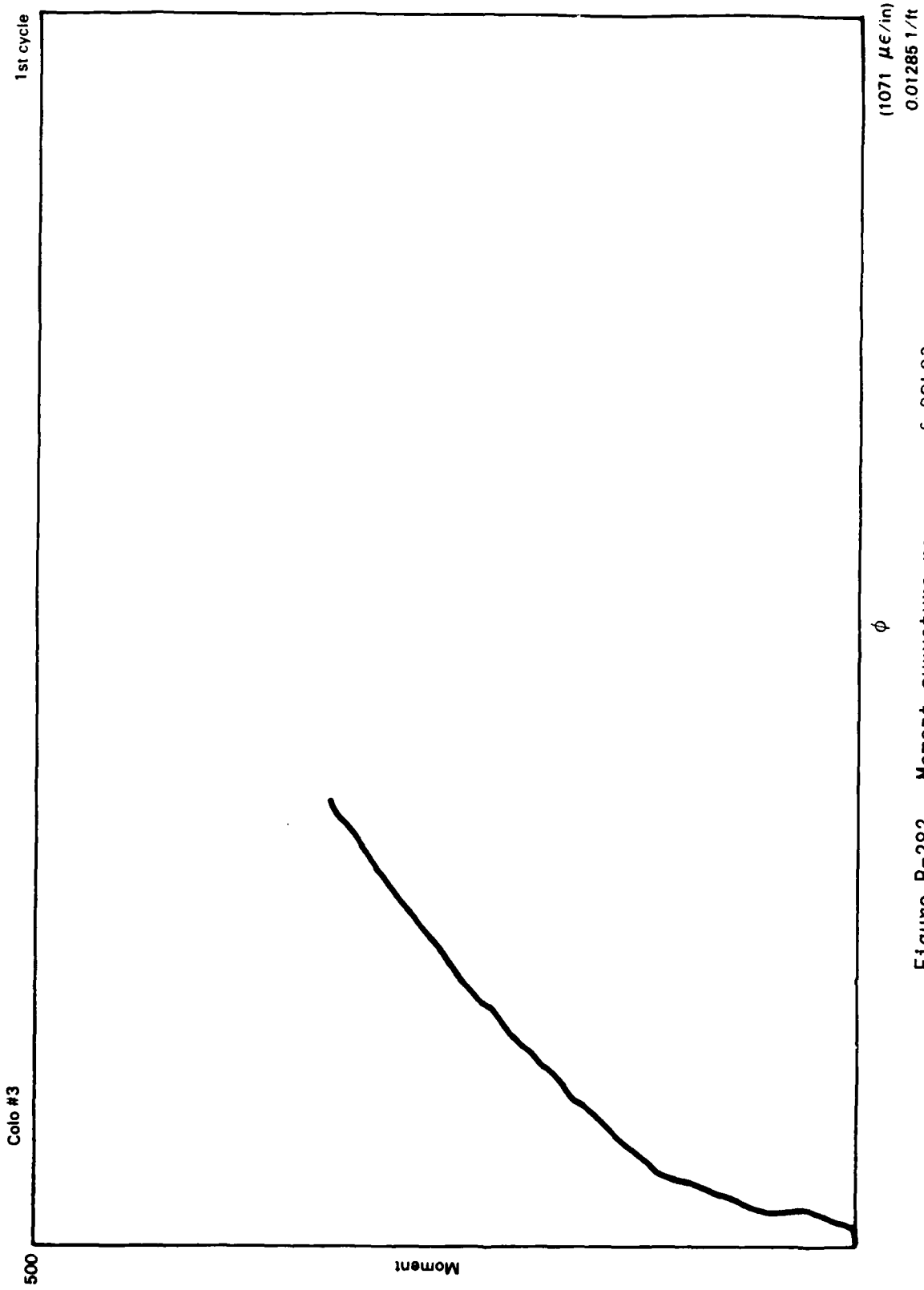


Figure B-282. Moment-curvature response of COL03.

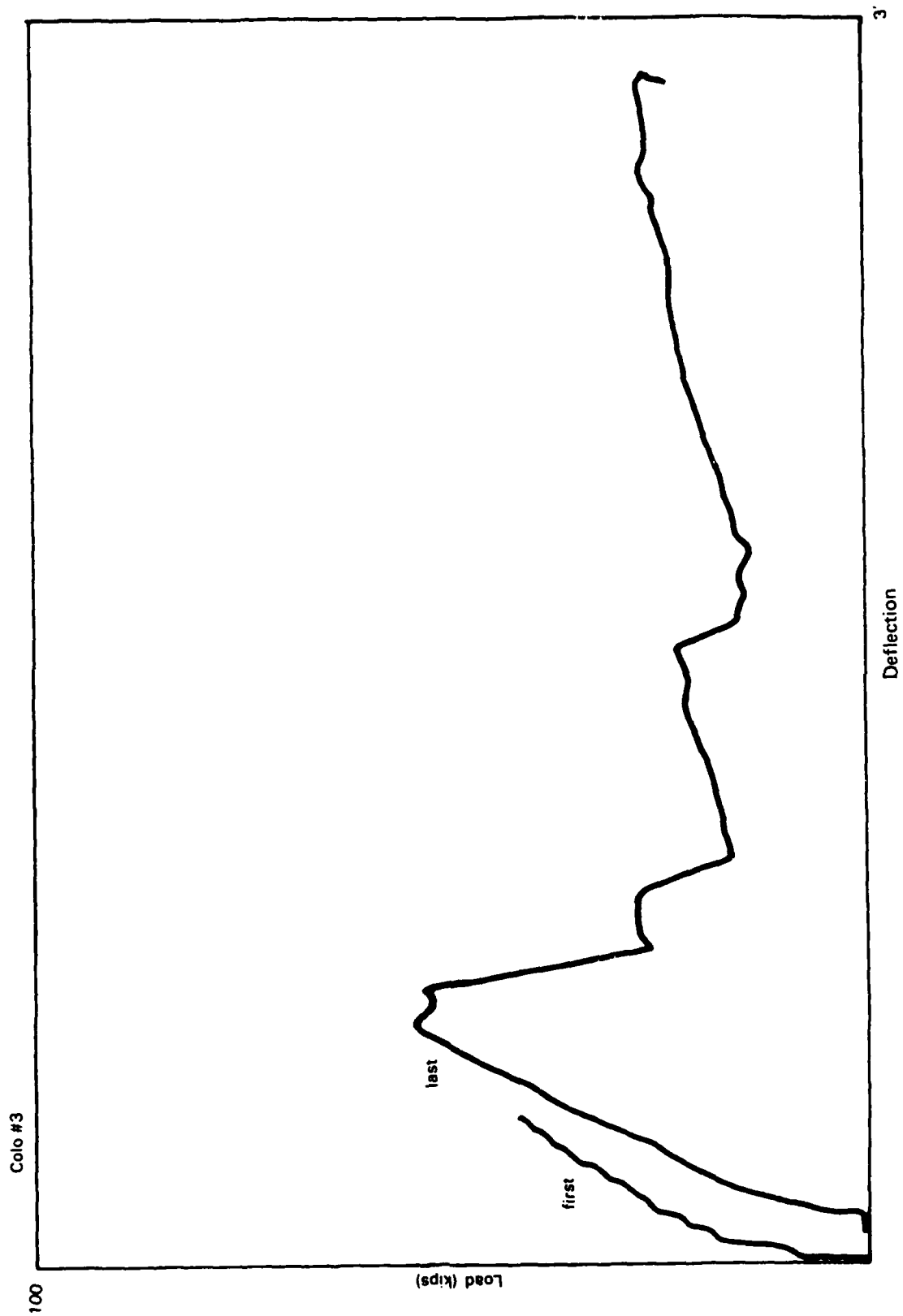


Figure B-283. Load-deflection plot of first and last cycle of COL03.

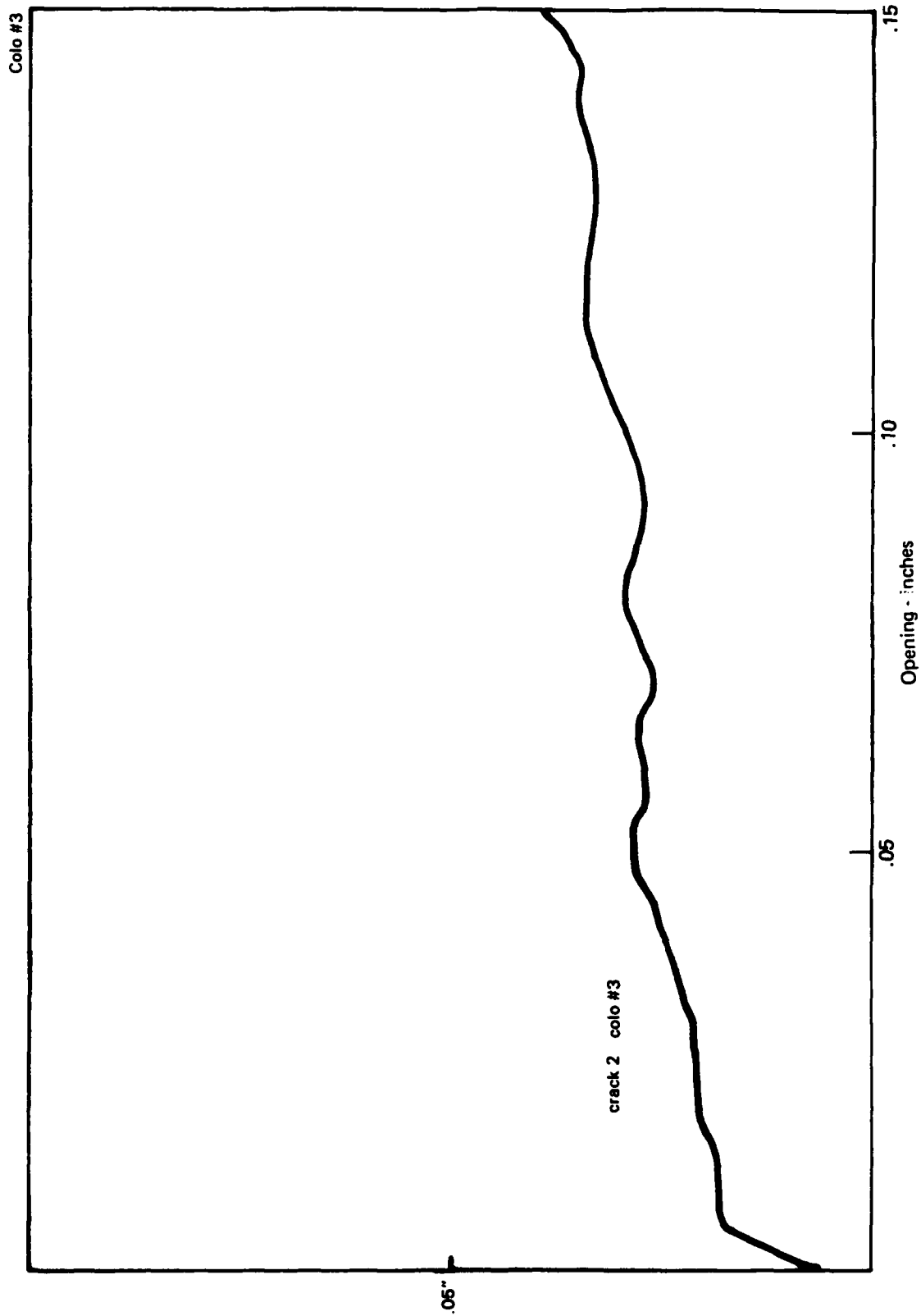


Figure B-284. Residual crack opening at load point of COL03.

Colo #3 2/12/87

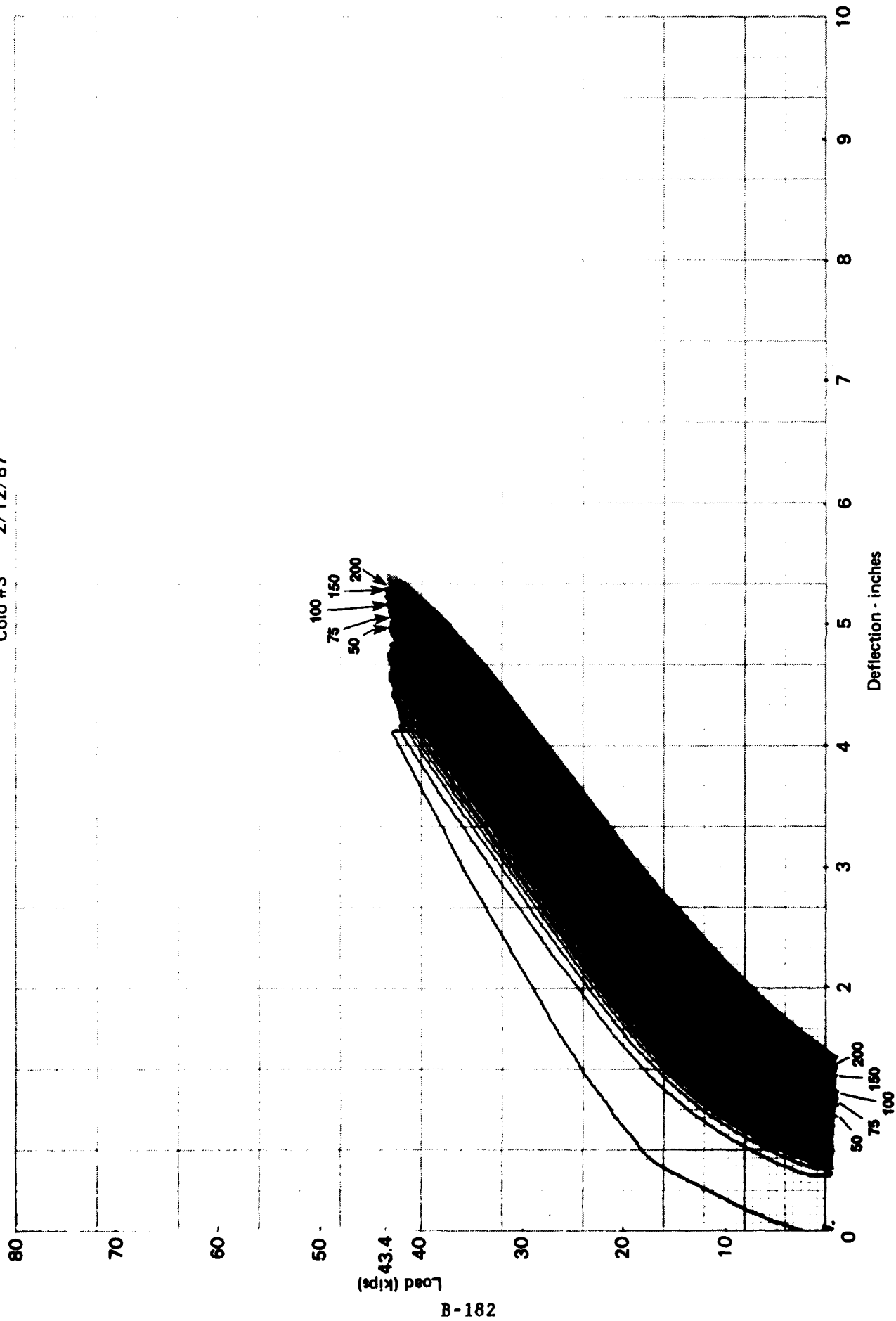


Figure B-285. Continuous deflection response of COL03 to cyclic load.

DISTRIBUTION LIST

AFESC TIC (library), Tyndall AFB, FL
 ARMY CECOM R&D Tech Lib, Ft Monmouth, NJ
 ARMY CERL CECER-EME (Hayes), Champaign, IL; Library, Champaign, IL
 ARMY CRREL A. Iskandar, Hanover, NH
 ARMY ENGR DIST LMVCO-A/Bentley, Vicksburg, MS; Library, Seattle, WA; Phila, Lib, Philadelphia, PA
 ARMY EWES GP-EC (Webster), Vicksburg, MS; Library, Vicksburg MS; WESCD (TW Richardson),
 Vicksburg, MS; WESCD-P (Melby), Vicksburg, MS; WESCV-Z (Whalin), Vicksburg, MS; WESCW-D,
 Vicksburg, MS; WESGP-E, Vicksburg, MS; WESGP-EM (CJ Smith), Vicksburg, MS
 ARMY MMRC DRXMR-SM (Lenoe), Watertown, MA
 BUREAU OF RECLAMATION D-1512 (GS DePuy), Denver, CO; Smoak, Denver, CO
 CBC Library, Davisville, RI; PWO (Code 400), Gulfport, MS; PWO (Code 80), Port Hueneme, CA; PWO,
 Davisville, RI; Tech Library, Gulfport, MS
 CBU 411, OIC, Norfolk, VA
 CNA Tech Library, Alexandria, VA
 CNO DCNO, Logs, OP-424C, Washington, DC
 COMDT COGARD Library, Washington, DC
 COMFAIR Med, SCE, Naples, Italy
 COMNAVACT G.T. Clifford, London, UK; PWO, London, UK
 DIRSSP Tech Lib, Washington, DC
 DTIC Alexandria, VA
 DTRCEN Code 172, Bethesda, MD; Code 4111, Bethesda, MD; Code 42, Bethesda MD
 EFA-SW Code 101.1, San Diego, CA
 LIBRARY OF CONGRESS Sci & Tech Div, Washington, DC
 MARCORBASE Code 405, Camp Lejeune, NC; Code 406, Camp Lejeune, NC; PWO, Camp Lejeune, NC
 MARITIME ADMIN MAR-770 (Corkrey), Washington, DC; MMA, Library, Kings Point, NY
 MCRDAC AROICC, Quantico, VA
 NAS Code 18700, Brunswick, ME; Code 8, Patuxent River, MD; PWO, Key West, FL; PWO, South
 Weymouth, MA; SCE, Norfolk, VA
 NAVAIRTESTCEN PWO, Patuxent River, MD
 NAVCAMS MED, SCE, Naples, Italy
 NAVCOASTSYSCEN Tech Library, Panama City, FL
 NAVFAC PWO, Oak Harbor, WA
 NAVFACENGCOM Code 00, Alexandria, VA; Code 03, Alexandria, VA; Code 03T (Essoglou), Alexandria,
 VA; Code 04A, Alexandria, VA; Code 04A1, Alexandria, VA; Code 04A1D, Alexandria, VA; Code 04A3,
 Alexandria, VA; Code 04A3C, Alexandria, VA; Code 04A4E, Alexandria, VA; Code 04B3, Alexandria,
 VA; Code 051A, Alexandria, VA; Code 0631, Alexandria, VA; Code 07, Alexandria, VA; Code 09M124
 (Lib), Alexandria, VA; Code 1002B, Alexandria, VA; Code 163, Alexandria, VA
 NAVFACENGCOM - CHES DIV. Code 112.1, Washington, DC; FPO-1PL, Washington, DC
 NAVFACENGCOM - LANT DIV. Code 1112, Norfolk, VA; Code 403, Norfolk, VA; Library, Norfolk, VA
 NAVFACENGCOM - NORTH DIV. CO, Philadelphia, PA; Code 04, Philadelphia, PA; Code 04AL,
 Philadelphia, PA; Code 11, Philadelphia, PA; Code 111, Philadelphia, PA; Code 202.2, Philadelphia, PA;
 Code 408AF, Philadelphia, PA
 NAVFACENGCOM - PAC DIV. Code 09P, Pearl Harbor, HI; Code 2011, Pearl Harbor, HI; Library, Pearl
 Harbor, HI
 NAVFACENGCOM - SOUTH DIV. Code 04A3, Charleston, SC; Code 0525, Charleston, SC; Code 1021F,
 Charleston, SC; Code 102H, Charleston, SC; Code 4023, Charleston, SC; Code 405, Charleston, SC; Code
 406, Charleston, SC; Library, Charleston, SC
 NAVFACENGCOM - WEST DIV. 09P/20, San Bruno, CA; Code 04A2.2 (Lib), San Bruno, CA; Code 04B, San
 Bruno, CA; Code 102, San Bruno, CA; Pac NW Br Offc, Code C/42, Silverdale, WA; Pac NW Br Offc,
 Code C/50, Silverdale, WA
 NAVFACENGCOM CONTRACTS OICC, Guam
 NAVHOSP SCE, Yokosuka, Japan
 NAVMAG SCE, Guam, Mariana Islands
 NAVOCEANO Library, Bay St Louis, MS
 NAVOCEANSYSCEN Code 9642B, San Diego, CA
 NAVPGSCOL Code 68 (C.S. Wu), Monterey, CA; Code 68WY (Wyland), Monterey, CA
 NAVPHIBASE SCE, San Diego, CA
 NAVSEASYS COM Code 56W23 (J Coon), Washington, DC; Code PMS296L22 (J Rekas), Washington, DC
 NAVSECGRUACT PWO, Sabana Seca, PR
 NAVSHIPREPFAC Library, Guam

NAVSHIPYD CO, Philadelphia, PA; Code 134, Pearl Harbor, HI; Code 202.4, Long Beach, CA; Code 202.5 (Library), Bremerton, WA; Code 308.3, Pearl Harbor, HI; Code 382.3, Pearl Harbor, HI; Code 420, Long Beach, CA; Code 443, Bremerton, WA; Code 903, Long Beach, CA; Library, Portsmouth, NH; Mare Island, Code 106.4, Vallejo, CA; Mare Island, Code 202.13, Vallejo, CA; Mare Island, Code 280, Vallejo, CA; Mare Island, Code 401, Vallejo, CA; Mare Island, Code 421, Vallejo, CA; Mare Island, Code 457, Vallejo, CA; Mare Island, PWO, Vallejo, CA; Norfolk, Code 380, Portsmouth, VA; Norfolk, Code 440, Portsmouth, VA; Norfolk, Code 450-HD, Portsmouth, VA; PWO, Bremerton, WA
 NAVSTA CO, Long Beach, CA; CO, Roosevelt Roads, PR; Engrg Dir, PWD, Rota, Spain; SCE, San Diego, CA; SCE, Subic Bay, RP
 NAVSUPPACT PWO, Naples, Italy
 NAVSWC PWO, Dahlgren, VA
 NAVWPNSTA Earle, PWO (Code 09B), Colts Neck, NJ
 NBS Bldg Mat Div (Mathey), Gaithersburg, MD; Bldg Tech (M. McKnight), Gaithersburg, MD
 NETC PWO, Newport, RI
 NETPMSA Tech Library, Pensacola, FL
 NOAA Library, Rockville, MD
 NRL Code 2530.1, Washington, DC; Code 6123 (Dr Brady), Washington, DC
 OCNR Code 1121 (EA Silva), Arlington, VA; Code 1234, Arlington, VA
 PWC ACE Office, Norfolk, VA; Code 10, Oakland, CA; Code 101 (Library), Oakland, CA; Code 101, Great Lakes, IL; Code 1011, Pearl Harbor, HI; Code 110, Oakland, CA; Code 123-C, San Diego, CA; Code 30, Norfolk, VA; Code 400, Guam, Mariana Islands; Code 400, Oakland, CA; Code 400, Pearl Harbor, HI; Code 400, San Diego, CA; Code 412, San Diego, CA; Code 420, Great Lakes, IL; Code 420, Oakland, CA; Code 420B (Waid), Subic Bay, RP; Code 421 (Kaya), Pearl Harbor, HI; Code 421 (Quin), San Diego, CA; Code 421 (Reynolds), San Diego, CA; Code 422, San Diego, CA; Code 423, San Diego, CA; Code 424, Norfolk, VA; Code 430 (Kyi), Pearl Harbor, HI
 PWC Code 430 (Kyi), Pearl Harbor, HI
 PWC Code 500, Norfolk, VA; Code 500, Oakland, CA; Code 505A, Oakland, CA; Code 590, San Diego, CA; Code 615, Guam, Mariana Islands; Code 700, San Diego, CA; Library (Code 134), Pearl Harbor, HI; Library, Guam, Mariana Islands; Library, Norfolk, VA; Library, Pensacola, FL; Library, Yokosuka, Japan; Tech Library, Subic Bay, RP
 SUBASE Bangor, PWO (Code 8323), Bremerton, WA; SCE, Pearl Harbor, HI
 USNA Mech Engrg Dept (Hasson), Annapolis, MD; Ocean Engrg Dept (McCormick), Annapolis, MD
 CALIF MARITIME ACADEMY Library, Vallejo, CA
 CALIFORNIA Nav & Ocean Dev (Armstrong), Sacramento, CA
 CITY OF MONTEREY Const Mgr (Reichmuth), Monterey, CA
 CLARKSON COLL OF TECH CE Dept (Batson), Potsdam, NY
 CLEVELAND STATE UNIVERSITY CE Dept (Akinmusuru), Cleveland, OH
 COLORADO STATE UNIVERSITY CE Dept (Criswell), Ft Collins, CO
 CORNELL UNIVERSITY Civil & Environ Engrg (Dr. Kulhawy), Ithaca, NY; Library, Ithaca, NY
 DUKE UNIVERSITY CE Dept (Muga), Durham, NC
 FLORIDA ATLANTIC UNIVERSITY Ocean Engrg Dept (Hart), Boca Raton, FL; Ocean Engrg Dept (McAllister), Boca Raton, FL
 FLORIDA INST OF TECH CE Dept (Kalajian), Melbourne, FL
 INSTITUTE OF MARINE SCIENCES Dir, Morehead City, NC; Library, Port Aransas, TX
 LEHIGH UNIVERSITY Linderman Library, Bethlehem, PA
 LONG BEACH PORT Engrg Dir (Allen), Long Beach, CA
 LOS ANGELES COUNTY PW Dept (J Vicelja), Alhambra, CA
 MAINE MARITIME ACADEMY Lib, Castine, ME
 MICHIGAN TECH UNIVERSITY CE Dept (Haas), Houghton, MI
 MIT Engrg Lib, Cambridge, MA; Lib, Tech Reports, Cambridge, MA
 NATL ACADEMY OF SCIENCES NRC, Naval Studies Bd, Washington, DC
 NORTHWESTERN UNIV CE Dept (Dowding), Evanston, IL
 NY CITY COMMUNITY COLLEGE Library, Brooklyn, NY
 OREGON STATE UNIVERSITY CE Dept (Hicks), Corvallis, OR; CE Dept (Yim), Corvallis, OR; Oceanography Scol, Corvallis, OR
 PENNSYLVANIA STATE UNIVERSITY Rsch Lab (Snyder), State College, PA
 PURDUE UNIVERSITY CE Scol (Altschaeffl), W. Lafayette, IN; CE Scol (Leonards), W. Lafayette, IN; Engrg Lib, W. Lafayette, IN
 SAN DIEGO PORT Port Fac, Proj Engr, San Diego, CA
 SAN DIEGO STATE UNIV CE Dept (Noorany), San Diego, CA
 SEATTLE PORT W Ritchie, Seattle, WA
 SEATTLE UNIVERSITY CE Dept (Schwaegler), Seattle, WA
 SOUTHWEST RSCH INST M. Polcyn, San Antonio, TX
 STATE UNIVERSITY OF NEW YORK CE Dept (Reinhorn), Buffalo, NY; CE Dept, Buffalo, NY

TEXAS A&I UNIVERSITY Civil & Mech Engr Dept (Parate), Kingsville, TX
 TEXAS A&M UNIVERSITY CE Dept (Herbich), College Station TX; CE Dept (Machemehl), College Station, TX; CE Dept (Niedzwecki), College Station, TX; CE Dept (Snow), College Station, TX; Ocean Engr Proj, College Station, TX
 UNIVERSITY OF ALABAMA Dir Fac Mgmt (Baker), Birmingham, AL
 UNIVERSITY OF ALASKA Biomed & Marine Sci Lib, Fairbanks, AK
 UNIVERSITY OF CALIFORNIA CE Dept (Fourney), Los Angeles, CA; CE Dept (Gerwick), Berkeley, CA; CE Dept (Taylor), Davis, CA
 UNIVERSITY OF DELAWARE Engrg Col (Dexter), Lewes, DE
 UNIVERSITY OF HARTFORD CE Dept (Keshawarz), West Hartford, CT
 UNIVERSITY OF HAWAII Manoa, Library, Honolulu, HI; Ocean Engrg Dept (Ertekin), Honolulu, HI
 UNIVERSITY OF ILLINOIS Library, Urbana, IL; Metz Ref Rm, Urbana, IL
 UNIVERSITY OF MICHIGAN CE Dept (Richart), Ann Arbor, MI
 UNIVERSITY OF NEW MEXICO NMERI (Falk), Albuquerque, NM; NMERI (Leigh), Albuquerque, NM
 UNIVERSITY OF RHODE ISLAND CE Dept (KW Lee), Kingston, RI
 UNIVERSITY OF TEXAS CE Dept (Thompson), Austin, TX; Construction Industry Inst, Austin, TX; ECJ 4.8 (Breen), Austin, TX; ECJ 5.402 (Tucker), Austin, TX
 UNIVERSITY OF WASHINGTON Applied Phy Lab Lib, Seattle, WA; CE Dept (Mattock), Seattle, WA
 UNIVERSITY OF WISCONSIN Great Lakes Studies Cen, Milwaukee, WI
 VENTURA COUNTY Deputy PW Dir, Ventura, CA
 WASHINGTON DHHS, OFE/PHS (Ishihara), Seattle, WA
 ADVANCED TECHNOLOGY, INC Ops Cen Mgr (Bednar), Camarillo, CA
 AMERICAN CONCRETE INSTITUTE Library, Detroit, MI
 ARVID GRANT & ASSOC Olympia, WA
 ATLANTIC RICHFIELD CO RE Smith, Dallas, TX
 BABCOCK & WILCOX CO Tech Lib, Barberton, OH
 BATTELLE D Frink, Columbus, OH; New Eng Marine Rsch Lab, Lib, Duxbury, MA
 BECHTEL CIVIL, INC Woolston, San Francisco, CA
 BLAYLOCK WILLIS & ASSOC T Spencer, San Diego, CA
 BROWN & ROOT Ward, Houston, TX
 CORRIGAN, LCDR S. USN, CEC, Stanford, CA
 CHILDS ENGRG CORP K.M. Childs, Jr, Medfield, MA
 COASTAL SCI & ENGRG C Jones, Columbia, SC
 COLLINS ENGRG, INC M Garlich, Chicago, IL
 COLUMBIA GULF TRANSMISSION CO Engrg Lib, Houston, TX
 CONSOER TOWNSEND & ASSOC Schramm, Chicago, IL
 CONSTRUCTION TECH LABS, INC G. Corley, Skokie, IL
 CONTINENTAL OIL CO O. Maxson, Ponca City, OK
 DILLINGHAM CONSTR CORP (HD&C), F McHale, Honolulu, HI
 EARL & WRIGHT CONSULTING ENGRGS Jensen, San Francisco, CA
 EASTPORT INTL, INC JH OSborn, Mgr, Ventura, CA
 GDM & ASSOC, INC Fairbanks, AK
 GEOTECHNICAL ENGRS, INC Murdock, Winchester, MA
 GLIDDEN CO Rsch Lib, Strongsville, OH
 HALEY & ALDRICH, INC. T.C. Dunn, Cambridge, MA
 HAYNES & ASSOC H. Haynes, PE, Oakland, CA
 HIRSCH & CO L Hirsch, San Diego, CA
 INTL MARITIME, INC D Walsh, San Pedro, CA
 LEO A DALY CO Honolulu, HI
 LIN OFFSHORE ENGRG P. Chow, San Francisco CA
 LINDA HALL LIBRARY Doc Dept, Kansas City, MO
 MARATHON OIL CO Gamble, Houston, TX
 MARINE CONCRETE STRUCTURES, INC W.A. Ingraham, Metairie, LA
 MARITECH ENGRG Donoghue, Austin, TX
 MC CLELLAND ENGRS, INC Library, Houston, TX
 MOBIL R&D CORP Offshore Engrg Lib, Dallas, TX
 MOFFATT & NICHOL ENGRS R Palmer, Long Beach, CA
 MT DAVISSON CE, Savoy, IL
 EDWARD K NODA & ASSOC Honolulu, HI
 NATL ACADEMY OF ENGRG Alexandria, VA
 NEW ZEALAND NZ Concrete Rsch Assoc, Library, Porirua
 NUHN & ASSOC A.C. Nuhn, Wayzata, NM
 PACIFIC MARINE TECH (M. Wagner) Duvall, WA

PILE BUCK, INC Smoot, Jupiter, FL
PORTLAND CEMENT ASSOC AE Fiorato, Skokie, IL
SEATECH CORP Peroni, Miami, FL
SIMPSON, GUMPERTZ & HEGER, INC E Hill, CE, Arlington, MA
THE KLING-LINDQUIST, INC Radwan, Philadelphia, PA
TREMCO, INC M Raymond, Cleveland, OH
TRW INC Rodgers, Redondo Beach, CA
TUDOR ENGRG CO Ellegood, Phoenix, AZ
VSE Ocean Engrg Gp (Murton), Alexandria, VA
WISS, JANNEY, ELSTNER, & ASSOC DW Pfeifer, Northbrook, IL
WOODWARD-CLYDE CONSULTANTS R. Cross, Oakland, CA; West Reg. Lib, Oakland, CA
CHAO, JC Houston, TX
FOWLER, J.W. Virginia Beach, VA
KLIEGER, PAUL CE, Northbrook, IL
PETERSEN, CAPT N.W. Pleasanton, CA
STEVENS, TW Dayton, OH
TAMPA PORT AUTHORITY Engrg Dept (Schrader), Tampa, FL

NCEL DOCUMENT EVALUATION

You are number one with us; how do we rate with you?

We at NCEL want to provide you our customer the best possible reports but we need your help. Therefore, I ask you to please take the time from your busy schedule to fill out this questionnaire. Your response will assist us in providing the best reports possible for our users. I wish to thank you in advance for your assistance. I assure you that the information you provide will help us to be more responsive to your future needs.



R. N. STORER, Ph.D, P.E.
Technical Director

DOCUMENT NO. _____ TITLE OF DOCUMENT: _____

Date: _____ Respondent Organization : _____

Name: _____ Activity Code: _____
Phone: _____ Grade/Rank: _____

Category (please check):

Sponsor _____ User _____ Proponent _____ Other (Specify) _____

Please answer on your behalf only; not on your organization's. Please check (use an X) only the block that most closely describes your attitude or feeling toward that statement:

SA Strongly Agree A Agree O Neutral D Disagree SD Strongly Disagree

	SA	A	N	D	SD		SA	A	N	D	SD
1. The technical quality of the report is comparable to most of my other sources of technical information.	()	()	()	()	()	6. The conclusions and recommendations are clear and directly supported by the contents of the report.	()	()	()	()	()
2. The report will make significant improvements in the cost and or performance of my operation.	()	()	()	()	()	7. The graphics, tables, and photographs are well done.	()	()	()	()	()
3. The report acknowledges related work accomplished by others.	()	()	()	()	()	<div>Do you wish to continue getting NCEL reports? <input type="checkbox"/> YES <input type="checkbox"/> NO</div> <p>Please add any comments (e.g., in what ways can we improve the quality of our reports?) on the back of this form.</p>					
4. The report is well formatted.	()	()	()	()	()						
5. The report is clearly written.	()	()	()	()	()						

Comments:

Please fold on line and staple

DEPARTMENT OF THE NAVY

**Naval Civil Engineering Laboratory
Port Hueneme, CA 93043-5003**

**Official Business
Penalty for Private Use \$300**



Code L03B
NAVAL CIVIL ENGINEERING LABORATORY
PORT HUENEME, CA 93043-5003

INSTRUCTIONS

The Naval Civil Engineering Laboratory has revised its primary distribution lists. The bottom of the label on the reverse side has several numbers listed. These numbers correspond to numbers assigned to the list of Subject Categories. Numbers on the label corresponding to those on the list indicate the subject category and type of documents you are presently receiving. If you are satisfied, throw this card away (or file it for later reference).

If you want to change what you are presently receiving:

- Delete – mark off number on bottom of label.
- Add – circle number on list.
- Remove my name from all your lists – check box on list.
- Change my address – line out incorrect line and write in correction (**DO NOT REMOVE LABEL**).
- Number of copies should be entered after the title of the subject categories you select.

Fold on line below and drop in the mail.

Note: Numbers on label but not listed on questionnaire are for NCEL use only. please ignore them.

Fold on line and staple.

DEPARTMENT OF THE NAVY

Naval Civil Engineering Laboratory
Port Hueneme, CA 93043-5003

Official Business
Penalty for Private Use, \$300

BUSINESS REPLY CARD

FIRST CLASS PERMIT NO. 12503 WASH. D.C.
POSTAGE WILL BE PAID BY ADDRESSEE

NO POSTAGE
NECESSARY
IF MAILED
IN THE
UNITED STATES

Commanding Officer
Code L34
Naval Civil Engineering Laboratory
Port Hueneme, California 93043-5003

DISTRIBUTION QUESTIONNAIRE

The Naval Civil Engineering Laboratory is revising its Primary distribution lists.

SUBJECT CATEGORIES

- 1 SHORE FACILITIES
- 2 Construction methods and materials (including corrosion control, coatings)
- 3 Waterfront structures (maintenance/deterioration control)
- 4 Utilities (including power conditioning)
- 5 Explosives safety
- 6 Aviation Engineering Test Facilities
- 7 Fire prevention and control
- 8 Antenna technology
- 9 Structural analysis and design (including numerical and computer techniques)
- 10 Protective construction (including hardened shelters, shock and vibration studies)
- 11 Soil/rock mechanics
- 14 Airfields and pavements
- 15 ADVANCED BASE AND AMPHIBIOUS FACILITIES
- 16 Base facilities (including shelters, power generation, water supplies)
- 17 Expedient roads/airfields/bridges
- 18 Amphibious operations (including breakwaters, wave forces)
- 19 Over-the-Beach operations (including containerization, material transfer, lighterage and cranes)
- 20 POL storage, transfer and distribution

TYPES OF DOCUMENTS

- 85 Techdata Sheets 86 Technical Reports and Technical Notes
83 Table of Contents & Index to TDS

28 ENERGY/POWER GENERATION

- 29 Thermal conservation (thermal engineering of buildings, HVAC systems, energy loss measurement, power generation)
30 Controls and electrical conservation (electrical systems, energy monitoring and control systems)
31 Fuel flexibility (liquid fuels, coal utilization, energy from solid waste)
32 Alternate energy source (geothermal power, photovoltaic power systems, solar systems, wind systems, energy storage systems)
33 Site data and systems integration (energy resource data, energy consumption data, integrating energy systems)
34 ENVIRONMENTAL PROTECTION
35 Hazardous waste minimization
36 Restoration of installations (hazardous waste)
37 Waste water management and sanitary engineering
38 Oil pollution removal and recovery
39 Air pollution

44 OCEAN ENGINEERING

- 45 Seafloor soils and foundations
46 Seafloor construction systems and operations (including diver and manipulator tools)
47 Undersea structures and materials
48 Anchors and moorings
49 Undersea power systems, electromechanical cables, and connectors
50 Pressure vessel facilities
51 Physical environment (including site surveying)
52 Ocean-based concrete structures
54 Undersea cable dynamics

- 82 NCEL Guides & Abstracts
91 Physical Security

☐ None-
remove my name